V

Focused Fundamental Research

V. Focused Fundamental Research

V.A Introduction

The focused fundamental research program is supported by the VTO to research and analyze new materials for high-performance, next generation, rechargeable batteries for use in HEVs, PHEVs, and EVs. The efforts in FY 2014 continued the increased emphasis on high-energy materials for PHEV and EV batteries and expanded efforts into technologies for enabling the use of Li metal anodes. (Note: at the beginning of the FY 2015, the focused fundamental research program, previously also called the Batteries for Advanced Transportation Technologies (BATT) Program, has been reorganized. It is now transitioning to a new program called the Batteries Materials Research (BMR) program. This report follows the structure of the program as it existed during FY 2014, i.e., the structure as outlined in the BATT program. Next year's progress report will describe the new BMR program in greater detail and follow its revised structure.)

Background and Program Context

The focused fundamental research program (until FY 2014, alternately referred to as the BATT Program, as explained above) addresses the fundamental problems of chemical and mechanical instabilities that have slowed the development of automotive batteries with acceptable cost, performance, life, and safety. The aim is to develop and test new materials and to use traditional and novel diagnostics and modeling methods to better understand cell and material performance and lifetime limitations before initiating battery scale-up and development. Emphasis is placed on the synthesis of components into cells with determination of failure modes, while continuing with materials synthesis and evaluation, advanced diagnostics, and improved model development. Battery chemistries are monitored continuously with timely substitution of more promising components. This is done with advice from within the program and from outside experts, including consultation with automotive companies and DOE. Also factored into the program direction is the monitoring of world-wide battery R&D activities. The Program not only supports research that leads to improvements to existing materials, but also into high-risk "leap-frog" technologies that might have a tremendous impact in the marketplace. An overview of the approach used in the BATT program is shown in Figure V - 1.

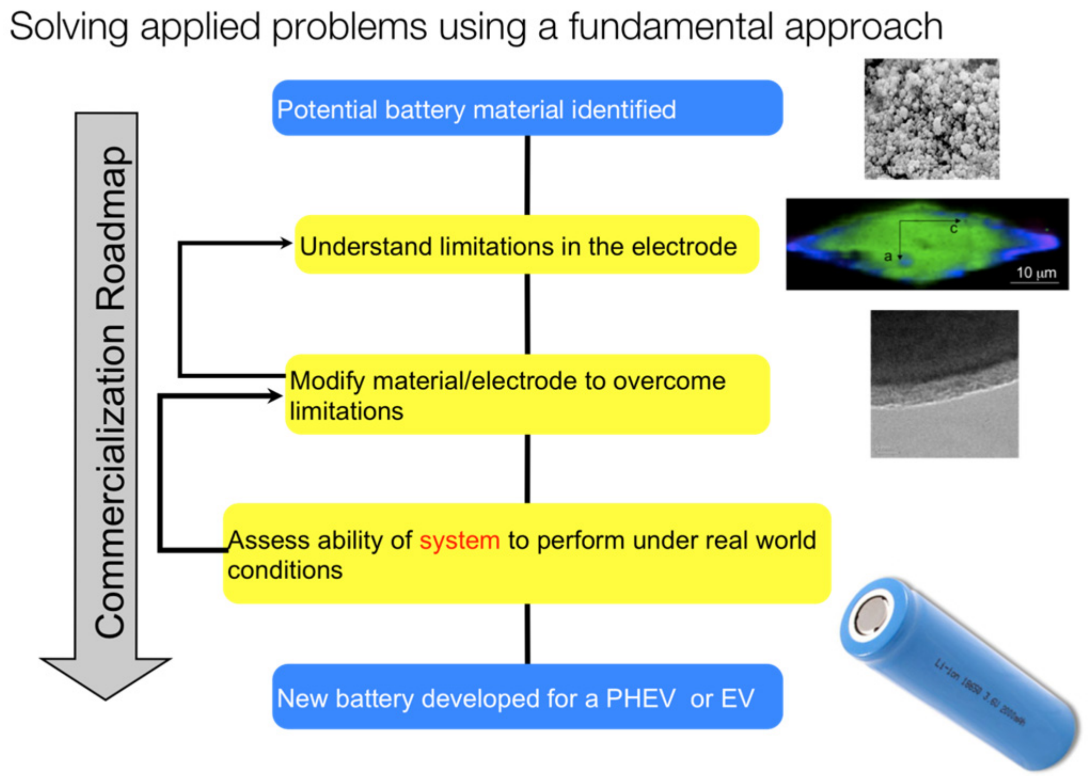

Figure V - 1: BATT approach overview

Under the BATT structure, which existed until FY 2014, the work was administered by the Lawrence Berkeley National Laboratory (LBNL), with principal researchers from LBNL, five additional national laboratories, fourteen universities, and two commercial companies participating. The program was organized into the following areas:

- Cathode Development.
- Anode Development.
- Electrolytes Development.
- Cell Analysis, Modeling, and Fabrication.
- Diagnostics.
- Beyond Lithium-ion Technologies.

Brief descriptions of each research area are as follows.

Cathode Development aims to find novel cathode materials and processing methods that offer significant improvements in volumetric and specific energy and/or power over current state of the art materials, like $LiCoO_2$. Current projects include work on the high voltage, high-energy layered/layered or Li rich cathode materials, investigating Li bearing mixed polyanion glasses, investigating polyanions that may cycle more than one Li ion per transition metal ion (e.g., silicates), optimization of ion transport in high-energy composite cathodes, and developing *in situ* reactors designed to investigate solvothermal synthesis reactions in real-time using synchrotron-based tools.

Anode Development involves a significant focus on silicon, which offers ten times the capacity of currently-used graphite anodes. Researchers are investigating several forms of Si, including nanowires, nanoparticles, clathrate structures, and others. They are also investigating methods for stabilizing Si and Sn composite negative electrodes, including the use of Cu foam current collectors, atomic layer deposition to stabilize alloy electrodes, and a number of Si/carbon nanocomposite materials. It also involves research on metal-based high capacity Li-ion anodes, layered nanolaminates for use in lithium battery anodes, nanoscale composite hetero-structures and thermoplastic resin binders.

Electrolyte Development includes research efforts focused on expanding the temperature range of cells, additives to stabilize the negative and positive interfaces, development of new overcharge shuttles to further stabilize Li-ion cells, new ionic liquids to enable higher voltage windows, sulfone liquids and sulfate/triflate solids for high voltage electrolytes, bifunctional electrolytes for lithium-ion batteries, interfacial and bulk properties and stability studies and first principles modeling to understand and construct a more stable SEI.

Cell Analysis, Modeling, and Fabrication involve several modeling approaches used to understand cell and fundamental material properties, including *ab-initio* calculations, macroscopic cell calculations, and finite element simulations. Standard cell making and testing techniques are developed and applied to provide a common evaluation process for new materials. Projects might involve predicting microstructure and performance for optimal cell fabrication, assembly of battery materials and electrodes, predicting and understanding novel electrode materials from first-principles, electrode fabrication and materials benchmarking, and the design and scalable assembly of high density low tortuosity electrodes.

Diagnostics involve the use of advanced diagnostics techniques, such as FTIR, X-ray absorption fine structure (XAFS), X-ray diffraction (XRD), nuclear magnetic resonance (NMR) and other techniques to investigate interfacial and other properties in Li-ion batteries. Sample projects include those using DOE's user facilities, advanced *in situ* diagnostic techniques, study of interfacial processes, *in situ* electron microscopy of electrical energy storage materials, microscopy investigation on the fading mechanism of electrode materials, and NMR and pulse field gradient studies of SEI and electrode structure.

Beyond Lithium-ion Technologies involve study of issues critical to the realization of beyond Lithium-ion technologies. Two of the most promising (Lithium/Sulfur and Lithium/Air) require the use of a lithium metal anode. The main focus is to devise new methods to understand and stabilize lithium metal anodes (against mossy Li formation and dendrites) to bring about leaps in energy density without compromising durability and safety. LBNL, ANL and ORNL have partnered to design a series of projects that utilize recent advances in ceramic electrolyte materials, polymer science, and materials characterization to stabilize lithium metal anodes. Inorganic solid state lithium-ion conductors have been proposed as protective electrolyte layers in a lithium metal cell that contains a second, liquid electrolyte in contact with the cathode. The team is also studying various Li metal protective films and dopants that lead to a stable Li/electrolyte interface and permit long-term and stable cycling. Some projects focus on lithium selenium and selenium sulfur couple and composite electrolytes to stabilize metallic lithium anodes.

In subsequent sections, this annual progress report, following the FY 2014 structure, describes individual projects in each of the above areas. The program includes an impressive team of principal investigators, many of them with international stature, who push the battery field forward in each of these areas. The focus areas include advanced architectures that increase the energy and decrease the cost of batteries via "engineering" approaches and new materials that focus on advancing the state of the art in the short term (e.g., silcon anodes, high voltage electrolytes) and leapfrog chemistries for the long term (e.g., lithium metal anode, sulfur and oxygen cathodes). This balanced materials effort is made more robust by coupling them with modeling at different length scale, microscopy and spectroscopy with in situ focus, and advanced electrochemical characterization. This is illustrated in Figure V - 2.

The whole effort is undertaken in a coordinated fashion with focus groups formed to solve big challenges. Two such focus groups that bear mention include one charged with solving the mechanical damage and surface instability of silicon anodes, and another with understanding and alleviating the problems at high voltages. Both teams bring together researchers with focus on material synthesis, advanced diagnostics and modeling to understand the issues and propose solutions.

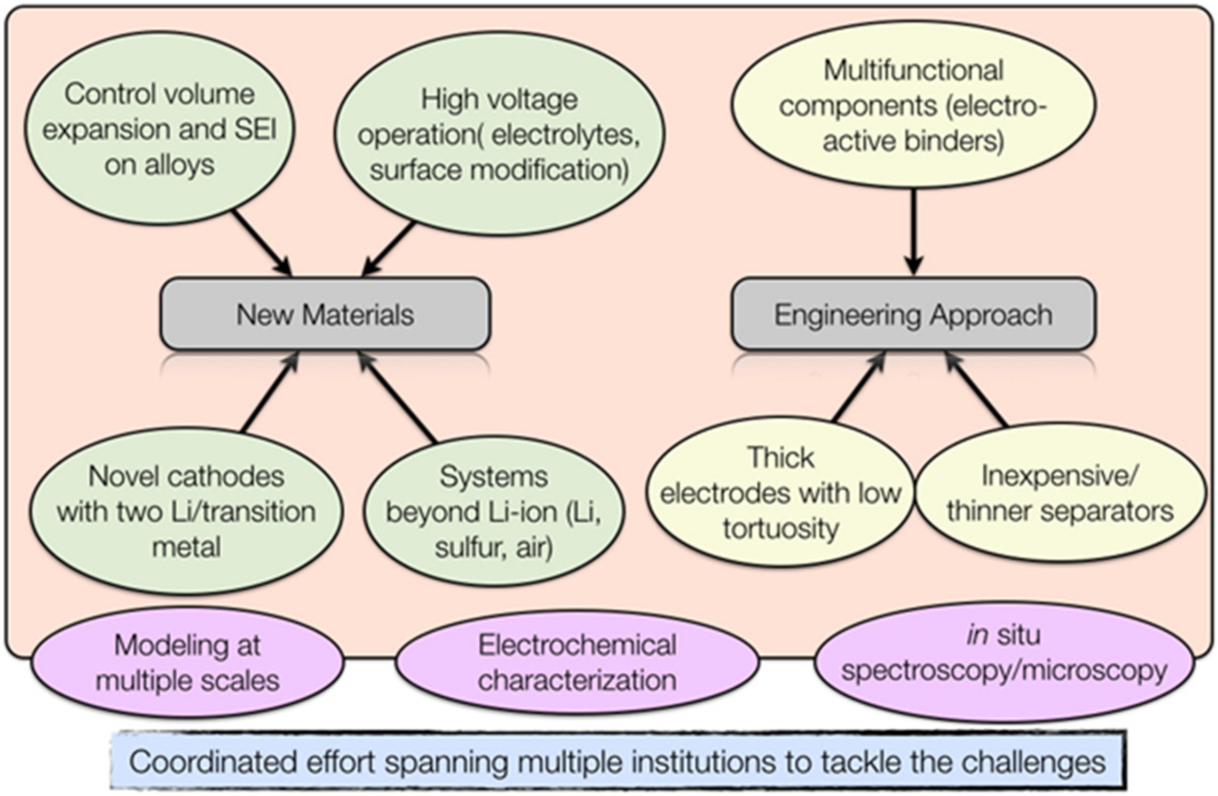

Figure V - 2: BATT focus areas

V.B Cathode Development

V.B.1 High Capacity Composite Cathode Materials (ANL)

Michael Thackeray
Argonne National Laboratory

Electrochemical Energy Storage
9700 South Cass Avenue
Argonne, IL 60439
Phone: (630) 252-9184; Fax: (630) 252-4176
E-mail: thackeray@anl.gov

Jason R. Croy
Electrochemical Energy Storage
9700 South Cass Avenue
Argonne, IL 60439
Phone: (630) 252-9184; Fax: (630) 252-4176
E-mail: croy@anl.gov

Start Date: October 2011
Projected End Date: September 2015

Objectives

- Design high capacity, high-power and low cost cathodes for PHEVs and EVs.
- Improve the design, composition and performance of Mn-based cathodes.
- Explore novel processing routes to prepare advanced electrodes with effective architectural designs.
- Use atomic-scale modeling as a guide to identify, design and understand the structural features and electrochemical properties of advanced cathode materials.

Technical Barriers

- Low energy density.
- Poor low temperature operation.
- Abuse tolerance limitations.

Technical Targets (USABC – End of life)

- 142 Wh/kg, 317 W/kg (PHEV 40 mile).
- Cycle life: 5,000 cycles.
- Calendar life: 15 years.

Accomplishments

- Evaluated high-capacity cation-substituted electrodes.
- Explored synthesis routes for controlled integration of a spinel component into ‘layered-layered’ cathodes.
- Developed a metal fluoride-based ALD process for coating electrode surfaces.
- Identified promising Mn-rich compositions with low Co content for high-energy Li-ion cells.

* * *

Introduction

Li- and Mn-rich $x\text{Li}_2\text{MnO}_3\bullet(1-x)\text{LiMO}_2$ (M=Mn, Ni, Co) electrodes are currently the most promising class of cathodes for next-generation, high energy Li-ion batteries. However, the structural instability of these electrodes at high potentials, involving both surface and bulk phenomena, has prevented their large-scale use in commercial systems. To advance the technology, more robust electrode structures and surfaces must be designed and fabricated.

Approach

- Exploit the concept, and optimize the performance, of structurally-integrated, high-capacity electrodes, particularly “layered-layered” $x\text{Li}_2\text{MnO}_3\bullet(1-x)\text{LiMO}_2$ (M=Mn, Ni, Co) and “layered-layered-spinel” $y\{x\text{Li}_2\text{MnO}_3\bullet(1-x)\text{LiMO}_2\}\bullet(1-y)\text{LiM}_2\text{O}_4$ electrodes.
- Explore new processing routes to prepare composite electrodes that provide acceptable capacity, power and life.
- Design effective surface structures to protect the underlying metal oxide particles from the electrolyte and to improve their rate capability when charged at high potentials.

Results

Effect of cation substitution on voltage fade: $x\text{Li}_2\text{MnO}_3\bullet(1-x)\text{LiMO}_2$ cathodes with $x \geq 0.5$ yield capacities >250 mAh/g but suffer from structural instability when continually cycled to 4.6 V. Cathodes with x≤0.33, however, show more promising electrochemical behavior. A layered-layered composition, $0.33Li_2MnO_3 \bullet 0.67LiMn_{0.375}Ni_{0.375}Co_{0.25}O_2$, was therefore selected as a baseline electrode and doped with either 2 mol% Mg^{2+} or Al^{3+}. Because Mg^{2+} and Al^{3+} are electrochemically inactive ions and can occupy and diffuse through tetrahedral and octahedral sites, it is anticipated that a small amount of these mobile ions could enhanced the stability of the electrodes during cycling. Figure V - 3(a) and (b) show the electrochemical data of baseline and Mg^{2+}/Al^{3+}-doped electrodes, after an initial activation to 4.6 V, when cycled between 4.45 – 2.0 V at 15 mA/g to minimize voltage fade. The cells delivered more than 200 mAh/g, converging to ~210 mAh/g. Figure V - 3(b) shows the dQ/dV plots of the 15th cycle for each cell; the undoped electrode shows a larger redox activity in the lower voltage region (<3.3 V) relative to the Mg^{2+}- and Al^{3+}-doped electrodes.

The hysteresis, manifest by the redox processes at ~4.3 V on charge and ~3.3 V on discharge, appeared less for the doped electrodes. The rate performance of the cells, shown in Figure V - 3 (c), demonstrates that all electrodes delivered ≥200 mAh/g at 150 mA/g (~C/1.3). The figure shows that discharge capacities of 240-250 mAh/g could be obtained but that high discharge rates resulted in significant polarization of the doped electrodes. This finding suggests that Li^+ diffusion may be hindered by tetrahedral site occupancy of Mg^{2+}/Al^{3+} ions; the polarization is highest for Mg^{2+}-doped electrodes. Similar data were obtained for Ru-doped samples (but are not shown here).

Synthesis routes to "layered-layered-spinel" structures: A strategy to mitigate the structural transformations in composite, 'layered-layered' (LL) electrodes that cause voltage fade was adopted by incorporating a stabilizing spinel component within LL structures. A spinel component, with the ideal 3:1 ratio of transition metal ions in the metal-rich and lithium-rich layers of the spinel structure, respectively, offers the possibility of using the transition metals (TMs) in the lithium layer to provide greater binding energy and stability to the oxygen planes at low lithium loadings, and to suppress further migration of the transition metal ions from the TM-rich layer into the lithium layer. However, controlling both elemental composition and structural configurations in such integrated materials is difficult when traditional synthesis routes are used. Previous work has demonstrated that layered Li_2MnO_3 can be successfully used as a template for producing composite LL structures. Studies were therefore conducted to evaluate this approach for synthesizing LLS electrodes. Figure V - 4(a) shows the first-cycle discharge (i.e., prior to charging) of a series of lithium cells with $x[Li_{1.2}Mn_{0.6}Ni_{0.2}O_2] \bullet (1-x)LiMn_{1.5}Ni_{0.5}O_4$ cathodes. The capacity of the electrode at ~2.75 V increases as a function of (1-x), i.e., the spinel content; it follows the expected trend for uptake of lithium in vacant octahedral sites of the spinel component. Figure V - 4(b) shows the evolution of the XRD patterns with x. The appearance of spinel peaks and minor NiO-like impurities are evident for x=0.5 and 0.75 (dashed lines). Figure V - 4(c) shows a high resolution TEM image of a LLS electrode with targeted composition: $0.85[0.25Li_2MnO_3 \bullet 0.75LiMn_{0.375}Ni_{0.375}Co_{0.25}O_2] \bullet 0.15LiMn_{1.5}Ni_{0.5}O_4$ in which the layered (A and C) and spinel (B) regions are clearly visible. An EDX analysis of the spinel region (B) revealed a Mn and Ni rich composition, whereas the cobalt was found to reside largely within the layered regions (A and C) of the composite structure.

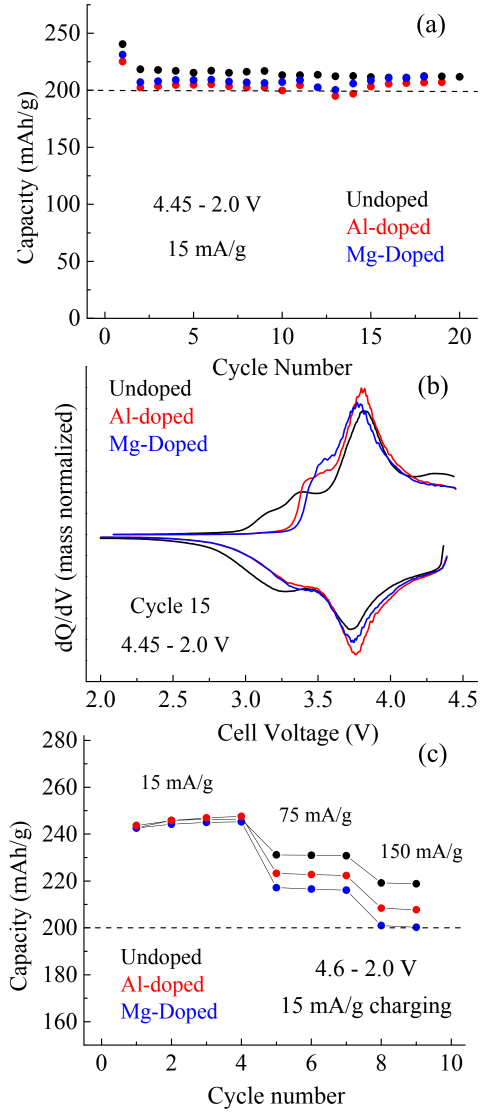

Figure V - 3: (a) Capacity, (b) dQ/dV, and (c) rate data for $0.33Li_2MnO_3 \bullet 0.67LiMn_{0.375}Ni_{0.375}Co_{0.25}O_2$ baseline and Mg^{2+}- and Al^{+}-doped (2 mol%) electrodes in Li half-cells at RT

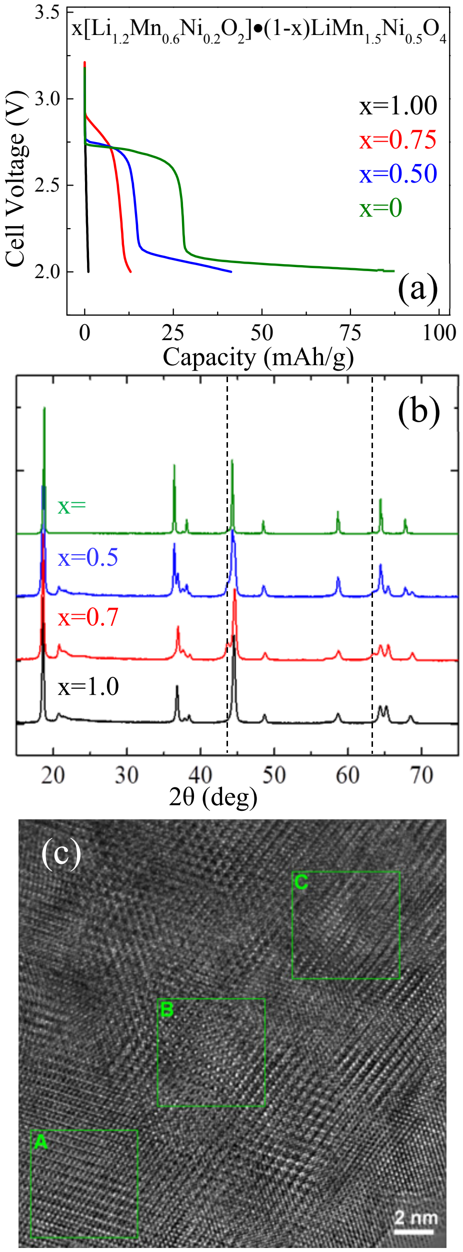

Figure V - 4: (a) Initial discharge capacities for $x[Li_{1.2}Mn_{0.6}Ni_{0.2}O_2]•(1-x)LiMn_{1.5}Ni_{0.5}O_4$ electrodes and the corresponding XRD patterns, (b). Dashed lines in (b) mark NiO-like impurities (c) High resolution TEM image of $0.85[0.25Li_2MnO_3•0.75LiMn_{0.375}Ni_{0.375}Co_{0.25}O_2]•0.15LiMn_{1.5}Ni_{0.5}O_4$ particle showing integrated, layered (regions A and C) and spinel (region B) components

Optimization of low Li_2MnO_3-content composite electrode structures: The performance of both the LL and LLS electrodes is dependent on factors such as the ratios of TM's (Mn:Ni:Co), Li_2MnO_3 content, and synthesis conditions. The contribution of cobalt is particularly sensitive as it can serve to enhance electrode performance (e.g., conductivity and layering); however, the amount of cobalt used should ideally be kept as low as possible because of practical considerations, such as cost and safety. In order to fully exploit the concept of LLS electrodes, systematic studies were undertaken to determine the key properties of the individual components (LL and spinel) and to identify the best synthesis procedures to optimize the integration of the layered and spinel components. Figure V - 5(a) shows the first-cycle capacities of a series of LL $0.05Li_2MnO_3•0.95LiMn_{0.5-y}Ni_{0.5+y/2}Co_{y/2}O_2$ electrodes (Li half-cells) in which $0≤y≤0.3$. The Co content is a critical parameter relative to the Mn and Ni concentrations; an optimum value is found at y~0.1. It appears that the overall cobalt content can be kept low (~5%) for selected Mn:Ni ratios, which is in line with the strategy to design a highly layered electrode that is rich in Mn and low in Co. Figure V - 5(b) reveals that, for y=0.1, the electrode can provide a cell energy density of approximately 750 Wh/kg of oxide with a 6% energy loss over 50 cycles. These compositions are being explored as precursor templates for synthesizing stabilized LLS structures. Because of the layered and composite nature of these materials, it is envisioned that selected cations can be inserted into the lithium layers with some degree of control, as has already been demonstrated in fabricating LL structures from a Li_2MnO_3 precursor. The ability to control the occupation of Li-layer sites by transition metal cations is consistent with the strategy of embedding spinel domains into structurally compatible LL electrode materials. This approach provides new possibilities for tuning not only the stability of high-capacity LL cathodes but also the voltage profiles of the cells.

Synthesis of novel fluoride-based coatings: Surface stability of all Li-ion cathodes (layered, LL, and LLS) is extremely important. For example, atomic layer deposition (ALD) of various oxide electrodes has been shown to enhance rate, capacity retention, and thermal stability. In particular, Al_2O_3 is known to improve the electrode properties further as a supposed HF scavenger. Consequently, AlF_3 has been used as an alternative to Al_2O_3 to bypass the corrosion and etching of Al_2O_3 coatings. In contrast to wet chemical methods that do not always lead to complete and uniform surface coatings, ALD can produce uniform and controllable surface films even though the deposition of fluorides by ALD can be complex. In this regard, a unique ALD coating process to deposit AlW_xF_y thin films on electrode laminates has been developed at Argonne.

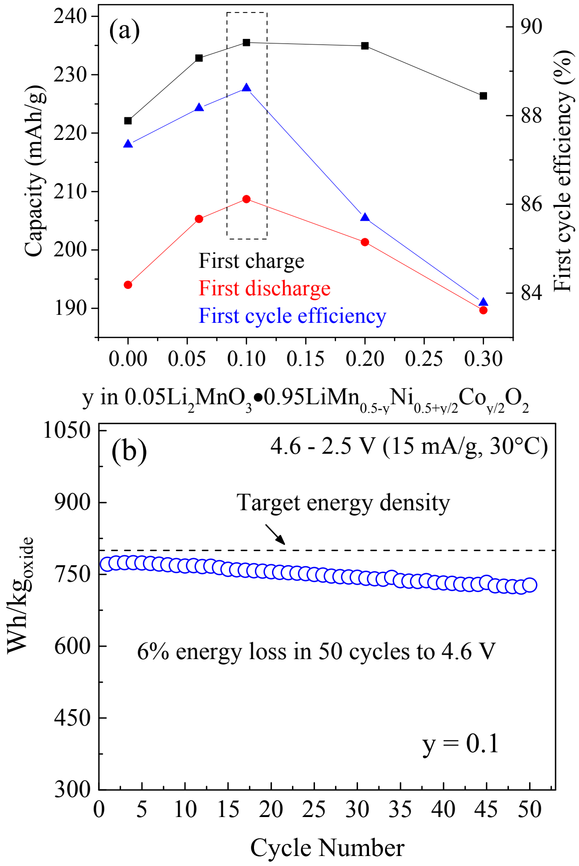

Figure V - 5: (a) First cycle capacities and efficiencies of $0.05Li_2MnO_3•0.95LiMn_{0.5-y}Ni_{0.5+y/2}Co_{y/2}O_2$ with y values from 0-0.3. (b) Specific energy density of the y=0.1 composition for 50 cycles between 4.6-2.0 V (half-cell at 30°C, 15 mA/g)

Figure V - 6(a) shows a standard $LiCoO_2$ electrode cycled between 4.4 – 2.5 V at 20 mA/g in a Li half-cell at room temperature (RT). Because $LiCoO_2$ shows predictably poor performance with respect to rate and capacity retention when cycled above ~4.3 V, it was selected as a baseline material for initial studies. As expected, the voltage profiles of cells with the bare $LiCoO_2$ show significant capacity loss and profile changes within 25 cycles. Figure V - 6(b) shows the performance of the same $LiCoO_2$ after the laminate had been protected by ALD with the newly developed AlW_xF_y thin film. Remarkable stability, with capacities >160 mAh/g, is observed for 50 cycles. In addition, the well-known phase transition, which occurs in $Li_{1-x}CoO_2$ electrodes after ~135 mAh/g (x≈0.5), is reversible throughout the 50 cycles. This finding reveals that the coating has indeed modified the surface properties and not the bulk of the $LiCoO_2$ electrode particles. Figure V - 6(c), which compares the performance of untreated and coated electrodes, reiterates this result. The coated electrodes demonstrate exceptional performance, showing >90% retention of the C/8 discharge capacity at 2.5 C and a full capacity recovery on returning to C/8 cycling, thereby highlighting the promise of these newly developed, surface-stabilizing materials.

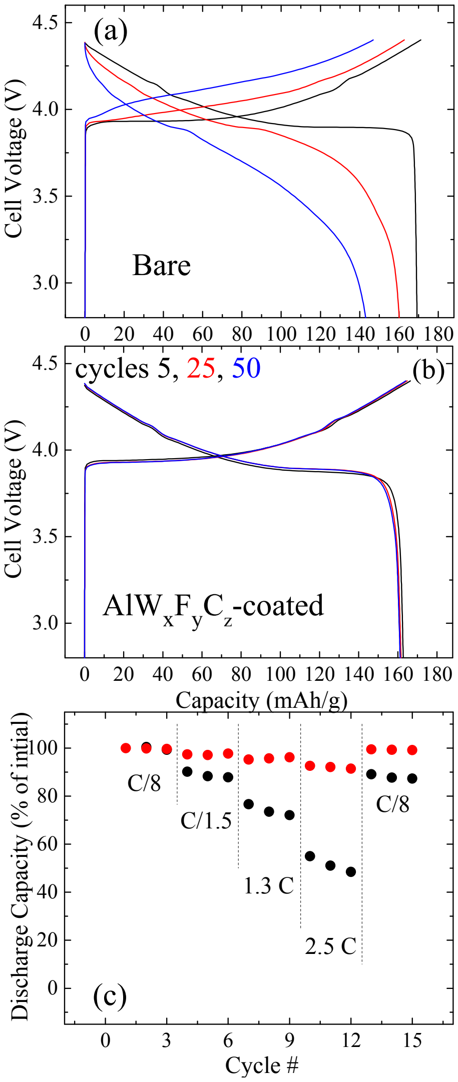

Figure V - 6: Charge and discharge profiles of cycles 5, 25, and 50 (4.4 – 2.5 V, 20 mA/g, half-cells at RT) for (a) bare and (b) ALD AlW_xF_y-coated $LiCoO_2$. (c) Comparison of rate capability for bare (black) and AlW_xF_y-coated (red) $LiCoO_2$

Conclusions and Future Directions

The synthesis and stabilization of composite, “layered-layered” (LL) and “layered-layered-spinel” (LLS) electrode structures has been explored. Cation-substitutions were found to impact the voltage profiles while the voltage fade phenomenon was mitigated by narrowing the operating voltage window. Synthesis of LLS electrodes using a Li_2MnO_3 precursor showed promise as an efficient route to the fabrication of complex composite electrode structures containing a spinel component. A large compositional space, both structural and elemental, was explored; high-energy, stable, LL electrode materials were identified, but at the expense of some capacity. Finally, metal fluoride-based coatings were fabricated by ALD using selected precursors and processing approaches. In particular, ALD coatings applied directly on electrode laminates, rather than on powders, resulted in stable, long-term cycling behavior. Future studies will focus on the synthesis and study of the singular components of these complex systems (layered-layered, spinel, and surfaces), how to best integrate them, and the optimization thereof to create high-energy, stable electrode architectures and surfaces. Theoretical modeling of LLS composite electrodes and protective surface structures will be initiated to complement the experimental efforts in FY2015.

FY 2014 Publications/Presentations

1. Jason R. Croy, J.R., Thackery, M.M. et al., (June 2014). “Design and Evaluation of High Capacity Cathodes.” Presented at the 2014 DOE Annual Merit Review and Peer Evaluation Meeting, Washington D.C.
2. Croy, J.R, K.G. Gallagher, K.G, Long, B.R., Balasubramanian, M., and Thackeray, M.M (2014). “Quantifying Hysteresis and Voltage Fade in xLi_2MnO_3●$(1-x)LiMn_{0.5}Ni_{0.5}O_2$ Electrodes as a Function of Li_2MnO_3 Content.” *J. Electrochem. Soc*. (161: A318).
3. Long, B.R., Croy, J.R., Dogan, F., Suchomel, M. R., Key, B., Wen, J. G., Miller, D. J., Thackeray, M.M., and M. Balasubramanian, M. (2014). “Effect of Cooling Rates on Phase Separation in $0.5Li_2MnO_3$•$0.5LiCoO_2$ Electrode Materials for Li-Ion Batteries.” *Chem. Mater.* (26); p. 3565.
4. Croy, J.R., Gallagher, K.G. Balasubramanian, M., Long, B.R., and Thackery, M.M. (October 2013). “Transformation Mechanisms in Composite xLi_2MnO_3•$(1-x)LiMO_2$ Electrode Structures.” Presented at the 224th Meeting of the Electrochemical Society, San Francisco, CA.
5. Croy, J.R., Gallagher, K.G., Balasubramanian, M., Long, B.R., Dogan, F., Suchomel, M., Key, B., Miller, D., and Thackery, M.M. (February 2014). “Transformation Mechanisms in Layered-Layered Composite Cathodes: The Role of Local Structure.” Presented at the AABC, Atlanta, GA.
6. Thackeray, M.M., Croy, J. R., Long, B. R., Park, J. S., Gallagher, K. G., Balasubramanian, M., Johnson, C. S., Trahey, L., Chan, M. K. Y., Lau, K.-C., Curtiss, L. A., Kirklin, S., Wolverton, C. (March 2014). “Recent Advances in Transition Metal Oxide Electrode Materials for Lithium Batteries.” Presented at the IBA, Brisbane, Australia.
7. Long, B.R., Croy, J.R., Gallagher, K.G., Balasubramanian, M., Dogan, F., Key, B., Miller, D.J., Suchomel, M.R., and Thackeray, M.M. (March 2014). “Recent Advances in Lithium and Manganese Rich Composite Cathodes.” Presented at the Gordon Conference -Batteries, Ventura, CA.
8. Thackeray, M.M., Croy, J. R., and Long, B. R. (June 2014). “Addressing the Limitations of Layered $LiMO_2$ Electrodes: Structural, Compositional and Electrochemical Control of Integrated ‘Layered-Layered-Spinel’ Cathode Structures.” Presented at the 17th International Meeting on Lithium Batteries, Como, Italy.

V.B.2 *In situ* Solvothermal Synthesis of Novel High Capacity Cathodes (BNL)

Feng Wang
Brookhaven National Laboratory

Sustainable Energy Technologies Department
Upton, NY 11973
Phone: (631) 344-4388; Fax: (631) 344-7905
E-mail: fwang@bnl.gov

J. Patrick Looney
Sustainable Energy Technologies Department
Upton, NY 11973
Phone: (631) 344-3798; Fax: (631) 344-7905
E-mail: jlooney@bnl.gov

Start Date: April 2012
Projected End Date: April 2016

Objectives

- Develop low-cost cathode materials that offer high energy density (>660 Wh/kg) and electrochemical properties (cycle life, power density, safety) consistent with USABC goals.

Technical Barriers

Present day Li-ion batteries are incapable of meeting the 40-mile all-electric-range within the weight and volume constraints established for PHEVs by DOE and the USABC. Higher energy density cathodes are needed for Li-ion batteries to be widely commercialized for PHEV applications.

The development of new, safer lithium batteries requires new tools to better understand the physical and chemical processes that occur during cycling and the ability to predict and ultimately control the key electrochemical properties such as capacity (power and energy density), durability (calendar and cycle life), abuse tolerance (safety characteristics) and cost.

Technical Targets

- Higher energy density.
- Lower cost.

Accomplishments

- Completed structural and electrochemical characterization of ε-$Cu_xV_2O_5$ cathodes, with the results indicating stabilized structure for long-term cyclability of the material.
- Developed solvothermal-assisted synthesis procedures to prepare phase-pure $Li_3V_2(PO_4)_3$ cathodes, with high rate capability and long-term cyclability enabled *via* particle size reduction and carbon coating.
- Completed structural and electrochemical characterization of new $CuVO_3$ cathodes, with extremely high capacity (*ca. 350 mAh/g*).
- Developed *in situ* ion-exchange synthesis of $Li_xNa_{1.5-x}VOPO_4F_{0.5}$ cathodes for precise control of the exchange process to synthesize final products of desired stoichiometry and electrochemical properties.

✧ ✧ ✧ ✧ ✧

Introduction

Despite considerable interest in developing new cathodes for Li-ion batteries, only a small number of known materials show real promise for achieving significant improvement in capacity and/or a reduction in cost. The preparation of new compounds or materials with unique properties often relies on trial and error as there are a variety of synthesis parameters (precursor concentration, temperature, pressure, *pH* value, cation type and reaction time) that can have a strong influence on the material properties (crystal structure, morphology, particle size) and electrochemical performance (e.g., capacity, rate capability, and durability). Most solution-based reactions are carried out in a sealed autoclave and therefore the reactor is a black box – the inputs and outputs are known, but little is known about intermediate phases and the overall reaction pathway. *In situ,* real-time probes of synthesis reactions can provide the details of reactions, elucidating intermediate phases and how temperature, pressure, time and the precursor concentrations affect the reaction pathways. The results of such studies enable strategies to optimize synthesis reactions, particularly the formation of materials of desired phases and properties. With a more fundamental understanding of the correlation between synthesis conditions, crystallization processes, and material properties, a more rational design of advanced lithium electrode materials should emerge.

Approach

In this effort, specialized *in situ* reactors were developed to investigate synthesis reactions in real time using synchrotron X-ray diffraction (XRD) techniques. With these techniques, crystal growth and structure changes can be monitored while leaving the reaction undisturbed. This approach provides a real-time measurement of how reaction conditions affect nucleation and crystallization, bonding, particle size, morphology and defect concentration. In addition, *in situ* measurements reveal the formation of intermediate and short-lived phases formed during the reaction without the need for quenching. These new tools are being used to prepare novel high-energy cathodes with desired properties (*e.g.* structure, stoichiometry).

The structural and electrochemical properties of synthesized materials are evaluated *via* synchrotron X-ray, and various electrochemical methods. The structural/chemical evolution of electrodes during cycling is systematically investigated using *in situ*, *operando* synchrotron XRD and X-ray absorption near-edge (XANES) and extended fine structure (EXAFS) and advanced TEM techniques, which help to identify the mechanism(s) responsible for the capacity fade and provide guidance to further optimizing the synthesis.

Results

Structural reversibility of ε-$Cu_xV_2O_5$

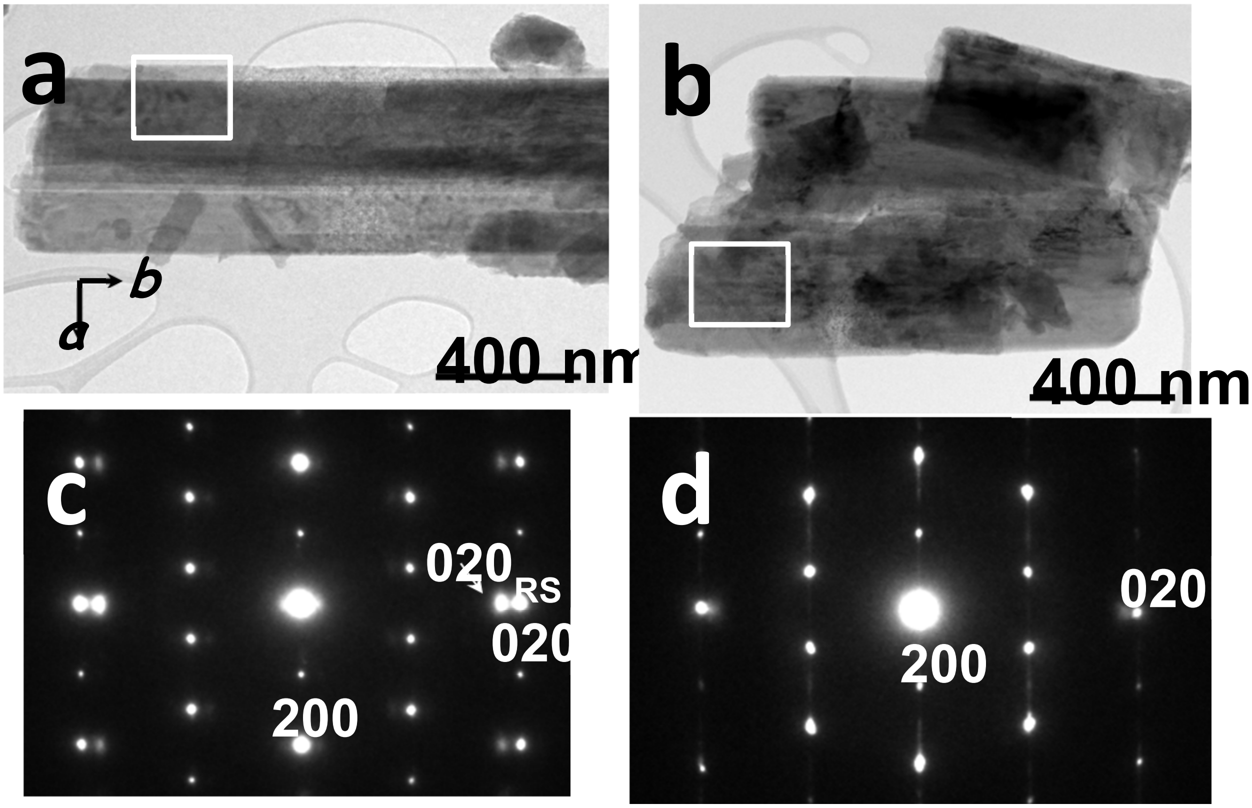

Figure V - 7: Local structural ordering of ε-CVO by TEM imaging and electron diffraction at pristine state (a, c) and after one cycle (b, d)

Following on from previous work on synthesis of high-capacity ε-$Cu_xV_2O_5$ (ε-CVO) electrodes, transmission electron microscopy (TEM) and synchrotron X-ray techniques were applied to study the correlation between structural ordering (both *short-range* and *long-range*) and electrochemical behavior of ε-CVO cathodes, aiming to understand the structural origin of their cycling reversibility. Figure V - 7 shows the representative TEM images and electron diffraction patterns from individual ε-CVO nanorods. The TEM results are consistent with XRD measurements, showing that the as-synthesized material has a monoclinic structure (C2/m), but with new local ordering likely due to Cu-deficiency (Figure V - 7a, and Figure V - 7c). TEM results from cycled electrodes show that a new ordered structure is formed after the 1st cycle (Figure V - 7b, and Figure V - 7d), and remains invariant during subsequent cycles.

Galvanostatic Intermittent Titration Technique (GITT) and *in situ* XAS studies on ε-CVO electrodes were used to identify Cu/V redox reactions and local structural evolution during the 1st two cycles. As illustrated in Figure V - 8a, there is a clear separation of Cu and V reduction reactions in the 1st discharge, which becomes overlapped in the 2nd discharge (shadowed region). At the same time, the reaction kinetics of Cu reduction is significantly improved compared to that during the 1st discharge. This implies that the *long-range order* of ε-CVO was changed during the 1st lithation/delithiation, while the *local structural ordering* is reversible according to the Fourier transform of the EXAFS spectra (Figure V - 8b). For example, VO_6 octehdra are recovered after one cycle (despite a slight increase in symmetry).The detailed structural analysis provides direct experimental evidence of the change in the long-range ordering during initial lithation and delithation, while the short-range ordering is maintained, which, in concert with electrochemical studies, explains the origin of the cycling reversibility found in ε-CVO electrodes.

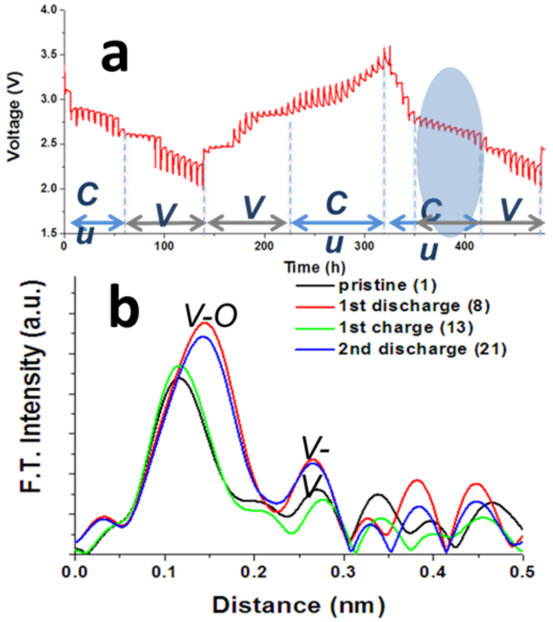

Figure V - 8: Lithium reaction pathways and reversibility of ε-CVO cathode, *via* (a) GITT, (b) V K-edge EXAFS

Electrochemical properties of α-CVO3 cathodes

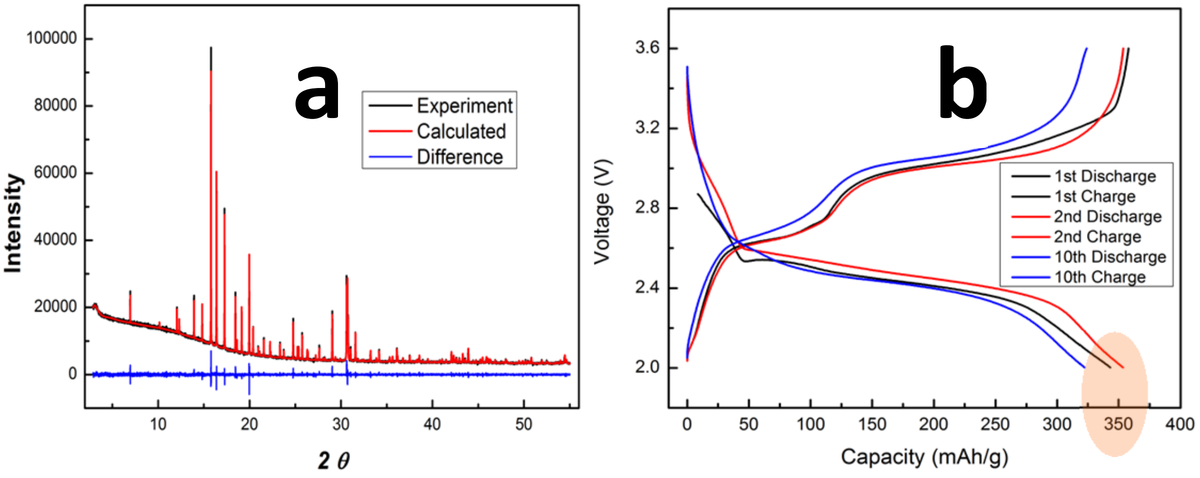

Figure V - 9: Structural (a) and electrochemical (b) properties of synthesized α-$CuVO_3$

An extensive evaluation was made of the key process parameters of solid state reactions (precursors, atmosphere, pressure, and temperature of reaction) by combining *ex situ* and *in situ* synthesis techniques to develop procedures for making phase-pure α-$CuVO_3$ at the lowest possible temperature. The structure of as-synthesized materials was determined by synchrotron XRD and refinement (Figure V - 9a). α-$CuVO_3$ has a rhombohedral structure (space group: R-3 (148)), with lattice parameters of a =12.855 Å, c =7.194 Å and stoichiometry of about $Cu_{6.89}V_6O_{19}$. Mixed valences of Cu (+1/+2) and V (+4/+5) were identified by XAS.

The as-synthesized α-$CuVO_3$ was generally composed of μm-sized particles with very low capacity. With post-processing (using a patent-protected procedure), a capacity as high as 350 mAh/g along with reasonable cycling reversibility was obtained in α-$CuVO_3$ electrodes under a moderate cycling condition (with the window 2.0-3.6 V and rate C/20; Figure V - 9a, Figure V - 9b). Such high, reversible capacity is attributed to the robust 3D framework of α-$CuVO_3$ that can accommodate multiple electron redox reactions. Cu dissolution in liquid electrolyte is one common issue for all Cu-containing electrodes (including α-$CuVO_3$). Given the extremely high capacity, α-$CuVO_3$ is an appealing cathode for solid-state batteries.

Synthesis of vanadium phosphates (Li-V-PO_4)

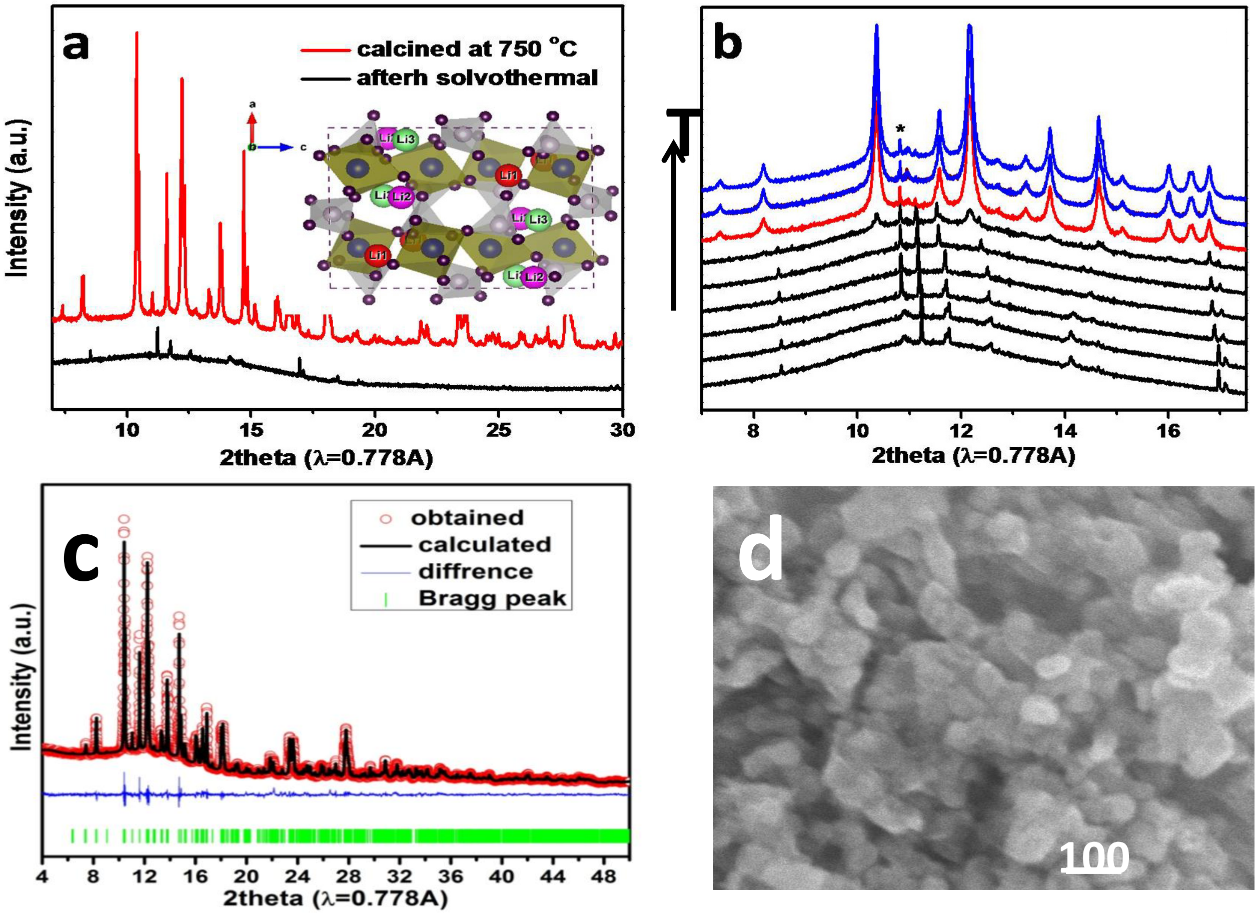

Figure V - 10: Synthesis and structural properties of LVP cathodes, (a) synchrotron XRD patterns recorded from intermediate and final product, (b) *in situ* synchrotron XRD studies of synthesis reactions, (c) XRD, structure refinement of synthesized LVP, and (d) SEM image of the as-synthesized LVP particles

There exists a large number and variety of polyanion-type cathodes, and among them vanadium-based (V) phosphates are particularly interesting given the potential for high energy density enabled by high voltage (induced by phosphate groups) and accessible multiple redox states of V, as well as the open yet potentially stable framework. Thermal-assisted synthesis procedures were developed for preparing monoclinic $Li_3V_2(PO_4)_3$ (LVP), one of the promising cathodes with a theoretical capacity of 197 mAh/g.

Direct solvothermal synthesis of LVP, *via* heat treatment of precursors in ethylene glycol solution at different temperatures was attempted, but only amorphous intermediates (along with residual Li_3PO_4) were observed. An additional calcination step was found to be necessary in obtaining the monoclinic LVP phase Figure V - 10a).

Additional efforts were focused on investigating and tuning the synthesis process. A combination of XAS of V K-edge, along with electron diffraction and high-resolution TEM imaging was used to identify the local structure and chemical states of V in the intermediate and final products, and *in situ* synchrotron XRD was applied for tracking the detailed phase evolution during calcination. Some of the diffraction patterns from *in situ* XRD measurements are given in Figure V - 10b, which clearly indicates no formation of crystalline LVP phase at low temperatures. At elevated temperatures, 630°C and above, LVP phase was detected while Li_3PO_4 precursor was consumed simultaneously. Eventually the monoclinic LVP phase was obtained at about 730°C. This investigation shows that LVP may not be synthesized *via* a "*one-pot*" solvothermal process. However the solvothermal step was found to play the role of reducing V (to the valence 3+) and reaching a similar local ordering in the intermediate as that of the final product, and thus is essential to the eventual formation of the final LVP phase.

Based on the investigation of synthesis reactions, a solvothermal-assisted procedure was developed for making pure phase of LVP with monoclinic structure (Figure V - 10c). The as-synthesized LVP particles are about 50 nm in size, single-crystalline and coated with thin layer of amorphous carbon (Figure V - 10d).

Following the synthesis of phase-pure vanadium phosphates, $Li_3V_2(PO_4)_3$ (LVP) and $Li(Na)_{1+x}VOPO_4F_x$ (LVOPF), their extensive electrochemical characterization was performed. The results from the investigation demonstrated that some desirable electrochemical properties, such as long-term cyclability and high rate capability, were enabled via a synthetic control of the morphology and stoichiometry of those cathodes.

Galvanostatic cycling measurements were performed on the LVP electrodes at a C/10 rate in two different voltage windows, 3.0-4.8 and 3.0-4.3 V (Figure V - 11a). A capacity as high as 190 $mAh \cdot g^{-1}$ was obtained during initial charge to 4.8 V, but the capacity fades quickly with cycling. With a restriction of the window to 3.0-4.3 V, while the capacity was reduced to120 $mAh \cdot g^{-1}$ (bottom panel), an extraordinary capacity retention of 95% was obtained after 200 cycles. The LVP electrodes also exhibit an excellent rate capability, of 88 $mAh \cdot g^{-1}$ measured at 10C, in stark contrast to the low capacity and large polarization obtained from the LVP synthesized *via* solid state reaction (Figure V - 11b). Although the ionic conductivity of LVP is intrinsically high due to the 3D Li diffusion pathways across the NASICON structure, it appears that carbon coating and particle size reduction achieved *via* synthetic control is essential to achieving such a high rate capability.

Electrochemical properties of vanadium phosphates.

Micron-sized LVOPF with pseudo-layered structure were synthesized *via* hydrothermal ion-exchange from the Na counterpart ($Na_{1.5-x}VPO_5F_{0.5}$). The exchange process is complicated, involving multiple-step phase transformation (reported previously). *In situ* ion exchange synthesis was used to systematically evaluate synthesis parameters, including the concentration of LiBr solution, reaction temperature, Li/Na ratio and heating rate. With the determined optimum exchange conditions, a series of LVOPF of different stoichiometry and structures were obtained. The preliminary electrochemical tests indicate a strong dependence of their electrochemical properties on the extent of Li^+ replacement. High capacity was achieved in the LVOPF with high lithium content and, interestingly, maximizing lithium ion exchange appears to also be essential to the long-term cyclability. This is likely due to the enhancement of structural stability with a close-to-complete replacement of Na^+ by Li^+.

Conclusions and Future Directions

During FY14, new *in situ* reactors and time-resolved XRD techniques were developed and utilized for studying hydrothermal ion exchange and solid-state reactions and the synthesis of phase-pure materials. Structural and electrochemical characterization of ε-$Cu_xV_2O_5$ cathodes was performed, demonstrating stabilized structure for long-term cyclability of the material. Solvothermal-assisted synthesis procedure was developed to prepare single-crystalline $Li_3V_2(PO_4)_3$ nanoparticles with high rate capability and long-term cycling stability. The electrochemical performance of α-CuVO3 cathode was optimized, achieving an extremely high capacity (350 mAh/g). *In situ* ion-exchange synthesis was used for evaluation of synthesis parameters, and thereby preparing $Li_xNa_{1.5-x}VOPO_4F_{0.5}$ cathodes of different stoichiometry and electrochemical properties.

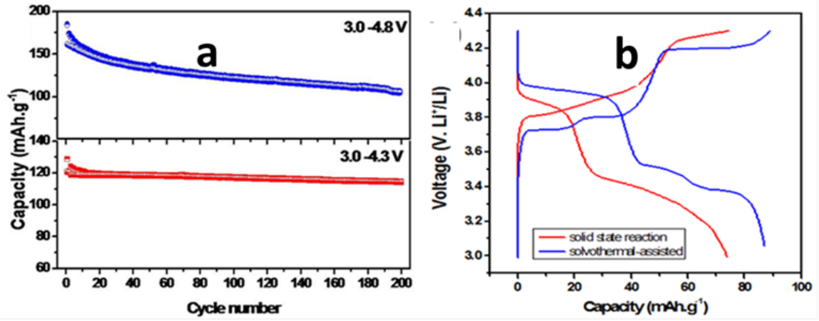

Figure V - 11: Electrochemical properties of LVP particles, shown by (a) galvanostic cycling at C/10 in two different voltage windows, (b) typical voltage profiles of LVP synthesized *via* two different routes

In FY15, new tools and techniques will be developed for high-throughput synthesis of new cathodes and diagnostic studies of electrochemical properties of synthesized electrodes. Efforts will be continued on synthesis and structural, electrochemical characterization of new polyanionic and other type of cathodes, in which multiple electron redox reactions may be potentially enabled for achieving high capacity.

FY 2014 Publications/Presentations

1. Looney, P., Wang, F. (June 2014), "*In situ* Solvothermal Synthesis of Novel High Capacity Cathodes Presented at the 2014 DOE Annual Merit Review and Peer Evaluation Meeting, Washington, D.C.
2. Gutierrez, A., Qiao, R., Wang, L., Yang, W., Wang, F., and Manthiram, A. (2014). "High-capacity, Aliovalently Doped Olivine LiMn$_{1-3x/2}$V$_x$ □$_x$/2PO$_4$ Cathodes without Carbon Coating." *Chem. Mater. (*26); p. 3018.
3. Li, X., Ma, X., Su, D., Liu, L., Chisnell, R., Ong, S., Chen, H., Toumar, A., Idrobo, J-C., Lei, Y., Bai, J., Wang, F., Lynn, J.W., Lee, Y. S., Ceder, G. (2014). "Direct Visualization of the Jahn-Teller Effect Coupled to Na Ordering in Na$_{5/8}$MnO$_2$." *Nat. Mater.* (13); p. 585.
4. Wang, F., Kim, S-W., Graetz, J. (Patent filed). "Ternary Transition Metal Fluorides as High-Energy Cathodes for Lithium Rechargeable Batteries."
5. Wang, F., Bai, J., Park, Y-U., Wang, L-P., Wang, X., Looney, P. (December 2013). "*In situ* Solvothermal Synthesis of Novel High Capacity Cathodes." Presented at the NSLS Triennial Review Meeting, BNL.
6. Wang, F., Kim, S-W., Wang, X., Wang, L., Bai, J. (April 2014). "*In situ* Hydrothermal Synthesis of Nanostructured High-Energy Cathodes for Li-Ion Batteries." Presented at the MRS 2014 Spring Meeting, San Francisco, California.
7. Kim, S-W., Wang, L-P., Su, D., Graetz, J., Wang, F. (April 2014). "Ternary Metal Fluorides as New Cathodes of Rechargeable Lithium Batteries with Ultrahigh Energy Density." Presented at the MRS 2014 Spring Meeting, San Francisco, California.
8. Bai, J., Hong, J., Chen, H., and Wang, F. (May 2014). "*In situ* Solvothermal Synthesis of Olivine Cathodes." Presented at OREBA 1.0, Montreal, HQ, Canada.
9. Wang, L., Bai, J., Kim, S-W., Wang, X., Wang, F. (November 2013). "*In situ* Synthesis of High-energy Cathode Materials for Lithium-ion Batteries." Presented at the Young Researcher Symposium, BNL.

V.B.3 Design of High Performance, High Energy Cathode Materials (LBNL)

Marca Doeff
Lawrence Berkeley National Laboratory

Environmental Energy Technologies Division
1 Cyclotron Road
Berkeley, CA 94720
Phone: (510) 486-5821
E-mail: mmdoeff@lbl.gov

Start Date: October 2011
Projected End Date: September 2015

Objectives

- To develop high-energy, high-performance cathode materials based on Ti-substituted NMCs and composites of $LiNi_{0.5}Mn_{1.5}O_4$ and coated powders, using spray pyrolysis and other synthesis techniques.
- To understand surface and bulk structural properties of Ti-NMCs that lead to enhanced energy densities.

Technical Barriers

The cost of vehicular batteries is too high and the energy density needs to be improved. Cost on a $/kWh basis will be lowered if a higher energy density can be obtained without adversely affecting cycle life. However, the performance of high-energy high voltage electrode materials like $LiNi_{0.5}Mn_{1.5}O_4$ needs to be improved by reducing its reactivity with the electrolyte. Alternatively, higher utilization of NMC cathode materials could lead to higher energy density provided cycling issues can be successfully addressed.

Technical Targets

- Explore feasibility of increasing utilization of NMCs by partial Ti-substitution of Co and using higher voltage cutoffs during cycling.
- Understand origins of Ti-substitution effects in substituted NMCs.

Accomplishments

- Successfully synthesized high-performance NMC materials by spray pyrolysis.
- Demonstrated that surface reconstruction of NMC particles is a function of cycling history, electrolyte exposure and the method of synthesis.
- Traced improved performance of Ti-substituted NMCs to stabilization against formation of surface rock salt phase.

◆ ◆ ◆ ◆ ◆

Introduction

Batteries for vehicular applications need improvements in energy density, ideally without compromising cost or safety. At present, cathodes are the limiting factor preventing achievement of this goal due to their relatively low specific capacities compared to graphite (~370 mAh/g) or silicon anodes (>4,000 mAh/g). NMCs, which have the general formula $Li[Ni_xMn_xCo_{1-2x}]O_2$, are a technologically important class of cathodes, but their practical capacities are limited to about 160 mAh/g, slightly more than half of the theoretical (280 mAh/g). While greater capacities can be achieved by cycling to higher voltage limits, this leads to a rapid capacity fading. Work on this project is directed towards development of higher capacity NMCs to improve energy density by attempting to understand the phenomena responsible for the capacity fade and using strategies to mitigate it, such as partial Ti-substitution.

Approach

A combination of synchrotron radiation and electron microscopy techniques (in collaboration with A. Mehta, D. Nordlund, and T.-C. Weng at SSRL and H. L. Xin at BNL) and computational methods (with M. Asta at U.C. Berkeley) were used to understand the surface and bulk characteristics of baseline and Ti-substituted NMCs. Materials were synthesized either by classic co-precipitation methods or by spray pyrolysis.

Electrochemical characterization was carried out in lithium half-cell configurations. Several physical techniques were used to characterize materials before and after electrochemical cycling under a variety of conditions. Soft X-ray absorption spectroscopy (XAS) experiments carried out at SSRL were used to probe oxidation states of transition metals at particle surfaces and in the bulk as a function of their electrochemical history. High-resolution transmission electron microscopy (HR-TEM) and electron energy loss spectroscopy (EELS) at Brookhaven National Laboratory was also used to characterize materials.

Results

Surface reconstruction of NMC particles: NMC cathodes typically cycle well in lithium half-cells when an upper voltage limit of 4.3V is used, but lose capacity rapidly when cycled to higher voltages. Partial previous results indicated that Ti-substitution ameliorates the fading observed during high voltage cycling to some extent. Understanding the reasons for the deterioration in performance during high voltage cycling is key toward developing variants of NMCs able to tolerate high-voltage cycling and deliver higher specific capacities safely and reliably. To this end, recent work on this project was focused on understanding the phenomena responsible for the poor high-voltage performance, particularly at particle surfaces, since bulk processes such as phase changes or decomposition are not observed. Another goal was to understand the role of Ti in ameliorating the capacity fading.

High throughput ensemble-averaged synchrotron soft XAS was used to determine the relative oxidation states of the transition metals as a function of depth in electrodes charged to 4.7V in half-cells. The Auger electron yield (AEY) typically probes the top 1-2 nm of a sample, the total electron yield (TEY) about 2-5 nm, and the fluorescence yield (FY) about 50 nm into the sample. A comparison of data shows that ratios of the L3 low and high peaks differ in the three modes, indicating that there is a gradient of oxidation states extending from the surface into the bulk, with the more reduced species at the surface. Figure V - 12 shows results for the Ni L-edge, but the gradients were also observed for Mn and Co (not shown).

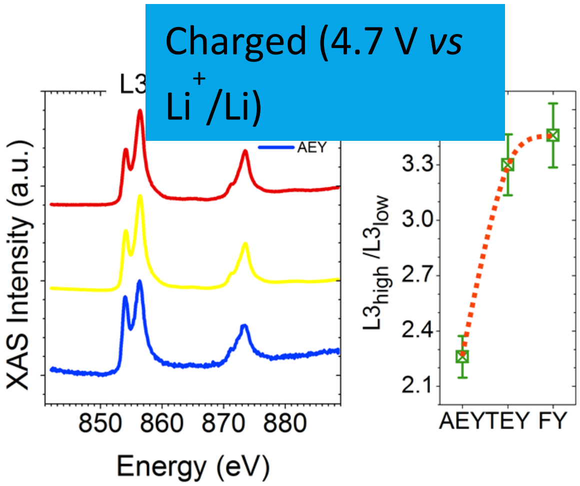

Figure V - 12: Soft XAS data showing the Ni L-edge of a charged electrode using three different modes. Auger electron yield (AEY) probes the top 1-2 nm of the sample, total electron yield (TEY) the top 2-5 nm, and fluorescence yield (FY) about 50 nm into the bulk

The gradient distribution of the oxidation states in individual particles obtained from the charged electrodes was confirmed by spatially resolved STEM-EELS experiments (not shown). HR-TEM images (Figure V - 13) clearly show the formation of a rock salt phase on particle surfaces. The surface reconstruction is anisotropic, with thicker rock salt layers forming on the facets through which Li ions diffuse. The growth of the rock salt phase, along with a more diffuse reaction layer consisting of LiF and organic matter on NMC particle surfaces, is thought to be responsible for the rise in impedance and rapid capacity fading observed in the cells charged to high voltages. Surface reconstruction also occurs to some extent after long exposures to electrolytic solution even without electrochemical cycling, and increases with increasing cycle number (see [5], [8]). The degree to which it occurs is dependent on how materials were synthesized (particularly in terms of calcination times, see [2]) and cycling regimes, with more severe changes observed for materials cycled potentiostatically rather than galvanostatically.

Figure V - 13: HR-TEM images of an NMC particle harvested from a charged electrode, showing the formation of a rock salt structure on the surfaces

Formation energies of the rock salt structure were determined as a function of the state-of-charge of NMC electrodes using first principle calculations (Figure V - 14, see [3]). From these data, it is clear that the tendency to form rock salt increases as more lithium is removed from the structure. At a lithium content of about 0.4 in the baseline material, rock salt is predicted to form. Substitution with 2% Ti, however, has a stabilizing influence, delaying the onset of transformation. This arises as a consequence of the stronger Ti-O bond compared to that of Ni-O, Co-O and Mn-O bonds, since formation of rock salt requires loss of oxygen.

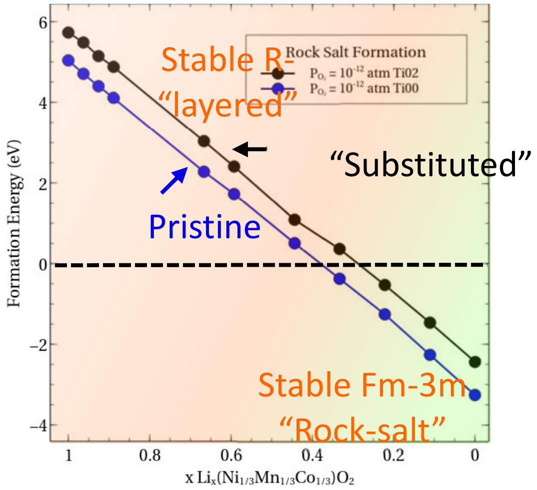

Figure V - 14: Formation energies of the rock salt structure as a function of state-of-charge of baseline and Ti-substituted NMC cathodes, determined by first principles calculations

Spray pyrolysis synthesis of NMCs: Spray pyrolysis synthesis of NMCs was carried out successfully. Figure V - 15 shows the uniform morphologies of the hollow spherical particles, which are composed of nanometric primary particles. The electrochemical performance of the spray-pyrolyzed materials equals or surpasses that of materials made by co-precipitation.

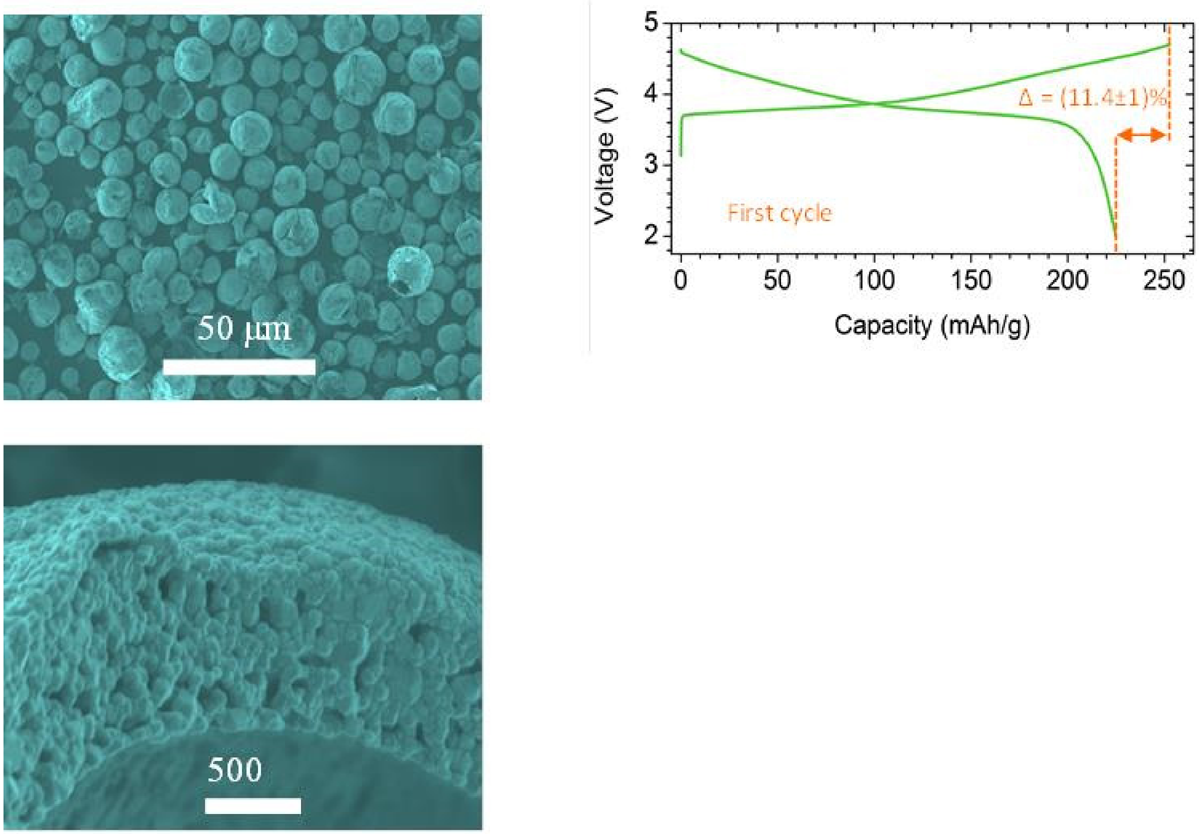

Figure V - 15: Scanning electron micrographs of spray-pyrolyzed NMC samples (left), and electrochemical performance in lithium half-cells (right)

Conclusions and Future Directions

Future work will be directed towards synthesis of Ti-substituted NMCs by spray pyrolysis, preparation of coated particles using atomic and molecular layer deposition (with Chunmei Ban of NREL), and investigation of the efficacy of these strategies using microscopy and synchrotron X-ray techniques.

FY 2014 Publications/Presentations

1. Doeff, M.M. (2014). “Design of High Performance, High Energy Cathode Materials.” Presented at the 2014 DOE Annual Merit Review and Peer Evaluation Meeting, Washington, D.C.
2. “Lin, F., Nordlund, D., Pan, T., Markus, I., Weng, T-C., Xin, H., and Doeff, M.M. (2014). “Influence of Synthesis Conditions on the Surface Passivation and Electrochemical Behavior of Layered Cathode Materials.” *J. Mater. Chem.* ***A*** DOI: 10.1039/c4ta04497e.
3. Markus, I., Lin, F., Kam, K., Asta, M., and Doeff, M.M. (2014). “Computational and Experimental Investigation of Ti Substitution in $Li_1(Ni_xMn_xCo_{1-x-y}Ti_y)O_2$ for Lithium-Ion Batteries.” *J. Phys. Chem. Lett.* (5); p. 3649.
4. Cheng, L., Crumlin, E.J., Chen, W., Qiao, R., Hou, H., Lux, S.F., Zorba, V., Russo, R., Kostecki, R., Liu, Z., Persson, K., Yang, W., Cabana, J., Richardson, T., Chen, G., and Doeff, M.M. (2014). “Origin of High Electrolyte-Electrode Interfacial Resistances in Lithium Cells Containing Garnet Type Solid Electrolytes.” *Phys. Chem. Chem. Phys.* (16); p. 18294.
5. Lin, F., Markus, I., Nordlund, D., Weng, T-C., Xin, H., and Doeff, M. M. (2014). “Profiling the Nanoscale Gradient in Stoichiometric Layered Cathode Particles for Lithium-ion Batteries.” *Energy & Environ. Sci.* (7); p. 3077.
6. Lin, F., Markus, I., Doeff, M. M., and Xin, H. (2014). “Chemical and Structural Stability of Lithium-Ion Battery Electrode Materials under Electron Beam.” *Scientific Reports* (4); p. 5694 DOI:10.1038/srep05694.
7. Iturrondobeitia, A., Goñi, A., Gil de Mur, I., Kim, C., Doeff, M. M., Cabana, J., and Rojo, T. (2014). “Modification of the Electrochemical Activity of $LiMn_{1.95}Si_{0.05}O_4$ Spinel via Addition of Phases with Different Physico-chemical Properties.” *J. Mater. Chem. A* (2); p. 3216.
8. Lin, F., Markus, I., Nordlund, D., Weng, T-C., Asta, M., Xin, H., and Doeff, M. M. (2014). “Surface Reconstruction and Chemical Evolution of Stoichiometric Layered Cathode Materials for Lithium-Ion Batteries.” *Nature Commun.* (5); p. 3529.
9. Cheng, L., Park, J., Hour, H., Zorba, V., Chen, G., Richardson, T., Cabana, J., Russo, R., and Doeff, M. M. (2014). “Effect of Microstructure and Surface Impurity Segregation on the Electrical and Electrochemical Properties of Dense Al-substituted $Li_7La_3Zr_2O_{12}$.” *J. Mater. Chem. A* (2); p. 172.
10. Lin, F., Markus, I., Nordlund, D., Weng, Weng, T-C., Asta, M., Xin, H. and Doeff, M.M. (August 2014). “Characterization at Complementary Length Scales: Fundamental Correlation between Structure and Electrochemistry of Electrode Materials in Lithium-ion Batteries.” Invited oral presentation given by Feng Lin, presented at the 248th ACS National Meeting & Exposition, San Francisco, CA.

V.B.4 Design and Synthesis of Advanced High-Energy Cathode Materials (LBNL)

Guoying Chen
Lawrence Berkeley National Laboratory

Environmental Energy Technologies Division
1 Cyclotron Road
Berkeley, CA 94720
Phone: (510) 486-5843; Fax: (510) 486-5467
E-mail: gchen@lbl.gov

Start Date: October 2012
Projected End Date: September 2016

Objectives

- Obtain fundamental understanding of structural, chemical and morphological instabilities during Li extraction/insertion and extended cycling.
- Establish and control the interfacial chemistry between the cathode and the electrolyte at high operating potentials.
- Determine transport limitations at both material and electrode levels.
- Rationally design and develop next-generation electrode materials.

Technical Barriers

Low-energy density, low power density, poor cycle life and poor safety.

Technical Targets

- PHEV40: 96 Wh/kg, 750 W/kg, 5,000 cycles.
- EV: 200 Wh/kg, 1,000 cycles.

Accomplishments

- Characterized crystal-plane specific chemistries at the electrode/electrolyte interface and demonstrated the effect of surface facets on self-discharge of Ni/Mn spinels.
- Investigated the thermal behavior of $Li_xMn_{1.5}Ni_{0.5}O_4$ (Li_xMNO) in the entire Li range and constructed the phase diagram.
- Isolated the solid solution phases in the Ni/Mn spinel system for the first time. Detailed characterization of the intermediates initiated.
- Synthesized and characterized phase-pure oxide cathode crystals with alternative morphologies by using solvothermal method for the first time.
- Diagnostic techniques were developed for the single-crystal studies pertaining to cathode performance and stability. Cycling-induced structural changes and variation in TM oxidation state visualized at the particle level.

✧ ✧ ✧ ✧ ✧

Introduction

To meet the DOE targets for Li-ion batteries intended for vehicular applications, electrode materials with high-energy density and high stability are needed. Critical performance issues, such as structural and morphological instabilities, side reactions with the electrolyte, and transport limitations, are sensitive to materials chemical compositions, crystal structures, surface facets, and particle sizes. Advances in materials development, therefore, require a better understanding of the relationships between their properties and functions. This project addresses these issues in a systematic way by synthesizing single-crystal version of the commercially promising yet complex electrode materials, obtaining new insights into the materials by utilizing state-of-the-art analytical techniques that mostly do not apply to conventional, aggregated secondary particles, and subsequently establishing the relationships between structure and function. The goal is to use these findings to rationally design and synthesize advanced electrode materials with an improved performance.

Approach

Prepare single crystals of Li-rich layered composites and high-voltage Ni/Mn spinels with well-defined physical attributes. Perform advanced diagnostic and mechanistic studies at both bulk and single-crystal levels. Global properties and performance of the samples will be established from the bulk analyses, while the single-crystal based studies will utilize time- and spatial-resolved analytical techniques to probe material’s redox transformation and failure mechanisms.

Results

Crystal synthesis: To complement the crystal samples prepared from high-temperature synthesis, the solvothermal method, which is known for its simplicity and versatility in preparing well-formed crystals, was explored. The low temperature and high pressure conditions typically promote nucleation and crystal growth that favor metastable surface facets. Careful adjustments on solvent, precursors, temperature and reaction time led to the synthesis of phase-pure spinel $LiMn_{1.5}Ni_{0.5}O_4$ (LMNO) with controlled morphology. Figure V - 16 shows the selected morphologies obtained by this method. The crystals were prepared by mixing stoichiometric amounts of MnO_2 with $NiCl_2$ and LiOH in water followed by thermal treatment in a Teflon-lined Parr autoclave at 250°C for 10 h. Upon post-synthesis annealing at 400°C for 2 h and then 800°C for 6 h in an oxygen atmosphere, thermodynamically favorable octahedron-shaped LMNO crystals were obtained (Figure V - 16a). The crystallinity of the MnO_2 had a large impact on morphology, as replacing the amorphous with crystalline MnO_2 resulted in the formation of truncated-octahedron-shaped LMNO crystals (Figure V - 16b). In the absence of LiOH, the reaction led to the formation of rod-shaped nickel manganese oxide intermediate. The morphology was largely preserved when immediate lithiation with LiOH was performed in ethanol, which led to the formation of micron sized, rod-shaped LMNO crystals (Figure V - 16c). The size and uniformity of the rods greatly improve with lithiation time. All the samples were treated with the same post-synthesis annealing procedure to improve the oxide quality, particularly with regard to site occupancy and structural ordering. Electrochemical evaluation, however, showed the presence of a large Mn^{3+} content in all samples, suggesting potential TM off-stoichiometry. The rate capability test also indicated poorer performance compared to those synthesized by the molten-salt method (Figure V - 16d).

Effect of surface facets on cathode self-discharge: One of the critical issues facing LMNO as a high-voltage cathode material is the severe self-discharge upon storage at charged state. Previous mechanistic studies have largely attributed the phenomena to the oxidative decomposition of the electrolyte at high potentials, with the insertion capacity mostly reversible upon subsequent cycling. This, however, reduces calendar life and has a major impact on cycling performance and stability considering the limited amount of electrolyte available in commercial Li-ion cells. Several factors, including state of charge, storage temperature, and the choice of electrolyte, have previously been shown to influence the rate of cathode relithiation. The goal was to investigate the role of cathode surface facet on relithiation.

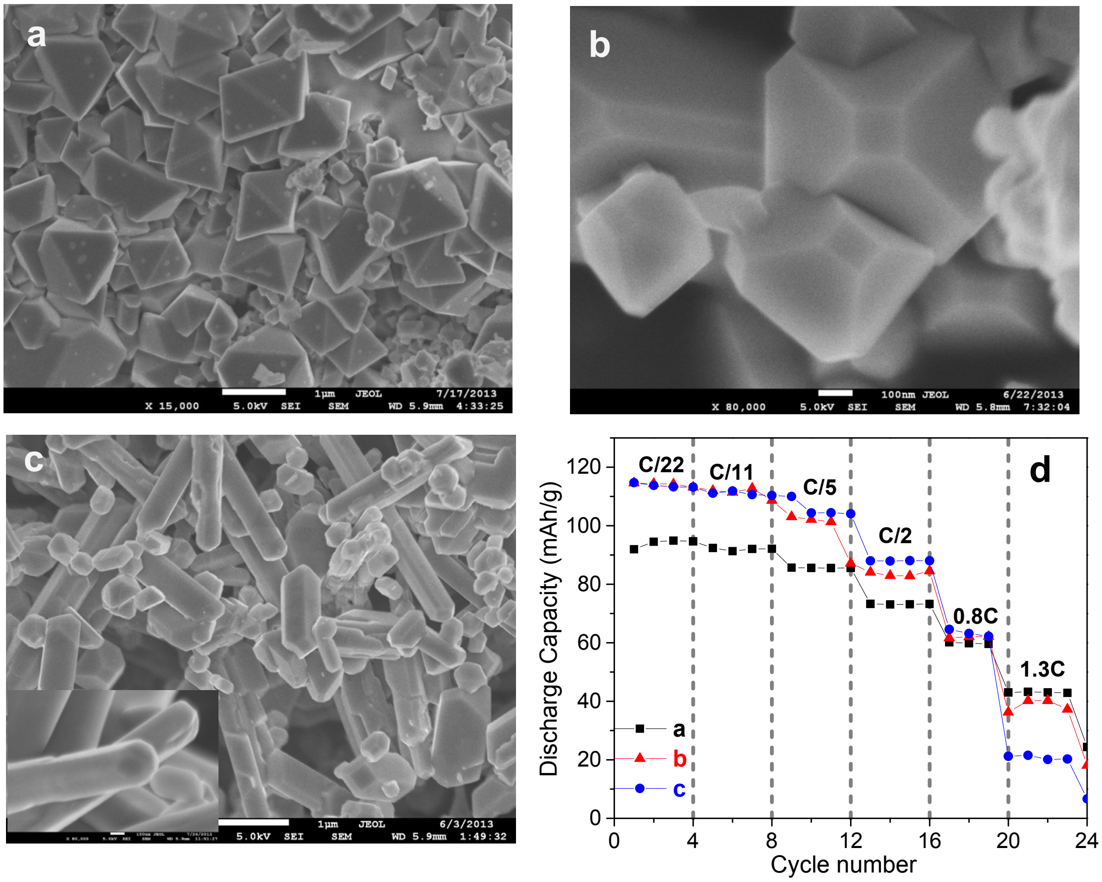

Figure V - 16: SEM images of solvothermal synthesized LMNO crystals: a) octahedrons, b) truncated-octahedrons and c) rods; d) rate capability of the crystal samples

Micron-sized LMNO single crystals with predominant (112) and (111) surface facets (plate and octahedron shapes, respectively) were fully delithiated by chemical oxidation with a NO_2BF_4 solution in acetonitrile and then aged at room temperature in a 1.0 M $LiPF_6$ in EC:DEC (1:1) (% v/v) electrolyte for 5 weeks. In both cases, a light brown color gradually developed in the electrolyte but the color was significantly darker in the solution containing the plate sample. Figure V - 17 shows the XRD patterns as well as the expanded view of (311), (400) and (440) peaks collected on the recovered crystals during the various stages of storage. Pristine LMNO was composed of a single cubic phase with a lattice parameter of 8.168 Å (Phase I) and the delithiated LMNO consists of a single cubic phase, $Mn_{1.5}Ni_{0.5}O_4$ (MNO), with a lattice parameter of 8.008 Å (Phase III). Aging of MNO in the electrolyte led to relithiation which is clearly shown by the appearance of a cubic phase with an intermediate Li content, previously determined to be $Li_{0.5}Mn_{1.5}Ni_{0.5}O_4$, with a lattice parameter of 8.089 Å (Phase II). For the plates, Phase II appeared during the first week of aging and then Phase I appeared after 3 weeks. The amount of both phases increased at the expense of Phase III, and after 5 weeks of storage, the plates were mostly composed of Phase I and II (Figure V - 17a). Relithiation was also observed in the octahedrons but the ratio between Phase III/Phase II remained high and Phase I did not appear even after 5 weeks of storage (Figure V - 17b). This suggests that the extent of Li reinsertion is much smaller in the latter case. Full-pattern Rietveld refinements of the XRD patterns were used to estimate the lithium content in the aged samples, which produced a range of 0.2-0.3 for the plates and 0.1-0.2 for the octahedrons after 5 weeks (Figure V - 18). The study suggests that relithiation may be used as a kinetic index for side reactions between cathode and electrolyte, and that particle morphology design provides an important route to minimizing self-discharge.

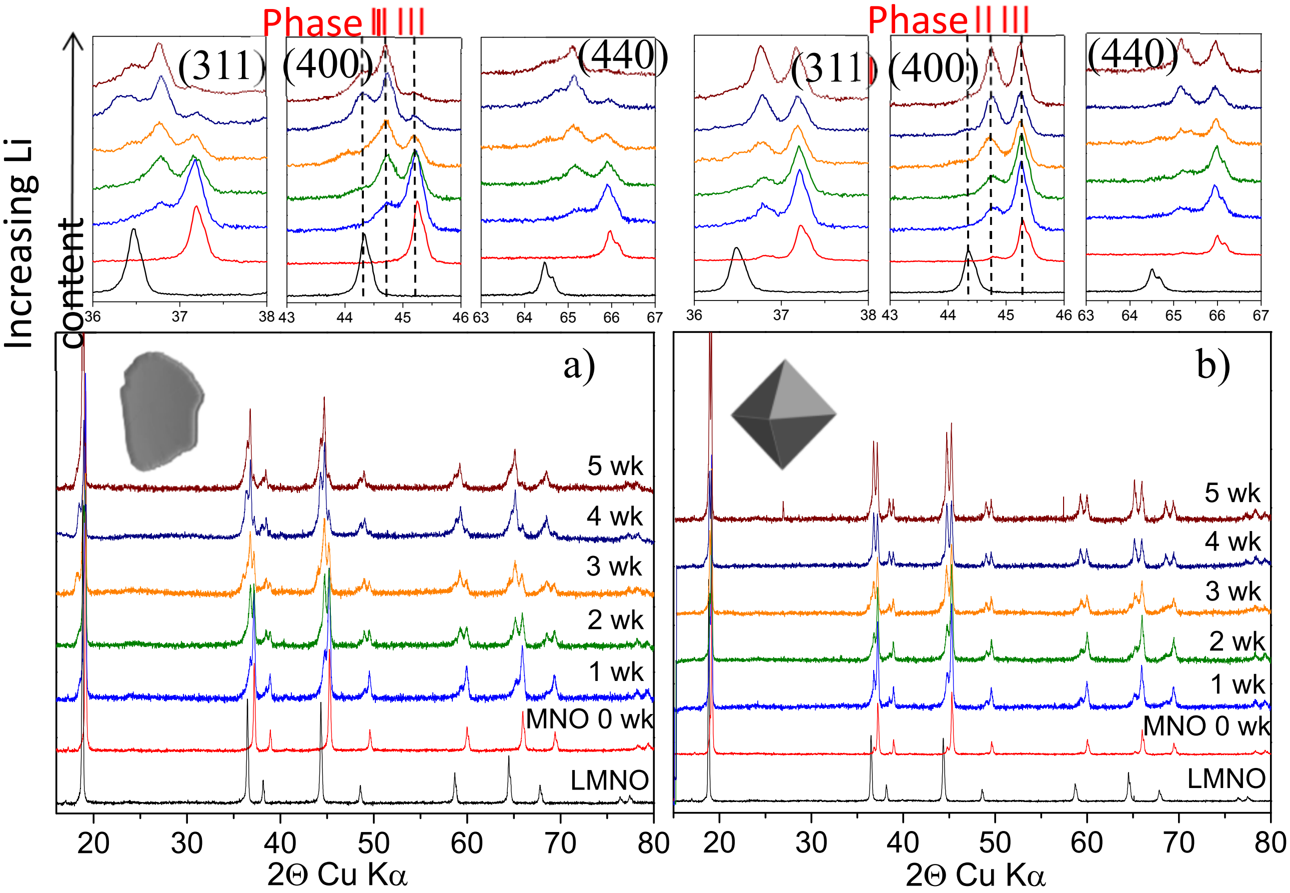

Figure V - 17: Evolution of the XRD patterns and the expanded view of (311), (400) and (440) peaks during room-temperature storage of fully delithiated LMNO in the electrolyte: a) plates and b) octahedrons

Solid solution in Ni/Mn spinel system: In the intercalation materials, single-phase transformation is considered kinetically advantageous over the two-phase process but the characteristics of solid solutions are largely unknown, largely hindered by their metastable nature. In the ordered LMNO, *in situ* XRD studies revealed a solid solution process at low state of charge (estimated Li content of $0.59<x<1$, Figure V - 19a), but the effort to isolate the single phases was unsuccessful. As shown in the *ex situ* XRD patterns collected on the cathodes recovered from partially charged cells, two-phase mixtures instead of single phases were obtained in Li_xMNO with a Li content of $0.7<x<1$ (Figure V - 19b). Nearly identical mixtures were obtained when Li was removed either by an electrochemical or chemical method (Figure V - 19c), suggesting that the solid solutions appearing during the *in situ* electrochemical charge and discharge are metastable transient intermediates that bear kinetic significance but are thermodynamically unstable.

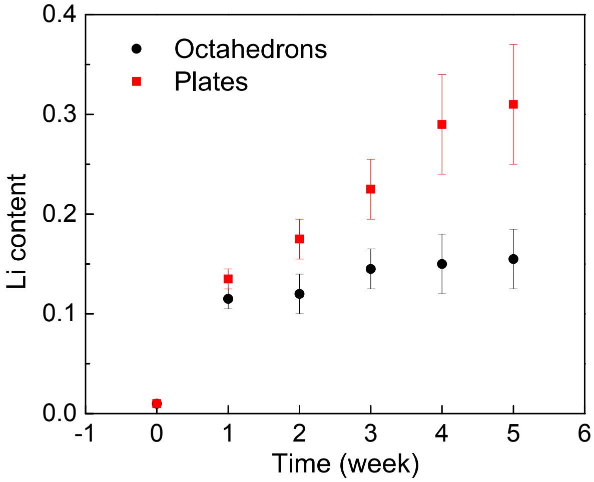

Figure V - 18: Li content in the crystal samples as a function of storage time

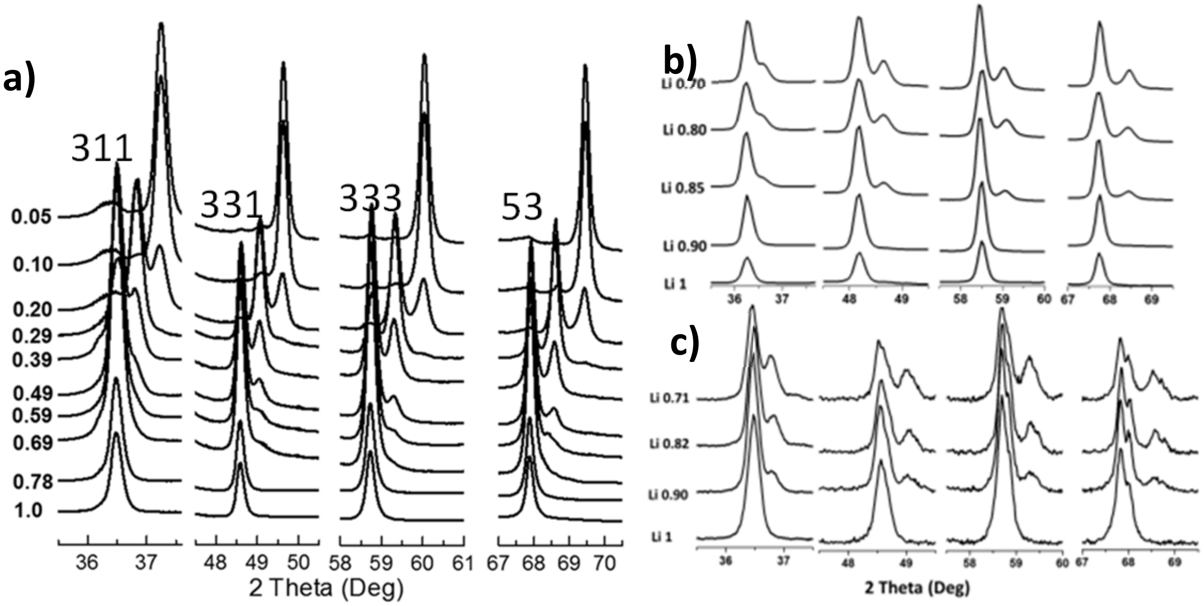

Figure V - 19: XRD patterns collected during: a) *in situ* electrochemical, b) *ex situ* electrochemical and c) chemical delithiation of LMNO

Efforts were directed to preparing solid solutions through thermal treatment, a technique that was successfully used in the synthesis of Li_xFePO_4 (Li_xFP) single phases at elevated temperatures. Temperature-controlled *in situ* XRD (TXRD) studies were performed to investigate the thermal behavior of Li_xMNO ($0 \leq x \leq 1$) and the synthesis of room-temperature solid solution intermediates that may lead to the understanding of their role in battery electrode performance. A series of delithiated Li_xMNO, with x=0.90, 0.82, 0.71, 0.51, 0.40, 0.25, 0.11, 0.06 and 0, were prepared by chemical oxidation with varying amounts of NO_2BF_4 in acetonitrile. The reactions resulted in a variety of mixtures among three cubic phases of Phase I, II and III: those with a Li content between 0.71 and 1 were composed of Phase I and II; those with a low Li content between 0 and 0.25 consisting of Phase II and III (with a dominant presence of Phase III); and those with an intermediate Li content between 0.25 and 0.71 were mixtures of all three cubic phases. The samples were subjected to heating and cooling in air at a rate of 5°C/min while collecting TXRD patterns at a step size of 25°C. The selected patterns from x=0.82, 0.25 and 0 are shown in Figure V - 20. In all cases, no significant changes were detected below 150°C. Between 150 and 225°C, the peaks from Phase I and II broadened and began to merge in x=0.82 (Figure V - 20a), with complete transformation into a single cubic phase observed at 225°C. In the fully delithiated sample composed of Phase III only (x=0, Figure V - 20c), a new spinel-type phase with expanded lattice dimensions appeared above 200°C, suggesting that Phase III is susceptible to thermal-induced phase conversion. Further characterization suggested that the process releases oxygen from the spinel lattice and triggers nickel reduction to a lower oxidation state as a compensation mechanism. For x=0.25, three components, Phase II, a new spinel-type phase and Phase III, were observed above 175°C (Figure V - 20b). At 225°C, the mixture was composed mostly of the spinel-type phase along with a small amount of remaining Phase III. The relationship between the lattice parameters of the phases present and the heating temperature is shown in Figure V - 21, established from the full-pattern Rietveld refinements of the TXRD patterns. It becomes clear that in samples with minimal presence of Phase III ($0.51 \leq x < 1$), the cubic lattice parameters grew closer to each other when the temperature is raised above 150°C which eventually became a single lattice parameter in the range of 200-250°C (Figure V - 21a).

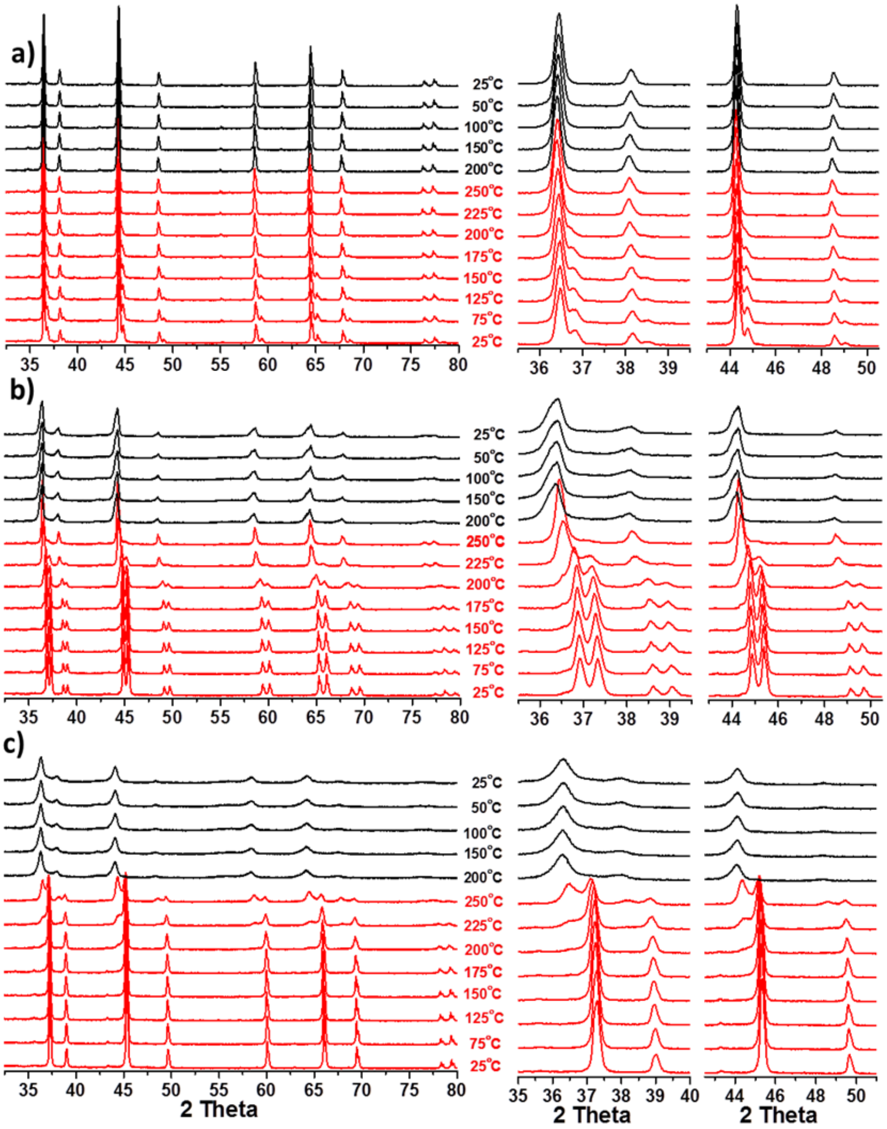

Figure V - 20: TXRD patterns of selected Li$_x$MNO crystal samples: a) x=0.82, b) x=0.25, and c) x=0

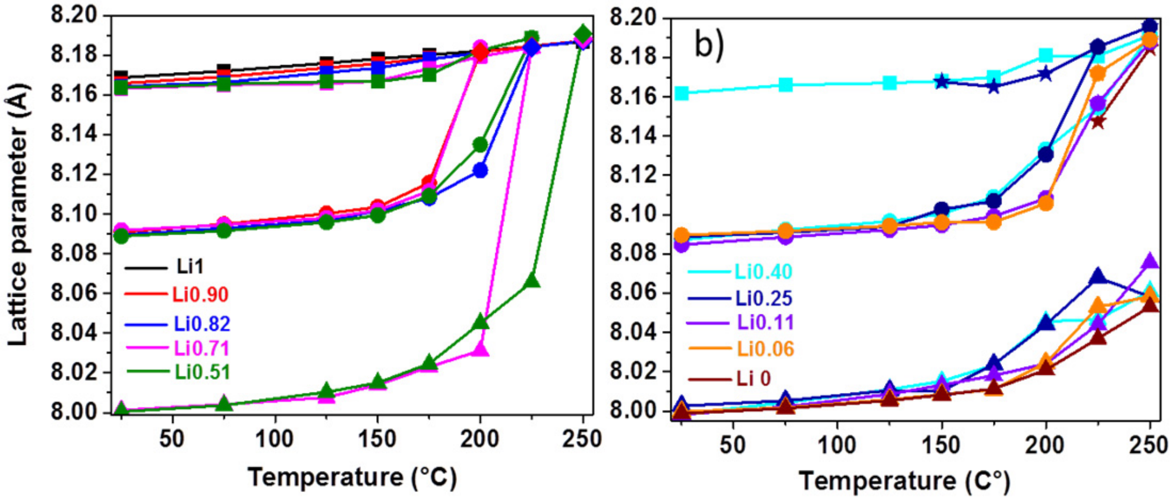

Figure V - 21: Changes in the lattice parameters upon heating the Li$_x$MNO crystal samples: a) 0.51≤x≤1 and b) 0≤x≤0.40. Phase I: square; Phase II: circle; Phase III: triangle; solid solution: diamond; spinel-type phase: star

The formed single phases remained phase pure after cooling to room temperature which rendered the isolation of Li$_x$MNO phases for the first time. For samples with 0<x≤0.40 that have a predominant presence of Phase III, the merge of the lattice parameters was not observed during heating (Figure V - 21b). Phase III remained in all samples even at 250°C, although its content was significantly reduced due to thermal decomposition. Although the miscibility gap between Phase I and II is reduced at elevated temperature, phase III decomposes before it can dissolve in either Phase I or II. Additional characterization by X-ray absorption and vibrational spectroscopies enabled us to further refine the structural evolution as functions of both Li content and temperature and the results are captured in the phase diagram shown in Figure V - 22.

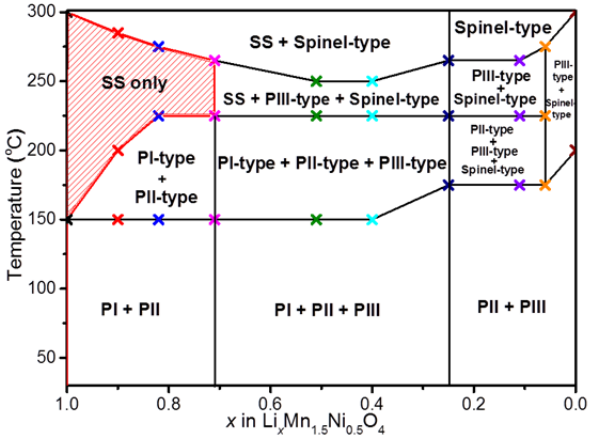

Figure V - 22: Phase diagram of Li$_x$MNO

The study clearly reveals the similarities in Li$_x$MNO and Li$_x$FP solid solutions: they are metastable in nature; they can appear as transient intermediates during electrochemical charge and/or discharge; and their formation is promoted by temperature. The former, however, appear to possess higher stability which rendered their isolation at room temperature. These findings pave the way for detailed evaluation of the properties of solid solution intermediates that may lead to the understanding of their kinetic role in intercalation electrode materials and the effect of phase transition mechanism in the performance of materials, both of which are long standing challenges.

Conclusions and Future Directions

In conclusion, the synthesis of oxide cathode crystals was explored using the low-temperature based solvothermal method and we evaluated the performance of the samples. The reactions at the electrode/electrolyte interface were characterized and the effect of surface facets on self-discharge during storage demonstrated. The thermal behavior of Li$_x$MNO was carefully investigated which led to the construction of a new phase diagram. Room-temperature solid solution intermediates in the Ni/Mn spinel system were isolated for detailed evaluation on their role in the performance of intercalation electrode materials.

Future work will characterize the properties of the Ni/Mn spinel solid solutions and illustrate the impact of phase transformation mechanism on rate capability. Focus will also be placed on the relationships between cathode surface properties and the interfacial reactivities between the electrode and the electrode. Controlled surface features, such as modified surface compositions and surface coatings, will be introduced to probe their effect on side reactions and interface stability at high operating voltages. Diagnostic techniques will be developed to further characterize the reactions and processes at the cathode-electrolyte interface relevant to cathode performance and stability.

FY 2014 Publications/Presentations

1. Duncan, H., Hai, B., Leskes, M., Grey, C. P., and Chen, G. (2014). “Relationships between Mn^{3+} Content, Structural Ordering, Phase Transformation and Kinetic Properties in $LiNi_xMn_{2-x}O_4$ Cathode Materials.” *Chemistry of Materials* (26); p. 5374.
2. Doeff, M., Chen, G., Cabana, J., Richardson, T. J., Mehta, A., Shirpour, M., Duncan, H., Kim, C., Kam, K, and Conry, T. (2013). “Characterization of Electrode Materials for Lithium Ion and Sodium Ion Batteries using Synchrotron Techniques.” *Journal of Visualized Experiments*. (81); p. e50594.
3. Boesenberg, U., Meirer, F., Liu, Y., Dell’Anna, R., Shukla, A., Tyliszczak, T., Chen, G., Andrews, J. C., Richardson, T., Kostecki, R., and Cabana, J., “Mesoscale Phase Distribution in Single Particles of $LiFePO_4$ Following Lithium Deintercalation.” *Chemistry of Materials* (25); p.1664.
4. Duncan, H., and Chen, G. (October 2013). “Morphology Design of High-Energy Cathode Materials for Rechargeable Li-Ion Batteries.” Presented at the Berkeley Energy and Resources Collaborative (BERC) Innovation Expo, Berkeley, CA. BERC poster award.
5. Duncan, H., Lux, S., Kostecki, R., and Chen, G. (October 2013). “Surface-Facet Dependent Reactivity between $LiMn_{1.5}Ni_{0.5}O_4$ and Carbonate Electrolytes.” Presented at The 224th ECS Meeting, San Francisco, CA.
6. Crumlin, E., Duncan, H., Chen, G., and Liu, Z. (October 2013). “Tender XPS studies of the interfacial reactivity between the high-voltage cathode, $LiMn_{1.5}Ni_{0.5}O_4$, and the electrolyte.” Presented at The 224th ECS Meeting, San Francisco, CA.
7. Kuppan, S., Duncan, H., and Chen, G. (March 2014). “Particle Design for Optimal Cathode Performance.” Presented at the Gordon Research Conferences, Ventura, CA.
8. Chen, G. (June 2014). “Design and Synthesis of Advanced High-Energy Cathode Materials.” Presented at the 2014 DOE Annual Merit Review and Peer Evaluation Meeting, Washington, D.C.
9. Shukla, A. K., Ramasse, Q., Duncan, H., Darbal, A., Das, P. P., Ophus, C., Mendoza, J., Estrade, S., Yedra, L., and Chen, G. (September 2014). “Study of structure and defects in Li-rich layered oxide material for Li-ion batteries.” Presented at the International Microscopy Congress (IMC), Prague, Czech Republic.

V.B.5 Studies on High Energy Density Cathodes for Advanced Lithium-ion Batteries (ORNL)

Jagjit Nanda (Principal Investigator)
Oak Ridge National Laboratory

Materials Science & Technology Division
Oak Ridge, TN 37831
Phone: (865) 241-8361; Fax: (865) 574-4066
E-mail: nandaj@ornl.gov

Collaborators:
Dr. Rose Ruther and Dr. Hui Zhou, ORNL
Dr. Yijin Liu & Joy Andrews, SSRL, SLAC
Dr. Kang Xu, Army Research Laboratory

Start Date: October-2011
Projected End Date: Continuing

Objectives

- Mitigate technical barriers associated with current high voltage cathode compositions: lithium-manganese rich NMC and Mn-Ni 5V spinel.
- Implement new diagnostic techniques to correlate electrode crystal structure and morphology with electrochemical performance.
- Develop a mechanistic understanding of how local inhomogeneity leads to cell degradation, using state-of-the-art characterization methods.
- Design new synthesis techniques for high capacity lithium-ion electrodes and approaches for interfacial modification.

Technical Barriers

This project addresses the following technical barriers as described in the USDRIVE and USABC goals: (i) performance: high energy density cells for plug-in electric vehicles (PEVs), such as 40 mile PHEV and beyond; (ii) life: 5,000 deep discharge cycles over the battery life for PEVs; and (iii) safety: thermally stable and abuse tolerant.[1,2]

Technical Targets

- PHEV specific energy targets (pack): 3.4 (min) to 11.6 (max) kWh[1].
- EV specific energy targets (pack): 80 (min) to 200 (max) Wh/kg[2].

Accomplishments

- We developed TXM-XANES methods to monitor and evaluate the Mn oxidation state and change in the morphology of LMR-NMC cathode particles under high voltage cycling. The study directly correlates the oxidation state of transition metal cations to the electrochemical signature of voltage fade observed through differential capacity measurements.
- We used Raman imaging/mapping of pristine, charged, and cycled LMR-NMC electrodes to measure (i) the structural degradation of the active materials under cycling, (ii) carbon distributions, and (iii) degradation of the conductive diluent (carbon) at strongly oxidizing potentials (> 4.5 V).
- We synthesized and characterized a new high capacity 4 V Li-ion cathode composition ($Li_2Cu_xNi_{1-x}O_2$) with initial capacities exceeding 200 mAh/g.

* * * * *

Introduction

Current R&D efforts in lithium-ion batteries are directed towards increasing their energy density while reducing cost and improving cycle-life and safety performance. Among other important factors, developing high energy density lithium-ion cathodes is a high priority research area. Recently, there has been significant progress made on a number of high voltage cathode chemistries such as Mn-Ni spinel cathodes, $LiMn_{1.5}Ni_{0.5}O_4$, and LMR-NMC.[3-6] Nevertheless, significant materials and cycle life technical challenges still need to be addressed for meeting automotive applications. These include (i) structural and phase stability of cathode materials under continuous high voltage cycling (>4.5V) (ii) Mn dissolution leading to capacity fade (iii) electronic and ionic transport limitations, and (iv) first cycle irreversible capacity loss (ICL) due to interfacial issues and oxygen loss. To address these technical barriers, we have studied pristine and cycled LMR-NMC material using various spectroscopic and microscopic methods to correlate the observed capacity and/or voltage fade behavior to their structural and morphological changes. Other efforts include development of high capacity cathode materials that are not lithium and manganese rich. The current effort is directed towards high capacity Cu-Ni phases having composition $Li_2Cu_{1-x}Ni_xO_2$, where x = 0.3-0.6.

Approach

High voltage LMR-NMC cathode materials having nominal composition $Li_{1.2}Mn_{0.525}Ni_{0.175}Co_{0.1}O_2$ were obtained from the pilot scale production facility of Toda-Kogyo Corporation, Japan. Cathode powders were fabricated into electrodes using the slurry coating method with PVDF binder (Sigma-Aldrich) and carbon diluent (super-P, Timcal). The electrodes were assembled in the form of half cells (Li-metal as counter electrode) or full cells using modified graphite powders obtained from Philips-66 using the standard ABR protocol. Local state-of-charge (SOC) studies on high voltage LMR-NMC electrodes were undertaken to correlate local structure with electrochemical properties. We employ techniques with both high spatial resolution and large field of view to understand and mitigate factors that lead to voltage fade and capacity loss in LMR-NMC. The methods include (i) micro-Raman mapping of high voltage cathodes to measure surface SOC inhomogeneity (if any) under continuous electrochemical duty cycle, (ii) X-ray imaging and spectroscopy (XANES) combined with 3D elemental mapping (tomography) and (iii) electron microscopy and ICP studies to monitor transition metal (TM) oxidation state, migration, and dissolution which lead to voltage fade and degradation.

Results

Quantifying the morphological changes, transition metal segregation, and phase redistribution in cycled high voltage LMR-NMC cathodes

In last year's annual progress report, we described 2D TXM-XANES analysis of LMR-NMC cathode materials that provided important information about the oxidation state evolution of Mn during repeated high voltage charge/discharge cycles. However, true 3D mapping is needed to distinguish the chemical heterogeneities and to fully characterize processes related to degradation of cathode performance. For this reason, 3D tomography was performed on electrode materials that were cycled once (1×) and two hundred times (200×) between 2.0 and 4.9 V. Details regarding the tomographic reconstructions are described in a journal publication.[7] More than 60 cathode particles in each group of samples were investigated, providing good statistics for the evaluation of morphological changes over electrochemical cycling. To interpret the observed changes, we evaluated the morphological complexity of individual cathode particles using tomography data collected with monochromatic X-rays at 6630 eV (90 eV above the Mn K-edge).

We used a dimensionless parameter, $\varepsilon = V^{1/3}/S^{1/2}$ (where V is the solid volume of the particle and S is the total surface area of the solid phase), to quantify morphological complexity of the cathode particles. For comparison, the ε values for a few standard 3D solid objects are shown in Figure V - 23e, illustrating that more 'complex' objects have smaller ε values. A plot of ε versus particle radius for more than 120 of the LMR-NMC particles (Figure V - 23e) scanned in our experiments from the 1×-cycled (green) and 200×-cycled (red) electrodes shows a wide range of ε values. It is important to clarify here that the particles are certainly not regularly shaped and the 'radius' mentioned is an averaged estimation using the formula $r = (3V/4\pi)^{1/3}$, in which V is the volume of the particle disregarding any internal macropores.

The plot in Figure V - 23e shows a clear separation in morphology of the 1×-cycled particles and the 200×-cycled particles. The particles that have been cycled only once have ε values varying between 0.45 and 0.3, with a median value close to 0.4. In the case of the 200×-cycled cathode particles, the ε value ranged between 0.35 and 0.2, indicating much larger deviation from spherical morphology for the secondary particle aggregates. This suggests that, during repeated charging and discharging, the electrode particles undergo internal stresses that could lead to events such as change in their internal porosities, amorphization, cracking, or fracture, affecting both internal as well as external morphologies.

It is also of great interest to correlate the changes in particle morphologies as they evolve under electrochemical cycling with their spatial elemental distribution in three dimensions. Figure V - 24 shows the 3D renderings of selected particles from the pristine (Figure V - 24a), 1×-cycled (Figure V - 24b), and 200×-cycled (Figure V - 24c) electrodes with elemental concentration color-coded (color legend shown in the inset).

The corresponding pie charts show the elemental TM associations in the cathode particles. In the pristine LMR-NMC particle, we notice about 76% Mn-Co-Ni association, indicating a majority phase as layered NMC. In addition, about 20.6% of the voxels in the pristine particle contain Mn-Ni; the rest of the phases occupy only ~3% of the total voxels. After the first full cycle, we expect activation of the Li_2MnO_3 component, leading to a final discharged phase, predicted to be a mixture of $Li_{1.2-y}(MnCoNi)O_2$ and Li_yMnO_2 phases [52]. Interestingly, we observe 8% as a pure Mn-based phase, in addition to 44% Mn-Co-Ni, 31% Mn-Ni and 12% Mn-Co. In the 200×-cycled particle, the Mn-Co-Ni phase drops down to ~37%, while the pure Mn- and Ni-based phases rise to ~10% each with minimal pure Co-based phase (~1%).

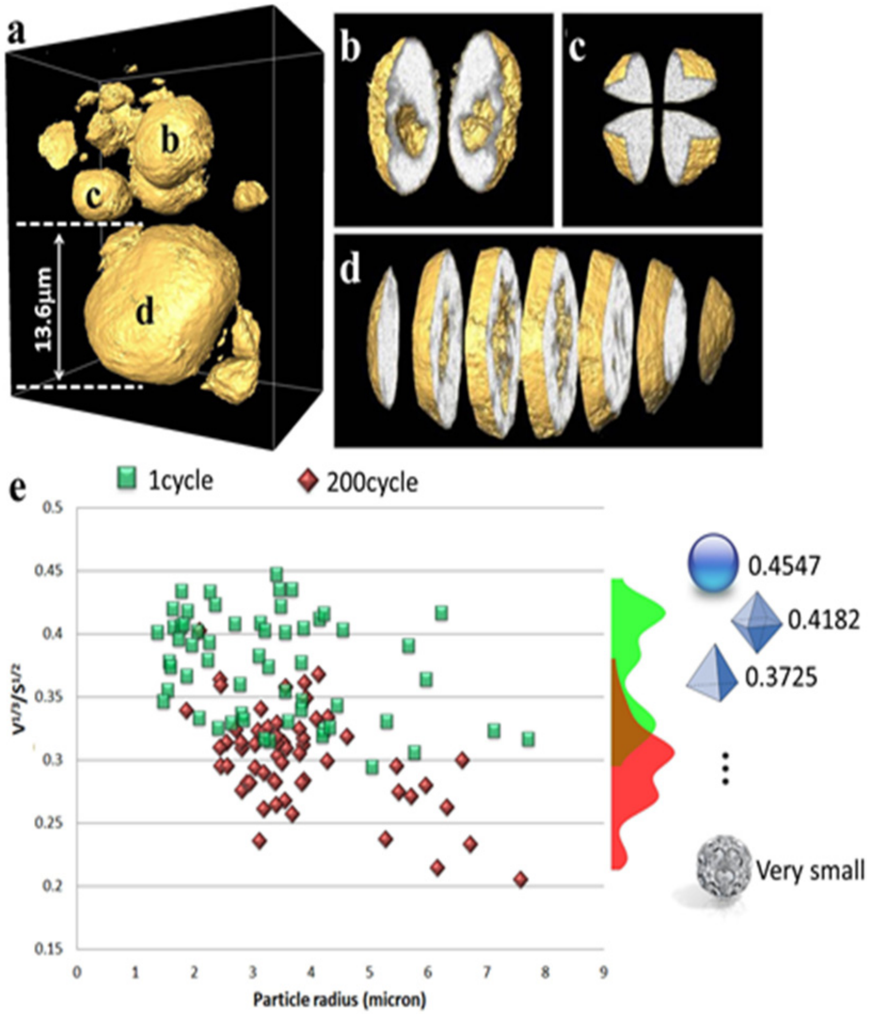

Figure V - 23: Three dimensional morphology of cycled particles and corresponding statistical analysis. Panel a: A selection of typical particles from the 1×-cycled electrode from tomography data acquired at 6630 eV. Panels b, c, d: Views of several particles magnified and virtually sliced/cut, indicating different types of morphology (solid and hollow). Panel e: A plot of ε parameter versus particle radius for two groups of particles cycled 1× (green) and 200× (red), indicates that the surface area of the particle structure increases with cycling. A histogram of the data points is plotted on the right hand side of panel e, along with a few selected standard geometric objects and their ε values for comparison

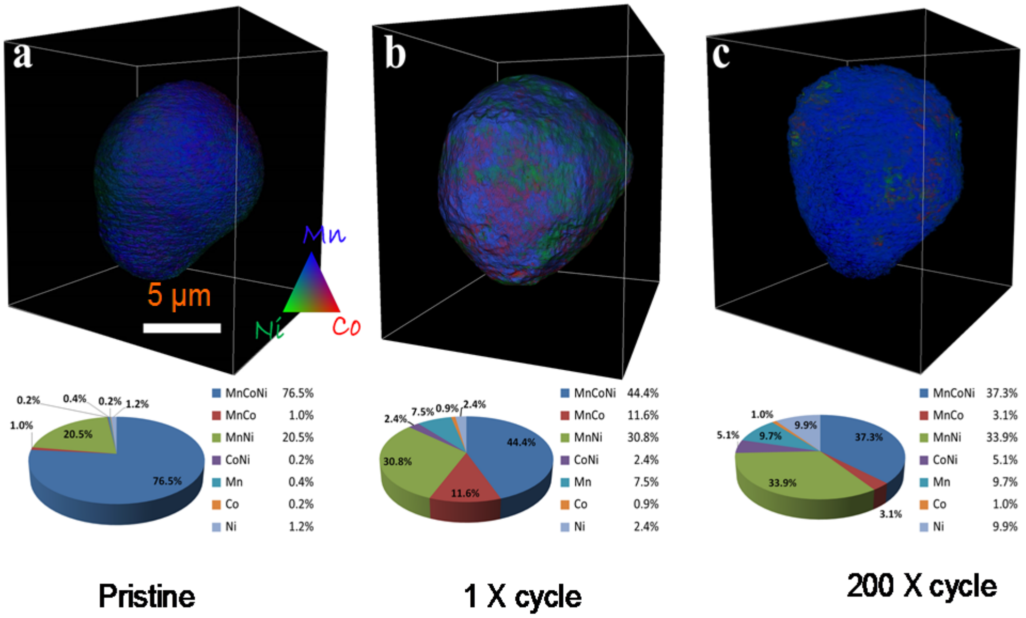

Pristine 1 X cycle 200 X cycle

Figure V - 24: 3D rendering of a selected cathode particle from (a) pristine, (b) 1×-cycled, and (c) 200×-cycled electrodes with elemental distribution resolved from tomography above and below the K-edges of Mn, Co and Ni. The color legend represents relative concentrations of the TM elements

State of charge (SOC) variation of LMR-NMC cathodes and their structural evolution: Raman microscopy studies

Raman spectroscopy is a powerful tool to monitor the crystal chemistry and correlate phase changes with electrochemical behavior.[8] While several groups have reported Raman spectra of lithium rich TM oxides, the data show considerable variability in terms of both the vibrational features observed and their interpretation. In this study, Raman microscopy is used to investigate lithium-rich and manganese-rich TM cathodes as a function of voltage and electrochemical cycling at various temperatures.

The Raman spectrum of LMR-NMC changes considerably when the electrode is charged and lithium is removed from the lattice. Figure V - 25 shows spectra from electrodes which were charged to different cut-off voltages during the first cycle charging. The electrodes were held at the cut-off voltages for 24 h prior to cell disassembly. The spectra are averaged over several particles derived from different regions of the electrode. The spectra of LMR-NMC at different states of charge show many broad overlapping bands which cannot be resolved uniquely. Nonetheless, the spectra show similar trends upon delithiation as the parent $LiMO_2$ and Li_2MnO_3 phases. Up to 4.5 V, the Raman modes of LMR-NMC tend to shift towards lower energy (Figure V - 25b). This corresponds to oxidation of the transition metals and an increase in the *c*-lattice parameter. The Raman spectrum of $LiCoO_2$ shows the same behavior with charging. Beyond 4.5 V, the Li_2MnO_3 component becomes activated and the LMR-NMC bands shift back to higher energy.

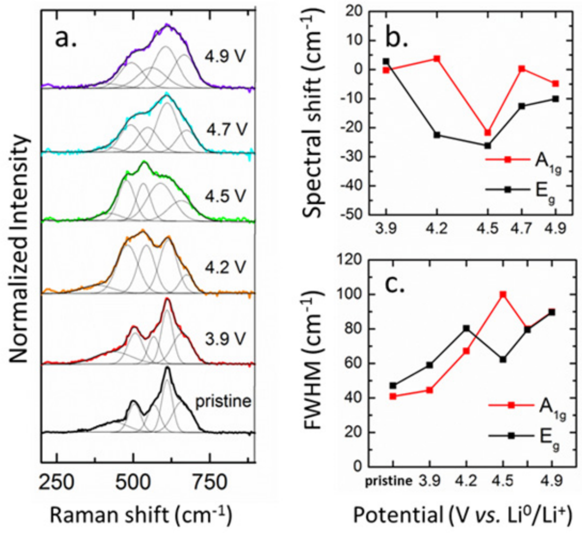

Figure V - 25: (a) Average Raman spectra of LMR-NMC cathodes charged to different cut-off voltages during the first cycle. (b) Shift of the A1g and Eg modes with respect to the pristine material as a function of voltage. (c) FWHM of the A1g and Eg modes as a function of voltage

This corresponds to extraction of lithium from the transition metal layers and a decrease in the *c*-lattice parameter. Similar high energy shifts are observed when Li_2MnO_3 is charged from 4.4 to 4.7 V. The LMR-

NMC bands also tend to become broader with charging (Figure V - 25c), likely due to increasing disorder, as has been observed previously for $LiCoO_2$ and Li_2MnO_3. We have also monitored the changes in Raman spectra of LMR-NMC cycled at 60°C. Results are reported in a journal article.[9]

Investigation on high capacity cathode composition: $Li_2Cu_xNi_{1-x}O_2$

In our search for stable high capacity (energy) cathodes for lithium-ion that are not manganese rich, we are in the process of screening other TM cathode oxide or phosphate compositions based on theoretical modelling predictions. One of the compositions under investigation is the two lithium Cu-Ni oxide having nominal composition $Li_2Cu_xNi_{1-x}O_2$ with x= 0.4-0.6.[10,11] Figure V - 26 shows preliminary electrochemical results of a stabilized composition $Li_2Cu_{0.5}Ni_{0.5}O_2$ synthesized using a solid-state route. The cathode composition shows an initial capacity in the range of 250 mAh/g. The electrochemical performance can be improved by reducing the particle size, which is in the range of 10 microns. We are also pursuing other approaches such as TM dopants or substituents that will stabilize the lattice upon lithium removal.

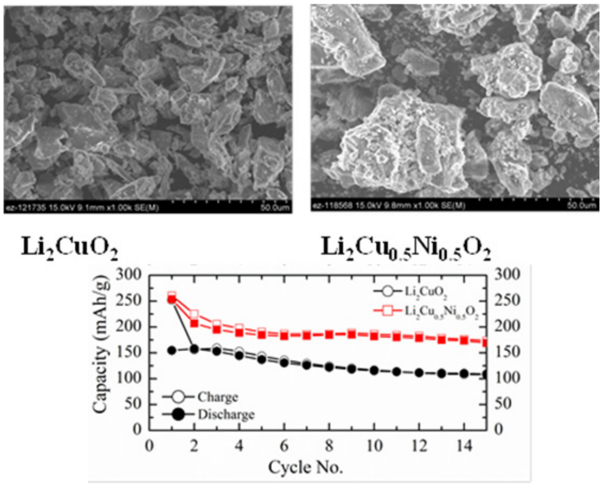

Figure V - 26: (Upper panel) SEM picture of as-synthesized Li_2CuO_2 and $Li_2Cu_{0.5}Ni_{0.5}O_2$ cathode materials. (Lower panel) Initial charge-discharge capacity of Li_2CuO_2 (black) and $Li_2Cu_{0.5}Ni_{0.5}O_2$ (red)

Conclusions and Future Directions

We have provided fundamental understanding and insights into the phenomenon of “voltage fade” in high voltage LMR-NMC cathode compositions using TXM-XANES and Raman microscopy. XANES tomography of cycled LMR-NMC electrodes provided a quantitative estimate of the extent of TM phase segregation compared to pristine material. Tomography analysis also provided direct evidence of changes in cathode particle morphology and densification as they were cycled. Raman spectroscopy of lithium-rich NMC cathode provides unique structural information which bridges the length scales probed by X-ray and neutron diffraction (bulk) and electron diffraction (nanoscale). Upon charging, the spectra evolve in a manner similar to the parent $LiMO_2$ and Li_2MnO_3 phases with shifts in the vibrational modes that correspond to changes in the *c*-lattice parameter. Finally, preliminary work is in progress to stabilize high capacity cathode materials belonging to $Li_2M^IM^{II}O_2$ and $Li_2M^IM^{II}O_3$ where M^I and M^{II} are TMs anionically coupled to oxygen. Work is continuing to stabilize the high capacity cathode composition $Li_2Cu_xNi_{1-x}O_2$ (x = 0.4-0.6) with choice of appropriate TM dopant.

FY 2014 Publications/Presentations

1. Jagjit Nanda, 2014 DOE Annual Peer Review Meeting Presentation, May 2014, Washington DC.
2. Nanoscale Morphological and Chemical Changes of High Voltage Lithium-Manganese Rich NMC Composite Cathodes with Cycling, F. Yang, Y. Liu, S. K. Martha, Z. Wu, J. C. Andrews, G.E. Ice, P. Pianetta, J. Nanda, Nano Letts. 2014, 14, 4334.
3. Raman Microscopy of Lithium-Manganese-rich Transition Metal Oxide Cathodes, R. E. Ruther, A. F. Callender, H. Zhou, S. K. Martha and J. Nanda,. Journal of the Electrochemical Society, 162 (1) A1-A5 (2015).
4. Role of Surface Functionality on the Electrochemical Performance of Silicon Nanowire Anodes for Rechargeable Lithium Batteries, H. Zhou, J. Nanda, S. K. Martha, R. R. Unocic, H. M. Meyer III, Y. Sahoo, P. Mickiewicz, T. F. Albrecht, ACS Appl. Mater. Interfaces, 2014, 6 (10) 7607.
5. Direct Synthesis and fabrication of $C\text{-}Si\text{-}SiO_2$ Monolithic Composite Electrodes Comprised of Lignin-derived Carbon Fibers Embedded with Silicon, O. Rios, S. K. Martha, M. A. McGuire, Wyatt Tenhaeff, K. More, C. Daniel, J. Nanda, Energy Technology 2014, DOI: 10.1002/ente.201402049.
6. Artificial SEI to Address the Electrochemical Degradation of Silicon Electrodes, J. C. Li, N.J. Dudney, J. Nanda and C. Liang, ACS Appl. Mater. Interfaces 2014, 6, 10083.
7. Multiscale Neutron and X-Ray Tomographic Studies on High Capacity Lithium Battery Chemistries, J. Nanda et al., ACS Fall Meeting August 10-14 2014 San Francisco, CA, U.S. (Invited).
8. Raman Mapping Study of Inhomogeneity in Lithium-Manganese-Rich Cathode Particles, J. Nanda R. Ruther, A. Callendar and H. Zhou,

Gordon Conference on Batteries,, March 2014, Ventura, CA, U.S.

9. Nanoscale XANES Tomography of Lithium-ion Electrodes: Bridging between Chemical State & Morphology, J. Nanda, F. Yang, Y. Liu, S.K. Martha, G. E. Ice, J. Andrews. Gordon Conference on Batteries,, March 2014, Ventura, CA, U.S. (Invited).
10. Local State-of -Charge Inhomogeneities in Charged and Cycled High Capacity Lithium-Manganese-Rich Composite Cathodes, Rose E. Ruther, Andrew F. Callender, Hui Zhou, Robert Kostecki, and Jagjit Nanda, 226th ECS Meeting October 5-9th 2014, Cancun, Mexico.
11. Local State of Charge Mapping and Analysis of Lithium-Manganese Rich NMC High Voltage Electrodes, J. Nanda R. Ruther A. Callendar, H. Zhou, ECS Spring Meeting, May11th-16th, 2014, Orlando, FL, U.S.
12. First-principles investigation of the structural changes in Li-rich cathode composites, H. Dixit, Wu Zhou, J.C. Idrobo J. Nanda and V. Cooper, APS March Meeting, March 2-7th 2014, Denver, CO, U.S.

References

1. Battery Test Manual For Plug-In Hybrid Electric Vehicles, Rev. 1, June 2010, INL/EXT-07-12536.
2. USABC Electric Vehicle Battery Test Manual, 2011.
3. Li, J. C.; Baggetto, L.; Martha, S. K.; Veith, G. M.; Nanda, J.; Liang, C. D.; Dudney, N. J. *Adv. Energy Mater.* **2013**, *3*, 1275.
4. Martha, S. K.; Nanda, J.; Veith, G. M.; Dudney, N. J. *J. Power Sources* **2012**, *216*, 179.
5. Martha, S. K.; Nanda, J.; Kim, Y.; Unocic, R. R.; Pannala, S.; Dudney, N. J. *J. Mater. Chem. A* **2013**, *1*, 5587.
6. Li, Y.; Bettge, M.; Polzin, B.; Zhu, Y.; Balasubramanian, M.; Abraham, D. P. *J. Electrochem. Soc.* **2013**, *160*, A3006.
7. Yang, F.; Liu, Y.; Martha, S. K.; Wu, Z.; Andrews, J. C.; Ice, G. E.; Pianetta, P.; Nanda, J. *Nano Lett.* **2014**, *14*, 4334.
8. Baddour-Hadjean, R.; Pereira-Ramos, J. P. *Chem. Rev.* **2010**, *110*, 1278.
9. Ruther, R. E.; Callender, A. F.; Zhou, H.; Martha, S. K.; Nanda, J. *J. Electrochem. Soc.* **2015**, *162*, A98.
10. Imanishi, N.; Shizuka, K.; Ikenishi, T.; Matsumura, T.; Hirano, A.; Takeda, Y. *Solid State Ionics* **2006**, *177*, 1341.
11. Love, C. T.; Dmowski, W.; Johannes, M. D.; Swider-Lyons, K. E. *J. Solid State Chem.* **2011**, *184*, 2412.

V.B.6 Lithium-Bearing Mixed Polyanion (LBMP) Glasses as Cathode Materials (ORNL)

Jim Kiggans (Principle Investigator)
Oak Ridge National Laboratory

P.O. Box 2008; MS 6087
Oak Ridge, TN 37831-6087
Phone: (865) 574-8863; Fax: (865) 574-4357
E-mail: kiggansjojr@ornl.gov

Andrew Kercher (Co-PI)
P.O. Box 2008; MS 6087
Oak Ridge, TN 37831-6087
Phone: (865) 576-5252; Fax: (865) 574-4357
E-mail: kercherak@ornl.gov

Start Date: June 2012
Projected End Date: June 2016

Objectives

- Synthesize mixed polyanion (MP) glasses for use as active cathode materials in Li-ion batteries.
- Demonstrate enhancement in electrochemical performance and key materials properties of glass cathode materials by tailoring the polyanion content.
- Produce MP glass cathode materials that undergo multi-valent transitions in the transition metal cations during electrochemical testing.
- Through laboratory-scale testing, demonstrate novel glasses with excellent overall cathode performance that are viable replacements for current cathode materials in electric vehicle applications.

Technical Barriers

MP glass cathode materials are being developed to address the key technical barriers of low energy density, poor high power performance, inadequate cycle life, safety, and high cost.

Technical Targets

- Produce an MP glass cathode with significantly greater capacity at high discharge rates than crystalline $LiFePO_4$.
- Develop an MP glass cathode material with at least 25% greater specific energy than $LiFePO_4$.
- Demonstrate multi-valent MP glass cathodes with specific capacities exceeding 200 mAh/g.

Accomplishments

- Glass-state conversion reactions have been demonstrated in iron, copper, and nickel-based glasses. X-ray absorption spectroscopy data confirmed the valence changes of the reactions.
- Through collaboration with Northwestern University, the voltages for hundreds of glass-state conversion reactions have been modeled using crystalline thermodynamic data from the Open Quantum Materials Database.
- Electrical conductivity measurements on a series of iron phosphate/vanadate glasses have directly shown a dramatic increase in electrical conductivity with increased vanadate content.
- Capacity fade and large hysteresis have been observed during the cycling of glass-state conversion reactions.

✧ ✧ ✧ ✧ ✧

Introduction

Polyanionic crystalline materials, such as $LiFePO_4$, are promising cathode materials for Li-ion batteries for electric vehicle applications, because they can have excellent safety and cycling performance due to their rigid covalently bonded structure. However, many polyanionic crystalline materials with theoretically excellent energy densities, such as $LiCoPO_4$, $LiFeBO_3$, and Li_2MnSiO_4, have not performed well as cathodes due to low electrical conductivity and/or crystal structure changes during cycling. Oak Ridge National Laboratory has proposed that mixed polyanion (MP) glasses can be excellent high capacity cathodes that can overcome the limitations of similar polyanionic crystalline materials.

Mixed polyanion glasses have three key advantages over similar polyanionic crystalline materials. First, with the proper choice of polyanion content, MP glasses can have higher electrical conductivities than similar polyanionic crystalline materials. For example, substitutions of molybdate or vanadate for phosphate in iron phosphate glasses have demonstrated increases in electrical conductivity by orders of magnitude. Second, the disordered covalently bonded structure of MP glasses limits the ability of the structure to rearrange, which holds the promise to prevent undesirable microstructural rearrangement during cycling. Third, the glass polyanion content can be tailored to produce cathodes with a maximized redox potential for a given electrolyte system. Changing the polyanion content of a polyanionic cathode material has been shown to change the redox potential due to the inductive effect of the polyanion (Isono, et al., J. *Power Sources*, 2010, 195: 593-598). Depending on the amount and electronegativity of the polyanion substituted in the glass, the voltage of a glass cathode could be increased or decreased to the desired optimal voltage.

Most polyanionic crystalline materials are phosphates, borates, or silicates. Phosphates, borates and silicates are renowned glass formers using conventional glass processing methods. Therefore, producing these novel glass cathode materials will not likely require exotic processing methods, but could be produced by low-cost conventional glass processing methods.

Approach

The research into MP glass cathode materials involves: (1) computational thermodynamic modeling, (2) glass processing, (3) glass structure and property characterization, and (4) electrochemical testing. Computational thermodynamic modeling of the electrochemical response of prospective MP glasses is being used to make decisions on the most promising glasses to pursue. Classical heat/quench glass processing has been the primary processing method. Characterization techniques are being used to confirm amorphous structure, to determine transition metal valences, and to measure fundamental glass properties. Electrochemical testing is being performed on coin cells with powdered glass cathodes produced by conventional slurry casting.

Results

Glass-state conversion reactions: In FY2013, a high capacity glass-state conversion reaction was unexpectedly discovered to occur during discharge of iron pyrophosphate/vanadate glass cathodes. Conversion reactions have not been previously reported in crystalline phosphate materials. Therefore, additional phosphate glasses were produced in hopes of discovering glass-state conversion reactions involving other transition metal cations at higher voltages.

Copper metaphosphate/vanadate (CMP50V) and nickel metaphosphate/vanadate (NMP50V) glasses were produced by splat quenching. Cathodes of both glasses demonstrated a high capacity electrochemical reaction at higher voltages than the previous iron pyrophosphate/vanadate glass. No significant intercalation reaction was observed in CMP50V or NMP50V. (See Figure V - 27.)

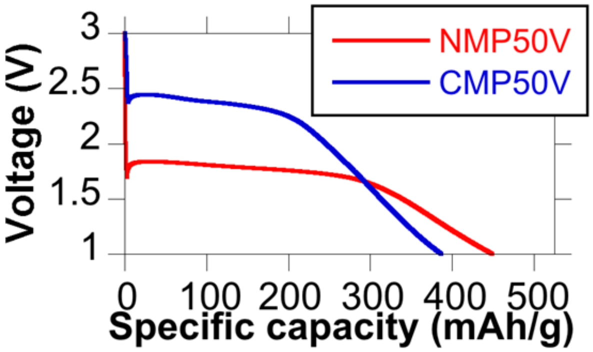

Figure V - 27: Copper (CMP50V) and nickel metaphosphate/vanadate (NMP50V) glasses demonstrate high-capacity glass-state conversion reactions

CMP50V and NMP50V glass cathodes at different electrochemical stages were analyzed *ex situ* by X-ray absorption spectroscopy (XANES) at the National Synchrotron Light Source at BNL in order to confirm and study the glass-state conversion reactions. XANES analysis was done in collaboration with Kyler Carroll, MIT. By comparing to Cu and Ni standards of known valence, transition metals in both glasses were shown to have 2+ cations at a fully charged state and fully reduced metal (0+) at a discharged state of 1V. A full reduction of transition metal cations to metal is consistent with a glass-state conversion reaction. Also, XANES at the Ni-K and V-K edges of charged, discharged, and recharged cathodes showed that the first cycle loss of NMP50V glass cathodes was primarily associated with an irreversible vanadium valence change. (See Figure V - 28.)

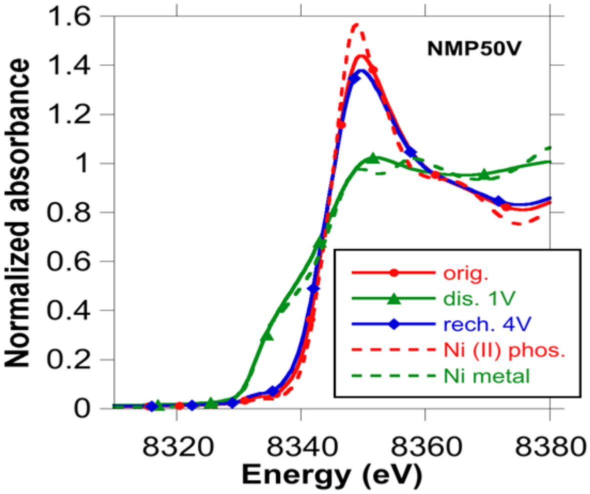

Figure V - 28: Ni-K edge XANES of nickel metaphosphate/vanadate (NMP50V) glass cathodes confirmed the Ni valence changes associated with a glass-state conversion mechanism

Thermodynamic modeling: Chris Wolverton's group at Northwestern University collaborated with the project team to predict the equilibrium voltages of hundreds of glass-state conversion reactions. Thermodynamic data from Northwestern's Open Quantum Materials Database was used to calculate the theoretical equilibrium voltages of polyanionic crystalline cathode materials as estimates of analogous polyanion glasses. This vast database of possible glass cathodes shows the effect of different polyanion structures, polyanion substitutions, and transition metal cations on glass cathode voltages. The predicted glass cathode voltages are being used to guide project decisions toward the most promising glasses. (See Table V - 1.)

Table V - 1: Predicted voltages, specific capacities, and specific energies of glass-state conversion reactions using thermodynamic data from Northwestern's Open Quantum Materials Database

	Predicted Voltage	Specific Capacity (mAh/g)	Energy density (mWh/g)
$Ir(PO_3)_3$	3.9 V	178	694
$Pd(PO_3)_2$	3.9 V	192	744
$Ru(PO_3)_3$	3.7 V	224	831
$Pd(P_2O_7)$	3.6 V	258	935
$Ag_3(PO_4)$	3.5 V	182	645
$Hg_3(PO_4)$	3.5 V	112	396
$Rh(PO_4)$	3.4 V	367	1244
$Hg_2(P_2O_7)$	3.4 V	177	599
$Cu_3(PO_4)_2$	3.3 V	380	1258
$Cu_2(PO_4)$	3.3 V	331	1079

Polyanion content effect on electrical conductivity: Based on literature measurements on glasses of similar composition, the electrical conductivity of iron phosphate glasses is expected to increase by orders of magnitude when vanadate is substituted into the glass. To confirm this effect in MP glass cathodes, electrical conductivity was measured on a series of iron metaphosphate/vanadate glass cathode materials. The conductivity specimens were as-produced glass splats with sputtered gold electrodes. The electrical conductivity of MP glasses increased by four orders of magnitude with vanadate substitution. (See Figure V - 29.)

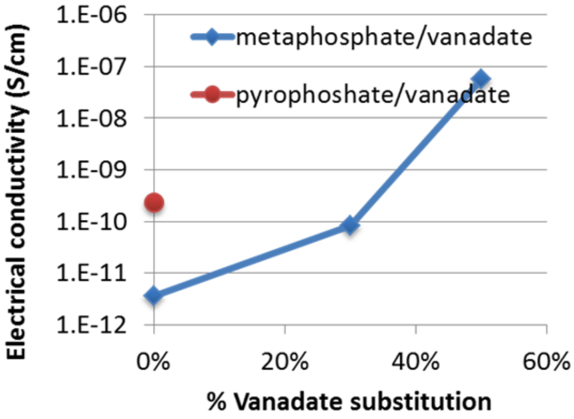

Figure V - 29: Electrical conductivity of iron phosphate glasses is strongly dependent on vanadate substitution

Cycling of glass-state conversion reactions: When they are electrochemically cycled, conversion reactions in crystalline oxides and halides typically exhibit substantial capacity fade and large hysteresis. Cycle testing was performed on glass cathodes to determine the cycling behavior of glass-state conversion reactions. For cycle testing on preliminary iron pyrophosphate glass cathodes with 0% and 50% vanadate substitution, large hysteresis and substantial capacity fade were observed. (See Figure V - 30.)

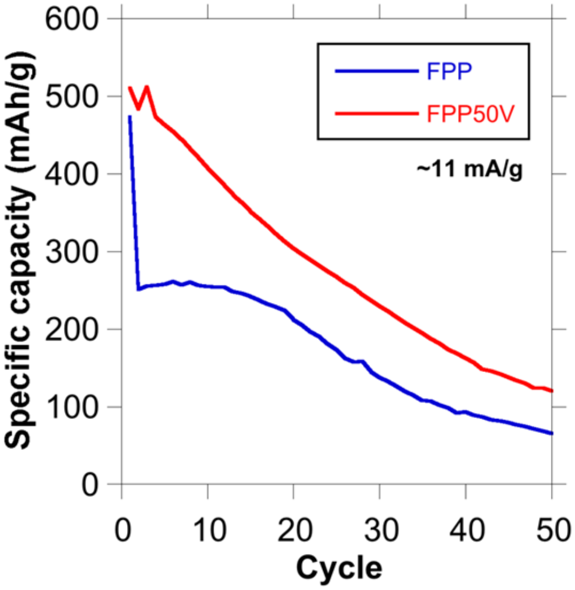

Figure V - 30: Substantial capacity fade was observed during cycle testing between 4V and 1 V of iron pyrophosphate glasses with 0% vanadate (FPP) and 50% vanadate (FPP50V) substitution

First attempts at multi-valent intercalation: Polyanion cathodes that can undergo multiple valence changes have the potential to exceed the specific energy of commercial cathodes by 40-80%. One potential multi-valent route is multi-valent intercalation. For polyanion materials, the predicted voltages of multiple valence changes for several cations (e.g., Mn, Cu, Sb, and V) fall within a reasonable electrolyte stability window (Hautier, et al., *Chemistry of Materials*, 2011, 23: 3495-3508).

Two MP glasses were produced that were theoretically capable of a multi-valent transition: a lithium copper metaphosphate/vanadate glass (LCMP50V) and a lithium manganese metaphosphate/vanadate glass (LMMP50V). The polyanion contents of these glasses were sufficient to balance the highest valence states of the cations. Unfortunately, neither glass exhibited an intercalation reaction with a significant capacity.

Conclusions and Future Directions

MP glass cathodes offer two potential routes to achieving high capacity: multi-valent intercalation and glass-state conversion. Both routes have demonstrated key challenges to their success. Multi-valent intercalation has not demonstrated close to theoretical capacity. Possible causes include insufficient electrical conductivity and low ionic diffusivity. Glass-state conversion reactions have poor cycling and large hysteresis. The mechanism of glass-state conversion reactions is not fully understood, but ionic diffusivity of the transition metal cations and lithium cations may have a strong effect.

Unlike most crystalline materials, large compositional variations are possible in glasses, which can produce large changes in key physical properties. The primary focus of future work is to improve the physical properties of MP glasses in order to produce cycleable high-energy cathodes. Glass compositions will be tailored to enhance electronic conductivity and ionic diffusivity, and these enhanced glasses will be electrochemically tested to look for improved performance. Secondly, because mechanisms for glass-state conversion reactions are not known, electron microscopy of *ex situ* MP glass cathodes will be used to better understand the structural changes and capacity fade of glass-state conversion reactions. Finally, MP glass research will move beyond phosphate/vanadate glasses and determine the possibilities in other glass systems (e.g., silicates, borates).

FY 2014 Publications/Presentations

1. Kercher, A.K, et al. (June 2014). “Lithium-bearing mixed polyanion (LBMP) glasses as cathode materials.” Presented at the 2014 DOE Annual Merit Review and Peer Evaluation Meeting, Washington, D.C.
2. Kercher, A.K, et al. (May 2014). “Mixed polyanion glasses as lithium ion battery cathode materials.” Presented at the 225th Electrochemical Society Meeting, Orlando, FL.

V.B.7 Development of High-Energy Cathode Materials (PNNL)

Ji-Guang Zhang
Pacific Northwest National Laboratory

Energy & Environment Directorate
902 Battelle Boulevard
Richland, WA 99352
Phone: (509) 372-6515; Fax: (509) 375-2186
E-mail: jiguang.zhang@pnnl.gov

Jie Xiao (Co-PI)
Energy & Environment Directorate
902 Battelle Boulevard
Richland, WA 99352
Phone: (509) 375-4598; Fax: (509) 375-2186
E-mail: jie.xiao@pnnl.gov

Start Date: October 2011
Projected End Date: September 2015

Objectives

- Develop high-energy cathode materials with improved safety.
- Develop low-cost synthesis routes for environmentally benign cathode materials with long cycle life.

Technical Barriers

High cost of materials and synthesis methods, limited energy density and cyclability, and safety.

Technical Targets

- Understand the failure mechanism of layered composite $xLi_2MnO_3\cdot(1-x)LiMO_2$ (M = Mn, Ni, Co; $0 \leq x \leq 1$).
- Investigate the interfacial properties between electrode and electrolyte by using standard thick Li-Mn-rich (LMR) cathode.
- Understand the synthesis-structure-performance relationship in LMR cathode.

Accomplishments

- Identified new synthesis method for LMR with significantly improved cycling stability though uniform elemental distribution at the atomic level.
- Confirmed the effects of new electrolyte additive on enhancing the cycling stability of thick LMR electrode.
- Identified functioning mechanism of AlF_3 coating on the LMR cathode materials.

✧ ✧ ✧ ✧ ✧

Introduction

Li-Mn-rich layered composites, for example, $Li[Li_{0.2}Ni_{0.2}Mn_{0.6}]O_2$, have attracted extensive interest because of their highest energy density among all cathode candidates in Li-ion batteries that can be employed for vehicle electrification. However, capacity degradation and voltage fading were usually observed in LMR due to the layered-to-spinel phase transition. Concurrently, oxygen was released from the lattice due to cation migration and reacted intensively with the electrolytes, generating insulating by-products. The end results were gradual voltage fade, limited rate performances, and poor capacity retention which prevented the practical application of LMR cathode material.

Approach

- Use advanced microscopic characterizations to investigate the phase transition of LMR during cycling.
- Use Hydrothermal-assisted solid synthesis to improve the uniform distribution transition metal(TM) cations in LMR.
- Use standard thick LMR cathode (supplied by ANL) to evaluate the effectiveness of electrolyte additive.

Results

Mitigation of voltage fade in cathode materials by improving atomic level uniformity of elemental distribution: For LMR cathode, both intrinsic phase transition and the surface parasitic reactions affected its electrochemical performances. While electrolyte additive may mitigate the side reactions, the internal structural evolution was difficult to modulate. It was found for the first time that the voltage and energy fade of LMR cathodes can be mitigated by improving the atomic level spatial uniformity of the chemical species. The samples with uniform atomic level spatial distribution demonstrate much better capacity retention and much smaller voltage fade as compared to those with significant non-uniform Ni distribution. The fundamental findings on the direct correlation between the atomic level spatial distribution of the chemical species and the functional stability of the materials may also guide the design of other energy storage materials with enhanced stabilities.

Three different synthesis routes, including traditional precipitation (CP), sol-gel (SG) method and hydrothermal-assisted (HA) solid-state methods, were adopted to prepare LMR cathode materials with the same stoichiometry of $Li[Li_{0.2}Ni_{0.2}Mn_{0.6}]O_2$. A new four-detector system (Figure V - 31a) was used in TEM to determine the local chemical species, in the bulk and at the surface, and quantitatively map of Mn, Ni, and O in these LMR particles. Both Mn (red) and O (blue) elements were uniformly distributed in all LMR prepared differently (Figure V - 31b - Figure V - 31d). However, the distribution of Ni (green) was not homogeneous in those prepared from co-precipitation (Figure V - 31b) and sol-gel methods (Figure V - 31c). The surface regions of LMR particles in Figure V - 31b and Figure V - 31c had enhanced contrast for Ni, implying a higher concentration of Ni on the surface. For LMR prepared from hydrothermal-assisted solid synthesis, Ni element showed much more uniform distribution without obvious aggregation on the particles surfaces.

To correlate the observed Ni-serration phenomenon to the LMR electrode performances, the electrochemical behaviors of LMR synthesized by three different approaches were further compared in Figure V - 32. The initial charge-discharge curves of the three LMR cathodes showed similar capacity and efficiency at C/10 rate between 2.0-4.8 V (Figure V - 32a). When the rate was increased to 1C, HA material began to show higher capacity retention at elevated current densities than those of CP and SG materials (Figure V - 32b). In terms of the cycling stability (Figure V - 32c), the differences became more obvious in these three LMR cathodes. Both CP and SG materials displayed fast capacity fading, while the HA material demonstrated very stable cycling with more than 95% capacity retention rate over 300 cycles. A closer inspection on the voltage profiles (Figure V - 32d, Figure V - 32e and Figure V - 32f) of the three LMR electrodes discovered that the voltage fading issue was also mitigated in HA material.

The atomic-level uniform TM cation distribution in LMR prepared by hydrothermal assisted method prevented the Ni-segregation that blocked Li^+ ion diffusion channels and enhanced the Ni-Mn interactions to stabilize crystal structure during repeated cycling. Therefore, the voltage fade issue of LMR was alleviated along with greatly improved cycling stability. This finding provided clues on the modification of synthesis approaches to improve the electrochemical performances of LMR series and was readily adaptable for mass production.

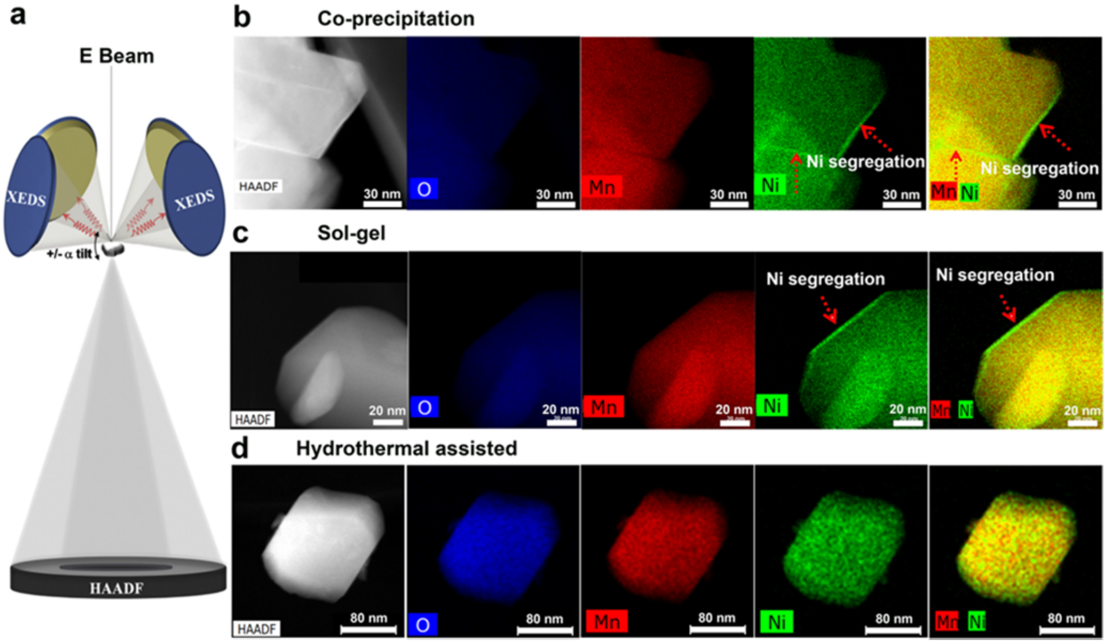

Figure V - 31: Z-contrast imaging and XEDS mapping of LMR prepared by different methods. (a) Schematic drawing of the newly developed four-detector system in a TEM, enabling efficient collecting of the EDS signal. Z-contrast images as well as XEDS maps of Mn, Ni and overlaid Mn/Ni maps of (b) coprecipitation-derived, (c) sol-gel method-derived and (d) hydrothermal-assisted method-derived LMR materials

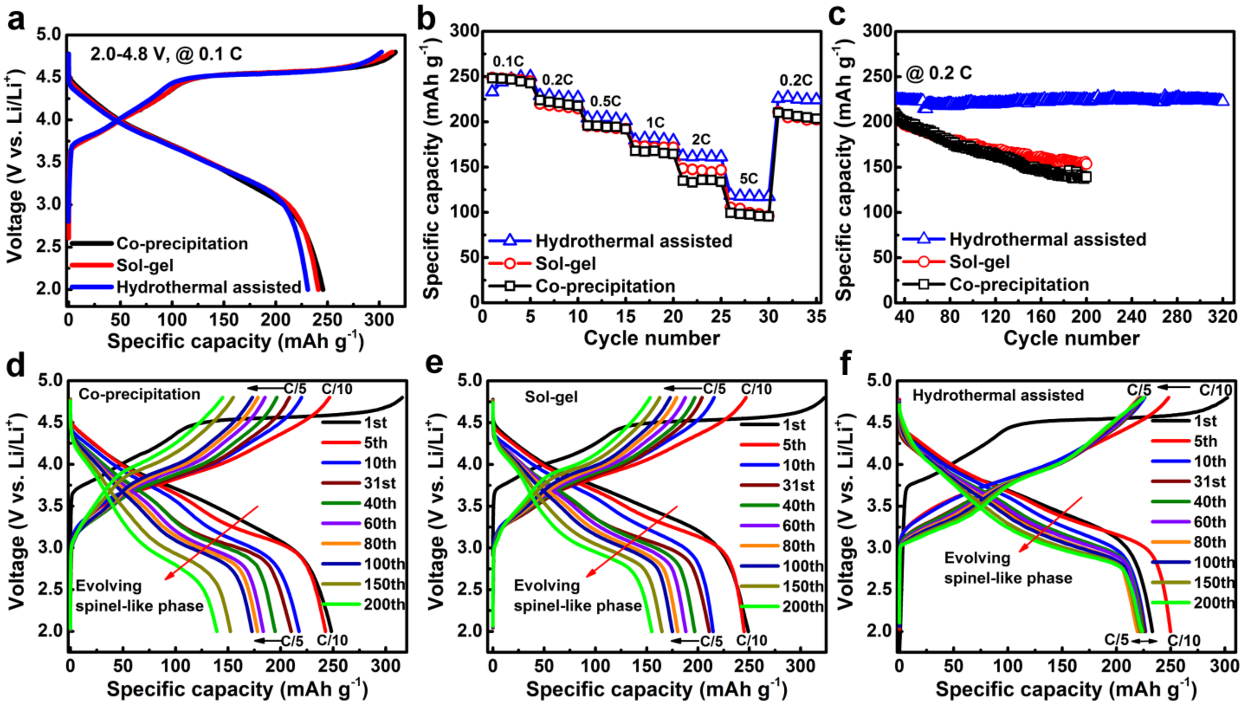

Figure V - 32: Charge/discharge characteristics of LMR cathodes prepared by different methods. (a) Initial charge/discharge profiles at C/10 in the voltage range of 2.0−4.8 V. (b) Comparison of rate performance. (c) Cycling performance at C/5 after rate performance tests. Corresponding charge/discharge profile evolutions of materials prepared by the (d) CP method, (e) SG method, and (f) HA method during the long-term cycling

Evaluation of electrolyte additive by using thick LMR electrode: It has been proved before that Tris (pentafluorophenyl) borane (($C_6F_5)_3B$, TPFPB)) can improve the cycling stability and mitigate the voltage fading of LMR when a thin electrode is used. In this work, the effectiveness of TPFPB additive was further evaluated by using a thick LMR electrode (supplied by ANL) and the testing protocol developed by ANL.

At a high LMR loading of 12.9 mg/cm^2, the first discharge capacity was still above 200 mAh/g for all the cells (Figure V - 33a). The addition of TPFPB did not change the voltage profiles during charge, consistent with previous report on TPFPB. During cycling, thick LMR baseline electrode decayed fast after only 50 cycles (Figure V - 33b). However, with 0.1M TPFPB, the stable cycling was extended to close to 100 cycles. In the presence of 0.2 M TPFPB, the capacity retention was further improved to 76.7% after 125 cycles, indicating that TPFPB is a promising additive to improve the electrochemical performance of LMR in the practical applications.Of note, based on 12.9 mg/cm^2 loading, C/3 translated to 1.08 mA/cm^2 which is detrimental to the lithium side during charge. In other words, the shortened cycling of thick LMR was caused by the anode side after extended cycling in half-cell testing.

The above results indicate that the proposed functioning mechanism for TPFPB e.g., the ability to modify the interfacial side reactions between LMR and electrolyte also works well in thick standard LMR electrodes and is worth further exploration for industry applications.

Functioning mechanism of AlF_3 coating on the Li- and Mn-Rich cathode materials: AlF_3 have been demonstrated to be one of most effective coating materials in enhancing the performance of high voltage cathode materials. However, the microstructural changes of materials with and without surface coating at different stages of cycling have not been systematically investigated to get insight on the improved performance. During the last year, aberration-corrected scanning/transmission electron microscopy (S/TEM) was combined with electron energy loss spectroscopy (EELS) to probe the atomic/electronic structure of uncoated and AlF_3-coated LMR cathode $Li_{1.2}Ni_{0.15}Co_{0.10}Mn_{0.55}O_2$ before and after high voltage cycling. The atomic contrast in high angle annular dark field (HAADF) STEM imaging identified the crystallographic structure changes in terms of stacking and ordering in the cycled particles while EELS chemical analysis revealed important electronic structure changes. Based on the results of S/TEM observations and the EELS characterization, a more profound understanding of the functioning mechanism of surface coating was obtained.

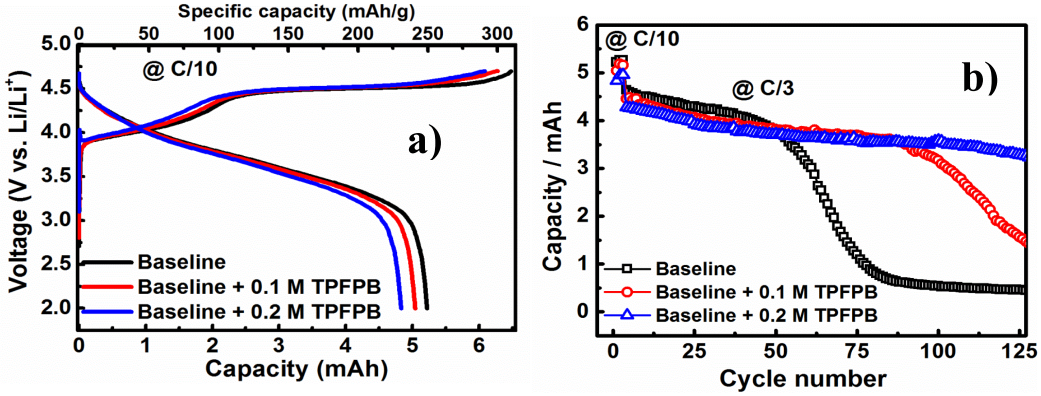

Figure V - 33: a) Charge-discharge curves and b) cycling ability of thick LMR electrode (LMR loading:12.9 mg/cm^2) supplied by ANL. Voltage range: 2.0-4.7 V, current: C/10 for 3 formation cycles followed by C/3 in the subsequent cycling (1C=250 mA/g)

Prior to the cycling, the bulk material is uniformly covered with an AlF_3 coating layer with a thickness of ca. 10 nm. O_2 molecules with much reduced activity can diffuse through the amorphous coating layer and lead to the suppressed decomposition of electrolyte. Figure V - 34 shows the S/TEM characterization results of uncoated material after 100 cycles. As shown in Figure V - 34a, there is a thick SEI layer (10~20 nm) formed on the particle surface owing to the aggressive side reactions occurring during each charge to high voltages, typically > 4.5 V. Accumulation of such a thick, poorly conducting SEI layer is one of the significant factors leading to the increase of cell polarization, fast capacity fading and poor rate capability of the LMR cathode materials. Figure V - 34 shows that the spinel-like structure is identified at surface regions over the whole particle of uncoated material after cycling. TEM image presented in Figure V - 34c as magnified from the green square in Figure V - 34b shows that the spinel-like structure well matches the [001] zone axis of a cubic spinel with Fd-3m space group. Formation of spinel-like phase is ascribed to the structural instability of LMR cathode material.

In contrast to that observed for uncoated material, there is no serious corrosion observed for the AlF_3-coated material after 100 cycles, as representatively shown in Figure V - 35a. Figure V - 35b indicates that the cathode material is still well protected by the AlF_3 coating layer, indicating that the dramatic surface reconstruction in the formation cycle and during the subsequent cycling does not destroy the AlF_3 surface coating. There is no thick SEI layer observed because the inert surface coating layer prevents direct contact between the electrode material and the electrolyte, which thus largely suppresses the side reactions between them. The amorphous coating layer, which is a good lithium-ion conductor after lithiation, can maintain the electrical contact between the bulk particle lattices separated by the microstreams. All of these advantages associated with surface coating guarantee the reversible Li-ion intercalation/de-intercalation, thus leading to significantly improved electrochemical performance.

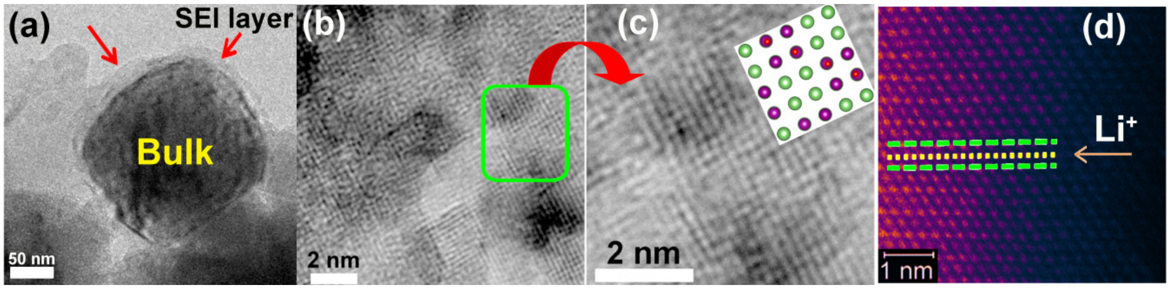

Figure V - 34: Characterization of uncoated material after 100 cycles. (a) TEM image showing a thick SEI layer formation. (b) TEM image showing the spinel formation distributed in nanoscale. (c) TEM image magnified from the green square in panel (b) showing cubic spinel lattice formation in this region; (d) High resolution Z-contrast image showing the formation of spinel-like phase at particle surface region

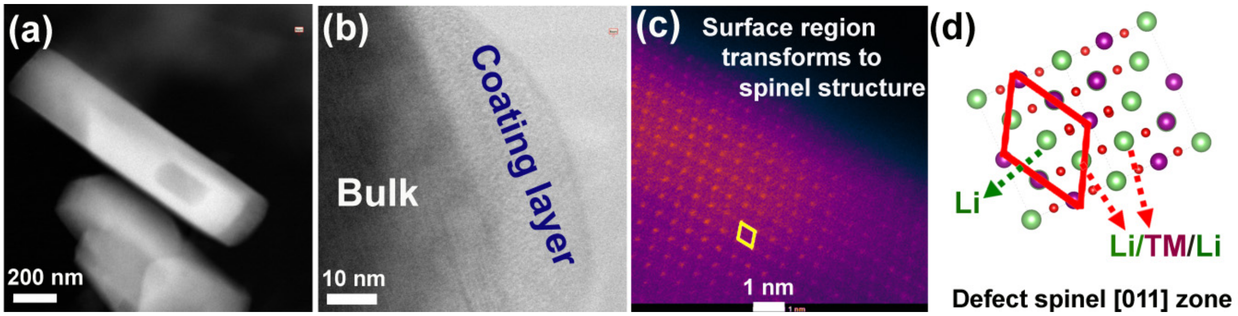

Figure V - 35: Characterization of AlF_3-coated material after 100 cycles. (a) Overview Z-contrast image of coated material after cycling. (b) TEM image showing that the surface region is protected by an AlF_3 coating layer. (c) Z-contrast image of the cycled particle. (d) Atomic model of the [011] zone projection of a cubic spinel with Fd-3m space group

Conclusions and Future Directions

The materials challenges in LMR cathode existed in both intrinsic irreversible structural changes and parasitic reactions on the surface caused by the oxygen release and electrolyte decomposition at high voltages. Improvement on the atomic uniformity of the elemental species throughout the whole crystalline particles was found to alleviate the voltage degradation and largely improves the cycling stability of LMR cathode. The LMR cathodes prepared by hydrothermal assisted method exhibits a much uniform distribution of cation species in LMR particles than those prepared by co-precipitation and sol-gel methods. As a result, the samples prepared by HA approach demonstrate much better capacity retention and much smaller voltage fade as compared to those prepared by other approaches.

Two approaches have been used to protect the surface stability of LMR cathode. TPFPB was proved to be an effective electrolyte additive to effectively mitigate the capacity loss of cathode by using thick LMR cathode and testing protocol developed at ANL. On the other hand, the fundamental mechanisms on the protection of LMR cathode byAlF_3 coating are also investigated. An AlF_3 coating layer prevents direct contact between the active material and the electrolyte, enhances structural stability of the electrode material, and mitigates the phase transformation from layered to spinel-like structure, therefore significantly improves the stability of voltage profiles during cycling.

Based on the knowledge obtained in FY14 on the failure mechanism of LMR cathode, future work will focus on improving the atomic level element uniformity of cathode materials and the performance of cathode. This new approach will be further explored to improve the performance of both $Li(Ni_{0.2}Mn_{0.6}Li_{0.2})O_2$ (LMR) and $LiNi_{1/3}Mn_{1/3}Co_{1/3}O_2$ (NMC). Various synthesis approaches and conditions will be investigated to improve the distribution of different transition metal cations in LMR and NMC at the atomic level. The synthesis conditions and surface coatings will be optimized to enable the stable operation of NMC cathode at higher voltages to increase its usable energy density while still maintaining its structure integrity and long lifespan.

FY 2014 Publications/Presentations

1. Zhang, J.-G., and Xiao, "Development of High Energy Cathode Materials." Presented at the 2014 DOE Annual Merit Review and Peer Evaluation Meeting, Washington, D.C.
2. Zheng, J., Gu, M., Genc, A., Xiao, J., Xu, P., Chen, X., Zhu, Z., Zhao, W., Pullan, L., Wang, C., and Zhang, J.-G. (2014)."Mitigating Voltage Fade in Cathode Materials by Improving Atomic Level Uniformity of Elemental Distribution." *Nano Letters* (14); pp. 2628–2635.
3. Xiao, J., Zheng, J., Zhang, J.-G., Nasybulin, E., Xu, W. U.S. Patent No. 61,716,908.
4. Zheng, J., Xiao, J., Gu, M., Zuo, P., Wang, C., and Zhang, J.-G. (2014). "Interface modifications by anion receptors for high energy lithium ion batteries." *J. Power Sources* (250); pp. 313-318.
5. Zheng, J., Shi, W., Gu, M., Xiao, J., Zuo, P., Wang, C., and Zhang, J.-G. (2013). "Electrochemical Kinetics and Performance of Layered Composite Cathode $Li[Li_{0.2}Ni_{0.2}Mn_{0.6}]O_2$." *Journal of the Electrochemical Society* (13:160); pp. A2212-2219.
6. Gu, M., Genc, A., Belharouak, I., Wang, D., Amine, K., Thevuthasan, S., Baer, D.R., Zhang, J.-G., Browning, N.D., Liu, J., and Wang, C.M. (2013). "Nanoscale Phase Separation, Cation Ordering, and Surface Oxygen Chemistry in Pristine $Li_{1.2}Ni_{0.2}Mn_{0.6}O_2$ for Li-Ion Batteries." *Chemistry of Materials* (25:11); pp. 2319-2236.
7. Zhan, H., Xiao, J., Nie, Z., Li, X., Wang, C.M., Zhang, J.-G., and Liu, J. (2013). "Nanostructured materials for rechargeable batteries: synthesis, fundamental understanding and limitations."

Current Opinion in Chemical Engineering (2:2); pp. 151-159.

8. Pan, A., Wang, Y., Xu, W., Nie, Z., Liang, S., Nie, Zimin, Wang, C., Cao, C., and Zhang, J.-G. (2014). "High-performance anode based on porous Co_3O_4 nanodiscs." *Journal of Power Sources* (255); pp. 125-129.
9. Jiang J., Shi, W., Zheng, J., Zuo, P., Xiao, J., Chen, X., Xu, W., and Zhang, J.-G. (2014). "Optimized Operating Range for Large-Format $LiFePO_4$/Graphite Batteries." *Journal of the Electrochemical Society* (161:3); pp. A336-A341. DOI:10.1149/2.052403jes.
10. Chen, X., Xu, W., Engelhard, M.H., Zheng, J., Zhang, Y., Ding, F., Qian, J., and Zhang, J.-G. (2014). "Mixed Salts of LiTFSI and LiBOB for Stable $LiFePO_4$-Based Batteries at Elevated Temperatures." *Journal of Materials Chemistry* (A2:7); pp. 2346-2352. DOI:10.1039/C3TA13043F.
11. Xiao, J., Meduri, P., Chen, H., Wang, Z., Gao, F., Hu, J.Z., Feng, J., Hu, M.Y., Dai, S., Brown, S., Adcock, J.L., Deng, Z., Liu, J., Graff, G.L., Aksay, I.A., and Zhang, J.-G. (2014). "Energetics of Defects on Graphene through Fluorination." *ChemSusChem* (7:5); pp. 1295-1300. DOI:10.1002/cssc.201301066.
12. Zheng, J., Gu, M., Xiao, J., Zuo, P., Wang, C., and Zhang, J.-G. (December 2013). "Structure Evolution of Li-Mn-Rich Cathodes and New Approaches to Improve Their Cycling Stability." Presented at the MRS Fall Meeting, Boston, Massachusetts.

V.B.8 Diagnostics – Optimization of Ion Transport in High-Energy Composite Cathodes (UCSD)

Ying Shirley Meng
University of California, San Diego

Department of Nanoengineering
9500 Gilman Drive, #0448
La Jolla, CA, 92093–0448
Phone: (858) 534-9553; Fax: (858) 534-9553
E-mail: shmeng@ucsd.edu

Start Date: April 2013
Projected End Date: March 2017

Objectives

- Probe and control the atomic-level kinetic processes that govern the performance limitations (rate capability and voltage stability) in a class of high energy composite electrodes.
- Conduct a systematic study with a powerful suite of analytical tools to pin down the mechanism and determine the optimum bulk compositions, surface characteristics for high rate, and long life.
- Help synthesis efforts to produce the materials at large scale with consistently good performance.
- Extend the suite of surface-sensitive tools to diagnose silicon type of anodes.

Technical Barriers

The technical barriers are low rate and poor voltage stability of high-energy Li rich composite cathodes.

Technical Targets

- PHEV: 96 Wh/kg, 5000 cycles.
- EV: 200 Wh/kg; 1000 cycles (80% DoD).

Accomplishments

- Established a suite of surface and interface characterization tools, such as STEM/EELS, XPS and FP computation.
- Identified the surface of coated materials (AlF_3, LLTO etc.) electrochemical performance matrices, including first cycle irreversible capacity, discharge energy density, voltage stability upon cycling, and rate capabilities.
- Proposed mechanism of surface modification and its impact on electrochemistry.
- Successfully applied XPS to characterize the solid electrolyte interphase (SEI) on amorphous silicon thin film anodes.

✧ ✧ ✧ ✧ ✧

Introduction

Advanced diagnostics are essential to investigate performance-limiting processes in batteries. Li transport is significantly more complex in composite structures which locally integrate different crystal structures at the nano-scales. Here, interfaces separating different local crystal structures can play a significant role on Li transport; however, this is not well understood. Some composite arrangements and spacings may promote significantly higher Li mobilities, while others may suppress Li transport. Insights into the role of nano-scale modulations in crystal structure and chemistry are lacking but essential for the directed design of composite electrodes with significantly improved rate capabilities. Careful engineering of the surface (coating) and bulk compositions (substitution) of these nanostructured materials may lead to significant improvement in ion transport. This project aims to combine a suite of diagnostic tools, including scanning transmission electron microscopy, electron energy loss spectroscopy as well as first principles computation to characterize new generation high-energy density Li transition metal oxides and high-capacity silicon carbon composites. In addition, the diagnostic tools developed here can also be utilized to study anode materials, such as silicon.

Approach

The approach uniquely combines atomic resolution scanning transmission electron microscopy (a-STEM) and electron energy loss spectroscopy (EELS), X-ray photoelectron spectroscopy (XPS) and first principles (FP) computation to elucidate the dynamic changes of the bulk and surface structural changes in the complex oxide materials during electrochemical cycling. A systematic study with powerful analytical tools is necessary to pin down the mechanism. This can also determine the optimum bulk compositions, surface characteristics for high rate and long life, and can help in synthesis efforts to produce the materials at large scale with consistently good performance.

Results

AlF_3 treatment for the $Li_{1.2}Ni_{0.2}Mn_{0.6}O_2$ lithium excess material: $Li_{1.2}Ni_{0.2}Mn_{0.6}O_2$ (LNMO) was synthesized by the hydroxide co-precipitation method without morphology control and treated with $Al(NO_3)_2$ and NH_4F to theoretically form a 1 wt.% AlF_3 coating. A comparison of the cyclic capacity and 1st and 60th discharge profiles for treated and untreated LNMO is provided in Figure V - 36a. After 60 cycles, it is evident that the treatment does not prevent voltage fade. With treatment the initial coulombic efficiency (CE) improved from 75.1% to 82.7% and the initial discharge capacity improved to 259 $mAhg^{-1}$; however, the treatment also resulted in faster capacity fade. A rate study compared the rate performance of untreated (Figure V - 36b) and treated (Figure V - 36c) LNMO. At a current density of 500 mAg^{-1} (2C) the treated LNMO delivered a specific discharge capacity of 181 $mAhg^{-1}$ which is an improvement over untreated LNMO. Characterization of the AlF_3-treated LNMO was carried out using XPS and a-STEM. XPS results indicate the presence of only Al-O bonds which shows that little or no AlF_3 was synthesized by the treatment process. TEM also revealed partial/incomplete coating on LNMO. However, a-STEM and the image fast Fourier transform (FFT) show that LNMO's surface structure changed after treatment. FFT of the a-STEM image near the surface of the LNMO particle indicates the presence of a spinel-like structure. The results show that the AlF_3 treatment, while beneficial for 1st cycle efficiency and rate, may not be the best choice for improving the performance of Li excess cathodes. Strategies to change the coating material for Li excess layered materials must be considered.

$Li_{1.133}Ni_{0.3}Mn_{0.567}O_2$ with LLTO surface modification: The LNMO particles were coated with a new type of coating - LLTO. A coating of certain amount was found to improve reversible capacity and voltage retention. Figure V - 37a presents the XRD of LNMO before and after LNMO coating. As the inset figure indicates, the intensity of the LLTO peak depends on the coating conditions. Figure V - 37b compares the first cycle voltage profile of LNMO, #1 LLTO coated LNMO and #2 LLTO coated LNMO. The CE improved from 73.1% to 79.1% and 91.4%, respectively.

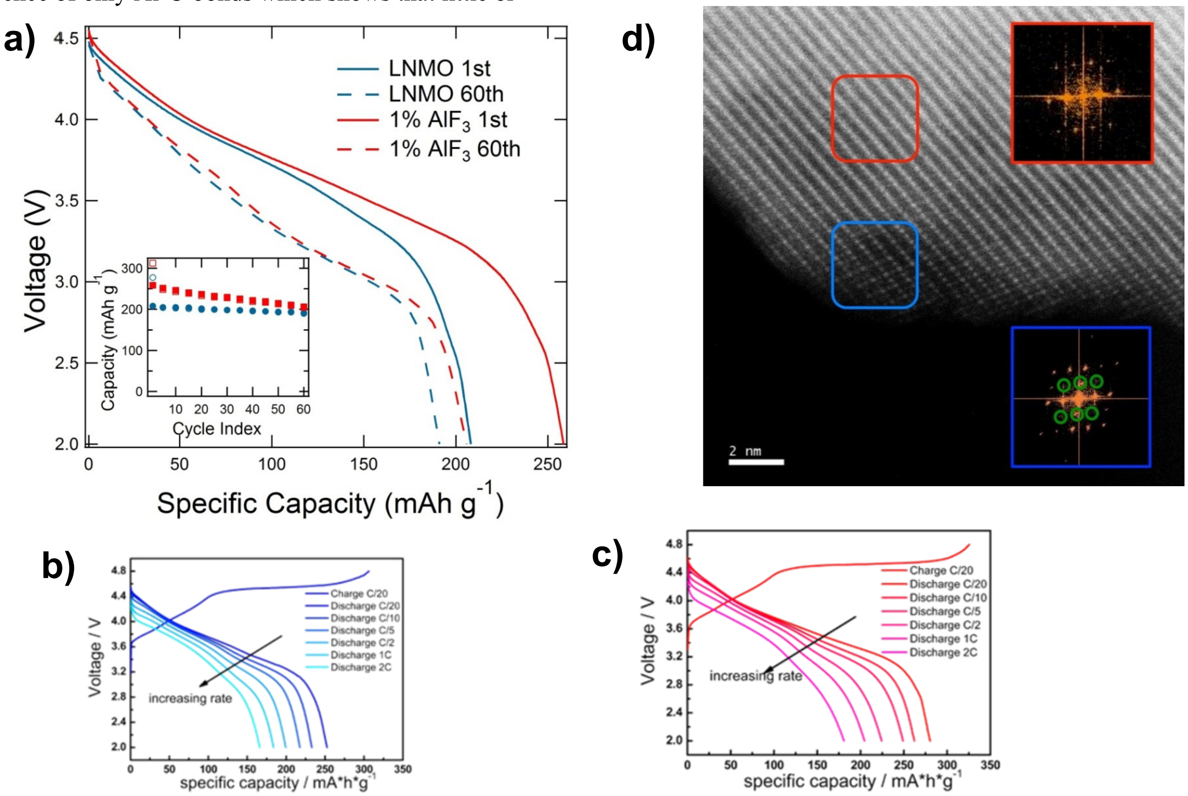

Figure V - 36: a) Voltage profiles and cyclic capacity of untreated (blue) and 1 wt.% AlF_3 treated (red) LNMO at C/10 with 2.0 - 4.8 voltage range. b, c) Rate profiles for untreated (blue) and treated LNMO (red). d) a-STEM and FFT of uncycled treated LNMO

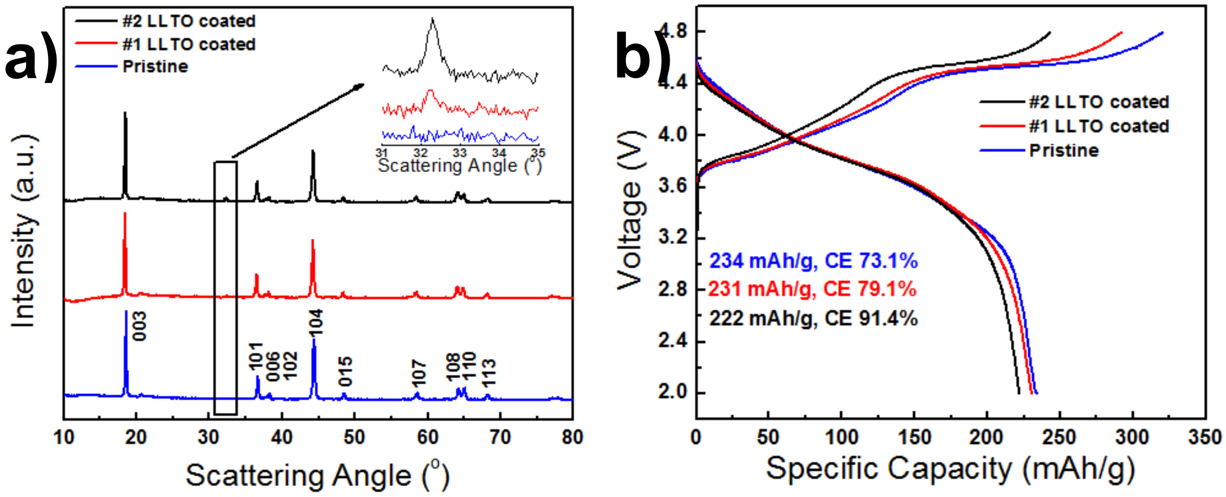

Figure V - 37: a) XRD of $Li_{1.133}Ni_{0.3}Mn_{0.567}O_2$ and crystalline LLTO surface modified LNMO. b) First cycle voltage profiles of pristine and LLTO surface modified sample at C/20, voltage range is 2.0-4.8V

Figure V - 38a compares the capacity versus cycles of these materials. The #1 LLTO coated LNMO shows 95.5% capacity retention after 200 cycles which is a better improvement than the LNMO pristine. The voltage profile showed in Figure V - 38b indicates that with help from the LLTO coating, there is less of a voltage fade This result suggests that the LLTO coating holds promise for eliminating LNMO's large initial irreversibility. Moreover, it also has the ability to maintain capacity and voltage retention.

Morphology control of $L_{1.2}Ni_{0.2}Mn_{0.6}O_2$ cathode materials: A modified synthesis method was employed to synthesize $L_{1.2}Ni_{0.2}Mn_{0.6}O_2$ (LNMO) particles with controlled morphology. This material preparation technique was found to improve capacity retention and reduce voltage fade. Figure V - 39 presents the 2nd, 20th, 40th, 60th and 80th dQ/dV profiles of the UCSD LNMO material when cycled under a current density of 25 mAg^{-1} (C/10) between 2.0 – 4.8V. A discharge capacity versus cycle number plot demonstrates a steady rise in capacity for the first 30 cycles with spherical LNMO delivering an initial discharge capacity of 220 $mAhg^{-1}$ and an 80th cycle discharge capacity of 230 $mAhg^{-1}$. The dQ/dV comparison of spherical LNMO shows remarkably stable electrochemical performance compared to the non-modified sample suggesting that the modified co-precipitation technique holds promise for resolving the lithium excess material's problems of capacity and voltage fading.

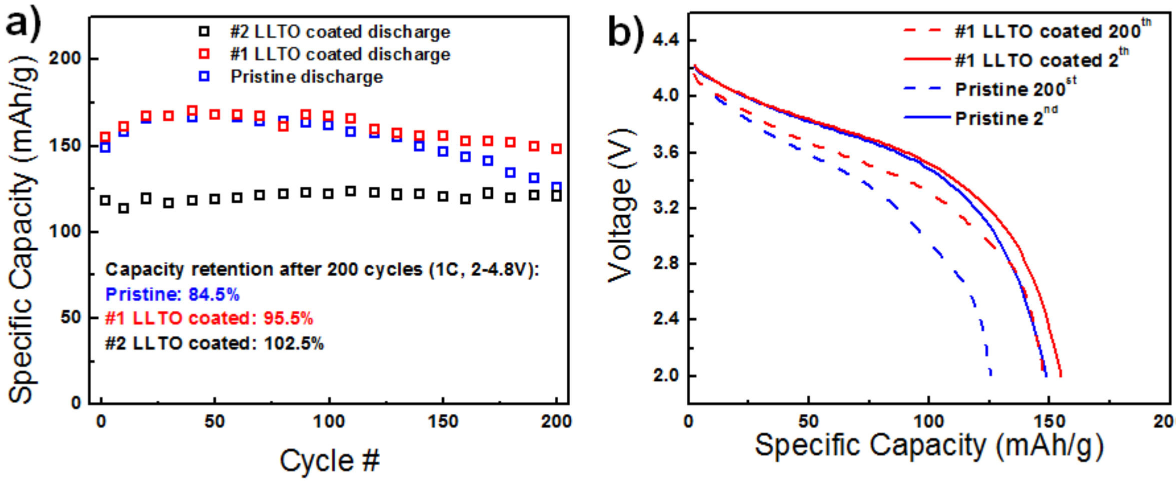

Figure V - 38: a) Cycling stability of $Li_{1.133}Ni_{0.3}Mn_{0.567}O_2$ and crystalline LLTO surface modified sample at 1C, voltage range is 2.0-4.8V, b) Comparison of voltage degradations between pristine and LLTO surface modified sample at 1C, voltage range is 2.0-4.8V

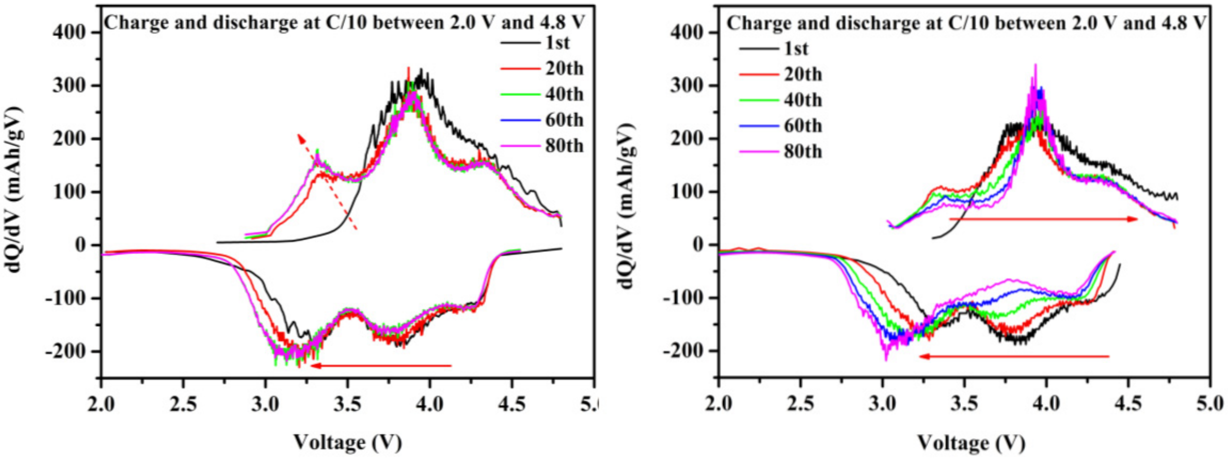

Figure V - 39: a) dQ/dV profiles for spherical LNMO cycled at C/10 between 2.0 – 4.8V, b) dQ/dV curves of the non-modified LNMO. The first cycle (not depicted) was conducted at a rate of C/20

Morphologically controlled $Li_{1.2}Ni_{0.2}Mn_{0.6}O_2$ with a gradient transition metal composition: In order to determine if the performance of morphologically controlled LNMO could be improved further, LNMO with a radially gradient composition was synthesized via the urea hydrolysis method. Figure V - 40a provides a SEM image of a focused ion beam FIB cut cross-sectioned LNMO particle. EDX was used to map the transition metals in the material. The ratio of Mn/Ni signals at points 1-4 is 0.96, 5.7, 3.17, and 2.91, respectively. The change in Mn/Ni ratio suggests particles with a Ni rich outer surface layer. EDX mapping and line scans (Figure V - 40b, Figure V - 40c) also suggest gradient distribution of Mn and Ni. The electrochemical performance of such a radially gradient spherical LNMO is now under investigation.

Characterizing the chemical stability of Si anodes: The large irreversibility associated with the formative cycle of Si anodes is primarily due to mechanical pulverization and chemical degradation (e.g., unstable SEI formation). It is not yet clear how to create a stable solid electrolyte interphase (SEI) between Si and the carbonate based organic liquid electrolytes in order to improve CE and long term stability. For this reason, a fundamental compositional study of the SEI formed on 50 nm amorphous-Si (a-Si) thin film electrodes fabricated by pulsed laser deposition and sputtering is being conducted. In order to reveal the reactivity of native Si with the 1M $LiPF_6$ in 1:1 EC:DEC electrolyte, the surfaces of a Si wafer before and after dipping etched (110) wafers in electrolyte was examined (Figure V - 41). Partial Si-H surface functionalization was achieved after etching. Nonetheless, after exposure in electrolyte, the highly reactive Si-H bonds disappear and a variety of new functionalities associated with electrolyte decomposition products are observed (blue). Removal of the native silicon oxide layer has been shown to improve the initial coulombic efficiency (CE); however, the high reactivity in etched Si promotes poor CE in subsequent cycles.

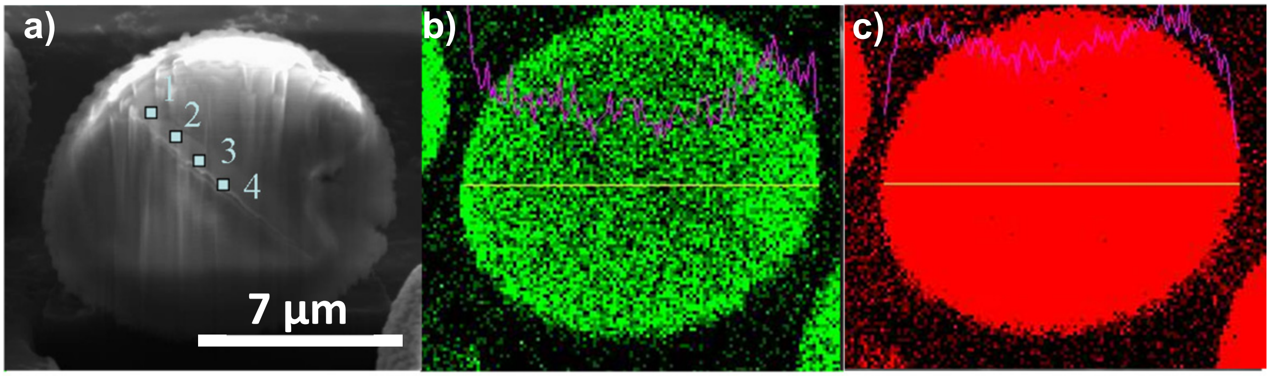

Figure V - 40: a) Cross sectional SEM image of a LMNO particle synthesized by the urea hydrolysis method with labeled EDX point scan locations. b) EDX mapping for Ni. c) EDX mapping for Mn

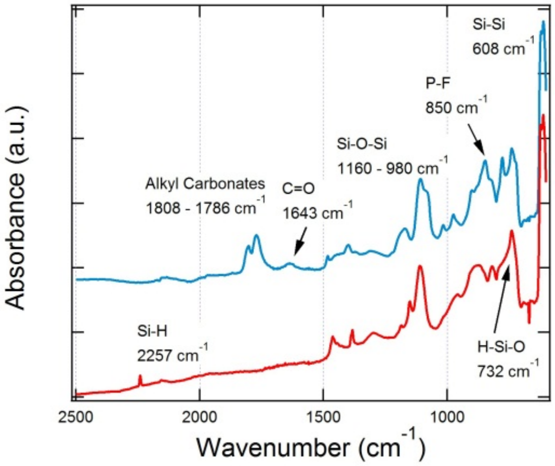

Figure V - 41: FTIR of etched Si wafer (red) compared to etched Si wafer that was exposed in EC:DEC electrolyte (blue).

XPS study on the effect of FEC additive on the interface stability of sputtered a-Si thin film electrodes: Sputtered a-Si thin film electrodes are binder- and additive-free. In this way, electrolyte additives and Si surface treatments can be properly investigated as strategies to improve the chemical stability of Si electrode surfaces. Fifty (50) nm thin-film sputtered amorphous Si (a-Si) electrodes were cycled under a variety of conditions. (Sample made by N. Dudney group, ORNL) Thin films < 80nm were chosen because they have been shown to be mechanically stable during cycling. In this way, chemical degradation can be isolated from mechanical degradation mechanisms. The variables in this study include a 10 wt. % FEC electrolyte additive and/or PEG functionalization via hydrosilylation. PEG was chosen for its similarity to polymeric electrolyte decomposition products previously identified in Si's SEI. According to the FTIR spectra for (100) crystalline Si wafers before and after PEG functionalization, it is confirmed a successful hydrosilylation reaction has occurred on treated *a*-Si thin-films. Figure V - 42 presents the electrochemical data for bare a-Si in 1:1 EC:DEC electrolyte (control), and bare Si in 45:45:10 EC:DEC:FEC 1M $LiPF_6$ electrolyte. Previously presented work confirms the proper functionalization of a-Si. Without any surface treatments or electrolyte additives, the first cycle CE is 86%. PEGylation of a-Si improves the first cycle CE to 88% but does not improve the subsequent cycle capacity retention. It is accepted by the battery research community that FEC preferentially decomposes during the first cycle to form inorganic LiF. The preferential decomposition of FEC should decrease first cycle CE not increase it, as reported in prior literature. In agreement with this notion, when 50 nm thick a-Si thin films were cycled with FEC the first cycle CE decreases to 80% and a dramatic improvement in cyclic capacity retention in subsequent cycles is observed.

Two early studies suggest that FEC reduces to VC which then self-polymerizes to form either polycarbonates or a poly(alkene). Computation studies by Balbuena et al. show that the most probable decomposition mechanism for FEC occurs via a ring opening reaction to form F^-, CO_2^{2-} and $CHOCH_2$. These reduction products can then react further to form LiF, RCOLi, and Li_2CO_3. Figure V - 43 presents the XPS spectra of a-Si surface after 1 full cycle in electrolyte with and without FEC additive. The F(1s) spectra suggest that the surface of the SEI contains more LiF in the presence of FEC. The C(1s) spectra provides evidence for the preferential formation of RCOLi, PEO and Li_2CO_3 in the presence of FEC. It is noted that polyethylene (C=C) may be convoluted with the C-C peak at 285 eV. Finally, polycarbonates are not observed in the O(1s) FEC spectrum at 534.5 eV. The XPS results correlate best with Balbuena et al.'s FEC decomposition mechanism.

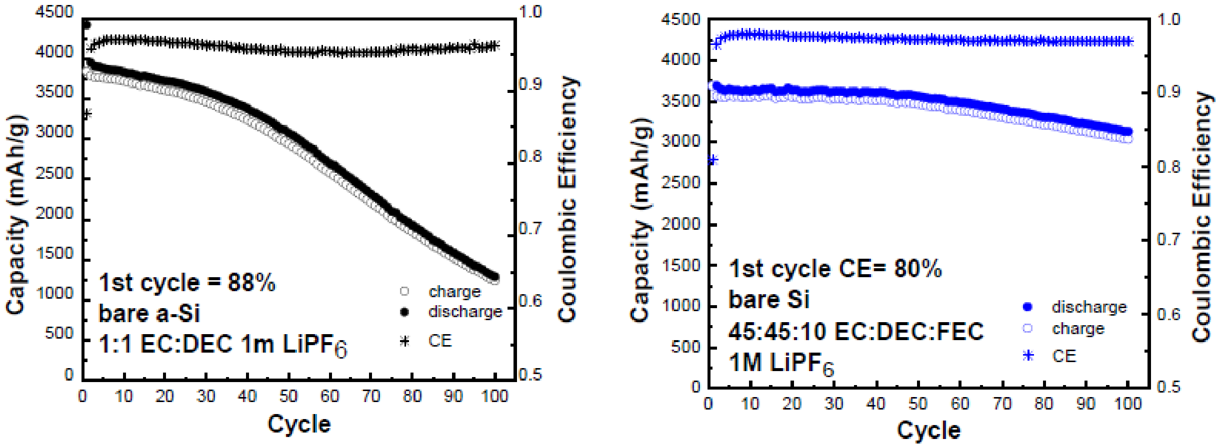

Figure V - 42: Cyclic capacity and coulombic efficiency for the control thin film electrode, and the thin film electrode cycled in electrolyte with the FEC additive

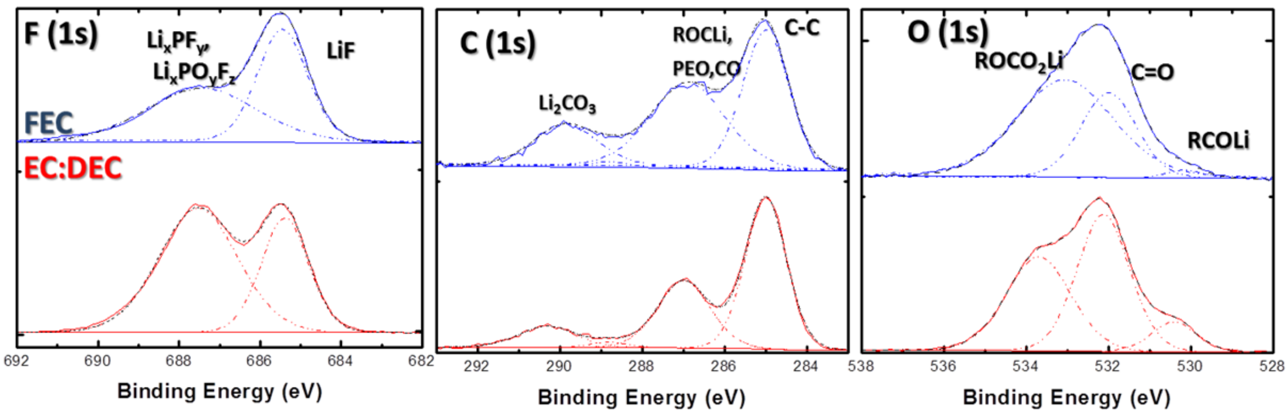

Figure V - 43: XPS spectra of a-Si surface after 1 full cycle in 1:1 EC:DEC 1M LiPF6 electrolyte (red) and 45:45:10 EC:DEC:FEC 1M LiPF6 electrolyte (blue)

Conclusions and Future Directions

For AlF_3 surface treatment, XPS results indicate the presence of only Al-O bonds which shows little or no AlF_3. In addition, TEM revealed partial/incomplete coating on LNMO and a-STEM shows that LNMO's surface structure transferred to spinel-like structure. The results show that the AlF_3 treatment, while beneficial for 1st cycle efficiency and rate, may not be the best choice for improving the cycling performance of Li excess cathodes. LLTO surface coating was explored to improve the voltage/ capacity stability of LNMO as well as initial CE. The effects of morphology control on voltage degradation of LNMO showed improvement in voltage stability, suggesting that the new co-precipitation technique holds promise for resolving the Li excess material's problems of capacity and voltage fading. More systematic investigation is underway.

The extreme surface reactivity of Si-H was demonstrated. The highly reacted H-terminated surface decomposed fresh electrolyte which was demonstrated in the FTIR spectrum. The use of electrolyte additive FEC showed a decrease in the initial CE which is due to the preferential decomposition of FEC to form LiF initially. XPS elucidated the possible reduction mechanism of FEC, which correlated best with Balbuena et al.'s ring opening reduction mechanism. In order to further understand how FEC stabilizes the cell over prolonged cycles while maintaining good capacity retention. Time of Flight Secondary Ion Microscopy (ToF-SIMs) will be used to explore SEI interphase, morphology, and film thickness at different cycles.

FY 2014 Publications/Presentations

1. Meng, Y.-S. (June 2014). "New *In situ* Analytical Electron Microscopy for Understanding Structure Evolution and Composition Change in High Energy Density Electrode Materials in Lithium Ion Batteries." Presented at the 2014 DOE Annual Merit Review and Peer Evaluation Meeting, Washington, D.C.
2. Qian, D., Xu, B., Chi, M., Meng, Y.-S. (2014). "Uncovering the roles of oxygen vacancies in cation migration in lithium excess layered oxides." *Physical Chemistry Chemical Physics* (14:16); p. 14665.

V.B.9 Novel Cathode Materials for High-Energy Lithium Batteries (U Texas)

Arumugam Manthiram
University of Texas at Austin

Materials Science and Engineering Program
204 E. Dean Keeton Street, Mail Stop C2200
Austin, TX 78712
Phone: (512) 471-1791; Fax: (512) 475-8482
E-mail: manth@austin.utexas.edu

Start Date: January 2012
Projected End Date: December 2015

Objectives

- Develop high-performance cathodes for lithium-ion batteries and gain a fundamental understanding of their structure-composition-performance relationships.
- Develop a fundamental understanding of the impact of aliovalent doping of $\mathrm{V^{3+}}$ for $\mathrm{Mn^{2+}}$ and $\mathrm{Co^{2+}}$ in $\mathrm{LiMnPO_4}$ and $\mathrm{LiCoPO_4}$, respectively, and improve their performance.
- Develop novel synthesis approaches for phosphate polyanion cathodes that can offer the reversible insertion/extraction of more than one lithium ion per transition-metal ion.
    - ○ Fabrication of nanostructured $\mathrm{LiVOPO_4}$ and $\mathrm{LiVOPO_4}$/graphene composite by microwave-assisted solvothermal (MW-ST) synthesis and template methods.

Technical Barriers

Focusing on the cathode materials, this project addresses the following technical barriers for lithium-ion batteries to be employed for vehicle applications: cost, safety, cycle life, energy, and power.

Technical Targets

- Realize high capacity through the reversible insertion/extraction of more than one lithium per transition-metal ion in polyanion cathodes.
- Develop nanostructured polyanion cathodes to overcome the poor ionic and electrical conductivities.
- Develop a fundamental understanding of aliovalent substitutions on the electrochemical performances of polyanion cathodes.

Accomplishments

- Successful synthesis of aliovalently doped $\mathrm{LiMn_{1-3x/2}V_x\square_{x/2}PO_4}$ and $\mathrm{LiCo_{1-3x/2}V_x\square_{x/2}PO_4}$ cathodes by a low temperature microwave-assisted solvothermal (MW-ST) process.
- Demonstration of a high reversible capacity of ~ 155 mAh/g for the $\mathrm{V^{3+}}$-doped $\mathrm{LiMn_{1-3x/2}V_x\square_{x/2}PO_4}$ ($x = 0.2$) cathode without any carbon coating.
- Understanding the roles of $\mathrm{V^{3+}}$ aliovalent substitution in the $\mathrm{LiMnPO_4}$ and $\mathrm{LiCoPO_4}$ cathodes.
- Synthesis of α_1-$\mathrm{LiVOPO_4}$/graphene nanocomposites by the microwave-assisted solvothermal (MW-ST) approach with low cost solvents of water and ethanol.
- Reversible extraction/insertion of more than one lithium per vanadium from/into the α_1-$\mathrm{LiVOPO_4}$.
- Understanding the phase evolution of $\mathrm{LiVOPO_4}$ cathodes by chemical and electrochemical lithiation.
- Development of synthesis methods for nanostructured α-$\mathrm{LiVOPO_4}$ with a carbon hard-template.

◆ ◆ ◆ ◆ ◆

Introduction

Cost, safety, energy, and power are the major issues that hamper the adoption of lithium-ion technology for vehicle applications. Accordingly, this project focuses on the design and development of high-energy, low-cost, safer polyanion cathodes by addressing the poor electronic and ionic transport in phosphate cathodes. For example, aliovalent substitution of $\mathrm{V^{3+}}$ in $\mathrm{LiMPO_4}$ (M = Mn and Co) could enhance the electrochemical performance. Similarly, novel low-temperature synthesis approaches to control the particle size and morphology could enhance the electrochemical utilization and capacity. Also, characterization of products obtained by chemical and electrochemical lithiation could enhance understanding of the behavior of polyanion cathodes. Accordingly, this project focuses on aliovalent doping and low-temperature synthesis approaches with polyanion phosphate cathodes.

Approach

Most phosphate cathodes, such as $LiMnPO_4$, $LiCoPO_4$, and $LiVOPO_4$, suffer from low electronic and ionic conductivities. Accordingly, synthesis and processing conditions play a critical role in realizing the full capacities of these polyanion cathodes. For instance, novel solution-based approaches such as microwave-assisted solvothermal (MW-ST) and template-assisted methods are pursued to control morphologies and particle size to maximize electrochemical performance. Additionally, low-temperature microwave synthesis enables high levels of aliovalent substitutions. Also, template-assisted synthesis is employed to control the particle size and morphology. The synthesized samples are characterized by a variety of techniques including X-ray diffraction (XRD), electron microscopy (SEM, TEM, and STEM), X-ray adsorption spectroscopy (XPS), Fourier transform infrared spectroscopy (FTIR), and in-depth electrochemical measurements. Based on the characterization data gathered, a fundamental understanding of the structure-composition-property-performance relationships is developed, which is then utilized to design better-performing cathodes.

Results

Aliovalent doping of $LiMnPO_4$: Aliovalent doping of V^{3+} for Mn^{2+} and Co^{2+} in $LiMnPO_4$ and $LiCoPO_4$ was pursued to determine its effect on electrochemical performance. Single-phase $\mathrm{LiMn}_{1-3x/2}\mathrm{V}_x\square_{x/2}\mathrm{PO}_4$ ($0 \le x \le 0.2$ and □ refers to cation vacancy) samples, in which the Mn^{2+} ions are substituted by V^{3+} ions, were obtained by a microwave-assisted solvothermal synthesis process at 300 °C. As seen in Figure V - 44a, scanning electron microscopy (SEM) showed rod-like morphology with 20 – 200 nm length for the substituted samples. Similar morphology was observed for the unsubstituted sample also (not shown here). Moreover, a homogenous distribution of Mn, V, and P was observed with energy dispersive spectroscopy (EDS) on the doped samples.

The oxidation state of the cations in the substituted samples was analyzed with X-ray absorption near edge spectroscopy (XANES). The manganese oxidation state was found to be 2+, as expected. Employing $LiVOPO_4$ and $Li_3V_2(PO_4)_3$ as standards, respectively, for V^{4+} and V^{3+} states, the XANES data indicated an oxidation state of near 3+ for vanadium. Furthermore, the pre-edge feature indicated that the VO_6 octahedra in the vanadium-doped samples is less distorted than in $LiVOPO_4$, but more so than in $Li_3V_2(PO_4)_3$, which is similar to what was found previously for vanadium-substituted $LiFePO_4$.

Electrochemical measurements were carried out in the voltage range of 1.5 – 5.0 V. Figure V - 44b compares the electrochemical charge-discharge profiles of the un-substituted ($x = 0$) and vanadium-substituted ($x = 0.05$, 0.10, 0.15, and 0.20) samples. As the amount of vanadium increases from $x = 0$ to 0.2, the first charge/discharge capacity increases from ~ 40 mAh/g to 155 mAh/g, respectively. Although carbon coating is generally needed to electrochemically cycle $LiMnPO_4$, the vanadium-doped samples exhibit high capacity without carbon coating. Moreover, the irreversible capacity loss drops from ~ 20 mAh/g in the unsubstituted ($x = 0$) sample to ~ 0 mAh/g in the $x = 0.2$ sample.

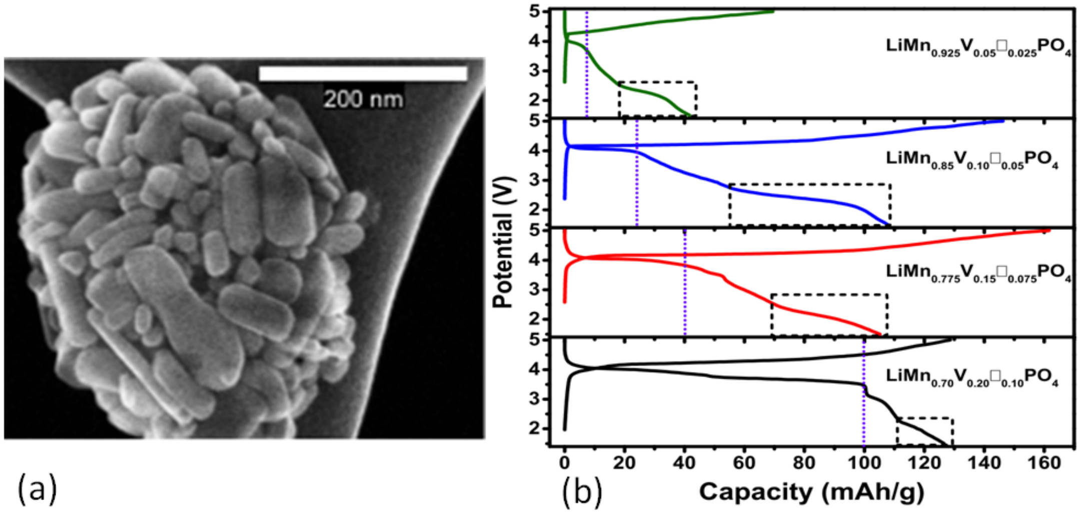

Figure V - 44: (a) SEM micrograph of the rod-like $\mathrm{LiMn}_{0.7}\mathrm{V}_{0.20}\square_{0.10}\mathrm{PO}_4$ and (b) first charge-discharge profiles of the $\mathrm{LiMn}_{1-3x/2}\mathrm{V}_x\square_{x/2}\mathrm{PO}_4$ ($0 \le x \le 0.20$) samples, showing the advantage of aliovalent vanadium doping on the performance

Aliovalent doping of $LiCoPO_4$: The substitution of V^{3+} for Co^{2+} in $LiCo_{1-3x/2}V_x\square_{x/2}PO_4$ (LCVP) with $0 \leq x \leq 0.2$ was explored. A phase-pure tetragonal form (space group: $Pn2_1$) of LCVP was first synthesized by a low-temperature MW-ST method at 260°C as the olivine form of LCVP could not be accessed. The tetragonal polymorphs were then converted to the olivine phase by heating in argon at 525°C (Figure V - 45).

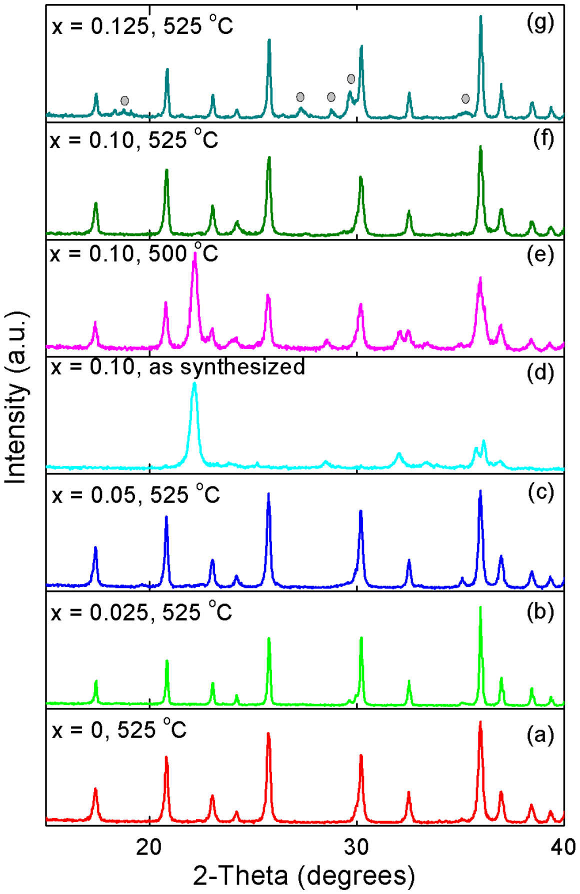

Figure V - 45: XRD patterns of $LiCo_{1-3x/2}V_x\square_{x/2}PO_4$ before and after heating

The temperature dependence of the conversion of $LiCo_{0.85}V_{0.1}\square_{0.05}PO_4$ from the tetragonal to olivine phase is shown by the X-ray diffraction (XRD) in Figure V - 45 (d)-(f). The compositions of the samples with varying vanadium substitutions were verified before and after heating at 525°C by inductively coupled plasma analysis. The XRD data indicate the formation of single-phase olivine LCVP for $x \leq 0.1$ and the formation of impurity phases for $x \geq 0.125$. However, no shifts in lattice parameters with x could be observed due to the similar ionic radii values of V^{3+} (78 pm) and Co^{2+} (79 pm). Additionally, the single-phase LCVPs disproportionate on heating to 725°C to give $LiCoPO_4$ and $Li_3V_2(PO_4)_3$.

The Fourier transform – infrared spectroscopy (FT-IR) data shown in Figure V - 46 indicate that the band corresponding to the antisymmetric stretching (υ_3) of PO_4^{3-} at 1070 cm^{-1} in the x = 0 sample shifts to lower wavenumbers while the peak corresponding to the symmetric stretching mode (υ_1) of PO_4^{3-} shifts to higher wavenumbers with increasing vanadium content.

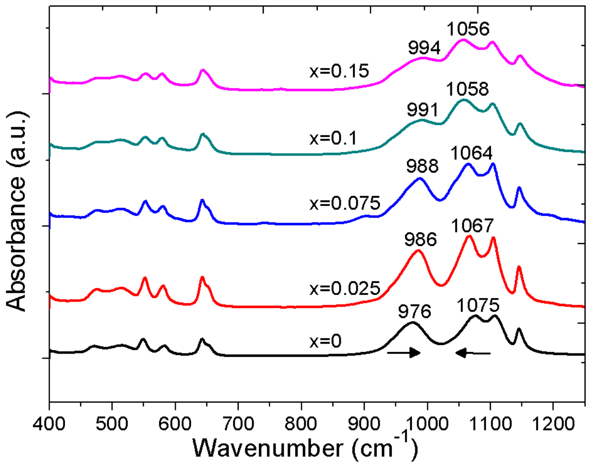

Figure V - 46: FT-IR spectra of $LiCo_{1-3x/2}V_x\square_{x/2}PO_4$ after heating at 525°C

Electrochemical data shown in Figure V - 47 indicate that the discharge capacity increases from 52 mAh g^{-1} for x = 0 to 109 mAh g^{-1} for x = 0.025 and then decreases.

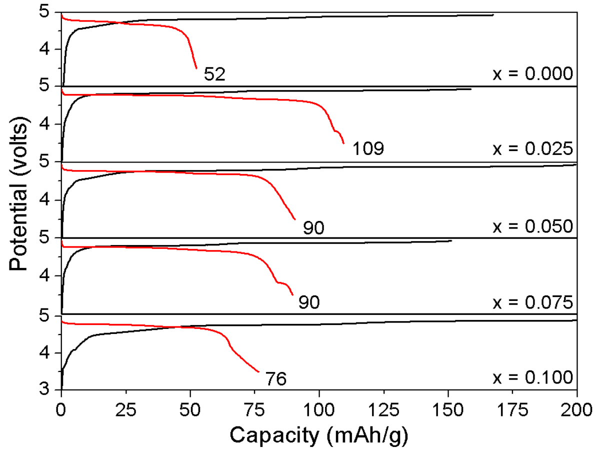

Figure V - 47: First charge/discharge profiles of $LiCo_{1-3x/2}V_x\square_{x/2}PO_4$ after heating at 525°C

Nanostructured $LiVOPO_4$ cathodes: α_1-$LiVOPO_4$/graphene nanocomposite was synthesized by the MW-ST process at 210°C in a mixed solvent consisting of water and ethanol. The α_1-$LiVOPO_4$ (tetragonal) sample exhibits a "flower-balls" morphology with an average particle size of ~ 5 µm, as shown in the SEM image in Figure V - 48a. Each "flower ball" is composed of uniform 80 – 100 nm "nano-petals" (see the inset in Figure V - 48a).

Graphene sheets were incorporated to form α_1-$LiVOPO_4$/graphene nanocomposite by the thermal reduction of graphene oxide (GO) during the microwave synthesis.

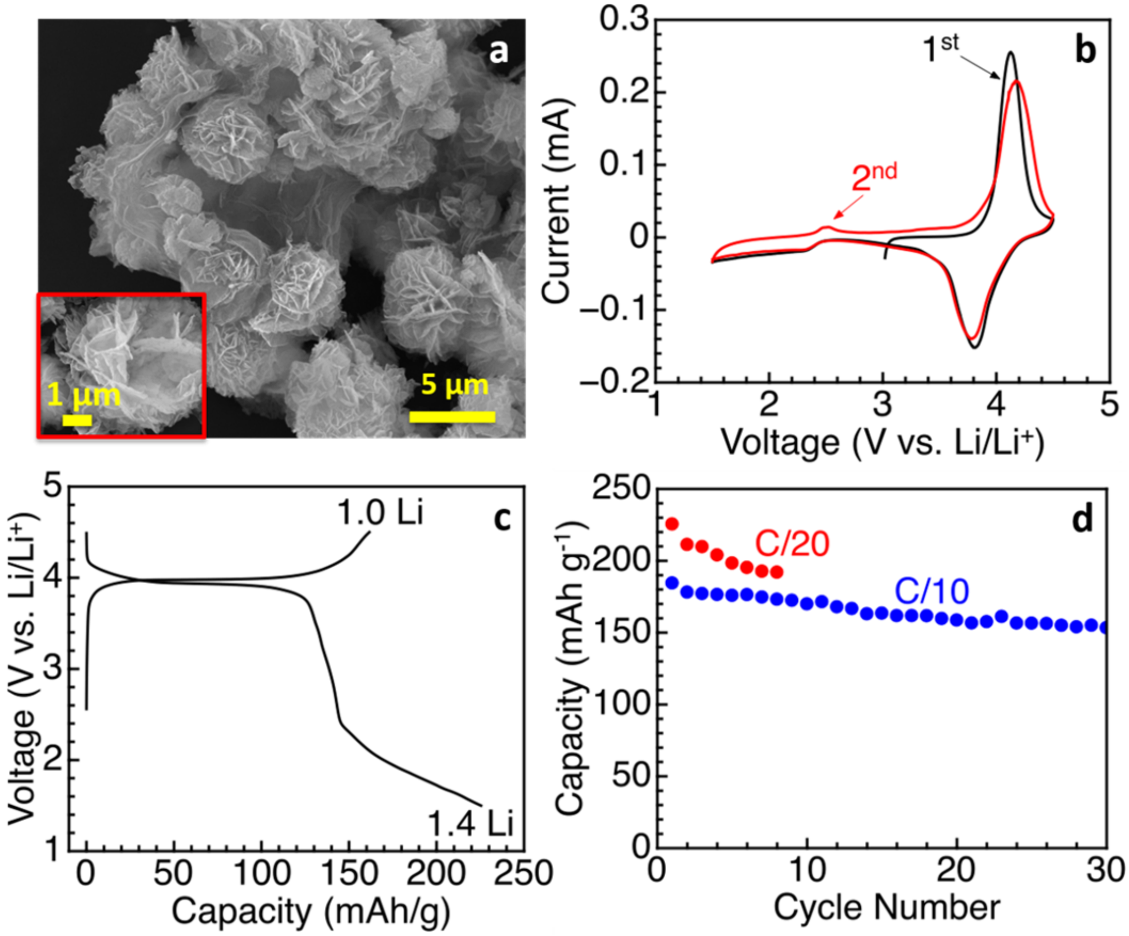

Figure V - 48: (a) SEM image, (b) CV plots, (c) first charge-discharge profiles at C/20 rate, and (d) cyclability at C/20 and C/10 rates of α_1-$LiVOPO_4$/graphene cathodes

As seen in Figure V - 48b, cyclic voltammetry (CV) of the $LiVOPO_4$/graphene nanocomposite at 0.01 mV s^{-1} shows two reduction peaks at 2.3 and 3.9 V and two oxidation peaks at 2.5 and 4.1 V. The two peaks correspond to the reversible insertion/extraction of two lithium (between $VOPO_4$ and Li_2VOPO_4), analogous to what was found before with both α-$LiVOPO_4$ (triclinic) and β-$LiVOPO_4$ (orthorhombic), although the lower-voltage (~ 2 V) profile is more sloping in α_1-$LiVOPO_4$ compared to those in α-$LiVOPO_4$ and β-$LiVOPO_4$. Figure V - 48(c) shows the first charge-discharge profiles at C/20 rate of α_1-$LiVOPO_4$/graphene cathodes. The first charge capacity of 160 mAh g^{-1} at ~ 4 V corresponds to the extraction of 1.0 lithium per formula. The first discharge capacity of 220 mAh g^{-1} corresponds to the insertion of 1.4 lithium per formula, with the sloping voltage profile below 2.4 V corresponding to the insertion of the second lithium into $LiVOPO_4$. These results are consistent with the CV data. Figure V - 48d shows the cyclability of the α_1-$LiVOPO_4$/graphene cathodes at C/20 and C/10 rates, and further optimization is needed to improve the cyclability.

Phase evolution of the α_1-$LiVOPO_4$/graphene nanocomposite was studied by both electrochemical and chemical lithiation. The *ex situ* XRD patterns of the α_1-$LiVOPO_4$/graphene electrodes at various depths of discharge show the phase evolution (Figure V - 49). For example, the intensity of the (001) peak is significantly reduced below 2.5 V, along with the growth of a new peak on the right side of the (001) peak. Similarly, the (020) peak is progressively replaced by another peak located on its left side upon discharge to 1.7 V. These results suggest a two-phase reaction of the electrochemical lithiation process. Additionally, the chemically-lithiated α_1-Li_2VOPO_4 displays an XRD pattern similar to the sample discharged to 1.5 V, indicating the consistency between the electrochemical and chemical lithiation processes. Similar studies were also carried out with α-LiVOPO$_4$ and β-LiVOPO$_4$. It was found that a significant amount of lithium can be inserted into α-LiVOPO$_4$ before a phase change occurs. In contrast, lithiation of β-LiVOPO$_4$ is more consistent with the formation of a two-phase mixture throughout most of the lithiation range.

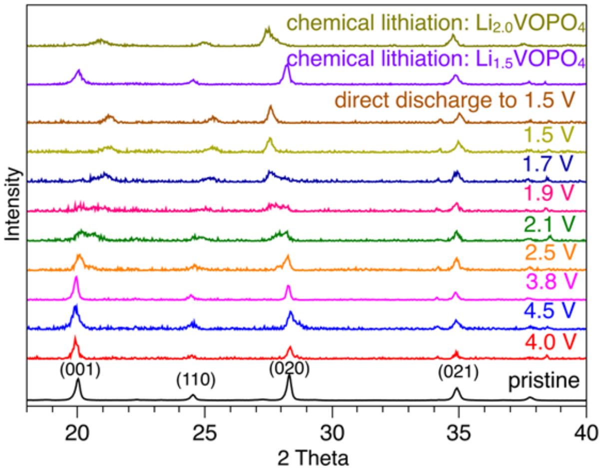

Figure V - 49: XRD patterns of the α_1-LiVOPO$_4$/graphene nanocomposite after various depths of electrochemical discharge and chemical lithiation with n-butyllithium.

The reversible extraction of more than one lithium with both α-LiVOPO$_4$ and α1-LiVOPO$_4$ has been demonstrated. In order to develop a systematic understanding of the performance of all three polymorphs of LiVOPO4, β-LiVOPO$_4$ was also prepared by a sol-gel approach. A smaller initial capacity of < 50 mAh g-1 was obtained with the sol-gel material due to the large particle size (> 10 µm). Macroporous carbon was then employed as a hard-template to confine the growth of the LiVOPO$_4$ particles during the calcination process. The resulting LiVOPO$_4$ had a much reduced particle size (< 500 nm), but the XRD pattern indicated this sample to be more like α-LiVOPO4 rather than β-LiVOPO$_4$. Further studies will focus on the microwave synthesis of the β-LiVOPO$_4$ to avoid this phase transformation.

Conclusions and Future Directions

Aliovalent substitution with V^{3+} in LiMnPO$_4$ and LiCoPO$_4$ has been accomplished by low-temperature microwave-assisted synthesis. The electrochemical performances are greatly improved with the substitution by lowering charge-transfer impedance and enhancing lithium-diffusion. In addition, reversible extraction of more than one lithium per transition-metal ion has been demonstrated with α1-LiVOPO$_4$ by employing novel microwave synthesis approaches to control the particle size and morphology. Also, investigation of the phase evolution of all three polymorphs of LiVOPO$_4$ (α: triclinic, β: orthorhombic, α1: tetragonal) with chemical and electrochemical lithiation has helped understand the composition-structure-performance relationships.

Future work is focused on (i) further optimization of the LiVOPO$_4$ cathodes by microwave and template-assisted approaches, (ii) aliovalent substitution with Ti$_4$+ in LiM$_{1-2x}$Tix$\square$x PO$_4$ to enhance the electrochemical properties, and (iii) aliovalent substitution in Li$_2$M$_{1-3/2x}$Vx$\square$x/2P2O$_7$ to extract more than one lithium (> 110 mAh/g).

FY 2014 Publications/Presentations

1. Manthiram, A., Chemelewski, K., and Lee, E.-S. (2014). "A Perspective on the High-Voltage LiMn$_{1.5}$Ni$_{0.5}$O$_{4)}$. Spinel Cathode for Lithium-ion Batteries." *Energy and Environmental Science* (7); pp. 1339-1350.
2. Lee, E.-S., and Manthiram, A. (2014). "Smart Design of Lithium-rich Layered Oxide Cathode Compositions with Suppressed Voltage Decay." *Journal of Materials Chemistry* (A2); pp. 3932-3939.
3. He, G., and Manthiram, A. (2014). "Nanostructured Li$_2$MnSiO$_4$/C Cathodes with Hierarchical Macro/Meso Porosity for Lithium-ion Batteries." *Advanced Functional Materials* (24); pp. 5277-5283.
4. Gutierrez, A., Qiao, R., Wang, L., Yang, W., Wang, F., and Manthiram, A. (20141). "High-capacity, Aliovalently Doped Olivine LiMn$_{1-3x/2}$V$_x\square_{x/2}$PO$_4$ Cathodes without Carbon Coating." *Chemistry of Materials* (26); pp. 3018-3026.
5. Harrison, K. L., Bridges, C. A., Segre, C. U., Varnado, C. D., Jr., Applestone, D., Bielawski, C. W., Paranthaman, M., and Manthiram, A. (2014). "Chemical and Electrochemical Lithiation of LiVOPO$_4$ Cathodes for Lithium-ion Batteries." *Chemistry of Materials* (26); pp. 3849-3861.
6. Gutierrez, A., and Manthiram, A. (2014). "Microwave-assisted Solvothermal Synthesis of Spinel AV$_2$O$_4$ (M = Mg, Mn, Fe, and Co)." *Inorganic Chemistry* (53); pp. 8570-8576.
7. Xiang, X., Knight, J. C., Li, W., and Manthiram, A. (2014). "Understanding the Effect of Co^{3+} Substitution on the Electrochemical Properties of Lithium-Rich Layered Oxide Cathodes for Lithium-Ion Batteries." *Journal of Physical Chemistry C* (118:38); pp. 21826-21833.

V.C Anode Development

V.C.1 Novel Anode Materials (ANL)

Jack Vaughey
Argonne National Laboratory

Chemical Sciences and Engineering
Building 205
9700 S Cass Avenue
Lemont, IL, 60439
Phone: (630) 252-8885; Fax: (630) 252-4176
E-mail: vaughey@anl.gov

Start Date: October 2010
Projected End Date: September 2014

Objectives

- Design electrode architectures containing main group metal, metalloid or intermetallic components that can tolerate the volumetric expansion of the materials and provide an acceptable cycle life.
- Exploit various deposition techniques to improve the design and performance of Si-based electrodes by controlling the surface functionality and chemistry of the active electrode.
- Develop methods to assess the internal changes within the electrode on cycling as a tool to improve performance.

Technical Barriers

There are several technical barriers to the utilization of silicon as an electrode material for Li-ion batteries. Notably, its high volume expansion on lithiation, reactivity with its environment, and a large kinetic resistance to lithiation leads to obstacles that must be addressed before silicon can be considered as a replacement electrode material for graphitic carbons. These barriers include:

- Low energy.
- Poor low temperature operation.
- Abuse tolerance limitations.

Technical Targets

- 142 Wh/kg: 317 W/kg (40 mile PHEV requirement).
- Cycle Life: 5000 Cycles.
- Calendar Life: 15 Years.

Accomplishments

- Utilized a combined synthesis, impedance spectroscopy, and MAS-NMR study to determine the types of functional groups that are at the silicon-electrolyte interface and how they can be changed as a function of synthesis.
- Utilized thin film deposition to make silicon electrodes with various surface passivation layers and determined the effect of electrolyte additive fluorethylene carbonate (FEC) on electrode side reactions.
- Studied the reactivity of the silicon electrode passivation layer (SiO_2) within the electrochemical cell and identified some surface reactivity of the compound Li_4SiO_4. Showed that this compound formed quickly but thermodynamically was not the most stable product and it gradually, on exposure to electrolyte solvent, transforms to the crystallographically denser phase Li_2SiO_3.
- Created synthetic SEI layers on a series of silicon electrodes and used EQCM (in collaboration with Mike Thackeray and ZhenZhen Yang (CEES-EFRC) to monitor the effect of cycling and electrolyte on SEI density and porosity.
- Maintained interactions with the EFRC – Center for Electrical Energy Storage - Tailored Interfaces (Argonne-Northwestern University-University of Illinois Urbana-Champaign) focused on EQCM studies and micro CT tomography electrode characterization.

✧ ✧ ✧ ✧ ✧

Introduction

Elemental silicon has received significant attention from the energy storage community as a viable alternative to graphitic carbon as the negative electrode in Li-ion batteries. Among the main group elements with high theoretical capacities (via room temperature formation of Li_xM), silicon has the highest gravimetric capacity and, when combined with its availability and low cost, is a very promising electrode material to be targeted. Unlike most commercial cathodes, silicon anodes do not work by intercalation but by a stepwise chemical reaction. With this storage mechanism Si can store ~3,800 mAh/g (or ~8,800 mAh/ml), nearly an order of magnitude higher than graphite (372 mAh/g and 818 mAh/ml, respectively), while inserting lithium only a few hundred millivolts above the potential of metallic lithium. However, the crystallographic expansion on lithiation translates to a significant electrode level volume expansion as the constituent Si atoms complete their p-orbitals and become much larger anions. Although this expansion among other kinetic issues (e.g., poor exchange current density) presently limits its utility, the high potential payoff has made silicon a focus for the BATT-Anode program.

A major objective is to understand how a silicon electrode interacts with its cell environment and how these interactions can be controlled to increase cycle life and limit capacity fade. Initial work, inspired by Yi Cui's work with silicon VLS nanowires, focused on designing methods to use metallic copper as both a binder and electrode current collector for a silicon-based electrode. This led to the development of host architectures that simplified the Li-ion battery electrode while providing an engineered void space within the electrode sufficiently large void volume to accommodate the volumetric expansion that occurs during charging. Utilizing these and related thin film electrode designs, synthesis and diagnostics efforts were combined to understand and adapt the excellent cycling performance seen for deposited silicon electrodes to the commercially utilized laminated electrodes. Specifically, the active surface of silicon, the interfacial region with the electrolyte, and role of electrode porosity was studied to improve the electrochemical performance of Si-based electrodes.

Approach

Utilizing a variety of methods to make silicon electrodes with defined structure and surface functionality, samples were created that are amenable to spectroscopic studies and determining the effect of processing and electrolyte additives (e.g. BATT standard electrolyte component FEC) on performance. These electrode materials were then evaluated by diagnostic techniques on different scales (nanometer to micron) to determine how their composition and surfaces interact with the electrolyte on cycling, leading to capacity fade via degradation reactions.

Results

Synthesis. The goal of the research has been to develop an understanding of how elemental silicon interacts with components of the typical electrochemical cell and how that is seen in the electrochemical performance. It was previously examined how the electrochemical properties of bulk silicon, electrodeposited Si thick films, and sputtered thin films are dependent on sample history and processing. In all of these studies, a critical variable was the surface functionality and how it interacted with the electrolyte. In response to this, a series of surface sensitive NMR spectroscopic techniques were developed to track the functionality and surface composition. Using these, development studies were continued by investigating how the surface passivation layer itself interacts with the electrolyte.

Previous studies have identified SiO_2, $Si(OH)_x$, or SiH_x as the predominant species passivating elemental silicon. The exact species and their ratios depend significantly on processing and history. For instance, SiH_x is the main species for SiH_4 derived thin films (C. Ban, NREL). For electrodes exposed to oxygen (air) the species tends to be SiO_2. In this instance a layer of SiO_2 coats the surface to a thickness dependent on time, temperature, and other variables. However, until recently this capping layer was thought to be inert. It could be overcome via cracking or other physical methods but remained as the base of the SEI layer. Recent work by Edstrom, et al., has shown that in fact the SiO_2 is reactive at the cell voltages seen in a LIB and reacts to form $Li_4[SiO_4]$ at the interface. This conclusion was supported by extensive XPS work and by first principles calculations that showed it to be the most thermodynamically stable phase (Y.-P. Kim, Michigan St).

In order to evaluate the reactivity of these lithium silicate phases in the cell, materials were synthesized at different scales to establish the role of reactivity and surface area (particle size). Samples of $Li_4[SiO_4]$, $Li_6[Si_2O_7]$, and Li_2SiO_3 were synthesized and characterized by solid state NMR, powder X-ray diffraction, FTIR, and TGA. The samples were exposed to various electrolytes (varying time, temperature, concentration) and the changes versus the baseline measurements were determined.

Characterization: It was found that after exposure to electrolyte, even in the absence of current being passed, Li_4SiO_4 was reactive with the electrolyte. The main mechanism was identified as gradual solvation of the lithium cation in the solid. This gradually weakens the bonding with the silicate anion, resulting in protonation (from electrolyte) and gradual condensation. The mechanism is shown in Figure V - 50.

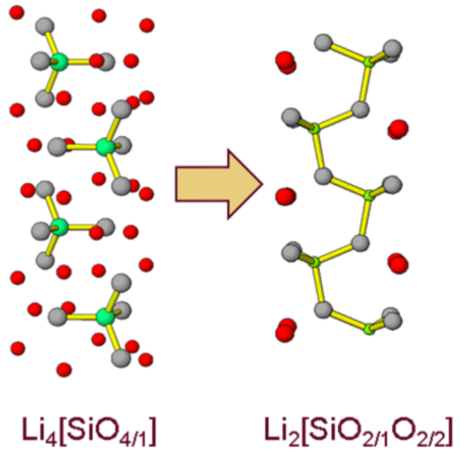

Figure V - 50: Structural relation showing condensation of molecular [SiO_4] to chains of [SiO_3]

Solid state NMR of a mixed phase sample is presented in Figure V - 51. The initial sample shows NMR signals from all three identified silicate species. After one week exposure to either BATT standard or Gen2 electrolyte, the ratio of the peaks changes in a way consistent with the proposed mechanism. The amount of [SiO_4] and [Si_2O_7] anions are diminished while the amount of anionic [SiO_3] chains has increased.

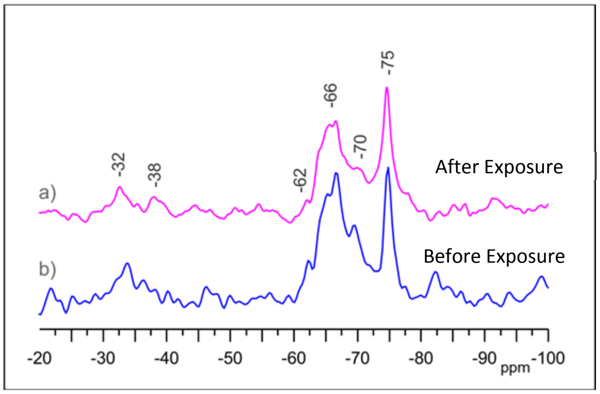

Figure V - 51: Solid State ^{29}Si NMR spectra of mixed Li-Si-O's before and after exposure to DME for 1 week

EQCM: Electrochemical quartz crystal microbalance (EQCM) studies were performed on simulated silicon and silicon coated with a thin film of silica. Cycling the thin film electrodes in a series of electrolytes was used to determine the disposition of the silica coating (after Li_4SiO_4 formation) and the role of FEC on the SEI layer. Cycling data and EQCM measurements were consistent with the NMR and XRD data. Evidence for weight loss was seen as the condensation reaction was happening. The FEC was found to have a strong effect on the SEI layer. The samples, especially when compared to Gen2, were found to have much denser SEI layers with FEC present. This is consistent with the mechanism proposed by modelers for FEC polymerization and its role in protecting the surface of the electrode.

Conclusions and Future Directions

During these studies, the role of interfaces in silicon electrodes was examined and the results were extrapolated to identify underlying mechanisms that cause capacity fade and poor coulombic efficiency. In this effort, it was shown that the passivation layer of the silicon is not an innocent bystander in the cell as often assumed. The material pulls in lithium on first charge and gradually releases lithia (Li_2O) as it reacts with the electrolyte. This reaction at the interface results in the formation, eventually, of a condensed polysilicate with poor Li-ion conductivity. Future directions will focus on:

Working with the BATT-Anode team to model and better describe the surfaces and materials present in a working electrode.

FY 2014 Publications/Presentations

1. Vaughey, J.T., Trahey, L., Dogan, F. (June 2014). "Novel Anode Materials: Three Dimensional Architectures." Presented at the 2014 DOE Annual Merit Review and Peer Evaluation Meeting, Washington, D.C.
2. Dogan, F., Joyce, C., Vaughey, J.T. (2013). "Formation of New Silicon Local Environments upon Annealing for Silicon Anodes: A ^{29}Si Solid State NMR Study." *J. Electrochem. Soc*, (160); p. A312.
3. Brushett, F.R., Trahey, L., Xiao, X., and Vaughey, J. T. (2014). "Full-Field Synchrotron Tomography of Non-Graphitic Foam and Laminate Anodes for Lithium-Ion Batteries." *ACS Applied Mater. Interfaces* (6); p. 4524.
4. Vaughey, J. T., Liu, G., Zhang, J.G. (2014). "Stabilizing the Surface of Lithium Metal." *MRS Bulletin*, (39); p. 429.
5. Hubaud, A., Ingram, B., Key, B., Schroeder, D., Vaughey, J. T. (2013). "Role of Al Substitution in Stabilizing the Structure of the Solid Lithium-Ion Conductor Li7-xAlxLa3Zr2O12." *J. Mat Chem. A* (1); p. 8813.
6. Neuhold, S., Vaughey, J. T., Grogger, C., López, C.M. (2013). "Enhancement in Cycle Life of Metallic Lithium Electrodes Protected with Fp-Silane Derived Coatings." *J. Power Sources* (254); p. 241.

7. Woo, J.-J., Marconi, V.A., Liu, G., Vaughey, J.T., Amine, K., Gosztola, D.J., Zhang, Z. (2014). “Symmetrical Impedance Study on Inactivation Induced Degradation of Lithium Electrodes for Batteries Beyond Lithium-ion.” J. *Electrochem. Soc.* (161); p. A827.
8. Dogan, F., Sanjeewa, D., Trahey, L., Vaughey, J.T. (October 2013). “Three-Dimensional Silicon Anode Architectures via Electrodeposition on Copper Foam Current Collectors.” Presented at the 224th Meeting of the Electrochemical Society, San Francisco, CA.
9. Hubaud, D. Schroeder, B.J., Ingram, Vaughey, J.T. (March 2014). “Thin Film Ceramic Electrolytes.” Presented at the Gordon Conference on Batteries, Ventura, CA.
10. Dogan, F., Proffitt, D., Hubbard, A., Schroeder, D. J., Key, B., Vaughey, J. T. (July 2014). “Materials Development for Energy Storage Applications.” Presented at the Gordon Conference on Solid State Chemistry, New London, NH.

V.C.2 Metal-Based High Capacity Li-Ion Anodes (SUNY Binghamton)

M. Stanley Whittingham
SUNY at Binghamton

Department of Chemistry and Materials S&E
Vestal Parkway East
Binghamton, NY 13902-6000
Phone: (607) 777-4623; Fax: (607) 777-4623
E-mail: stanwhit@binghamton.edu

Start Date: January 2011
Projected End Date: December 2014

Objectives

- To replace the presently used carbon anodes with:
    - Materials that have double the volumetric energy density of carbon
        - 1.6 Ah/cm^3, and
        - ≥ 500 Ah/kg.
    - Materials that are compatible with low cost layered oxide and phosphate cathodes and the associated electrolyte.
    - Lower cost materials and approaches.

Technical Barriers

This project addresses the following technical barriers facing the use of Li-ion batteries in PHEV and all-electric vehicles:

- Materials and manufacturing cost of Li-ion batteries.
- Safety of Li-ion batteries, including abuse-tolerance.
- Volumetric capacity limitations of Li-ion batteries.

Technical Targets

- Determine the reaction mechanism of the nano-Sn-Fe-C system.
- Identify the cause of the first cycle excess lithium capacity and propose approaches to mitigate it.
- Identify an anode candidate having an energy density of 2 Ah/cm^3 for at least 100 cycles.
- Determine the electrochemistry of the leached nano-silicon material, and compare to the standard silicon.

Accomplishments

- Determined the reaction mechanism of the nano-Sn-Fe-C system.
- Identified the key parameters causing the first cycle excess.
- Shown more than 100 cycles at low and at C rates with a capacity of at least 1.6 Ah/cm^3.
- Determined that the solvothermal approach for the synthesis of the Sn-Fe-C composite is a No-Go.
- Identified two promising approaches for nano-silicon.

✧ ✧ ✧ ✧ ✧

Introduction

Achieving the DOE cost and energy/power density targets will require improved anode materials that have higher volumetric energy densities than carbon, and lower cost production methods. At the same time, the material must have higher lithium diffusion rates than carbon and preferably be at a slightly higher potential to improve the safety. Replacing the present carbon anode with a Si or Sn based composite will increase the overall cell capacity by at least 50%.

Approach

The anode approach is to synthesize, characterize and develop inexpensive materials that have higher volumetric energy densities than carbon. Emphasis is being placed on simple metal alloys/composites at the nano-size. The initial focus is being placed on tin, building on what was learned from previous studies of the tin-cobalt anode, the only commercial anode besides carbon. All materials will be evaluated electrochemically in a variety of cell configurations, and for thermal, kinetic and structural stability to gain an understanding of their behavior. Ideally these will have a potential slightly higher than that of carbon and above that of pure lithium, so as to minimize risk of Li plating and thus enhance safety, while allowing for rapid charging. As Figure V - 52 shows, incorporating as little as 2.3 Li into tin will allow a doubling of the volumetric capacity and an increase of the gravimetric capacity.

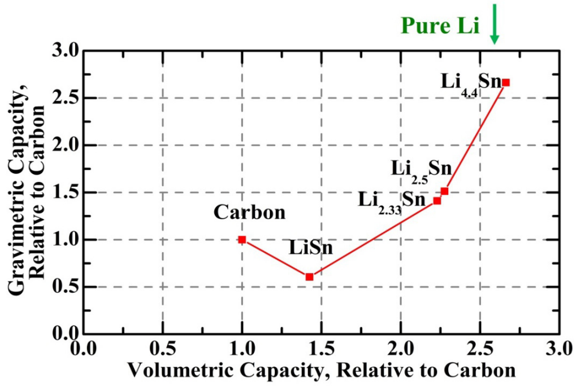

Figure V - 52: Capacity of tin-based anodes compared to carbon. The volumetric capacity of Li ≈ $Li_{4.4}Sn$≈$Li_{4.4}Si$

Results

Mechanism of reaction of Sn-Fe-C composite: *In situ* X-ray diffraction of an operating cell at Brookhaven National Laboratory showed the presence of Sn and Sn_2Fe in the pristine electrode before discharge, and their complete disappearance on lithiation with the formation of Li_xSn compounds. On recharge, the Sn and Sn_2Fe are reformed. Similar behavior was observed on the 2nd cycle. This shows the total reversibility of the Sn-Fe-C composite. These results are consistent with the X-ray absorption spectroscopy (XAS) reported last year, which reveals that the mechanism is a conversion reaction that converts Sn and Sn_2Fe to Li-Sn alloys. (See Figure V - 53.)

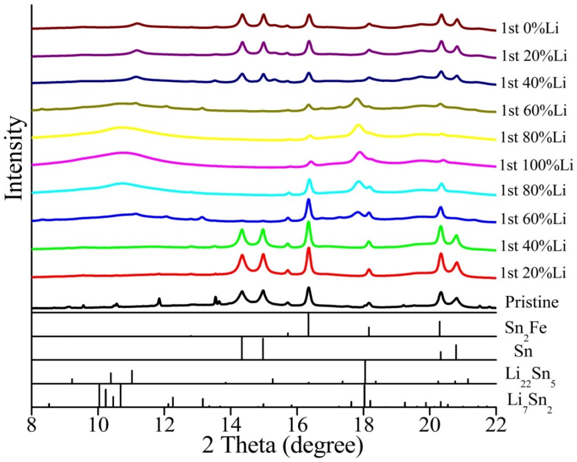

Figure V - 53: X-ray diffraction pattern performed on operating electrochemical cells as a function of discharge and charge. λ=0.728 Å

Identified the key parameters causing the first cycle excess capacity: The Ti/Sn molar ratio used in the synthesis of the nano-sized Sn-Fe-C composite was varied to reduce the first cycle excess capacity (first cycle capacity loss). As shown in Figure V - 54(top), when the Ti/Sn ratio increases from 0 to 1, the first cycle capacity loss is continuously decreases from 610 mAh/g to 390 mAh/g. This decrease mainly occurs when the Ti/Sn ratio varies from 0 to 0.5, and after that (i.e., Ti/Sn ratio from 0.5 to 1) the decrease is less. This observation indicates that the Ti content of this material has a marked impact on the chemistry/electrochemistry on the initial reaction with lithium; it is however not the only contributor to the capacity. From an overall capacity retention point of view, an optimum Ti/Sn ratio appears to be between 0.25 and 0.5 (Figure V - 54 bottom).

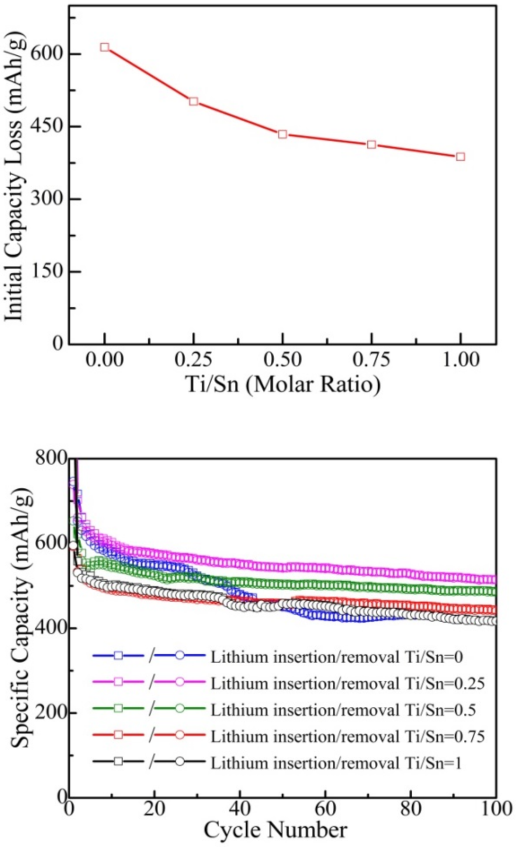

Figure V - 54: (top) First cycle capacity as a function of the Ti/Sn ratio, and (bottom) electrochemical capacity of Sn-Fe-C composites as a function of the Ti/Sn ratio

The impact of varying the graphite/Sn molar ratio used in synthesizing the Sn-Fe-C composite was determined. Figure V - 55 shows that when the graphite/Sn molar ratio decreases from 10 to 5, a small decrease of both the first capacity loss and the overall capacity is observed. This decrease suggests that although the graphite contributes to the first capacity loss, the overall electrochemical performance does not benefit from reducing the amount of graphite. Moreover, the capacity retention is worse when less graphite is added. It is noteworthy that a lower graphite/Sn ratio results in a higher crystallinity of the material, which can be associated with degradation of the capacity retention.

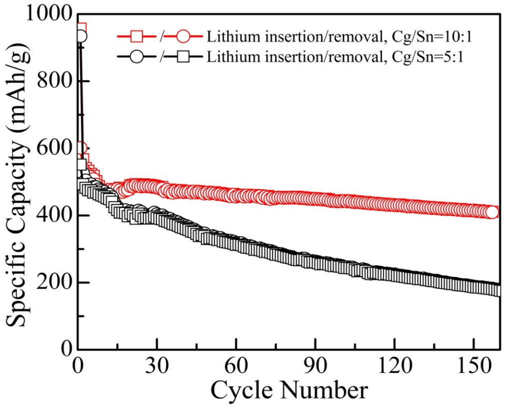

Figure V - 55: Carbon plays a critical role in the maintenance of capacity on cycling

The capacity after the first cycle is greater than expected from just the reaction of Li with Sn to form $Li_{4.4}Sn$. The reaction of Li with some of the carbon to form the phase LiC_2 must be invoked. The first cycle excess capacity is believed to be associated with reaction with the titanium oxides to form Li_xTiO_y and the formation of titanium carbides TiC_y.

Extended cycling shows capacity around 1.6 Ah/cm^3: The optimum synthesis approach for nano-tin anode is the mechanochemical method, with the initial ratio of SnO, Ti and graphite of 1:0.25:10 (ball-milling for 8 h). This nano-sized Sn-Fe-C composite shows excellent extended cycling at the C/10 rate as shown in Figure V - 56. The calculated volumetric capacity exceeds 1.6 Ah/ cm^3 for 100 cycles, which is double the capacity of carbon. The cycling efficiency exceeds 99% for most of the cycles.

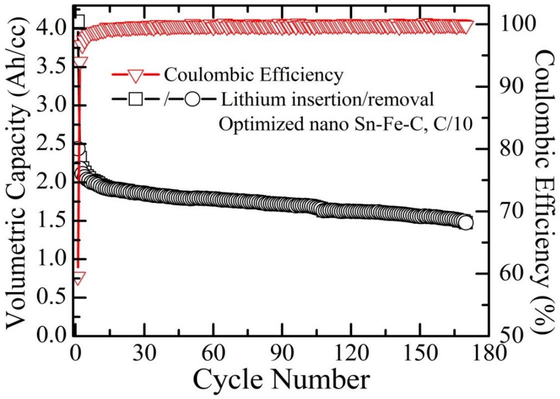

Figure V - 56: The volumetric capacity and cycling efficiency of the Sn-Fe-C composite over 100 cycles

At a C rate on both discharge and charge, the capacity retention is not as good as at C/10 as shown in Figure V - 57(top). However, the capacity still exceeds that of a carbon anode cycled under the same conditions for more than 140 cycles. However, shortly thereafter, the cell failed as indicated in Figure V - 57 (middle). This was believed to be due to the failure of the lithium anode. On replacement of the lithium anode, separator and electrolyte, the cell capacity was recovered as shown in Figure V - 57(bottom). It is therefore likely that the Sn-Fe-C composite can be cycled more than 200 times.

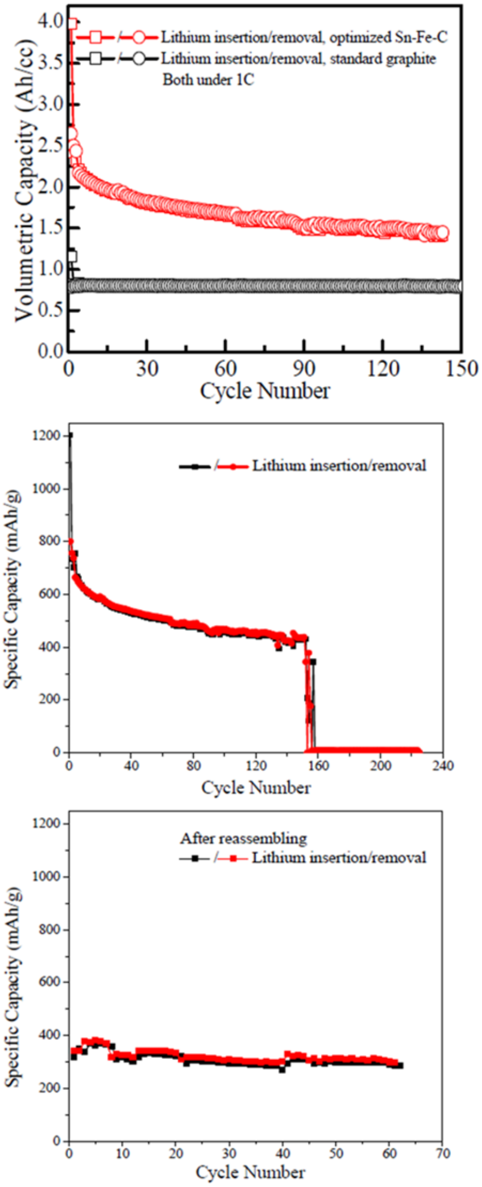

Figure V - 57: (top) Volumetric capacity comparison of the optimized Sn-Fe-C composite with standard graphite cycled under 1C rate (1C corresponding to a current density of 600 mA/g for Sn-Fe-C, 372 mA/g for standard graphite). The cycling curves of optimized Sn-Fe-C composite (middle) before and (bottom) after replacing lithium the anode in the coin cell

Determined that the solvothermal approach for the synthesis of the Sn-Fe-C composite is a No-Go: The nano-sized Sn-Fe-C composite made using a hydrothermal approach showed a more rapid loss in capacity than mechanochemical synthesized composite even when only Sn_2Fe was present. The presence of any tin caused an extremely rapid loss of capacity, 80% over 20 cycles.

Determined the synthetic approaches for silicon: The synthesis approaches for nano-silicon were narrowed to the two most promising. In the first approach, nano-silicon was formed from a readily available Al-Si alloy by leaching out most of the Al; around 3-5% Al remains dissolved in the nano-silicon and favorably impacts the electrochemical behavior. The electrochemical behavior of the leached alloy was described last year. In the second approach, nano-silicon was made by the titanium reduction of "SiO", similarly to the method used for formation of the nano-tin material reported above. The latter method is a modification from the earlier approach of reducing the SiO using magnesium metal. The use of Ti gave a higher capacity material than found for the Mg produced material. The capacity and cycling efficiency of this material is shown in Figure V - 58.

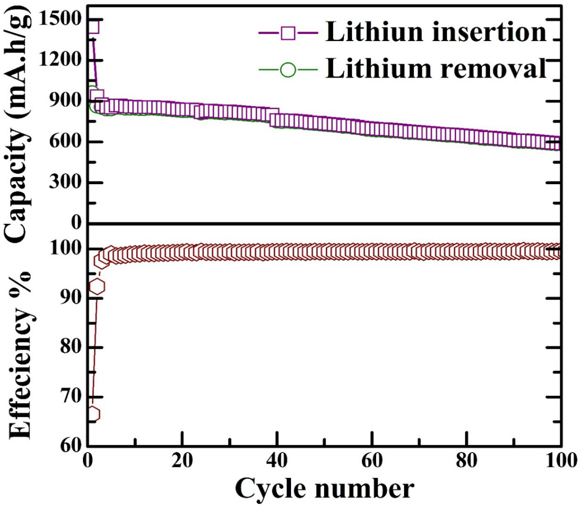

Figure V - 58: Capacity and efficiency versus cycle number of Si-Ti-C between 0.002 and 2 V at C/20 rate (0.4 mA/cm²)

Conclusions and Future Directions

Nano-tin: Two synthesis methods were explored for making the Sn-Fe-C composite – mechanochemical and hydrothermal. The mechanochemical approach gave material with the better electrochemical behavior. The optimum carbon and titanium contents in the synthesis were determined; a 10:1 ratio of C:Sn and 0.25 Ti:Sn ratio gave the best cell behavior. The excellent electrochemical behavior of this nano-Sn_2Fe has been determined, and matches the SONY Sn-Co-C anode in capacity and rate capability. This Sn-Fe-C composite shows all the capabilities to double the volumetric capacity of carbon, while also exceeding the gravimetric capacity of carbon. More than 100 cycles were obtained at both C/10 and C rates. The mechanism of reaction of this composite was determined to be that of a conversion reaction, with no structure retention. The $SnFe_2$ compound forms lithium tin alloys and iron metal on reaction with lithium, and the reaction is fully reversible. In addition the carbon not only provides a protective coating for the tin compound but also is an active electrochemical component. A composition of LiC_2 is formed; the nature of the material will be studied in future efforts. This Sn-Fe-C composite will be the anode component of a new BATT award.

Nano-silicon: Nano-silicon was formed by two different methods. That formed by leaching an Al-Si alloy has a unique morphology and the presence of a little dissolved Al improved the capacity retention. Nano-silicon was also formed from SiO by mechanochemical reaction with titanium. It had a slightly lower capacity than the Si-Al alloy, but a higher capacity of Si formed by Mg reduction of SiO. The future effort on the nano-Si will emphasize reducing the first cycle loss and improving the cycling performance.

FY 2014 Publications/Presentations

1. Whittingham, S. (June 2014). "Metal-Based High Capacity Li-Ion Anodes." Presented at the 2014 DOE Annual Merit Review and Peer Evaluation Meeting, Washington, D.C.
2. Dong, Z., Zhang, R., Wang, Q., Chernova, N. A., Whittingham, S. (December 2013). "Synthesis and Characterization of Nanosized Sn_2Fe as Anode Materials for Lithium-Ion Batteries." Presented at the Materials Research Society Fall Meeting, Boston, MA.
3. Jiang, T., Zhang, R., Zhou, W., Whittingham, S. (December 2013). "Morphology, Composition and Electrochemistry: A Comparative Study of Si Anodes for Lithium-Ion Batteries." Presented at the Materials Research Society Fall Meeting, Boston, MA.
4. Wang, Q., Dong, Z., Chernova, N.A., Omenya, F., Jung, H., Grey, C.P., Whittingham, S. (December 2013). "Understanding Sn-Based Anode Materials for Li-Ion Batteries: X-Ray Absorption Spectroscopic Studies." Presented at the Materials Research Society Fall Meeting, Boston, MA.

V.C.3 New Layered Nanolaminates for Use in Lithium Battery Anodes (Drexel U)

Yury Gogotsi (Principal Investigator)
Drexel University

Department of Materials Science and Engineering
3141 Chestnut Street
Philadelphia, PA 19104
Phone: (215) 895-6446; Fax: (215) 895-1934
E-mail: gogotsi@drexel.edu

Michel W. Barsoum (Co-PI)
Department of Materials Science and Engineering
3141 Chestnut Street
Philadelphia, PA 19104
Phone: (215) 895-2338; Fax: (215) 895-6760
E-mail: barsoumw@drexel.edu

Start Date: January 2011
Projected End Date: December 2014

Objectives

- Replace graphite with a new material selected from a group of layered (two-dimensional) binary carbides and nitrides known as MXenes, which may offer combined advantages of graphite and Si anodes with a higher capacity than the former, less expansion, longer cycle life and a lower cost than the latter.

Technical Barriers

This project aims to address the following technical barriers facing modern Li-ion batteries technology:

(A) Short life-span of modern batteries,

(B) Low charge density, and

(C) Compromised safety.

Technical Targets

- Perform the a*b initio* simulation of Li incorporation into MAX phase carbides.
- Screening electrochemical experiments on a variety of MAX phases to select the most promising ones for more detailed study.
- Studying the effect of particle size on the capacity of the three best materials.
- Improvement of capacity by selective extraction of A atoms, to add space for the Li.
- Investigation of solid electrolyte interface (SEI) formation on selected carbides.
- Optimization of the material. Testing the rate capability of the anode.
- *In situ* study of charge/discharge processes and better understanding of the mechanisms of Li insertion.
- Comparison of powder vs. solids with 10-20% porosity.

Accomplishments

- Completed *in situ* and *ex situ* studies of the lithiation and delithiation mechanisms.
- Predicted theoretical capacity values for MXenes of different chemistry.
- Discovered, synthesized and electrochemically tested a new Mo containing MXene, Mo_2TiC_2.
- Completed study of the effect of carbon additives on the performance of multilayered MXenes in LIBs.
- Achieved highly reversible gravimetric and areal capacities for Nb_2C-based composite anodes that are well above those currently reported for other anode systems.

✧ ✧ ✧ ✧ ✧

Introduction

In FY 2011, a new family of two-dimensional materials was discovered, which were labeled MXenes. A number of MXenes of different chemistries (such as Ti_3C_2, Ti_2C, $Ti_3(C_{0.5}N_{0.5})_2$ and Ta_4C_3) were successfully produced by selectively etching Al from the corresponding MAX phases and tested showing excellent potential as anode material in LIBs. In FY 2013, the main focus shifted to lighter MXenes of M_2X formulae and additive-free anodes. In order to understand the mechanism of Li insertion and further maximize capacity, the charge/discharge behavior of MXene anodes and the effect of carbon additives on their performance was initiated in FY 2013 and continued in FY 2014. In FY 2014, the effect of chemistry and particle size was also investigated to select the most promising MXenes as improved cycle-life anodes for LIBs. Herein are highlights of some results obtained during FY 2014.

Approach

Since at this time the exact relationship between capacity and MXene phase chemistry is unknown, a rapid screening of as many MXene phases as possible is being carried out to determine the most promising chemistry, by testing their performance in Li-ion batteries, LIB. This work is also guided by *ab initio* calculations.

Results

Study of lithiation/delithiation mechanisms: To understand the lithiation and delithiation mechanisms, *in situ* X-ray absorption spectroscopy (XAS) and X-ray photoelectron spectroscopy (XPS) were used. The X-ray absorption near edge spectroscopy (XANES) showed a shift of Ti K edge spectrum to lower and higher energies after lithiation and delithiation, respectively, implying the Ti oxidation states change reversibly from lower to higher oxidation states (Figure V - 59). This is evidence for a redox process. No evidence for a conversion reaction was observed. The variation of the Ti edge energies during lithiation and delithiation (not shown) also suggests the formation of a second Li layer on the $Ti_3C_2O_2Li_2$ layers. Theoretical calculations confirmed that the formation of additional atomic layers of Li on $Ti_3C_2O_2Li_2$ is possible.

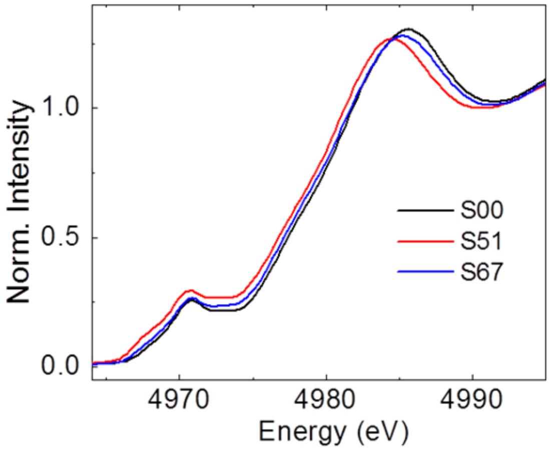

Figure V - 59: *In situ* Ti K-edge XANES analysis of lithiation and delithiation of Ti_3C_2.

Ex situ XPS study of the lithiation, down to 5 mV, and delithiation to 3 V during electrochemical cycling of Ti_3C_2 showed that the 1st cycle irreversibiliy is affected mostly by the irreversible formation of LiF and Li_2O and partially by $ROCO_2Li$ and/or TiF-Li by the end of the first cycle (Figure V - 60). This implies that SEI is not the strongest contributor to the 1st cycle irreversibility. On the another hand, the shift to higher binding energy values in the Li 1s (Figure V - 60B), O 1s and F 1s regions was also observed and assigned to Li interacting with/absorbing onto the MXene O and F surface groups that could correspond to the reversible lithiation and delithiation mechanisms. The XPS peaks after 8 cycles were not too different from those after the 1st cycle. Only a slight increase in the LiF and decrease of TiO-Li peak intensities were observed that would correspond to a small drop in capacity values upon cycling.

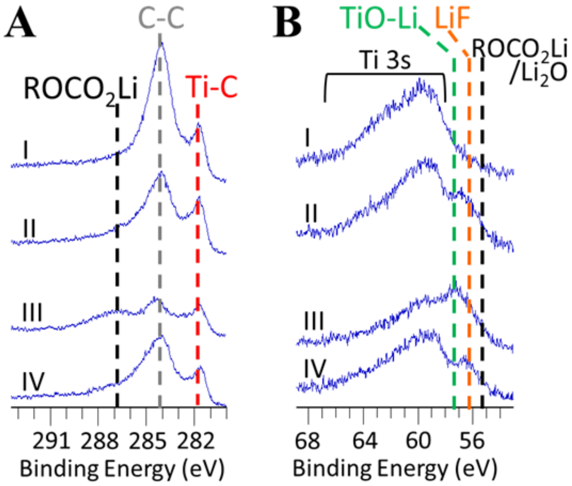

Figure V - 60: *Ex situ* XPS spectra in (A) C1s region and (B) Li1s region for Ti_3C_2 after electrochemical cycling: I – initial Ti_3C_2 soaked in the electrolyte; II – lithiated from OCV to 1 V; III – lithiated from OCV to 5 mV; IV – lithiated from OCV to 5 mV, then delithiated to 3 V

Theoretical capacity of MXenes: Using density functional theory, the theoretical capacities of different MXene monolayers with bare, O– and OH–terminated surfaces were calculated (Table V - 2). Bare MXenes were found to have higher capacities than surface terminated ones. Among those, V_2C and Ti_2C showed the highest values. Experimentally, V_2C gives a specific capacity of 260 $mAh.g^{-1}$ at 1 C and 125 $mAh.g^{-1}$at 10 C after 150 cycles, being the most promising among the multilayered MXenes listed in Table V - 2. Nb_2C yields 170 $mAh.g^{-1}$at 1 C, and 110 $mAh.g^{-1}$ at 10 C after 100 cycles. Both, Ti_3C_2 and Ti_2C, yield ≈110 $mAh.g^{-1}$ at 1 C after 50 cycles. These values, listed in Table V - 2, assume MXene monolayers, with one Li layer formation per surface. These results suggested that predicted theoretical values can be reached and even exceeded by maximizing the MXene active surface area through delamination (it was experimentally confirmed for delaminated Ti_3C_2 in FY 2013) and/or modifying the MXenes chemistry.

Table V - 2: Capacities (mAh.g^{-1}) corresponding to one Li layer on bare, O- and OH-terminated MXene monolayers

	$M_{n+1}X_n$	$M_{n+1}X_nO_2$	$M_{n+1}X_n(OH)_2$
Ti_2C	439	383	95
V_2C	418	335	91
Nb_2C	252	219	58
Ti_3C_2	294	250	67

Effect of carbon additives on performance of binder-free multilayered MXene anodes: To maximize areal capacity of multilayered MXenes by increasing their conductivity, the effect of different carbon additives (carbon black, CB; carbon onions, and carbon nanotubes, CNT) was tested. The additives were mixed with multilayered Ti_3C_2, pressed into free-standing discs, with loadings of ≈50 mg.cm^{-2} and tested as anodes. The resulting areal capacities vs. cycle number are summarized in Figure V - 61. Among those, the Ti_3C_2/CB mixture showed the highest reversible areal capacity – 5.9 mAh.cm^{-2} after 50 cycles – at a rate of ≈ C/3, a value ≈ 5 times higher compared to bare Ti_3C_2 pressed discs.

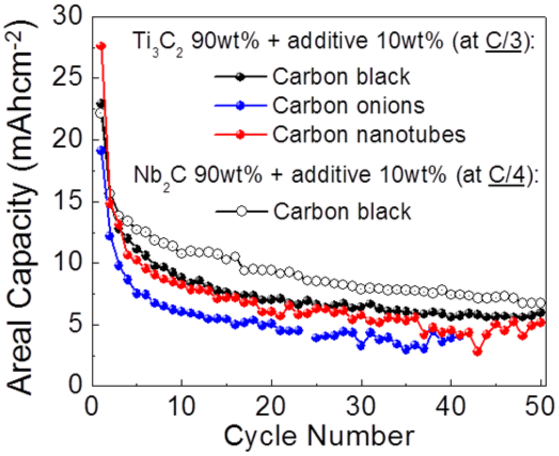

Figure V - 61: Areal capacity *vs.* cycle # for pressed Ti_3C_2 and Nb_2C discs with 10 wt.% of different carbon additives at C/3 and C/4, respectively

The performance of other multilayered MXenes was also improved by using CB. Nb_2C anodes pressed with 10 wt.% of CB showed a capacity of 7 mAh.cm^{-2} after 50 cycles at a current of 1.5 mA.cm^{-2} (represented by unfilled circles in Figure V - 61). The values achieved for both Ti_3C_2 and Nb_2C are above those reported for other anodes (Figure V - 62).

To enhance the volumetric capacity while retaining the high areal capacity, thinner Ti_3C_2 electrodes were produced, with mass loading of ≈15 mg.cm^{-2} compared to ≈50 mg.cm^{-2}. And while this decreased the areal capacity to 2 mAh.cm^{-2}, it is still comparable to literature values. The volumetric capacity, on the other hand, was doubled compared to original high mass loading films and reached ≈260 mAh.cm^{-3}.

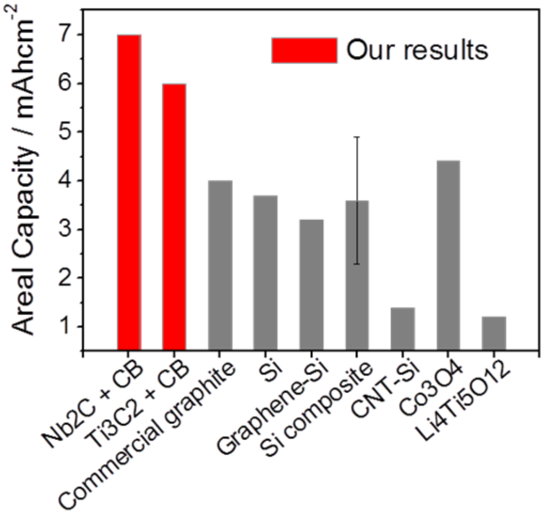

Figure V - 62: Comparison of areal capacities for Ti_3C_2 and Nb_2C discs with 10 wt.% of CB with other systems

Effect of carbon additives on performance of binder-free delaminated MXene anodes: To maximize gravimetric capacity and improve the rate performance, delaminated d-Ti_3C_2 and d-Nb_2C were mixed with CNTs to form composite electrodes. The latter acted as spacers to allow the electrolyte to penetrate between the MXene layers, and as a conductive agent to facilitate electron transfer at higher rates. Nb_2C was delaminated into single flakes by intercalation with isopropylamine followed by sonication in water for 1 h; dimethyl sulfoxide was used to delaminate Ti_3C_2 (reported in FY 2013). Nanocomposite papers were prepared by filtering a mixture of corresponding delaminated MXene colloidal solution and 10 wt.% CNT dispersion. A SEM image of *d-*Nb_2C*/CNT* paper can be seen in inset of Figure V - 63B.

A reversible capacity of over 150 mAh.g^{-1} was achieved for the *d-*Ti_3C_2*/CNT* electrode during 300 cycles instead of 20 mAh.g^{-1} for pure d-Ti_3C_2 at the same cycling rate of 1 C. At 0.5 C, the capacity yielded by the *d-*Nb_2C*/CNT* paper (≈430 mAh.g^{-1} over 100 cycles) was almost double that for *d-*Ti_3C_2*/CNT* paper at the same current density (Figure V - 63A; also see inset in Figure V - 63B). Note that the capacities for both electrodes continue to increase even after tens of cycles signifying that cycling improves access of Li-ions to the interlayer spaces. This result is quite encouraging since it clearly implies that further improvement through optimization of the electrode architecture is possible.

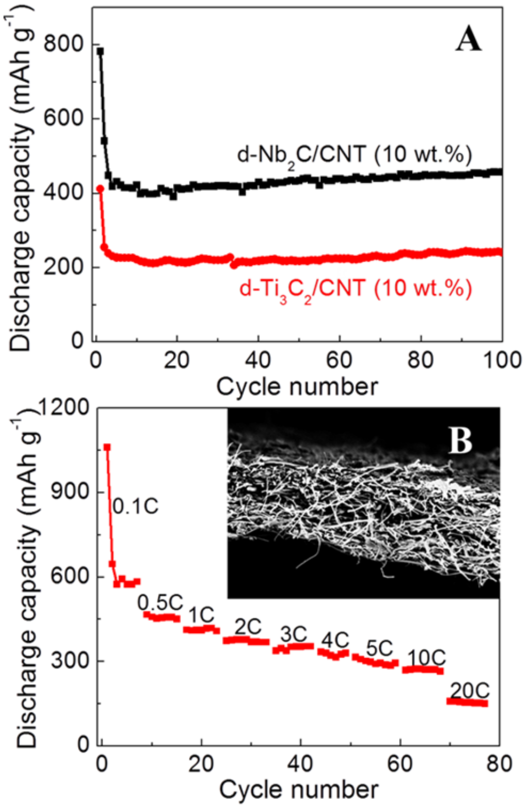

Figure V - 63: Electrochemical performance of d-Nb_2C/CNT nanocomposite paper: (A) cycling performance compared to d-Ti_3C_2/CNT paper at 0.5 C; (B) rate performance. Inset in (B) shows a cross-sectional SEM image of d-Nb_2C/CNT paper

A highly reversible capacitance of ≈600 mAh.g^{-1} was achieved for *d-Nb_2C/CNT* paper at 0.1 C (Figure V - 63B). This value is even higher than the theoretical values for d-Nb_2CO_2 (466 mAh.g^{-1}) assuming 2 Li layers on each side of each flake. This result thus implies that more than two Li layers are deposited on each d-Nb_2C flake or the presence of additional storage mechanisms in the composite paper. At 10 C, the capacitance was stable at ≈270 mAh.g^{-1}, greatly exceeding the performance of any commercial electrodes at that rate. A capacitance of ≈150 mAh.g^{-1} was still preserved at 20 C indicating outstanding rate performance of this d-Nb_2C/CNT paper.

A new Mo containing MXene as anode for LIBs: With the goal of exploring MXenes that are expected to have even larger Li uptakes, a new Mo containing MXene, Mo_2TiC_2, was synthesized and tested as anode. Cyclic voltammetry curves, at a rate of 2 mVs^{-1}, for the Mo_2TiC_2 anode with conductive carbon black additive and polyvinylidene fluoride (PVDF) binder in a 70:20:10 ratio (Figure V - 64) showed that the majority of lithiation and delithiation capacity is at voltages below 2.5 V. Also, in the contrary to other MXene materials, a clear lithiation peak was observed at voltages lower than ≈ 0.5 V. The discharge curves at 0.3C showed a voltage plateau for potentials lower than 0.5 V - first for MXenes - and a capacity of ≈120 mAh.g^{-}1 (see inset in Figure V - 64). These experiments were performed using one of the first produced batches of Mo_2TiC_2 and a higher capacity is expected once the processing conditions are optimized and non-reacted MAX and other impurities are eliminated.

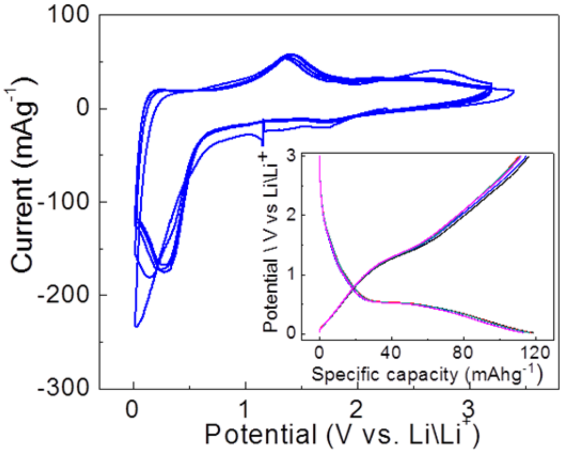

Figure V - 64: Cyclic voltammetry curves of Mo_2TiC_2 recorded at 2 mVs^{-1}. Inset shows the galvanostatic charge-discharge curves (5 cycles) at 0.3C recorded after CV measurements.

Conclusions and Future Directions

During FY 2014, all milestones were reached. Lithiation/delithiation studies confirmed that the main mechanism is based on redox reactions. It was also found that the 1st cycle irreversibility is mostly affected by irreversible formation of LiF and Li_2O and partially by $ROCO_2Li$ and/or TiF-Li by the end of cycle. Bare MXenes are predicted to have higher capacities than surface terminated one.

The effect of carbon additives on the performance of multi-layered stacks and delaminated flakes of Ti_3C_2 and Nb_2C in LIBs was studied. The carbon black at 10 wt.% loading was found to be the best additive resulting in areal capacities of 5.9 and 7 mAh.cm^{-2} for multilayered Ti_3C_2 and Nb_2C composite anodes, respectively, after 50 cycles at a current of 1.5 mA.cm^{-2}. It was also found that gravimetric capacity can be enhanced by using delaminated MXene and CNTs additive. The highest values were achieved for the d-Nb_2C/CNT electrode – 600 mAh.g^{-1} at a 0.1C and 270 mAh.g^{-1} at 10C.

A new MXene – Mo_2TiC_2 – was synthesized and tested resulting in a capacity of ≈120 mAh.g^{-1} at 0.3C and, for the first time, a clear voltage plateau for potentials lower than 0.5 V.

Approaching the end of the project, future work will focus on delivering MXene-based anodes of optimized structure, which show the highest capacities, both gravimetric and areal, at high cycling rates. The performance of the most promising MXenes and the effect of each carbon additive (carbon black, onion-like carbons, carbon nanotubes) will be summarized. Also, electrochemical study of recently discovered Mo_2TiC_2 will be continued by optimizing etching conditions, particle morphology and electrode structure, and investigating the effects on the plateau in the galvanostatic charge-discharge curves. Work on decreasing 1st cycle irreversibility is also ongoing. Based on the results, the most promising system will be defined, and the optimum structure will be chosen. The designed electrodes are expected to meet the main project goal showing capacities that are higher than those of commercial anodes.

Six plenary lectures, 20 invited talks, and 1 invited webinar were conducted in FY 2014. Also, numerous posters and conference papers were presented by PhD students. Received 2 Graduate Student Awards at the Spring 2014 MRS meeting (U.S.) and E-MRS meeting (France); Best Poster Award at the 6th PCGMR-NCKU Symposium in Taiwan.

FY 2014 Publications/Presentations

1. Gogotsi, Y. (June 2014). “New Layered Nanolaminates for Use in Lithium Battery Anodes.” Presented at the 2014 DOE Annual Merit Review and Peer Evaluation Meeting, Washington, D.C.
2. Er, D., et al. (2014). ACS Appl Mater Inter (6:14); 11173.
3. Xie, Y., et al. (2014). *ACS Nano 2014* (8:9); p. 9606.
4. M. Naguib, et al., *Adv Mater 2014* (26:7); p. 992.
5. Shi, C., et al., *Phys Rev Letts 2014* (112); p. 125501.
6. Xie, Y. et al., *J Am Chem Soc 2014* (136:17); p. 6385.
7. Naguib, M., et al., *J Am Chem Soc 2013* (135:43); p. 15966.
8. Barsoum, M.W., et al., U.S. Patent No. 2,012,177,712 (Jun. 20, 2012).

V.C.4 A Combined Experimental and Modeling Approach for the Design of High Current Efficiency Si Electrodes (GM, Michigan State U)

Xingcheng Xiao
General Motors LLC

Global Research and Development Center
30500 Mound Road
Warren, MI 48090
Phone: (248) 912-8132; Fax: (586) 986-3691
E-mail: Xingcheng.xiao@gm.com

Yue Qi
Michigan State University
Department of Chemical Engineering and Materials Science
3509 Engineering Building
East Lansing, MI 48824
Phone: (517) 432-1243; Fax: (517) 432-1105
E-mail: yueqi@egr.msu.edu

Brian W. Sheldon, Huajian Gao (Brown University)
Yang-Tse Cheng (University of Kentucky)

Start Date: May 2013
Projected End Date: April 2017

Objectives

- Combine modeling and experimental approaches to understand, design, and fabricate stabilized nano-structured Si anode with high capacity and high coulombic efficiency.

Technical Barriers

- The real challenges to developing a model that allows us to design high current efficiency Si electrodes with electrochemically and mechanically stable artificial SEI layer are: a) poor understanding of SEI failure mechanisms; b) lack of accurate mechanical properties of the SEI; and c) difficulty in validation of the model. All of these are due to the extreme challenges associated with characterizing the properties of nano-meter thin SEI layer on lithiated Si in real battery systems. Therefore, these questions will be first addressed based on simpler thin film electrodes.

  Technical Targets

- Fundamentally understand the mechanical degradation of SEI (including artificial coatings) on Si electrodes.
- Establish a correlation between the capacity loss (or current efficiency) and such mechanical degradation.
- Develop a multi-scale model to predict the stress/strain in the SEI layer on Si.
- Predict and measure the basic material properties required in the mechanics model.
- Use the model the guide the design of nanostructured Si electrode.
- Ultimately, assist USABC achieve its goal on EV energy storage: 200 Wh/kg (EV requirement); 96 Wh/kg, 316 W/kg, 3,000 cycles (PHEV 40 mile requirement). Calendar life: 15 years and improved abuse tolerance.

Accomplishments

- Computed the basic elastic properties of ALD coatings (e.g., Al_2O_3) from MD simulations with ReaxFF and measured by AFM and acoustic wave for method validation.
- Predicted the interface strength of amorphous carbon, SiO_2 and Al_2O_3 coatings on Si substrate from atomic simulations.
- Developed a continuum framework to model SEI deformation and stability on Si film and compared with *in situ* MOSS measurement.
- Demonstrated that multi-component and multi-functional artificial SEI coatings paired with a variety of Si nanostructure can be mechanically and chemically stable, based on both experiment and simulation results.

* * *

Introduction

Volume changes of up to *ca.* 300 vol.% for Si during lithiation and delithiation leads to fracture of Si and/or loss of electrical contact with the conductive phase or the current collectors. Nano-structured Si effectively mitigates Si cracking/fracture. Unfortunately, the high surface to volume ratio in nanostructures leads to unacceptable amounts of solid-electrolyte interphase (SEI) formation, thereby lowering current efficiencies. Artificial SEI coated Si nanostructures will resolve this contradiction, if the coating can be stable. Based on mechanics models, it was demonstrated that the SEI coating can be mechanically stable despite the volume change in Si, if the material properties, thickness of the SEI and the size/shape of Si are optimized. Engineering such a system is extremely difficult due to the large number of variables involved, especially when many of them are unknown.

In order to develop a validated model, it is critical to fundamentally understand the mechanical and chemical stability of SEI (hereafter, SEI refers to both naturally formed native SEI and artificial SEI coatings) in electrochemical environments, the correlation between the coulombic efficiency and the dynamic process of SEI evolution, and the structural optimization of both the SEI and the Si electrode. However, it is extremely difficult to characterize the structure and to measure the mechanical properties of SEI layers tens of nm thick on complicated geometries. This project will use thin-film geometry simplifies the investigations, while providing fundamental parameter values. Many measurements (e.g., AFM, indentation, XPS and TOF-SIMS depth profile) can be readily conducted with thin films, whereas similar measurements on particles or nanofibers are difficult. These thin-film electrodes can be appropriately modeled using continuum-based models, thus allowing the direct comparison of measurements with models to support model validation.

Approach

In this project, four steps will be taken: a) Develop a multi-scale model to predict the stress/strain in the SEI layer (including the artificial SEI layer) on thin-film Si and establish a correlation between the capacity loss (or current efficiency) and mechanical degradation of SEI on Si. b) Use atomic simulations combined with experiments performed on Si-thin-films to provide critical material properties used in the continuum modeling. c) Investigate the impact of the SEI formation on the stress/strain evolution, combined with modeling to quantify the current efficiency related to a variety of artificial SEI layers using *in situ* electrochemical experiments. d) Use the validated model to guide surface coating design and Si size/geometry optimizations that mitigate mechanical degradation to both SEI and Si.

Results

A combined experimental and atomic scale model has been established to understand the mechanical properties of both natural and artificial SEI layers. A 2D-melt method was developed to generate amorphous ALD- Al_2O_3 coatings structures at different densities. It was found that: 1) Young's modulus, En (along film growth direction), is always higher than Et (in plane direction); the modulus does not vary with film thickness; 2) E increases linearly with film density (Figure V - 65). Since the modulus of the coating is one of the important parameters for its mechanical stability on Si electrode, it is very important to correlate deposition conditions with film density and its modulus.

The growth rate and density of ALD-coated Al_2O_3 coating has been verified by X-ray reflectometry and ellipsometry. The same techniques have also been used to characterize SEI layers. The typical growth rate at 80°C is around 0.15 nm/cycle and density is about $3.26 g/cm^3$. The values have been applied to calibrate the modulus of Al_2O_3 coatings measured by a laser acoustic wave system and the modulus is around 170±5 GPa.

Compare experiments and modeling: For the same density ($3.26 g/cm^3$), atomic modeling predicted modulus is *ca.* 130GPa, lower than the experimental values (170 GPa). For the next stage, the continuum mechanics model will be developed to understand the effect of Al_2O_3 coating on the mechanical failure in Si thin film and particle, and will be validated with *in situ* electrochemical-nanomechanical experiments including *in situ* nanoindentation.

A multiscale modeling approach was developed to predict the mechanically stable size of Si-C core-shell structure: First, *ab initio* simulations were used to calculate interface properties for lithiated a-Si/a-C interface structures and combine these results with linear elasticity expressions to model conditions that will avert fracture and debonding in core-shell structures. The a-Si/a-C interface was found to retain good adhesion even at high stages of lithiation. For average lithiated structures, it has been observed that the strong Si-C bonding averts fracture at the interface; instead, the structure ruptures within lithiated a-Si.

As shown in Figure V - 66, the predicted safe zone for Si-C core-shell structures is when the thickness of the core is less than 200 nm and the thickness of the shell is approximately 10 nm.

Develop a continuum frame work to model SEI deformation and stability on Si film and compare with *in situ* MOSS measurement: Finite element simulations suggested a potentially new and important failure mode of SEI layer from plastic ratcheting in the a-Si electrode. In the model, SEI is considered a nanoscale thin layer attached on the a-Si anode and cyclic Li flux is applied on the top surface to simulate the lithiation/delithiation half cycles (Figure V - 67a). During cycling, a ratcheting mechanism of accumulative plastic deformation in the a-Si has been observed, leading to the gradual wrinkling and delamination of SEI (Figure V - 67b), which may result in battery degeneration. Analytical approach and molecular dynamics simulation will be conducted in the near future to confirm and interpret the simulation results.

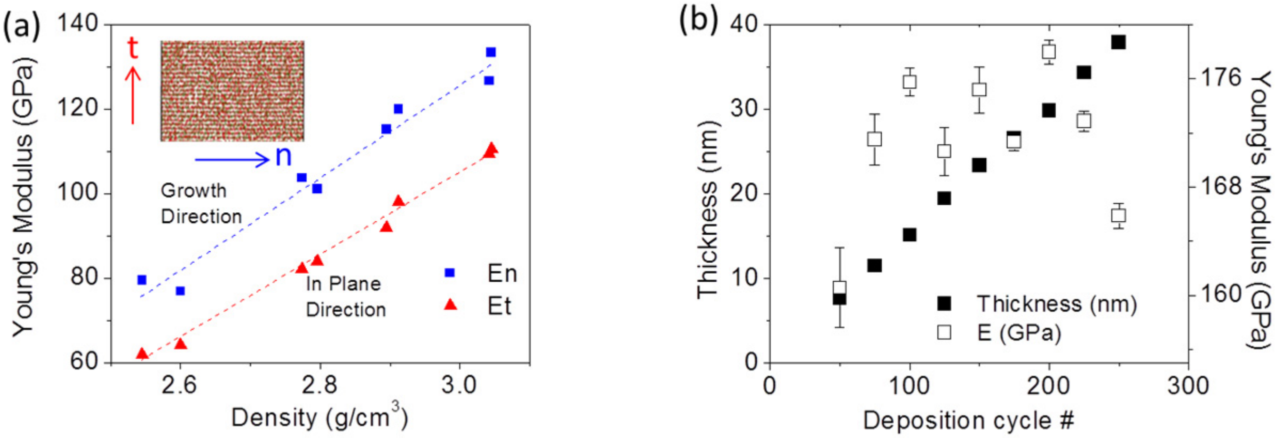

Figure V - 65: (a) MD predicted Young's modulus as a function of a-Al_2O_3 film thickness, (b) Experimentally measured the cycle number vs. thickness and calibrated modulus

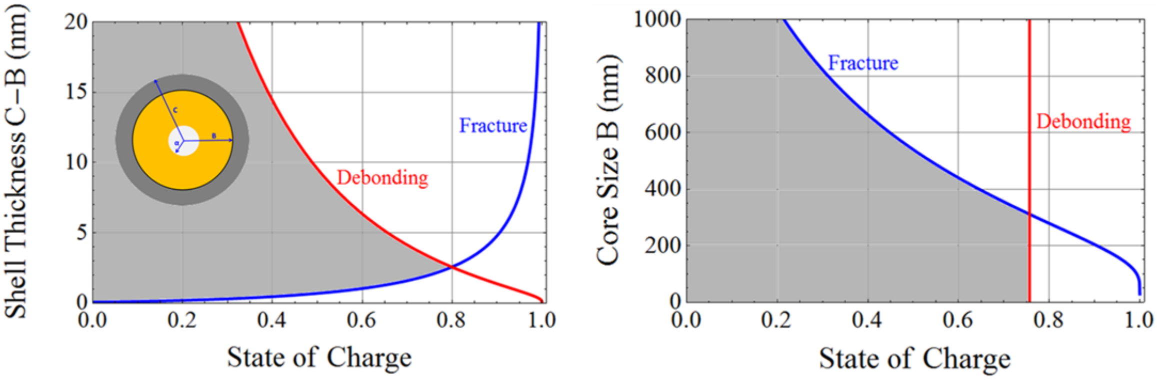

Figure V - 66: The optimized core-size and coating-thickness region for a Si-core and C-shell structure as a function of SOC

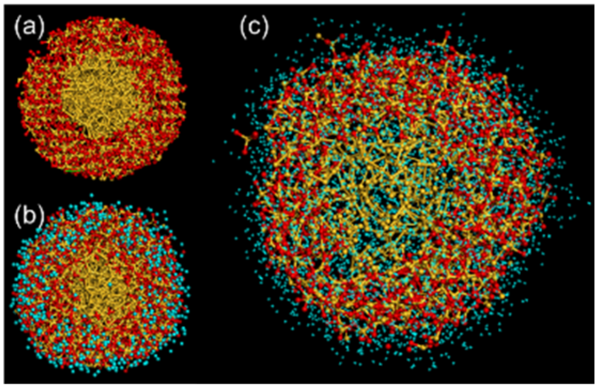

Figure V - 67: (a) Schematic of the finite element model; (b) Snapshots of the finite element results during 1st cycle and 4th cycle, respectively

Develop multi-component and multi-functional artificial SEI paired with a variety of Si nanostructure from both experiment and simulation. Identify the critical coating properties as the artificial SEI: The main possible pathways for electron leakage from LiF are via: 1) movements of ionic defects and 2) polaron migration. First principle calculations predicted the ionic defects carrying electrons have negligible concentration, thus the electron leakage through ionic defects is unlikely in LiF coated on an anode surface. Comparing the performance of various synthesized surface coatings of natural SEI components, suggested that the desirable SEI should have high LiF concentration, uniform SEI morphology, high Young's modulus, and low impedance. Atomic simulation of Si-core/SiO_2-shell nanowires revealed mechanically stable coating thickness. Reactive molecular dynamics simulations of the lithiation of Si-core/SiO_2-shell nanowires were performed. The coating structural integrity and stability vs. its thickness were investigated. (See Figure V - 68.) Upon lithiation SiO_2 shell was immediately lithiated without volume expansion, followed by the lithiation of Si core. When the thickness of SiO_2 is comparable to the size of Si, the lithiated coating remained intact. For thinner coatings, the SiO_2 coating is spread out and lost its structural integrity. These results indicated the existence of an optimal coating thickness to tolerate the volume expansion of Si anode.

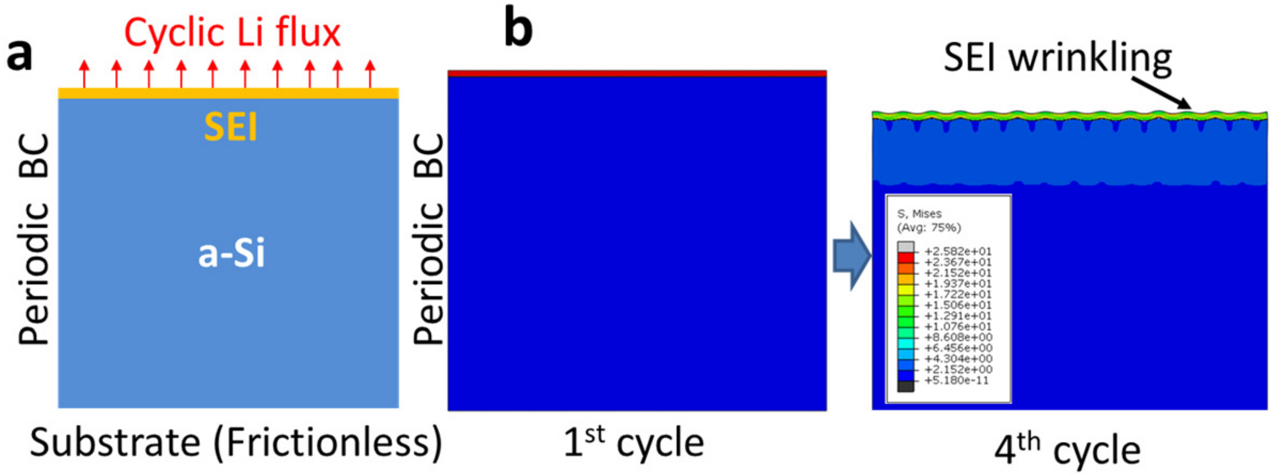

Figure V - 68: MD simulation of the lithiation process of a SiO_2 covered Si nanowire structure.

Conclusions and Future Directions

A combination of experimental approaches and MD simulations which have been developed to investigate the mechanical properties of ultrathin natural formed SEI and artificial SEI layers can be validated by the tests on ADL- Al_2O_3 coating. By comparing the performance of various synthesized surface coatings of natural SEI components, it is suggested that the desirable SEI should have high LiF concentration, uniform SEI morphology, high Young’s modulus, and low impedance. A combined DFT and continuum model has been developed to predict the mechanically stable Si-C core-shell structures, which stabilize the SEI layer and accommodate the volume expansion of Si. As a result, the breathing effect of electrodes has been significantly suppressed. These results allowed us to make a “Go” decision that multi-component and multi-functional artificial SEI coatings paired with a variety of Si nanostructure can be mechanically and chemically stable.

The next step is to identify SEI failure modes by using combined *in situ* electrochemical experiments and modeling techniques developed in this year. This was built based on previous work on patterned Si model system with controllable deformation. The *ab initio* MD simulations, supported by experimental measurements, explained that Si segregation at the interface decreased the interfacial resistance by one order of magnitude, responsible for interfacial sliding. Particularly, detailed SEI failure mode will be revealed by using MD simulations with ReaxFF for Li-Si-Al-O-C system to model the deformation of SEI on a Si as it undergoes large strain. The desirable material properties for stable SEI will also be correlated and determined by applying the continuum model and experimental nanomechanics, therefore establishing the material property design methodology for stabilizing SEI on Si.

FY 2014 Publications/Presentations

1. Stoumara, M. E., Qi, Y., and Shenoy, V. B. (2014). “From Ab Initio Calculations to Multiscale Design of Si/C Core–Shell Particles for Li-Ion Anodes.” *Nano Letters* (14:4); pp. 2140–2149.
2. Su, X., Wu, Q., Li, J., Xiao, X., Lott, A., Lu, W., Sheldon, B. W., Wu, J. (2014). “Silicon-based Nanomaterials for Lithium Ion Batteries - A Review.” *Advanced Energy Materials* (4); pp. 1-23.
3. Hassan, F. M., Chabot, V., Elsayed, A., Xiao, X., Chen, Z. (2014). “Engineered Si electrode nano-architecture: A scalable treatment for the production of next-generation Li-ion batteries.” *Nano Letters* (14:1); pp. 277–283.
4. Tokranov, A., Xiao, X., Lu, P., Sheldon, B. W. (2014). “The origin of stress in the solid electrolyte interphase on carbon electrodes for Li ion batteries.” *Journal of Electrochemistry Society* (161:1); pp. A58-A65.
5. S. Kim, Y. Qi. (2014). “Property Evolution of Al_2O_3 Coated and Uncoated Si Electrodes: A First Principles Investigation”, *Journals of the Electrochemical Society* (161:11); pp: F3137-F3143.
6. Q. Zhang, X. Xiao, Y. Cheng, and M. W. Verbrugge. (2014). “A non-destructive method to measure the mechanical properties of ultrathin film prepared by atomic layer deposition”, *Applied Physics Letters*, 105, 061901 (2014).
7. Zhang, Q., Xiao, X., Zhou, W., Cheng, Y., Verbrugge, M. W. (2014). “Towards High Cycle Efficiency of Silicon-Based Negative Electrodes by Designing Solid Electrolyte Interphase.” *Advanced Energy Materials*. DOI: 10.1002/aenm.201401398.

8. Zhou, W., Xiao, X., Cai, M., Li, Y. (2014). “Polydopamine Coated Nitrogen Confused Hollow Carbon–Sulfur Core–Shell Structure for Improving the Lithium–Sulfur Batteries.” *Nano Letters* dx.doi.org/10.1021/nl502238b.
9. Hassan, F.M., Elsayed, A., Chabot, V., Batmaz, R., Xiao, X., and Chen, Z. (2014). “Subeutectic Growth of Single-Crystal Silicon Nanowires Grown on and Wrapped with Graphene Nanosheets High-Performance Anode Material for Lithium-Ion Battery.” *ACS Appl. Mater. Interfaces* (6:16); pp. 13757–13764.
10. Tokranov, A., Sheldon, B.W., Li, C., Minne, S., and Xiao, X. (2014). “*In situ* AFM Study of Initial SEI Formation on Silicon Electrodes for Li Ion Batteries.” *ACS Applied Materials & Interfaces* (6); pp. 6672-6686.
11. Chabot, V., Feng, K., Park, H. W., Hassan, F. M., Elsayed, A., Yu, A., Xiao, X., Chen, Z. (2014). “Graphene wrapped silicon nanocomposites for enhanced electrochemical performance in lithium ion batteries.” *Electrochimica Acta* (130); pp. 127-134.
12. Qi, Y. (August 2014). “Defect facilitated electron leakage through the solid electrolyte interphase in Li-ion batteries.” Invited talk presented at the 248th ACS, Division of COMP, SESSION: Modeling and Simulations of Electrochemical Interfaces and Materials for Energy Storage, San Francisco, CA.
13. Qi, Y. (July 2014). “Predicting interface properties in Li-ion batteries.” Presented at the 1st International Symposium on Energy Challenges and Mechanics, Aberdeen, Scotland.

V.C.5 Hierarchical Assembly of Inorganic/Organic Hybrid Si Negative Electrodes (LBNL)

Gao Liu
Lawrence Berkeley National Laboratory

Environmental Energy Technologies Division
1 Cyclotron Road, MS 70R108B
Berkeley, CA 94720
Phone: (510) 486-7207; Fax: (510) 486-7303
E-mail: gliu@lbl.gov

Start Date: October 2013
Projected End Date: September 2014

Objectives

- Develop new conductive polymer binder materials to enable large volume-change Li storage materials to be used in Li-ion electrode.
- Explore and modify different aspects of conventional polymer binder, which allow the design of new types of electrode materials.

Technical Barriers

This project addresses the following technical barriers from the Energy Storage section of the Vehicle Technologies Program Multi-Year Research, Development and Demonstration Plan: 1) calendar and cycle life, 2) energy density and 3) cost.

Technical Targets

Relevant USABC goals:

EV

- \$150/kWh.
- 230 Wh/dm^3.
- 1000, 80% capacity, discharge cycles.
- 10-year system life.

PHEV 40-mile

- \$220/kWh.
- 193 Wh/dm^3.
- 2750, 75% capacity, discharge cycles +80,000 HEV cycles.
- 15-year system life.

Accomplishments

- High-energy density SiO enabled by conductive polymer binder and stabilized Li metal powder (SLMP) prelithiation.
- Polarity of the conductive polymer binder manipulated, an optimized electrolyte uptake leads to improved cell performance.
- Flexibility of polymer binder is correlated with cell cycling performance.
- A new polymer binder is inspired by an effective electrolyte additive, which highlights important concerns in the design of binders for Li-ion battery.

✧ ✧ ✧ ✧ ✧

Introduction

Achieving the DOE energy, cycle life and cost targets will require materials of higher capacity and improved coulombic efficiency or cells with higher voltage. High-capacity Si alloy-based anode material has the potential to fulfil the energy density requirements for EV/HEV applications. However, full capacity cycling of the alloy anode materials results in a significant capacity fade due to a large volume change during Li insertion and removal. Decreasing the particle size to nanometer scale can be an effective means of accommodating the volume change. However, it is very challenging to insure electric connections between all the alloy nanoparticles in the electrode by using similar size acetylene black conductive additives. The repeated volume change of the alloy nanoparticles during cycling can lead to a repositioning of the particles in the electrode matrix and result in particle dislocation from the conductive matrix. This dislocation of particles causes the rapid fade of the electrode capacity during cycling. An effective polymer binder must enable satisfactory cycling performance of Si-containing anode. Previous work established the advantage of conductive polymer as a binder of Si anode. Subsequent investigations indicate an excellent cycling of SiO anode enabled by using a dual strategy of conductive polymer and SLMP prelithiation. Other properties of a polymer binder are also studied, as part of the ongoing effort toward an ideal polymer binder design.

Approach

Use functional polymer design and synthesis to develop new conductive polymers with proper electronic properties, strong adhesion and improved flexibility to provide electric pathways in the electrode, and to accommodate large volume change of the Si or Sn alloy active material during Li insertion and removal. The rational design of binder is assisted with advanced diagnostic techniques such as XAS at the Advanced Light Source and with advanced molecular computation at National Energy Research Scientific Computing Center – both of which are DOE User Facilities.

Results

SiO electrodes enabled by conductive polymer and SLMP prelithiation: Only 2% (by weight) functional conductive polymer binder Poly (9,9-dioctylfluorene-co-fluorenone-co-methyl benzoic ester) (PFM) without any conductive additives was successfully used with a micron-size SiO anode material, demonstrating stable and high gravimetric capacity (>1,000 mAh/g) for *ca.* 500 cycles and more than 90% capacity retention. Prelithiation of this anode using SLMP improves the first cycle coulombic efficiency of a SiO/NMC full cell from *ca.* 48% to *ca.* 90%. The combination enables good capacity retention of more than 80% after 100 cycles at C/3 in a Li-ion full cell. (See Figure V - 69.)

Manipulating the polarity of polyfluorene-type binder: Figure V - 70a shows the synthesis schematic of the conductive polymers under study, where P represents polyfluorene with octyl side chains, E represents triethyleneoxide monomethylether side chains, F represents fluorenone and M represents benzoate ester. The molar ratio among P, E, F and M was demonstrated by a, b, c, and d. In terms of their functionality, P contributes to the electric conductivity as polyfluorene type polymer block; E was introduced into the polymer to enhance its polarity, therefore its electrolyte uptake capability; F was incorporated to tailor the electronic structure of the polymer; M groups were copolymerized to improve the chain flexibility of the polymer and therefore strengthen the mechanical adhesion force between the active materials and the polymer binder.

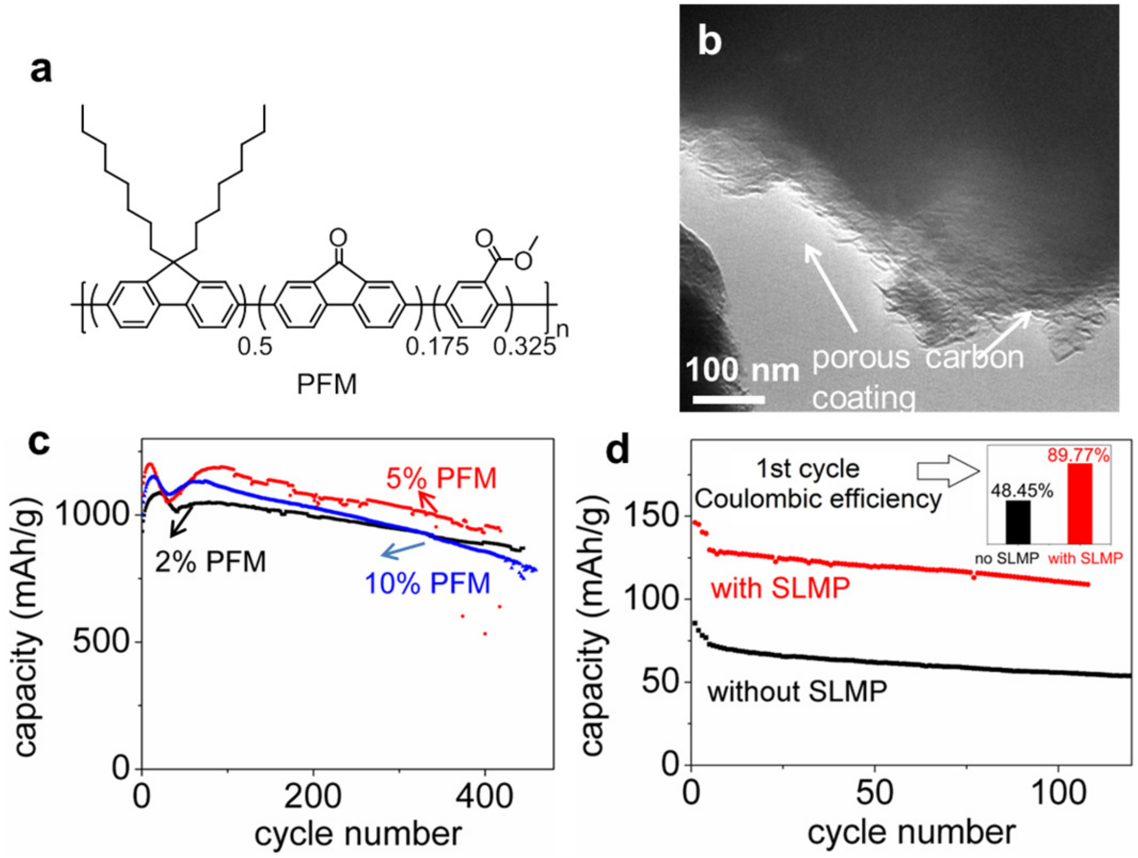

Figure V - 69: (a) Chemical structure of PFM conductive polymer binder. (b) HRTEM of the carbon coated SiO pristine particles. (c) cycling performance of the PFM/SiO half cells at C/10 (200 mA/g). (d) cycling performance of the NMC/SiO full cell with or without prelithiation by SLMP, C/20 for 2 cycles, C/10 for 2 cycles and then C/3

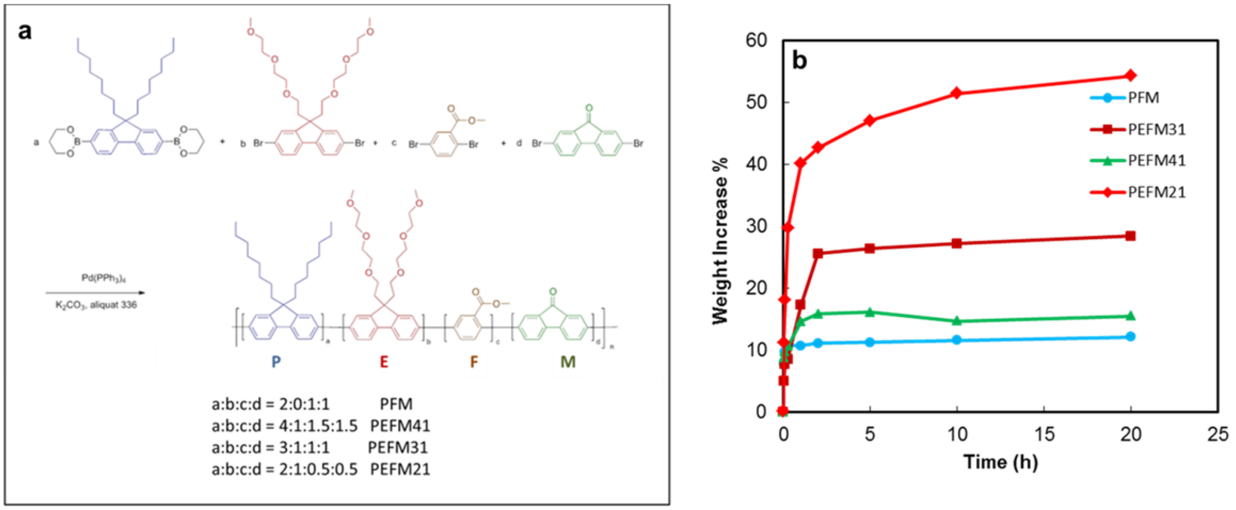

Figure V - 70: (a) Synthetic scheme and the relative molar ratio of four functional block of polymer binders. (b) The swelling tests of polymer films in the EC/DEC (1/1) electrolyte

The polarity of polymers, particularly, was designed from low to high by controlling the relative molar ratio of polar side chain E from low to high. The swellability of the polymer films in ethylene carbonate (EC) and diethylene carbonate (DEC) (1:1 w/w) was measured at room temperature (Figure V - 70b). The trend of the swelling of four polymer binders is consistent with the increase of ethyleneoxide contents, indicating the chemically attached ether side groups in the binder helps to improve the overall electrolyte uptake. The swellability of the polymer binders suggests the level of polymer/electrolyte interaction as higher swellability of polymer binders indicates that it should behave as a more deformable material.

Optimizing the flexibility of conventional polymer binders: The mechanical failure in the electrode interfaces (laminate/current collector and binder/particle interfaces) leads to particle isolation and delamination, which has been regarded as one of the main reasons for the capacity decay and cell failure for Li-ion batteries (LIBs). The polymer binder has been known to provide this key function for a good interface property and to maintain the electrode integrity in LIBs. Incorporation of triethyleneoxide monomethylether moieties in the polymer is supposed to increase both the interface adhesion and the ductility to better eliminate stress-induced fracture. To unveil the role of the polymer binders in the inhibition of failure of electrode interfaces, a rigid binder was chemically modified to improve its flexibility and resulting electrode laminate. As shown in Figure V - 71a, both PMAA and PMAA-5%PTEGMA show similar performance, the PMAA-10%PTEGMA enables a stable cycling at 270 mAh/g at 1C.

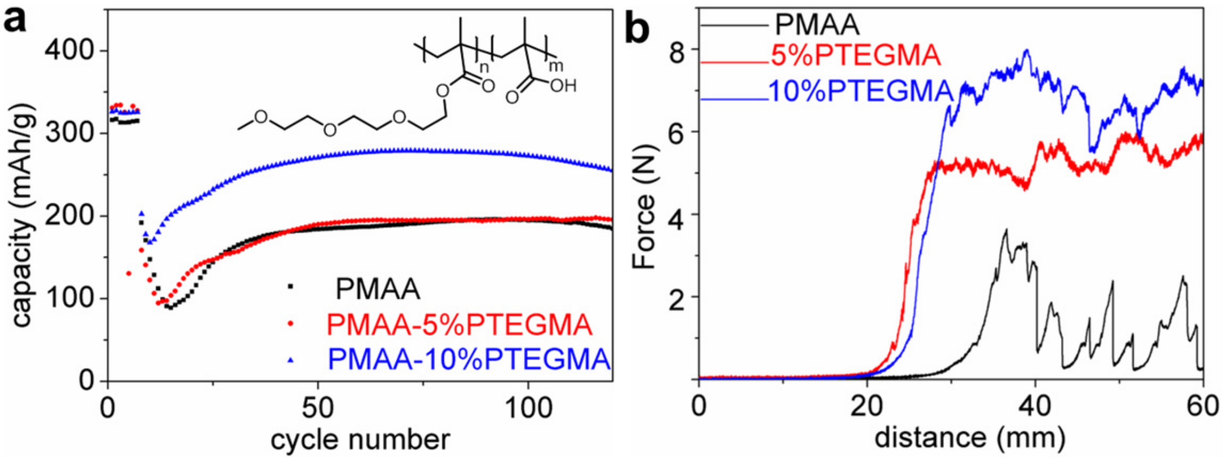

Figure V - 71: (a) Cycling performance of graphite half-cells with different binders, C/25 for 2 cycles, C/10 for 5 cycles and then 1C, with the PMAA-based polymer structure embedded. (b) Peel test results of the graphite electrodes using PMAA-based binders

The improved flexibility of the polymer and the enhanced adhesion strength is confirmed by the peel test (Figure V - 71b.) As more compliant polymer binder is supposed to significantly strengthen the mechanical binding force and enhance the particle/particle cohesion strength, the peel-off workloads started with a quite high value (*ca.* 5 N for PMAA-5%PTEGMA and *ca.* 7 N for PMAA-10%PTEGMA), confirming this high cohesion strength.

New polymer binders inspired by an effective electrolyte additive: Vinylene carbonate (VC) has been proven to be an effective additive for LIBs, previous studies indicate that the sacrificial decomposition of VC before carbonate solvents forms a stable SEI, which enables a reversible cycling of graphite in PC-based electrolytes. The use of polymerized vinylene carbonate (polyVC) as a binder for graphite anodes was investigated in Li-ion cells. It functions not only as a traditional binder, but also plays an important role in surface stabilization of graphite in propylene carbonate (PC)-based electrolytes. In an electrolyte with PC content as high as 30 wt%, the polyVC binder enhanced battery performance, with a reversible capacity of *ca.* 170 mAh g^{-1} at a delithiation rate of 1C, whereas a comparable graphite cell fabricated with a polyvinylidene fluoride (PVDF) binder failed to cycle, as shown in Figure V - 72.

Conclusions and Future Directions

The combined strategy of using both a functional conductive polymer binder and an SLMP prelithiation solves the volume expansion and low first-cycle coulombic efficiency problems associate with SiO anodes, leading to high-energy Li-ion chemistry. To further optimize the design of polymer binders for Li-ion batteries, different aspects of binder properties are modified and the effects studied. By exclusively manipulating the polarity of conductive polymer binders, the effect of polymer binder polarity, therefore the electrolyte uptake properties on the electrochemical performance of Si based anodes is illustrated. By systematically improving the flexibility of a rigid binder, laminate/current collector delamination and particle/particle isolation is inhibited during cell cycling, an improved cell performance was demonstrated based on the flexible binder. Inspired by an electrolyte additive, vinylene carbonate, its polymerized form, polyVC is chemically synthesized and used as binder, which shows promise as an optimized binder compared to conventional binders. Enlightened by this study, it is proposed that design of polymer binders should take into consideration of their behavior in a real Li-ion cell. For example, once the electrode is assembled into a Li-ion cell and begins to cycle, the polymer binder is swelled by the electrolytes and voltage is applied. This is a much different chemical and electrochemical environment than that of the electrode in a dry state. A successful binder design should take these factors into account.

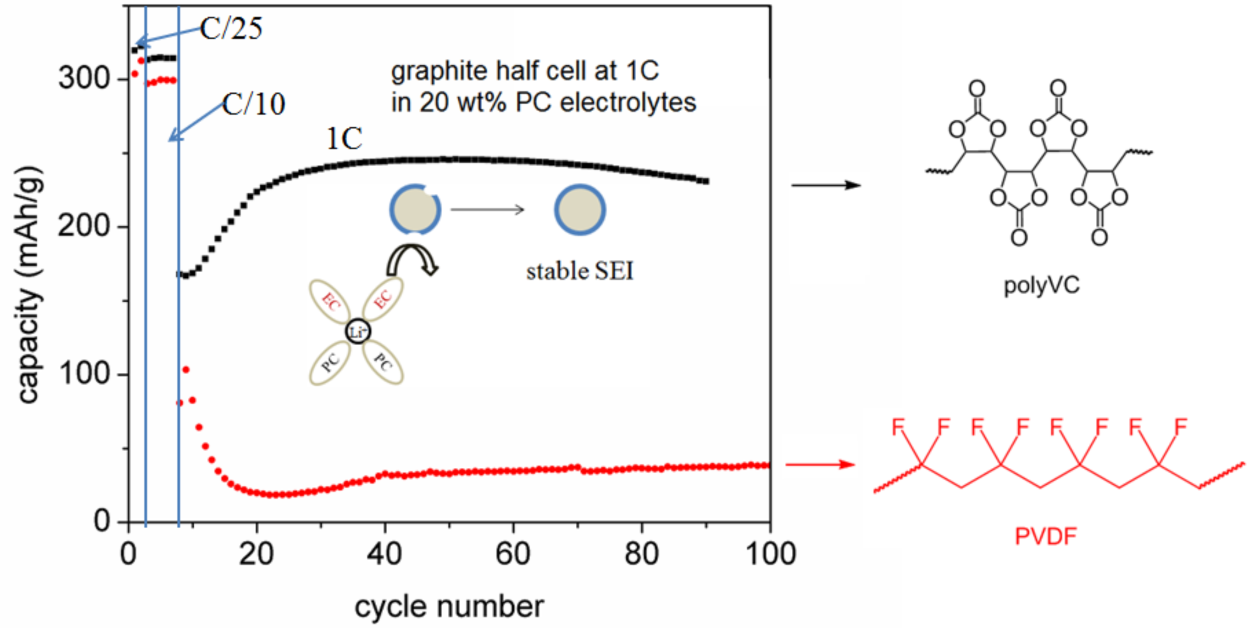

Figure V - 72: Cycling performance of graphite (CGP-G8, ConocoPhillips) half-cells based on polyVC or PVDF binder, using 20% PC, 40% EC, 40% DEC and 1 M $LiPF_6$. The cell was put into formation for two cycles C/25, five cycles C/10 before cycling at 1C

Instead of focusing on pure Si anode, different types of Si-based anode materials, such as SiO_2 (*Adv. Mater*. 2014, **26**, 4527-4532), Si-alloys (J. *Electrochem. Soc*. 2014, **161**, A783-A791), Si/C materials (*Adv. Functional Mater*. 2014, **24**, 5904-5910), materials having different specific capacities, volume changes during cycling, particles sizes, surface chemistries, which pose new challenges for designing suitable polymer binders. A recent work via *in situ* TEM (*Sci. Rep.*, 2014, 4, 3684) demonstrates an obvious advantage of conductive polymer binder-based Si electrode compared to a conventional polymer/conductive additive/Si electrode. A new generation of conductive polymer binder, is highly desirable, which allows facile synthesis, easy modification toward specific anode active materials.

FY 2014 Publications/Presentations

1. Liu, G. (June 2014). “Hierarchical Assembly of Inorganic/Organic Hybrid Si Negative Electrodes.” Presented at the 2014 DOE Annual Merit Review and Peer Evaluation Meeting, Washington, D.C.
2. Zhao. H.; Wang, Z.; Lu, P.; Jiang, M.; Shi, F.; Song, X.; Zheng, Z.; Zhou, X.; Fu, Y., Guerfi, A.; Xiao, X.; Liu, Z.; Battaglia, V.; Zaghib, Z.; Liu, G. (2014). *Nano Lett.* DOI: 10.1021/nl503490h.
3. Yuca, N., Zhao, H.; Song, X.; Dogdu, M.F.; Yuan, W.; Fu, Y.; Battaglia, V.S.; Xiao, X.; Liu, G. (2014). *ACS Appl. Mater. Interfaces* (*6)*; pp: 17111-17118.
4. Zheng, Z.; Wang, Z.; Song, X.; Xun, S.; Battaglia, V.; Liu, G. (2014). *ChemSusChem* (7); pp: 2853-2858.
5. Feng, C.; Zhang, L.; Wang, Z.; Song, X.; Sun, K.; Wu, F.; Liu, G. (2014). *J. Power Sources* (*269); pp:* 550-555.
6. Shi, F.; Zhao, H.; Liu, G.; Ross, P.N.; Somorjai, G.; Komvopoulos, K. (2014) *J. Phys. Chem. C* (118: 27); pp: 14732–14738.
7. Wang, Z.; Zhang, Y.; Xia, T.; Murowchick, J.; Liu, G.; Chen, X. (2014). *Energy Technology* (*2)*; pp: 1-8.
8. Xia, T.; Zhang, W.; Wang, Z.; Zhang, Y.; Song, X., Murowchick, J.; Battaglia, V.; Liu, G.; Chen, X. (2014). *Nano Energy* (6); pp: 109-118.
9. Vaughey, J.T.; Liu, G.; Zhang, J.-G. (2014) *MRS Bull.* (39); pp: 429-435.
10. Wang, Z.; Chen, Y.; Battaglia, V.; Liu, G. (2014). *J. Mater. Res.* (29); pp: 1027-1033.
11. Zhao, H.; Zhou, X.; Park, S.-J.; Shi, F.; Fu, Y.; Ling, M.; Yuca, N..; Battaglia, V.; Liu, G. (2014). *J. Power Sources* (263); pp: 288-295.
12. Wang, Z.; Fu, Y.; Zhang, Z.; Yuan, S.; Amine, K.; Battaglia, V.; Liu, G. (2014). *J. Power Sources* (260); pp: 57-61.
13. Dai, K.; Zhao, H.; Wang, Z.; Song, X.; Battaglia, V.; Liu, G. (2014). *J. Power Sources* (263); pp: 276-279.
14. Zhao, H.; Park, S.-J.; Shi, F.; Fu, Y.; Battaglia, V.; Ross, P.N.; Liu, G. (2014). *J. Electrochem. Soc.* (161); pp: A194-A200.
15. Dai, K.; Mao, J.; Li, Z.; Zhai, Y.; Wang, Z.; Song, X.; Battaglia, V.; Liu, G. (2014). *J. Power Sources* (248); p: 22.
16. Gu, M.; Xiao, X.-C.; Liu, G.; Thevuthasan, S.; Baer, D. R.; Zhang, J.-G.; Liu, J.; Browning, N. D.; Wang, C.-M. (2014). *Sci. Rept* (4); pp. 3684-3688.
17. Zhao, H., *et. al.*, U.S. provisional patent application 61/944,976, filed Feb. 2014.
18. Liu, G., *et. al.*, U.S. provisional patent application 62/012,876, filed June 2014.
19. Liu, G. (May 2014). “Hierarchical Electrode Design for Si and Sn Based Anode.” Presented at the Spring Korea Battery Society meeting, Seoul, Korea.
20. Dai, K. (April 2014). “Recent progress on anode and cathode for sodium-ion batteries.” Presented at the 2014 MRS Spring Meeting, San Francisco, CA.
21. Wang, Z. (April 2014). “Applications of SLMP in lithium ion batteries.” Presented at the 2014 MRS Spring Meeting, San Francisco, CA.
22. Zhao, H. (August 2014). “Conductive polymer binders for Si-based anode in lithium-ion batteries.” Presented at the 2014 ACS Fall Meeting, San Francisco, CA.
23. Yuan, W. (August 2014). “*In situ* Formed Si Nanoparticle Network with Micron-sized Si Particles for Lithium-ion Battery Anodes.” Presented at the 2014 ACS Fall Meeting, San Francisco, CA.
24. Wang, Z. (August 2014). “Improving the performance of lithium-sulfur batteries using conductive polymer binder and ionic liquid based electrolyte.” Presented at the 2014 ACS Fall Meeting, San Francisco, CA.

V.C.6 Electro-Deposition of Silicon and Other Metals for Li-Ion Battery Anodes (NETL)

Dr. Manivannan Ayyakkannu
Contractor: NETL, DOE

Dr. Prashant N. Kumta
Subcontractor: University of Pittsburgh, Pittsburgh.

Project Start Date: October 2010
Project End Date: September 2014

Objectives

- This research is aimed at exploring electrodeposition as a low cost and scalable approach to replace graphite with other metal alloy systems such as Li, Sn, Sb, etc. as a high energy density anode system. The main objectives of this research are
    - Develop thin films of Si and other electroactive metal alloy systems as high capacity Li-ion anodes.
    - Similar or lower irreversible loss compared to graphite.
    - Attain high specific capacities (>1,000 mAh/g).
    - Similar or better cyclability and calendar life of the developed anode systems.
    - Obtain a columbic efficiency close to 100%.
    - Attain good rate characteristics for high load applications.

Technical Barriers

One of the major challenges of silicon based anodes is the loss of mechanical integrity and poor cyclability due to the colossal stress related problems associated with the huge volumetric changes in Si (>300%) during lithium alloying and delloying.

Technical Targets

- Synthesize amorphous Si films for Li-ion system by cost effective electrodeposition process.
- Improve the cyclability of Si anode based system for Li-ion cell.
- Lower the first cycle irreversible loss of Si anodes.
- Application of pulse plating electrodeposition technique to control the morphology of the Si anode.

Accomplishments

- Synthesized binder-free amorphous silicon films on copper substrate by electroreduction of Si salts from an inorganic solvent bath.
- The amorphous Si films exhibited a stable and reversible capacity of 1,300 mAh/g with a columbic efficiency of 99.5% up to 100 cycles.
- Modified the morphology of the electrodeposited Si thin films using pulse plating techniques.
- Improved the cycling stability of a-Si thin films by using pulse current electrodeposition leading to a decrease in the fade rate caused by increasing the frequency of the deposition.

✧ ✧ ✧ ✧ ✧

Introduction

Silicon, with a theoretical capacity of 4,212 mAh/g, corresponding to the maximum lithiated phase of $Li_{22}Si_5$, was identified as an alternative anode which can store nearly 10 times more charge than that of graphite. However, during alloying and dealloying of lithium of the Si anode there is a very large volumetric change leading to mechanical stresses in the electrode causing cracking and consequently loss of inter – particle contact. Hence, there is delamination of the electrode layer leading to a rapid capacity fade for the battery.

Nanostructured and amorphous Si synthesized by physical and chemical vapor deposition show improved performance but are not economically viable for secondary batteries. Electrodeposition is a very inexpensive process which has been widely studied and used in many industrial applications for plating metals and alloys. Electrodeposition of silicon from organic solvents and ionic liquids on metallic and graphite substrates has previously been reported in the literature. Additionally, the electrodeposition technique offers to provide the deposited films with different morphologies and functional properties by controlling parameters such as electrolyte composition, applied voltage/current density and time of deposition.

Approach

Silicon thin films were electrodeposited using galvanostatic and pulse current conditions (Figure V - 73) from an electrolyte of 0.5M silicon tetrachloride

($SiCl_4$) and 0.1M tetrabutylammonium chloride (TBACL) in propylene carbonate (PC) solution in an argon environment (<0.1 ppm oxygen and <0.1 ppm water) on copper substrate. The current density of the deposition done at constant current (galvanostatic condition) was -1mA/cm^2. The frequencies of negative cycle at the same deposition current density for pulse conditions were 0Hz (galvanostatic), 500Hz, 1,000Hz, 2,000Hz, 3,000Hz, 4,000Hz, and 5,000Hz. The duty cycle (active deposition time/total time) of the deposition was maintained constant at 50%.

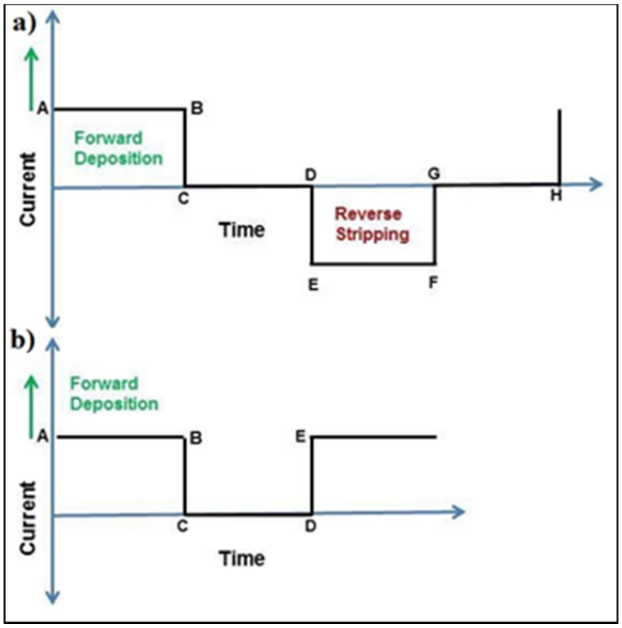

Figure V - 73: a) Standard input current cycle during pulse electrodeposition and b) input current cycle for pulse current electrodeposition in the current study

Electrochemical investigations were performed on the electrodeposited Si thin films on copper foil which served as the working electrode. A 2016/2025 coin cell assembly in a half cell configuration was used by employing lithium (Li) foil as counter electrode and 1 M $LiPF_6$ in ethylene carbonate and di-ethyl carbonate (EC:DEC = 1:2, by volume) as the electrolyte. The assembled cells were tested by cycling between 0.02 and 1.2 V vs. Li^+/Li employing a constant current density of 400 mA/g.

Results

Materials Characterization: The glancing angle X-Ray diffraction for all the electrodeposited films did not show any peaks corresponding to crystalline silicon. Raman spectra showed the presence of broad peak between 480 cm^{-1} - 485 cm^{-1} for the films deposited at all frequencies, which is indicative of the transverse optical phonon mode of amorphous silicon.

The EDAX indicated the presence of Si, C, O and Cu; the oxygen present was due to the surface oxidation and carbon present from the residual PC and acetone. A major change in the morphology of the electrodeposited Si was observed with the change in the frequency of deposition, as can be observed in Figure V - 74.

The morphology of thin films for 0Hz (galvanostatic) showed islands of Si, 500Hz showed islands of Si formed from Si particles and 1,000Hz resulted in continuous thin films of Si. The formation of continuous films at high frequency deposition can be attributed to the increased diffusion of Si^{4+} ions in the depletion layer close to the electrode-electrolyte interface during the relaxation time (zero current) of the deposition cycle.

Electrochemical Testing: The electrochemical testing (Figure V - 75) of these pulse current electrodeposited films as Li-ion anode system showed stable cycling data with charge capacities of 800mAh/g – 950mAh/g with an improvement in the stability of the films. The improvement in the stable capacity of the films with increase in frequency is due to the decrease in the fade rate of these films during the initial charge/dicharge cycles marked by the vertical red line in Figure V - 75.

The films showed a decrease in the percentage loss per cycle with the increase in the frequency of the deposition cycle (Figure V - 76).

This may be attributed to the increased adhesion of the films to the substrate and improvement in the strength of the films with the increase in the frequency of the deposition due to improved monolayer assembly of the atoms caused by enhanced deposition/diffusion kinetics. However, no significant improvement was observed on the first cycle irreversible loss (FIR) in these films with the change in frequency which indicates that the FIR in these films is essentially immune to the change in the morphology of the film but dependent on Si composition.

The post cycling SEM analysis (Figure V - 77) of the pulse electrodeposited *a*-Si films showed that they were stable even after 100 cycles of testing as anode material. The thin films develop cracks in the initial 10 cycles which corresponds to the higher fade rate during the initial charge/discharge cycles, however, no major change in the film morphology is observed after 10 cycles and 50 cycles indicating good stability of the films on lithiation and de-lithiation during the electrochemical testing.

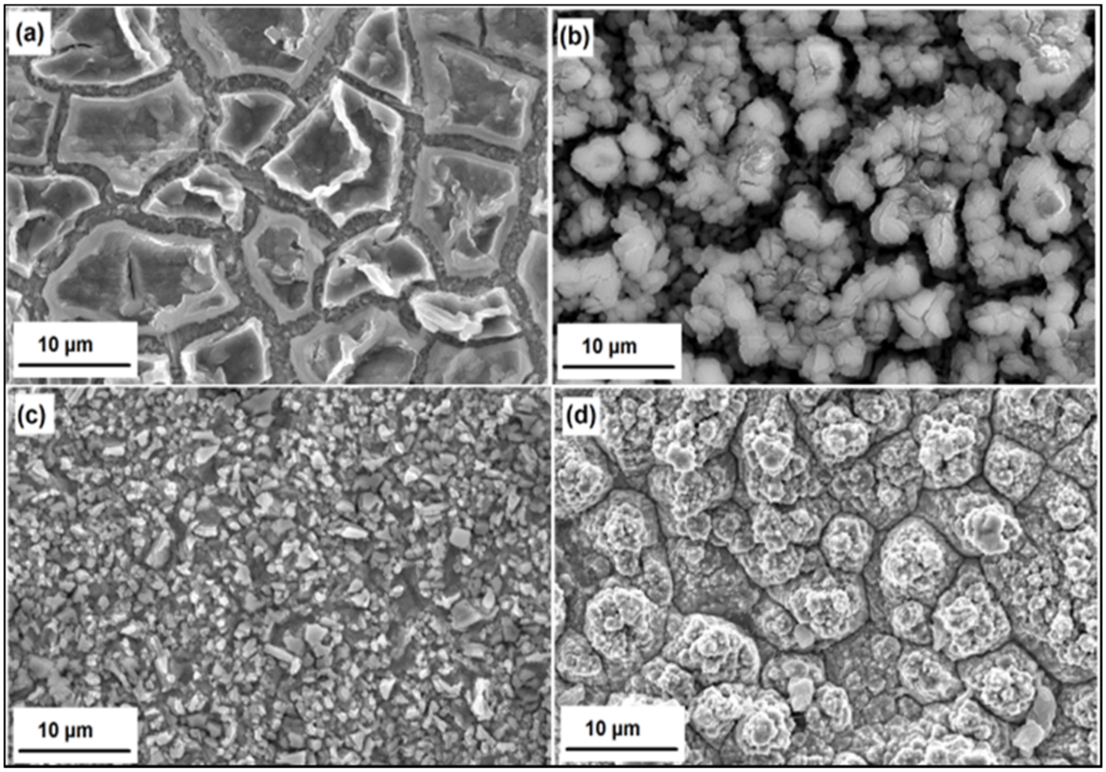

Figure V - 74: SEM images of electrodeposited Si films at (a) 0Hz, (b) 500Hz, (c) 1000Hz and (d) 5000Hz pulse frequency

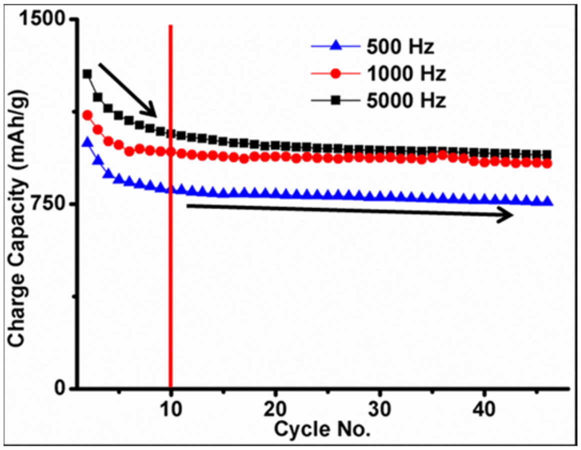

Figure V - 75: Charge capacity of *a*-Si thin films deposited at 500Hz, 1000Hz and 5000Hz current cycle frequencies for Li/Li$^+$ system

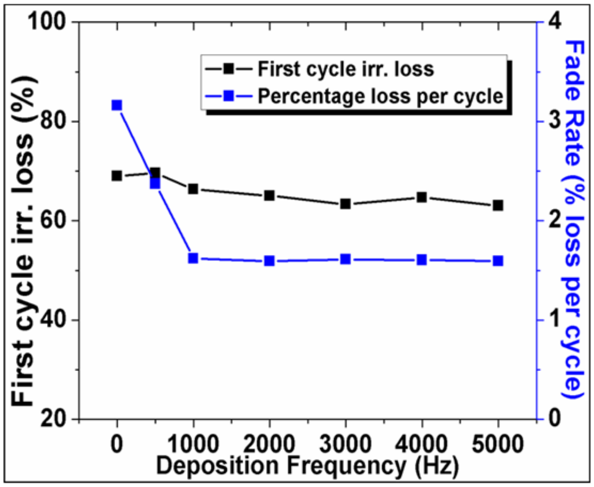

Figure V - 76: First cycle irreversible loss and Percentage loss per cycle vs Frequency of electrodeposition for a-Si films for Li/Li$^+$ system

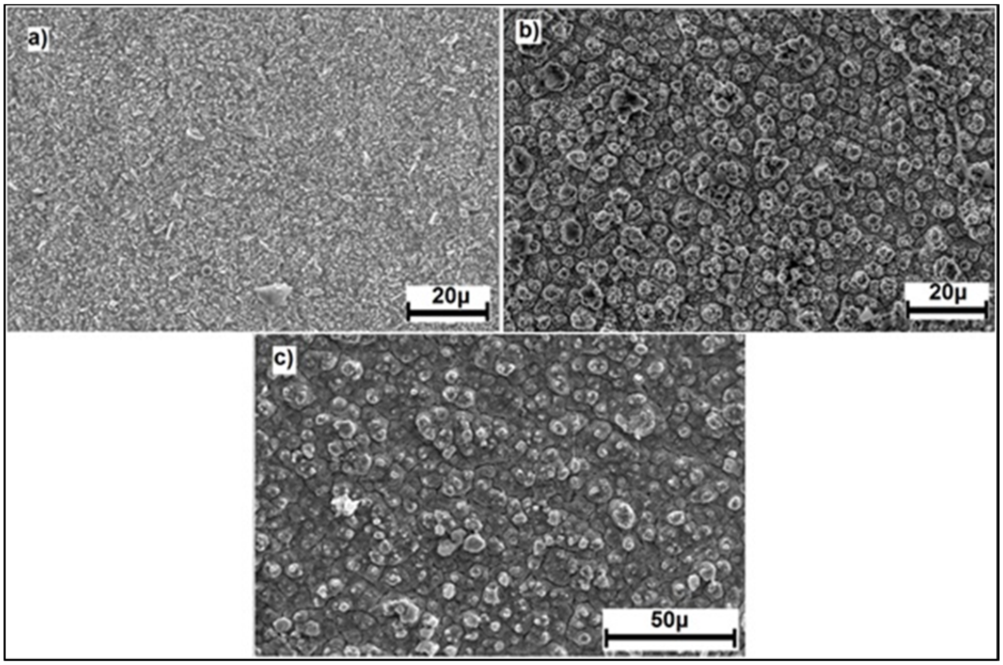

Figure V - 77: SEM images of amorphous Si films electrodeposited at 1000Hz a) before cycling; b) after 10 and c) after 50 cycles

Conclusions and Future Directions

Electro-reduction of $SiCl_4$ was carried out at a cathodic potential ~−1.6 V vs. Pt.QRE using a PC based solvent to obtain amorphous silicon thin films on copper substrates. Pulse current electrodeposition was carried out at different frequencies of the current cycle to change the morphology of the deposited Si thin films.

Films obtained by galvanostatic deposition (0 Hz) showed a mud-crack (island) morphology, 500Hz pulse current deposition showed cracked morphology with the islands consisting of agglomerated discrete particle deposits and 1,000Hz pulse current deposition shows a continuous thin layer comprised of Si particles. At pulse current frequency greater than 1,000Hz (2,000Hz, 3,000Hz, 4,000Hz, and 5,000Hz) show a continuous layer of *a*-Si deposited on the substrate with a decrease in the size of the particles containing the films.

The electrochemical testing of these Si films showed stable capacity for 100 cycles and the percentage loss per cycle decreased with increase in the deposition frequency however, without any major impact on the first cycle irreversible loss. The post cycling SEM analysis shows development of cracks within the first 10 charge/discharge cycles after which no major change in observed upon cycling as anode for Li/Li^+ system.

Development of electrodeposited Si anode systems can be further carried out to decrease the first cycle irreversible loss by changing the electrolyte, post deposition heat treatment and by developing multilayer coatings on the Si thin films. Further multi-layer Si film systems can be developed to increase the loading capacity of the active Si material on the electrode.

FY 2014 Publications/Presentations

1. Bharat Gattu, Rigved Epur, Moni Kanchan Datta, A. Manivannan and Prashant N Kumta, "Pulse Electrodeposition of Amorphous Si Film Anodes for Li-Ion Battery", 225th ECS Meeting, ORLANDO, FL, U.S.: May 11-15, 2014.

V.C.7 Atomic Layer Deposition for Stabilization of Amorphous Silicon Anodes (NREL, U Colorado)

Chunmei Ban (Principal Investigator)
National Renewable Energy Laboratory

15013 Denver West Parkway
Golden, CO, 80401
Phone: (303) 384-6504; Fax: (303) 384-6432
E-mail: Chunmei.ban@nrel.gov

Steve M. George and Sehee-Lee
University of Colorado Boulder
Department of Chemistry and Department of Mechanical Engineering
914 Broadway, Boulder, CO, 80309
Phone: (303) 493-7471; Fax: (303) 492-7889
E-mail: steve.george@colorado.edu and sehee.lee@colorado.edu

Start Date: October 2010
Projected End Date: September 2014

Objectives

- Develop a low-cost, thick and high-capacity silicon anode with sustainable cycling performance, via advanced surface modification.
- Synthesize novel stable and elastic coatings for Si anodes using Atomic Layer Deposition (ALD) & Molecular Layer Deposition (MLD).
- Demonstrate durable cycling performance of thick Si anodes by using new ALD/MLD coatings and electrode designs.
- Investigate coating mechanism on electrochemical cycling performance via
    - Study of the mechanical properties of MLD coating materials.
    - Research on the morphology and structural evolution during lithiation/delithiation
- Explore the importance and mechanism of various coatings via the BATT Coating Group.
- Collaborate within the BATT Program with the aim of developing high-rate plug-in hybrid electric (PHEV) compatible electrodes (both anodes and cathodes).

Technical Barriers

- Cost: Inexpensive processing techniques are employed to fabricate conventional thick electrodes.
- High Capacity: Silicon is predominantly being explored as a high-capacity anode material. There is also a collaborative emphasis to enable high-capacity cathode materials.
- High Rate: Both ALD and MLD coatings are being developed such that high-rate capability is demonstrated for emerging materials.
- Safety: The ALD/MLD coatings are targeted to improve safety for a variety of electrode materials.

Technical Targets

- Stabilize the high-capacity silicon anodes by employing the advanced surface coating techniques, ALD and MLD.
- Demonstrate the stable high-rage cycling performance of Si anodes.
- Relevant to USABC goals: 200Wh/kg (EV requirement), 96Wh/kg, 316W/kg, 3000 cycles (PHEV 40 miles requirement). Calendar life: 15 years. Improved abuse tolerance.

Accomplishments

- Developed new aluminum alkoxide polymer (alucone) film using the sequential reactions of MLD sequential reactions of trimethylaluminium (TMA) and hydroquinone (HQ).
- Achieved sustainable cycling behavior with 2,000 mAh g^{-1} at 50 cycles, and enhanced rate performance for this new MLD-engineered thick Si anodes.
- Characterized the morphology and structure evolution of both uncoated and MLD-coated silicon anodes during cycling.
- Investigated the effect of coatings on the properties of additives and current collectors, in order to further mitigate the irreversible capacity loss.

✧ ✧ ✧ ✧ ✧

Introduction

Significant advances in both energy density and rate capability for Li-ion batteries will be critical for their implementation in next generation EVs. Due to the high theoretical capacity of Si, 3,579 mAh g^{-1} for $Li_{15}Si_4$, and its natural abundance, Si has attracted much attention as a promising Li-ion anode material. However, progress towards a commercially viable Si anode has been impeded by its rapid capacity fade caused by the large volumetric expansion. Such a massive volumetric change can result in cracking and pulverization of the Si particles, which then lead to the interruption of electronic transport pathways and the electrochemical isolation of pulverized particles.

The overall goal of this project is to stabilize the silicon anodes with conformal ultrathin coatings. Both ALD and MLD have been developed to fabricate the nanoscale coatings with desirable elastic properties and good conductivity, to accommodate the volumetric expansion, protect the surface from the reactive electrolytes and ensure the electronic paths through the composite electrodes.

In past years, the project has developed ALD Al_2O_3, cyclized polyacrylonitrile (PAN) and MLD aluminum glycerol (AlGL) coatings. The coatings have greatly improved electrochemical cycling performance of silicon anodes. Among the developed coatings, MLD coatings show the best performance for a thick electrode and the potential of scalable assembly for battery manufacturing. Using sequential and self-limiting reactions, the MLD method not only enables the formation of conformal and ultrathin coatings, but also integrates inorganic materials (herein Al_2O_3) into polymeric organic matrix. Thus, the resulting MLD aluminum alkoxide (alucone) materials have much lower elastic moduli than the pure aluminum oxide coating via the ALD method. The MLD coating creates a strong, flexible network within the electrode that binds the materials and ensures sufficient contact area throughout cycling.

The synthesis strategy has been recently applied to synthesize a new alucone coating composed of polymeric aluminum hydroquinone (AlHQ) to further enhance the mechanical strength and stability. Both high rate and durable cycling have been achieved in AlHQ coated Si anodes. Moreover, *in situ* characterization has been applied to investigate the effect of coating on morphology and chemical evolution of the electrodes during lithiation and delithiation. The results confirm that the coating is stable and conductive in the electrolyte, and resilient enough to host the extreme volumetric changes of silicon particles. This favorable combination of mechanical and electrochemical properties allows the alucone coating to greatly enhance the performance of nano-Si electrodes.

Approach

MLD method has been applied to synthesize the hybrid inorganic-organic coatings. Both AlGL and ALHQ films were grown directly on the nano-Si composite electrodes using a pancake reactor.

The nano-Si based composite electrodes were prepared by spreading nano-Si powder (50 nm, Alpha Aesar), acetylene black (AB), and PVDF (polyvinylidene fluoride binder) mixed in N-methyl pyrolidinone solvent (60:20:20 weight ratio) on a piece of Cu foil. The electrochemical measurements were all normalized based on the mass of nano-Si in each electrode (typically 0.5-0.8 mg/cm^2).

The typical growth rate is ~2.5 Å for the AlGL chemistry per cycle at a substrate temperature of 140 °C. The reaction sequence for AlGL coating is using sequential, self-limiting reaction of trimethylaluminium ($Al(CH_3)_3$) and glycerol ($C_3H_5(OH)_3$) according to:

(A) $R\text{-}OH^* + Al(CH_3)_3 \rightarrow R\text{-}O\text{-}Al(CH_3)_2{}^* + CH_4$

(B) $R\text{-}Al(CH_3)^* + C_3H_5(OH)_3 \rightarrow R\text{-}Al\text{-}OC_3H_5(OH)_2{}^* + CH_4$

where asterisks indicate surface species. Due to the presence of more than two hydroxyl groups per glycerol molecule, sequential reactions between $Al(CH_3)_3$ and ($C_3H_5(OH)_3$) produce large degrees of crosslinking between polymer chains which strengthen the alucone films and lead to higher fracture toughness.

The same strategy is applied to fabricate the AlHQ coating based on the reaction between trimethylaluminum ($Al(CH_3)_3$) and hydroquinone ($C_6H_4(OH)_2$). The typical growth rate is *ca.*7 Å for the AlHQ chemistry at a substrate temperature of 180 °C.

Results

Alucone coating enhances the cohesion of the composite electrodes*:* Figure V - 78 presents the TEM images of bare and coated electrodes after first delithiation. The severance between the nano-Si particles and the electrode network was observed after delithiation (during volumetric contraction), as shown in Figure V - 78a and Figure V - 78b. As depicted in Figure V - 78c, the massive volume change during lithiation/delithiation of Si particles contributes to the isolation of Si particles, and results in fast capacity degradation. In contrast, the alucone-coated electrode shows an intimate adherence between Si particles and surrounding network during cycling. The alucone coating grown by MLD was covalently bound on the surface of the electrode, which dramatically enhances the cohesion of the components in the electrode. It is the covalent coating that ensures the continuous and conductive matrix even while large volume changes occur during cycling.

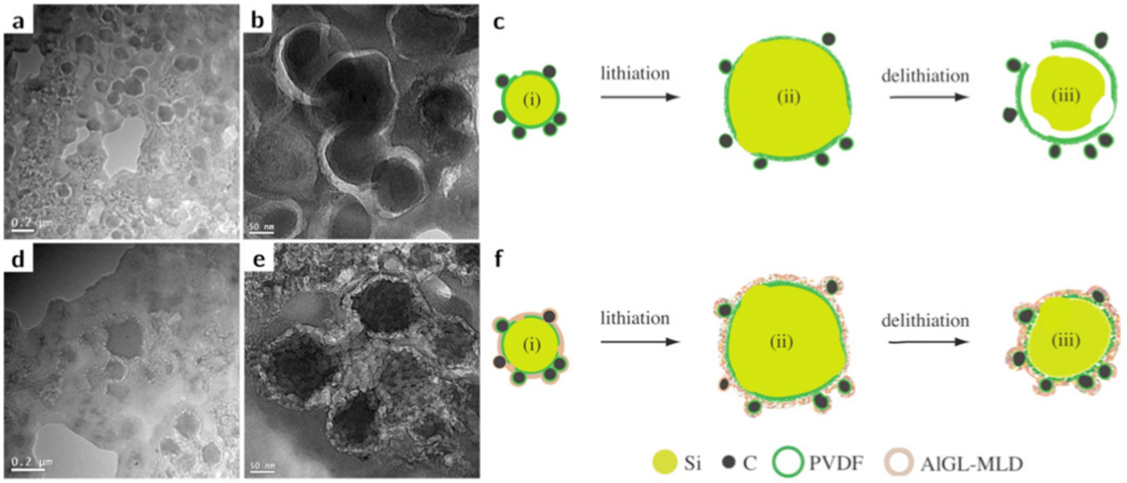

Figure V - 78: TEM images of the bare electrode (a and b) and coated electrode (d and e); schematics of the bare and coated electrodes during lithiation/delithiation (c and f)

MLD synthesis of AlHQ coating: A new alucone coating has been developing on the Si anodes recently by using MLD sequential reactions of trimethylaluminium (TMA) and hydroquinone (HQ). HQ ($C_6H_4(OH)_2$) is an aromatic diol that has a rigid structure with a central benzene ring, which can potentially increase electronic conductivity due to the conjugated π-electrons in the aromatic rings. As illustrated in Figure V - 79, the aromatic rings have enclosed the AlO_x and appear polymerized after annealing above 200°C in Argon. The cross-linked alucone coating has shown greatly improved critical tensile strain from 1.0% to 1.8%. The improved mechanical properties of this conductive coating can ensure the structural integrity of the composite electrodes, which is critical to high-capacity Si anodes with massive volume changes.

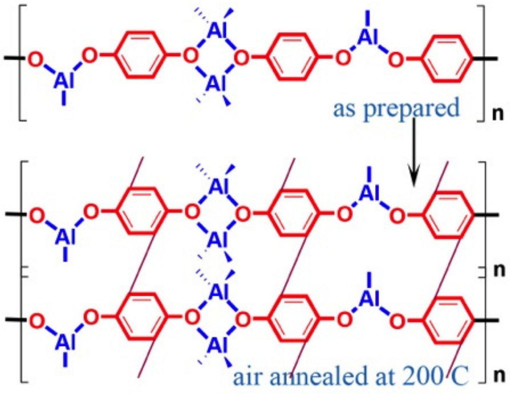

Figure V - 79: Chemistry structure of TMA-HQ MLD coating: as-prepared coating (top) and the cross-linked coating after annealing at 200°C in Argon

Different from ALD Al_2O_3 layer, an organic group was integrated in the MLD alucone coating from the reaction between trimethylaluminum and glycerol/hydroquinone. The organic group results in largely reduced elastic modulus from *ca.* 195 GPa in ALD Al_2O_3 coating to *ca.* 39 GPa in the AlGL coating, and *ca.* 29 GPa in the AlHQ coating. The flexible alucone coating greatly accommodates the massive volume changes in cycling Si anodes, which ensures the highly reversible capacity in the alucone-coated Si anodes. Among the coating developed in this project, MLD AlHQ coating shows the best mechanical properties in terms of elasticity and robustness.

Electrochemical performance of alucone coated Si anodes: The AlHQ coated Si anodes showed greatly improved performance as indicated in Figure V - 80. The Si anode, coated with this new ALHQ coating, has even higher reversible capacity than the ALGL coated Si anode. Both coatings have improved the 1st cycle coulombic efficiency from 65% in bare Si anode to 85% for the coated anode. Interestingly, both MLD-coated anodes show different 1st voltage profiles than that of bare Si anode. The reaction at *ca.* 0.7 V, mainly attributed to the SEI formation in the bare Si anode, has largely been mitigated in the coated anodes. This behavior implies that the coatings modify the interfacial chemistry, as well the SEI formation. Since the hybrid coatings chemically grow on the surface of electrode, the conformal coatings act as an artificial SEI to prevent the direct contact between Si and electrolyte.

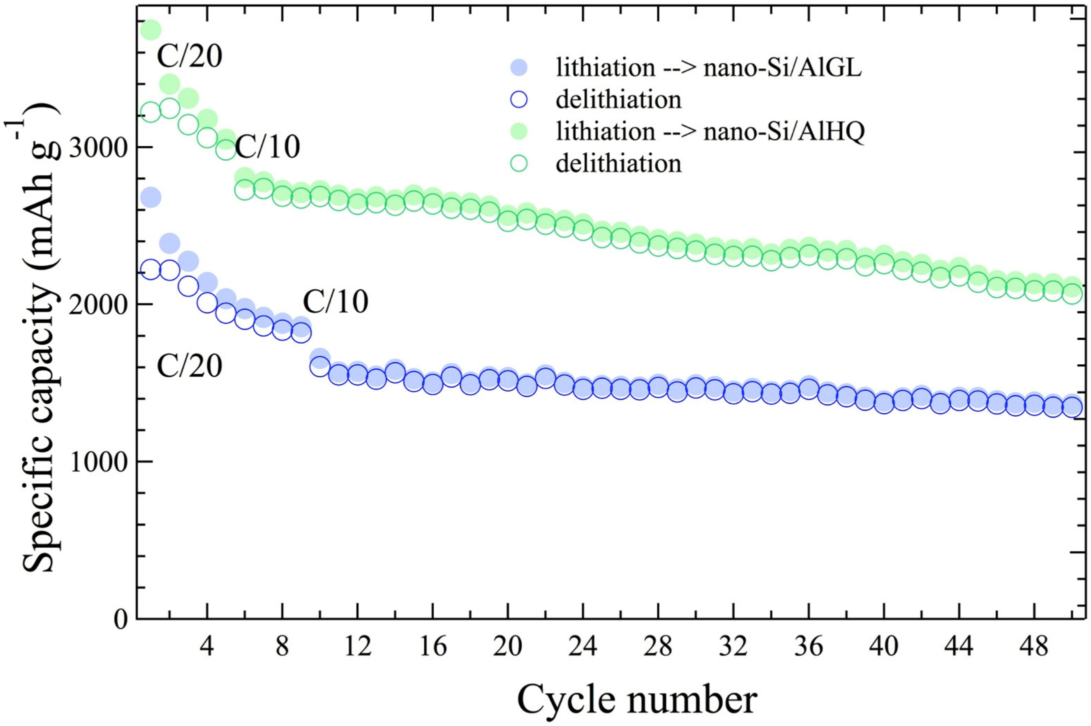

Figure V - 80: Significantly improved cycling performance achieved in MLD AlGL and AlHQ coated Si anodes

Further enhanced rate performance was achieved after post-annealing resulting from the cross-linked polymerization of the aromatic rings in the AlHQ coating. These results are displayed in Figure V - 81. After annealing, the AlHQ coated Si anode exhibits a higher rate capability than the as-prepared AlHQ coating. This behavior suggests that the enhanced conductivity results from the cross-linking in the AlHQ coating.

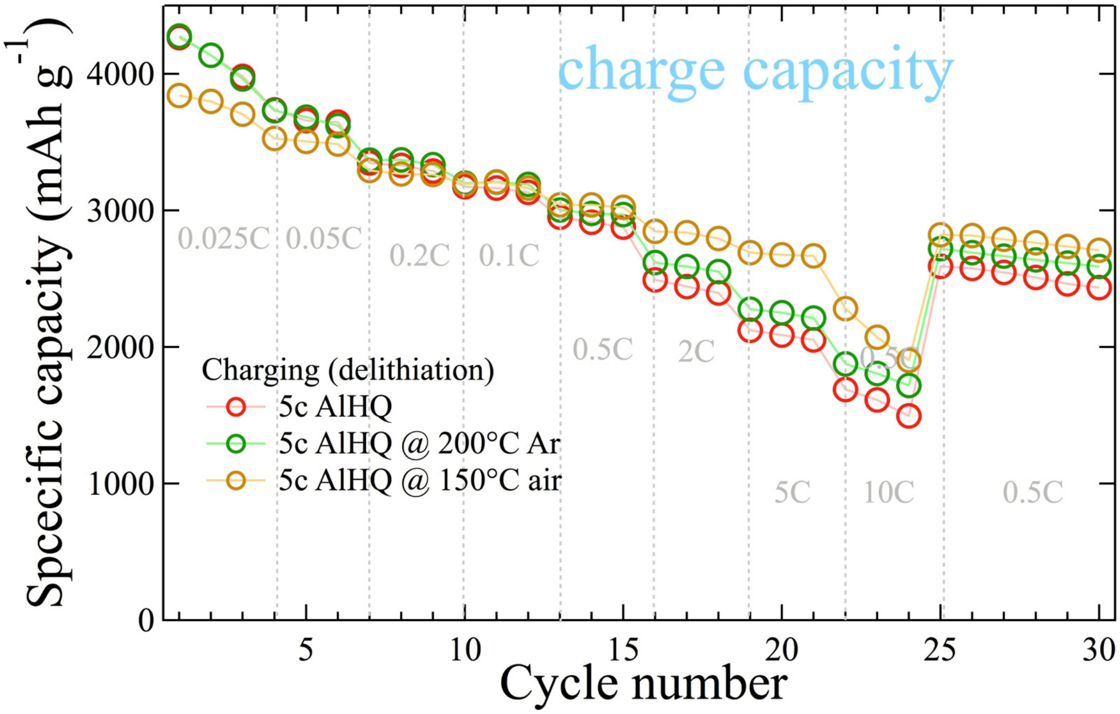

Figure V - 81: Rate capability of MLD ALHQ coated electrodes under different annealing conditions

***In situ* characterization of morphology and chemical evolution of the uncoated and coated Si particles:** Surface modification via MLD method has been proven to significantly improve the electrochemical performance of Si anodes. Here, a specially designed *in situ* TEM equipped with electron diffraction was used to investigate the impact of coating on the morphology and chemical evolution of Si particles upon cyclic lithiation /delithiation. The results show that the native oxide layer (silicon oxide) on the surface of Si converts to crystalline Li_2O islands during initial lithiation. (See Figure V - 82.) The formation of crystalline Li_2O islands essentially increases the impedance on the particle, resulting in ineffective lithiation/delithiation, and therefore low columbic efficiency. In contrast, the alucone MLD coated particles show extremely fast, thorough and highly reversible lithiation behaviors, which are clarified to be associated with the mechanical flexibility and fast Li^+/e^- conductivity of the alucone coating. Surprisingly, the alucone MLD coating process chemically changes the silicon surface, removing the native oxide layer and therefore mitigates side reaction and detrimental effects of the native oxide. This study provides a vivid picture of how the MLD coating works to enhance the columbic efficiency and preserve capacity and clarifies the role of the native oxide on Si nanoparticles during cyclic lithiation and delithiation. Most broadly, this work also demonstrated that the effect of the chemical modification of the surface during the coating process might be of equal importance to the coating layer itself.

Conclusions and Future Directions

MLD method has been used to grow a mechanically robust, flexible coating for high capacity Si nanocomposite anodes. Different from ALD, using MLD can form hybrid polymeric inorganic-organic coatings by integrating various organic groups into an inorganic structure, such as aluminum oxide. The thin, conformal, and flexible MLD coating is able to penetrate the electrode's porous structure and covalently bind to available surfaces.

The employment of alucone coatings on conventional nano-Si composite electrodes provides significant improvement in cycling stability, rate, and coulombic efficiency. The stable coating acts as a passivating agent to protect the active material from unwanted secondary reactions. Due to its unique mechanical properties, the alucone coating proves to be robust and resilient enough to accommodate the extreme volumetric changes of the Si nanocomposite electrodes, helping maintain an intimately linked conductive network and allowing for faster ionic and electronic conduction.

In situ characterization was applied to understand the impact of coating on the morphology and surface chemistry of Si particles. Instead of forming crystalline Li_2O islands in the uncoated Si particles, the native oxide was removed during MLD coating process. The continuous and conductive coating has been observed under *in situ* characterization. Without forming Li_2O, the mechanically flexible and electron/Li^+ conductive alucone coating effectively facilitates fast and thorough reversible electrochemical reactions.

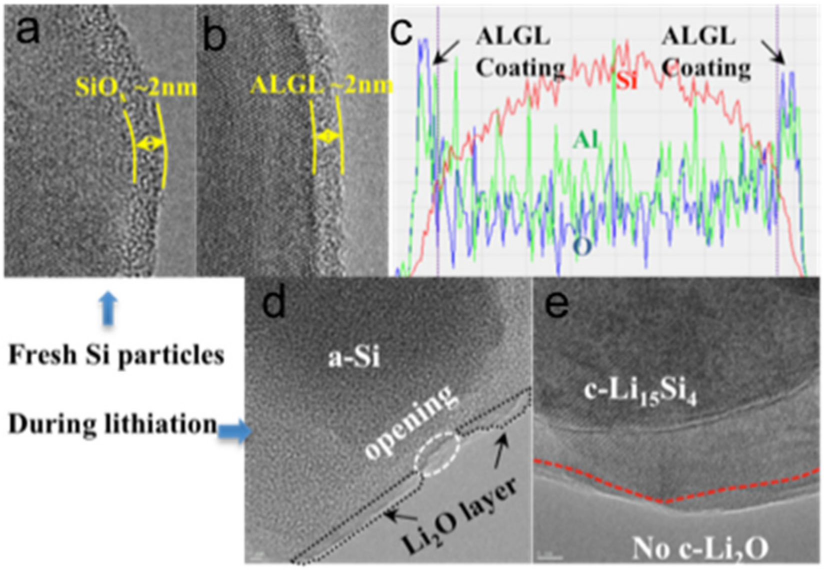

Figure V - 82: Morphology of as-received (a) and alucone coated Si nanoparticle (b), featuring a native amorphous oxide layer of ~2 nm in the as-received uncoated particle and ~2 nm alucone MLD coating in coated particle. Morphology of lithiated uncoated Si nanoparticle (d) and lithiated coated Si nanoparticle (e), showing the appearance of Li2O islands only in uncoated Si nanoparticle and continuous lithiated-AlGL coating. (f) EDS with elemental line across the coated Si nanoparticle

FY 2014 Publications/Presentations

1. Piper, D. M., Travis, J. J., Young, M., Son, S.-B., Kim, S. C., Oh, K. H., George, S. M., Ban, C. and Lee, S.-H. (2013). *Adv. Mater.* DOI:10.1002/adma.201304714.
2. Li, Z., Ban, C., Chernova, N. A., Wu, Z., Upretia, S., Dillon, A., Whittingham, S. (2014). *J Power Sources* DOI: 10.1016/j.jpowsour.2014.05.142.
3. Ban, C. (June 2014). "Atomic Layer Deposition for Stabilization of Silicon Anodes." Presented at the 2014 DOE Annual Merit Review and Peer Evaluation Meeting, Washington, D.C.
4. Ban, C. (December 2013). "Atomic Layer Deposition for Stabilization of Si Anodes for Lithium-ion Batteries." Invited talk, presented at THERMEC' 2013, Las Vegas, Nevada.
5. Ban, C. (March 2014). "Understand the effect of conformal coatings on electrochemical performance and interfacial chemistry of Si anodes." Invited talk, presented at the 247th ACS, Dallas, TX.
6. Ban, C. (March 2014). "Different behavior of lithium interaction with SiO2 and Al2O3." Presented at the APS March Meeting, Denver, CO.
7. Ban, C. (August 2014). "Surface modification of silicon anodes for advanced Li-ion batteries." Invited talk, presented at the 40^{th} Annual Symposium AVS, East Lansing, MI.

V.C.8 Synthesis and Characterization of Structured Si/SiO$_x$-based Nanocomposite Anodes and Functional Polymer Binders (PS U)

Donghai Wang (Principle Investigator)
Pennsylvania State University

Department of Mechanical and Nuclear Engineering
328 Reber Building
University Park, PA 16802
Phone: (814) 863-1287; Fax: (814) 863-4848
E-mail: dwang@psu.edu

Michael A. Hickner (Co-PI)
Department of Materials Science and Engineering
310 Steidle Building
University Park, PA 16802
Phone: (814) 867-1847; Fax: (814) 865-2917
E-mail: hickner@matse.psu.edu

Start Date: January 2011
Projected End Date: October 2014

Objectives

- Synthesis and characterization of Si/SiOx-based nanocomposite Li-ion battery anodes.
- Identify and evaluate the electrochemical performance of the Si/SiOx-based nanocomposite and the polymer binder.
- Develop understanding of long-lifetime Si anodes for Li-ion batteries by considering both the Si active phase and the polymer binder and surface interactions between the electrode components.

Technical Barriers

There are several technical barriers to developing Si/SiO$_x$-based anodes for lithium-ion batteries including:

- Poor capacity cycling.
- Large initial irreversible capacity and corresponding low coulombic efficiency.
- Need to add a high percentage of conductive carbon to obtain good rate (C/3) performance.

Technical Targets

- Optimize surface modifications of Si and Si/SiOx-carbon composites (including carbon, metal oxides, non-oxidic metal composite coating) to improve the long-cycling stability.
- Synthesize and characterize Si alloy and Si/Si alloy composites to obtain optimized energy densities and electrochemical properties.
- Achieve reversible capacity of at least 1,200 mAh/g and a cycle life of at least 200 cycles with the first cycle efficiency of 80% and efficiency of above 99% in cycles thereafter.
- Measure surface interactions of functional polymers and Si composites.
- Synthesize new functional binders with acidic and semiconducting functionalities.

Accomplishments

- Prepared hierarchical silicon-carbon (Si-C) composites simultaneously possessing primary carbon-coated sub-10 nm Si particles and secondary micro-sized aggregation, which show specific capacity >1,500mAh/g with good cycling stability and rate capability.
- Successful synthesis of titanium nitride (TiN) coated silicon nanoparticles (Si@TiN) via the reduction of TiO2-coated silicon nanoparticles (Si@TiO2) in nitrogen, which exhibit good cycling performance, high efficiency and good rate capability.
- Synthesized graft copolymer binders with mechanically stable backbones and semiconducting grafts.
- Tested new crosslinked SPEEK and sulfonated semiconducting binder compositions to improve upon previous best-tested SPEEK binders.

✧ ✧ ✧ ✧ ✧

Introduction

An increase in energy and power densities of Li-ion cells clearly depends on improvements in electrode materials performance. The commercial anode, graphite has the theoretical capacity of 372 mAh/g, which is low relative to the requirement of high-energy applications. Thus, the search for an alternative anode to replace graphite in Li-ion batteries has been underway for many years. So far, silicon has the highest theoretical capacity ($Li_{4.4}Si$ ~ 4,200 mAh/g) of all known materials, and is abundant, inexpensive, and safer than graphite (it shows a slightly higher voltage plateau than that of graphite, and lithiated silicon is more stable in typical electrolytes than lithiated graphite). Unfortunately, the practical use of Si powders as anodes in Li-ion batteries is still hindered by several problems. One of the problems is severe volume changes during Li insertion/extraction, leading to loss of electric contact and poor cycling performance.

One approach to obtain a high-performance Si anode is to use silicon/carbon composites. This project aims to develop novel Si/SiO$_x$-carbon nanocomposite to improve cycling performance of Si anodes. On the other hand, many important battery characteristics, including stability and irreversible capacity losses, are critically dependent on the polymer binder's properties. High capacity electrochemically active Si particles that exhibit significant volume changes during insertion and extraction of Li require improved binder characteristics to ensure electrode integrity during use.

Inspired by these features, this project seeks to mitigate the electrochemical limitations of Si-based anodes during charge/discharge by designing novel Si/SiO$_x$-carbon nanocomposite and polymer binders to tolerate volume change, improve electrode kinetics, and decrease initial irreversible capacity loss.

Approach

The approach is 1) to synthesize different Si-based nanocomposites and identify novel commercially available binders to tolerate volume change upon lithiation/delithiation so as to improve cycling performance; and 2) to develop novel polymer binders with controlled elastic properties, ion-conductive moieties, and SiO$_x$ surface binding functionality, in order to stabilize and bridge SiO$_x$ particles to improve cycling performance of Si-based anodes.

Results

Si-based anode materials: Hierarchical silicon-carbon (Si-C) composites have been prepared, which simultaneously possess primary carbon-coated sub-10 nm Si particles and secondary micro-sized aggregation. The synthesis process involves facile thermal annealing of silsesquioxane with size-controlled formation of Si primary particles and subsequent carbon coating steps. The Si-C composites are composed of micro-sized particles having the size of about 10 µm, as shown in Figure V - 83a. In addition, the carbon was uniformly coated on Si particles as a similar intensity of silicon (red) and carbon (blue) was observed in the same region by EDS analysis. Si-C composites exhibited high reversible capacity of 1,660 mAh/g and excellent cycling stability within 150 cycles (Figure V - 83b). It also delivers a relatively high initial coulombic efficiency of 76.0%, then quickly increases to ~97.8% at the third cycle, 99.0% at the tenth cycle, and finally stabilizes at ~99.5% in the subsequent cycles. Besides, this Si-C composite with micro-sized secondary aggregation exhibited a high tap density of 0.68 g/cm^3, leading to a high volumetric capacity of 1,088 mAh/cm^3.

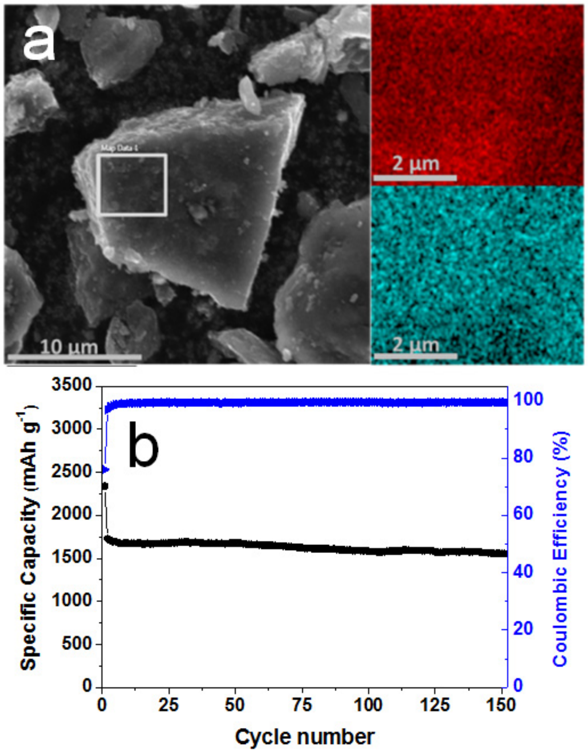

Figure V - 83: (a) SEM image and (b) cycling performance of the hierarchical silicon-carbon (Si-C) composites

Titanium nitride (TiN) coated silicon nanoparticles (Si@TiN) were synthesized via the reduction of TiO$_2$-coated silicon nanoparticles (Si@TiO$_2$) in nitrogen. The TiO$_2$ layers were coated on the surface of commercial silicon via a solution approach, and subsequent thermal annealing in N$_2$ led to a formation of titanium nitride coating on Si to obtain TiN-coated Si nanoparticles. Si nanoparticles in Si@TiN are coated with a crystalline TiN layer composed of TiN nanoparticles with an average particle diameter of around 10 nm, as shown in Figure V - 84a. Ti and N elements are uniformly distributed in the Si@TiN particles as shown in EDS elemental mapping of Si (Figure V - 84b), Ti (Figure V - 84c) and N (Figure V - 84d). The Si@TiN composite shows initial discharge and charge capacities of 2,650 mAh/g and 1,990 mAh/g, respectively, with an initial coulombic efficiency of 76%. Si@TiN has a high efficiency of above 99% during cycling. It also shows better cyclability than Si@TiO$_2$ and Si, with 75% capacity retention (1,900 mAh/g) with respect to the first discharge capacity after 100 cycles at 400 mA/g (Figure V - 84e). Impedance studies indicate that the TiN coating can enhance the conductivity of the Si@TiN and promote formation of a more stable SEI layer than the Si and Si@TiO_2.

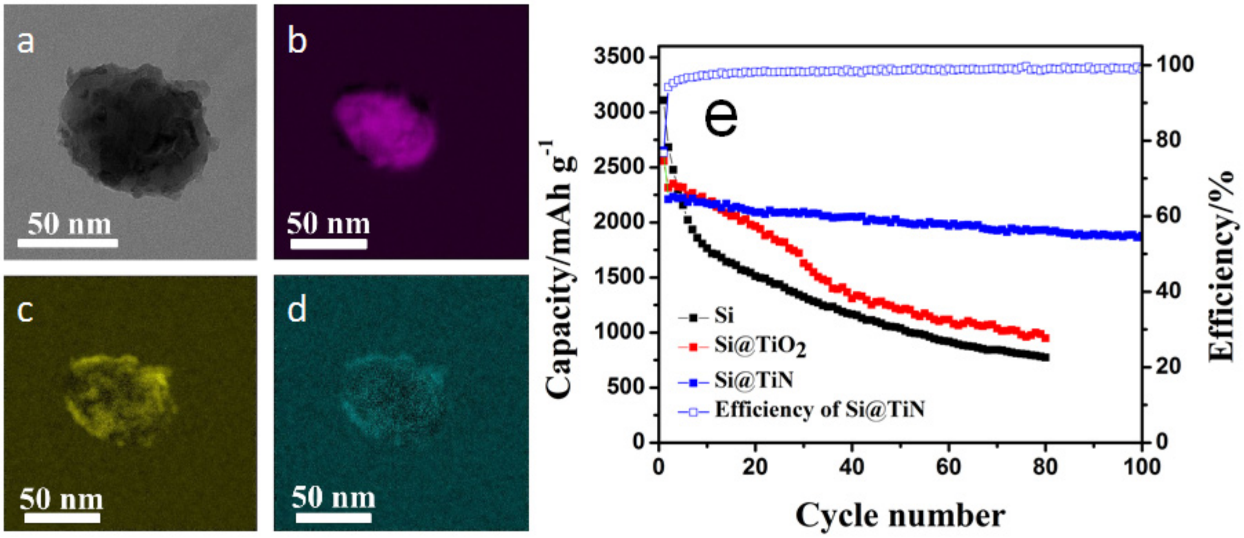

Figure V - 84: (a) TEM image, (b) Si, (c) Ti and (d) N EDS mapping, and (e) cycling performance of Si@TiN

A micro-sized porous Si-C composite (PSi/C) has been developed by reduction of $SiCl_4$ with alkaline alloy followed by a thin layer of carbon coating by thermal deposition of acetylene. Both the pore size and Si building blocks size are about 10 nm (Figure V - 85a). The initial discharge and charge capacity of PSi/C are 1,862 mAh/g and 1,044 mAh/g (2,482 mAh/g and 1,392 mAh/g based on Si, at current density of 0.4 A/g), giving a coulombic efficiency of 56%. After 100 cycles, the material shows a reversible capacity of 990 mAh/g (1,320 mAh/g based on Si) with capacity retention of 94.8% (Figure V - 85b). The coulombic efficiencies reach 99% after 10 cycles and remain at > 99%.

A Si-based anode material (boron doped Si/SiO2/C) with controlled electrochemical prelithiation and with superior high rate performance by element doping has been demonstrated as the anode in a Li-ion hybrid supercapacitor to enable high energy and power densities. Benefitting from the high capacity and good rate performance, a large portion of capacity is reserved even under lower voltage, for example, 0.2 V as marked by dash line in Figure V - 86a. A Li-ion hybrid supercapacitor was constructed by coupling the prelithiated Si-based anode with porous carbon cathode in conventional Li-ion electrolyte. Figure V - 86b shows the voltage profiles of the Li-ion hybrid supercapacitor at different current densities. The curves show little deviation from the linear slope of an ideal supercapacitor, which is due to the relatively flat charge/discharge plateau of the Si-based anode. The energy and power densities of the hybrid supercapacitor were calculated based on these curves. A high energy density of 128 Wh/kg can be achieved at a power density of 1,229 W/kg. Even at an ultra-high power density of 9,704 W/kg, which is on a par with conventional supercapacitors, the hybrid supercapacitor can still deliver 89 Wh/kg. The capacity retention is 70% after 6,000 cycles at 1.6 A/g. This work demonstrates that incorporating high-performance Si-based anodes is an effective approach to boost the energy and power densities of Li-ion hybrid supercapacitors.

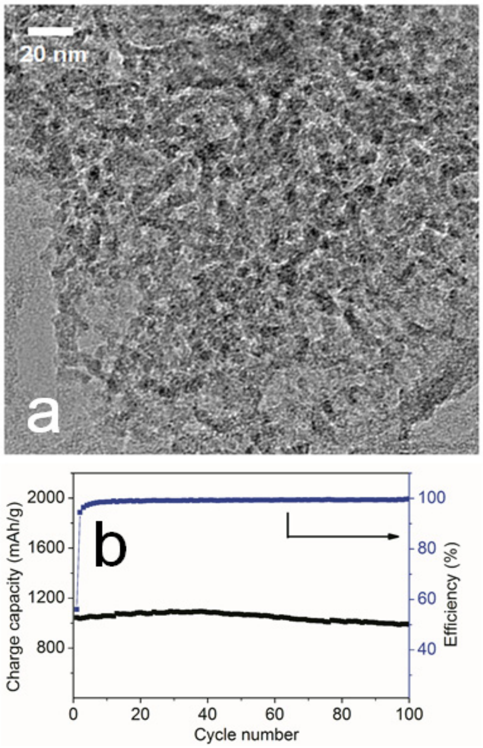

Figure V - 85: (a) TEM image and (b) cycling performance of PSi/C

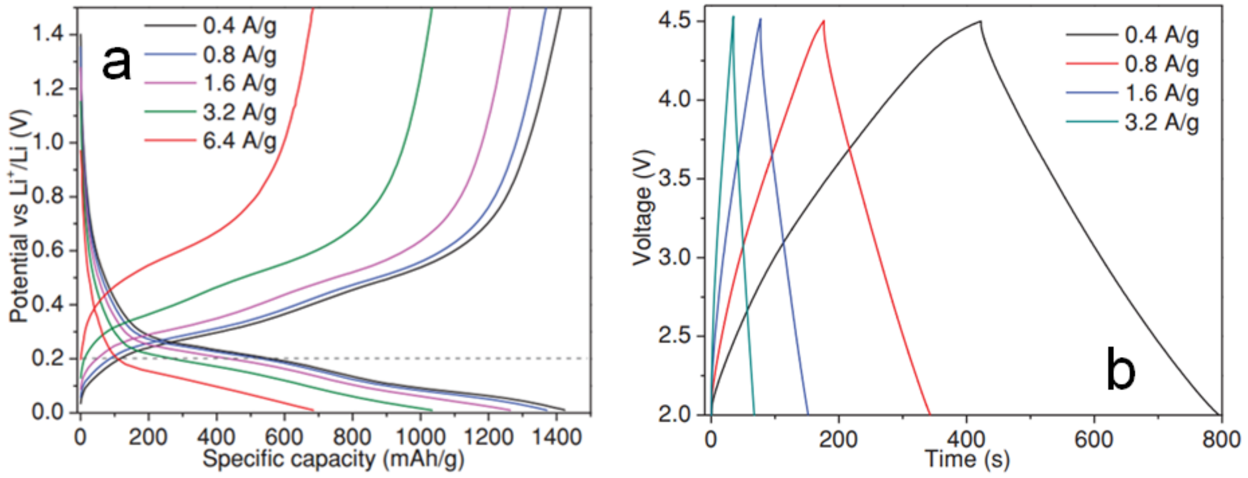

Figure V - 86: (a) Voltage profiles of boron doped Si/SiO$_2$/C at different current densities and (b) charge-discharge curves of the hybrid supercapacitor at different current densities

Synthesis and evaluation of polymer binders: A range of polymer chemical structures for mechanically robust binders were screened (Figure V - 87). Carboxylic acid (CA) and nitrile-containing polymers (SPAEN) were synthesized and tested as Si binders. The purpose of these experiments was to investigate other chemistries on binder performance. Strongly interacting functional groups like carboxylate, sulfonate, and nitrile are sought to help mitigate capacity fade in Si anodes.

The CA and SPAEN binder performance data is shown in Figure V - 88. None of these binders performed up to the level of the previous SPEEK system. Therefore, this line of inquiry was discontinued on mechanically robust polymers with sulfonate, carboxylate, and nitrile functional groups to investigate other types of structures, including semiconducting graft copolymers.

To improve upon the SPEEK structure semiconducting graft binders were synthesized from poly(phenylene oxide) backbones using a Suzuki grafting-from approach, Figure V - 89. The key step in this reaction is the complexation of the catalyst on the brominated backbone structure. This allows for a chain-growth type of polymerization mechanism using an A-B semiconducting monomer. Since sulfonation has been shown to be advantageous in previous work, the graft polymers were then post-sulfonated and tested as binders in Si-anode cells.

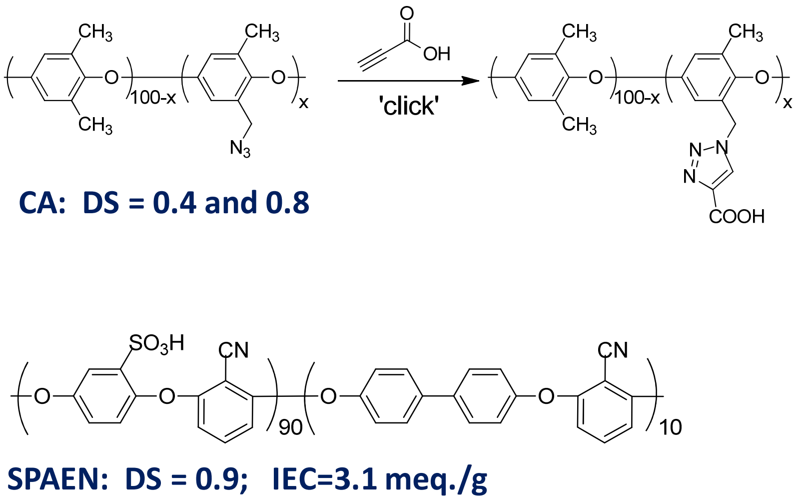

Figure V - 87: Chemical structures of carboxylic acid (CA) and nitrile (SPAEN) containing binders

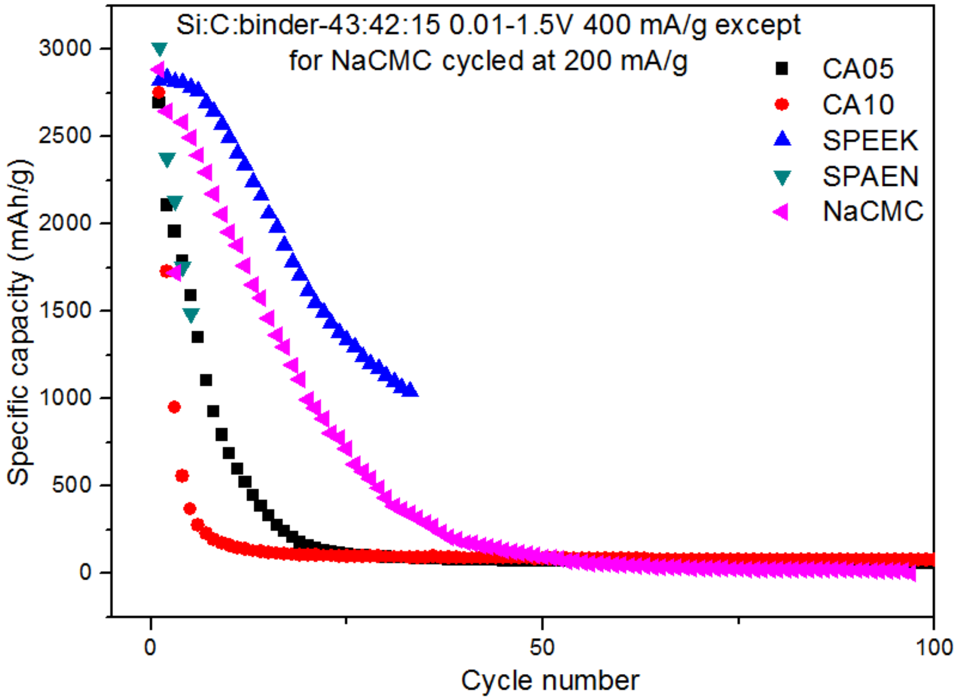

Figure V - 88: Capacity fade as a function of cycle number for CA and SPAEN binders

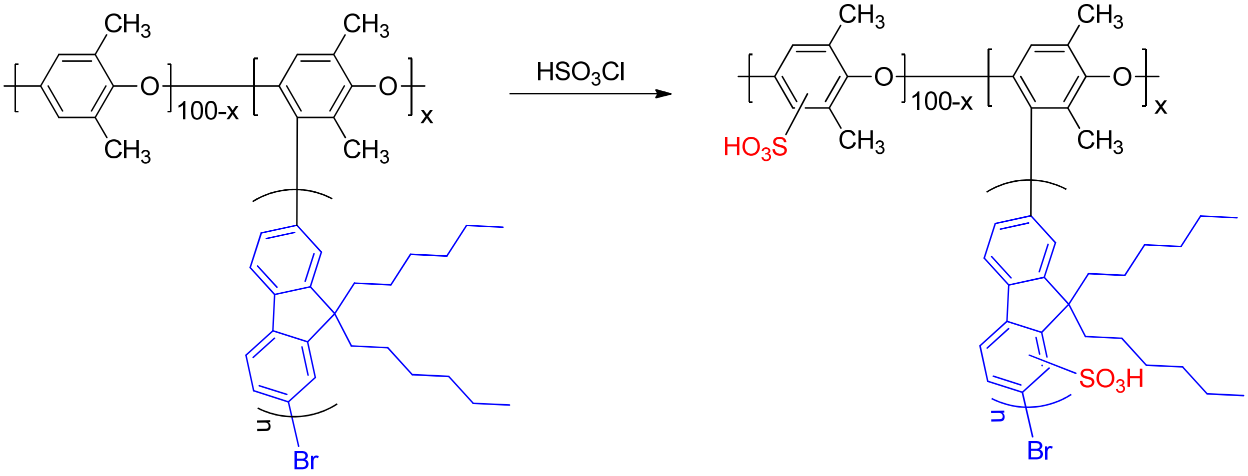

Figure V - 89: Suzuki graft synthesis of semiconducting side chains and mechanically robust backbones

Initial testing with these binders showed poor performance and significant capacity fade after only a few cycles (Figure V - 90). This type of rapid fade is similar to that observed with other non-interacting Si binders, like PVDF. It is hypothesized that carbonyl or carboxylic acid groups might be needed to improve the performance of these binder structures. The poor performance of the latest round of binder testing is currently trying to be diagnosed through collaboration with LBNL researchers on baseline Si anode compositions.

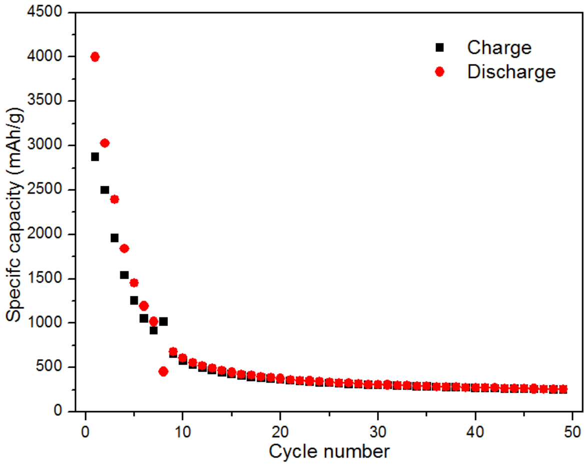

Figure V - 90: Capacity as a function of cycle number for sulfonated semiconducting binder shown in the previous figure

Conclusions and Future Directions

Hierarchical silicon-carbon (Si-C) composites have been prepared. Si-C composites exhibited high reversible capacity of 1,660 mAh/g and excellent cycling stability within 150 cycles. A novel coating of titanium nitride (TiN) has been developed for silicon nanoparticles (Si@TiN), which help achieve good cycling performance, high efficiency and good rate capability. A micro-sized porous Si-C composite (PSi/C) has been developed by reduction of $SiCl_4$ with alkaline alloy followed by a thin layer of carbon coating by thermal deposition of acetylene. It shows a reversible capacity of 990 mAh/g with a high capacity retention of 94.8% after 100 cycles. A Si-based anode material (boron doped $Si/SiO_2/C$) with controlled electrochemical prelithiation and with superior high rate performance by element doping has been demonstrated as the anode in a Li-ion hybrid supercapacitor. A high energy density of 128 Wh/kg can be achieved at a power density of 1,229 W/kg. Even at an ultra-high power density of 9,704 W/kg, it can still deliver 89 Wh/kg.

Continued synthesis and testing of binders will continue to the end of the project. The goal is to improve upon the previous best-observed SPEEK composition and provide a path to crosslinked binders and graft copolymers that are based on commercially-available backbones.

During the remaining period of the project, future work will be focused on: 1) optimizing modifications of micro-sized Si/carbon composite (including particle size and carbon content) to further improve the long cycling stability; 2) evaluating combinations of binders and Si-based anode materials developed in this project aiming to obtain an optimized Si-based anode composition.

FY 2014 Publications/Presentations

1. Wang, D. (June 2014). “Development of High Energy Density Lithium-Sulfur Cells.” Presented at the 2014 DOE Annual Merit Review and Peer Evaluation Meeting, Washington, D.C.
2. Song, J. X., Chen S. R., Zhou, M. J., Xu, T., Gordin, M. L., Lv, D. P., Long T. J., Melnyk M., Wang, D. H. (2014). *Journal of Material Chemistry A* (2); p. 1257.
3. Tang, D. H., Yi, R., Gordin, M. L., Melnyk, M., Dai, F., Chen, S. R., Song, J. X., Wang, D. H. (2014). *Journal of Material Chemistry A* (2); 10375.
4. Song, J. X., Chen S. R., Wang, D. H. (May 2014). “Micro-Sized Silicon-Carbon Composite Composed of Carbon-Coated Sub-10 nm Si Primary Particles As High-Performance Anode Materials for Lithium-Ion Batteries.” Presented at the 225th ECS Meeting, Orlando, FL.

V.C.9 Development of Silicon-Based High Capacity Anodes (PNNL)

Ji-Guang Zhang
Pacific Northwest National Laboratory

Energy & Environment Directorate
902 Battelle Boulevard, Mail Stop K2-44
Richland, WA 99352
Phone: (509) 372-6515; Fax: (509) 375-2186
E-mail: jiguang.zhang@pnnl.gov

Jun Liu (Co-PI)
Energy & Environment Directorate
902 Battelle Boulevard, Mail Stop K2-01
Richland, WA 99352
Phone: (509) 375-4443; Fax: (509) 351-6242
E-mail: Jun.Liu@pnnl.gov

Start Date: October 2010
Projected End Date: September 2014

Objectives

- Develop Si-based anodes with high capacity, high cycle stability, and high rate capability.
- Develop low-cost synthesis routes for Si-based anodes.
- Advance the fundamental understanding of the electrolyte additive effect, stress/volume expansion effects, and degradation mechanisms of Si-based anodes.

Technical Barriers

Low-energy density, limited cycle life, and high cost.

Technical Targets

- Identify the fading mechanisms in both thick and thin Si anodes.
- Achieve high-loading Si-based anodes with a capacity retention of >1.2 mAh/cm^2 after 150 cycles.
- Achieve improved cycling stability of thick electrodes of >3 mAh/cm^2.
- Achieve a first cycle Coulombic efficiency of > 90% for Si anodes through the application of stabilized lithium metal powder.

Accomplishments

- Demonstrated > 85% capacity retention after > 150 cycles for high-loading Si-based anodes of ~1.5 mAh/cm^2 with mesoporous sponge Si porous (MSS) and modified Si/B4C/graphite composites.
- Demonstrated ~90% capacity retention after 100 cycles for thick porous (MSS) Si electrodes of ~3 mAh/cm^2.
- Demonstrated capacity retention of ~87% and an areal capacity of ~1.85 mAh/cm^2 for porous Si prepared by a low cost thermite reaction.
- Identified the effect of the charge voltage on the cycling stability of Si anodes.
- Revealed the differences in the fading mechanisms of thick vs. thin Si electrodes.

✧ ✧ ✧ ✧ ✧

Introduction

Si has a very high theoretical capacity of ~4,200 mAh/g and a strong potential to be used as an anode for next generation Li-ion batteries. However, the large volume expansion during the lithiation process usually leads to a rapid capacity fade, thus hindering its use for practical applications. Several nanostructured Si materials have demonstrated excellent performance, but most of these work well only for low active material loadings and the electrode performance degrades quickly with the increased loadings required for practical applications. Another barrier in this field is that most high capacity Si-based electrodes must be prepared using expensive processes that are difficult to scale up. Therefore, to pave the road for practical applications, a cost effective and scalable approach needs to be developed to produce Si-based anodes that can retain excellent performance under high-loading conditions.

Approach

The focus of this year's work was to improve the cycling stability of thick Si-based anodes with high active material loadings (> 1 mAh/cm^2). Both the mesoporous, sponge-like Si particles (MSS) and rigid, skeleton-supported Si composites (Si/B_4C/graphite) developed recently in the laboratory have been used in this study. As a comparison, porous Si prepared by a low-cost thermite reaction was also investigated.

The MSS active material with nano-sized pores and high porosity was synthesized using a scalable anodization method. The etched material was then coated with a thin layer of carbon using chemical vapor deposition to improve its electronic conductivity. Although the etched samples exhibit a size of >20 µm, it was not pulverized during the cell reactions, even after thousands of charge/discharge cycles. This is a significant improvement compared to the performance of conventionally used large Si particles. The large volume expansion of the MSS material during the lithiation process is primarily accommodated by the inner channels so that an overall particle expansion of only ~30% was observed.

The Si/B_4C/graphite active materials were prepared by a cost-effective and scalable ball-milling method. The syntheses methods have been further optimized to improve the cycling stability and rate performance of the samples with high areal specific capacity. In this composite, a conductive B_4C material with a high Mohs hardness rating serves not only as micro-/nano-millers in the high energy ball-milling process to break down the micron-sized Si, but it also improves the electronic conductivity of the composite. A low-energy ball milling process was then used to coat a thin layer of conductive carbon on the resulting material to further enhance the conductivity of the composite.

In a separate effort, porous Si synthesized through a thermite reaction was provided by David Ji of Oklahoma State University. The as-received material exhibited a low capacity due to its poor electronic conductivity. Therefore, a thin layer of conductive carbon (~10 nm) was coated on the Si surface by chemical vapor deposition as described in a previous report (*Nat. Comm.*, 5, 4105–4111 (2014)).

Results

High-loading mesoporous silicon sponge anodes: The MSS particles prepared in this work exhibited large pore sizes of ~50 nm. Most of the volume change in this material can thus be accommodated by the inner channels. Therefore, large Si particles (>20 µm) with such large pore sizes underwent a volume expansion of only ~30% in their outside dimensions enabling them to serve as highly stable anodes, even for high active material loadings. The batteries with MSS were cycled using the BATT protocol: 0.005 to 1 V; three formation cycles at 0.06 mA/cm^2; 0.75 mA/cm^2 for delithiation and 0.5 mA/cm^2 for lithiation. The electrolyte used was 1M $LiPF_6$ in EC:DEC:FEC (0.45:0.45:0.1).

Figure V - 91 shows the areal capacity as a function of cycle number for a porous Si anode with a loading of ~2 mg/cm^2. This anode had a capacity of 1.85 mAh/cm^2 at low current density and ~1.5 mAh/cm^2 at higher rates. The capacity retention was ~96% after 300 cycles. Excellent cycling stability of the anode was also demonstrated for higher Si loadings. For example, Figure V - 92 shows the long term cycling of an MSS Si anode with the loading of ~2.9 mg/cm^2. This anode had a capacity of ~2.9 mAh/cm^2 at low current density and ~2.2 mAh/cm^2 at higher charge/discharge rate. The sample retained 86% of its capacity after 300 cycles. Figure V - 93 shows the cycling performance of MSS Si anodes with a high-loading of ~3.5 to 4 mg/cm^2. A capacity of ~3 mAh/cm^2 with ~90% capacity retention after 100 cycles was obtained.

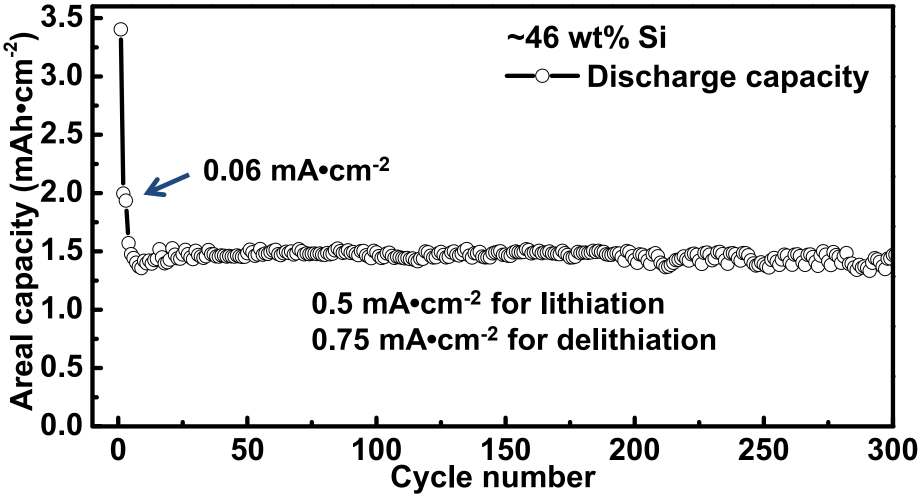

Figure V - 91: Cycling stability of a MSS Si anode with a high areal discharge capacity of ~1.5 mAh/cm^2

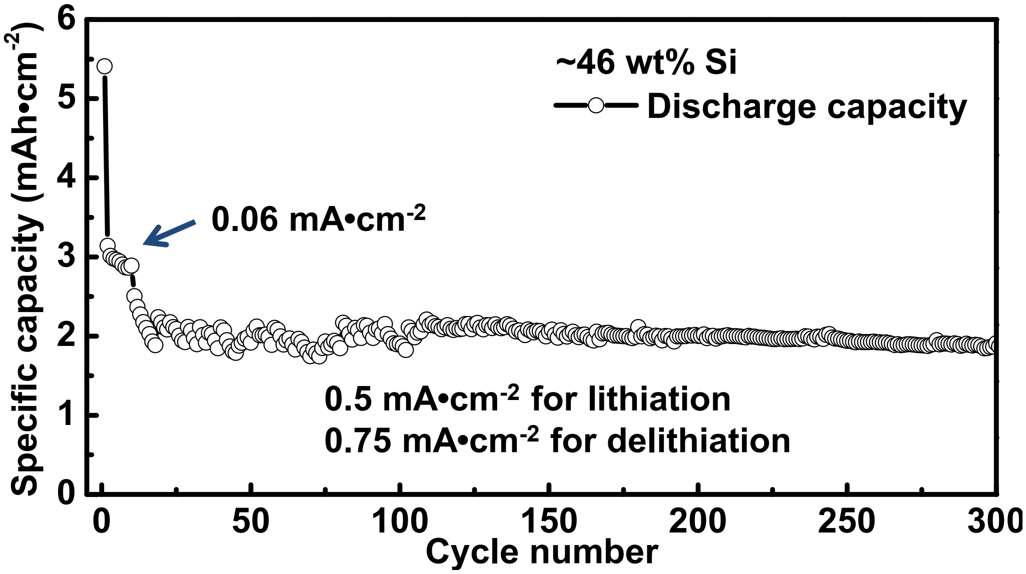

Figure V - 92: Cycling stability of a MSS Si anode with a high areal discharge capacity of ~2.2 mAh/cm^2

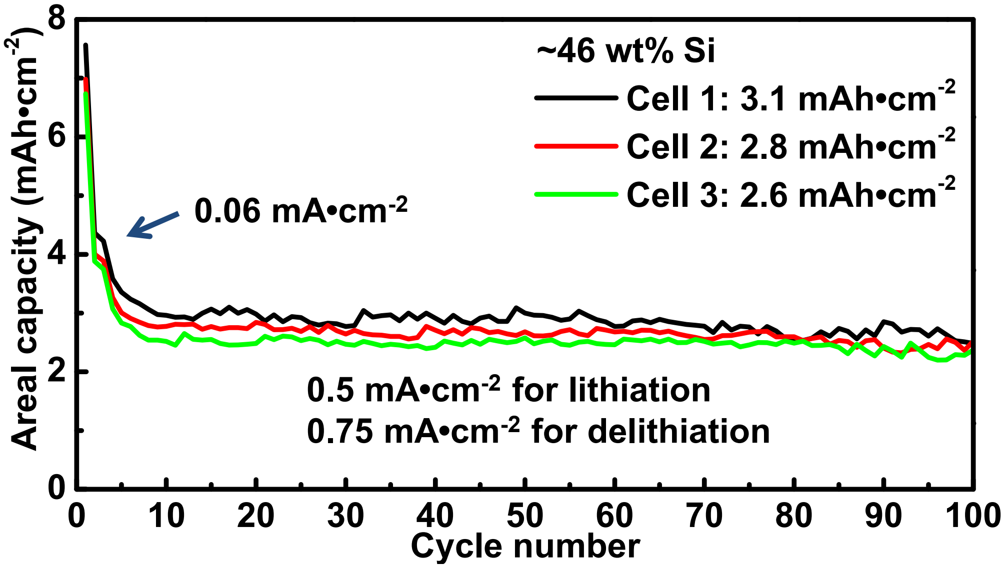

Figure V - 93: Cycling stability of a MSS Si anode with a high areal discharge capacity of ~3 mAh/cm^2

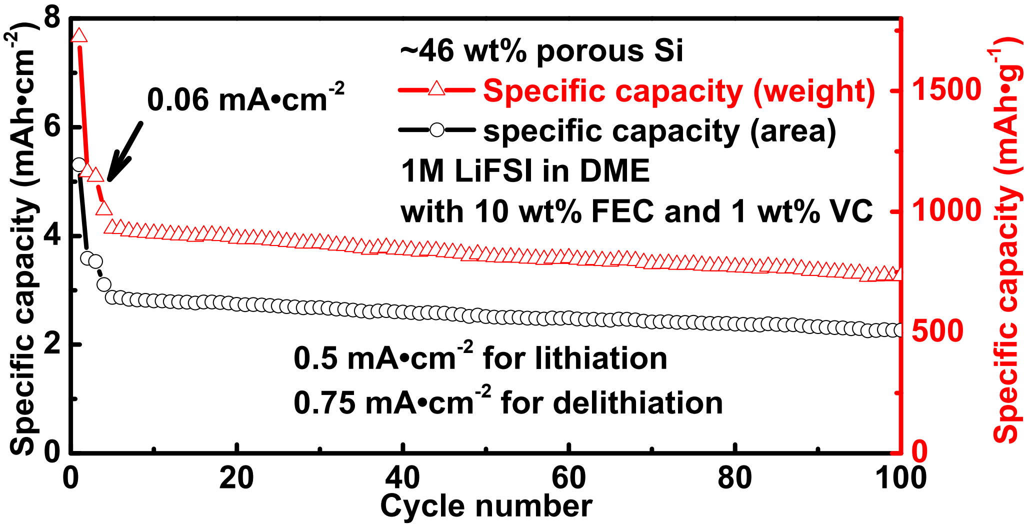

Figure V - 94: Cycling stability of a MSS Si anode with the electrolyte 1M LiFSI in DME with 10 wt% FEC and 1 wt% VC

To further improve the cycling stability of the MSS Si, the influence of the electrolyte was further investigated. It was reported recently that ether-based electrolytes (such as 1M LiFSI in DME) can improve the cycling stability of Li metal anodes. This electrolyte has been used to test the Si-based anodes with the addition of 10 wt% FEC and 1 wt% VC. Figure V - 94 shows the long term cycling stability of a MSS Si anode with a loading of ~3.1 mg/cm^2, using this new electrolyte. This anode was cycled at a low current density of 0.06 mA/cm^2 for 3 cycles and then charged at 0.75 mA/cm^2 and discharged at 0.5 mA/cm^2. The anode had a capacity of ~3.5 mAh/cm^2 (~1,150 mAh/g) at low current density and ~2.9 mAh/cm^2 (~930 mAh/g) at higher rates. Its capacity retention is ~79% after 100 cycles. Although these results are close to those observed in the conventional electrolyte (1M $LiPF_6$ in EC:DEC:FEC (0.45:0.45:0.1)), this electrolyte may not be suitable for high-voltage cathode materials because the solvent DME is less stable than EC and DEC at high-voltage conditions. Further optimization of the electrolyte is needed to improve the electrochemical performance of the Si-based anodes without compromising the possible use of high-voltage cathodes in Li-ion batteries.

High-loading anode with Si/B_4C/graphite composite: The Si/ B_4C/graphite composite shows an improved cycling stability after further modification. Figure V - 95 shows the specific capacity of this anode material as a function of cycle number. This anode was conditioned at 0.06 mA/cm^2 for three cycles, and then cycled at 0.75 mA/cm^2 for delithiation and 0.5 mA/cm^2 for lithiation. The battery was cycled between 0.005–1 V. 1M $LiPF_6$ in EC:DEC:FEC (0.45:0.45:0.1) was used as the electrolyte. The modified material exhibits a high areal specific capacity of ~1.42 mAh/cm^2 and a capacity retention of ~85% after 150 cycles.

High-loading anode with porous Si prepared by thermite reaction: In a separate effort, a thermite reaction (a potentially low cost synthesis approach) has been used to prepare porous Si. Excellent performance of the Si obtained from such a reaction is demonstrated in Figure V - 96 which shows that the porous Si can have a capacity of ~1.85 mAh/cm^2 with ~87% capacity retention after 100 cycles. A similar test protocol to that described above was used in this study.

Cycling stability – charge voltage dependence: The effect of the charge voltage on the cycling stability of the Si/B_4C/graphite composite anodes was investigated. Figure V - 97a shows the cycling stability of a Si/B_4C/graphite composite anode (2.4 mg/cm^2) cycled between 0.005 V–1 V. This anode exhibited a capacity of ~2.25 mAh/cm^2 (~950 mAh/g) at low current density and ~1.85 mAh/cm^2 (~780 mAh/g) at higher rates. Its capacity retention was ~65% after 100 cycles. In contrast, Figure V - 97b shows the cycling stability of a Si/B_4C/graphite composite anode (2.8 mg/cm^2) when it was cycled between 0.005 V–0.6 V. This anode had a capacity of ~2.1 mAh/cm^2 (~770 mAh/g) at low current density and ~1.71 mAh/cm^2 (~620 mAh/g) at higher rate. Its capacity retention was ~85% after 100 cycles. By lowering the voltage from 1 V to 0.6 V, the capacity retention of a Si/B_4C/graphite composite anode of similar loading can be improved by 20% with the sacrifice of ~20% of the capacity.

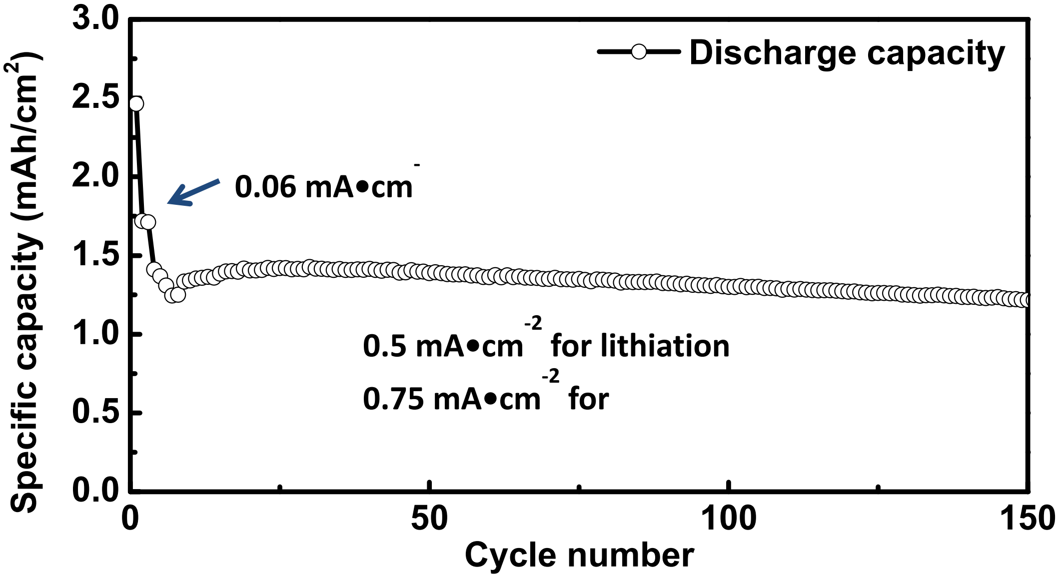

Figure V - 95: Cycling performance of a modified SBG composite anode

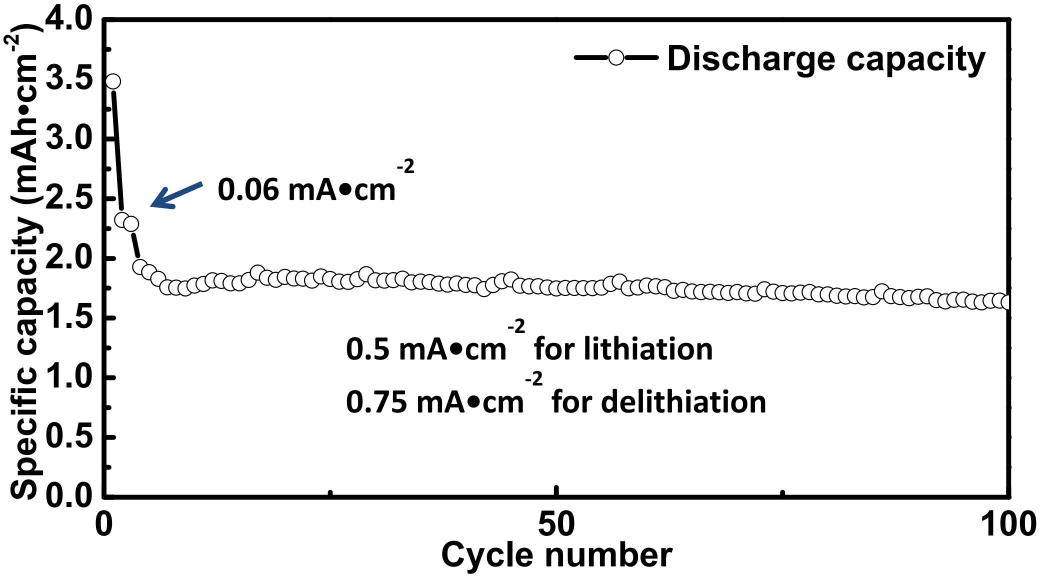

Figure V - 96: Cycling stability of a porous Si anode obtained from the thermite reaction

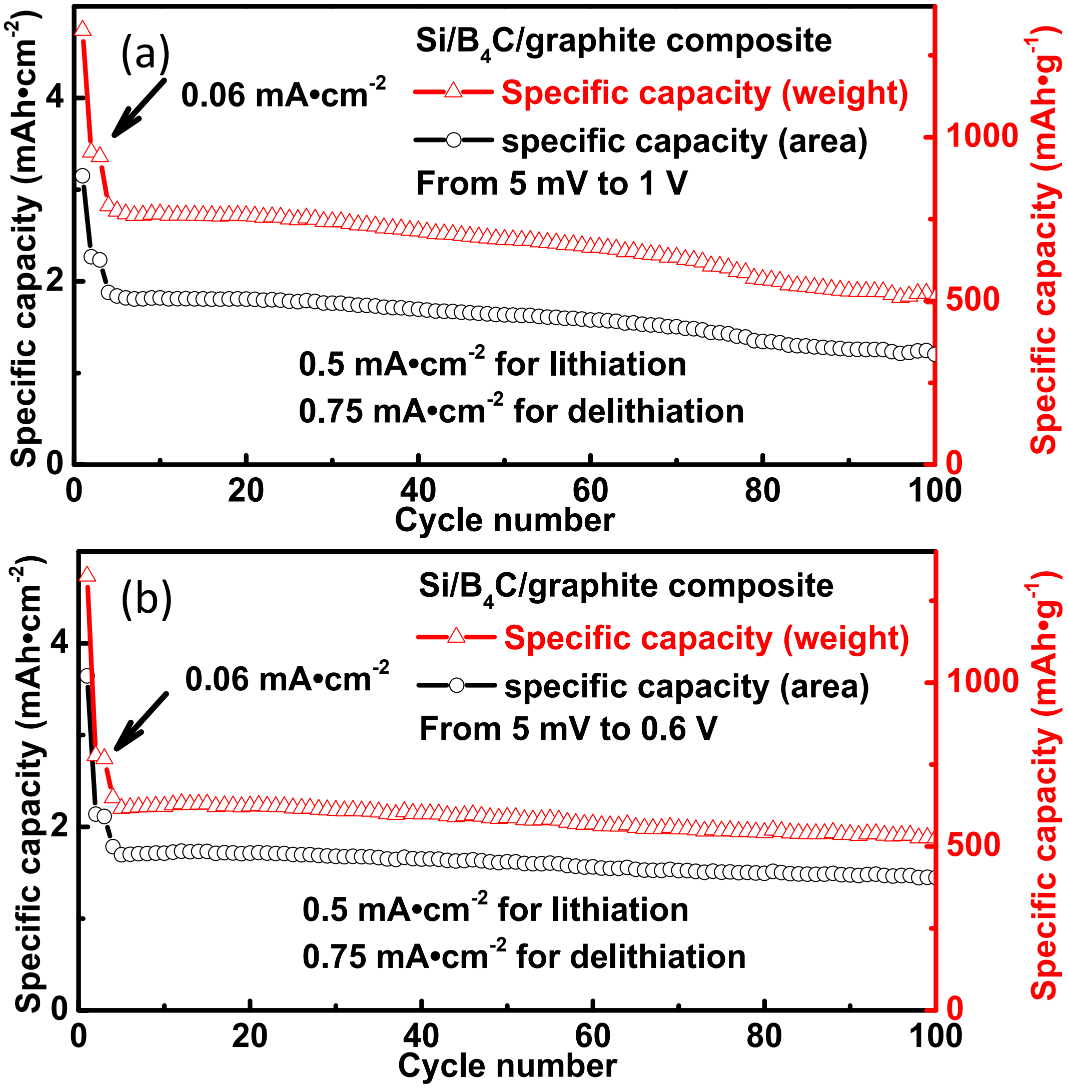

Figure V - 97: (a) Cycling stability of a Si/B$_4$C/graphite composite anode of ~2.4 mg/cm^2 between 0.005–1 V. (b) Cycling stability of the Si/B$_4$C/graphite composite anode of ~2.8 mg/cm^2 between 0.005–0.6 V

Conclusions and Future Directions

The main focus of the project during the last year has been to improve the performance of Si-based anodes at high-loading conditions. A capacity retention of > 85% after > 150 cycles has been achieved for Si-based anodes with a loading of ~1.5 mAh/cm^2 for both the MSS Si and modified Si/B$_4$C/graphite composites. The porous Si prepared by the anodization method exhibits excellent long term cycling stability because its mesoporous structure can effectively accommodate the volume change during the cycling process. This anode has retained ~96% of its capacity after 300 cycles. Excellent cycling stability at higher loadings of ~2-3 mAh/cm^2 was also demonstrated with the electrochemically-etched porous Si. This anode has an ~86% capacity retention after 300 cycles at ~2.2 mAh/cm^2 and ~90% capacity retention after 100 cycles at ~3 mAh/cm^2. To further reduce the cost, a relatively low cost thermite reaction was also used to synthesize porous Si. With a similar porous structure, the thermite Si shows excellent cycling stability with a capacity retention of ~87% and the areal capacity of ~1.85 mAh/cm^2.

By studying the cycling stability of the Si electrodes with differing thickness, the differences in the fading mechanisms of thick vs. thin Si-based electrodes has been revealed. Although the porous Si used in this work exhibits only minor degradation due to pulverization of the Si particles, the continuous formation of an SEI layer consumes the electrolyte (as well as the Si active material) resulting in a high cell impedance. In the Si/Li coin cells used in this investigation, the amount of electrolyte added to each coin cell was the same. The quick fading of an electrode with a high Si loading was attributed to the rapid consumption of electrolyte because much more SEI was formed on the Si surface due to the larger active surface area, as compared with similar electrodes with a low Si loading. The formation of a large amount of SEI per unit area in the high-loading electrodes leads to a rapid increase in the cell impedance and loss of electrical contact between the electrode components and the current collector. This consumption of the electrolyte and increasing impedance eventually leads to (often sudden) failure of the cells. Although the FEC additive can improve the cell cyclability because of the thinner and more stable SEI formed on the Si surface in FEC-containing electrolytes, the factors that affect the stability of these SEI layers need to be more extensively investigated.

In addition to the accelerated degradation in the electrical properties of the cells, a thick Si-based electrode may also easy separate from the substrate (current collector) due to the larger mechanical stresses induced by cell cycling which may also result in premature cell failure. Electrodes with 3D current collectors have the advantage of a high gravimetric capacity for the cell pack, but their volumetric capacity will be lower. A binder with good adhesion and flexibility may help to maintain the integrity of the electrode. Strong binding among the electrode components and between the electrode and current collector is therefore critical to ensure stable cell cycling.

Future work will focus on the following areas:

- Development of more cost-effective methods to synthesize porous Si.
- Investigate new binders to improve the cycling stability of high-loading electrodes.
- Identify an optimized combination of porous Si with conventional graphite anodes—both the ratio of Si to graphite, as well as the synthesis methods will be investigated.
- Development of new approaches and electrode structures to enable electrodes with high Si mass loading without compromising the long-term cell cycling stability.

FY 2014 Publications/Presentations

1. Zhang, J.; Liu, J. (June 2014). “Development of Si-based High Capacity Anodes.” Presented at the 2014 DOE Annual Merit Review and Peer Evaluation Meeting, Washington, D.C.
2. Li, X.; Gu, M.; Hu, S.; Kennard, R.; Yan, P. Chen, X.; Wang, C.; Sailor, M.J.; Zhang, J.-G., Liu, J. (2014). “Mesoporous Silicon Sponge as an Anti-Pulverization Structure for High-Performance Lithium-Ion Battery Anodes.” *Nat. Comm.* (5); pp: 4105–4111.
3. Chen, X.; Li, X.; Mei, D.; Feng, J.; Hu, M.Y.; Hu, J.; Engelhard, M.; Zheng, J.; Xu, W.; Xiao, J.; Liu, J.; Zhang, J.-G. (2014). “Reduction Mechanism of Fluoroethylene Carbonate for Stable Solid–Electrolyte Interphase Film on Silicon Anode,” *ChemSusChem* (7:2); pp: 549–554.
4. Wang, C.M.; Gu, M.; Wang, Z.; Gao, F.; Zhang, J.-G.; Baer, D.R.; Thevuthasan, S.; Browning, N.; Liu, J. (2013). “*In situ* TEM study of Lithiation of Si and Phase Transformation.” *Microsc. Microanal.* (19:S2), pp: 1468–1469.
5. Zhan, H.; Xiao, J.; Nie, Z.; Li, X.; Wang, C.M.; Zhang, J.; Liu, J. (2013).“Nanostructured Materials for Rechargeable Batteries: Synthesis, Fundamental Understanding and Limitations.” *Curr. Opin. Chem. Eng.* (2:2); pp: 151–159.
6. Zhang, J. (September 2014). “Development of Next Generation of Li-Ion Batteries.” Presented at the PNNL-UNIST Workshop, Ulsan, Republic of South Korea.
7. Li, X.; Gu, M.; Kennard, R.; Hu, S.; Chen, X.; Wang, C.; Sailor, M.J.; Liu, J.; Zhang, J.-G. (October 2013). “Macroporous Silicon as Highly Stable Anodes for Lithium Rechargeable Batteries.” Presented at the 224th ECS Meeting, San Francisco, CA.

V.C.10 Wiring up Silicon Nanoparticles for High Performance Lithium Ion Battery Anodes (Stanford U)

Yi Cui
Stanford University

Department of Material Science and Engineering
476 Lomita Mall, McCullough 343
Stanford. CA 94305
Phone: (650) 723-4613; Fax: (650) 725-4034
E-mail: yicui@stanford.edu

Start Date: January 2011
Projected End Date: December 2014

Objectives

- Go beyond the charge capacity limitation of conventional carbon anodes by designing nano-architectured silicon electrodes.
- Design, synthesize and characterize Si nanostructure-based anodes to overcome the volume change-induced materials challenges and to realize high performance.
- Understand the fundamental structure-property relationship on electrode materials with large structure and volume changes.
- Develop low-cost material processing methods.

Technical Barriers

The large structure and volume changes of Si during battery cycling causes multiple materials challenges: 1) mechanical breaking; 2) unstable solid electrolyte interface; 3) difficulties in maintaining good electrical connections. These fundamental challenges result in the following technical barriers to good battery performance:

- Large first cycle irreversible capacity loss.
- Poor cycle life.
- Inadequate coulombic efficiencies.
- Low areal mass loading of active materials.

Technical Targets

- Develop fundamental material guidelines through structure and property correlations.
- Design nanostructured Si anodes to address the four material challenges outlined above.
- Develop synthesis techniques to produce the designed nanostructured Si anodes.
- Develop low-cost material processing methods.

Accomplishments

- Designed and synthesized Si pomegranate structures to overcome the challenges of Si anodes, and achieve high battery performance.
- Developed unique porous Si structures and CNT-Polymer-SiNP interconnected architectures for better anode performance.
- Developed electro-less copper plating to improve electrical conductivity of Si anodes.
- Used *in situ* TEM and *ex situ* SEM methods to understand how neighboring Si particles affect each other during cycling.

✧ ✧ ✧ ✧ ✧

Introduction

Next generation high capacity electrode materials are needed in order to develop high energy battery technologies to meet the demands of the transportation sector. Silicon is an exciting and promising anode material for replacing carbon in Li-ion batteries due to: 1) a high gravimetric capacity of ~4,200 mAh/g, ten times higher than graphite (~370 mAh/g); 2) a high volume capacity of 9,786 mAh/cm^3; 3) its relatively low working potential (~ 0.5 V Vs Li/Li$^+$), which makes it suitable as an anode; 4) the abundance and environmentally friendly nature of Si; and 5) the ability to leverage the fundamental and manufacturing knowledge that has been established in the Si semiconductor industry and solar industry. However, there exist several scientific and technical challenges for silicon anodes: 1) *Mechanical fracture caused by large volume changes.* The electrochemical alloying reaction of Li with Si involves volume expansion of up to 300% and significant contraction during lithium extraction. The stress induced by the large volume changes causes cracking and pulverization of silicon, which leads to loss of electrical contact and eventual capacity fading. 2) *Unstable solid electrolyte interface (SEI).* The repetitive volume expansion/contraction causes the continuous movement of the interface between Si and organic electrolyte, which makes it challenging to form a stable SEI layer, resulting in low coulombic efficiency and capacity loss during cycling. 3) *Good electrical contact.* It is challenging to maintain good electrical contact between Si materials and the current collector, especially in high areal-mass-loading case. Even though mechanical fracture does not take place in Si nanostructures below critical sizes, large volume changes can still cause the movement of Si nanostructures and their detachment from the conducting framework during long-term battery cycling. 4) Challenges associated with generating Si materials to address the above three challenges with low-cost and scalable processing.

The goal of this project is to study the fundamental principles related to alloy anodes, to design nanostructured Si anodes for solving the fundamental challenges, and to develop low-cost and scalable processing for these materials.

Approach

This project takes a two-pronged approach to solving the above-listed problems. First, *ex situ* and *in situ* observation techniques are developed and used to uncover the fundamental nature of the Li-Si reaction, such as Si volume changes and particle-particle interactions during cyclings. Insight gained from this fundamental study is used as the framework for designing new nanostructured anodes that feature minimal structural damages and are dimensionally stable SEI regions. A focal point of the project is to also develop low-cost and scalable methods to synthesize these designed nanostructured Si anodes.

Results

Pomegranate-inspired nanoscale design for Si anodes: Inspired by the structure of a pomegranate fruit, a novel secondary structure for Si anodes was designed (Figure V - 98). Si nanoparticles (SiNPs) are embedded within a spherical micron-sized porous carbon framework. The porous carbon framework of nanoscale thickness connects all the SiNPs, and also conformally covers the whole secondary particle surface, so that most of the SEI only forms on the outside of the secondary particle. Well-defined void space is engineered around each nanoparticle, allowing the Si to expand without changing the secondary particle morphology or breaking the SEI layer. Such a design has multiple advantageous features, including (i) the nano-sized primary particle size prevents fracture; (ii) the micron-sized secondary structure makes it easier to maintain electrical contact; (iii) the well-defined internal void space allows the SiNPs to expand without destroying the secondary particle morphology; (iv) the carbon framework functions as an electrical highway and a mechanical backbone so that all SiNPs are electrochemically active; (v) carbon also completely wraps the secondary particle surface to limit most of SEI formation to the outer surface, which not only limits the amount of SEI, but also retains the internal void space for Si expansion; and (vi) the dilemma of high surface area and low tap density introduced when using nano-sized primary feature is partially solved.

The pomegranate design affords remarkable battery performance. As shown in Figure V - 99a, its reversible capacity reached 2,350 mAh/g at a rate of C/20. From the second cycle to the 1,000th cycle at a rate of C/2, the capacity retention was more than 97%. After 1,000 cycles, over 1,160 mAh/g still remained, which is more than three times the theoretical capacity of graphite. Unprecedentedly stable cycling (100 cycles with 94% capacity retention) with high areal capacity (3.7 mAh/cm^2) was also demonstrated, similar to the areal capacity of commercial Li-ion batteries (Figure V - 99b). The SEM images confirm that the pomegranate structures remain intact after 100 cycles (Figure V - 99c).

Moreover, the specific SEI area (the surface area in contact with the electrolyte divided by the mass of silicon) decreases from 90 m^2/g for single yolk–shell particles to 15 m^2/g for 1 μm pomegranate particles and to only 1.5 m^2/g for 10 μm particles. As a result, the initial coulombic efficiency of pomegranate can reach 82%, compared with ~70% for yolk-shell structures. The successful design principles developed in this study can be widely applied to other high-capacity Li battery electrodes.

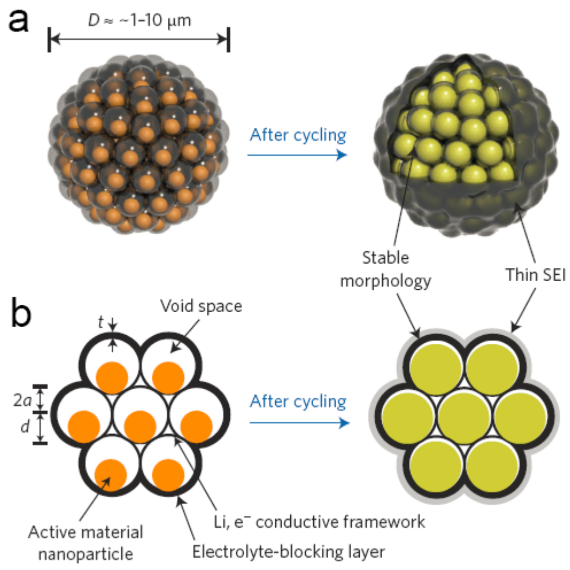

Figure V - 98: Schematic of the pomegranate-inspired design. (a) Three dimensional view and (b) simplified two-dimensional cross-section view of one pomegranate microparticle before and after electrochemical cycling (in the lithiated state)

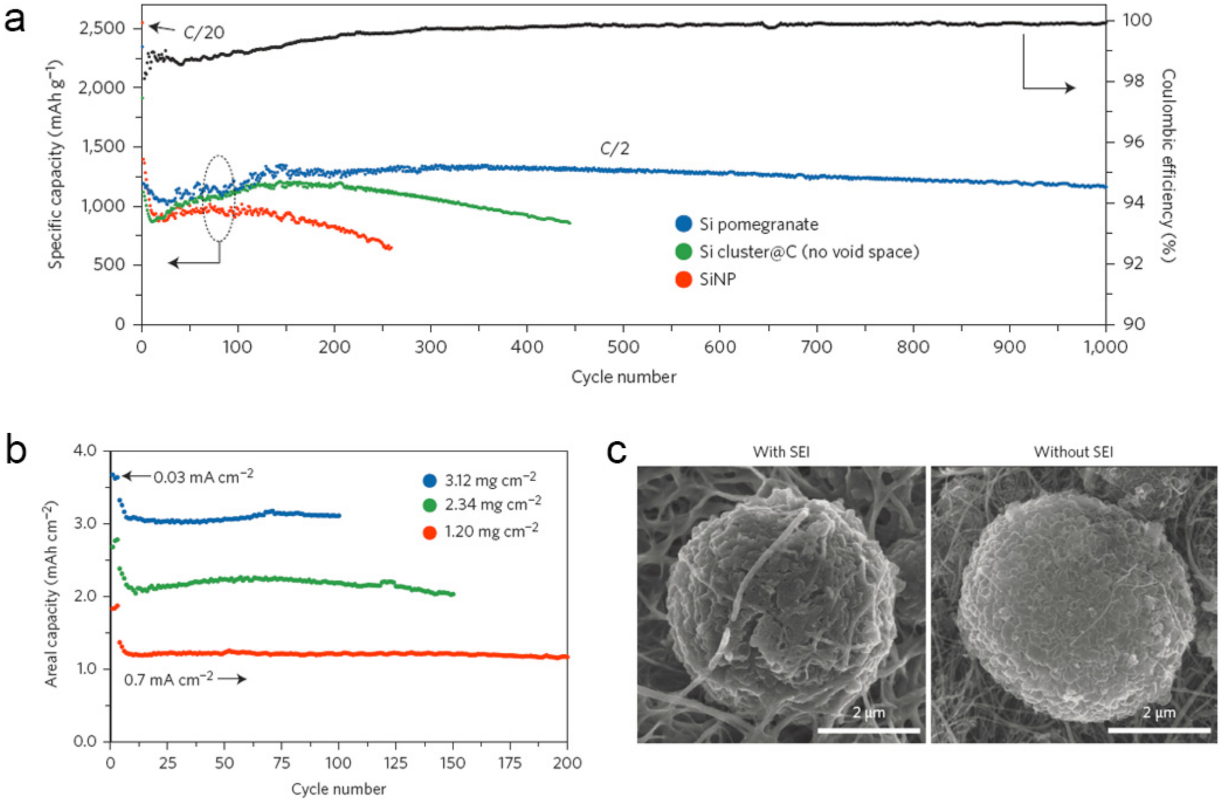

Figure V - 99: (a) Reversible delithiation capacity for the first 1000 galvanostatic cycles of Si pomegranate and other structures tested with the same conditions. (b) High areal mass loading test (up to 3.12 mg/cm^2 active material) of Si pomegranate anodes. (c) Typical SEM images of Si pomegranates after 100 cycles

Low-cost and high-mass-loading silicon anode from rice husks: A method was developed to synthesize Si porous structures for Si batteries directly from agricultural waste product rice husks (Figure V - 100a). Rice husks were first converted to pure silica by burning in air and then reduced to silicon by magnesium. The synthesis process results in a 5 wt% yield of Si according to the weight of the initial rice husks. Considering the abundance (1.2x10^8 tons/year) and the low price (~$18/ton) of the rice husks, the synthesis dramatically reduces the cost of nanostructured silicon, which may paves the way for large scale application of Si anodes in vehicles.

This method results in a porous Si structure composed by interconnected nanoparticles, as shown by the SEM image in the Figure V - 100b. These nanoparticle domains were physically connected with each other in the synthesis, resulting in good contact during cycling, which finally ensures the good battery performance under high mass loading. In addition, the gap between the nanoparticles provides the space for volume expansion during lithiation. The late-cycle capacity of this porous structure is about 1,700 mAh/g with areal mass loading 0.6 mg/cm^2. Thus, an anode with areal capacity above 1 mAh/cm^2 and cycle life above 100 cycles was demonstrated. Even higher mass loading and longer cycle life can be achieved by combining the protection layer design via different coating method.

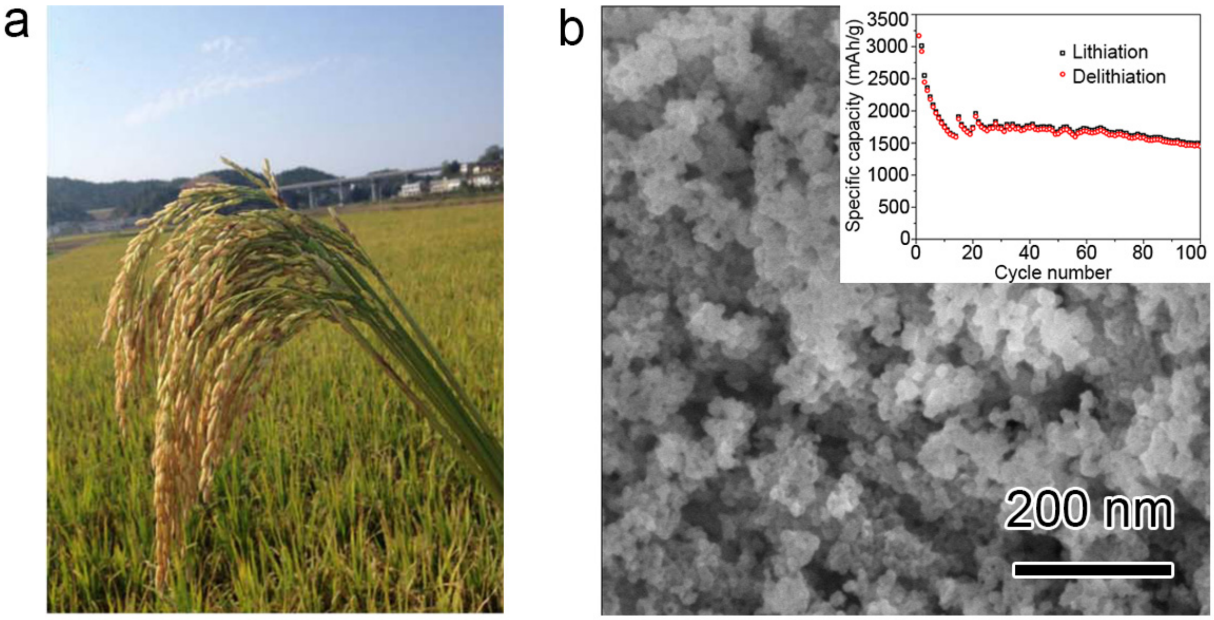

Figure V - 100: (a) A panicle of ripe rice. (b) SEM images of porous Si structure from rice husk. Inset is lithiation/delithiation capacity of the first 100 galvanostatic cycles. The rate was C/20 for the first cycle, then C/2 for the later cycles

A three-dimensionally interconnected carbon nanotube-conducting polymer hydrogel network for high-mass-loading Si anode: An aqueous-based solution process has been developed for efficient fabrication of high performance flexible Si electrodes using a synergistic combination of conducting polymer solution, CNTs, and Si nanoparticle building blocks (Figure V - 101a). The resulting interpenetrating network of CNT-conducting polymer network provided good mechanical properties, high conductivity and facile ion transport, thus leading to facile electrode kinetics and high strain tolerance during volumetric changes. Due to these structural merits, high cycling stability is achieved for SiNP electrodes at high mass loading. As shown in Figure V - 101c, the areal capacity of the interpenetrated electrode architecture reached 2.2 mAh/cm^2 within the initial cycle and retained to 1.8 mAh/cm^2 during the following 100 cycles. The realization of such high areal capacity using CNT-conducting polymer network opens great opportunities to fabricate flexible, light-weight and high-energy lithium battery for practical applications.

Copper coating for performance improvement of Si anode: Coatings help to increase the electrical conductivity, buffer the large volume change, form a stable solid electrolyte interface (SEI), and prevent aggregation of Si particles. Carbon is the most common material for accomplishing these purposes. However, the conductivity of carbon is affected by its quality, which is often not as good as graphite. Moreover, carbon coating produced at a low temperature (below 1,000°C) traps considerable Li in the initial cycles, which leads to a large decrease in first coulombic efficiency (CE). Copper coating is a good alternative due to its high electrical conductivity. A convenient, scalable electro-less plating method for uniform copper coating on Si pomegranate structures was developed. The presence of coated copper layer significantly enhances the inter-particle electrical conductivity in electrode. As a result, the copper coated structure exhibited excellent electrochemical performances, including a stable cycling performance at high mass loading (a areal capacity of 3.13 mAh/cm^2 at mass loading 4.10 mg/cm^2 after 100 cycles), and excellent rate capability (861mAh/g at 1C rate and 467 mAh/g at 4C rate). This copper electro-less plating route may open up an effective way to improve electrical conductivity of anode materials.

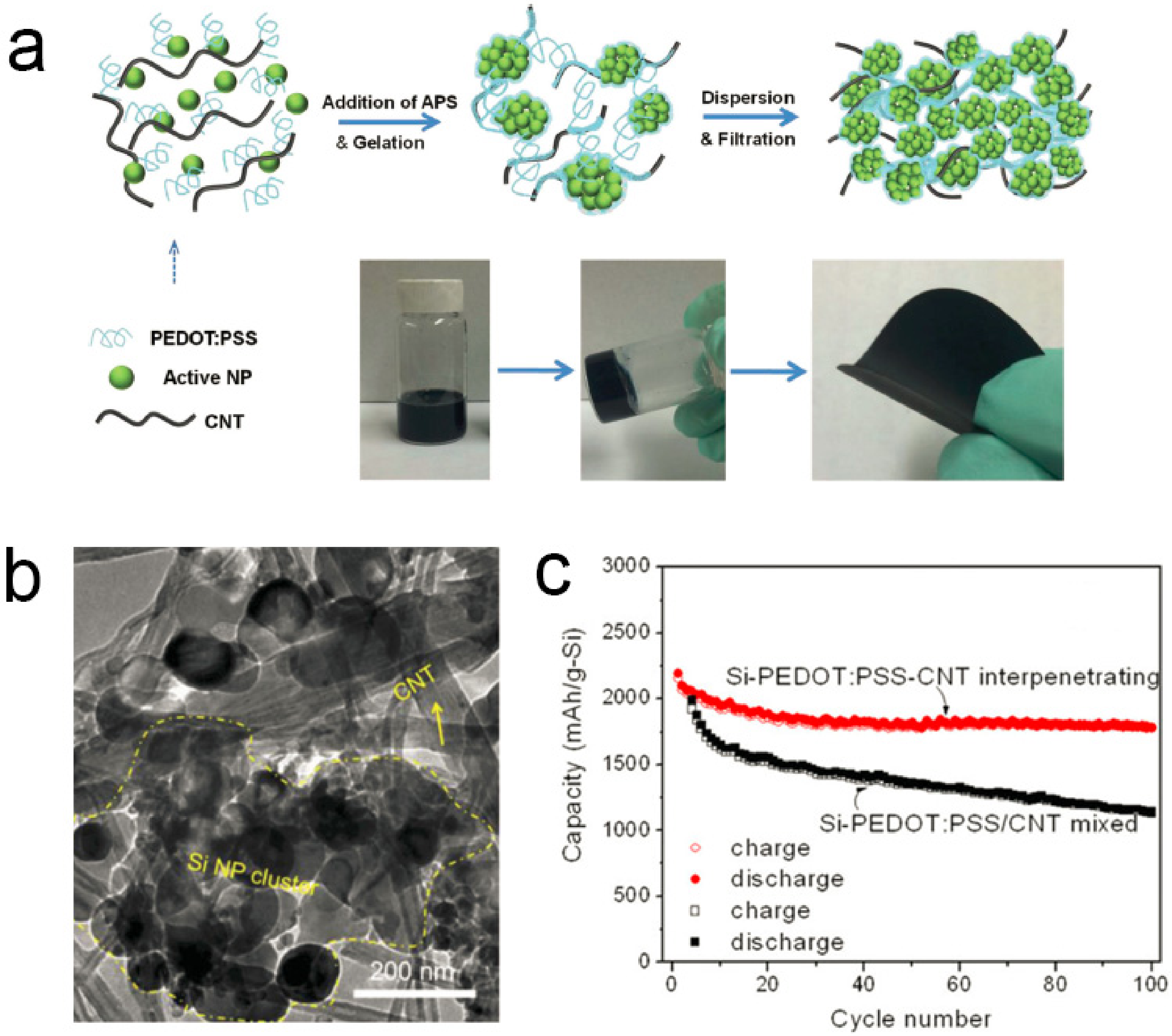

Figure V - 101: (a) Schematic of the aqueous solution process to fabricate flexible electrodes using Si nanoparticles CNT and PEDOT:PSS. (b) TEM image of the composite film. (c) Cycling stability of a thick Si-PEDOT:PSS-CNT electrode at C/10 rate. Cycling result of a control electrode made by simply mixing Si-PEDOT:PSS with CNT is also presented

Understand how neighboring Si particles affect each other during cycling: Accompanying the search for high performance Si anodes, fundamental studies have provided a better idea of how Si lithiates, swells and fractures, leading to a basis for the rational design of Si structures. Fundamental studies have revealed that crystalline Si expands preferentially in <110> directions during electrochemical lithiation and that the corresponding mechanical stresses affect the reaction kinetics and mechanical fracture of single Si particles or pillars upon lithiation. However, in a real battery system, electrochemical lithiation occurs simultaneously in clusters of individual Si structures in a confined medium. Hence, understanding how the individual Si structures (e.g. particles) interact during lithiation in a closed space is necessary to fully understand the lithiation process in whole electrode. Herein, various physical/mechanical interactions of swelling Si structures during electrochemical lithiation using well-defined Si nanopillar pairs were demonstrated. *Ex situ* SEM and *in situ* TEM studies reveal that the swelling Si nanopillars are pushed by obstacles and translated toward open space. When the pillars are mechanically clamped, compressive stresses change the reaction kinetics so that preferential lithiation occurs at free surfaces exposed to open spaces, even if lithiation does not normally occur rapidly on such surfaces. Such mechanical interactions enhance the fracture resistance of lithiated Si by lessening the tensile stress concentrations that develop in isolated Si pillars. An analytical model and numerical analysis are used to explain how mechanical interaction affects the reaction kinetics and fracture resistance of lithiated Si. This study will contribute to improved design of Si structures at the electrode level for high performance Li-ion batteries.

Conclusions and Future Directions

Much progress has been made on these projects this year. In Si pomegranate structures, silicon nanoparticles were embedded in a carbon framework with internal void spaces that accommodate the vast volume increases during charging. The carbon framework allows Li-ions and electrons to be transported while keeping the electrolyte and SEI away from the nanoparticles. The nanostructured anode can maintain a specific capacity of over 1,160 mAh/g after 1,000 lithiation cycles; and an areal capacity of 3 mAh/cm^2 over 100 cycles. Several methods were developed to achieve high areal mass loading by improving the electrical conductivity of electrode, such as 3D interconnected CNT-polymer-Si architectures and copper coating. Various physical/mechanical interactions of swelling Si structures were studied during electrochemical lithiation using well-defined Si nanopillar pairs. It demonstrated that mechanical interactions enhance the fracture resistance of lithiated Si by lessening the tensile stress concentrations that develop in isolated Si pillars.

Future directions include: 1) further developing and exploring conducting polymer additives, coatings, and binder to improve the connectedness of the Si electrode framework during cycling. 2) Other conducting coating materials will be evaluated to increase the coulombic efficiency and cycling stability. 3) Simple and scalable synthesis and electrode preparation method will be developed for practical applications. 4) Study of multiple Si nanostructures during cycling will be continued to understand how neighboring particles affect each other, and then guide the nanostructure design. 5) Prelithiation of Si structures will be used to increase the first cycle coulombic efficiency.

FY 2014 Publications/Presentations

1. Cui, Y. (June 2014). “Wiring Up Silicon Nanostructures for High Performance Lithium-Ion Battery Anodes.” Presented at the 2014 DOE Annual Merit Review and Peer Evaluation Meeting, Washington, D.C.
2. Liu, N.; Lu, Z.; Zhao, J.; McDowell, M.T.; Lee, H.-W.; Zhao, W.; Cui, Y. (2014). “A pomegranate-inspired nanoscale design for large-volume-change lithium battery anodes.” *Nature Nanotechnology* (9); pp: 187-192.
3. Chen, Z.; To, J.W.F.; Wang, C.; Lu, Z.; Liu, N.; Chortos, A.; Pan, L.; Wei, F.; Cui, Y.; Bao, Z. (2014). “A Three-Dimensionally Interconnected Carbon Nanotube–Conducting Polymer Hydrogel Network for High-Performance Flexible Battery Electrodes.” *Advanced Energy Materials* (4); pp: 1400207.

V.C.11 First Principles Modeling of SEI Formation on Bare and Surface/Additive Modified Silicon Anode (TAMU)

Perla Balbuena (Principle Investigator)
Texas A&M University

Department of Chemical Engineering
3122 TAMU
College Station, TX, 77843
Phone: (979) 845-3375; Fax: (979) 845-6446
E-mail: balbuena@tamu.edu

Jorge M. Seminario (Co-PI)
Department of Chemical Engineering
3122 TAMU
College Station, TX, 77843
Phone: (979) 845-3301; Fax: (979) 845-3301
E-mail: seminario@tamu.edu

Start Date: October 2012
Projected End Date: September 2016

Objectives

- Develop fundamental understanding of the molecular processes that lead to the formation of a solid electrolyte interphase (SEI) layer due to electrolyte decomposition on Si anodes.
- Develop a rational selection of additives and/or coatings.

Technical Barriers

Description of the electrode surface chemistry; characterization of the electron transfer rate through the SEI layer; description of the SEI layer structure and its evolution as well as that of the electrode during cycling.

Technical Targets

- Determine SEI reaction mechanisms and products for decomposition of ethylene carbonate (EC), fluorethylene carbonate (FEC) and vinylene carbonate (VC) as a function of degree of lithiation (voltage) of the Si surface.
- Develop a mesoscopic model able to predict SEI nucleation and growth at realistic time and length scales.
- Analyze voltage effects on SEI reactions on lithiated Si surfaces.

Accomplishments

- SEI reaction mechanisms and products of EC, FEC, and VC as a function of lithiation degree elucidated.
- Differences and similarities between products and mechanisms of additives FEC and VC revealed.
- New model explaining electron transfer through thick SEI layers developed.

✧ ✧ ✧ ✧ ✧

Introduction

Investigation of formation/growth mechanisms of the SEI layer on bare surfaces requires incorporation of effects from surface structure and chemical state: presence of functional groups, surface oxidation, nature of exposed facets, and electrolyte composition including additive species. Finding the correspondence between additive molecular properties and SEI formation mechanism, structure, and properties in additive-induced SEI layers will allow identification of new/improved additives. Including the state of lithiation of the surface is also a key factor to determine possible changes in the electrolyte reduction mechanism and/or nature of the products. Finally, it is crucial to understand how the electron transfer from the electrode to the electrolyte is modified by deposition of the initial SEI intermediates or products of the SEI formation reaction.

Approach

A comprehensive first-principles computational approach employed in this work includes density functional theory, *ab initio* molecular dynamics, and *ab initio*-Green's function theory. Static density functional theory (DFT) is utilized within two approaches: cluster models are used to investigate electrolyte reduction on model Si surfaces with ultra-low state of lithiation, whereas periodic surfaces represent both quasi-amorphous low lithiated surfaces and well-characterized crystalline Si_xLi_y alloys. The studied degrees of lithiation include $LiSi_{15}$, $LiSi_4$, $LiSi_2$, LiSi and $Li_{13}Si_4$ (from~0.8 V to ~0.2 V against Li/Li+). Adsorption of solvent (ethylene carbonate, EC) and additives (fluorinated ethylene carbonate, FEC and vinyl carbonate, VC) on the surface and the potential energy surfaces including activation barriers for their decomposition are studied with these methods. Models of periodic surfaces in contact with liquid electrolyte mixtures are also utilized to investigate mechanisms of electrolyte reduction using *ab initio* molecular dynamics (AIMD). Electron transport through the composite material (electrode/SEI layer/electrolyte molecule) is determined using *ab initio* Green's functions calculations. In addition, a multiscale modeling approach is utilized to develop a mesoscopic model able to predict SEI layer nucleation and growth at realistic length/time scales.

Results

Effects of degree of lithiation on SEI reactions: The reductive decomposition mechanisms of EC and FEC in very low-lithiated surfaces modeled with a Si cluster showed that Li^+ ions bind on the Si surface and form adsorption sites for EC/FEC bindings. In this ultra-low lithiated surface Li atoms are adsorbed above the surface plane whereas in the Li_xSi_y surfaces at intermediate and high degrees of lithiation Li atoms are on the surface or below the surface plane. This geometric dissimilarity induces significant differences in the electronic distribution and therefore in the reduction mechanisms. EC/FEC adsorption on the Li^+-adsorbed Si cluster is energetically favorable, and the decomposition mechanism starts with a C_E-O cleavage: the (negatively charged) oxygen atoms from EC bond with the Si atoms (slightly positively charged) that are not directly interacting with Li, forming a Si-O_E bond whereas the CH_2 radical moves away from the surface. In $2e^-$ transfers, two C_E-O bonds are broken. For EC decomposition at ultra-low degrees of lithiation, either the $1e^-$ or $2e^-$ induced ring openings are feasible, as both steps are exothermic and possess similar barriers, therefore both mechanisms may coexist for the EC reduction on the Si anode surface. Similar conclusion was found for the cases of the intermediate degrees of lithiation on Li_xSi_y alloyed surfaces. However, intermediate and higher lithiated surfaces show formation of a Si-Cc bond and then the Cc-O bond is broken. Both 2 and 4 e^- mechanisms are observed at intermediate degrees of lithiation, but only very fast 4 e^- mechanisms are detected at higher degrees of lithiation and direct transfer of two electrons to EC molecules in liquid phase was also found possible.

FEC reduction may undergo more pathways due to the multi- possible breaking sites in the ring and the high reactivity. At very low degree of lithiation, the one-electron ring-breaking reactions are either slightly exothermic or slightly endothermic, and the corresponding barriers are higher than those of the 2 e^- mechanisms. In contrast, the C_C-O_E bond cleavages show more negative reaction energy as well as very low barriers. This suggests that FEC breakdown undergoes the $2e^-$ mechanism on the very low-lithiated Si surfaces, and the C_E-F bond-breaking may take place through a moderate barrier. In contrast, multi-electron reaction pathways are found in intermediate and high degrees of lithiation, as discussed below.

VC reduction mechanisms and products: A $2e^-$ mechanism was found operative for VC at low/intermediate lithiation stages ($LiSi_2$ and LiSi), which results in an adsorbed VC^{2-} anion with a broken C_c-O_c bond. Two additional electrons are transferred to VC^{2-} at the higher lithiated $Li_{13}Si_4$ surface, yielding CO^{2-} (ads) and $\cdot OC_2H_2O^2$. Although no direct formation of CO_2 is observed upon VC reduction on Li_xSi_y surfaces, spontaneous reactions between VC and EC reduction species revealed that CO_2 can be released upon reaction of VC with CO_3^{2-}, present in the liquid phase of the electrolyte after reduction of the solvent EC. This is an alternative mechanism to that where CO_2 is produced via reaction of VC with EC^-. These simulation results suggest that the $1e^-$ reduction of EC is much less frequent on Si surfaces at intermediate or high stages of lithiation, where the proposed reaction of VC with CO_3^{2-} should be prevalent. (See Figure V - 102.)

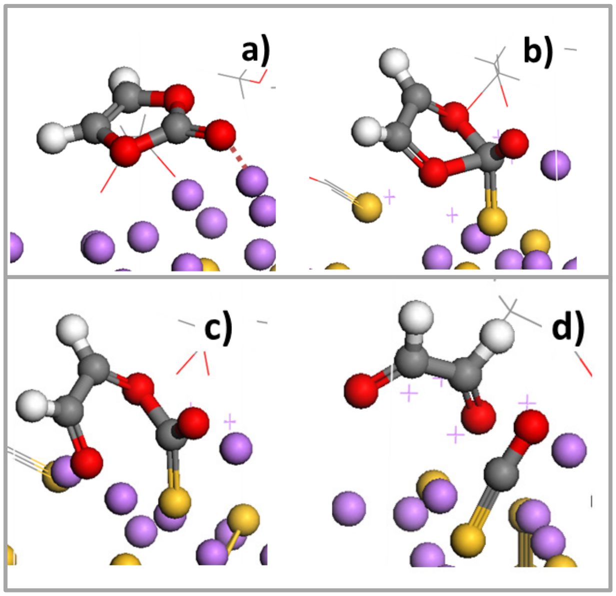

Figure V - 102: Reduction of VC on a $Li_{13}Si_4(010)$ surface. (a) VC adsorption starts with electrostatic interaction between the negatively charged carbonyl oxygen of the molecule and Li^+ ions on the surface (b) A Cc-Si bond is formed (c) Upon adsorption and transfer of 2 e^- from the surface to the molecule a Cc-Oc bond is broken. The resultant adsorbed species is opened VC $^{2-}$. (d) The cleavage of a 2nd Cc-Oc bond is observed upon transfer of 2 additional e^- to the adsorbed VC anion. Color code: Li is purple, Si yellow, O red, C black, and H white

FEC reduction mechanisms and products: Due to its high reactivity, reduction of FEC on Li_xSi_y surfaces was found to be extremely fast, independent of the degree of lithiation, and able to proceed through three different mechanisms. One of them leads to the adsorbed VC^{2-} anion upon release of H and F atoms from the FEC molecule (pathway III in Figure V - 103). This is a very interesting finding showing that in some cases the reduction of FEC and VC leads to the exact *same reduction products*, and explaining similarities in SEI layers formed in the presence of these additives. FEC molecules can also be reduced through two other mechanisms, involving the sequential transference of electrons to the molecules that result in formation of CO_2^{2}, F^- (pathway I in Figure V - 103), or CH_2CHO^- or CO^{2-}, F^-, and $\cdot OCH_2CHO^-$ (pathway II in Figure V - 103). These two groups of reduction products, which are different to the ones produced from VC reduction (pathway III), may oligomerize and form SEI layers with different components to those formed in the presence of VC. Additionally, in every FEC decomposition pathway observed, the fluorine atom leaves the FEC molecule being reduced and forming LiF moieties on the anode surface.

Multiscale modeling for prediction of SEI nucleation and growth: Electrodes modeled through AIMD simulations at various degrees of lithiation demonstrated rapid formation of LiF on the surface of lithiated Si anodes. These incipient nucleation sites have an irregular structure, and showed the possible continuation of solvent/additive reduction on parts of the surface that were not covered by LiF. Based on these structures, model SEI layers made of LiF fragments were constructed in various thicknesses and configurations, and by analogy, Li_2O model films were also built and examined with DFT/Green function's methods. It was found that at the same thicknesses and similar configurations, the LiF films offer a higher resistance to electron transfer than Li_2O. In each case, the resistance of the films is also larger if the fragments are separated at Van der Waals distances. As expected, increasing the thickness increases the film resistance. A rapid decay of the electron transfer was found within the 1st nanometer SEI thickness through these and other SEI blocks. This suggested that a different electron transfer mechanism must be prevalent for the SEI growing to thicknesses in the order of hundreds of nanometers. Thus, a new model has been formulated to describe the SEI layer nucleation and growth behavior within realistic time and length scales; the schematic shown in Figure V - 104 illustrates the main concepts. The model is designed based on the following hypotheses: a) Electron transfer through the SEI is done via the SEI intermediate anion products that carry the charge from the surface of the anode, where they are formed, to the SEI layer/electrolyte interface where they further decompose other electrolyte molecules. b) Such anion transport is done via channels formed between blocks (see schematic Figure V - 104). c) As the anion travels in the channels, it may combine with Li^+ forming

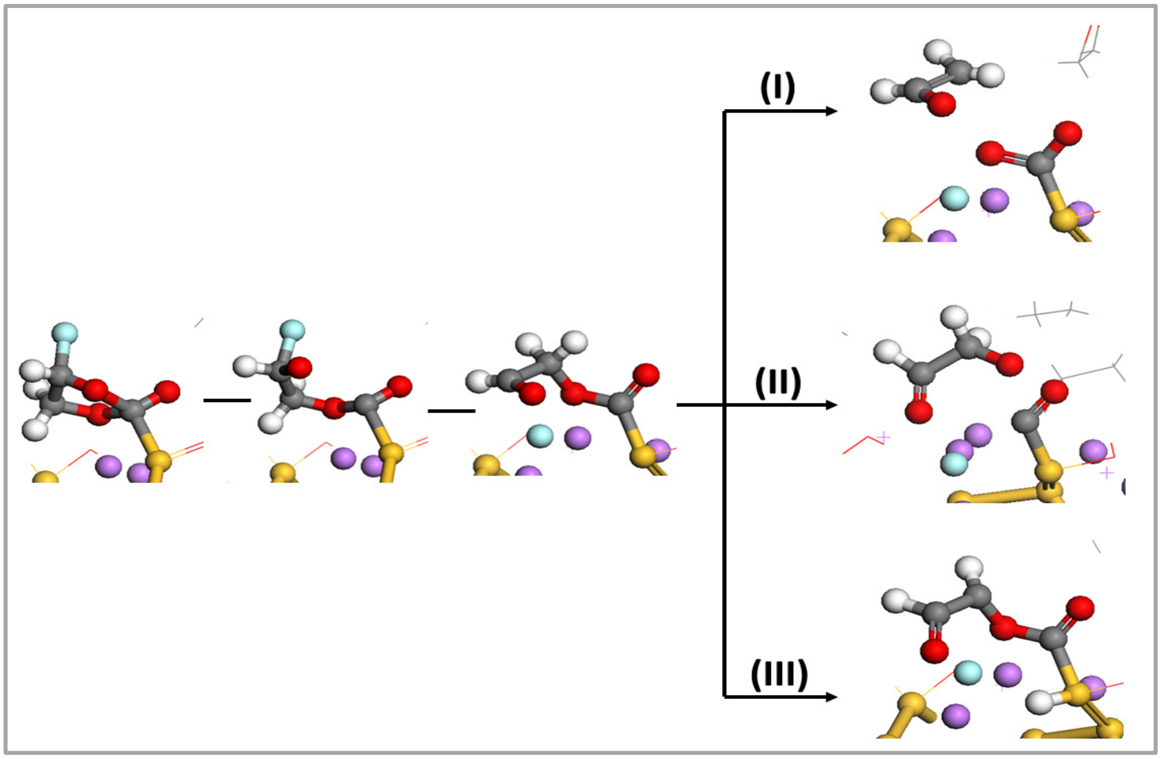

Figure V - 103: Reduction mechanisms of FEC on Li_xSi_y surfaces. Color code for the atoms: light blue: F, red: O, yellow: Si, purple: Li, grey: C, white: H

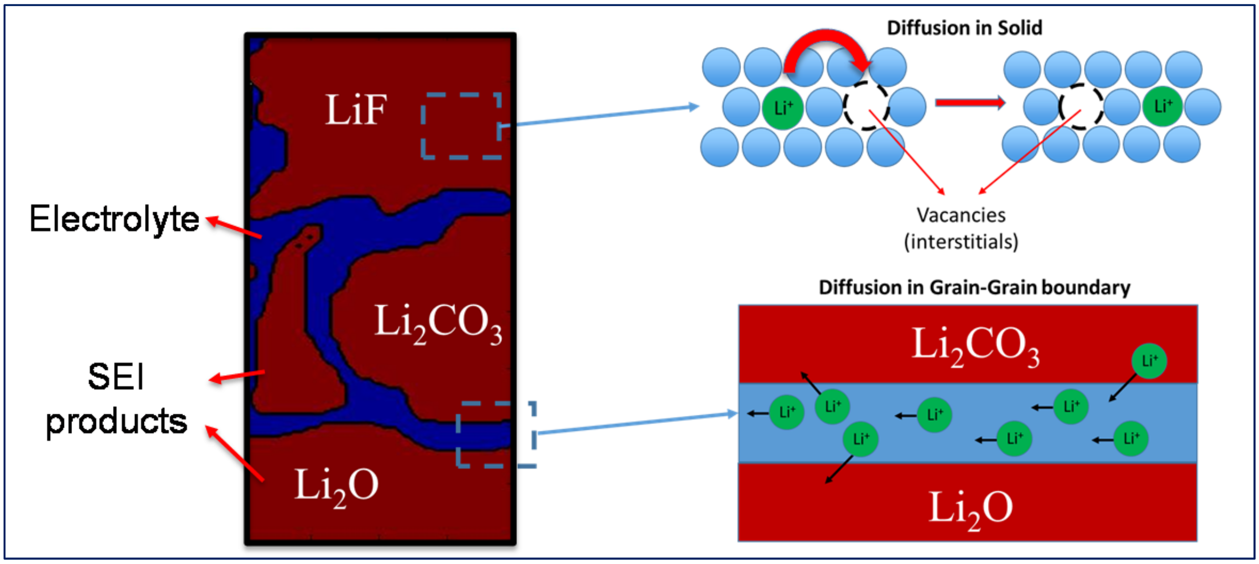

Figure V - 104: Schematic of SEI mesoscopic model. Ionic transport may occur through the blocks and/or through the ion channels separating blocks

neutral species. These species may get adsorbed partially blocking the channels or continue traveling towards the surface where they will contribute to increasing the SEI thickness. d) Thus, the channel thicknesses are also functions of time. e) The SEI layer grows until all channels are blocked to anion transport, although cation transport will continue. At that point the SEI layer growth will stop because electron transfer will be no longer possible.

Based on the above hypotheses, a mesoscopic model based on continuum mechanics was formulated to determine ionic composition profiles, evolution of channel thickness, evolution of SEI thickness, and maximum thickness when electron transfer is no longer possible. The parameters to the mesoscopic model are carefully determined from first principles simulations. Describing the interfaces between blocks and between the blocks and the anode surface is carried out at two different levels: a) AIMD simulations; b) Classical molecular dynamics (CMD) simulations. The AIMD simulations provide information about mixing of the various SEI species at the molecular level: if the species do not mix, it provides information about the geometry and atomic constitution of the channel walls. The CMD simulations provide similar insights at higher length and time scales. For example nucleation involves longer times that cannot be detected via AIMD but can be detected via CMD. Further, diffusion coefficients of Li^+ and anions through the channels are also obtained from CMD. The transport information is then fed to a mesoscopic model (in collaboration with Partha Mukherjee, TAMU) where formation of cracks, evolution of channels structure, and other large scale/long time phenomena will be investigated.

Initially, the model has yielded these conclusions: 1) Since in most tested cases, the diffusion through the channels is much higher than that inside the SEI blocks, a Li^+ concentration gradient is established at the SEI boundaries; 2) The concentration profile of Li ions in the SEI structure is dependent on the ionic conductivity of the blocks and on the structure, thickness, and nature of the channels; 3) the ionic diffusion may lead to microcrack formation within the SEI; 4) the SEI microstructure (arrangement of blocks) affects the propagation of microcracks and therefore the subsequent SEI growth.

Conclusions and Future Directions

The following conclusions are drawn from work performed so far: 1) the degree of lithiation of the surface has a strong influence on the SEI reaction mechanisms, especially because of its effect on atomic lithium distribution and surface structure which determine the adhesion of the solvent/additive/salt species on the surface and the extent of electron transfer from the surface to the species being reduced; 2) FEC and VC have similar effects on the SEI because one of the possible reduction pathways of FEC leads to open VC anion; 3) electron transfer decays rapidly within 1 nm SEI thickness through SEI blocks of typical species such as LiF, LiO_2, and Li_2CO_3; 4) a new electron transfer mechanism is suggested whereby anions convey charge traveling through ion channels formed among the various interfaces between SEI blocks; however the anionic species may combine with Li^+ forming neutral species that can block channels and eventually lead to ending SEI growth.

Regarding the mesoscopic model, the following aspects will be implemented: 1) compute presence of SEI anion intermediates and products inside the ion channels and possibility of reaction with Li^+ to form neutral species; 2) compute channel blockage effect due to adhesion of species to the channel walls; 3) incorporate effect on neutral species and channel blockage effect on SEI growth; 4) determine SEI thickness as a function of anion transport. All of these aspects will be investigated with first-principles models and fed into the continuum model.

Voltage effects on the SEI reactions are currently being investigated with AIMD simulations of the anode potential in a simulation cell with explicit $Li_{26}Si_8$/liquid EC interfaces. A prerequisite of a successful potential determination is that no redox reaction occurs during the trajectory, which allows equilibrium sampling. But even when 4 PF_6^- anions added to the liquid electrolyte region make the surface positively charged and cause the voltage to rise, EC decomposition occurred in ps time scales, which prevented voltage determination. This suggested that (1) the voltage associated with the anode surface remained low despite its positive charge; or (2) the surface is "catalytic" and reacted chemically rather than electrochemically. To proceed further, the (lithiated) silicon surface was coated with a monolayer of LiF so that no Si remains exposed to the liquid. LiF force fields are being fitted for pre-equilibration simulations and AIMD potential calculations will resume afterwards. This aspect of the work is carried out by project collaborator Kevin Leung from the Sandia National Laboratories.

SEI reactions on SiO_2 surfaces are currently being investigated by sequentially studying lithiation of the oxidized surface and posterior reaction. Also, work in collaboration with Chunmei Ban from NREL is carried out to evaluate the formation of a molecularly deposited coating of alucone films on bare Si surfaces investigated using DFT and AIMD analyses. Cross-linking reactions within the film (~ 2nm thick) at the experimental density will be characterized using DFT. Li diffusion and migration barriers through the film down to the interface with the Si surface will be obtained and possible film restructuring as lithiation increases is evaluated. SEI reactions will be tested for various degrees of lithiation of the Si surface using AIMD simulations.

FY 2014 Publications/Presentations

1. Balbuena, P.B. (June 2014). “First Principles Modeling of SEI Formation on Bare and Surface/Additive Modified Silicon Anodes.” Presented at the 2014 DOE Annual Merit Review and Peer Evaluation Meeting, Washington D.C.
2. Martinez de la Hoz, J.M.; Leung, K.; Balbuena, P.B. (2013). “Reduction Mechanisms of Ethylene Carbonate on Si Anodes: Effects of Degree of Lithiation and Nature of Exposed Surface.” *ACS Appl. Mater. Inter.* (5); pp: 13457-13465.
3. Leung, K.; Rempe, S.B.; Foster, M.E.; Ma, Y.; Martinez de la Hoz, J.M., Sai, N.; Balbuena, P.B. (2014). “Modeling Electrochemical Decomposition of Fluoroethylene Carbonate on Silicon Anode Surfaces in Lithium Ion Batteries.” *J. Electrochem. Soc.* (161:3); pp: A213-A221.
4. Benitez, L.; Cristancho, D.; Seminario, J.M. Martinez de la Hoz, J.M.; Balbuena, P.B. (2014). “Electron transfer through SEI layers formed on Si anodes of Li-ion batteries.” *Electrochim. Acta* (140); pp: 250-257.
5. Ma, Y.; Balbuena, P.B. (2014). “DFT Study of Reduction Mechanisms of Ethylene Carbonate and Fluoroethylene Carbonate on Li+-adsorbed Si Clusters.” *J. Electrochem. Soc.* (161:8); pp: E1-E13.
6. Martinez de la Hoz, J.M.; Balbuena, P.B. (2014). “Reduction Mechanisms of Additives on Si Anodes of Li-Ion Batteries.” *Phys. Chem. Chem. Phys.* (16); pp: 17091-17098.

V.C.12 Analysis of Film Formation Chemistry on Silicon Anodes by Advanced *In situ* and *Operando* Vibrational Spectroscopy (UCB)

Gabor Somorjai
University of California, Berkeley

Department of Chemistry
Berkeley CA 94720
Phone: (510) 642-4053; Fax: (510) 643-9668
E-mail: somorjai@berkeley.edu

Philip Ross
Lawrence Berkeley National Laboratory
Materials Sciences Division
1 Cyclotron Rd.
Berkeley CA 94720
Phone: (510) 486-5821
E-mail: pnross@lbl.gov

Start Date: October 2012
Projected End Date: September 2015

Objectives

- Understand the composition, structure, and formation/degradation mechanisms of the solid electrolyte interface (SEI) on the surfaces of Si anodes during charge/discharge cycles by applying advanced *in situ* vibrational spectroscopies.
- Determine how the properties of the SEI contribute to failure of Si anodes in Li-ion batteries in vehicular applications. Use this understanding to develop electrolyte additives and/or surface modification methods to improve Si anode capacity loss and cycling behavior.

Technical Barriers

High-energy density Si anodes have large irreversible capacity and are not able to cycle. These failures are due in part to loss of electrolyte by reduction and a SEI that is not stable on the surface with repeated cycling.

Technical Targets

- EV: >200 Wh/kg with >1,000 cycles to 80% DOD.

Accomplishments

- Developed a method to fabricate Si micro/nanostructures to an electrode substrate that can be used in the spectroelectrochemical cell.
- Determined the oxidation and reduction potentials and products of the additives fluoroethylene carbonate (FEC) and vinylene carbonate (VC).
- Determined the role of the Si micro/nanostructure on electrolyte reduction chemistry.

✧ ✧ ✧ ✧ ✧

Introduction

Major efforts are under way to develop novel materials that provide higher battery capacity for increased driving distances of electric vehicles. A high capacity alternative to graphitic carbon anodes is Si, which stores 3.75 Li per Si versus 1 Li per 6 C yielding a theoretical capacity of 4,008 mAh/g versus 372 mAh/g for C. Unfortunately this high capacity comes at a cost: the Si anodes exhibit excessive irreversible capacity losses and short cycling lifetime. The irreversible capacity loss is believed to be caused by lattice expansion accompanying lithiation that is followed by particle cracking, continued reduction of electrolyte and formation of solid electrolyte interphase (SEI) on freshly exposed surface. Detachment of the SEI from the Si surface occurs even when the potential region of cycling is restricted to produce a degree of expansion similar to that of graphite. These observations suggest that the SEI on Si is not intrinsically passivating and that the chemistry of the SEI on the Si surface is different from that of the SEI on graphite. Nonetheless, there are no studies to date suggesting that the SEI on Si is significantly different from graphite.

Studies of the electrolyte reduction products (i.e. SEI) have been performed on both inert (Au, Ni, or Cu) and electroactive (Li or graphite) materials where many properties of the SEI including its chemical composition, electrical resistance, and Li^+ ion conductivity have been determined. The SEI is considered to contain organic and inorganic components that are comprised of lithium carbonates (e.g. $(CH_2OCO_2Li)_2$, $ROCO_2Li$, Li_2CO_3, polycarbonates), oxalate and alkoxides (e.g. $Li_2C_2O_4$, ROLi, HCOLi) and inorganic materials (e.g. LiF, Li_2O, LiOH). The formation mechanism of the interphase on anodes is still under debate, yet there are some properties that are generally agreed upon. Formation is suggested to occur in two voltage stages: at 1.5-0.8 V vs. Li/Li^+ a porous, resistive, and dimensionally unstable phase is formed by electrochemical reduction of electrolyte components; a second stage of reduction occurs concomitantly with intercalation or lithium deposition forming a compact phase that prevents further electrolyte reduction, i.e., passivation, yet allows Li-ion conduction, i.e., the solid electrolyte interphase. While lithium diethylcarbonate (LEDC) is considered to be a primary product from the one electron reduction of EC in the first stage, the overall composition of the inhomogeneous compact passivating SEI layer remains unclear. It is not known whether the SEI on graphite is unique to that electrode material, or that the cyclability of graphite is entirely due to the relatively small lattice change accompanying lithiation/delithiation.

The uncertainty regarding composition, structure, and formation and degradation mechanisms of the SEI is in general due to the poor interfacial sensitivity obtained using conventional spectroscopies. These issues will be addressed with a development of advanced *in situ* vibrational spectroscopies, sum frequency generation (SFG) and a new type of attenuated total reflection (ATR) Fourier transform infrared spectroscopy. Using these new tools, focus will be placed on determining the failure modes of an operating Si/Li electrochemical system for vehicular applications. These results will lead to an improved understanding of:

- The chemical composition and structure of the SEI at the Si and electrolyte interface
    - Which electrolyte components are involved?
    - How is Li-ion solvation involved?
- The formation mechanisms as a function of potential, time, and number of cycles.
- The degree of SEI inhomogeneity across Si electrodes.
- The stability of the SEI with respect to
    - Physical changes of Si that incur with lithiation and delithiation.
    - Crystal size, structure, and orientation of Si.
    - Doped or undoped Si.
    - Electrolyte composition.

This knowledge will be used to develop and tailor SEI films for Si anodes that reduce irreversible capacity loss, improve long term stability and cyclability for vehicular applications.

Approach

Model Si anode materials including single crystals, e-beam deposited polycrystalline films and nanostructures are studied using baseline electrolyte and promising electrolyte variations. A combination of *in situ* and *operando* Fourier Transform Infrared (FTIR), Sum Frequency Generation (SFG), and UV-Raman vibrational spectroscopies are used to directly monitor the composition and structure of electrolyte reduction compounds formed on the Si anodes. Pre-natal and post-mortem chemical composition is identified using X-ray photoelectron spectroscopy. The Si films and nanostructures are imaged using scanning and transmission electron microscopies.

Results

Electrochemistry of additives FEC and VC: As shown in *ex situ* IR spectra in Figure V - 105, Si electrodes in 5% VC additive show wide peak at higher wavenumber (1,831 cm^{-1}) compared to the EC residual electrolyte peak (1,799, 1,769 cm^{-1}). Based on the synthesized poly-VC standard spectra, the VC additive reduction compound has been assigned to poly-VC or its oligomer, which is consistent with previous reports. However, for Si electrode in FEC additive, the original C=O stretch (1829, 1802 cm^{-1}) in FEC disappeared or shifted to lower wavenumber. The exact reduction product of FEC degradation has not been confirmed yet, due to the lack of significant feature except residual electrolyte; however, it is clear that FEC goes different path from VC: for VC, the path is polymerization and remains a “ring” structure (C=O stretch peak shift to higher wave number); while FEC goes open “ring” pathway like EC. It is noted that if FEC were to react under the same pathway as EC to form LEDC, the fluorine ends up exclusively as difluoroethylene. The solid phase product would thus be identical to that from EC. More experiments are required to explore more details (i.e. concentration dependence, rigorous derivation of reaction path) of VC and FEC reduction with Si nanoparticle electrodes. However, results to date suggest replacing as much linear co-solvent with FEC as possible consistent with other needed properties of the electrolyte.

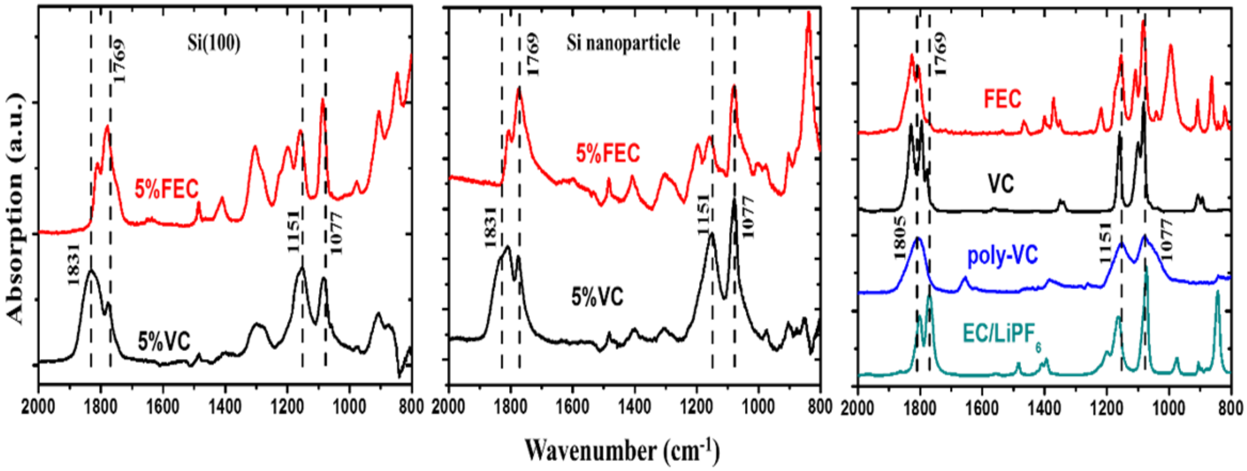

Figure V - 105: *Ex situ* ATR-FTIR spectra of Si (100) p-type doped wafer and for Si nanoparticles after 3 CV cycles with 0.1mV/s scan rate (2V-0.01V vs. Li/Li$^+$) and rinsing with DMC to remove residual electrolyte

Fabrication of Si micro/nanostructures. Binder-free Si micro/nano structures were fabricated using high resolution photolithography and reactive ion etching. By adjusting the photomask alignment direction, selective crystal planes (i.e. (100), (110)) of the sidewall could be exposed. An *in situ* FTIR spectroelectrochemical cell accompanied with the fabricated Si microstructure-on-Si wafer has been developed to investigate electrolyte reduction chemistry on Si micro/nano structures. As shown in Figure V - 106, the IR beam goes from the backside of prism and patterned Si wafer, thus the chemical species signal from Si micro/nano structure surface can be collected. In this way, both representative electrochemistry and adequate FTIR signals could be obtained on well-controlled Si surfaces with no surfactant or binder contamination.

Electrochemistry of electrolyte reduction on Si microstructures. The first cycle galvanostatic curves in Figure V - 107 show that the patterned Si sample has a much larger irreversible capacity, which indicates much more electrolyte reduction from the surface of Si microstructure electrode during the first discharge. The main reasons for the larger irreversible capacity are as follows: the catalytic activity of the etched Si walls for the initial reduction to dissolved species at E > 1 V; the space between those microstructures allow for more dissolved product to accumulate locally before precipitation occurs passivating the surface. The *ex situ* FTIR results shows SEI component signals of the same chemical species on both surfaces. It was concluded therefore that the microstructure of the Si surface does not cause a change in the chemistry of electrolyte reduction and passive film formation.

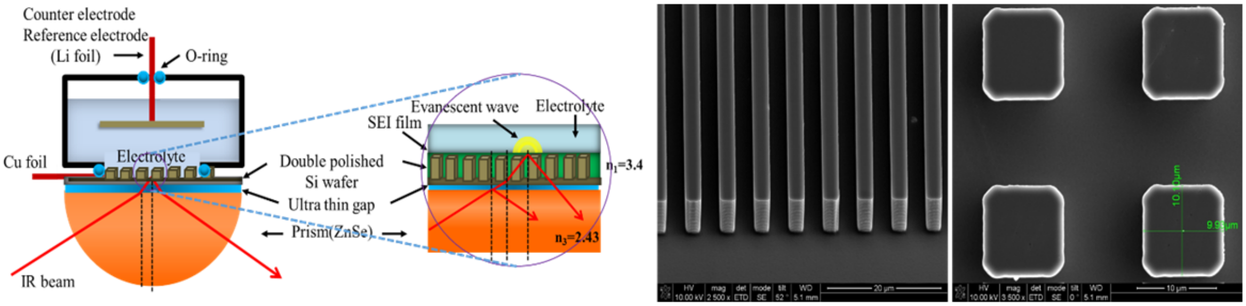

Figure V - 106: (left) ATR geometry of the *in situ* IR spectroelectrochemical cell using a patterned Si microstructure shown at left (10 micron feature size)

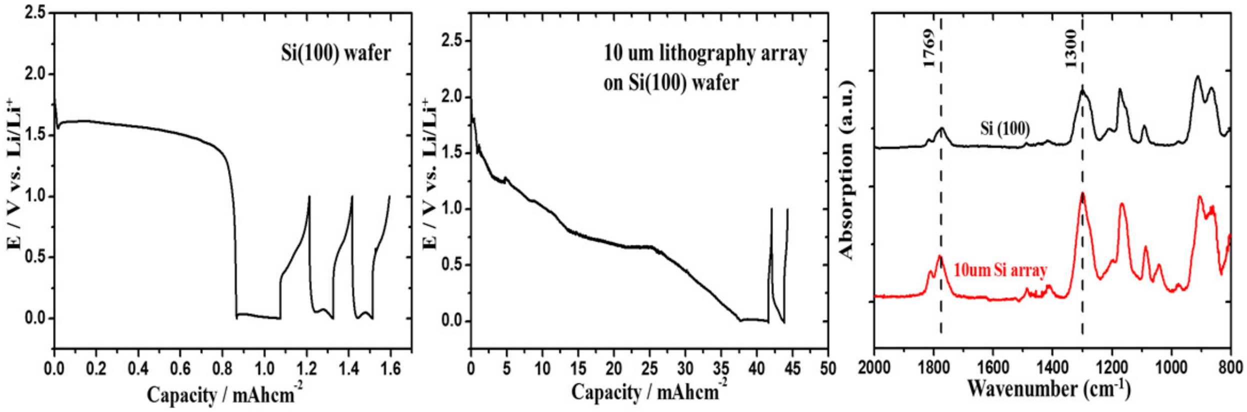

Figure V - 107: First cycle galvanostatic curve comparison between Si (100) wafer and 10 µm array on Si (100) wafer; *ex situ* FTIR spectra of Si (100) wafer and 10 µm array samples after 5 cycles with 5µAcm^{-2} charging rate

Conclusions and Future Directions

Silicon surfaces are catalytic for electrochemical reduction of the linear alkylcarbonate co-solvents, e.g., diethylcarbonate (DEC), in typical Li-ion electrolytes. This results in electrolyte reduction at potentials above 1 V, well positive of the potential for lithiation of the Si. The reduction products are partially soluble, much more than products of EC reduction, resulting in irreversible capacity much larger than on graphite and very dependent on Si surface chemistry. It is concluded that an alternative to linear alkylcarbonate co-solvents for EC be developed. Alternatively, electrolyte additives or surface pre-treatments that passivate the Si surface for reaction with the linear alkylcarbonates should be pursued.

The electrolyte additive fluoroethylene carbonate (FEC) is electrochemically reduced on Si electrodes in essentially the same manner as EC, producing the same products, or possibly the flouro compound. The beneficial effect of FEC appears to be only from displacement of DEC in the electrolyte. The additive vinylene carbonate is electrochemically reduced to a polymer chemically similar to one produced by polymerization of VC with an initiator. This polymer is stiff and does not swell in electrolyte and with Si anodes causes an increase in impedance and does not improve cycle life, although it does reduce first cycle irreversible capacity.

In future, the study of interfacial processes with advanced vibrational spectroscopies will be extended to high voltage oxide cathode materials. The particular oxide to study will be chosen based on materials of interest at that time and availability of the material in a form suitable for these studies, e.g., sufficiently large crystals or sufficiently smooth/reflective thin films. The effect of electrolyte composition, electrolyte additives, and surface coatings will be determined and new strategies for improving cycle life developed.

FY 2014 Publications/Presentations

1. Ross, P.N.; Somorjai, G.A. (June 2014). "Analysis of Film Formation Chemistry on Silicon Anodes by Advanced *In situ* and Operando Vibrational Spectroscopy." Presented at the 2014 DOE Annual Merit Review and Peer Evaluation Meeting, Washington, D.C.
2. Shi, Feifei; Zhao, Hui; Liu, Gao; et al. (2014) "Identification of diethyl 2,5-dioxahexane dicarboxylate and poly-ethylene carbonate as reduction products of ethylene carbonate-based electrolytes by FTIR", *Journal of Physical Chemistry C* (118:27); pp. 14732-14738.
3. Zhao, Hui; Zhou, Xin; Park, Sang-Jae; et al. (2014). "A Polymerized vinylene Carbonate Anode Binder Enhances Performance of Lithium-ion Batteries." Journal of Power Sources (263:10); pp. 288-295.
4. Zhao, Hui; Park, Sang-Jae; Shi, Feifei; et al. (2014). "Propylene Carbonate Based Electrolytes with High Coulombic Efficiency for Lithium-ion Batteries." (161:1); pp. A194-A200.

V.C.13 Nanoscale Composite Heterostructures and Thermoplastic Resin Binders: Novel Li-ion Anode Systems (U Pittsburgh)

Prashant N. Kumta
University of Pittsburgh

Department of Bioengineering, Chemical and
Petroleum Engineering, Mechanical Engineering
and Materials Science
Pittsburgh, PA 15261
Phone: (412) 648-0223; Fax: (412) 624-8069
E-mail: pkumta@pitt.edu

Start Date: October 2010
Projected End Date: December 2014

Objectives

- Identify new alternative nanostructured anodes to replace synthetic graphite providing higher gravimetric and volumetric energy densities.
- Similar or lower irreversible loss (≤15%) in comparison to synthetic graphite.
- Similar or better coulombic efficiency (>99.9%) in comparison to synthetic graphite.
- Similar or better cyclability and calendar life in comparison to synthetic graphite.
- Improve the coulombic efficiency, available energy density, rate capability and cycle life of high specific capacity Si based electrodes.
- Investigate nano-structured Si (*nc*-Si) and amorphous Si (*a*-Si) based composite or hybrid hetero-structured anode.

Technical Barriers

The important technical barriers of alternative anodes for Li-ion batteries (LIBs) to be used in electrical vehicles or plug in hybrid electrical vehicles are the following: 1) low energy density, 2) large first cycle irreversible (FIR) loss (>25-40%), 3) inadequate coulombic efficiencies, 4) poor cycle life, 5) poor rate capability and 6) low charge/discharge rates.

Technical Targets

- Synthesize nano-structured Si (*nc*-Si) and amorphous Si (*a*-Si) based composite or hybrid structured anodes using simple, cost effective processing techniques.
- Achieve reversible capacity of ≥1,200 mAh/g.
- Reduce FIR loss to less than *ca.* 15%.
- Improved coulombic efficiencies higher than 99.9%.
- Improved rate capability.
- Characterize the nano-scale hetero-structures for structure and composition using electron microscopy techniques such as SEM, TEM and HREM.

Accomplishments

- Developed a scalable approach to generate carbon coated hollow silicon nanotubes (h-SiNTs) using a low cost and high throughput sacrificial inorganic nanowire (INW) template and CVD technique.
- Developed active coatings on h-SiNTs and solution treatment of coated SiNTs to reduce the FIR loss.
- Obtained initial reversible capacities of *ca.* 1,500 mAh/g at a current rate of 300 mA/g and long term stable capacity of *ca.* 1,000 mAh/g at 1A/g utilizing carbon coated h-SiNTs for 200 cycles.
- The FIR was reduced to 13% with a stable cycling capacity of 1,100 mAh/g (high current rate 1A/g) at the end of 120 cycles by solution treating carbon coated h-SINTs.
- Novel high strength and elastomeric natural and modified polymer binders, PGG and PGG-PVA were identified and developed which exhibited comparable FIR loss and better capacity retention (0.01-0.04% loss per cycle) compared to the commercial PVDF and Na-CMC-based binder (0.37% loss per cycle).

✧ ✧ ✧ ✧ ✧

Introduction

Several novel approaches have been explored previously to achieve DOE BATT technical targets for Si based anodes: high specific capacity (>1,200 mAh/g), lower FIR loss (<15%), high coloumbic efficiency (>99.9%), good cyclability and rate capability. These approaches involved the development of nano-scale hetero-structures of vertically aligned carbon nanotube (VACNT) forests coated with nanocrystalline/amorphous silicon films/droplets, thin films of interface control agent (ICA), thin films of electrodeposited amorphous silicon and high strength thermoplastic binders. The VACNT-Si composites exhibited capacities >2,800 mAh/g with a very low irreversible loss (~12%) with moderate cyclability. The adhesion of Si film was improved by the addition of a thin layer of ICA between the VACNT and Si resulting in better cyclability and capacity retention. Electro-deposition of amorphous silicon films also showed excellent cyclability with a capacity of 1,300 mAh/g over 100 cycles.

Hollow Si nanostructures such as silicon nanotubes (*h*SiNTs) offer mechanical strain relaxation against the colossal volume expansion of Si occurring in the lithiation process, thus preventing mechanical failure and hence improving the cyclability of the electrode for hundreds of cycles. In the previous year, scalable quantities of smooth and long nanowire templates were generated by a scalable approach using inexpensive precursors and equipment. Reaction parameters including pH of the precursor solution and heat treatment conditions were further optimized to produce uniform and smooth inorganic nanowires (INWs) with a high aspect ratio. These INWs were used to develop *h*SiNTs by the thermal decomposition of silane gas and RF sputtering of silicon.

Water soluble natural green binders were explored as a replacement to the currently used PVDF which is the accepted commerical binder for anodes and cathodes. The large volume expansion of Si results in a significant stress field in the PVDF binder matrix leading to mechanical failure of the electrode. A high fracture strength binder is hence necessary to accommodate the volume strain that arises due to the large related Si volume exansion. In this report, results obtained on the electrochemical properties of Si/C composite with the newly developed modified natural polymer binders, named PGG, MAB and PGG-PVA has also been explored.

Approach

Sacrificial one dimensional inorganic nanowire template (INW) was first synthesized in an autoclave reactor under hydrothermal conditions. Surfactants were added to improve the dispersibility and the pH of the precursor solution and heat treatments were optimized to generate smooth and very high aspect ratio nanowire template. A thin layer of amorphous silicon was deposited on the surface of these nanowires by thermal cracking of silane gas (SiH_4) in a low pressure CVD reactor resulting in a core-shell (INW/Si) structure. This composite structure, when treated with a mineral acid to dissolve the nanowire template, generated the hollow silicon nanotubes (*h*SiNTs). Further, the time for the deposition of Si during the CVD was varied to modify the thickness of the *h*SiNTs obtained after dissolution of the INW template. A thin layer of carbon was directly deposited on these *h*SiNTs by thermal decomposition of hydrocarbon gas at 700°C to obtain carbon-coated *h*SiNTs. These carbon-coated *h*SiNTs were further washed and treated in dilute solutions following filtering.

The newly identified water soluble natural and modified elastomeric binders (PGG, PGG-PVA and MAB) were tested against a high specific capacity Si/C system derived by high energy mechanical milling (HEMM). The modified binders were synthesized using alkylation method of natural polymer AB. In this method, sodium monochloroacetate has been used as a crosslinking agent to the AB polymer in order to improve the mechanical properties such as fracture strength. NMR spectroscopy was employed to study the stability of molecular structure of these binders before and after electrochemical testing.

Results

Hollow silicon nanotubes (*h*SiNTs): The h-SiNTs structures reported previously exhibited a FIR of ~27% and stable reversible capacities of ~1,500 mAh/g at 2A/g charge/discharge rate. The time of Si deposition during the CVD process was increased beyond 10 min to obtain a thicker silicon shell in the h-SiNTs resulting in an increased active material density or higher areal loading on the current collector. Furthermore, the weight fraction of the conductive additive, Super-P was increased from 10% to 25% at the expense of the natural polymer based binder to achieve better electronic conduction through the h-SiNTs.

As shown in Figure V - 108, increasing the deposition time to 15 min and 20 min resulted in significant reduction in FIR of 19% and 15%, respectively, probably due to a decrease in the effective specific surface area (SSA) exposed to the electrolyte, resulting in decreased Li^+ consumption in the solid electrolyte interphase (SEI) layers formed.

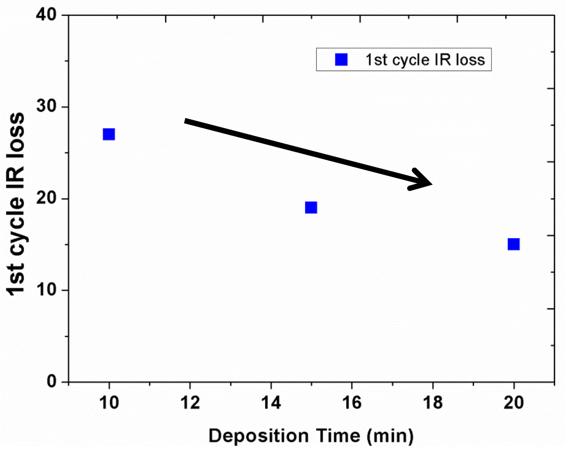

Figure V - 108: First cycle irreversible loss vs. Si-CVD deposition

Electrochemical cycling implementing the DOE-recommended test protocol of h-SiNTs obtained using a

CVD deposition time of 15 min (Figure V - 109) shows a first discharge capacity of 1,814 mAh/g and a first cycle irreversible loss of only 19% at an areal current density of 0.02 mA/cm^2.

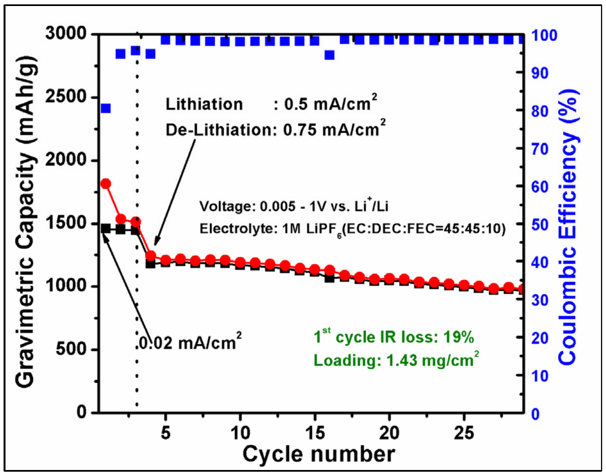

Figure V - 109: Variation of gravimetric specific capacity vs. cycle number of h-SiNT (15min deposition time)

A high loading density of 1.43 mg/cm^2 was achieved for these h-SiNTs. It should be noted that the capacities reported herein are based on the total weight of the dry laminate on the current collector. SEM analysis was conducted on h-SiNTs electrodes after 1st cycle lithiatioon and delithiation of the h-SiNTs (Figure V - 110a, b and c). The lithiated electrodes displayed large volume expansion due to the formation of the intermetallic phases of silicon with lithium, as can be observed by the increase in the diameter of the h-SiNTs. The delithiated electrodes showed the expected volumetric shrinkage of the h-SiNTs corresponding to the formation of Si accordingly, without causing any disintegration of the nanostructure and the mechanical integrity of the electrode is preserved.

Subsequently, SEM analysis was conducted on the electrode consisting of the h-SiNTs following 500 cycles of lithiation and delithiation (Figure V - 110d and e). The hollow nanotube architecture of the h-SiNTs was retained even after repeated cycling thus

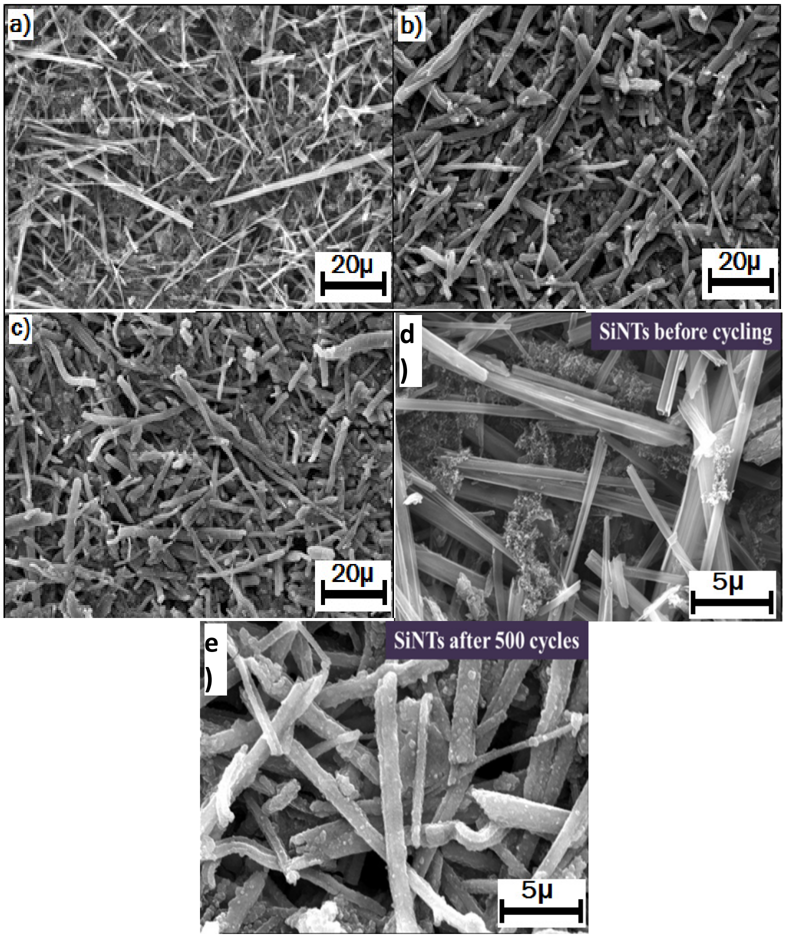

Figure V - 110: SEM images of h-SiNTs electrodes a) as prepared, b) after lithiation, c) after delithiation, d) before cycling, and e) after 500 cycles withstanding the colossal volume expansion and contraction during the lithiation and delithiation cycles, respectively, directly correlating to the stable cycling of these electrodes seen over large number of cycles. The surface of the h-SiNTs appears roughened upon cycling due to the formation of the SEI during the first charge/discharge cycle.

The first cycle discharge capacity and charge capacity at initial current rates of 300mA/g for carbon coated h-SiNTs were 1,780 mAh/g and 1,520 mAh/g, respectively, while for the solution washed material, the capacities were accordingly, 1,800 mAh/g and 1,565 mAh/g (Figure V - 111).

Both materials showed stable long term cycling exhibiting charge capacities of 975 mAh/g for carbon coated h-SiNTs and 1,100 mAh/g for solution washed active material, at the end of 100 cycles at 1A/g. The first cycle irreversible (FIR) loss for the carbon-coated h-SiNTs was 14.5%, while the solution treated material exhibited a lower FIR loss (13%). This may be due to reduction in unwanted phases. Similar reason could be attested to the slight increase in charge capacity of the solution treated carbon coated h-SiNTs. The loading density in the electrode was approximately 0.8-1.1 mg/cm^2 of active material leading to a first cycle areal charge capacity greater than 1.5Ah/cm^2 for both the materials at a modest current rate of 300 mA/g. The carbon content in the active material was approximately, 25-30 wt% as determined by EDAX analysis which explains the decrease in the specific capacity as compared to uncoated h-SiNTs however, with a drastic reduction (~50%) in FIR loss.

High strength and elastomeric binders: Effects of improved mechanical properties of a "mechanical binder" on the structural stability and long term cyclability of the Si/C based system has been studied. In this regard, PVDF, Na-CMC of elastic modulus ~1,000MPa, and ~2,300MPa, respectively, and a novel new polymer family named PGG of elastic modulus ~3,200MPa has been chosen as a suitable binder for the Si/C system. The Si/C composite, derived by high energy mechanical milling, exhibiting a reversible specific capacity ~780mAh/g and ~620mAh/g at a charge/discharge rate of ~50mA/g and ~200mA/g, respectively, was selected as the model active electrode system. It has been identified that the long term cyclability of the Si/C system depends on the mechanical properties of the binder such as high elastic modulus. PGG and Na-CMC binder show better cyclability (~0.04% loss per cycle upto 100 cycles) than the low elastic modulus PVDF binder (0.2% loss per cycle up to 100 cycles). To further confirm the degradation/disintegration of the matrix binder at a molecular level, the chemical structure of the polymer before and after electrochemical cycling was characterized by ^{1}H NMR. The ^{1}H-NMR data showed the structural degradation of the low elastic modulus PVDF following cycling (Figure V - 112a), whereas the high elastic modulus Na-CMC and PGG show no permanent deformation or structural damage (Figure V - 112b). This result clearly suggests that the newly developed high elastic modulus PGG based modified polymer is a promising binder family for Si/C based anodes.

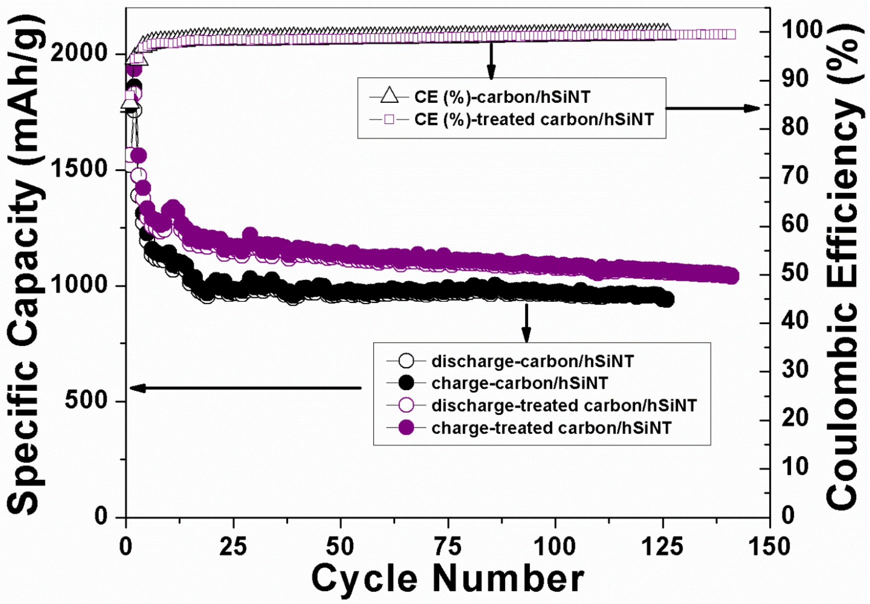

Figure V - 111: Specific charge/discharge capacity and coulombic efficiency vs. charge/discharge cycles of carbon coated h-SiNTs (black) and solution treated carbon coated h-SiNTs (violet) electrodes in Li/Li$^+$ battery

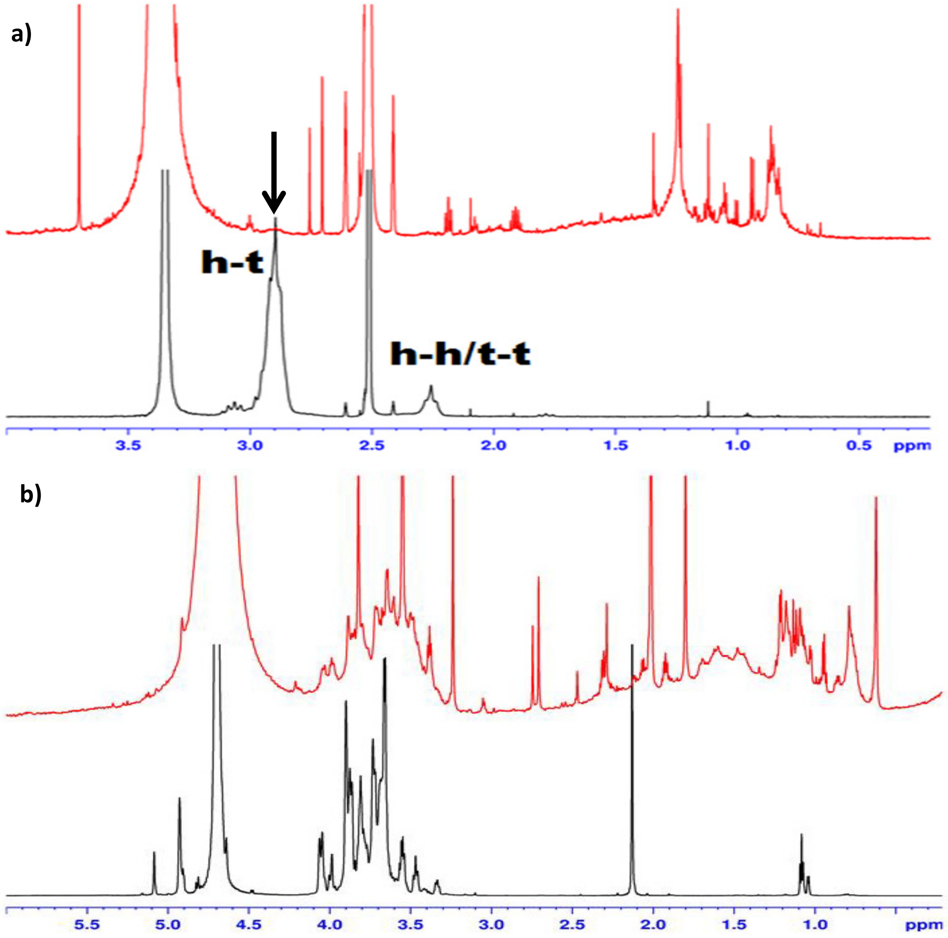

Figure V - 112: ^{1}H-NMR spectra of (a) PVDF before and after cycling; (b) PGG before and after cycling, for 111 cycles in DMSO-d_6. Black spectra indicates before cycling and red spectra indicates after cycling. Black arrow indicates the absence of the characteristic peak in PVDF

Conclusions and Future Directions

A cost effective and scalable approach has been developed to generate *h*SiNTs using a scalable, sacrificial inorganic nanowire template approach. The SEM analysis of the *h*SiNTs electrode shows stable mechanical integrity of the electrode upon 500 cycles and preservation of the nanostructures even in the lithiated state which explains the stable cycling for LIB application. By increasing the time of Si-CVD deposition (hence, the wall thickness in *h*SiNTs), the loading of active material is improved to 1.43 mg/cm^2 and the FIR loss decreased to 15%. The *h*SiNTs coated with carbon and solution treated, exhibited capacities >950 mAh/g after 200 cycles and a drastic reduction in first cycle irreversible loss to less than 15% meeting the desired DOE goal. The morphologies a-Si thin films were modified using a simple pulse current electrodeposition and their stability was improved by increasing the frequency of the deposition. High strength water soluble elastomeric polymers, PGG, Na-CMC and amine based MAB binder were chemically modified to achieve excellent capacity retention (fade rate of < 0.04% loss/cycle) compared to the commercially PVDF (~0.35% loss/cycle). Proton NMR spectroscopy of the binder after cycling indicated degradation of the PVDF binder at the molecular level while the PGG and Na-CMC remain unaffected which explains the better performance of PGG and Na-CMC as compared to PVDF.

In the future, the performance of the *h*SiNTs will be tested for high loading and areal capacities. The FIR loss in the binderless electrodeposited a-Si films will be reduced and further employed to develop a layered composite film to increase the loading density. Co-polymer and blend polymer binders will also be developed generating active functional interfaces to improve the performance of the Si/C based system.

FY 2014 Publications/Presentations

1. Kumta, P.N. (June 2014). "Nanoscale Heterostructures and Thermoplastic Resin Binders: Novel Li-ion Anode Systems." Presented at the 2014 DOE Annual Merit Review and Peer Evaluation Meeting, Washington, D.C.
2. Beck, F.R.; Epur, R.; Hong, D.; Manivannan, A.; Kumta, P.N. (2014). *Electrochimica Acta*, (127), pp: 299-306.
3. Epur, R.; Kumta, P.N. (December 2013). "Scalable synthesis of silicon nanotubes: A high capacity and stable anode system for lithium ion batteries." Presented at the 2013 MRS Fall Meeting, Boston, MA.
4. Gattu, B.; Epur, R.; Datta, M.K.; Manivannan, A.; Kumta, P.N. (May 2014). "Pulse Electrodeposition of Amorphous Si Film Anodes for Li-Ion Battery." Presented at the 225th ECS Meeting, Orlando, FL.

V.C.14 Pre-Lithiation of Silicon Anode for High Energy Li Ion Batteries (Stanford U)

Yi Cui (Principal Investigator)
Subcontractor: Stanford University

Department of Material Science and Engineering
476 Lomita Mall, McCullough 343
Stanford. CA 94305
Phone: (650) 723-4613; Fax: (650) 725-4034
E-mail: yicui@stanford.edu

Start Date: August 2013
Projected End Date: July 2017

Objectives

- Design and synthesize lithiated silicon to prelithiate various anode materials.
- Increase first-cycle Coulombic efficiency of various anode materials.
- Design and fabricate fully lithiated Si anodes to pair with high capacity lithium-free cathodes.

Technical Barriers

The high chemical reactivity of prelithiation reagents makes them difficult to synthesize and survive multiple battery fabrication processes (exposure to air and solvents, slurry mixing, coating and baking). This fundamental challenge results in the following technical barriers:

- Restrictive synthesis conditions.
- Instability in the slurry solvents.
- Instability in the dry and humid air conditions.

Technical Targets

- Design various methods to synthesize lithiated silicon with different nanostructures.
- Increase the stability of lithiated silicon in the slurry solvents.
- Increase the stability of lithiated silicon in the dry air.

Accomplishments

- Designed and synthesized Li_xSi-Li_2O core-shell nanoparticles to increase first-cycle Coulombic efficiency of various anode materials.
- Increased dry air stability of lithiated silicon.
- Used TEM, STEM and EELS methods to characterize morphology and composition.

✧ ✧ ✧ ✧ ✧

Introduction

Rechargeable lithium-ion batteries are widely used for consumer electronics and exhibit great potential for electrical vehicle and grid-scale energy storage. The first charging process, in which lithium ions and electrons move from cathode to anode, is critical for lithium-ion battery operation. When the potential of the anode is below ~1 V versus Li metal, the organic electrolyte is reduced on the anode surface to form a layer of solid electrolyte interphase (SEI) that consists of a complex composition of inorganic and organic lithium compounds. In addition, some lithium may be trapped in the electrode upon lithiation. As a result, the first charging process irreversibly consumes a fraction of the lithium ions, giving rise to a net loss of storage capacity. Such first cycle irreversible capacity loss is usually compensated by additional loading of cathode materials in current lithium-ion batteries. However, lithium metal oxide cathodes have a much lower specific capacity (mostly less than ~200 mAh g^{-1}) than anodes. Excessive loading of cathode material causes appreciable reduction of battery specific energy and energy density. It is therefore desirable to develop an alternative method that suppresses this loss and consequently increases the 1st cycle Coulombic efficiency.

The goal of this project is to design and synthesize lithiated silicon with different nanostructures to prelithiate various anode materials. Further, the synthesized nanoparticles should be processible in a slurry and exhibit high capacity under dry air conditions.

Approach

This project takes advantages of Li-rich compound as excellent prelithiate reagents to increase first-cycle Coulombic efficiency of various anode materials. Nano-coating is utilized to increase the stability of prelithiate reagents in the slurry solvents and day air condition.

Results

Li_xSi-Li_2O core-shell nanoparticles were developed as excellent prelithiation reagents with a high specific capacity to compensate the first cycle capacityloss. These nanoparticles were produced with a facile and scalable synthesis approach by direct alloying of Si nanoparticles with Li metal foil. Li_xSi-Li_2O core-shell nanoparticles are compatible with the conventional slurry process and exhibit high capacity under the dry air conditions with the protection of Li_2O passivation shell. Using 1,3-dioxolane or toluene as the slurry solvent, Li_xSi-Li_2O NPs show high extraction capacities of 1,200-1,400 mAh/g, which suffices as the prelithiation reagent. After exposing to dry air for one day, there is 1,175 mAh/g capacity, only 9% decay from time zero, indicating the Li_xSi-Li_2O core-shell NPs are compatible with the whole battery fabrication process in the dry room. Li_xSi-Li_2O NPs, exposing to dry air for 5 days, are still active to prelithiate MCMB graphite, which yields a 20% improvement in 1st cycle Coulombic efficiency, indicating the potential of long-term storage. Both Si and graphite anodes are successfully prelithiated with these nanoparticles to achieve high 1st cycle Coulombic efficiencies of 94% to 99%. It suppresses the undesired consumption of Li from cathode materials during SEI formation. (See Figure V - 113.)

Conclusions and Future Directions

Much progress has been made on this project this year. We have demonstrated a one-step thermal alloying process to synthesize Li_xSi-Li_2O core-shell NPs without using specialized capital equipment. These nanoparticles exhibit high capacity under dry air conditions with the protection of the Li_2O passivation shell, indicating that Li_xSi-Li_2O NPs are potentially compatible with industrial battery fabrication processes in a dry room. Both commercial Si nanoparticles and graphite are prelithiated with Li_xSi-Li_2O NPs, thereby remarkably increasing the 1st cycle Coulombic efficiency. The approach is generally applicable to various anode materials involving complex nanostructures. In addition, Li_xSi alloy also serves as a new anode material with the potential to pair with all high capacity lithium-free cathodes for next generation high-energy-density lithium-ion batteries.

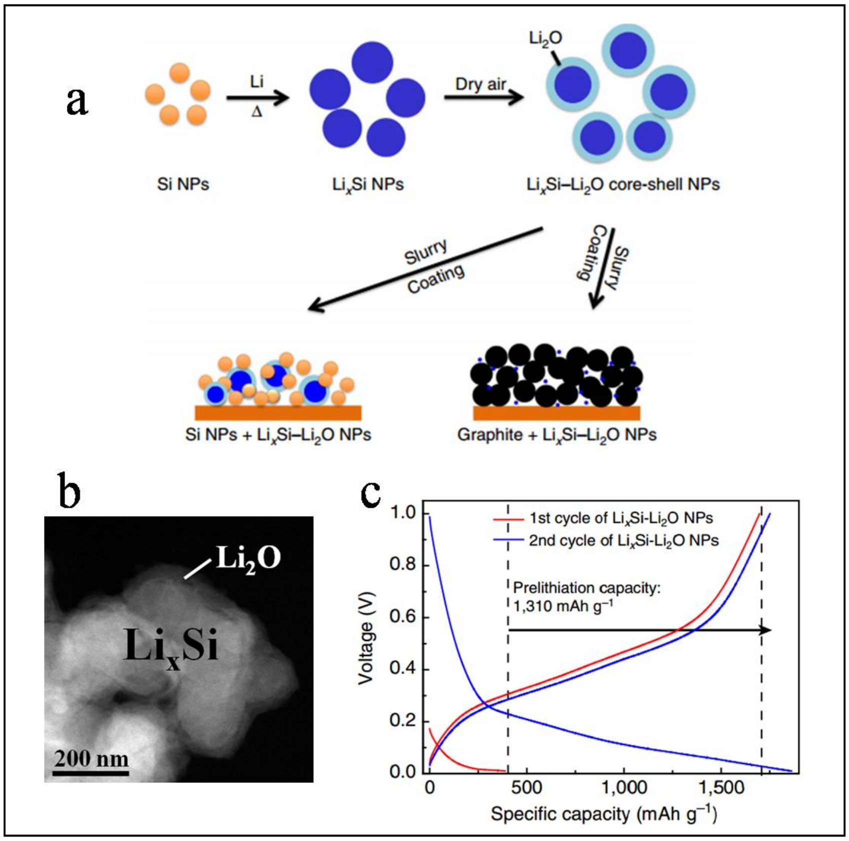

Figure V - 113: (a) Schematic diagrams showing Si NPs react with melted Li to form Li_xSi NPs. A dense passivation layer is formed on the Li_xSi NPs after exposure to trace amounts of oxygen, preventing the Li_xSi alloy from further oxidation in dry air. As-synthesized Li_xSi-Li_2O core-shell NPs, compatible with the existing battery manufacturing environment, can be mixed with various anode materials during slurry processing and serve as an excellent prelithiation reagent. (b) STEM image of Li_xSi-Li_2O core-shell NPs. (c) Galvanostatic discharge/charge profiles of Li_xSi-Li_2O NPs in 1st and 2nd cycles

Future directions include: 1) Synthesizing prelithiate reagents with higher specific capacity. 2) Developing different coatings to increase the stability of prelithiate reagents in the humid environment. 3) Simple and scalable synthesis and electrode preparation method will be developed for practical applications.

FY 2014 Publications/Presentations

1. J. Zhao, Z. Lu, N. Liu, H. Lee, M. McDowell, Y. Cui, "Dry-air-stable lithium silicide–lithium oxide core–shell nanoparticles as high-capacity prelithiation reagents." *Nat. Commun.* 5:5088 (2014).

V.D Electrolyte Development

V.D.1 Development of Electrolytes for Lithium Ion Batteries (URI)

Brett Lucht
University of Rhode Island

Department of Chemistry
51 Lower College Road, Pastore
Kingston, RI 02881
Phone: (401) 874-5071; Fax: (401) 874-5072
E-mail: blucht@chm.uri.edu

Start Date: April 2009
Projected End Date: December 2014

Objectives

- Develop an understanding of the mechanism of improved capacity retention for Si nano-particle electrodes in the presence of electrolyte additives FEC and/or VC.
- Conduct a direct comparison of the cycling performance of electrolytes with different concentrations of added FEC and/or VC to determine an optimized electrolyte for use with Si nano-particle electrodes.
- Suggest electrolyte formulation as a standard formulation for BATT Program researchers to allow for better cross comparison of electrochemical cycling data for different novel Si anode materials.
- Conduct *ex situ* surface analysis of cells cycled with different electrolytes to develop a mechanism for capacity retention enhancement via addition of fluoroethylene carbonate (FEC) or vinylene carbonate (VC).

Technical Barriers

Due to the large volume expansion and subsequent surface area changes for Si anode materials, the reactions of the electrolyte to generate a stable solid electrolyte interphase (SEI) are critical to the cycling stability of the electrode. This project is being conducted to develop a better understanding of the role of the electrolyte in capacity fade for Si nano-particle electrodes. Developing an understanding of the mechanism of stabilization of currently utilized additives, VC and FEC, can lead to the development of superior additives which afford improved cycling performance.

Technical Targets

- Complete electrochemical cycling of Si nano-particle electrodes with electrolytes containing added VC or FEC.
- Determine the best electrolyte formulation for Si nanoparticle electrodes and suggest as standard for BATT researchers.
- Complete surface analysis of Si nano-particle electrodes with electrolytes containing VC or FEC.
- Develop mechanism for the beneficial cycling performance for electrolytes with added FEC or VC for Si nano-particle electrodes.

Accomplishments

- Conducted a comparative investigation of seven different electrolytes with a standard Si nano-particle electrode.
- Determined the best electrolyte formulation for Si electrodes is 1.2 M $LiPF_6$ in 90% EC/DEC (1:1) with 10% added FEC.
- *Ex situ* surface analysis of Si electrodes revealed that the cells with the best capacity retention had an SEI composed of a combination of LiF, Li_2CO_3, lithium alkylcarbonates, and poly(FEC).
- The superior performance is likely due to the combination of conducting Li salts and crosslinked polymer.

✧ ✧ ✧ ✧ ✧

Introduction

There has been significant interest in the development of Li-ion batteries for electric vehicles (EV). However, in order to improve energy density, the development of anode and cathode materials with higher energy density than the anode and cathode materials used in traditional Li-ion batteries is needed. Silicon is one of the most promising candidates for an anode material in LIBs due to its high theoretical capacity, 3,580 mAh/g. This theoretical capacity is *ca.* 10 times that of commercial graphite (372 mAh/g) currently used in Li-ion batteries. However the silicon electrodes have a very large volume expansion (300-400%) during lithiation resulting in large stresses, mechanical damage, and surface area changes. The problems associated with the large volumetric changes have prompted the design and application of nano-structured Si materials. It is well known that during the first charging cycles a solid electrolyte interphase (SEI) is generated on the surface of the graphite anode in Li-ion batteries. Significant research has been conducted on the structure and composition of the graphite SEI. The structure and stability of the graphite SEI has been reported to depend on the composition of the electrolyte, salt, solvent, and additives. A related SEI was reported to have been generated on the surface of Si electrodes in Li-ion batteries. However, the instability of the solid electrolyte interphase on Si electrodes is a significant problem leading to poor capacity retention. While the two most frequently utilized additives for silicon electrodes are vinylene carbonate (VC) and fluoroethylene carbonate (FEC), a systematic comparison of the effects of added FEC or VC at multiple concentrations has not been conducted. In this project electrochemical cycling of uniform Si nano-particle electrodes with electrolytes without additives and with different concentrations of VC and/or FEC has been conducted.

Approach

Electrochemical cycling silicon nano-particle electrodes with electrolytes containing VC or FEC has been conducted. After cycling, the electrodes have been removed and *ex situ* surface analysis of extracted electrodes was conducted. Investigation of the composition of the solid electrolyte interphase (SEI) on the silicon anode is conducted by a combination of X-ray photoelectron spectroscopy (XPS), Infra-Red spectroscopy (FT-IR) with Attenuated Total Reflectance (ATR), and Scanning Electron Microscopy (SEM). The results enhance the understanding of the relationship between cell performance and electrolyte composition for Li-ion batteries.

Results

Electrochemical behavior: The specific capacities and efficiency as a function of cycle number are depicted in Figure V - 114. The cells containing electrolyte with added FEC show a higher initial capacity, *ca.* 3,500 mAh/g, compared to cells containing the standard electrolyte or electrolyte with added VC, 3,000 mAh/g, (Figure V - 114a). The first cycle efficiency of the cells with standard electrolyte is 90% while the cells containing electrolyte with added FEC or VC have slightly lower first cycle efficiency, 87-89%. After formation cycles, the capacity of the cells with standard electrolyte continuously decreases to 1,000 mAh/g over the next 50 cycles while the efficiencies hover around 98%. The capacity retention and efficiencies were not improved for cells containing electrolyte with added VC. However, all the cells containing electrolyte with added FEC show a significant improvement in capacity retention and efficiency. The cells with electrolyte containing 10% and 15% of added FEC have the best capacity retention, *ca.* 2,500 mAh/g after 53 cycles. The cell with electrolyte containing 5% FEC has a rapid capacity fade after 20 cycles, while the cells containing electrolyte with 25% FEC have a lower but stable capacity.

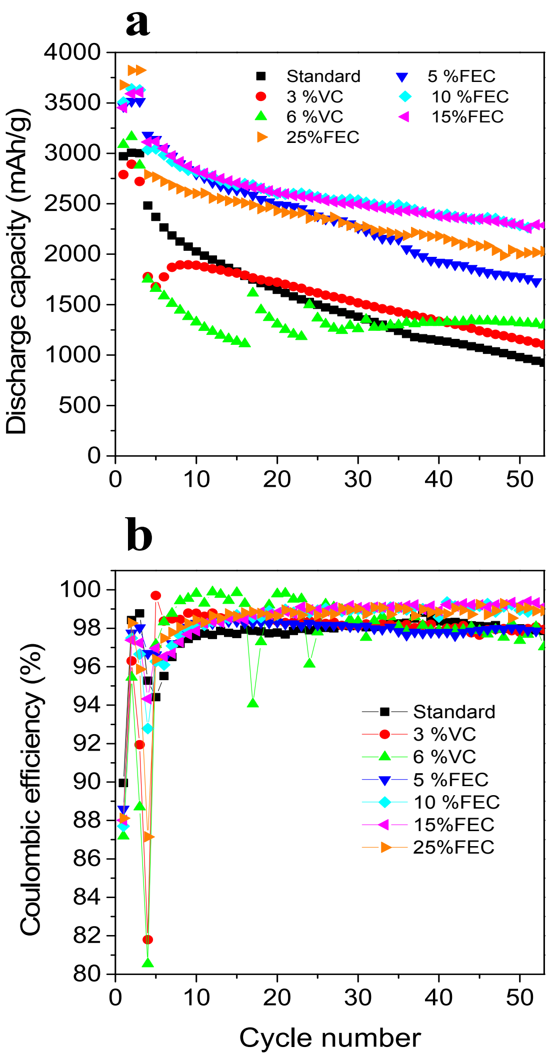

Figure V - 114: Discharge capacity vs. cycle number plots and cycling efficiency of Si electrodes

Electrochemical impedance spectroscopy (EIS): The electrochemical impedance spectroscopy of cycled Si anodes with various electrolytes was conducted at the end of discharge after formation cycles and after 53 cycles. After formation cycles (Figure V - 115a), the cells containing electrolyte with added VC have greater impedance compared to cells containing the standard electrolyte while the cells containing electrolyte with a low content of added FEC (5-15%) have the smallest impedance. However, increasing the FEC content of the electrolyte to 25% results in an increase in the impedance. This may contribute to the low capacity observed in Figure V - 114. Interestingly, the impedance of the cells cycled in standard electrolyte increases significantly after 53 cycles while the impedance of the cells containing electrolyte with added FEC or VC alters only slightly.

Surface analyses: X-ray photoelectron spectroscopy (XPS): High-resolution XPS spectra for fresh and cycled Si electrodes were acquired. The electrode cycled with electrolyte containing 3% VC has a similar elemental concentration to the electrode cycled with the standard electrolyte while the electrode cycled with electrolyte containing 6% VC has an increased O concentration. This is likely related to the increased concentrations of Li_2CO_3 as observed by IR spectroscopy (discussed below). The electrodes cycled with electrolytes containing FEC have a regular increase in the F concentration, and consequent decrease in the C and O concentrations, as the percentage of FEC is increased.

The C1s spectrum of the fresh electrode contains a peak at 284 eV from Super P and peaks at 287 eV and 289 eV for the C-O and C=O from CMC binder. The O1s spectrum contains a single broad peak at 533 eV from the CMC and surface silica, SiO_x. After cycling with the standard electrolyte, new peaks appear at 290 eV in the C1s spectrum and 531.8 eV in the O 1s spectrum consistent with the presence of ROCOOLi and Li_2CO_3. The F1s spectrum contains peaks at 685 eV and 687 eV characteristic of LiF and $Li_xPF_yO_z$, respectively. The electrode cycled with electrolyte containing 3% VC has similar C 1s, O 1s and F1s spectra to the electrode cycled in standard cells, while the electrode cycled with 6% VC has an increase in the intensity of the C=O peaks at 289 eV in the C1s spectrum. The C1s and O1s spectra of the electrode cycled with electrolyte containing 5% FEC are also very similar to the standard electrolyte. However, the peak associated with LiF in the F1s spectrum (685 eV) has greater intensity. The C1s spectra of electrodes cycled with electrolytes containing higher concentrations of FEC have lower intensity C=O and C-O peaks in both the C1s and O1s spectra while the F1s spectrum is completely dominated by the peak for LiF at 685 eV.

IR-ATR: The IR-ATR spectra for fresh and cycled Si electrodes are presented in Figure V - 115. The IR spectrum of the fresh electrode contains a strong absorption at 1,593 and 1,413 cm^{-1} characteristic of the carboxylate (COO) of the CMC binder. Absorptions characteristic of C-H bonds of the CMC binder are observed at 2,950-2,850 cm^{-1}. The absorptions from 1,250-900 cm^{-1} are due to the C-O-C and Si-O-Si groups from CMC and silicon oxide surface, respectively.

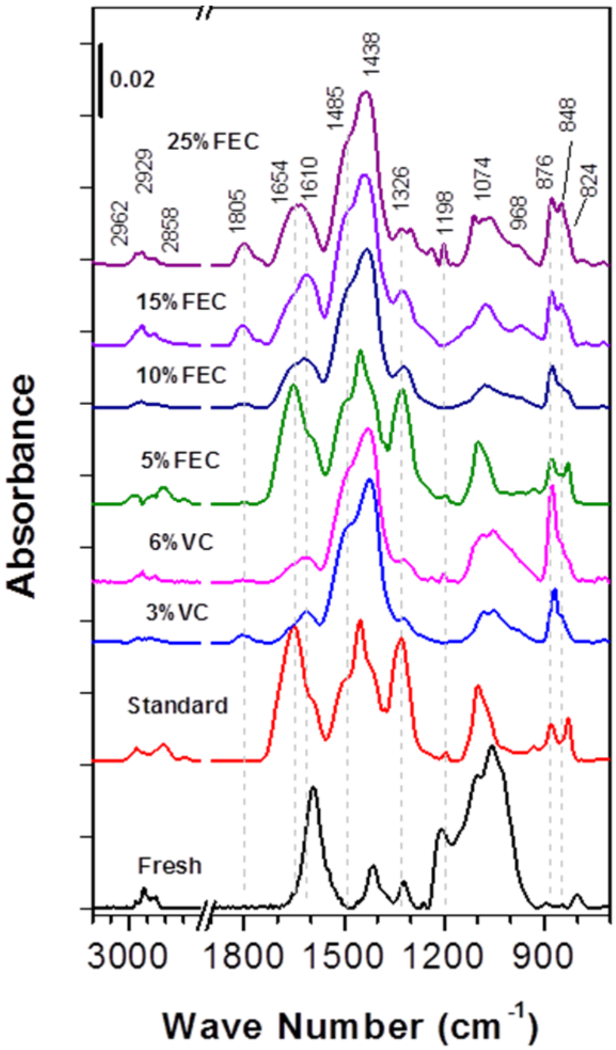

Figure V - 115: FT-IR spectra for Si anode before and after 53 cycles

The absorptions characteristic of the CMC binder and SiO_2 surface are not observed on electrodes after 53 cycles suggesting that a thick SEI is generated on the silicon surface. The IR spectrum of the silicon electrode cycled with the standard electrolyte is dominated by peaks characteristic of lithium alkyl carbonates, ROCOOLi, at 1,650, 1,325 and 825 cm^{-1} and lithium carbonate (Li_2CO_3), at 1,485 and 870 cm^{-1}. Incorporation of VC into the electrolyte results in a significant change in the SEI. The IR spectrum is dominated by the absorption of Li_2CO_3 at 1,485 and 876 cm^{-1}. The intensity of the absorptions characteristic of ROCOOLi are significantly weaker when compared to the electrode cycled with the standard electrolyte. In addition, a new peak is observed at 1800 cm^{-1}, attributed to poly(VC). The IR spectrum of the electrode cycled with electrolyte containing 5% FEC is similar to the electrode cycled with the standard electrolyte except a small peak is observed at 1,805 cm^{-1}, characteristic of poly(FEC). The similarity of the IR spectra of the electrodes cycled with standard electrolyte and electrolyte with 5% added FEC is consistent with the cycling results and suggests that incorporation of 5% FEC is not sufficient to form a stable SEI layer on the silicon anode. The IR spectra of Si electrodes cycled with electrolyte containing higher percentages of FEC (10, 15, and 25%) are similar to each other and differ from the IR spectra with the standard electrolyte. The intensity of the absorptions for Li_2CO_3 is stronger than those observed with the standard electrolyte, but weaker than the absorptions observed for electrolyte with added VC. The peaks for ROCOOLi are present but have lower relative intensity than that observed for the standard electrolyte. The intensity of the absorption for poly(FEC) at 1,805 cm^{-1} increases with increasing concentrations of FEC. The increase in the concentration of poly(FEC) on the electrode surface correlates with the improved capacity retention of Si electrodes as observed in Figure V - 114a and the decrease of the crack size observed by SEM. The poly(FEC) appears to effectively preserve electrode structure during cycling. However, very high concentration of poly(FEC) generated with the electrolyte containing 25% FEC has a worse capacity retention which likely results from the high observed impedance (Figure V - 115a and b).

Conclusions and Future Directions

A direct comparison of the electrochemical and cycling performance of Si nano-particle anodes has been conducted for a series of electrolytes containing different concentrations of FEC or VC. *Ex situ* surface analysis of the cycled electrodes has been conducted to provide a better understanding of the source of performance differences for the different electrolytes. The cells prepared with electrolyte containing 10-15% FEC have the highest specific capacity, best capacity retention and smallest impedance. *Ex situ* surface analysis of the cycled electrodes provides insight into the differences in cycling performance. The electrodes cycled with the standard electrolyte undergo severe cracking and have a surface film which is primarily composed of lithium alkyl carbonates and lithium carbonate with low concentrations of LiF and $Li_xPF_yO_z$. The surface of electrodes cycled with electrolyte containing added VC have much less cracking and the surface films are dominated by lithium carbonate with low concentrations of poly(VC), lithium alkyl carbonates, LiF and $Li_xPF_yO_z$. The electrodes cycled with electrolytes containing different concentrations of FEC have several clear trends with increasing FEC content. The cracking of the electrode decreases with increasing FEC concentration, while the concentrations of poly(FEC) and LiF are gradually increased. In addition, the oxygen concentration on the surface of the electrode gradually decreases while the ratio of Li_2CO_3 to lithium alkyl carbonates is increased. This suggests that the primary reduction products of FEC are poly(FEC), LiF, and Li_2CO_3 while the primary reduction products of the standard electrolyte are lithium alkyl carbonates and LiF, as previously reported. An electrolyte containing 10% FEC appears to have the best combination of reasonable cost, low impedance and high capacity retention. This is likely due to the formation of an SEI which contains both a flexible polymer and a high Li salt content (LiF and Li_2CO_3). However, if the polymer content is too high, as observed for cells cycled with electrolyte containing added VC or high concentrations of FEC (25%), or the SEI films are too thick the cell resistance may dominate cycling performance.

FY 2014 Publications/Presentations

1. Lucht, B. (June 2014). “Development of Electrolytes for Lithium-ion Batteries.” Presented at the 2014 DOE Annual Merit Review and Peer Evaluation Meeting, Washington, D.C.
2. Nguyen, C.C.; Lucht, B.L. (2014). “Comparative Study of Fluoroethylene Carbonate and Vinylene Carbonate for Silicon Anodes in Li-ion Batteries.” *J. Electrochem. Soc.*, (161), pp: A1933-A1938.
3. Lucht, B. (October 2013). “Improved performance of graphite/$LiNi0_{.5}Mn_{1.5}O_4$ cells with electrolyte additives.” Presented at the 224th ECS Meeting, San Francisco, CA.
4. Lucht, B. (February 2014). “Advances in Electrolytes for Lithium Ion Batteries: A Mechanistic Understanding.” Presented at the Advanced Automotive Battery Conference, Atlanta, GA.
5. Lucht, B. (February 2014). “Improved performance of graphite/$LiNi_{0.5}Mn_{1.5}O_4$ cells with electrolyte additives.” Presented at the TMS Meeting, San Diego, CA.
6. Lucht, B. (March 2014). “Advances in Electrolytes for Lithium Ion Batteries: A Mechanistic Understanding.” Presented at the International Battery Seminar, Ft. Lauderdale, FL.
7. Lucht, B. (September 2014). “Advances in Electrolytes for Lithium Ion Batteries: A Mechanistic Understanding.” Presented at Electrochemistry 2014, Mainz, Germany.

V.D.2 Fluorinated Electrolyte for 5-V Li-ion Chemistry (ANL, ARL, BNL)

Zhengcheng Zhang
Argonne National Laboratory

Chemical Sciences and Engineering Division
9700 S. Cass Avenue, B200
Argonne, IL 60439
Phone: (630) 252-7868; Fax: (630) 972-4440
E-mail: zzhang@anl.gov

Kang Xu
US Army Research Laboratory
2800 Powder Mill Road
Adelphi, MD 20783
Phone: (301) 394-0321
E-mail: Conrad.k.xu.civ@mail.mil

Xiao-Qing Yang
Brookhaven National Laboratory
Chemistry Department
Building 555
Upton, NY 11973
Phone: (631) 344-3663; Fax: (631) 344-5815
E-mail: xyang@bnl.gov

Start Date: September 2013
Projected End Date: October 2015

Objectives

- To develop a new advanced electrolyte system with outstanding stability at high voltages and high temperatures, and improved safety characteristics for an electrochemical couple consisting of a high voltage $LiNi_{0.5}Mn_{1.5}O_4$ (LNMO) cathode and graphite anode.
- To gain a fundamental understanding of the interaction between electrolyte and high voltage electrode materials, the dependence of SEI functionality on electrolyte composition, and the effect of high temperature on full Li-ion cells using the advanced electrolyte system.

Technical Barriers

To meet the energy density requirements for Li-ion batteries established by DOE and the USABC, higher voltage and/or higher capacity cathode materials are needed for their wide commercialization in PHEV applications.

However, state-of-the-art (SOA) electrolytes (originally designed for 4 V Li-ion chemistry) show a poor performance in 5 V Li-ion systems due to oxidative decomposition, especially at high temperatures, imposing a barrier to the application of any new cathode chemistry operating beyond 4.5 V, such as next-generation $LiNi_{0.5}Mn_{1.5}O_4$ (LNMO) or Li-Mn-rich high capacity $xLi_2MnO_3\cdot(1-x)Li(Ni_xMn_yCo_z)O_2$. Additionally, these electrolytes also incur safety concerns due to their high flammability.

Technical Targets

- New solvents to render intrinsic voltage and thermal stability in the entire electrochemical window of 5V.
- New additives to enhance the formation of a robust solid electrolyte interphase (SEI), tailored to the new electrolyte.
- Fundamental understanding of the interaction between the electrolyte and the high-voltage electrode.

Accomplishments

- Synthesized a series of new carbonate solvents with F- and F-alkyl substitution.
- Established an efficient method/floating test for screening high voltage electrolytes.
- Identified electrolytes with enhanced oxidation stability.
- Developed and evaluated the effect of a Li reservoir for LNMO/graphite cells.
- Characterized the high voltage working/failing mechanism by TEM, ICP, GC-MS, and NMR.

✧ ✧ ✧ ✧ ✧

Introduction

To meet or exceed the 40-mile electric drive range target for PHEV, it is the most efficient approach to further increase either the capacity or the voltage of the cathode materials on the chemistry level. High-voltage, high-capacity cathode materials have been developed, such as $LiNi_{0.5}Mn_{1.5}O_4$ (4.8 V), $LiCo_{0.5}Mn_{1.5}O_4$ (5.1 V), and $LiCoPO_4$ (5.1 V). However, their increased operating voltage presents challenges to conventional electrolytes, whose carbonate-based components tend to oxidatively decompose above 4.5 V. Recent research on

Gen 2 electrolytes with LNMO/graphite couples suggests that the SOA electrolytes are not suitable for high-voltage Li-ion batteries that operate beyond 4.8 V, especially at high temperatures.

In this project, it was attempted to resolve these issues with new solvents and additives, and a LNMO/graphite couple as a screening baseline was used to demonstrate the feasibility of the proposed high voltage electrolytes.

Approach

To achieve the above-mentioned goal, the approach was to explore intrinsically stable fluorinated electrolyte solvents to provide thermodynamic stability that addressed the voltage instability of the current electrolyte. The selection, design, and synthesis of the fluorinated solvents were guided by highly accurate quantum chemistry modeling. Development of the optimal high-voltage electrolyte formulation was greatly accelerated by a floating test. To further mitigate the surface reactivity of high-voltage cathodes such as LNMO, advanced additives based on highly fluorinated carbonate and phosphates that help in delivering F-alkyls onto cathode surfaces were made, as well as SEI additives tailored for the graphite anode. Extensive material surface and bulk diagnosis using X-ray techniques and atomic force microscopy (AFM) were employed to gain a deep understanding of the success/failure mechanism of the proposed new fluorinated electrolyte under various operating conditions.

Results

Quantum chemistry calculation of oxidation stability of fluorinated solvents: The oxidation potentials of the proposed fluorinated carbonate solvents and additives were calculated using density function theory (DFT) and the results of a selected few examples are shown in Table V - 3. Fluorinated solvents show a 0.5 to 1.3 V increase in oxidation potentials compared to their non-fluorinated counterparts. Furthermore, calculations that take the anion effect into account show that the anion plays a significant role in the oxidation stability of electrolyte solvents. The anion lowers the oxidation stability of solvents due to its negative charge; however, the TFSI$^-$ anion lowers the oxidation potential by 0.5 V more on average than the PF_6^- anion, indicating that TFSI$^-$ is not suitable for high voltage applications. Table V - 3 also summarizes the reduction potential of the fluorinated solvents which are higher than their non-fluorinated solvents. This information directs us to the tailored additive to passivate the anode side if SEI formation becomes an issue for the fluorinated electrolyte.

Table V - 3: DFT calculation for predicting the oxidation potentials of fluorinated molecules

Molecular Structure	Oxidation Potential (P_{ox}/V)	Anion Effect Potential (P_{ox}/V)	Reduction Potential (P_{red}/V)	Stretch Bond Potentials (P_{red}/V)
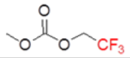	7.10 (6.62)*	6.26 (PF_6: HF forms) 5.79 (TFSI: H transfer)	0.03	1.40 (CF_3CH_2-O) 1.49 (CH_3-O)
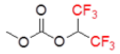	7.70 (6.46)*	6.28 (PF_6) 5.83 (TFSI)	0.30	
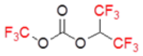	7.96 (6.46)*	7.69 (PF_6) 5.76 (TFSI)	1.29	1.54 (CF_3CH_2-O) 2.39 ($(CF_3)_2$CH-O 1.47 (CF_3-O)
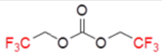	7.25 (6.51)*	7.35 (PF6) -	0.22	1.65 (CF_3CH_2-O)
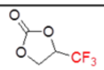	7.30 (6.80)*	6.21 (PF_6) 5.33, 5.44, 5.87 (TFSI)	1.54 (spontaneous C-O bond opening)	
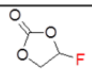	7.24 (6.95)*	6.44 (PF_6) 5.80 (TFSI)	0.33	1.56 (CHF-O)
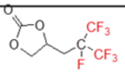	6.97			
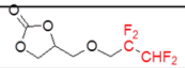	6.24	6.05 (PF_6) 5.90, 5.19, 5.22 (TFSI)	0.01	1.50
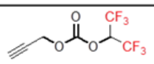	6.08 (gauche) 6.09 (trans)	-	2.44	

*The values in parenthesis are oxidation potentials of non-fluorinated versions of the molecules to the left.

Synthesis of new fluorinated solvents: The calculated fluorinated carbonate solvents were synthesized during the first two quarters of FY14. The typical synthetic routes for F-linear carbonates and F-cyclic carbonates are shown in Figure V - 116a. The synthesized fluorinated solvents illustrated in Figure V - 116b were analyzed by ^{1}H, ^{13}C, ^{19}F NMR to identify the chemical structure and GC-MS to ensure purity over 99.5%. The moisture level of these synthesized compounds was determined using the Karl Fischer titration method and controlled below 20 ppm.

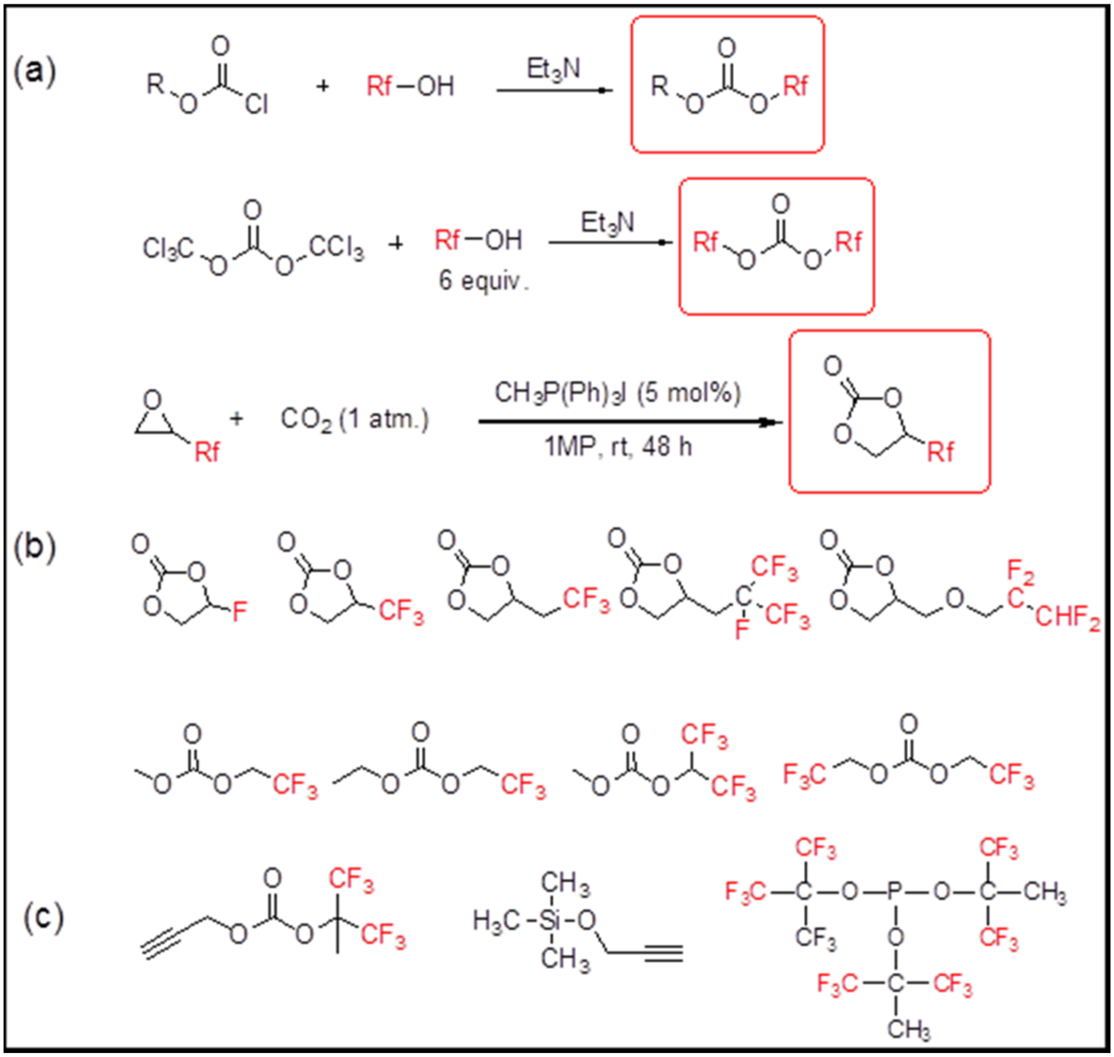

Figure V - 116: (a) General synthetic schemes of fluorinated carbonates, (b) structures of the synthesized fluorinated carbonate solvents, and (c) structures of the synthesized fluorinated additives

Electrochemical validation of oxidation stability of the new fluorinated solvents: The anodic stability of the new fluorinated carbonate solvents was investigated by electrochemical floating test. LNMO/Li cells were assembled with various formulations of electrolyte containing fluorinated cyclic and linear carbonates (1:1 ratio, 0.5 M $LiPF_6$) and the cells were then fully charged and maintained at 4.9 V, 5.0 V, 5.1 V and 5.2 V, respectively, for 10 hours. Figure V - 117 illustrates the leakage current of various electrolyte formulations. The electrolytes with F-cyclic carbonates showed similar leakage current at RT; however, a tremendous difference was observed when the temperature was raised to 55°C, with FEC being the most stable and TFE-PC-E being the least stable (Figure V - 117b) F-cyclic carbonate. For the linear carbonates, the partially fluorinated F-EMC shows a similar level of stability with DMC and EMC, but the highly fluorinated linear carbonates and F-ethers are more stable than DMC and EMC (Figure V - 117c, d). To this end, both theoretical calculations and experimental results prove that fluorinated solvents are more stable against oxidation than their non-fluorinated solvents.

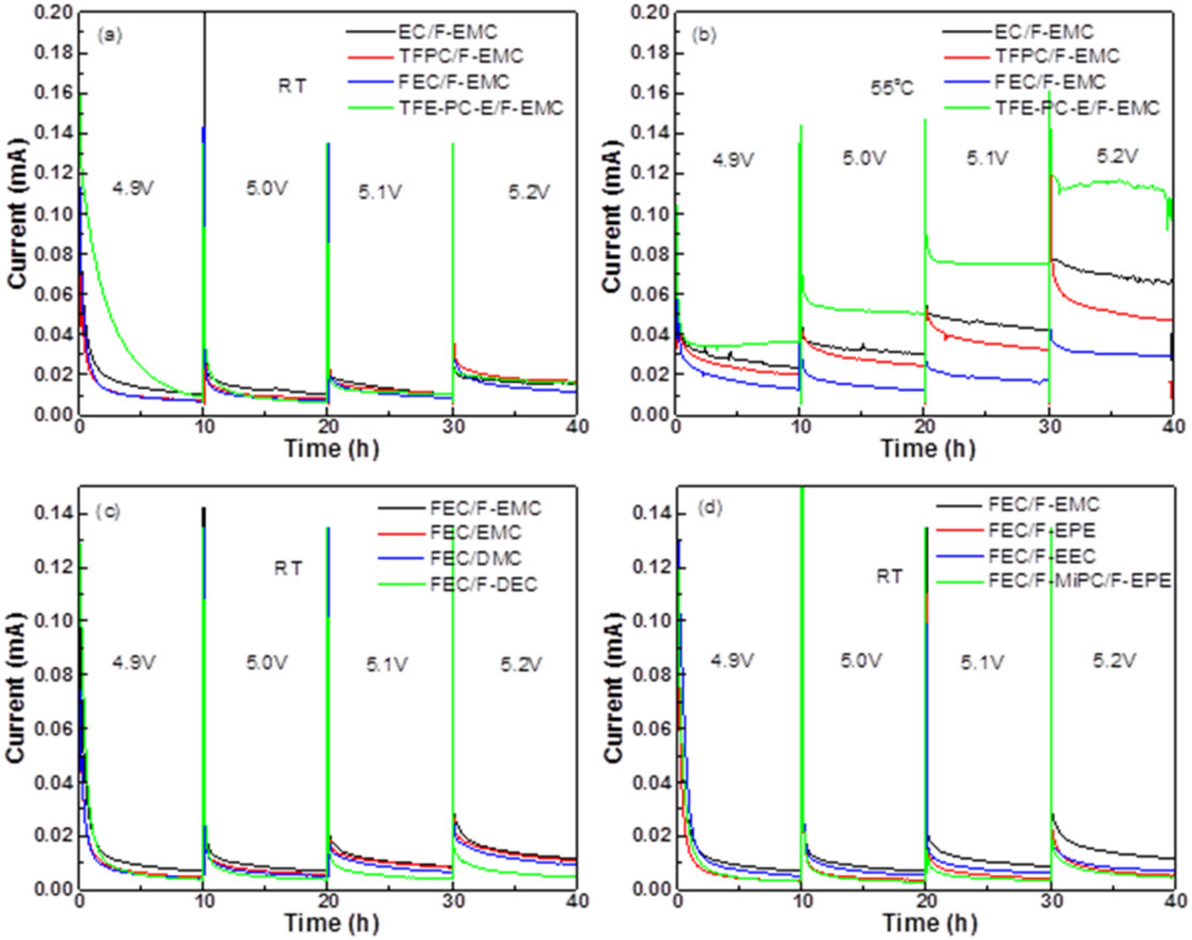

Figure V - 117: Leakage current from the electrochemical floating tests of EC, TFPC, FEC and TFE-PC-E with F-EMC at (a) RT, (b) 55°C; (c) EMC, DMC, F-DEC and (d) F-EPE, F-EEC, F-MiPC with FEC compared with F-EMC/FEC at RT

Cell performance of fluorinated electrolyte formulations: Based on the electrochemical floating test results, a library of electrolyte formulations was prepared using the fluorinated solvents. A few of these formulations have shown greatly enhanced cell performance in a LNMO/A12 graphite couple compared with the baseline electrolyte (Gen 2, 1.2 M $LiPF_6$ in EC/EMC =3/7 w/w). Formulation HVE1 comprises 1.0 M $LiPF_6$ in FEC/F-EMC/F-EPE=3/5/2 v/v/v with 1% LiDFOB and it improved the capacity retention of the LNMO/A12 cell cycled at 55°C (Figure V - 118a). HVE 2 (1.2 M $LiPF_6$ in FEC/DMC=1/1 v/v with 1% LiDFOB) showed a much improved capacity retention at RT (Figure V - 118b). HVE3 (1.0 M $LiPF_6$ in TFPC/F-EMC/F-EPE=3/5/2 v/v/v with 1% LiDFOB) comprised of TFPC, a trifluoromethyl substituted EC, showed excellent capacity retention; however, the initial capacity is low due to an SEI formation issue on the graphite anode (Figure V - 118c). Other than the cell cycling test, cell self-discharge from a fully charged condition has also been evaluated and the fluorinated electrolyte HVE1 shows at least twice the storage life of the Gen 2 electrolyte (Figure V - 118d). In FY14, tailored additives were made and their structures are shown in Figure V - 116c. Initial tests indicate that these additives can sufficiently suppress the co-intercalation of PC-based electrolytes by forming a good SEI on the graphite surface. The efficiency of these additives for F-electrolytes is under investigation.

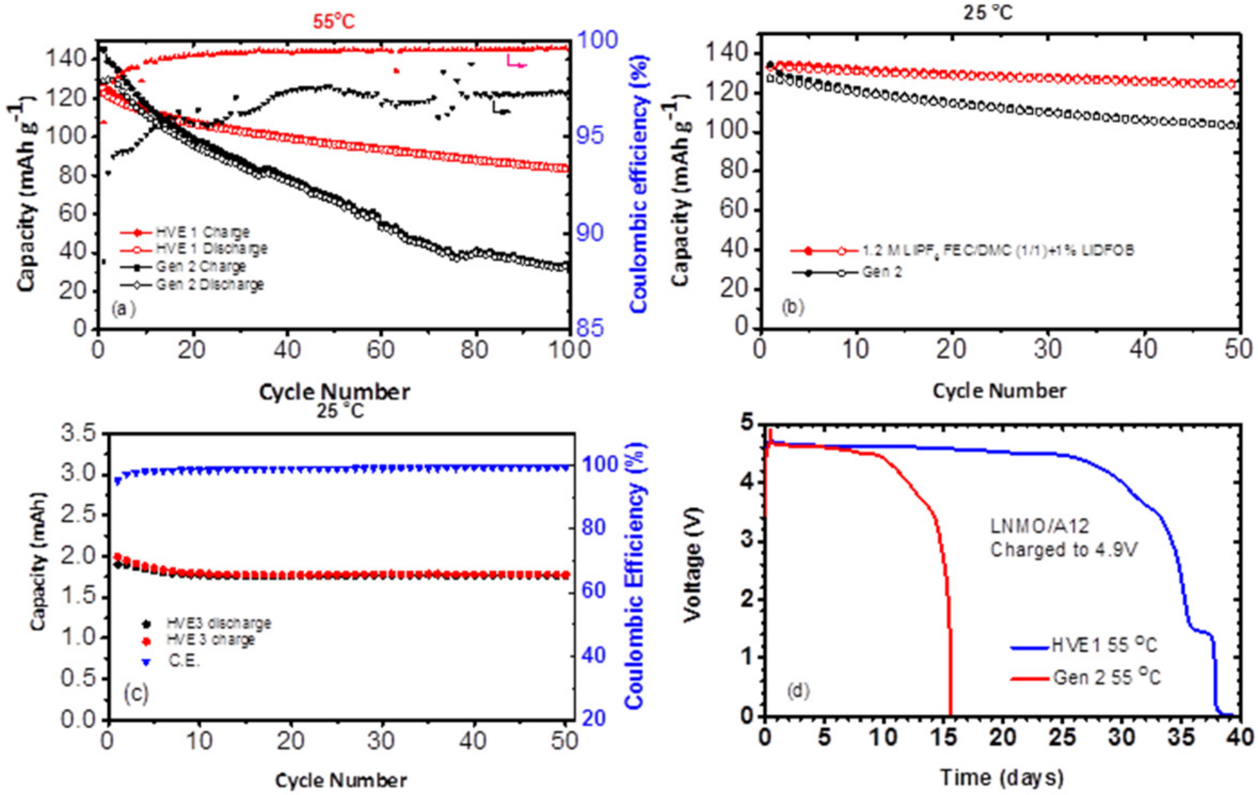

Figure V - 118: Cycle performance of LNMO/A12 cells with cutoff voltage of 3.5-4.9 V at C/3 with (a) HVE 1 electrolyte compared to Gen 2 electrolyte at 55°C, (b) HVE 2 electrolyte compared to Gen 2 electrolyte at RT, (c) HVE 3 electrolyte at RT, and (d) cell self-discharge test at 55°C

Post-test analysis of LNMO/A12 cells with fluorinated electrolyte: A variety of techniques have been employed to analyze the cycled electrodes and electrolytes to obtain mechanistic information on how the improvement was achieved when switching to fluorinated electrolytes. The HVE 1 electrolyte was selected as a model system for post-test analysis. The harvested electrolytes were analyzed by GC-MS and NMR for organic decomposition products and ICP-MS for transition metal dissolution. GC-MS and NMR analysis confirm the extensive trans-esterification reactions occurring in the Gen 2 electrolyte, while minimal side products were detected for the fluorinated electrolyte. The ICP-MS data (Table V - 4) reveal that the transition metal dissolution into the electrolyte is not significant at room temperature, and all the electrolytes show similar levels of concentration. However, the Gen 2 electrolyte shows much more dissolution than the fluorinated electrolyte at 55°C. The low solubility of transition metal in the F-electrolyte is beneficial to the stabilization of the electrode/electrolyte interphase, thus improving the cell’s performance.

Table V - 4: ICP-MS results of Mn and Ni dissolution in Gen 2; HVE1 electrolyte with and without LiDFOB additive harvested from LNMO/A12 cells cycled at RT and 55°C

Cycling Temp. (°C)	Electrolyte	Total Mass of Element in Harvested Electrolyte (µg)	
		Mn	Ni
RT	Gen 2	0.009	0.010
	HVE 3	0.008	0.023
	HVE 3 + LiDFOB	0.006	0.005
55 °C	Gen 2	18.1	19.0
	HVE 3	3.00	1.77
	HVE 3 + LiDFOB	0.022	0.017

The harvested electrodes were analyzed by SEM and TEM for chemical and morphological changes on the electrode and particle surfaces. SEM images of harvested graphite anodes and LNMO cathodes from the Gen 2 and HVE 1 electrolytes cycled at 55°C are shown in Figure V - 119. Heavy deposition of electrolyte decomposition products were observed on both the anode and the cathode from the Gen 2 cells. In the case of the HVE 1 electrolyte, the deposition on the anode surface is much less (Figure V - 119c) and the cathode surface almost resembles a pristine cathode (Figure V - 119f).

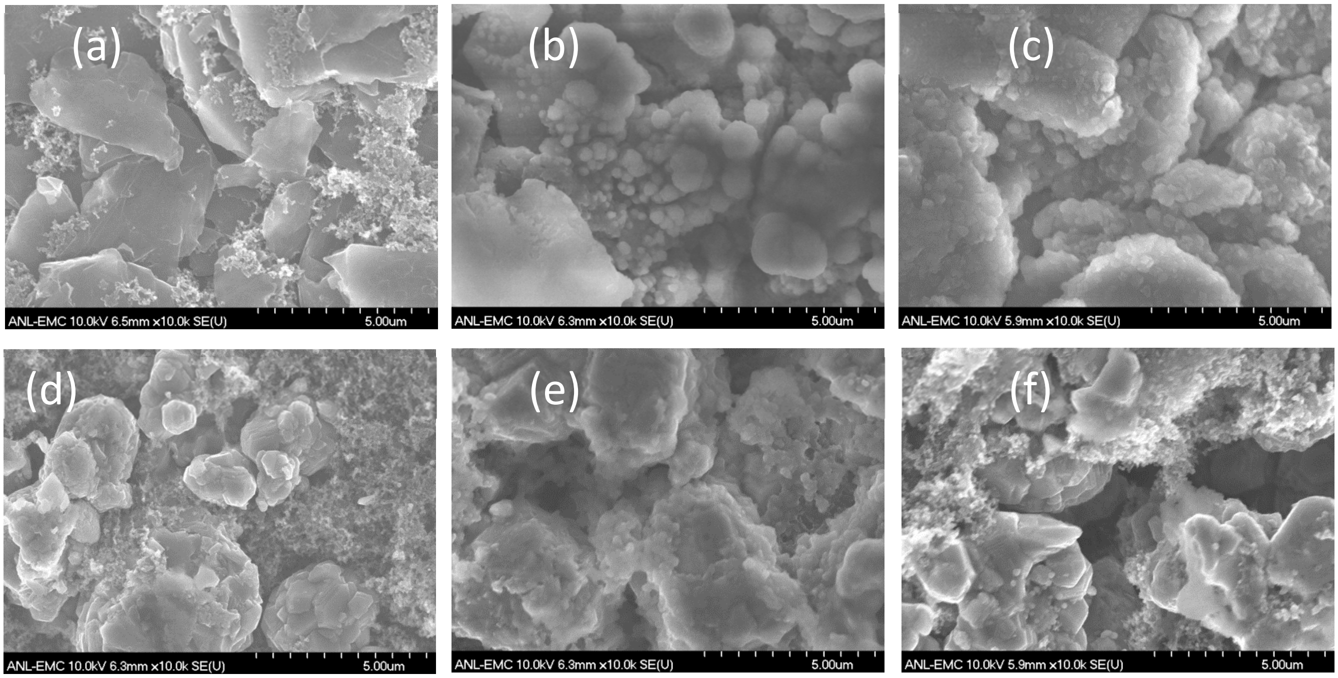

Figure V - 119: SEM image of (a) a pristine graphite anode and harvested graphite anode from (b) a Gen 2 cell, and (c) a HVE 1 cell; (d) pristine LNMO cathode and harvested LNMO cathode from (e) a Gen 2 cell, and (f) a HVE 1 cell. (100 cycles at 3.5–4.9 V, C/3 and 55°C)

TEM revealed more detailed information about the morphological change to the active material particles after cycling. TEM images of harvested LNMO cathodes from the Gen 2 electrolyte, and HVE 1 electrolyte with and without additive LiDFOB are shown in Figure V - 120. The cathode harvested from the Gen 2 cell showed severe degradation of the active material particles, with edge thinning and cracking (Figure V - 120a), while particle integrity is well maintained in the cathode harvested from the fluorinated electrolyte cell (Figure V - 120b). Even better results were obtained for the case where LiDFOB was the additive (Figure V - 120c). This result matches with the ICP-MS data shown in Table V - 4, and suggests that the transition metal dissolution phenomenon and the cathode material degradation are closely related.

FT-IR and XPS analyses of these electrodes were also performed and the results are consistent with the SEM/TEM data.

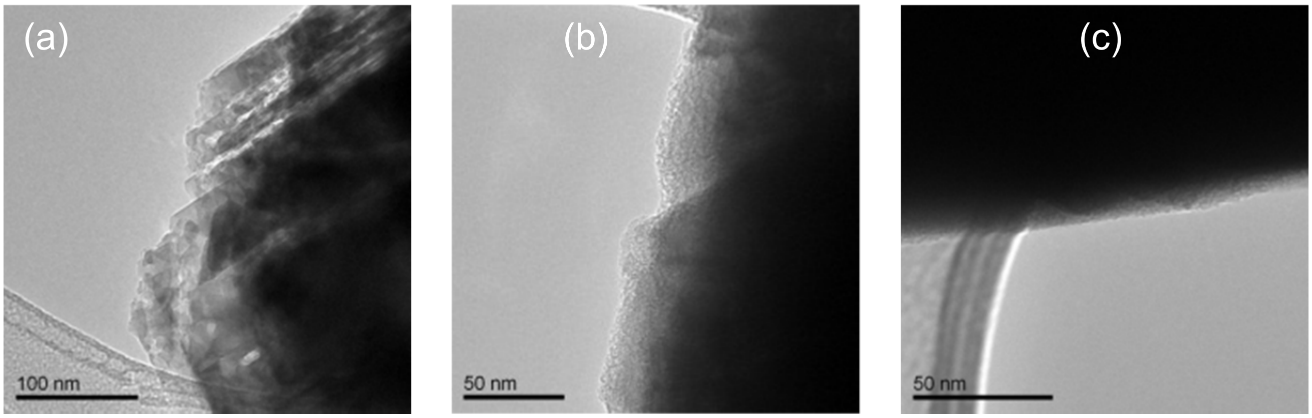

Figure V - 120: TEM image of harvested LNMO cathode cycled at 55°C for 20 cycles with (a) Gen 2 electrolyte, (b) HVE 1 electrolyte without additive, and (c) HVE 1 electrolyte with 1% LiDFOB

Conclusions and Future Directions

The fluorinated electrolytes comprised of fluorinated cyclic and linear carbonates were designed and synthesized as high-voltage electrolytes for a high voltage Li-ion battery. The FEC-based, high-voltage electrolyte for the LNMO/graphite was evaluated by comparing it with the conventional EC-based Gen 2 electrolyte. The HVE electrolyte shows much better cycle performance at both room temperature and at 55°C. In post-test analysis, SEM and FT-IR of the harvested anode and cathode cycled under 55°C indicate that the HVE has less solid decomposition products deposited on both the anode and the cathode. This finding is direct proof of the enhanced stability of the HVE in the high-voltage LNMO/graphite system on both the LNMO cathode and graphite anode at high temperature cycling conditions. The extraordinary electrochemical stability of this electrolyte makes it a suitable candidate for other high voltage cathode materials, i.e., $LiMPO_4$ (M=Ni, Co, Mn), as well.

Future research will focus on the electrolyte additive to further extend the cycle life of the LNMO/graphite cell with fluorinated electrolyte. In FY15, new fluorinated electrolytes containing fluorinated solvents other than fluorinated carbonates will be developed, including sulfones, ethers, and nitriles to further explore more anodically stable electrolyte candidates for high-voltage Li-ion cells.

FY 2014 Publications/Presentations

1. Croy, J.R.; Abouimrane, A.; Zhang, Z. (2014). “Next-generation lithium-ion batteries: The promise of near-term advancements.” *MRS Bulletin*, (39), pp: 407-415.
2. Hu, L.; Amine, K.; Zhang, Z. (2014). “Fluorinated electrolytes for 5-V Li-ion chemistry: Dramatic enhancement of $LiNi_{0.5}Mn_{1.5}O_4$/graphite cell performance by a lithium reservoir.” *Electrochem. Commun.,* (44), pp: 34-37.
3. Hu, L.; Xue, Z.; Amine, K.; Zhang, Z. (2014). “Fluorinated Electrolytes for 5-V Li-Ion Chemistry: Synthesis and Evaluation of an Additive for High-Voltage $LiNi_{0.5}Mn_{1.5}O_4$/ Graphite Cell.” *J. Electrochem. Soc.,* (161:12), pp: A1777-A1781.
4. Zhang, Z.; Hu, L.; Xue, Z.; Azimi, N. (May 2014). “Fluorinated Electrolytes for 5 V Li-Ion Chemistry.” Presented at the 225th ECS Meeting, Orlando, FL.
5. Hu, L.; Zhang, Z.; Johnson, C.S.; Amine, K. (May 2014). “Lithium Compensation to Mitigate Capacity Fading in High Voltage $LiNi_{0.5}Mn_{1.5}O_4$/ graphite Li-ion Cells.” Presented at the 225th ECS Meeting, Orlando, FL.

V.D.3 Daikin Advanced Lithium Ion Battery Technology – High Voltage Electrolyte (Daikin)

Ron Hendershot
Daikin America

Daikin America Technical Center
2749 Highway 20
Decatur, AL 35601
Phone: (256) 260-6302
E-mail: hendershot@daikin-america.com

Joe Sunstrom
Daikin America Technical Center
2749 Highway 20
Decatur, AL 35601
Phone: (256) 260-6314
E-mail: sunstrom@daikin-america.com

Start Date: October 2013
Projected End Date: September 2015

Objectives

- To develop and optimize an advanced electrolyte containing fluorochemical compounds to achieve
    - 300-1000 cycles at 4.6 V with a cut off capacity retention of 80%.
    - Reduced/no flammability.

Technical Barriers

This project is focused on the improvement of cycle/calendar life at high voltage (4.6 V) using advanced electrolytes which have improved safety characteristics.

Technical Targets

- Development and optimization of formulations containing fluorinated molecules.
- Increased high voltage cycle life.
- Improved safety through intrinsic properties of the electrolyte and reduced interaction with charged electrodes.

Accomplishments

- Comprehensive internal/external review of current data on fluorinated electrolytes was completed. Two baseline compositions for a fluorocarbon- and hydrocarbon-based electrolyte were chosen and baseline data was established.
- Composition maps around the baselines have been mostly completed for base solvent optimization. The base solvent compositions are optimized using properties of the electrolytes both in and out of cells.
- Preliminary work on additive behavior has been completed to establish which additive combinations will be optimized. In particular, the film formation energies of the additives was examined as a function of concentration and temperature. Voltammetry has been used to study film formation.
- A collaboration was initiated with Coulometrics Inc. (Chattanooga, TN). The primary focus is the production of high voltage pouch cells which includes electrode coating and cell fabrication. Coulometrics is also collecting variable temperature cycle data which is being guided by high precision coulometric techniques.

✧ ✧ ✧ ✧ ✧

Introduction

The use of small fluorinated molecules to enhance electrolyte stability is the focus of this project. Fluorinated small molecules show increased chemical and thermal stability due to the inherent strength of the C-F bond. These low molecular weight materials also exhibit viscosities low enough to make viable electrolyte solvents/additives. The stability of these fluorochemicals will allow routine operation to 4.6 V. There are two separate strategies involved to achieve this: 1) increasing intrinsic stability of the electrolyte solvents and 2) design of fluorinated molecules with functional moieities to bond with electrode surfaces as functional films. This technological advance would allow reduction in the number of cells needed for a target application, thus reducing overall cost.

Approach

Drawing on a large library of fluorinated molecules synthesized at Daikin, optimization of high voltage electrolytes will be achieved by a PDCA (Plan-Do-Check-Act) cycle method. Specifically, this involves multiple cycles to optimize electrolyte solvent composition based on intrinsic properties (e.g., conductivity, voltage stability). Optimization of SEI and gassing additives will then be superimposed over the optimal solvent combinations to propose candidate electrolytes. This is accomplished by the construction and manipulation of composition/property maps. Finally, the best candidate electrolytes will be evaluated using high performance coulometric techniques and real time cycling data to achieve the target

Results

Hydrocarbon and fluorocarbon baseline data

Two baseline compositions were chosen based on availability of current data in a variety of cell chemistries. They are: 1.0 M LiPF6 EC/EMC (7:3) and 1.2 M LiPF6 FEC/EMC/fluorether (2:6:2) + additive which are nominally hydrocarbon and fluorocarbon electrolytes, respectively. Figure V - 121 shows the room temperature C-rate cycling behavior of the baselines as measured in NMC/graphite commercial cells. There is no appreciable difference in the cycle performance at 1C even in an electrolyte which contains nominally 40% fluorocarbon solvent.

Using the same NMC/graphite commercial cells, the cells were cycled to 4.2, 4.3, 4.35, 4.4 and 4.5 V to determine the energy gain attained by cycling at a higher voltage. The energies are calculated by integrating the capacity curves with respect to voltage. Figure V - 122 shows the capacities and normalized energies for commercial NMC/graphite cells discharged at 0.2 C (top graphs) and 1C (bottom graphs) for the baseline electrolytes containing hydrocarbon (right graphs) and fluorocarbon/hydrocarbon (left graphs).

It can be seen that charge/discharge at 4.5 V results in a 25% and 31% energy gain for cells containing hydrocarbon and fluorocarbon/hydrocarbon electrolytes, respectively. The results shown in the graph are only for the first charge/discharge cycle. Cycle stability of these two electrolytes will be the subject of a future report. It has been noted that there appears to be a decomposition of hydrocarbon electrolyte at or above 4.35 V.

Optimization of electrolyte solvents and additives through property mapping

Electrolyte solvent/additive combinations are being examined and optimized by use of PDCA (Plan-Do-Check-Act) cycles. A total of 4 PDCA cycles will be completed which include 2 cycles for solvent, 1 cycle for SEI additive, and 1 cycle for gassing additive optimization. For this study, solvents are defined as components with >10% v/v and additives are materials with <5% w/w in the finished electrolyte. Variations of the baseline electrolytes are currently being optimized using a composition property map technique.

Table V - 5 shows an overview of the systems being studied. Four solvent combinations, all containing Daikin proprietary F-solvent, are being optimized with different carbonate solvents (DEC, EMC, DMC) varied with (FEC/EC) substitution.

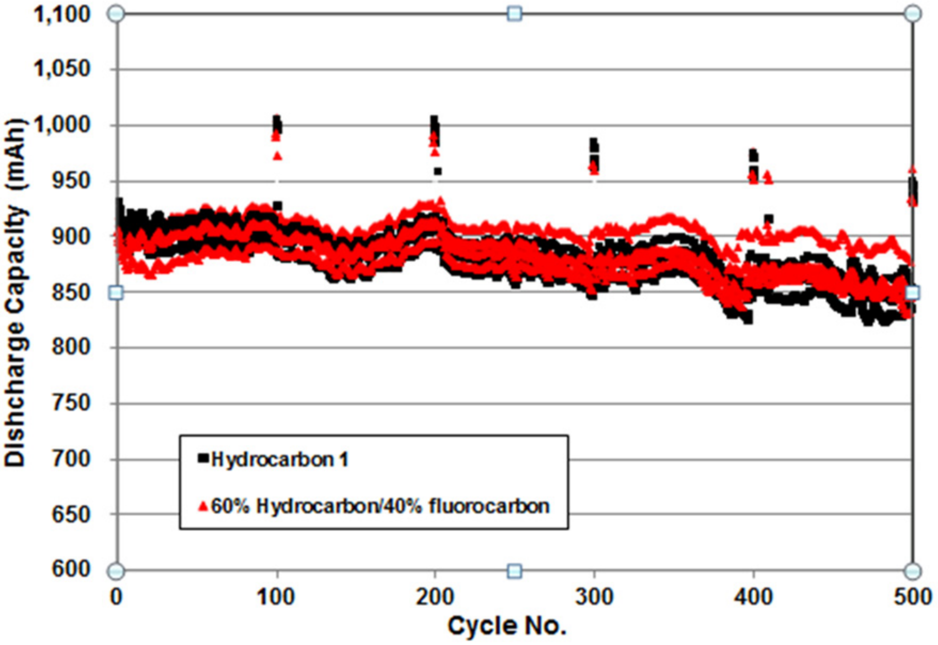

Figure V - 121: Room Temperature C-rate cycling comparison of hydrocarbon (black) vs. fluorocarbon/hydrocarbon (red) electrolyte

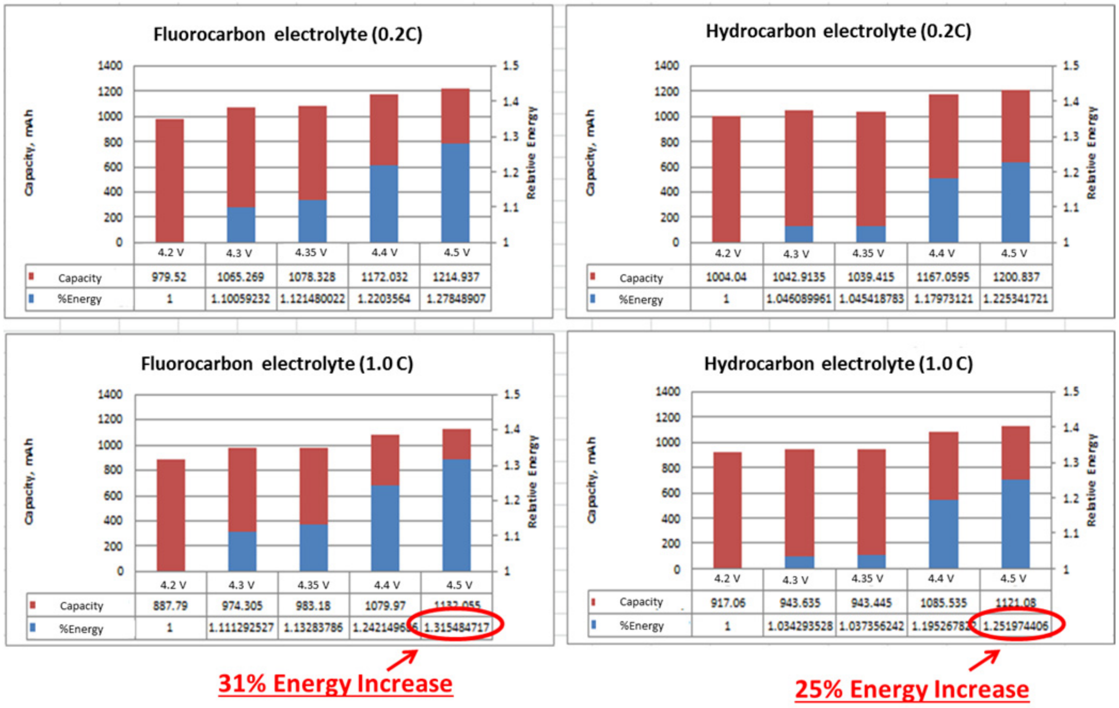

31% Energy Increase

25% Energy Increase

Figure V - 122: Energy comparison of commercial NMC/graphite cells containing fluorocarbon vs hydrocarbon electrolyte at variable voltage (4.2-4.5 V)

Table V - 5: Solvent and additive combinations for electrolyte optimization

Solvents

8 compositions each

- FEC/EMC/***F-solvent***
- EC/EMC/***F-solvent***
- FEC/DMC/***F-solvent***
- FEC/DEC/***F-solvent***

Best composition each

Additives

6-8 compositions each

- ***SEI additive-1***/VC/PS
- ***SEI additive-2***/VC/PS
- ***SEI additive-1***/VC/***gassing additive-3***

The first two PDCA cycles are nearing completion and property data is now being compiled. The properties under consideration are: conductivity, voltage stability, gassing, and battery properties (cell impedance, first capacity, OCV). The creation of composition- property maps like the one shown in Figure V - 123 for conductivity in an FEC/EMC/D7 mixture is now in progress. The intention is to overlay the maps to optimize base solvent compositions. An example of the methodology is shown in Figure V - 124 which shows addition conductivity, voltage stability, gassing, and initial capacity maps. The best guess compositions from this technique will then be used as vehicles for different additive packages for enhance cycle life.

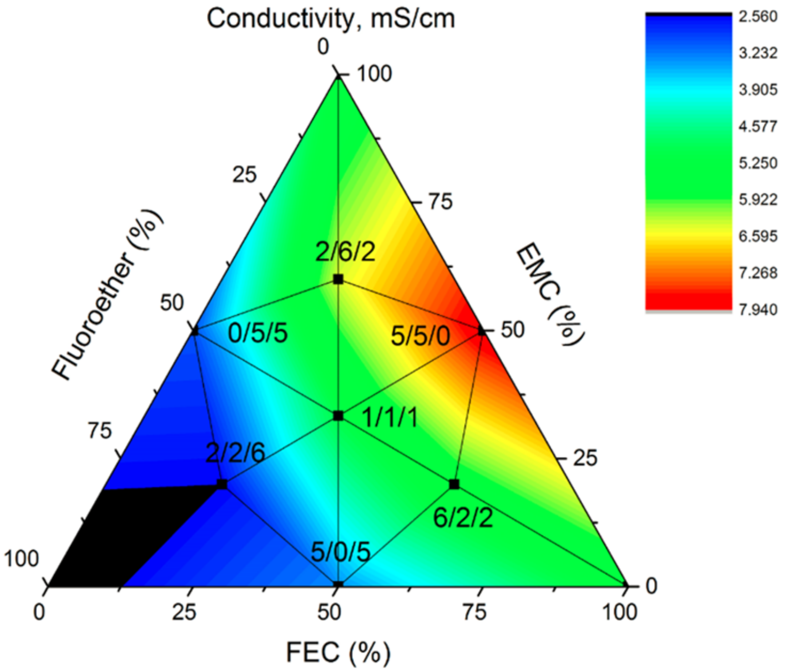

Figure V - 123: Representative property map for FEC/EMC/F-solvent for room temperature conductivity.

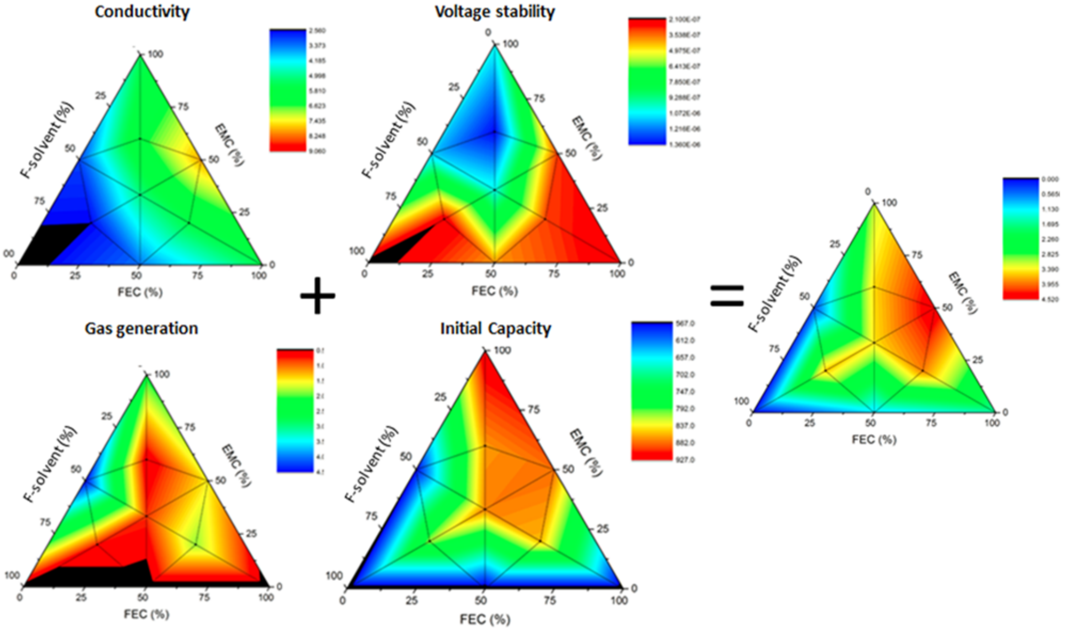

Figure V - 124: Representative additive of property maps to optimize solvent composition of electrolyte

Examination of the film forming properties of additives

Preliminary work for PDCA cycle 3 (which will involve optimizing additives) was completed. This work is being completed to best understand the implementation of additives (i.e., formation cycle parameters) and their intrinsic stability.

It is believed that FEC works well for two reasons: it improves the voltage stability of the solvent mixture and it works like an SEI layer making additive. The comparison of FEC to Daikin fluoroadditives (A9, HFEEC) as well as hydrocarbon (VC, EC) SEI forming additives is being examined. Examination of first charge cycle data is being used as the screening tool. The first charge data is measured for an electrolyte with and without the additive. The difference in energy between the two samples is considered to be proportional to the film formation energy. Figure V - 125 shows a comparison of FEC/A9/VC.

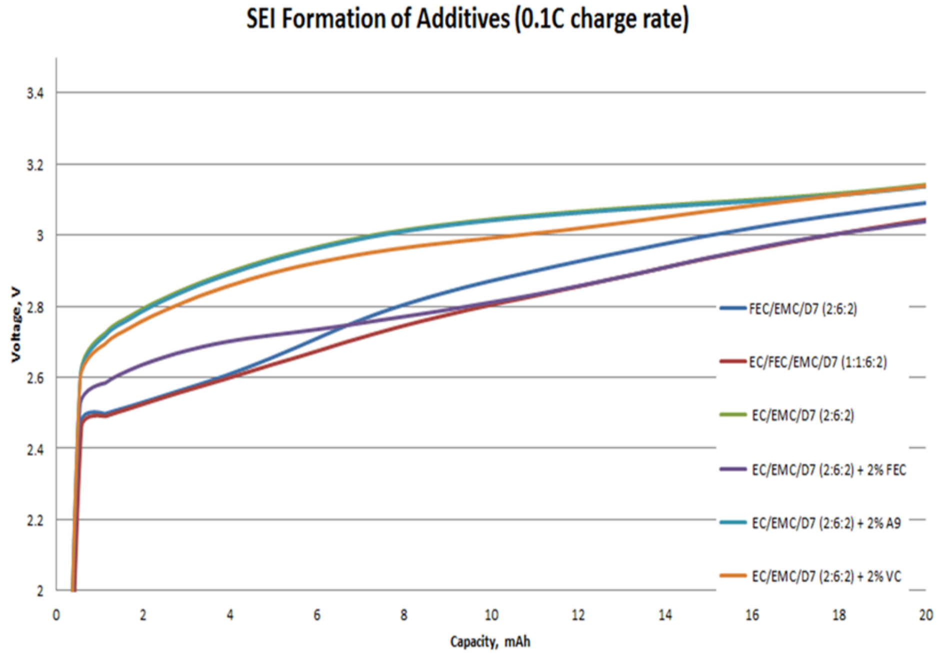

Figure V - 125: Comparison of first charge (film formation) curves of FEC, A9 (cyclic fluorocarbonate), VC

The data show that FEC has a bigger parasitic energy (film formation). It unclear that all the parasitic energy is due to surface films which would be proportional to the concentration of additive as well as surface area of carbon.

Measurements were made to vary the FEC concentration and watch the parasitic energy to determine an upper limit for forming the film (i.e., if the parasitic energy keeps increasing with increasing FEC content, then there is another process). The first charge as a function of FEC content is shown in Figure V - 126. The upper limit of the parasitic energy as a function of FEC concentration is still not known and additional experiments are being run.

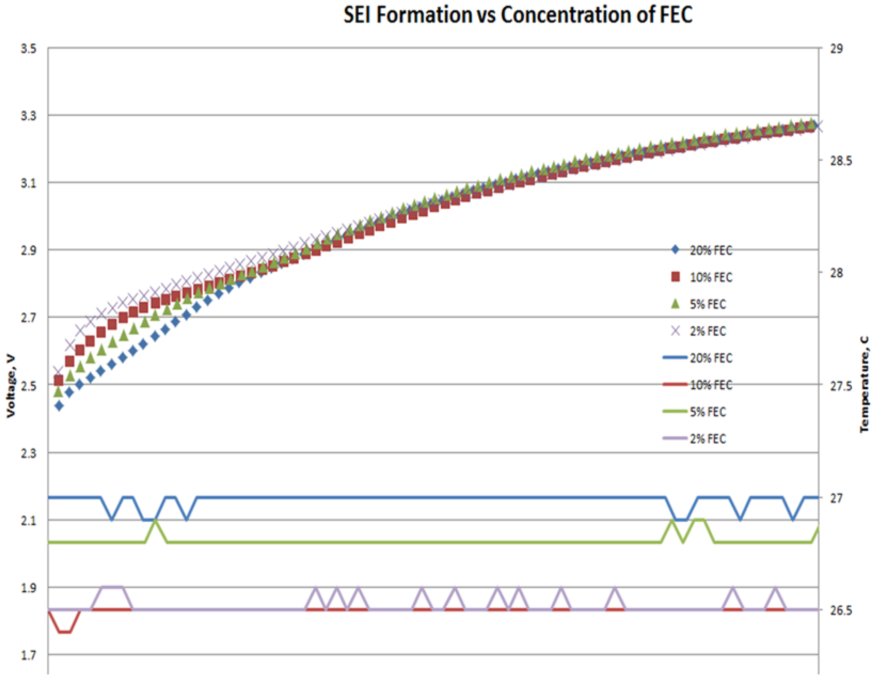

Figure V - 126: Comparison of first charge (film formation) curves of FEC at different FEC concentrations

An additional round of first charge experiments was done on the same electrolyte at various temperatures. The hypothesis was that due to wetting and viscosity of fluorochemicals, more efficient film formation would be possible if the batteries were formed at higher temperature. Some examples are shown in Figure V - 127.

In general, the parasitic energy increased with higher temperature which would be a product of more efficient film formation. However, when we cycled the batteries formed at 80 C, the cycle behavior became poorer for the batteries containing FEC (see Figure V - 128). This is attributed to the poor thermal stability of the FEC as evidenced by the photos in the inset of Figure V - 128. The photos show the electrolytes heated to 60 C and 85 C. The discoloration of the electrolyte at 85 C is due to decomposition involving FEC.

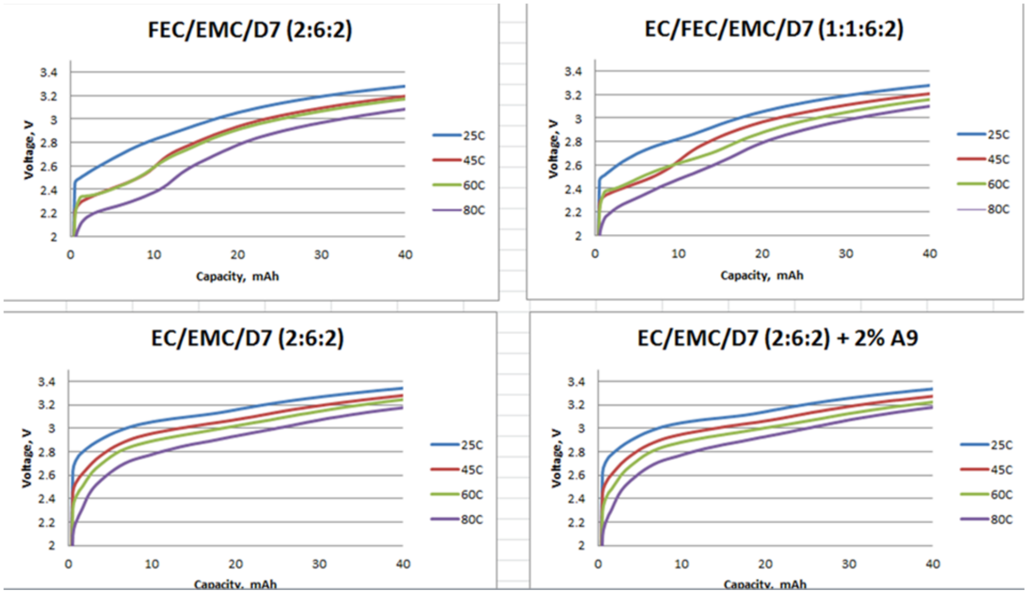

Figure V - 127: Comparison of first charge (film formation) at 25, 45, 60, 80 C for several electrolyte compositions

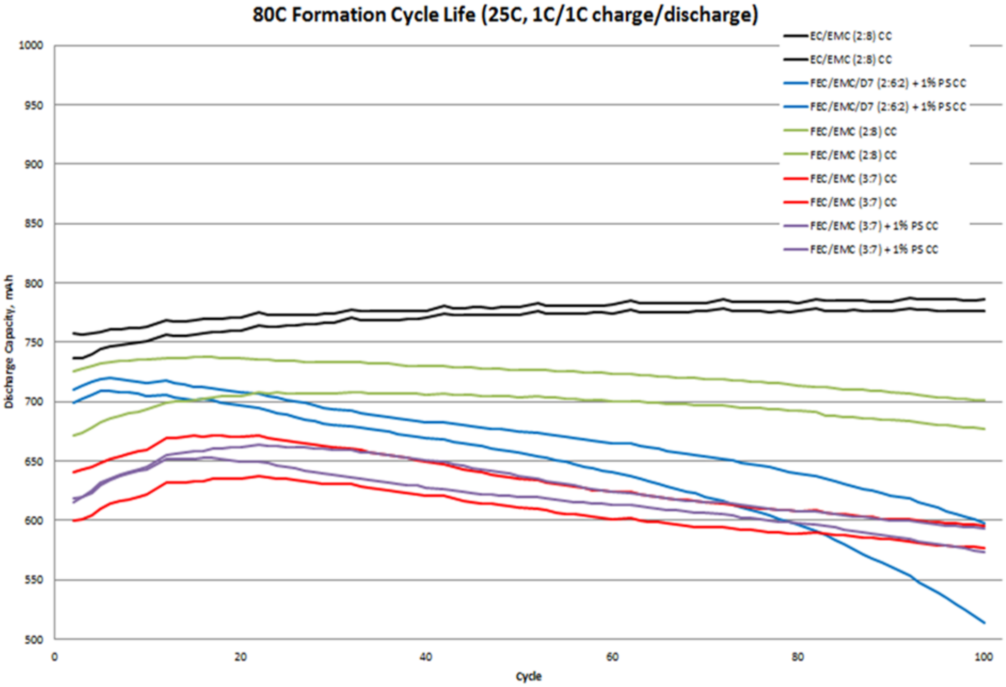

Figure V - 128: Cycle behavior of batteries with various electrolytes formed at 80 C (inset shows electrolytes exposed to 60 C and 85 C showing decomposition of electrolyte containing FEC)

Fabrication of high voltage cells

The agreement with Coulometrics Inc. LLC (Chattanooga, TN) was signed. The fabrication of high voltage electrodes is currently in progress. The first round of electrodes are LMNO cathode obtained from NEI and Mag D anodes. Efforts are underway to secure several other options to broaden the high voltage profile.

Conclusions and Future Directions

Two baseline electrolyte compositions have been selected as a starting point for this study. One is a conventional hydrocarbon electrolyte similar to industry standards and the other is a nominally 50:50 mixture of fluorocarbon/hydrocarbon solvents. The baselines have similar rate/capacity performances under normal (4.2 V) as well as high voltage (4.5 V) conditions. It has been shown that charge/discharge experiments show an appreciable (30%) energy gain when cycled at the higher voltage. Future work is being centered around the cycle life and stability of the baselines at high voltage.

Property-composition maps have been generated around variations on the solvent systems in the baseline. These maps were generated based on intrinsic properties of the electrolyte (e.g., Conductivity, voltage stability) as in cell properties (gassing, first capacity, cell impedance). This data has been collected and is currently being compiled for analysis. The best solvent combinations will then be used to study various additive packages by using property-composition maps based on cycling properties.

Out of cell studies on the best methods of implementing SEI forming and gas inhibiting additives is near completion. The additives will be then examined in various combination/concentrations according to methods described above.

Work to fabricate the high voltage cells needed to complete this project has begun with a partner (Coulometrics). Electrodes are being coated and cell fabrication tooling is being put in place along with a tenable cell balance and design.

FY 2014 Publications/Presentations

1. 2014 DOE Annual Peer Review Meeting Presentation.
2. Joseph Sunstrom, Hitomi Miyawaki, Shinichi Kinoshita, Akiyoshi Yamauchi, Michael Gilmore, Ron Hendershot, “High Voltage Electrolytes: Safety and Performance through the Use of Fluorochemicals” (invited), Advanced Automobile Battery Conference, Atlanta, GA, Feb. 3-7 2014.
3. Joseph Sunstrom, Michael Gilmore, Hitomi Miyawaki, Akiyoshi Yamauchi, Ron Hendershot, “Solids Meet Liquids: Interfaces, Surfaces and Batteries” (invited), Gordon Conference on Solid State Chemistry, 2014.

V.D.4 Novel Non-Carbonate Based Electrolytes for Silicon Anodes (Wildcat)

Deidre Strand
Wildcat Discovery Technologies

6985 Flanders Drive
San Diego, CA 92121
Phone: (858) 550 1980; Fax: (858) 638 7533
E-mail: dstrand@wildcatdiscovery.com

Start Date: October 2013
Projected End Date: December 2015

Objectives

- Develop electrolyte formulations based on non-carbonate solvents and novel additives that:
  - Form stable solid electrolyte interphase (SEI) layers on 3M Si alloy anode.
  - Enable coulombic efficiency > 99.9% after cycle 1.
  - Enable cycle life > 500 cycles (80% capacity) in NMC full cells.
  - Have comparable ionic conductivity to carbonate formulations.
  - Are oxidatively stable to 4.6V.
  - Do not increase cell costs over today's carbonate formulations.

Technical Barriers

While Si anodes can provide very high specific energy due to their high capacity and favorable voltage profile, they suffer from large volumetric changes on lithiation and delithiation. These large changes in volume are detrimental to the SEI layer, which continuously cracks and reforms, resulting in rapid capacity fade. The project objective is to develop electrolyte additives to provide more mechanically robust SEI layers. However, the use of such molecules may be detrimental to battery performance such as rate/power. Furthermore, the SEI may not passivate the anode well enough to prevent loss of bulk electrolyte with long cycling times. A key technical challenge is the difficulty in performing analytical evaluation of the SEI after formation in order to fully understand the positive or negative effects on the SEI with different additive structures.

Technical Targets

- > 99.9% coulombic efficiency after cycle 1.
- > 500 cycles to 80% capacity in NMC full cells.
- > 5 mS/cm ionic conductivity at 25°C.
- > 1 mS/cm ionic conductivity at -30°C.
- Oxidatively stable to 4.6V.
- Similar cost to carbonates.

Accomplishments

- Evaluation of over 180 additives in EC/EMC and PC/EMC formulations (EC=ethylene carbonate, EMC=ethyl methyl carbonate, PC=propylene carbonate).
- Initial identification of additives that significantly improve PC/EMC performance in full cells.
- Evaluation of combinations of over 20 high dielectric constant solvents and over 20 low viscosity solvents with initial additives.
- Identification of most promising solvent combinations for further optimization.
- Repeat testing of all favorable compositions to ensure benefits.

◆ ◆ ◆ ◆ ◆

Introduction

Improvements in energy density are vital for mass market adoption of electric vehicles. At present, commercial vehicle batteries employ cells based on $LiMO_2$ (M = Mn, Ni, Co), $LiMn_2O_4$, and/or $LiFePO_4$ coupled with graphite anodes. Next-generation cathode candidates include materials with higher specific capacity or higher operating voltage, with a goal of improving overall cell energy density. However, to achieve substantial increases in cell energy density, a higher energy density anode material is also required. Si anodes demonstrate very high specific capacities, with a theoretical limit of 4,200 mAh/g and state-of-the-art electrodes exhibiting capacities greater than 1,000 mAh/g.

Si-based anodes suffer from major disadvantages relative to graphite. First, during cycling, Si exhibits a volume change of up to 300% (vs. 5-10% for graphite), causing severe mechanical stress and electrical disconnection of particles. This mechanical stress can be managed by careful control of particle size/morphology, including nanoparticles, nanowires, and nano-pillared materials. Such nanostructured materials have high surface areas (e.g., >10 m^2/g) and often require a composite matrix to prevent electrochemical sintering. Second, carbonate-based electrolyte formulations do not form a stable SEI on Si, with subsequent high irreversible capacity losses and poor cycle life (typically >15% and <100 cycles, respectively).

Approach

This project consists of three stages. In the first, an additive package was developed in a PC. PC does not form a stable SEI on the anode, so the effect of additive(s) on the resulting SEI will be measureable. Once the promising additive package was identified, new solvent candidates were enabled. Therefore, the second stage consists of identification of novel solvents that maintain good first cycle capacity and coulombic efficiency, and also have good capacity retention with the new additives. The development of an effective additive package to form an SEI practically enables electrolyte solvents that might not otherwise be considered, and substantially increases the number of potential candidates. Finally, optimization of the electrolyte is necessary to ensure that the final solution can meet all of the PHEV/EV cell level goals, including ionic conductivity and oxidative stability to 4.6V.

In order to consider a large number of additives, solvents, and salts, Wildcat is utilizing its novel high throughput work flow. This enables the testing of large numbers of formulations in full cells. In addition, Wildcat has extensive experience in experimental design in a complex formulation space.

Results

Primary additive screening in EC/EMC: While the objective of this project was to identify noncarbonate electrolyte formulations, additives were initially screened in an EC/EMC (1:2), 1M $LiPF_6$ baseline electrolyte in NMC/Si full cells. This enables comparison of results for this set of additives with 1) those obtained in EC/EMC electrolyte in NMC/graphite cells and 2) those obtained in PC/EMC formulations in NMC/Si cells. In all additive screens, first cycle capacity and coulombic efficiency (CE) are used as primary metrics. Formulations resulting in decreased capacity and CE relative to the baseline (no additives) are not considered further. Therefore, capacity retention data shown throughout this report are only presented for formulations that show first cycle capacity and CE similar to the control. Figure V - 129 shows a subset of the capacity retention results for several additive categories. The green band in Figure V - 129 represents +/- one standard deviation around the mean for the baseline EC/EMC electrolyte with no additives. All screening was performed on NMC//Si full cells cycled from 2.8-4.2V.

Primary additive screening in PC/EMC: The same set of electrolyte additives were also screened in a base electrolyte that contains no EC. In this case, the base electrolyte, PC/EMC (1:4), 1M $LiPF_6$, does not form an effective SEI layer. Therefore, performance improvements due to additive effects on SEI can be clearly differentiated. Again, first cycle capacity and CE were used to eliminate formulations with negative effects. The capacity retention on cycling was then determined for the remainder of the formulations. A subset of the results is shown in Figure V - 130. The capacity retention on cycling of the baseline electrolyte (green band) is quite poor, as expected. All screening was performed on NMC/Si full cells cycled from 2.8-4.2V.

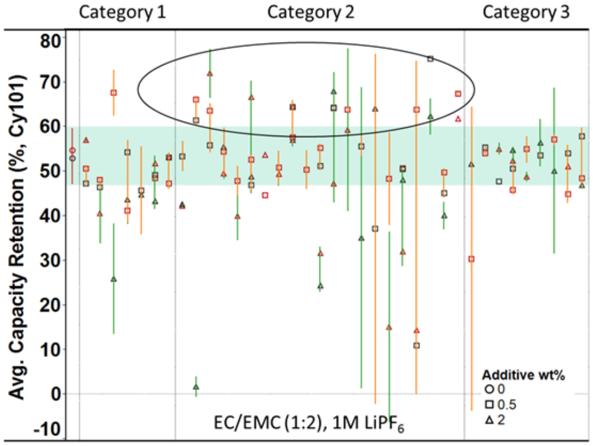

Figure V - 129: Category 2 additives improve cycle life in EC/EMC formulations

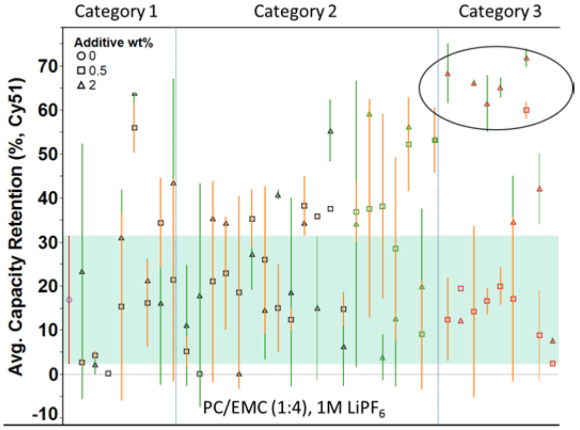

Figure V - 130: Category 3 additives improve cycle life in PC/EMC formulations

For this subset of results, it is of interest to note that the chemistry categories demonstrate different cycle life enhancement in the two baseline electrolyte formulations. In EC-based formulations, Category 2 was a reactive monomer type additive family. These additives appear to have a synergistic effect with the EC on the SEI performance. However, no synergies can occur in the PC based formulation as the PC does not participate in SEI formation. Therefore, Category 2 additives do not show benefit in Figure V - 130. However, polymer based additives (Category 3) do benefit the PC based formulation. These polymer additives do not improve the cycle life in EC based formulations, most likely due to the fact that EC itself forms high molecular weight species upon reduction in the SEI. Thus, polymer additives that impart higher molecular weight species into the SEI in the PC based formulations are beneficial.

High dielectric constant (polar) solvent screening: The selection of solvent candidates for this project was based upon a number of factors considered to be "ideal" for the application, including: aprotic, liquid over useful temperature range, appropriate reduction potential (avoid SEI formation by solvent), appropriate oxidation potential (stable on cathode). In addition, the solvents were categorized as either high dielectric constant solvents (HD) or low viscosity solvents (LV). It is anticipated that a blend of these two categories is required, as most of the high dielectric constant solvents have a viscosity too high for practical use as a sole solvent in a battery. All screening was performed on NMC/Si full cells cycled from 2.8-4.2V.

Prior to cell testing, the electrolyte combinations were tested for salt solubility and electrode stability. All the high dielectric constants were blended with a low viscosity solvent (EMC) in ratios of 1:1 and 1:3, and all low viscosity solvents were blended with a high dielectric constant solvent (EC) in ratios of 1:1 and 3:1. These solutions were then formulated with $LiPF_6$ at *ca.* 1.0M. Any formulations which did not completely dissolve the salt or showed any signs of reaction (e.g., color change, precipitate) were eliminated from future consideration.

Electrode stability was also tested, as some of the high dielectric constants are expected to solubilize or soften the binders used in the anode and cathode. Thus, a small piece of each electrode was soaked in each of the formulations. Any formulations that showed a residue or changes in the electrode were removed from further study.

Electrochemical screening of the non-carbonate solvents was done using the following design. First, 20 high dielectric constant solvents were blended with EMC at a single ratio (previously shown to have adequate $LiPF_6$ solubility). These solvent blends were screened in cells with the five best single additives (two concentrations) identified previously. Similar to the additive screening, formulations with significantly reduced first cycle capacity and/or CE were eliminated from further study. Capacity retention on cycling for the five best formulations is shown in Figure V - 131. The combination of cycle 1 capacity and capacity retention on cycling for a number of electrolytes vs. the control (gray bands) is shown in Figure V - 132.

Low viscosity solvent screening: Based on this analysis, the six best performing HD solvents were selected for further screening. These six solvents were blended with 22 low viscosity solvents (single ratio) containing a single additive. Capacity retention results are shown in Figure V - 133, along with first cycle capacity. Cycle life curves for some of the best performing non-carbonate formulations containing single additives are shown in Figure V - 134.

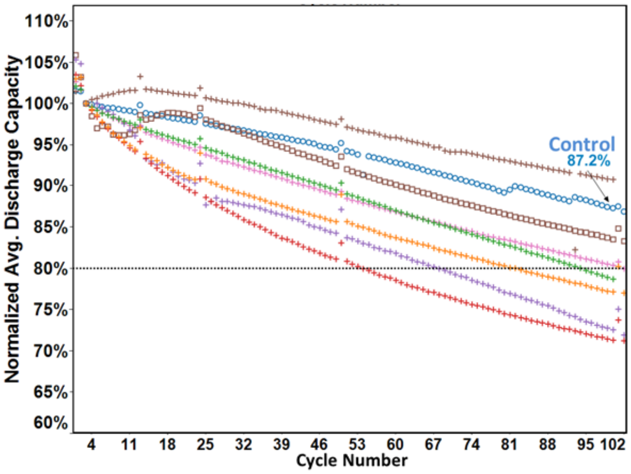

Figure V - 131: Several HD solvents/EMC blends with single additives perform similarly to baseline EC/EMC electrolyte

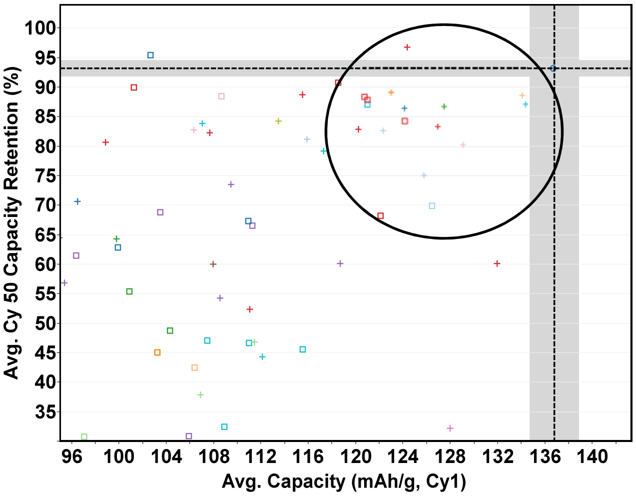

Figure V - 132: Promising HD solvents/EMC formulations show similar capacity and cycle life to control EC/EMC electrolyte

To date, more than 3,000 full cells have been tested to identify both promising SEI additives and solvents for use in NMC/Si full cells. Initial lead candidates have been selected for further combinations and optimization. In addition, specific additives are being synthesized to test hypotheses regarding effects on the mechanical and electrochemical stability of the resulting SEI.

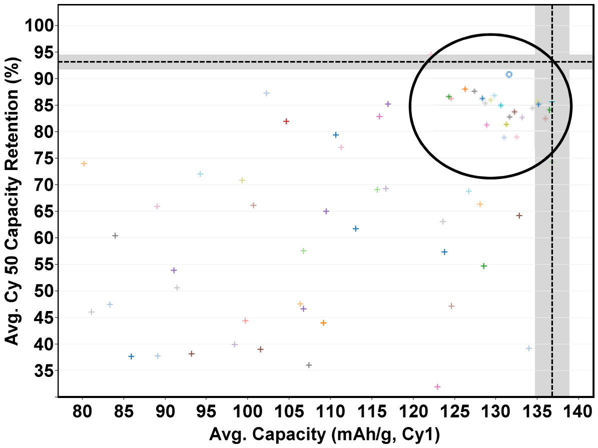

Figure V - 133: Promising non-carbonate HD solvent/LV solvent combinations perform similar to the EC/EMC control

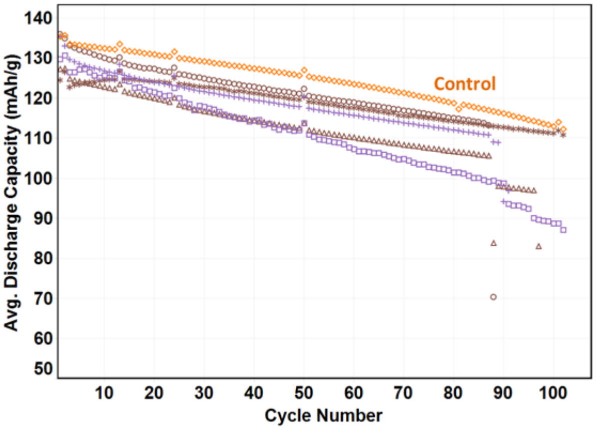

Figure V - 134: Cycle life of selected non-carbonate electrolyte formulations relative to EC/EMC control

Conclusions and Future Directions

Wildcat is in the second phase of the approach outlined above. Initial additives identified as effective SEI formers in PC-based electrolyte formulations were used to screen alternative non-carbonate solvents. Several of the non-carbonate formulations perform similar to the control EC/EMC electrolyte, with only a single additive.

The project will focus next on further screening of additional solvent formulations. In addition, alternative salts and co-salts (to $LiPF_6$) are currently under evaluation. As mentioned previously, new additives are being synthesized to test hypotheses and further demonstrate structure-property relationships. These hypotheses were described in Wildcat's original proposal, and emphasize the influence of additives to enhance mechanical stability of the SEI layer. Therefore, reactive monomers and higher molecular weight polymers will be fully evaluated. Once these experiments are completed, combinations of effective solvents and additives will be evaluated. It is anticipated that co-solvents and combinations of additives will further improve the NMC/Si cycle life.

Finally, phase 3 of the project will address optimization of the best formulations to maximize ionic conductivity and high voltage stability. This may involve the use of additional salts, co-solvents, and additives.

Throughout the course of this project, 3M electrodes (NMC and silicon alloy anode) are used for all screening of solvents, salts, and additives. In the second year of the project, additional silicon materials may be tested with the best formulations to test the robustness of the solutions.

FY 2014 Publications/Presentations

1. Strand, D. (June 2014). "Novel Non-Carbonate Based Electrolytes for Silicon Anodes." Presented at the 2014 DOE Annual Merit Review and Peer Evaluation Meeting, Washington, D.C.
2. Strand, D. (September 2014). "Development of Non-Carbonate Based Electrolytes for Silicon Anodes." Presented at the 2014 Battery Show, Novi, MI.
3. Three provisional patent filings filed on Apr. 15, 2014.

V.E Cell Analysis, Modeling, and Fabrication

V.E.1 Predicting Microstructure and Performance for Optimal Cell Fabrication (BYU)

Dean Wheeler
Brigham Young University

Department of Chemical Engineering
350 Clyde Building
Provo, UT 84602
Phone: (801) 422-4126
E-mail: dean_wheeler@byu.edu

Brian Mazzeo (Co-PI)
Department of Electrical and Computer Engineering
459 Clyde Building
Provo, UT 84602
Phone: (801) 422-1240; Fax: (801) 422-0201
E-mail: bmazzeo@ee.byu.edu

Start Date: October 2012
Projected End Date: September 2016

Objectives

- Develop rapid, reliable, and standardized methods for measuring electronic and ionic conductivities in porous electrodes.
- Determine and predict microstructures for porous electrodes.
- Understand tradeoffs and relationships between fabrication parameters and electrode performance.

Technical Barriers

One main technical barrier to improved battery performance is an insufficient understanding of electrode conductivity and spatial variability. Within a cell there are inhomogeneities on multiple length scales, from sub-particle size up to hundreds of microns and across the width of full rolls of commercially-prepared electrode films. New approaches must be devised to quantify and better understand these variations. Additionally, while, X-ray tomography (nano-CT) and SEM/FIB can be used to determine a few Li-ion electrode microstructures at a very fine resolution, a 3D microstructure prediction model needs to be developed to routinely generate structures for new materials and fabrication conditions, especially over much larger length scales. Because electronic and ionic transports take place in different phases that cannot occupy the same volume, new experimental and modeling techniques are needed to bring greater clarity to the relationships between electrode composition and morphology.

Technical Targets

- Measure variability and average electronic conductivity for five candidate electrode compositions using four-line probe.
- Ensure that probe measurement variability is significantly less than sample-to-sample variability.
- Measure microstructure of three candidate electrodes using SEM/FIB.
- Determine appropriate sets of descriptors or metrics that effectively characterize previously observed microstructures.

Accomplishments

- Electronic conductivity probe and testing protocol have been refined to include a computer-controlled test fixture with pressure control and measurement repeatability.
- The numerical inversion procedure has been sped up to allow real-time conductivity measurement.
- Multiple electrode samples have been sourced from A123 and ANL and tested for conductivity variations.
- Preliminary microstructure analysis (in preparation for microstructure model in FY2015) has been completed.

✧ ✧ ✧ ✧ ✧

Introduction

A great deal of effort is expended by battery researchers and battery manufacturers worldwide to develop improved materials for Li-ion storage batteries; yet greater understanding is necessary in order to best turn those materials into composite porous electrodes with optimized and uniform performance. A lack of fundamental understanding about the relationships between fabrication parameters, microstructure, and performance prevents appropriate feedback and hurts the development of next-generation battery materials and process improvement in battery manufacturing.

Either experimental measurements or predictive models can be used to make the processing-structure-property connection for battery electrodes. In this project, both are used. The effort on this project is intended to be general and system-agnostic, but must of necessity focus on a few key materials in a validation and test environment. For this reason, synergistic collaborations with other researchers, for example, at ANL and A123 Systems, are an important part of this work.

Approach

The general approach of this project is to use particle-based microstructural modeling, coupled with extensive experimental validation and diagnostics, to understand relationships between fabrication processes, microstructure, and corresponding electron and ion transport in composite electrodes. The fabricated probes will be used to assess electronic and ionic conductivities of porous electrodes attached to current collectors, including local heterogeneities and anisotropic effects, through the use of newly designed instrumentation. The measurements will be used to validate and parameterize the particle model using experimental microstructural and macroscopic properties. Then, these modeling and diagnostic tools will be used to suggest processing conditions that will improve cell performance. In FY2014, the focus was on validating the local electronic conductivity probe and performing preliminary analysis necessary for the forthcoming microstructure model.

Results

Materials: BYU has received electrode materials for testing from ANL, A123, and Hydro-Quebec. These include Toda HE5050 and 523 cathodes and graphite anodes from ANL. Not all received materials were tested in FY2014; the key results are given later. In addition, for validation purposes a conductive sheet made of carbon-impregnated silicone was obtained from Parker Chomerics and tested using the conductivity apparatus.

Refinement of four-line-probe design: The planar probe design allowed the surface of the probe to be placed directly upon electrode materials and thus allow an even pressure to be applied to the films while remaining mechanically robust. Prototype micro-four-line probes were fabricated in the BYU Cleanroom as described in the FY2013 report. Improvements to the design were continued in FY2014. This includes refinements of the masking and plating steps to produce metal lines of the desired configuration. Different versions of the probe with varied geometry were produced and tested. In each case, the geometry is designed to sample local values of electronic conductivity and contact resistance with the current collector. The probes do this without being unduly influenced by the stray current passing through the current collector metal film.

Construction of automated measurement apparatus: To consistently make measurements with the fabricated four-line-probe, an apparatus was constructed to make automated measurements. As shown in Figure V - 135, the electrode material was mounted on an X-Y stage with a force gauge under the target position. Then, the wafer probe was clamped in an inverted configuration to a Z-axis stage that descended on the electrode material. The entire measurement procedure with current source and multimeters was controlled using a computer control and data-logging interface. The design of this apparatus was finalized at the beginning of FY2014, and has been shown to produce consistent results in terms of measurement repeatability.

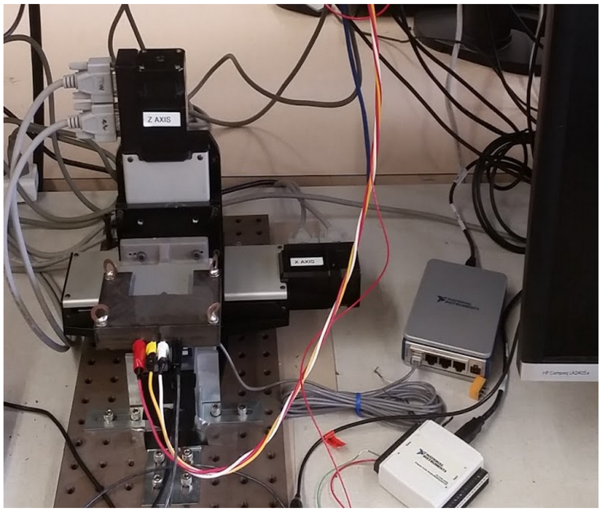

Figure V - 135: Measurement apparatus for electronic conductivity measurements. The probe wafer is clamped in an inverted orientation to an aluminum block that descends upon the electrode target. Electrical connections are made to the exposed connection pads. The electrode film target is mounted on a disc that is attached to a force gauge to measure and allow the control of the applied pressure

Numerical inversion procedure: To be able to properly interpret the micro-four-line probe measurements, a numerical inversion procedure was developed. In FY2013 the inversion procedure used COMSOL finite element simulations of the conduction paths. However, in FY2014, an analytic solution to Laplace’s equation was completed. This allowed a large increase in the speed of the mathematical model, allowing the inversion process to take place in real time in a desktop computer. In combination with experimental voltage and current data, the model allows simultaneous determination of bulk conductivity and contact resistance with the current collector and external probes.

Conductivity variation on commercial films: Conductivity variations were determined for 5 candidate electrodes. The results are summarized in Table V - 6. In the table, uncertainties indicate spatial variability across a 3mm x 3mm sample, not uncertainty in the probe measurements themselves. The average values determined here are consistent with reported values for similar materials and alternative measurement techniques. Another conclusion one can reach is that even for commercial-grade electrodes there can be significant spatial variability in conductivity performance.

Table V - 6: Summary of conductive properties and spatial variability for commercial-grade candidate electrodes

Electrode Sample	Bulk Electronic Conductivity (mS/cm)	Current collector interfacial contact resistance (Ω cm²)
NCM (A123)	76.73 ± 29.47	0.0703 ± .0121
LFP (A123)	14.24 ± 1.26	
Graphite Anode (A123)	4009.76 ± 844.97	0.0474 ± 0.0017
Toda 523 (ANL)	229.66 ± 33.37	0.0448 ± 0.0033
Toda HE5050 (ANL)	13.95 ± 1.55	0.116 ± 0.011

Table V - 7: Validation of micro-four line probe by other conductivity measurement methods for conductive polymer sheet

Method	Bulk Electronic Conductivity (mS/cm)
Van der Pauw	265.4 ± 1.1
Four-Line-Probe	276.5 ± 16.4

Method	Current Collector contact R (Ω cm²)
Direct	0.134 ± 0.028
Four-Line-Probe	0.146 ± 0.008

Figure V - 136 shows, for the Toda 523 example material, the analysis used to construct the results in Table V - 6. As shown in part A, the repeatability of measurements at single locations was very high, and was made by repeatedly lifting the probe off the sample and returning it to the same location. On other hand there was significant conductivity variability at different X-Y locations on the film (analyzed on a grid with 1-millimeter spacing). A more complete study of such spatial variations is planned in FY2015.

Table V - 7 shows results from a validation study of the probe using a commercially available conductive polymer sheet (Parker Chomerics), in this case meant to imitate a battery electrode. This material was used because it is not attached to a current collector and, it was hoped, would have more uniform properties. Results from the four-line probe were compared to the van der Pauw technique and contact resistance measurements based on sandwiching variable numbers of film layers between copper plates. The agreement between the different methods is satisfactory.

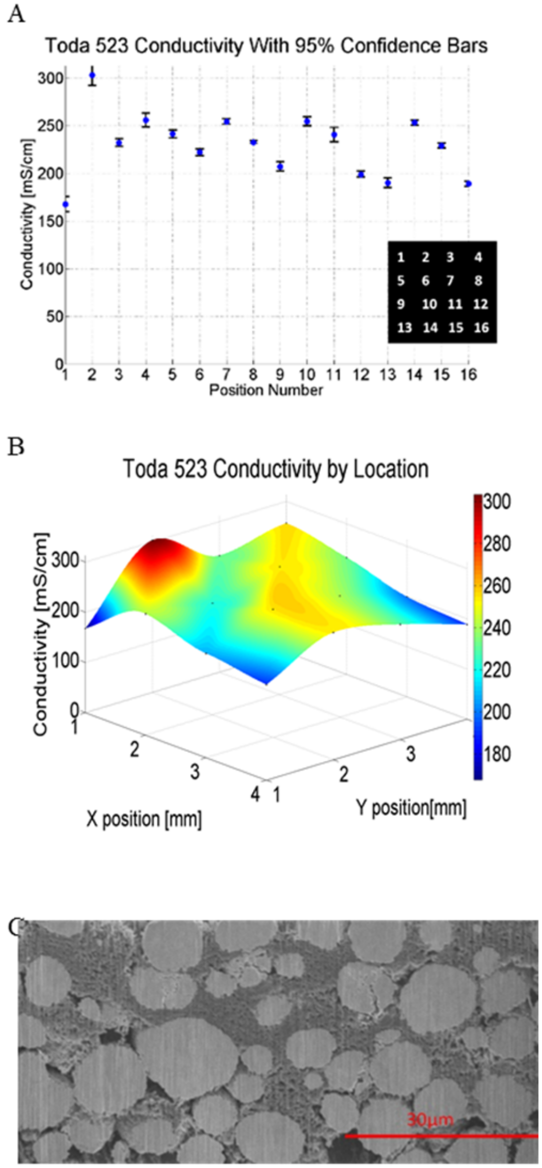

Figure V - 136: Analysis of Toda 523. (a) Conductivity (with 95% confidence intervals based on repeated sampling) of multiple locations on a 3 mm x 3mm grid (shown on inset). (b) Resulting conductivity map, showing significant spatial variability of the sample electrode compared to probe variability. (c) FIB/SEM cross-section of material used for structure analysis

Determination of metrics for analyzing structure of candidate electrodes: In preparation for the structure modeling milestones of FY 2015, metrics capable of describing relevant information from the electrode structure were developed. The primary metrics are volume fraction of phases, voxel contact probabilities, Fourier spectra, and geometrically computed ionic and electronic conductivities. To date, cathodes containing Toda 523 and Toda 5050 active materials have been examined by means of these metrics.

Figure V - 136c shows an example cross section that can be used for analysis, obtained by FIB/SEM. Significant effort was expended to develop satisfactory image processing algorithms for these materials. The algorithm is used to segment such images into three phases: active material, nanoporous carbon/binder domains, and macroscopic pores. These segmented images can then be analyzed according to key structural metrics. These data allow validation of microstructural models. They can also be used to correlate with experimentally observed conductive properties

Conclusions and Future Directions

One and a half years of the four-year contract are now completed. The work has met all milestones and technical targets for FY 2013 and 2014. Iterations of the micro-four-line-probe device and associated computer model took place during the year, leading to improved utility of the design. The accuracy of the method was validated using other techniques. Preliminary analysis of conductivity variations in commercial-grade electrodes was completed. This included both anodes and cathodes. Looking forward, materials obtained from multiple sources, including BATT researchers, will continue to be tested in this fashion, and transfer of the technology to commercial enterprises is being pursued.

Significant advancements are expected over the coming fiscal year in the following two areas: (1) extension of the micro-four-line-probe concept to the measurement of ionic conductivity, and (2) development of a particle-based predictive microstructure model. The extension to ionic conductivity will allow a comparison of local ionic and electronic conductivities to determine tradeoffs that affect cell performance. Furthermore, in many cases, such as for anodes, there is strong evidence that ionic conductivity is the more limiting of the two conductive properties. The development of the microstructure model will allow a better understanding of how fabrication steps, including slurry application and drying, determine the resulting microstructure and hence cell performance. Preliminary simulations and validation studies for the model are already underway.

FY 2014 Publications/Presentations

1. Wheeler, D.R.; Mazzeo, B.A. (June 2014). “Predicting Microstructure and Performance for Optimal Cell Fabrication.” Presented at the 2014 DOE Annual Merit Review and Peer Evaluation Meeting. Washington, D.C.
2. Lanterman, B.; Flygare, J.; Cutler, A.; Mazzeo, B.A.; Wheeler, D.R. (October 2013). “Development of a micro four-line probe for the measurement of thin-film battery electrode conductivity.” Presented at the 224th ECS Meeting, San Francisco, CA.
3. Mazzeo, B.A.; Lanterman, B.; Flygare, J.; Cutler, A.; Gates, N.; Wheeler, D.R. (November 2013). “Conductivity measurements of thin-film battery films.” Presented at the 3rd SHPE Engineering Research Symposium, Indianapolis, IN.
4. Zielke, L.; T. Hutzenlaub, T.; Wheeler, D.R.; Manke, I.; Arlt, T.; Paust, N.; Zengerle, R.; Thiele, S. (2014). “A combination of x-ray tomography and carbon binder modeling: Reconstructing the three phases of $LiCoO_2$ Li-ion battery cathodes,” *Adv. Energy Mater*.; p. 1301617.
5. Lanterman, B.; Flygare, J.; Cutler, A.; Gates, N.; Mazzeo, B.A.; Wheeler, D.R. (March 2014). “Probing local conductivity variations in particle-based electrodes.” Presented at the Gordon Research Conference on Batteries, Ventura, CA.
6. Nevers, D.R.; Peterson, S.W.; Robertson, L.; Chubbuck, C.; Flygare, J.; Cole, K.; Wheeler, D.R. (2014). “The effect of carbon additives on the microstructure and conductivity of alkaline battery cathodes.” *J. Electrochem. Soc.* (161); pp: A1691-A1697.
7. Peterson, S.W.; Wheeler, D.R. (2014). “Direct measurement of effective electronic transport in porous Li-ion electrodes.” *J. Electrochem. Soc.* (161); pp: A2175-A2181.

V.E.2 Assembly of Battery Materials and Electrodes (IREQ)

Karim Zaghib
Hydro-Québec (IREQ)

1800 Lionel Boulet
Varennes, QC J3X 1S1, Canada
Phone: (450) 652-8019; Fax: (450) 652-8204
E-mail: Zaghib.Karim@ireq.ca

Start Date: October 2012
Projected End Date: September 2016

Objectives

- Develop high-capacity, low-cost electrodes with good cycle stability and rate capability to replace graphite in Li-ion batteries.
- Identify an alternative supplier of Si powder material as baseline for the BATT Program.
- Fabrication of large format stacking Li-ion cells of 21 Ah capacity based on Si-anode and LiMnNiO cathode.

Technical Barriers

The technical barriers to overcome are the electrochemical capacity limitations (both gravimetric and volumetric) of conventional carbon anodes by developing low-cost electrode architectures based on Si. One of the biggest challenges for this anode material is its volume expansion and structural changes which lead to capacity fade and shorter cycle life.

These failures are due in part to loss of electrolyte by reduction and a SEI that is not stable on the surface with repeated cycling due to the exposure of fresh surfaces of Si particles.

Technical Targets

- Redesign the anode architecture based on Si-nano produced at Hydro-Québec (HQ).
- Design the architecture of the high-voltage cathode (LMNO) to match with anode.
- Identify the optimum parameters for large-scale electrodes fabrication.
- Deliver laminate electrodes and large format Li-ion cells (20 Ah) to BATT PIs.

Accomplishments

- Successfully produced kgs of Si-nano at HQ facility and shipped 1 kg to BATT PIs.
- Si-nano electrodes were successfully redesigned that demonstrated > 200 cycles at 40% DoD with reversible capacity of 1600 mAh/g.
- Laminated Si-electrodes (10 m) were shipped to BATT PIs.
- Large format stacking cells with 21 Ah capacity and Si-nano/LMNO chemistry were shipped to BATT PIs.

* * *

Introduction

The target of the BATT Program is to identify the next generation of high-energy batteries. Achieving this target will require materials of higher capacity and improved coulombic efficiency or cells with higher voltage. High-capacity anode materials such as Si or Sn alloys have the potential to fulfill the energy density requirements for EV/PHEV applications. However, large volume expansion during the lithiation process of these materials usually leads to a fast capacity fade that hinders its practical applications. Real-time SEM studies on charge/discharge of Si-anodes have demonstrated that decreasing the particle size to nanometer scale can be an effective means of accommodating the volume change.

HQ proposed a strategy to design the architecture of the Si-anode material that can tolerate the volumetric expansion and provide acceptable cycle life with low capacity fade. The particle size, binder type and electrode composition are the main parameters that define the formulation of the Si-anode. The porosity of the electrode has a direct impact on the performance, and therefore was optimized by investigating various mixing methods.

Approach

- Explore a variety of synthesis methods to produce low cost Si-nano materials with controlled purity and particle morphology. Develop an appropriate Si anode architecture that can tolerate volumetric expansion and provide an acceptable cycle life with low capacity fade.

- Identify a binder and an electrode composition by investigating parameters that define the electrode structure such as porosity, loading and electrode density. Use *in situ* techniques such as SEM and impedance spectroscopy to monitor the particle and electrode environment changes during cycling. The optimized Si-anode will be matched with high-voltage LMNO cathode to fabricate large format Li-ion cells.

Results

Si-anode: The binder type, mixing method and electrode loading are key parameters that control the architecture of the anode. These parameters affect its porosity and tortuosity. Other parameters can also affect the electrochemical performance of the electrode, such as the cut-off voltage, depth of discharge and cycling rate. It was found that monitoring the stress on Si-particles is another key parameter that affects the cycling performance, and studies identified the optimum range of anode composition (Si:Alginate:carbon) as between (50:25:25) and (60:20:20), which was expected to produce longer cycle life. The porosity of the electrode, which is strongly influenced by the electrode composition, is another major parameter affecting the electrode performance. A high carbon content and low Si ratio in the anode composition yielded significantly better performance. Therefore, to investigate the cycling life of this anode material, the formulation with (50:25:25) was adopted for an optimized Si-anode and electrode architecture by using the Si reference material from Umicore.

The effect of volume change on cycle life of the anode was determined as a function of the depth of discharge (DoD), which helps define the upper limit of the stress sustained by the particles. The stress level was controlled by varying the DoD; the Si particles will experience minimum stress at low DoD. This study clearly revealed the effect of DoD on the cycling stability. The capacity fade is severe when the anode is cycled at a high%DoD, which results in the particles experiencing high stress that induces cracks.

At 40% DoD, a very stable reversible capacity of around 1,670 mAh/g with good coulombic efficiency is obtained after 200 cycles at C/6 (Figure V - 137). This result indicates that sacrificing a little capacity is an acceptable compromise to achieve a longer cycle life and provides an acceptable anode for Li-ion cells.

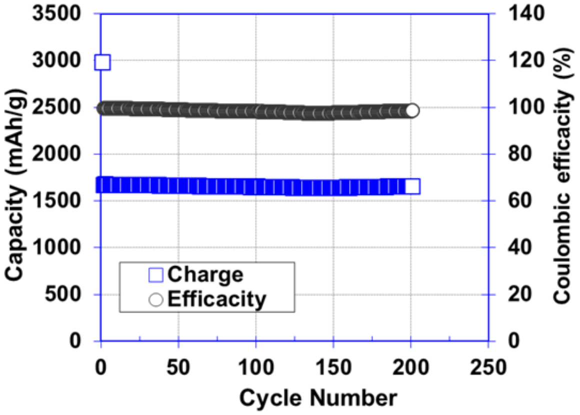

Figure V - 137: Cycle life at C/6 of Li/EC-DEC-1MLiPF$_6$/Si-nano cell at 40% DoD

Studies revealed that at 40% DoD a stable cycling life was obtained with good coulombic efficiency, however, with the cell cycled at 50% DoD, the capacity failed after less than 100 cycles. The discharge/charge curves for the first cycle and cycle 66 show clearly a different behaviour (Figure V - 138). When the cell is cycled at 100% DoD, the capacity fades rapidly and is comparable to the 50% DoD cell after 66 cycles. This result indicates that the capacity buffer is rapidly consumed when the particles and whole electrode experience high stress. Based on the stable cycle life obtained, a longer cycle life with an acceptable capacity of 1,600 mAh/g can be achieved if the threshold of the stress is controlled.

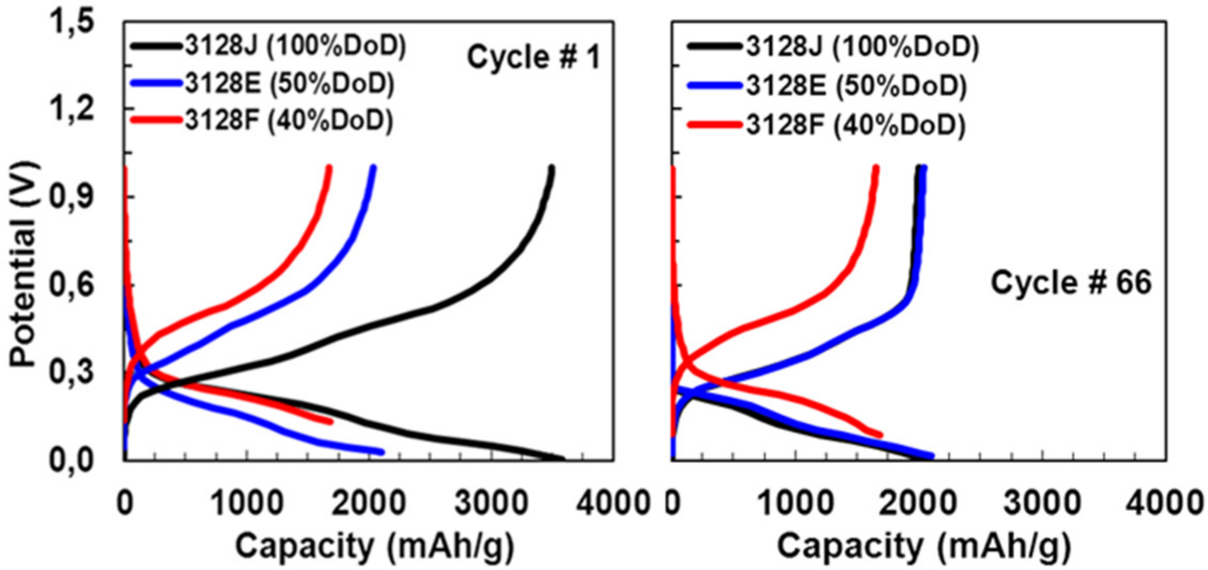

Figure V - 138: Discharge/charge curves at C/6 of Li/EC-DEC-LiPF₆/Si-nano cells for cycle 1 and 66 at different %DoD

The voltage profile of cells with stable cycle life was investigated. Cells cycled at less than what may be called the threshold stress (i.e., in this case 40% DoD), yielded a stable capacity and an improved end of life. However, when the voltage at end of discharge is shifted towards the cut-off voltage corresponding to 100% DoD (Figure V - 139), a stable capacity is not achieved.

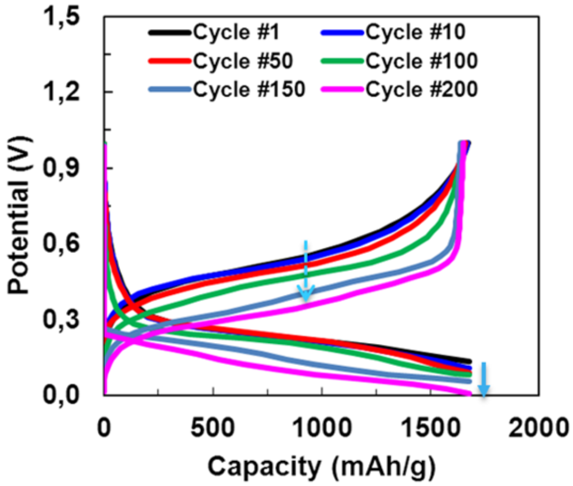

Figure V - 139: Voltage profiles of at C/6 of Li/EC-DEC-LiPF₆/Si-nano as function of cycle life

The volume change of the Si particles produced a loss of contact between the particles with cycling, and then the residual capacity between 40% to 100% DoD will be consumed. This finding was confirmed previously by *in situ* SEM, and the delamination and cracks were reduced by using smaller particles. With Si-nano particles, a high reversible capacity is obtained, but to achieve a much longer cycle life or a higher reversible capacity, further work is necessary to understand the failure mode. Impedance spectroscopy was used to monitor the interfacial resistance changes during the initial cycles to help improve the quality of the electrodes.

Impedance spectroscopy study: In order to improve understanding of the failure mode of the Si anode, *in situ* measurements using impedance spectroscopy were conducted. This technique is non-destructive and useful to study the electrochemical behavior of electrode materials and their interfacial properties, such as resistance and capacitance of SEI film formation. The first discharge/charge cycle was conducted at low rate (C/24) between cut-off voltages of 10 mV on discharge and 1.0 V on charge using EC-DEC-1M $LiFP_6$+2% VC as electrolyte. The impedance measurement was monitored continuously on discharge and charge at capacity rates of 20% based on theoretical capacity (Figure V - 140). The impedance was measured after each 10% DoD or charge (SOC).

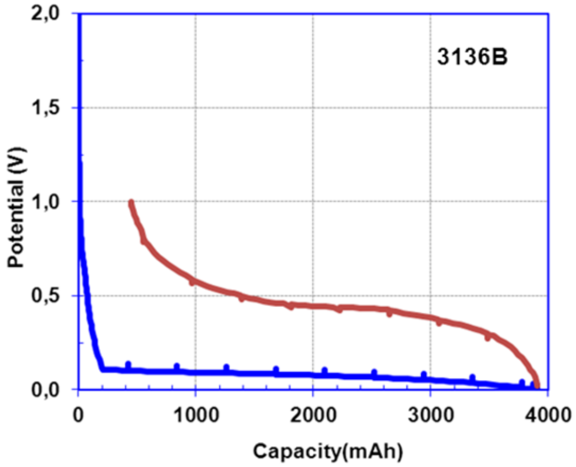

Figure V - 140: 1st discharge/charge curves at C/24 of Li/EC-DEC-LiPF6/Si-nano cells with positions where the impedance measurement were taken

Figure V - 141 shows typical impedance spectra with semicircles, and a tail at 0% DoD and 90 and 100% SOC, which implies mixed kinetics and diffusion process. It was observed that the internal resistance (R_{int}) on the discharge curve showed a small increase from 4.1 Ω before cycling to 4.5 Ω at 10% DoD, which is associated with SEI layer formation. However, this resistance doubled to 8.4 Ω at 20% DoD, then relaxed to 7.5 Ω at 100% DoD. This behavior is probably related to the volume expansion of the lithiated state. These results indicate that the major volume change occurred after 20% of lithiation, which corresponds to *ca.* 100 mV on the discharge plateaus. The charge transfer resistance (R_{tc}) decreased with increased lithiation from 146 Ω to 103 Ω, a sign of surface changes on the Si particles, such as breakdown of the thin resistive Si-O layer and an enhanced surface area due to volume expansion of Si particles.

This process is associated with an increased ionic conductivity and lower charge transfer resistance. On the other hand, when the cell is charged (delithiated), the R_{int} was reduced continuously to 2.7 Ω and 2.6 Ω, respectively, for 10 and 20% SOC, then to 2.2 Ω at 30% SOC and remains almost unchanged at SOC >30%. This decrease in R_{int} is probably related to the volume contraction of the delithiated Si particles after volume expansion during lithiation, and thus the particles are closer together. The biggest change occurs during the first 30% SOC. The R_{tc} continues to decrease from 98 Ω to 48 Ω when the Si-anode is delithiated at 10% and 80%, respectively, which demonstrates that cycling at lower depth of discharge is less stressful to the electrode.

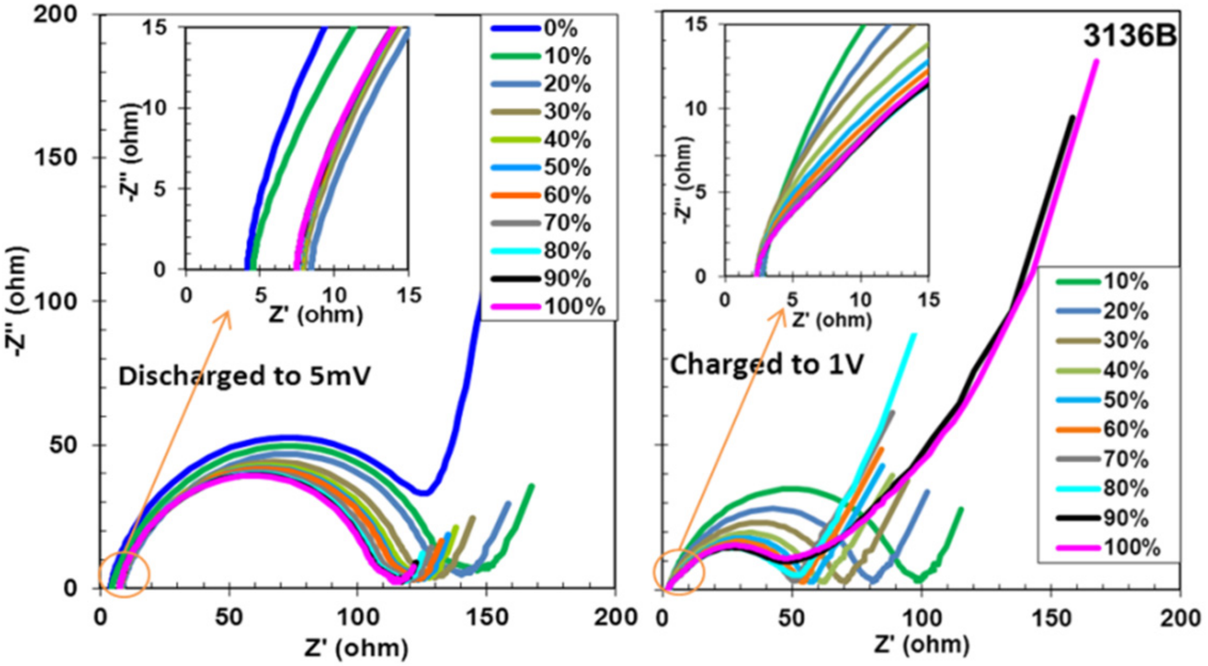

Figure V - 141: Impedance spectra of Li/EC-DEC-LiPF6/Si-nano cells at different states of discharge or charge

Large format Li-ion cell: The final part of this study to qualify this Si-anode material involved the assembly of large format stacking cells (21 Ah) using the HQ automatic assembly line. These cells are based on the high-voltage LMNO cathode and Si-nano anode, as defined by DOE.

Large films of anodes and cathodes were produced by the pilot coating machine at HQ. It was noticed that a gas was generated during anode film preparation due to the large surface area of the nano-Si. This material has high area and surface energy, which makes it extremely reactive with water. Thus, some precautions must be considered during slurry preparation and film coating (Figure V - 142). Parameters such as loading and electrode density were investigated in half-cells before assembling the full Li-ion cells.

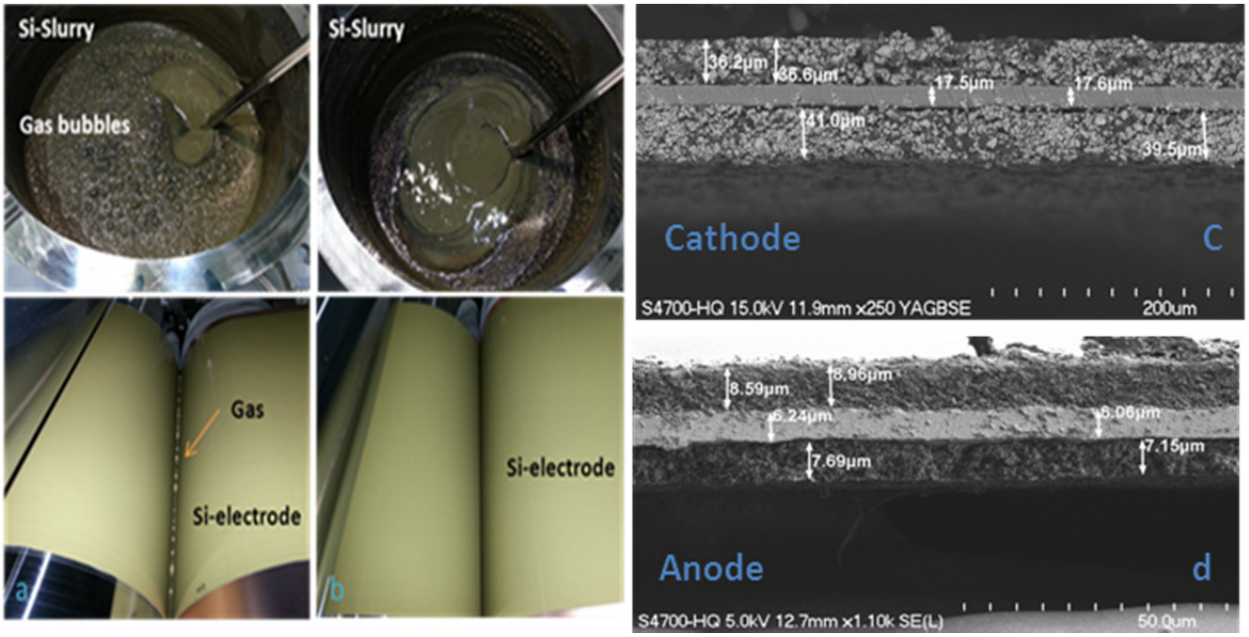

Figure V - 142: Slurry and electrode of Si-nano; a) after mixing, b) after 8 hours relaxing for degasing. SEM cross-section of cathode (c) and anode (d) used in 21Ah stacking cells

It was found that the Si-slurry must stand for a minimum of 8 hours to eliminate the gas bubbles. Based on the results of the anode, stable cycling was obtained at 40% DoD with a capacity of 1,600 mAh/g. This criterion was adopted to prepare the stacking cell.

This study identified the optimum critical parameters such as the anode loading and electrode cathode density. The high capacity of the Si-anode involves thin films having a thickness of about 10 µm per side, which makes the lamination step of the anode more critical. In addition, this high anode capacity requires a high cathode loading. The cathode thickness used in this cell configuration was about 4x that of the anode. Figure V - 142c and d show the SEM photos of the cross-section of the double side coating of the cathode and anode, respectively.

Since a new technology is being explored, many parameters were investigated, including the formation protocols. Cells with a capacity of 21Ah were successfully assembled (electrolyte composition EC/DEC-1M$LiPF_6$-10%FEC) using the pilot-stacking line machine at HQ. To achieve this capacity, 35 anode films and 34 cathode films were automatically stacked together.

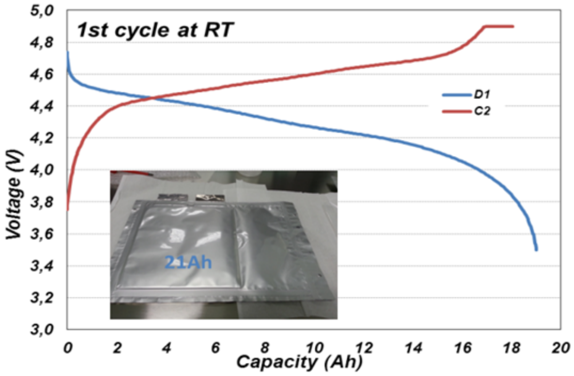

Figure V - 143: Charge/discharge curves of Si-nano/Li/EC-DEC-FEC-$LiPF_6$/LMNO stacking cell (21Ah) between 4.9V and 3.5V at RT

Different formation protocols were used to maximize the reversible capacity, such as cut-off voltage, temperature and degassing steps. Figure V - 143 shows the charge/discharge curves of the cell from 4.9 V to 3.5 V at RT. The highest reversible capacity obtained with different formation protocols is 19 Ah compared to the installed capacity of 21 Ah (90.5%).

One of the challenging problems is gas generation; it was observed that the gas was generated continuously with cycling up to 7 cycles, even after 3 degassing steps. This behavior with coin-type cells was not observed due to the small quantity of the active material. Therefore, since the optimizations studies were made with coin-type cells, a significant effort is needed to optimize the pouch-cell. It is thought that the use of aqueous media and the exposure of fresh Si surface during cycling are the main factors responsible for gas evolution. With this in mind, the binder and the formation protocols will be reevaluated to limit gas generation.

Conclusions and Future Directions

With Si-nano particles, high reversible capacity is obtained, but to achieve much longer cycle life requires improving the electrode architecture. The *in situ* impedance spectroscopy (IS) analysis and cycling studies on the Si-anode indicate that controlling the rated capacity by limiting %DoD improves cycle life. The net result is that stress is minimized and the mechanical integrity of the particles is maintained. The IS analysis shows R_{int} decreases, which indicates volume contraction of the delithiated Si particles after volume expansion (during lithiation) and the particles becomes closer together. The biggest change of the particles and their surrounding occurs during the first 30% of SOC. This study demonstrates that cycling at a lower depth of discharge is less stressful to the electrode. Thus, sacrificing some capacity could be an acceptable compromise to obtain Li-ion cells with a longer cycle life.

HQ proposes to continue development of high-energy batteries based on Si-nano material by improving the architecture of the anode and increasing its loading. It is proposed that optimization of the electrode composition be obtained by increasing the active material ration in order to increase the energy density. This effort will require further investigations of the binder, mixing protocol, and the further surface treatment of the Si-nano particles will also be considered.

FY 2014 Publications/Presentations

1. Zaghib, K. (June 2014). “Electrode Architecture – Assembly of Battery Materials and Electrodes.” Presented at the 2014 DOE Annual Merit Review and Peer Evaluation Meeting, Washington, D.C.
2. Liu, D.; Zhu, W.; Trottier, J.; Gagnon, C.; Barray, F.; Guerfi, A.; Mauger, A.; Groult, H.; Julien, C.M.; Goodenough, J.B.; Zaghib, K. (2014). *Review, RSC Adv*. (4); pp: 154–167.
3. Liu, D., Gagnon, C.; Trottier, J.; Guerfi, A.; Clément, D.; Hovington, P.; Mauger, A.; Julien, C.M.; Zaghib, K. (2014). *Electrochemistry, Communications* (41); pp: 64-67.
4. Wang, J.S.; Liu, P.; Soukiazian, S.; Tataria, H.; Dontigny, M.; Guerfi, A.; Zaghib, K.; Verbrugge, M.W. (2014). *Journal of Power Sources* (256); pp: 288-293.
5. Julien, C.M., Mauger, A.; Zaghib, K.; Groult, H. (2014). *Inorganics 2014* (2); pp: 132-154.

V.E.3 Predicting and Understanding Novel Electrode Materials from First-Principles (LBNL)

Kristin Persson
Lawrence Berkeley National Laboratory

Environmental Energy Technologies Division
1 Cyclotron Road
Berkeley, CA 94720
Phone: (510) 486-7218
E-mail: kapersson@lbl.gov

Start Date: October 2012
Projected End Date: September 2016

Objectives

- Model and predict the behavior of electrode materials from first-principles.
- Understand the atomistic interactions underlying the behavior and performance of the high-capacity lithium excess and related composite cathode materials.
- Predict new materials using the recently developed Materials Project high-throughput computational capabilities at LBNL.

Technical Barriers

Investigating electrode materials with atomistic modeling requires rigorous bench marking as well as insight into the materials chemistry and its effect on electrode performance. In case of Li-excess materials, it is challenging, as there are increased number of variables associated with the unknowns regarding possible composite or solid solution structure of the material, the amounts of each phase, synthesis procedure, etc.

Technical Targets

- Elucidate the phase space of the layered $L_{i2}MnO_3$, and associated defect spinel phases that can form as function of different Mn and Li sites and migration patterns.
- Understand the charging mechanism in $L_{i2}MnO_3$.
- Chart out and elucidate the transformation paths in $L_{i2}MnO_3$ as a function of charge.
- Increase the number of predicted battery compounds available on the Materials Project.

Accomplishments

- The redox mechanism in Li_xMnO_3 is found to be predominantly due to anion (oxygen) oxidation.
- Oxygen release is inhibited from the bulk region due to large oxygen migration barriers, but oxygen release on the surface is deemed possible.
- The voltage profile of defect-layered Li_xMnO_3 shows qualitative agreement with the voltage fade shown in experiments.
- To minimize the driving force for Mn migration (and subsequent voltage fade) it is recommended that the activation and charge be kept below 4.7 V so that no (even local) region of the material reaches $x_{Li} < 0.5$.

✧ ✧ ✧ ✧ ✧

Introduction

There is increasing evidence that many of the performance limiting processes present in electrode materials are highly complex reactions occurring at the atomic level. The Persson BATT effort at LBNL is studying these processes using first-principles density-functional theory modeling tools. By understanding the underlying reasons for the electrode materials' working performance, improvements or design schemes can be directed at the root cause of the process.

The composite cathode materials show great promise for high voltage and high capacity, however, they also present voltage fade, structural degradation and safety concerns. The voltage and capacity fade of the composite cathode materials are due to 1) possible dissolution of the transition metal ions and 2) structural transformation reactions as a function of rate and cycling. There are safety concerns relating to oxygen loss and electrolyte breakdown. All these aspects will in turn be addressed in this project. During the first year the main focus was to understand the structural and chemical changes in the layered Li_2MnO_3 structure, which is a key material to explain the high capacity in layer-layer or layer-spinel composite electrode materials. Layered Li_2MnO_3 has been assumed to be largely electrochemically inactive due to the high oxidation state of Mn (4+ in the discharged state). Additions of Li_2MnO_3 to other spinel and/or layered materials have been used to increase the structural stability of the composite materials and allow more Li extraction than for the layered or spinel materials alone. However, many recent experimental works have shown that the Li_2MnO_3 component is actually electrochemically active, which demands a re-examination of the conventional belief on the structural and chemical behavior of Li_2MnO_3 and the existing explanation of the origin of high capacity in the composite materials.

Approach

The Persson Group uses atomistic modeling to study the relevant thermodynamic and kinetic processes. The calculations are performed at NERSC and on the Lawrencium cluster at LBNL. To elucidate the atomistic interactions, first-principles zero-temperature calculations are employed and coupled with the cluster expansion technique to examine the structural and chemical space, establish ground states, and resulting electrochemical signature of the materials. To examine temperature-induced properties, statistical mechanics and kinetic Monte Carlo methologies are utilized.

Results

Structural transformation of Li_2MnO_3: In the 2013 Annual Report, it was reported that the structural deviations of Li_xMnO_3 significantly increase with the amount of Li extracted from the compound, especially at $x_{Li} < 1$. Furthermore, in the low Li content region ($x < 1$), it was noted that all stable structures are defect-layered supporting experimental evidence that Li_2MnO_3 and related materials are at far from equilibrium when activated. In all these defect-layered structures, a fraction of Mn ions are displaced to the Li-layer which implies a strong driving force for the pristine material to exhibit Mn migration into the Li-layer.

As part of the structural transformation, ionic migration patterns are investigated. The degree of ionic migration is determined by thermodynamic as well as kinetic factors, which means that the migration could be slow enough for material to retain its original structure during fast Li-extraction even if the structure is thermodynamically unstable. In this respect, Mn migration energies are calculated to characterize the transformation. The elastic band method is employed for several different hypothesized Mn migration paths at several different Li contents. The charge and positions of the ions along the transformation paths have been analyzed, as well as for the included larger supercells to benchmark the conclusions. From these calculations, the Mn^{4+} ion is predicted to move rapidly to the Li layer, if Li is almost depleted (even locally) through a local cooperative displacement of the oxygen environment. Two paths were examined, as a function of state-of-charge; the dumbbell path and a direct transition through an oxygen edge. While the dumbbell path exhibits sluggish but feasible migration energetics for x=1, the edge path becomes almost mechanically unstable (Figure V - 144) for an almost depleted Li region. This indicates a severe structural instability of the material as Li is extracted at a high charge.

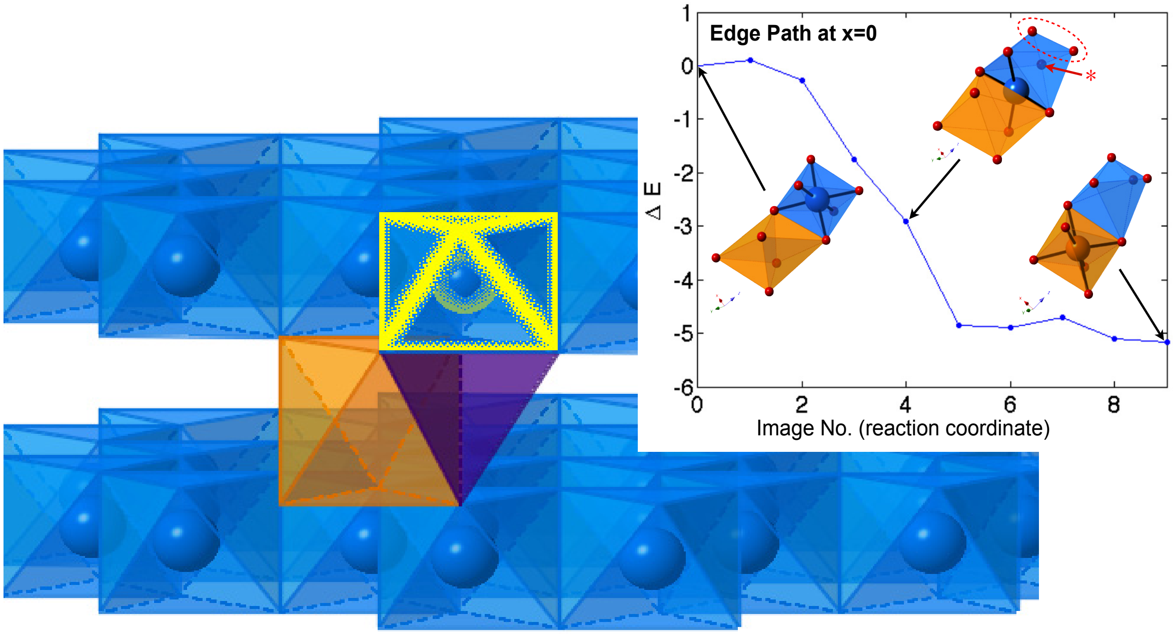

Figure V - 144: Illustration of a Mn migration path in Li_xMnO_3. Inset shows the Mn4+ activation energy as a function of path coordinate for migrating through the oxygen edge accompanied by a dramatic local oxygen bond stretching

Redox mechanism and possible oxygen release: To elucidate the activation process and the structural evolution of Li_2MnO_3 as a function of charge and discharge, the role of Mn and O in this process was investigated, using first-principles methods and a ternary cluster expansion.

For every extracted Li-ion in $L_{ix}MnO_3$, the charge of one electron should be compensated. To analyze whether these electrons are primarily originating from orbitals associated with Mn and/or O, the charge of each ion from the magnetic moment was calculated. Cognizant of the fact that the chosen DFT functional determines the degree of localization and charge sharing between the cations and anions, both the GGA, GGA+U and the HSE scheme were employed for a range of structures near the convex hull. A priori, it was expected that the GGA+U and the more computationally expensive HSE scheme, which uses Hartree-Fock hybrid functionals to provide better representations of the electron distribution in a Mn-O system, compared to the GGA. Indeed, a high level of consistency exists between the GGA+U and HSE results, which lends credibility to them. Using both descriptions of the many-body electron interactions, it was observed that Mn remains largely in the 4+ state and the majority of the redox activity occurs on orbitals primarily associated with the oxygen species.

Oxygen release has been suggested as another possible mechanism for charge compensation in Li_2MnO_3 during delithiation. To examine the thermodynamic stability of oxygen, the oxygen vacancy formation enthalpy was calculated (Figure V - 145). For each chosen composition ($0<x<2$) formation of an O^{2-} or O^{1-} (if applicable) vacancy was examined as a function of local cation environment and symmetry and we present only the lowest energy, most favorable, case. Figure V - 145 shows that oxygen vacancy formation, e.g., evolution from the material, is indeed favorable for $x<1$ and hence provides another possible mechanism for the material to compensate the charging process.

However, the oxygen release process is also dependent on favorable oxygen transport. While Li_xMnO_3 exhibits a thermodynamic instability towards oxygen release for $x<1$, the oxygen migration barriers (even for the O^{1-} species at high charge) were found to be too high which inhibits facile oxygen diffusion in the bulk region of the material. On the other hand, oxygen release in the surface region of the particles is deemed possible, where local under-coordination and strain may also facilitate the diffusion.

Voltage profile: To compare the findings, particularly pertaining to a presumed tendency towards defect layered phase transformation, to the experimental evidence of voltage fade, the evolving voltage profile of bulk Li_xMnO_3 was calculated. The voltage profile for the first charge process was obtained based on the intermediate stable structures that were predicted from the previous calculations (see the 2013 Annual Report), assuming that the original layered structure stays intact. To examine the voltage change as a function of the presumed structural evolution, the structure set was explored, as a function of increasing Li content, where all Mn ions belong to a spinel-nuclei (in a defect-layered phase). It was noted that it could not be predicted which of the defect-layered structures would first form, and it may be that a continuous degradation of the structure may occur as a function of cycling and increased number of migrated Mn, but the calculated voltage profile for the defect structures should follow the same discharge trend as found in experiments. The results are shown in Figure V - 146, where the calculated voltage profiles were compared to recent experimental work. Note that the charge and discharge process corresponds to decreasing and increasing x, respectively. The blue thick line indicates the voltage profile during the first charge, and clearly indicates that Li_2MnO_3 is activated at voltages above 4.5 V, in agreement with experiments. The discharge (red) curve corresponds to a scenario where the original structure has transformed to a defect phase, where a significant amount of Mn resides in the Li layer. This defect structure is substantially more stable at a high charge and less stable at high Li content, compared to the original layered structure. It is remarked that this structural transition alone (without any presumed oxygen release and/or creation of Mn^{3+}) can give rise to a significant voltage drop – compared to the first charge. At high charge (even locally), the defect migration and subsequent local re-arrangement of Mn is predicted to occur rapidly, and reverting back to the original phase at high Li content is kinetically impeded as the previous computation predicted high Mn activation barriers for that. Results indicate that the phase transformation can be suppressed if the voltage is maintained under ≈4.7 V and no part of the material reaches high charge or the critical composition $x<0.5$ where Mn migration becomes favorable. It is noted that the capacity obtained in experiments is significantly less than the theoretical maximum capacity and speculate that an increasing amount of the material becomes inactive.

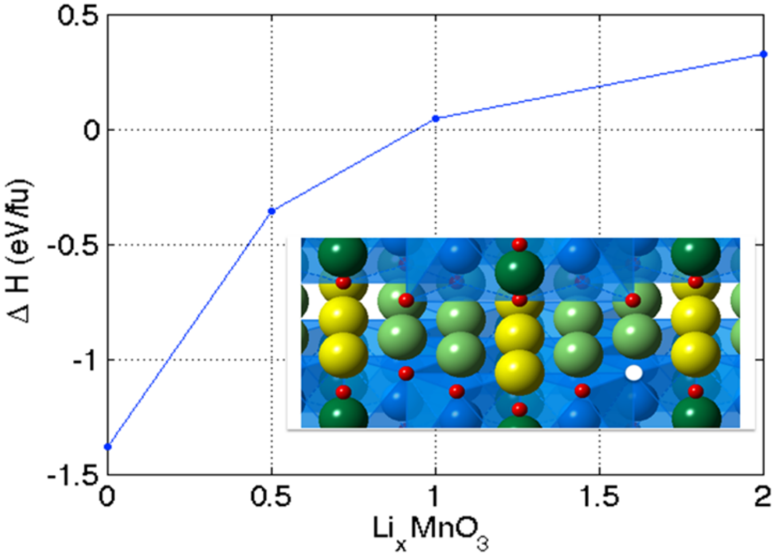

Figure V - 145: The lowest oxygen formation enthalpy as a function of charge state in Li_xMnO_3. Inset illustrates one possible vacancy in the lattice (white circle)

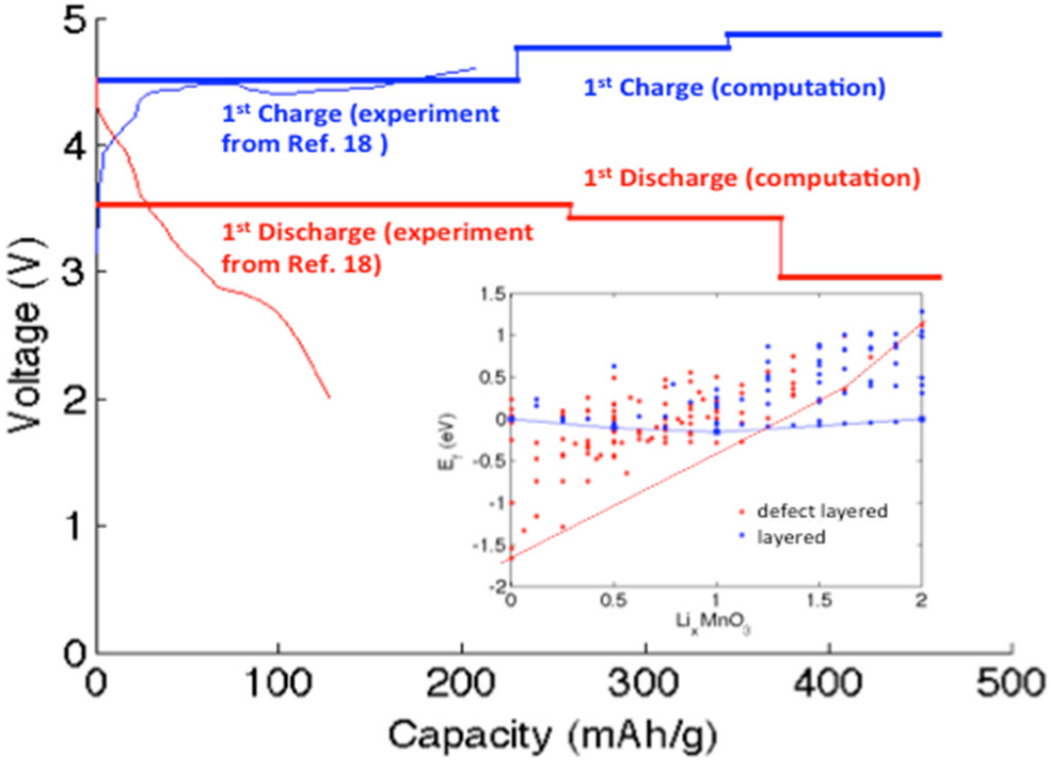

Figure V - 146: Voltage profiles of Li_xMnO_3 for the first charge (blue lines) and the discharge process (red lines) assuming a structural transformation, originating from Mn migration

Conclusions and Future Directions

It was found that the redox mechanism in Li_xMnO_3 is predominantly due to anion (oxygen) oxidation. Oxygen release is thermodynamically favorable for x<1 but is inhibited in the bulk region because of the large oxygen migration barriers. On the other hand, oxygen release from the surface is deemed possible. The voltage profile of defect layered Li_xMnO_3 shows qualitative agreement with the voltage fade shown in experiments. To minimize the driving force for Mn migration (and the resulting voltage fade) it is recommended that the Li concentration $x_{Li}>0.5$, even locally.

During year 1-2 the phase stability of Li_2MnO_3 and related layered and spinel defect structures was determined, and the instability towards Mn migration was established. For future studies, Li activation barriers for the pristine material will be obtained and also the most favorable defect structures as a function of Li content. Furthermore, stable crystal facets of the layered and spinel phases will be explored, as a function of O_2 release from surface and oxygen chemical potential.

FY 2014 Publications/Presentations

1. Persson, K. (June 2014). “Predicting and Understanding Novel Electrode Materials from First-Principles.” Presented at the 2014 DOE Annual Merit Review and Peer Evaluation Meeting, Washington, D.C.
2. Persson, K.; Lee, E. (March 2014). “Structural and Chemical Transformations in Li_xMnO_3 from First-principles.” Presented at the International Battery Association 2014, Brisbane, Australia.
3. Lee, K.; Persson, K. (2014). “Structural and Chemical Evolution of the Layered Li-excess Li_xMnO_3 as a function of Li content from First-Principles Calculations.” *Advanced Energy Materials*. DOI: 10.1002/aenm.201400498.

V.E.4 Electrode Fabrication and Materials Benchmarking (LBNL)

Vincent Battaglia
Lawrence Berkeley National Laboratory

Environmental Energy Technologies Division
1 Cyclotron Road
Berkeley, CA 94720
Phone: (510) 486-7172; Fax: (510) 486-4260
E-mail: vsbattaglia@lbl.gov

Start Date: October 2012
Projected End Date: September 2016

Objectives

- To advance Li- and Li-ion-based technologies to facilitate their use as traction batteries in vehicles.
- To produce electrodes and fabricate cells that provide a particular material the ability to perform to at its optimum level.
    - Assess the materials performance.
    - Identify source or sources of the material's deficiencies toward automotive applications.

Technical Barriers

The barriers to batteries being widely deployed in vehicles to provide traction and the recapture of energy lost to braking are the upfront cost, the limited lifetime, the weight, and the size.

Technical Targets

- Cost: 110 \$/kWh EV; 293 \$/kWh PHEV.
- Lifetime: 15 years EV; 15 years PHEV.
- Weight: 235 Wh/kg EV; 97 Wh/kg PHEV40.
- Size: 500 Wh/L EV; 145 Wh/L PHEV40.

Accomplishments

- Fabricated low-loading $LiFePO_4$ (LFP) half cells that cycle with a very high coulombic efficiency and negligible capacity fade.
- Fabricated high-loading $LiFePO_4$ electrodes with a very high coulombic efficiency, low capacity fade, and no cracks.
- Fabricated and tested a possible NCM baseline material under several conditions in full cells and half cells.
- Fabricated half cells and full cells of Graphite/LFP and Si/LFP to emphasize cyclability differences.

✧ ✧ ✧ ✧ ✧

Introduction

The BATT Program consists of a large number of individual projects all working towards solving the technical barriers that have been preventing the widespread adoption of EVs and PHEVs. Among the projects there typically are groups of PIs engaged with the same material. When this is the case, a Focus Group is established on that material. For 2014, the Focus Groups are 1) High-voltage NCM and 2) Si Anodes. The responsibility of the NCM Focus Group is to identify a good NCM material and provide an overview of its performance capabilities. The responsibility of the Si Focus Group is to test the Si in full cells and establish its performance capabilities and identify sources of failure for high-loading Si electrodes.

For this year, the effort in High-voltage NCM has been toward benchmarking an NCM material from a major supplier. The initial goal is to make an electrode and test it under conditions where there is high coulombic efficiency and excellent cyclability. The effort in the Si-anode focus group has been to assess the performance in half cells of Si electrodes provided by the Liu Group, compare that performance to graphite electrodes in half cells, develop the ability to fabricate an LFP electrode of any loading that cycles extremely well as a counter electrode for graphite and Si, and test graphite and Si in full cells.

Approach

A Focus Group is identified by the BATT management. A chemistry is identified specifically in the Focus Group, or is appropriately selected to accentuate the problem. Battery-grade materials are obtained from reliable, industrial sources. Performance metrics are obtained, and eventually shared with other BATT PIs at periodic meetings and through Quarterly Reports. Progress is made through a group effort focused on common materials.

Results

The fabrication of a $LiFePO_4$ electrode: $LiFePO_4$ is considered a moderate energy cathode material for Li-ion batteries. It has a theoretical capacity of 170 mAh/g but a flat voltage profile of 3.4 V. The material itself is a very poor conductor of electrons and has a low migration rate for Li and is therefore prepared in sub-micron particle size. The poor electronic conductivity calls for a high level of carbon black in order that all of the nanomaterials are connected to each other and to the current collector. It was chosen as a good counter electrode for testing Si because it has a high capacity, a flat voltage, a low voltage, and good cyclability. Because of these properties, it should have little impact on the performance of the anode and be easy to follow the progress of the anode's performance in a full cell.

Because LFP is a moderate energy density cathode material, the group has little experience in working with it as it is not considered a viable option for EVs. The group was essentially starting from scratch. Some of the first electrodes produced did not cycle well in half-cells (Figure V - 147).

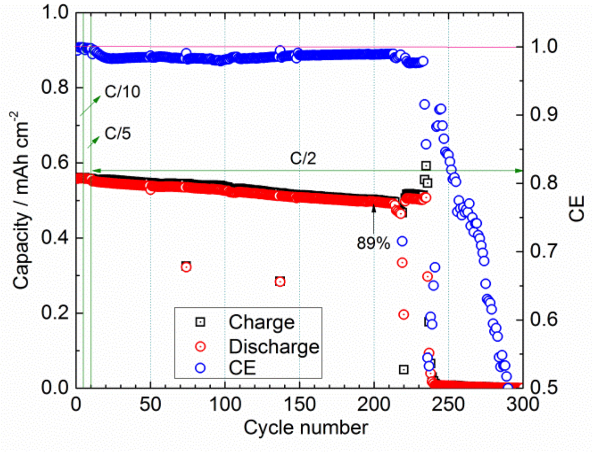

Figure V - 147: LiFePO$_4$ half-cell cycled at C/2 with an electrolyte of 1 M LiFePO$_4$ in EC:DEC 1:2

It took a little while to realize that this was an effect of the cycling rate using Li. Assembling a similar electrode in a half-cell but keeping the charging rate at C/10, resulted in much improved cyclability. It is believed that charging Li at high rate results in a very poor surface with rising resistance. Cycling at C/10 solved this problem and resulted in the cycling shown in Figure V - 148. With a cyclable LFP electrode in hand, it was time to try to produce a high loading LFP electrode.

High-loading LFP electrodes: One of the tasks of the Si-Anode Focus Group is to understand why the cyclability of Si is a strong function of loading, i.e., why electrodes of capacities greater than 1 mAh/cm^2 show a severe capacity fade with cycling. Thus, the goal is to make electrodes of up to 4 mAh/cm^2 that cycle well against Li or a cathode. For this reason, it is important that the group knows how to make cyclable electrodes of high loading cathodes.

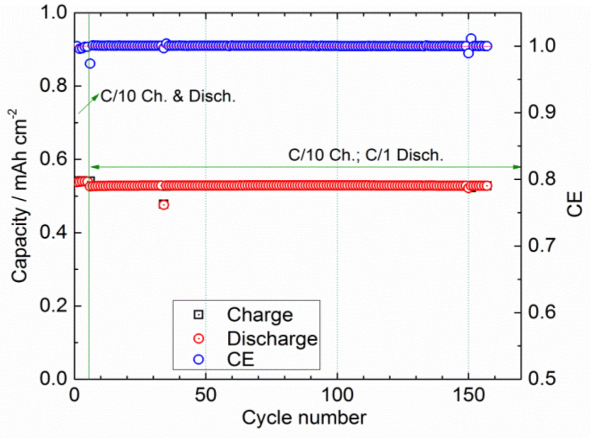

Figure V - 148: Similar cell as cycled in Figure V - 147 but charged at C/10 and discharged at C/1

The electrode performance of LFP shown in the previous section, especially the excellent performance at low charge rates, does not tell the full story of this electrode. After the fresh electrodes are dried but before they are calendered, they display "dried mud" cracks throughout the laminate, especially the higher loading electrodes. Such cracks have not previously been seen by this group for other cathode or anode chemistries. Because the active material is sub-micron for transport purposes and because a lot of high surface area carbon is added to make up for the poor conductivity, there is a preponderance of nanomaterials in the electrode. Even though the materials are sonicated to keep them from aggregating during the mixing step, these high surface area particles apparently agglomerate during the drying step of the cast laminate. The agglomeration during drying leads to cracked electrodes.

Several changes to the processing procedures were made to alleviate the cracking. First, the rate of drying was slowed down by covering the freshly cast laminates with a bowl to increase the vapor pressure of the solvent. Second, the amount of solvent in the slurry was reduced in order to cast more viscous slurries. In the end, the change that worked the best was to increase the amount of polymer in the composition. Polymer as much as 8% was found to be satisfactory for reducing cracking and still provide good cycling performance as seen in Figure V - 149.

Fabrication of NCM electrodes: The High-Voltage Focus Group, started three years ago, shifted its attention from LiNi$_{1/2}$Mn$_{3/2}$O$_4$ to NCM this year. The goal of the research will be understand why NCM 333 does not cycle well above 4.3 V and then to modify the cell chemistry to push the voltage to higher values. To start the project, an NCM baseline material needs to be identified. A large manufacturer of battery cathode material has agreed to work with us on this project and the other BATT PIs interested in participating.

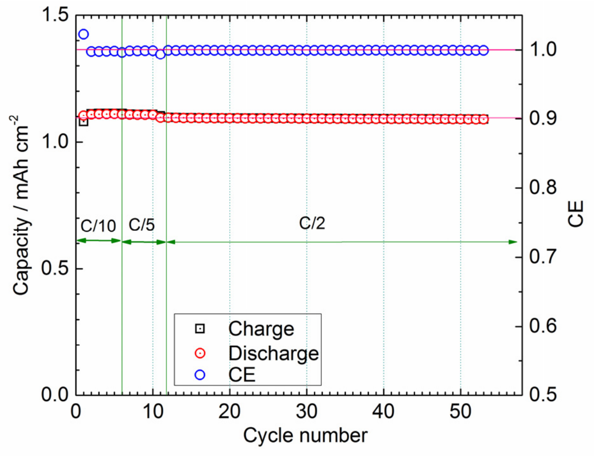

Figure V - 149: Cycling data of an LFP electrode with increased binder content to eliminate cracking

NCM was received from the supplier in August 2013. Since this will be a study of the active material and may require study of its surface, laminates were made of two different inactive material loadings: one with 4% binder and 3.6% carbon additive and the other with half of those values. Cells of the two laminates were assembled and tested. One of the tests performed was a rate test. The cells were charged and discharged at different rates and the amount of capacity removed on discharge was compared. The results showed no difference in rate performance. The cells were then tested for cyclability and again the results were similar. However, the cycling data was not perfect, as can be seen in Figure V - 150.

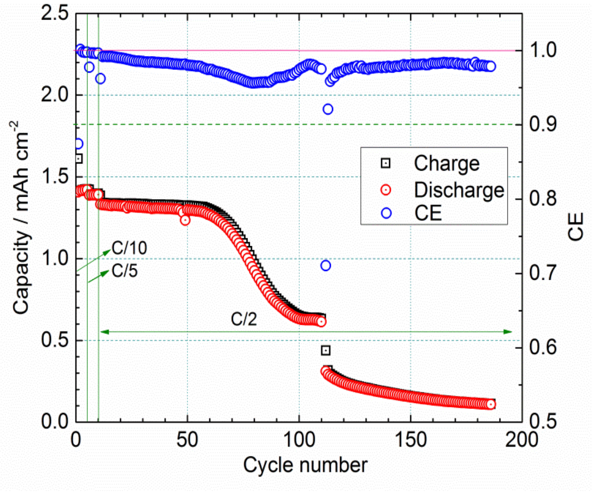

Figure V - 150: Charge, discharge, and coulombic efficiency of the cycling data of an NCM half-cell cycled at difference C-rates

The data presented is for a cell of 1.4 mAh/cm^2 cycled between 3 and 4.2 V *versus* lithium at different C-rates. The intention is to start with a cell that cycles very well at low voltages and then to understand the changes that occur as the upper cut-off voltage is increased. Here, it is seen that the discharge capacity is dropping a little bit with each cycle and the difference between the charge and discharge capacity is widening with each cycle for the first 60 cycles. Better cycling data than this was anticipated. To get to a point where there was no capacity fade and high coulombic efficiency, several changes were made: the electrode loadings were decreased, new electrolyte was obtained, the upper cutoff voltage was lowered to 4.1 V, and an earlier batch of NCM from the same company dating back to 2010 was used. However, despite all of those changes, the cycling data remained virtually unchanged.

It is thought that the source of the efficiency decline may not be the NCM but the Li. It is possible that soluble reduction products from the Li are migrating to the cathode where they are oxidized. Cells will be made to test this hypothesis.

A comparison of graphite and Si: Although graphite only demonstrates a coulombic efficiency in half cells of around 99.8%, full cells made with graphite have shown much better cyclability than would be expected from a loss of 0.2% of cyclable Li per cell. Recently, some of the Si-based materials reported in the literature and in the BATT Program have shown coulombic efficiencies in half-cells approaching those of graphite. The task of the Si Focus group is to make full cells with either graphite or Si anodes and to test to see if there are differences in the full cells not seen in the half-cells.

LFP-based cathodes of approximately 1 mAh/cm^2 were constructed for the comparison. The electrode in a half cell showed excellent capacity retention with cycling and a coulombic efficiency approaching 99.95%. A graphite electrode of slightly larger capacity was tested in a half cell and against this LFP electrode. In the half-cell, the graphite showed excellent capacity retention and a coulombic efficiency approaching 99.9%. In the full cell, the coulombic efficiency decreased a little to 99.8% and the capacity fade was consistent with this level of coulombic efficiency, i.e., the cell lost 0.2% of its capacity on each cycle. (See Figure V - 151.) This may not sound like much, but by 200 cycles, this amount to a full cell capacity loss of nearly 30%. From the analysis, this loss in capacity is attributed almost entirely to the coulombic inefficiency of the anode where the anode is walking off the cathode.

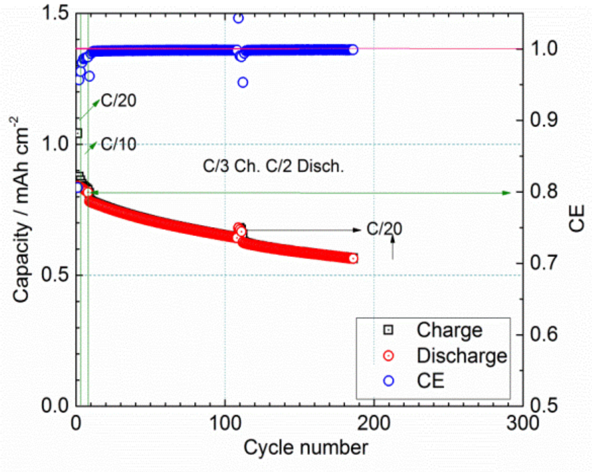

Figure V - 151: Charge and discharge capacities and the coulombic efficiency of a Graphite/LFP cell at different C-rates

Si-based electrodes were provided by Gao Liu's Group. These electrodes were of a cyclable capacity below the LFP cathodes and were Si limited on both charge and discharge. When tested in a half cell, these electrodes lost 70% of their capacity by the 200th cycle. Nearly all of this lost could be attributed to the loss of sites for Li intercalation, i.e., either the locations in the Si decreased with cycling or the Si was falling apart leading to material isolation. When the Si electrode was tested in a full cell against LFP where the Si was the limiting electrode, the cell behaved nearly identically to that of a Si half-cell. The presence of the LFP had little impact on the cells cyclability. The cell lost 80% of its capacity by the 300th cycle, as seen in Figure V - 152.

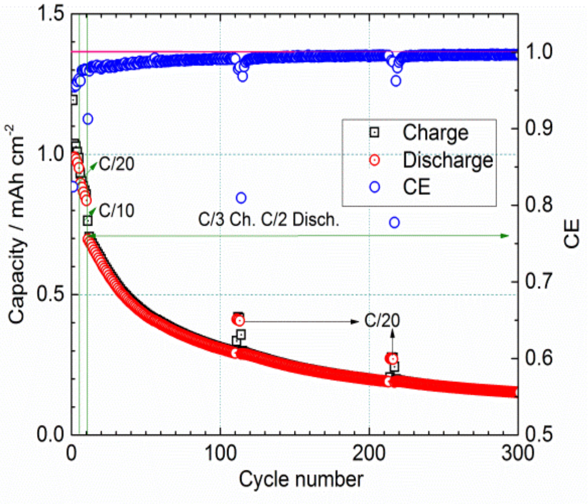

Figure V - 152: Charge and discharge capacities and coulombic efficiency of a Si/LFP cell cycled at different C-rates

Conclusions and Future Directions

This year, through the work with Focus Groups, four materials were benchmarked for battery performance: LFP, NCM, Si, and Graphite by fabricating and testing them in half cells and full cells. Some of the aspects of battery design learned this year include: 1) lithium may play a role in the performance of the counter electrode, especially with regards to side reactions, 2) LFP forms cracks during processing that have little impact on cyclability, 3) the cracks in LFP can be eliminated by increasing the binder content, 4) the NCM material being investigated is showing an increase in coulombic inefficiency with cycling, 5) the Si baseline electrodes are suffering from particle isolation during cycling, 6) the full cell data of the baseline Si electrode behaves as expected from the half-cell data, 7) Graphite/LFP cells show capacity fade proportional to the rate of side reaction on graphite, which indicates that either a better graphite is used in commercial cells or an additive has been found that is crucial to their success.

Future plans include the following: 1) testing half-cells at different rates to identify possible erroneous results coming from the Li, 2) comparing half-cell data to full cell data to subtract out effects from Li, 3) fabricating LFP laminates of higher loading to test higher loading Si anodes, 4) testing other sources of NCM material, 5) determining a rate of cycling where Si cracking stops, 6) testing Si electrodes in a LFP capacity-limited full cell, 7) testing other sources of graphite in graphite/LFP cells, 8) testing the effect that a small addition of VC to the electrolyte has on the cycling performance of graphite/LFP cells.

FY 2014 Publication/Presentation

1. Battaglia, V. (June 2014)."Scale-up and Testing of Advanced Materials from the BATT Program." Presented at the 2014 DOE Annual Merit Review and Peer Evaluation Meeting, Washington, D.C.

V.E.5 First-Principles Calculations of Existing and Novel Electrode Materials (MIT)

Gerbrand Ceder
Massachusetts Institute of Technology

Department of Materials Science and Engineering
77 Massachusetts Avenue, 13-5056
Cambridge, MA, 02141
Phone: (617) 253-1581
E-mail: gceder@mit.edu

Start Date: May 2013
Projected End Date: December 2016

Objectives

- Identify the structure of layered cathodes that leads to high capacity.
- Clarify the role of the initial structure as well as those of structural changes upon first charge and discharge.
- Give insight into the factors that control the capacity and rate of Na-intercalation electrodes, and make suggestions for novel Na-intercalation cathode materials.
- Generate insight into the behavior of alkali-intercalating electrode materials.

Technical Barriers

- Low rate capabilities.
- High cost.
- Poor stability.
- Low energy-density.

Technical Targets

- Identifying higher capacity Li-ion cathode materials and novel chemistries for higher energy density storage devices.

Accomplishments

- Discovered a high-capacity disordered rocksalt materials ($Li_{1.211}Mo_{0.467}Cr_{0.3}O_2$).
- Through percolation theory, generated a unified understanding of Li diffusion in rocksalt oxides (including the effect of cation disorder and Li excess) that relates cathode structure and composition to practical capacity.
- Catalogued Na-orderings using first-principles calculations and characterized co-operative Jahn-Teller distortion using TEM observed in Na_xMnO_2.

✧ ✧ ✧ ✧ ✧

Introduction

Improving cathode performance is an important step towards higher energy density batteries. Currently, the BATT Program has multiple new cathode materials under investigation, including several high-voltage materials and the high capacity layered materials. This BATT project is a systematic approach towards higher energy density using a combined first principles modeling and experimental approach to provide insight into how these materials function and what their limitations are.

To achieve large specific and volumetric capacity requires a large amount of intercalant (Li or Na) to be cycled in and out of a compact and light crystal structure. The relation between theoretical and practical capacity and chemistry is being investigated and tested in this program.

Approach

First principles computations are being used to evaluate existing and novel materials. Voltages and intercalation curves are calculated with GGA+U, and if highly accurate results are required, HSE methods are used. Phase diagrams are calculated with the Materials Project infrastructure. Configurational disorder for elevated temperature and off-stoichiometry is modeled with either point defect models (when off-stoichiometry is small) or with the cluster expansion for larger disorder. Ion mobility is evaluated with the Nudged Elastic Band Method or with direct Molecular Dynamics Simulations. Thermal stability is investigated using a previously-developed approach under this program. Some of the computational work is performed in collaboration with Kristin Persson and the Materials Project. Work on Li-excess layered materials is done in coordination with Kristin Persson (computational) and the experimental efforts in the BATT Program (e.g. Clare Grey).

Results

Unlocking the potential of disordered oxides for rechargeable Li batteries: The structure evolution in cation-disordered $Li_{1.211}Mo_{0.467}Cr_{0.3}O_2$ (LMCO) upon cycling was investigated. While LMCO forms as a layered rocksalt, it transforms to a disordered rocksalt after just a few charge-discharge cycles (Figure V - 153a) [1]. In general, disordering leads to poor electrochemical performance in rocksalt-like materials. Nevertheless, LMCO cycles remarkably well upon disordering (*ca.* 265 mAh/g, Figure V - 153c). Through *ex situ* X-ray diffraction (XRD), it was found that the change in lattice parameters and volume during charge and discharge is negligible in cation-disordered LMCO.

The unit cell volume only varies by *ca.* 0.12% (Figure V - 154), which is much less than in layered materials. In layered materials, the c-lattice parameter tends to decrease substantially upon high delithiation, leading to limited Li diffusion at highly charged states, and thus makes it challenging to achieve very high specific capacities. In contrast, the stable topology of disordered structures can allow for facile Li diffusion even at highly charged states so that very high capacities can be achieved in disordered materials. Furthermore, such stable structures result in reduced mechanical stress in the electrodes, which in turn extends the cycle-life in Li-ion batteries.

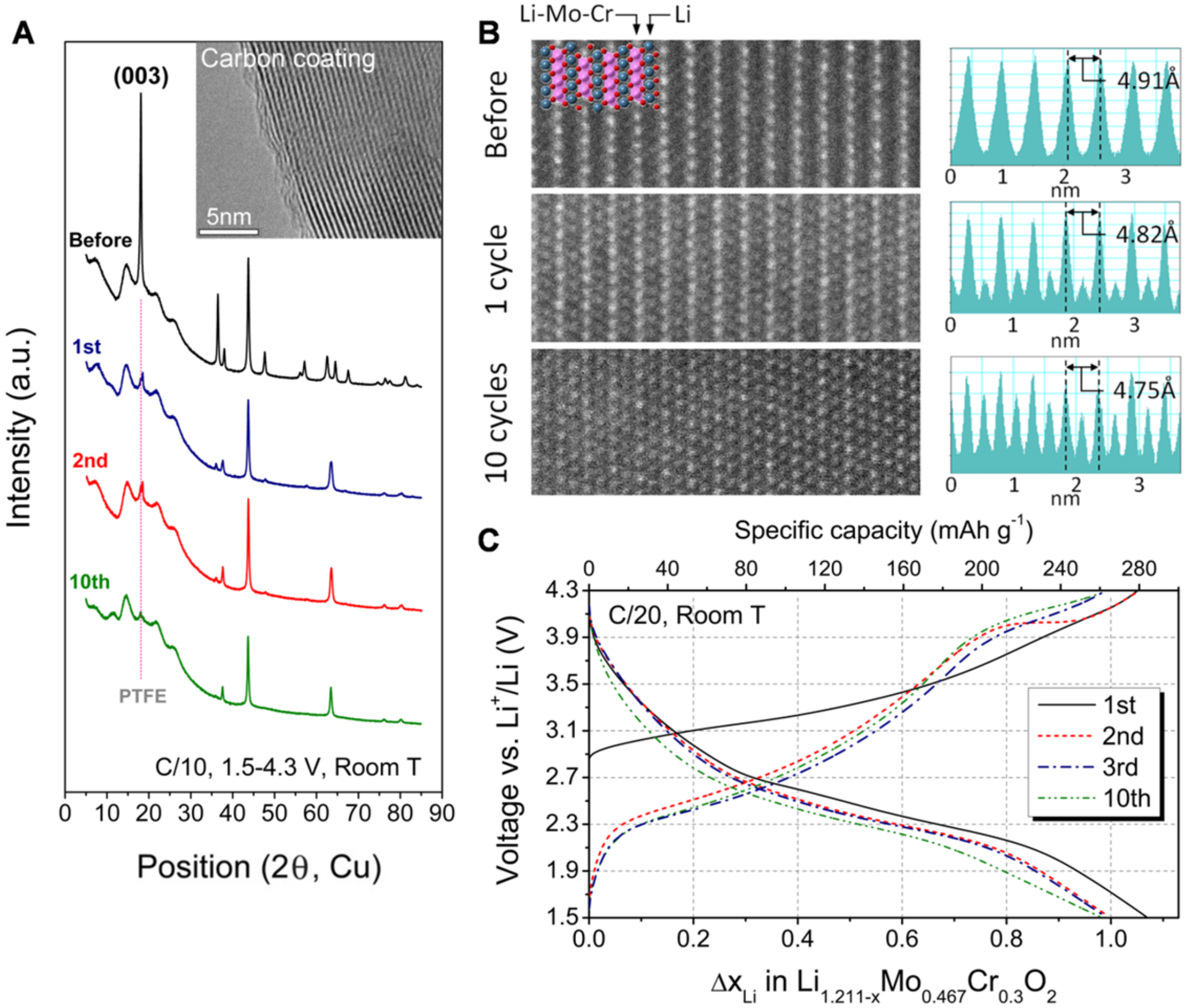

Figure V - 153: (a) XRD pattern of $Li_{1.211}Mo_{0.467}Cr_{0.3}O_2$ (LMCO) before and after 1, 2, and 10 cycles. (b) Scanning transmission electron microscopy images of LMCO particles before and after 1 and 10 cycles. (c) The voltage profile of carbon-coated LMCO. The figure has been reproduced from Ref. [1]

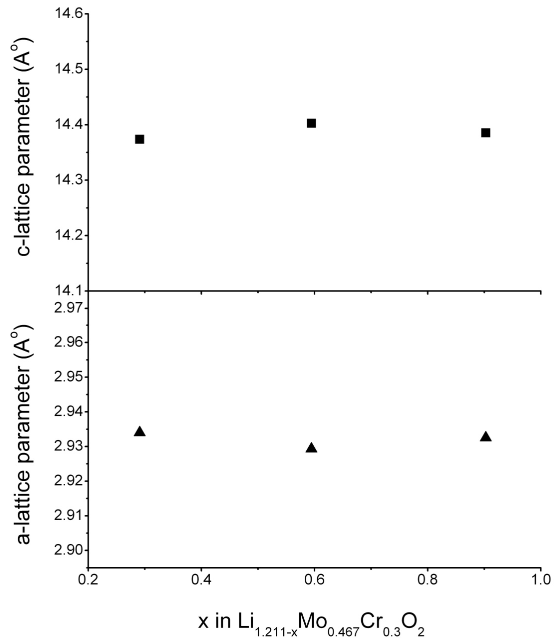

Figure V - 154: The c- and a-lattice parameter in disordered-LMCO upon delithiation

Using this cation-disordered Li-excess Mo/Cr oxide ($Li_{1.211}Mo_{0.467}Cr_{0.3}O_2$) as a prototype material, it was possible to gain a fundamental understanding of Li transport in general Li transition metal (TM) oxides [1]. In rocksalt-like Li-TM oxides, Li migration between two octahedral sites proceeds via a tetrahedral activated state (*o-t-o* diffusion, Figure V - 155a).[2] The activation barrier for this process is mainly determined by the electrostatic repulsion between the tetrahedral Li and the species (cation or vacancy) on its two face sharing sites (Figure V - 155c). In stoichiometric layered materials, exactly one face-sharing site is a TM site, while the second one is a Li site. The Li migration barrier for such a 1-TM diffusion channel is correlated with the TM valence and the Li-TM separation that varies with the height of the Li slab (*ca.* 2.6–2.7 Å).[3] This model for cation-disordered structures was generalized by taking into account all possible cation arrangements around the tetrahedral site, namely 0-TM, 1-TM, and 2-TM channels (Figure V - 155b-c).[1] It was found that due to spatial constraints in disordered materials (slab distances *ca.* 2.4 Å) the majority of 1-TM and 2-TM channels are not active at room temperature, but 0-TM channels can support facile Li migration. However, around 10% Li excess is required to achieve a sufficiently large concentration of 0-TM diffusion channels to form a percolating 0-TM network (Figure V - 156).[1]

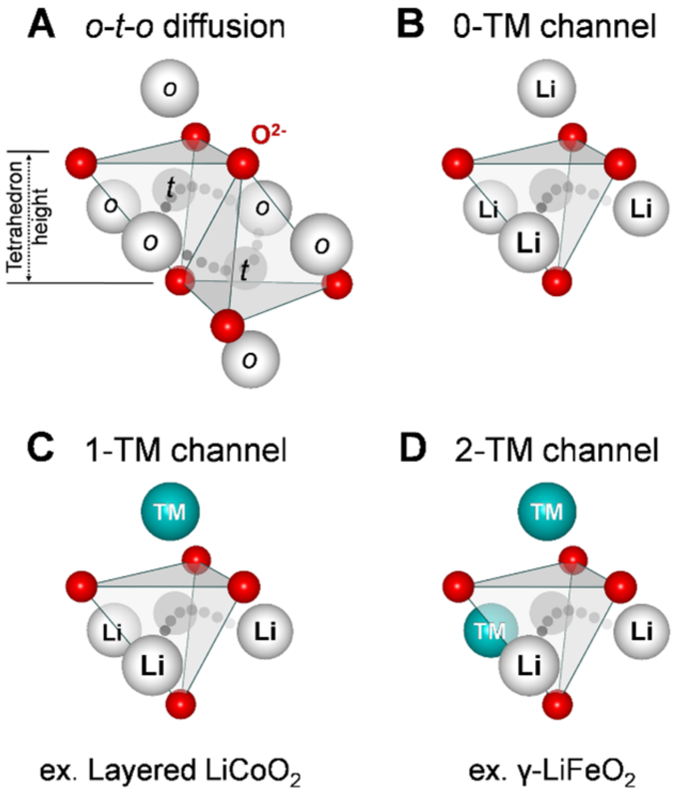

Figure V - 155: (a). Li migration between two octahedral sites via a tetrahedral activated state. (b.-c.) The three different diffusion channel types that occur in cation-disordered Li metal oxides. The figure has been reproduced from Ref. [1]

This new insight into Li percolation allows for definition of clearer boundaries for the expected capacity of new Li excess cathode materials, by evaluating the percentage of the Li contents that is accessible via 0-TM migration as a function of the composition (Figure V - 156). It also opens up the entirely new compound space of disordered materials, which have so far mainly been disregarded as cathode materials.

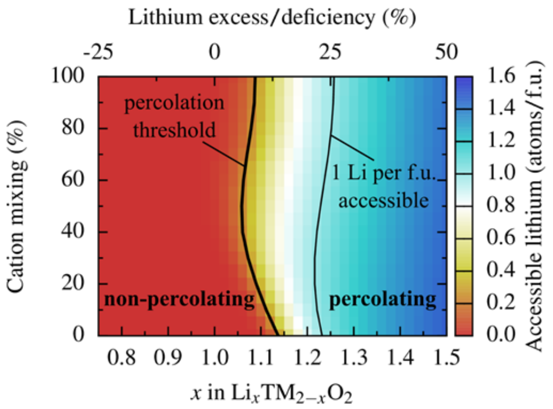

Figure V - 156: 0-TM percolation and accessible Li contents as function of the composition and the degree of disorder (cation mixing) in layered Li transition metal oxides ($Li_xTM_{2-x}O_2$). The figure visualizes the results of Monte-Carlo percolation simulations, which has been reproduced from Ref. [1]

The configurational space of rocksalt-type oxides for high-capacity Li-battery electrodes: Excess Li enables macroscopic Li migration in cation-disordered $Li_{1+x}M_{1-x}O_2$ by activating a percolating network of fast 0-TM Li diffusion channels [1]. To complete our understanding of Li migration through rocksalt-type oxides, this percolation analysis was extended beyond the layered and disordered (DO) rocksalt structures to the other common ordered $LiMO_2$ phases: the γ-$LiFeO_2$ structure and the spinel-like low-temperature $LiCoO_2$ structure [2].

The percolation thresholds of the four crystal phases (Figure V - 157) are notably different, indicating that the γ-$LiFeO_2$ structure is not well suited as Li conductor, since it would require a very large amount of Li excess to become 0-TM percolating. However, the spinel-like structure exhibits excellent percolation properties and is 0-TM percolating even at Li-deficient compositions. In addition, the beneficial properties of the spinel-like structure are robust against some amount of cation disorder, as is evident from the percolation maps (Figure V - 158).

As a result of the percolation analysis, the group now possesses a complete map of the Li conduction properties throughout the configurational space of rocksalt-type Li transition-metal oxides. Based on the knowledge of the 0-TM accessible Li content, it is now possible to estimate the practical capacity of any rocksalt-type Li battery electrode material given its crystal structure and the amount of cation mixing. Thus, the percolation maps (Figure V - 158) provide direct guidelines for the design of new battery materials and for the improvement of existing materials.

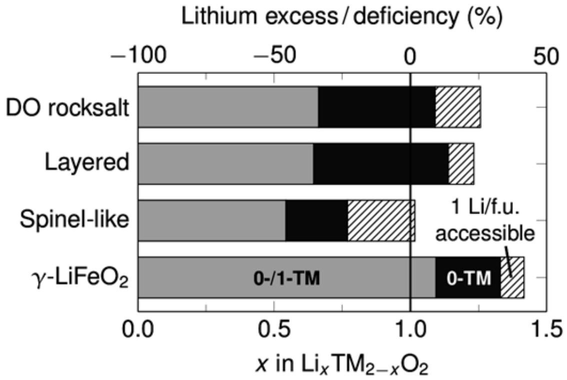

Figure V - 157: Critical Li concentrations in the most common $LiMO_2$ crystal phases [2]. The gray region indicates the percolation threshold for 1-TM diffusion (only active in the layered structure), the black region indicates 0-TM percolation, and the hatched region represents the Li content at which 1 Li atom per formula unit becomes 0-TM accessible

Sodium ordering in layered cathode materials: The ground state hull for Na_xMnO_2 (Figure V - 159) was computed and in doing so, confirmed a newly characterized superstructure at x=0.625. This superstructure provides direct visualization of a cooperative Jahn-Teller effect via a correlated distortion of atoms in the layered structure, seen both in extensive experimental characterization and in the density functional theory (DFT) model [3]. Figure V - 160 shows the Na and Na-vacancy ordering in one layer of this structure, as well as the ordering of transition metal charge and ferrimagnetic and AF stripe orderings. The structure is particularly unusual because it shows Na ions as being displaced from their original octahedral environments.

The convex energy hull shown in Figure V - 159 is constructed by several computational means. Enumeration algorithms enumerate possible atomic arrangements for Na ions within the Na layer and their formation energies are calculated by DFT. This set of calculated structural energies can then be used to formulate parameters for a cluster expansion, which is applied through Grand Canonical Monte Carlo methods to calculate a full voltage curve.

As well as providing the opportunity to confirm observed ground state phases, these methods can be used predictively to explore the nature of the voltage curve and all phases formed during the electrochemical cycling of a potential battery cathode.

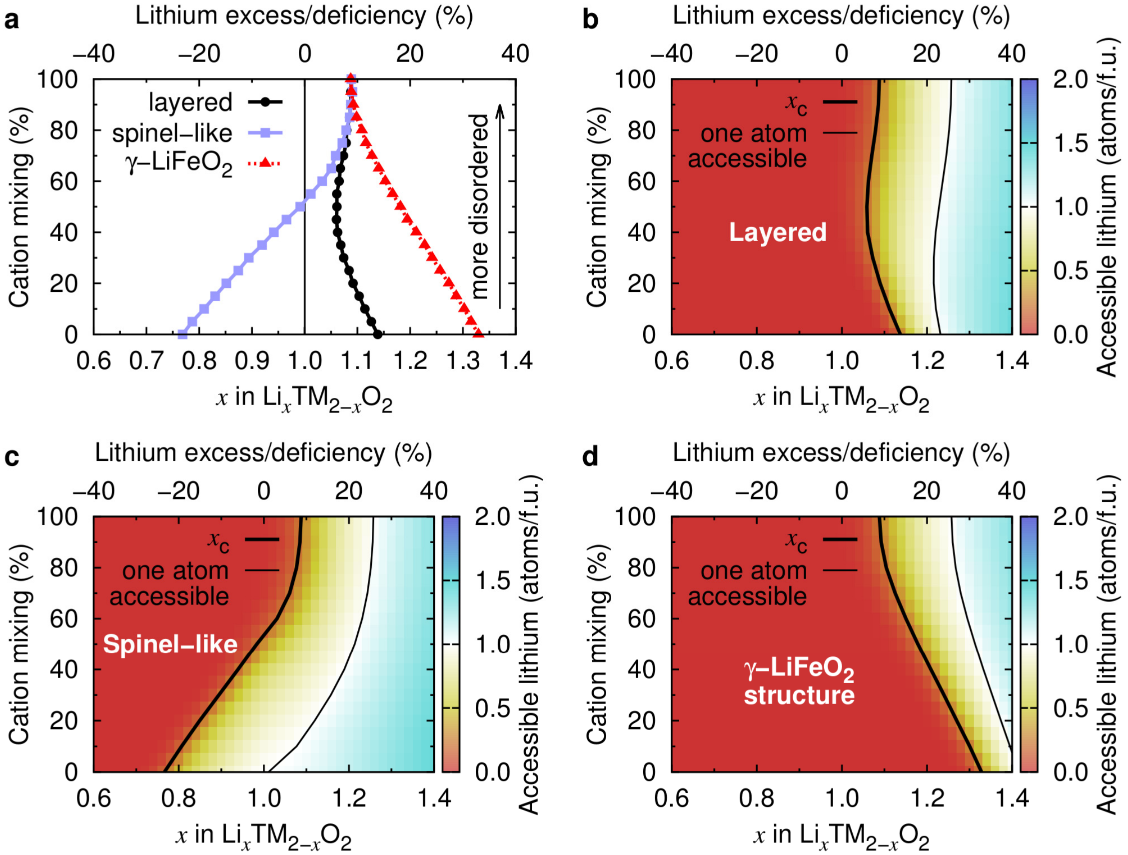

Figure V - 158: (a) 0-TM percolation thresholds and (b)-(d) 0-TM accessible Li content in different $LiMO_2$ crystal phases as function of Li content and degree of cation mixing (0%=ordered, 100%=cation-disordered) [2]. The thick and thin black lines in panels (b)-(d) indicate the percolation thresholds and the Li content at which 1 Li atom per formula unit is 0-TM accessible, respectively

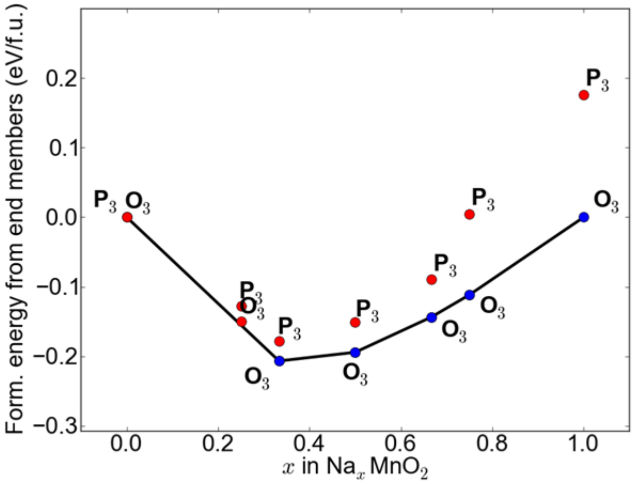

Figure V - 159: Calculated ground state hull for Na_xMnO_2, including predicted superstructure at x = 0.625

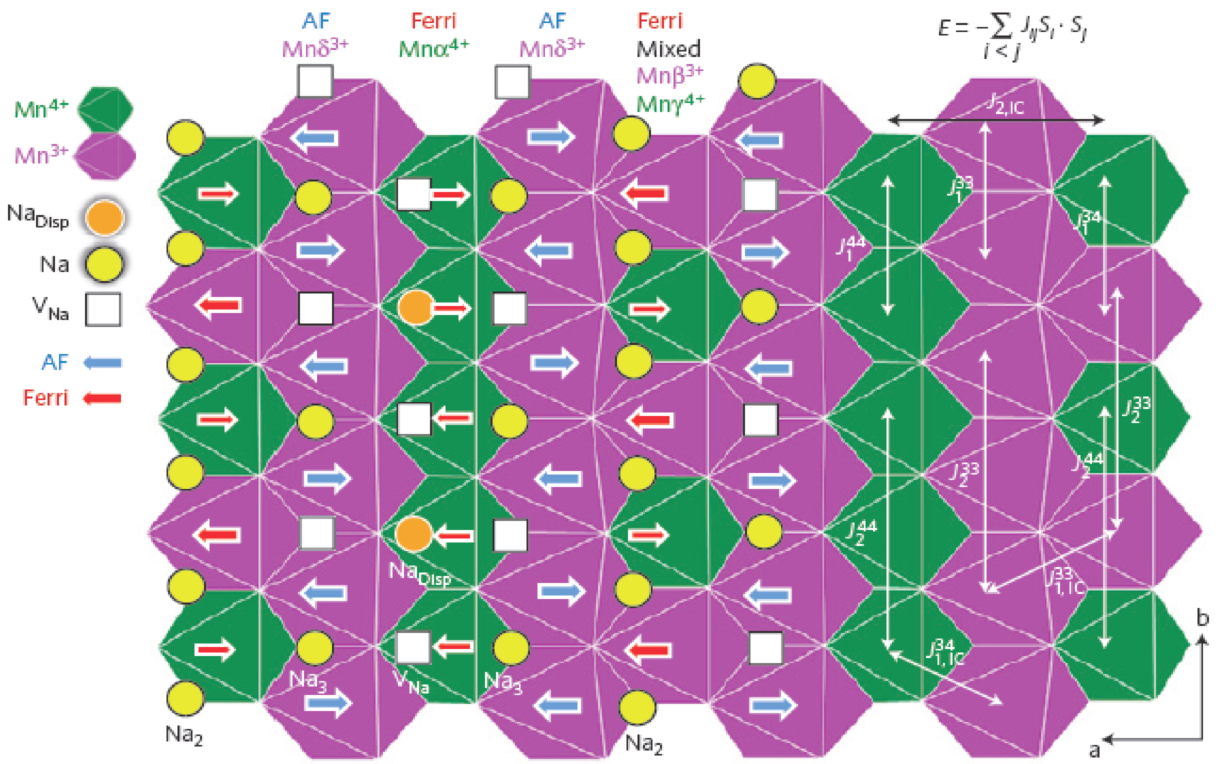

Figure V - 160: $Na_{5/8}MnO_2$ superstructure with vacancy (V_{Na}) ordering, Mn charge and magnetic stripe orderings.

Conclusions and Future Directions

In conclusion, a new high-capacity layered cathode material based on cation-disordered Li-excess Mo/Cr oxide ($Li_{1.211}Mo_{0.467}Cr_{0.3}O_2$) has been identified, synthesized, and cycled, and can achieve large practical and reversible capacities *ca.* 265 mAh/g. Furthermore, a comprehensive and fundamental understanding of the role of cation ordering Li-composition on the accessible capacity has been developed, validated against known cathode materials, and now provides a framework to design new compositions and structures that can also offer high capacity. In Na layered cathode materials, pronounced Na-orderings have been identified from first-principles computations and observed experimentally in the Na_xMnO_2 system, to predictively explore the voltage curve.

Future work will focus on using the existing principles from percolation theory identified in this work to identify other promising layered cathodes, as well as elucidating the role of overcharge on the first cycle observed in many Li-excess layered materials, and its effect on the practical capacity. In Na materials, the focus will be next on studying Na diffusion and clarifying the impact of Na-ordering and structure on diffusion.

FY 2014 Publications/Presentations

1. Ceder, G. (June 2014). “First Principles Calculations of Existing and Novel Electrode Materials.” Presented at the 2014 DOE Annual Merit Review and Peer Evaluation Meeting, Washington, D.C.
2. Lee, J.; Urban, A.; Li, X.; Su, D.; Hautier, G.; Ceder, G. (2014). *Science* (343); pp. 519-523.
3. Urban, A; Lee, J.; Ceder, G. (2014). *Adv. Energy Mat.* DOI: 10.1002/aenm.201400478.
4. Li, X.; et al. (2014). *Nature Materials* (13); pp:586-592.
5. Kim, J.-C.; et al. (2014). *Chemistry of Materials* (26); pp: 4200–4206.

V.E.6 Design and Scalable Assembly of High Density Low Tortuosity Electrodes (MIT, LBNL)

Yet-Ming Chiang
Massachusetts Institute of Technology

Department of Materials Science and Engineering
77 Massachusetts Avenue
Cambridge, MA 02139
Phone: (617) 253-6471; Fax: (617) 253-6201
E-mail: ychiang@mit.edu

Antoni P. Tomsia (Collaborator)
Lawrence Berkeley National Laboratory
Materials Science Division
1 Cyclotron Road
Berkeley, CA 94720
Phone: (510) 486-4918; Fax: (510) 486-4761
E-mail: aptomsia@lbl.gov

Start Date: October 2012
Projected End Date: September 2016

Objectives

- Develop scalable high-density, binder-free, low-tortuosity electrode designs and fabrication processes to enable increased cell-level energy density compared to conventional Li-ion technology.
- Characterize electronic and ionic transport as a function of state-of-charge in relevant electrode systems and downselect based on the superior performance.
- Maximize active material utilization and lower the cost of Li-ion cells for EVs applications.
- Testing electrochemical performance of freeze casting electrodes in continuous and pulse modes.

Technical Barriers

- Achieving sufficient electronic conductivity.
- Avoiding mechanical failure upon cycling.
- Meeting automotive duty cycles.
- Lowering cost.

Technical Targets

- Identify high-energy density cathode compositions with electronic transference number >0.5 across the State of Charge (SOC) range for use in directional freeze-casting processing.
- Fabricate conductive-additive free sintered cathodes with controlled pore volume fraction and topology yielding a tortuosity values less than 2.
- Increase cell-level specific energy and energy density, and lower inactive materials cost, by achieving area capacity of 5mAh/cm^2 at C-rates or current densities commensurate with operating conditions for PHEV and EV.

Accomplishments

- Measured pure-phase electronic and ionic transport in NCA ($LiNi_{0.8}Co_{0.15}Al_{0.05}O_2$) and Fe-LNMO.
- Downselected NCA for higher electronic conductivity.
- Optimized freeze casting process for obtaining desired microstructures.
- Demonstrated NCA electrodes with 3x the area capacity of conventional Li-ion at 1C rate.
- Demonstrated pulse power capabilities using Hybrid Pulse Power Characterization (HPPC) test protocol.

✧ ✧ ✧ ✧ ✧

Introduction

This project aims to develop alternative electrode architectures and scalable fabrication methods that result in thick, high-density electrodes with low-tortuosity porosity oriented normal to the electrode plane, using electrode actives of interest for future EV battery systems. Previously, it was showed that sintered-$LiCoO_2$ cathodes with aligned, low tortuosity porosity fabricated by co-extrusion or directional freeze-casting could reach area capacities of 7.5-9.5 mAh/cm^2 at 1C rate and 6.5-7.5 mAh/cm^2 at 2C rate (Figure V - 161). Here, a key technical performance target is to achieve at least triple the capacity per unit area at 1C-2C rate (e.g., >10 mAh/cm^2) that the same active materials can deliver in a conventional calendared electrode, and in cathodes of interest for automotive Li-ion batteries. The electrode density and thickness at which the discharge energy and discharge power are optimized for PHEV and EV applications critically depends on the pore topology of the sintered electrodes. Data on capacity per unit area and tortuosity of conventional calendared electrodes is available from literature and prior work under BATT. Even in the absence of controlled pore structure, the open porosity of sintered electrodes allows for ion transport with a lower tortuosity. However, in order to maximize the area capacity for PHEV and EV duty cycles, it is desirable to introduce lower-tortuosity porosity into the dense sintered electrodes.

Efforts have been, firstly, focused towards identifying cathode compositions with sufficiently high electronic conductivity that conductive additives need not be incorporated. Secondly, the bulk Li transport of candidate cathodes has been characterized in order to define the microstructural scale that is necessary to achieve the target performance without solid-state transport becoming rate-limiting. Thirdly, NCA electrodes have been fabricated by directional freeze-casting and sintering, and finally, electrochemical characterization under HPPC test procedures has been conducted.

Approach

The pure-phase electronic and ionic conductivity of candidate cathodes is measured as a function of Li concentration (state-of-charge) and was used to downselect cathodes. Directional freeze-casting and sintering studies are carried out to create aligned pore structures in sintered electrodes. Fabricated electrodes are tested using galvanostatic and HPPC test procedures. Modeling of continuous and pulse discharge response is used to help understand performance of these electrodes.

Results

Downselection of cathode: A key milestone for the project this year was the downselection of a cathode composition for follow-on work on the basis of measurement of electronic and ionic transport, and the fabrication and testing of freeze-cast electrodes in two candidate systems, Li(Ni,Co,Al)O_2 (NCA) and Fe-doped, high-voltage spinel $Li_{1-x}Mn_{1.5}Ni_{0.5}O_4$ spinel. Previously under BATT support, it was shown that the introduction of aligned dual-scale porosity into sintered $LiCoO_2$ cathodes where electronic conductivity is not limiting permits *ca.* 3x higher area capacity (mAh/cm^2) than in conventional electrodes at up to 2C rates. However, $LiCoO_2$ is exceptional amongst intercalation cathodes in having an unusually high electronic conductivity when delithiated beyond a few percent, $\sigma_e > 1$ S/cm. Thus the measurement of electronic conductivity, and its dependence on state-of-charge, is critical to identifying systems which as a dense additive-free electrode can obtain very high area capacity electrodes (>10 mAh/cm^2) without having electrode polarization become limiting. Ionic conductivity in the solid phase is less concerning since in the dense thick electrode limit, salt depletion in the pore space becomes limiting (as shown by porous electrode models). To date, $LiCoO_2$, NMC (1:1:1), NCA, LMNO and Fe-LMNO have been evaluated (Fe-LMNO being preferred to LMNO for its greater electrochemical shock resistance).

Of the candidate cathodes, NMC and the LMNOs appear to have too low electronic conductivity, and have been excluded in the downselect. NCA is also too electronically resistive in the fully dense limit, but is promising as a porous electrode in which electronic and ionic transport paths can be tuned through microstructure. Going forward, NCA and LCO are viable candidates in the absence of additional conductive phase being added.

Freeze casting and sintering optimization: First, directional freeze-casting of $LiMn_{1.5}Ni_{0.42}Fe_{0.08}O_4$ (Fe-LMNO) was carried out, bringing the list of cathodes successfully fabricated by this method to LCO, NMC, NCA and Fe-LMNO. However, as anticipated from the measured electronic conductivity of Fe-LMNO, polarization prevents high utilization of single-phase sintered electrodes. In contrast, freeze-cast samples of NCA show at C/50 rate a remarkably high area capacity of 20 mAh/cm^2, which is nearly 10x that of a conventional Li-ion electrode, in a sample 520 µm thick (Figure V - 161). However, at C/20 rate, significant polarization was observed. Efforts were therefore directed towards tailoring the microstructure to improve transport.

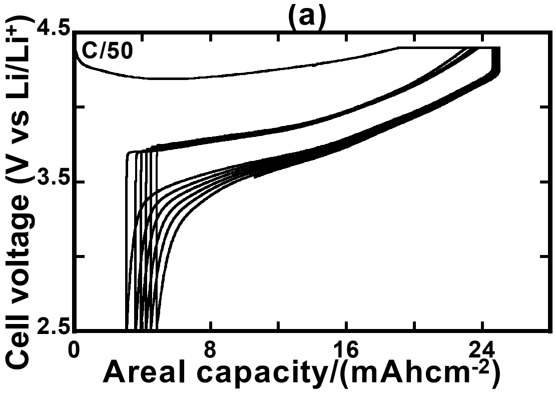

Figure V - 161: NCA freeze-cast electrode with 20 mAh/cm^2 capacity at C/50 rate

It is crucial to understand and control the evolution of the microstructures during freeze-casting of the $LiNi_{0.8}Co_{0.15}Al_{0.05}O_2$ (NCA) electrodes with aligned porosity. The microstructure can be triggered by controlling the processing parameters such as the solid content in the slurry, the cooling rate during freezing, the sintering conditions etc. Figure V - 162a illustrates the impact of the freeze-casting cooling rate, on the lamellae thickness of final sintered electrodes. As expected for a directional solidification process, the lamellae thickness (i.e., the thickness of the dense electrode regions) increases as the cooling rate decreases. The microporosity of the lamellae is furthermore a function of sintering time and temperature. Thus the dual-scale porosity of the electrodes, are mainly defined by the separation between lamellae and the porosity that can be controlled by the cooling rate and the sintering profile, respectively. Figure V - 162b, c and d depict microstructural features obtained at different rate of cooling.

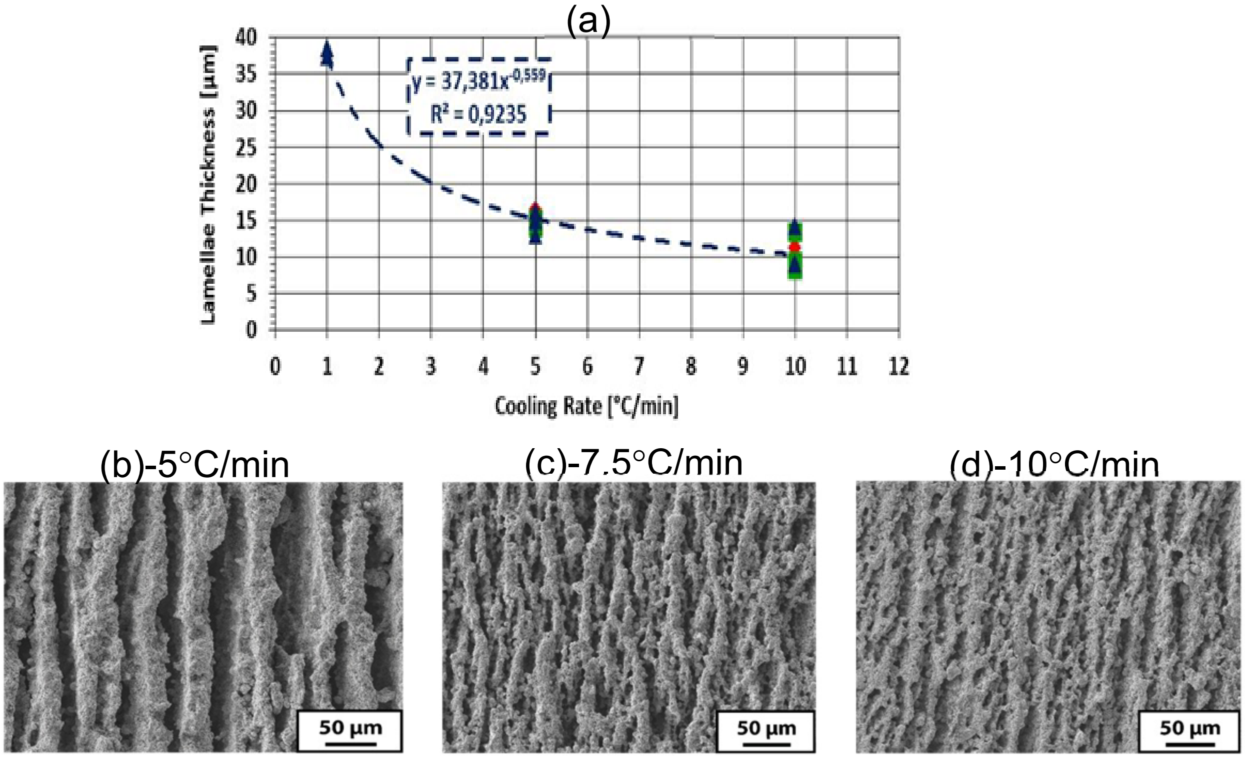

Figure V - 162: (a) Dependence of lamellae thickness on cooling rate in the freeze casting process, (b), (c) and (d) SEM micrograph of freeze casted-sintered NCA at three different cooling rates

The resulting sintered electrodes were electrochemically tested in Li half-cells (Swagelok type). The electrodes had the directional solidification direction oriented normal to the electrode plane, and were electrically connected to the stainless steel current collectors using a carbon paste. For continuous discharge at relatively low C-rates (C/5-C/10) (Figure V - 163), a 330 µm thick electrode had an area capacity exceeding 12 mAh/cm^2, which is about four times higher than current lithium ion electrodes. At 1C rate, over 5 mAh/cm^2 was obtained, meeting a quarterly milestone.

Hybrid pulse power characterization (HPPC) test: The hybrid pulse power characterization (HPPC) test was then performed on freeze-casted and sintered $LiNi_{0.8}Co_{0.15}Al_{0.05}O_2$ (NCA) electrodes with aligned porosity and high areal capacity. Key results are shown in Figure V - 164. The NCA electrode tested has area capacity of 16 mAh/cm^2 when measured at C/10 rate (compared to 3-4 mAh/cm^2 for conventional Li-ion cathodes), and has a thickness of 300 µm. The HPPC test was intiated with galvanostatic charging at C/5 rate followed by an open circuit hold for 1h. A 10s charge/10s discharge pulse at 2C current was then applied, followed by galvanostatic discharge at 1C rate to 90% of the cell capacity (i.e., 6 min). This sequence was repeated for every 10% depth of discharge.

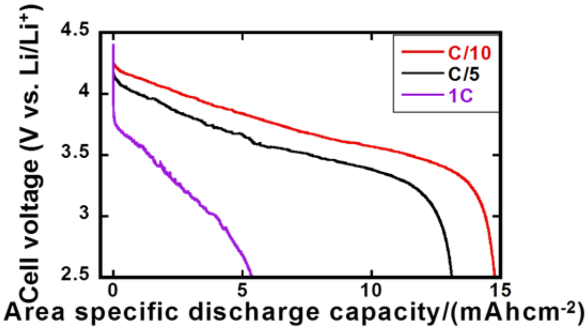

Figure V - 163: Voltage vs. capacity of directionally-solidified and sintered NCA electrode of 330 µm thickness, with discharge capacity plotted as area capacity (mAh/cm^2)

Figure V - 164 a shows the voltage profile of the cell during the HPPC test; note that the cell remains within the specified voltage limits throughout the 10s, 2C charge/discharge pulses. Figure V - 164 b shows the voltage vs. cumulative area capacity during the test, where it is seen that the cumulative capacity reaches *ca.* 12 mAh/cm^2. Note that in Figure V - 163, a similar electrode exhibits *ca.* 5 mAh/cm^2 capacity under continuous 1C discharge. The results (Figure V - 164a, b, and c) show that a much higher area capacity can be obtained from these novel electrodes under tests that more closely resemble vehicle duty cycles.

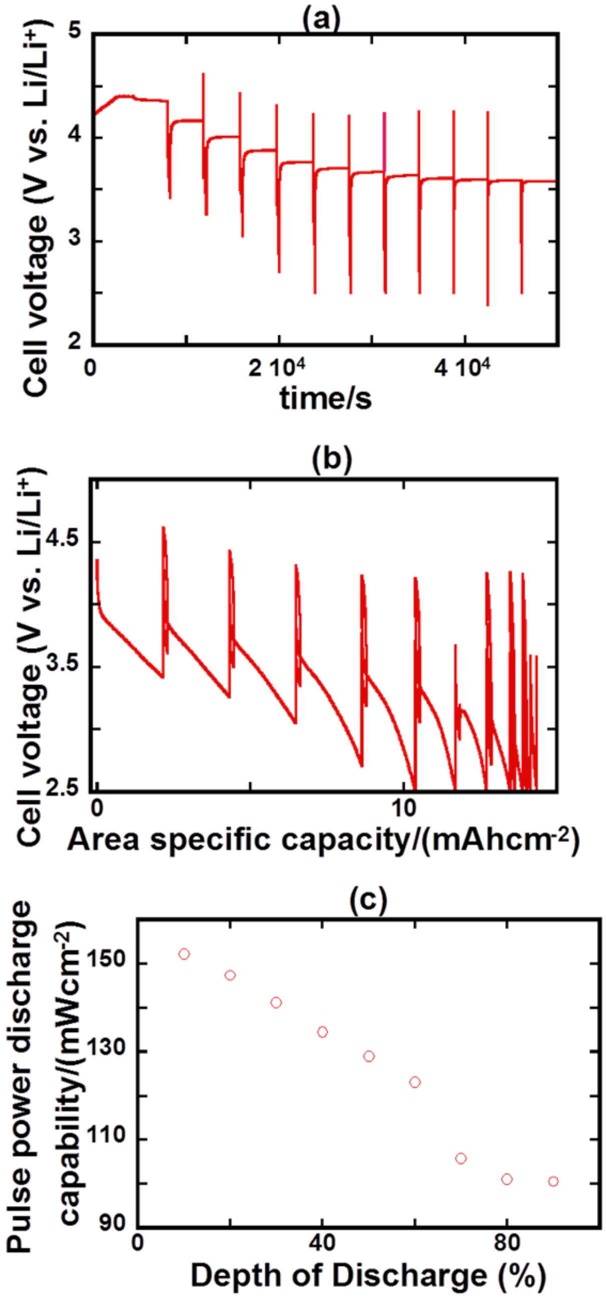

Figure V - 164: (a) Voltage vs. time for hybrid pulse power characterization (HPPC) test, (b) Area specific discharge capacity of the freeze-cast and sintered NCA electrode of 300μm thickness during HPPC test, and (c) Voltage vs. time for hybrid pulse power characterization (HPPC) test of NCA electrode of 300 μm thickness

The discharge power during the 2C/10s pulses is shown in Figure V - 164 c, plotted as area-specific power against depth of discharge. The values range from 150 mW/cm^2 at a low Depth of Discharge (DoD) to 95 mW/cm^2 at a high DoD, which is more than 2x higher and 4x higher, respectively, than reference data for a conventional NCA composite electrode (tested under 3.75C pulses, J. Shim and K. A. Striebel, *Journal of Power Sources* 122 (2003), 188–194). Since the 3-4 times greater area capacity of the present electrodes would dictate correspondingly lower electrode area for the same cell capacity, the higher area-specific power is promising, and necessary, to meet power requirements for vehicle applications.

Conclusions and Future Directions

NCA has sufficient electronic and ionic conductivity to be used as an additive free sintered cathodes, whereas both Fe-doped and undoped LMNO are electronically too resistive. Microstructure optimization in freeze-cast and sintered NCA electrodes results in areal capacity of 15 mAh/cm^2 at C/10 rate and >5 mAh/cm^2 at 1C rate. However, under HPPC test procedures with the same 1C rate during the discharge segment, >12 mAh/cm^2 was obtained, showing that the present electrodes have unexpectedly high pulse capacity relative to continuous discharge capacity, compared to conventional Li-ion electrodes.

Future work will use porous electrode modeling to understand this performance in detail. In addition, in the coming year, directionally-freeze cast negative electrodes will be fabricated and characterized, and full Li-ion cells constructed using these cathode counterparts.

FY 2014 Publication/Presentation

1. Chiang, Y.-M. (June 2014). “Electrochemically-Driven Phase Transitions in Battery Storage Compounds.” Presented at the 2014 DOE Annual Merit Review and Peer Evaluation Meeting, Washington, D.C.

V.E.7 Electrode Materials Design and Failure Prediction (LBNL)

Venkat Srinivasan
Lawrence Berkeley National Laboratory

Environmental Energy Technologies Division
1 Cyclotron Road, MS 70R0108B
Berkeley, CA 94720-8168
Phone: (510) 495-2679; Fax: (510) 486-4260
E-mail: vsrinivasan@lbl.gov

Start Date: October 2012
Projected End Date: September 2016

Objectives

- Quantify the usefulness of alloy anodes for use in PHEVs.
- Understand the mechanical degradation of electrodes used in EVs and PHEVs.
- Model reaction distribution in battery electrodes.

Technical Barriers

Low energy efficiency; low calendar/cycle life; high cost.

Technical Targets

- Available energy: 56 Wh/kg (10 mile) and 96 Wh/kg (40 mile).
- 10-s discharge power: 750 W/kg (10 mile) and 316 W/kg (40 mile).

Accomplishments

- Obtained Young’s modulus values for binder and conductive material composites saturated in electrolyte solution, and incorporated these into mechanical simulations of Si electrodes.
- Quantified polarization losses at liquid/single ion conductor interfaces for different electrolytes.
- Determined that available surface area was a likely reason for the dynamic nature of polarization loss at the single ion conductor/liquid interface.
- Quantified the impact of interfacial polarization at the liquid/single ion conductor interface in a Li-S cell for a given power to energy ratio.

✧ ✧ ✧ ✧ ✧

Introduction

High energy density and long cycle life are critical for reducing the cost of rechargeable Li-ion batteries. Thick porous electrodes result in large energy densities, and mathematical modeling is useful for understanding electrode processes and optimizing design parameters in such systems.

The primary goal of this project is to develop mathematical models for candidate Li-ion chemistries. The layered $LiNi_{1/3}Co_{1/3}Mn_{1/3}O_2$ (NMC) cathode material has been selected as the baseline system to study the rate performance associated with the transport limitations in the solid and electrolyte phases.

Approach

The Srinivasan group uses continuum-level mathematical modeling along with controlled experiments on model cells to understand the performance and failure modes associated with next-generation battery materials and to design battery materials and electrodes to alleviate these challenges.

Results

Stress and strain in Si electrodes. Equipment for mechanical testing of binder materials submerged in solvent was designed and fabricated. The simple but effective equipment designs are adaptable to common commercially-available tensometer equipment, so that the material testing procedures can be easily adopted by other research groups. Only small volumes of solvent are needed to keep samples submerged, and care has been taken to ensure that material samples can be brought quickly and easily into proper alignment for consistent testing.

Procedures for obtaining fairly consistent material samples have also been created. Samples of polyvinylidene fluoride (PVDF) in two different thicknesses, with and without conductive additive, have been tested when dry and when submerged in an ethylene carbonate/diethyl carbonate (EC/DEC) 1:1 solution. Results suggest that sample thickness, presence of additive, and exposure to solvent can all have a significant effect on the mechanical behavior.

As a description of binder stress-strain response, Hooke’s law was retained in the simulation code developed last year. A procedure for extracting Young’s modulus values from the raw material testing data was developed and automated; the values calculated for samples containing conductive additive and immersed in solvent, which are expected to best represent conditions within an actual cell, differ significantly from the mechanical properties of dry PVDF taken from literature and used in earlier simulations. A set of simulations incorporating the newly measured values has been performed.

Quantifying polarization loss at single-ion conductor/liquid electrolyte interface: Next-generation chemistries like Li-S have much higher theoretical energy densities than current Li-ion batteries. To prevent self-discharge due to polysulfide migration to the Li anode and to limit dendrite growth, the use of ceramic single ion conductors has been proposed. A single ion conductor (SIC) acts as a physical barrier that prevents dendrites from propagating and also prevents the transfer of polysulfides, while allowing the passage of Li ions. The junction polarization loss, which is the drop in potential due to the transfer of Li ions across such an interface, has implications for cell power. It is therefore necessary to quantify the polarization loss at the SIC/liquid electrolyte interface.

In the first quarter, a novel methodology to account for polarization loss at the SIC/liquid electrolyte was developed. Constant current cycling experiments were first performed in a custom Li-Li symmetric diffusion cell in the absence of the SIC. Thereafter, the SIC was incorporated in the cell by sandwiching it between two electrolyte chambers. Polarization loss at the SIC/liquid electrolyte interface was then extracted from these two sets of experiments after accounting for Ohmic drop in SIC and concentration polarization effects in the liquid electrolyte, using a mathematical model. Figure V - 165 shows the I-V plot extracted from these cycling experiments with and without SIC (red and blue dots). The solid black line shows the model predictions of a Li-Li symmetric cell with SIC (without polarization loss). The difference between the experimental data for the cell with SIC (red dots) and the model predictions (black line) gives the polarization loss at different current densities. All cases show substantial polarization losses at the SIC/electrolyte solution interface.

In the second quarter, polarization losses at the SIC/liquid electrolyte interface were measured for different concentrations of $LiPF_6$ in three different solvents (Figure V - 166): ethylene carbonate/diethyl carbonate (1:1), dimethyl sulfoxide (DMSO), and propylene carbonate (PC). Figure V - 166 shows that the polarization losses at the interface are substantial for all solvents tested. This will lead to a decrease in cell voltage at high currents.

Work in the third quarter focused on determining the source of these losses. Experiments were performed using a Li-Li symmetric cell with a Li reference electrode and 1 M $LiPF_6$ in EC/DEC (1:1) to compare energies of solvation and desolvation of Li-ions at the Li electrode/electrolyte solution interfaces. The cells were polarized for two minutes under a range of current densities, then allowed to relax for three minutes, after which the potentials were recorded. The measured potentials for the solvation and desolvation processes differ in magnitude by only a few millivolts at 1 mA/cm^2. Furthermore, the combined losses, determined by comparison with the mathematical model developed earlier in this project, are significantly smaller than those found for the SIC interface.

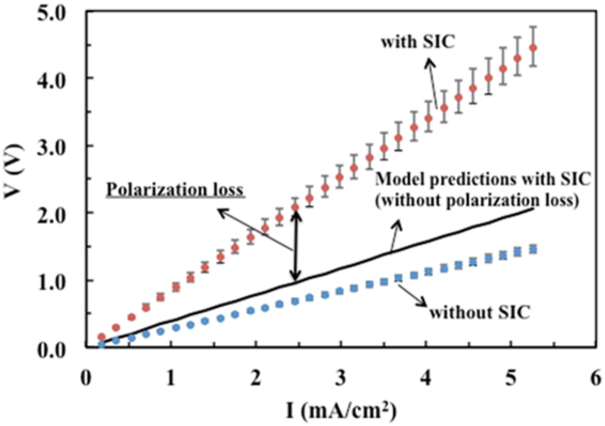

Figure V - 165: Experimental I–V curves for a Li-Li symmetric cell with and without SIC for 0.5M $LiPF_6$ in EC:DEC (1:1). Also shown are model predictions (solid line) for a Li-Li symmetric cell with SIC (without polarization loss)

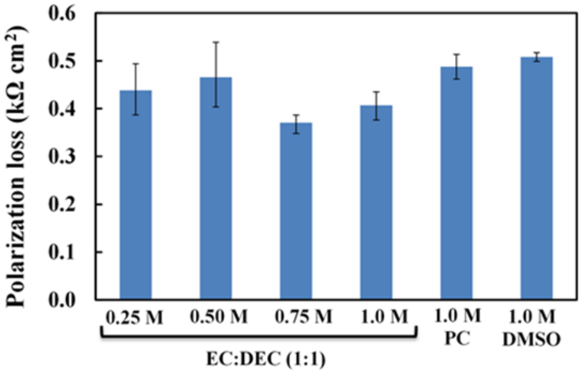

Figure V - 166: Polarization loss for different concentrations of $LiPF_6$ in various solvents: ethylene carbonate: diethyl carbonate [EC/DEC(1:1)], dimethyl sulfoxide (DMSO), propylene carbonate (PC)

These findings suggest that the polarization losses at the SIC interface include a net energy loss from desolvation and solvation. Application of the Butler-Volmer equation to the electrolyte solution/SIC interface further suggests that the difference in magnitude with losses at the Li electrodes may reflect differences in surface area. The electrodes used in this experiment were prepared using the formation protocol developed previously as part of this project for the purpose of stabilizing cell potential. For this reason, their actual surface areas may be significantly larger than their initial cross-sectional areas. In contrast, the surface area of the SIC is fixed. The computed value of the exchange current density for the SIC interface is comparable to those calculated for composite electrodes with much larger interfacial areas.

Polarization losses in Li-S cells: The impact of polarization losses on the energy density of Li-S batteries was then investigated through simulation. Figure V - 167 shows the specific energy of batteries at different C-rates (ranging from C/50 to C/2) with different battery designs: (1) batteries without a SIC and with an electrode loading of 0.5 mg/cm^2 of sulfur, (2) batteries with a SIC and the same 0.5 mg/cm^2 sulfur loading, and (3) batteries with a SIC and a loading of 3 mg/cm^2. The specific energy is calculated based on the mass of active material only, and it was assumed that the rate performance is not dependent on the degree of sulfur loading.

The results plotted in Figure V - 167 suggest that the presence of a SIC makes little difference to the specific energy of a battery when the sulfur loading is low (0.5 mg/cm^2). This is because the applied current density is correspondingly small. However, the low energy densities of these batteries make such a design impractical. If the sulfur loading is increased to 3 mg/cm^2, the specific energy at the highest C-rate is a small fraction of that obtained in the low-loading cases. The higher loading is associated with a larger applied current density, which is in turn associated with a large liquid electrolyte/SIC junction polarization loss. This huge loss of energy would limit the usefulness of Li-S batteries containing this SIC. Although incorporation of a SIC improves Li-S battery stability, polarization losses at the liquid/SIC interface must be reduced in order to make such a battery practical.

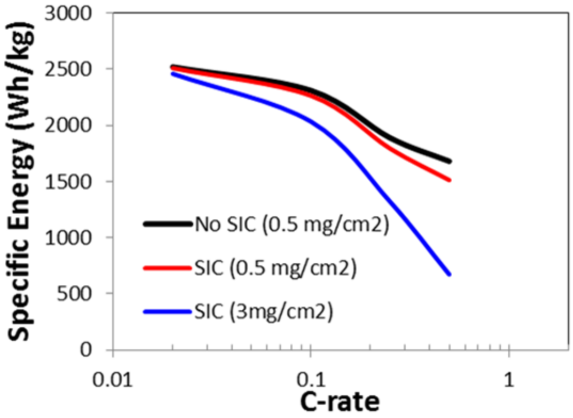

Figure V - 167: Specific energy densities of Li-S batteries with different designs, at a range of C-rates: 0.5 mg/cm^2 sulfur loading in batteries without a SIC, 0.5 mg/cm^2 loading in batteries with a SIC, and 3 mg/cm^2 loading of batteries with a SIC

Conclusions and Future Directions

Work in FY 2014 has focused on obtaining realistic material data for improving the accuracy of mechanical simulations of Si electrodes developed in the previous year, as well as on measuring polarization losses at SIC/electrolyte solution interfaces and applying this information in predictive simulations.

Stress-strain testing of PVDF samples has demonstrated that the presence of electrolyte solution and the inclusion of conductive material have significant effects on material behavior.

Measurements with a custom cell using a ceramic SIC have demonstrated that polarization loss is significant in all solvents and all salt concentrations examined. Additional experiments, coupled with mathematical modeling, suggest that these losses are likely to be a consequence of the low surface area of the SIC.

Subsequent modeling of a Li-S cell with and without a SIC has demonstrated that the polarization losses limit the practicality of cells incorporating this SIC when operating at large current densities.

Li-S-related work in FY 2015 will involve the further development of the Li/S model through the inclusion of a concentrated solution framework, as well as the development of a new custom Li/S cell with a small catholyte layer, for use in rate experiments.

In addition, microscale electrode models will be developed and compared against macroscale models and experimental data produced earlier by this project, in order to determine the importance of microstructural detail to simulation accuracy.

FY 2014 Publications/Presentations

1. Mehrotra, A.; Srinivasan, V. (October 2013). “Quantifying Polarization Loss at Organic Liquid Electrolyte/Single Ion Conductor Interface.” Presented at the 224th ECS Meeting, San Francisco, CA.
2. Higa, K; Srinivasan, V. (October 2013). “Stress and Strain in Silicon Electrode Models.” Presented at the 224th ECS Meeting, San Francisco, CA.

V.F Diagnostics

V.F.1 Energy Storage Materials Research using DOE's User Facilities (ANL)

Michael Thackeray
Argonne National Laboratory

9700 South Cass Avenue
Argonne, IL 60439
Phone: (630) 252-9184; Fax: (630) 252-4176
E-mail: thackeray@anl.gov

Collaborators:
ANL: Jason Croy, Brandon Long, Joong Sun Park
Advanced Photon Source, ANL: Mali Balasubramanian, Matthew Suchomel
Electron Microscopy Center, ANL: Dean Miller
Rutherford Appleton Laboratory, UK: Bill David

Start Date: October 2012
Projected End Date: September 2015

Objectives

- The primary objective of this project is to broaden the scope of studies of electrode materials relevant to the BATT program, using DOE and international user facilities through collaborative efforts.
- More specifically, the goal is to use a range of x-ray spectroscopic techniques, including *in situ* methods, such as X-ray diffraction (XRD), X-ray absorption (XAS), and X-ray reflectivity (XR) at the Advanced Photon Source (APS); high-resolution transmission electron microscopy (HRTEM) at Argonne's Electron Microscopy Center (EMC); and neutron scattering at the ISIS facility, Rutherford Appleton Laboratory (RAL), UK and/or ORNL's Spallation Neutron Source (SNS).

Technical Barriers

- Low energy density.
- Poor low temperature operation.
- Abuse tolerance limitations.

Technical Targets (USABC – End of life)

- 142 Wh/kg, 317 W/kg (PHEV 40 mile).
- Cycle life: 5,000 cycles.
- Calendar life: 15 years.

Accomplishments

- Evaluated methods for the synthesis of isotopically enriched composite cathodes for neutron studies.
- Conducted studies on a series of single and multi-component cathode materials by:
  - High-resolution synchrotron X-ray diffraction (at APS)
  - X-ray absorption spectroscopy (at APS)
  - Neutron diffraction (at RAL).

✧ ✧ ✧ ✧ ✧

Introduction

Multi-component electrodes, $y\{xLi_2MnO_3{\bullet}(1-x)LiMO_2\}{\bullet}(1-y)LiM_2O_4$ (M=Mn, Ni, Co), are currently the most promising class of cathodes for next-generation Li-ion batteries. However, the degradation mechanisms of these cathodes are not well understood. This lack of understanding is due to the complexity of the pristine materials as well as the complex atomic-level processes that occur on cycling. In order to create more robust structures, a detailed understanding of the structure-electrochemical properties of these materials must be obtained.

Approach

- Utilize DOE's user facilities to gain fundamental insights into complex $y\{xLi_2MnO_3{\bullet}(1-x)LiMO_2\}{\bullet}(1-y)LiM_2O_4$ electrodes.
- Combine data sets from multiple, advanced characterization techniques to enable a complete understanding of complex structures across multiple length scales.
- Combine experimental results with computation to advance the design of robust cathode structures.

- Establish national and international collaborations with experts in the field to foster innovation.

Results

Synchrotron studies of composite and end-member cathode structures

A series of composite and end-member cathode structures was selected for study. Table V - 8 lists the sample compositions, in layered and composite notation, and identification numbers. The end-members, Li_2MnO_3 (C2/m) and $LiMn_{0.5}Ni_{0.5}O_2$ (R3-m), were chosen, as well as materials in the compositional space around $0.5Li_2MnO_3$•$0.5LiMn_{0.5}Ni_{0.5}O_2$. In addition, the spinel $Li_{0.5}Mn_{0.75}Ni_{0.25}O_2$ was included. These structures are representative of those found in pristine, high-energy cathode materials where of all the above phases can be integrated at the nano-scale in complex arrangements.

Table V - 8: Sample compositions in layered and composite notation

#	Layered composition	Composite notation
1	$LiMn_{0.5}Ni_{0.5}O_2$	-
2	$Li_{1.2}Mn_{0.6}Ni_{0.2}O_2$	0.5 Li_2MnO_3● 0.5 $LiMn_{0.5}Ni_{0.5}O_2$
3	$Li_{0.5}Mn_{0.75}Ni_{0.25}O_2$	-
4	$Li_{1.16}Mn_{0.58}Ni_{0.26}O_2$	0.38 Li_2MnO_3● 0.62 $LiMn_{0.5}Ni_{0.5}O_2$
5	$Li_{1.15}Mn_{0.58}Ni_{0.27}O_2$	0.35 Li_2MnO_3● 0.645 $LiMn_{0.5}Ni_{0.5}O_2$
6	Li_2MnO_3	-
7	$Li_2Mn_{0.66}Ni_{0.34}O_3$	-

Figure V - 168(a) and (b), and Figure V - 169(a) and (b) show Mn and Ni K-edge XANES and EXAFS data, respectively, for the series of samples listed in Table V - 8. Detailed analyses of the X-ray absorption data were carried out and are summarized in Figure V - 170 and Figure V - 171. The data show how the metal-metal (Mn/Ni-Mn/Ni) and metal-oxygen bond distances, as well as the associated metal-metal coordination numbers, change as a function of the lithium to transition metal (TM) ratios of the as-prepared materials. The Li:TM ratios were determined by inductively-coupled plasma mass spectrometry (ICP). The Mn-M coordination falls to ~3 as the Li:TM ratio increases, indicating Li and Mn ordering, forming $LiMn_6$ regions within the TM layers. Conversely, the Ni-M coordination remain closer to 5 or above, indicating $LiMO_2$ like, Ni-rich domains, revealing the inhomogeneous and composite nature of these complex materials. Figure V - 172 shows high-resolution, synchrotron X-ray diffraction (HR-XRD) data for the same series of samples. The analyses of these data will be combined with the analyses of neutron powder diffraction data collected at Rutherford Appleton Laboratory (ISIS), U.K., as well as the X-ray absorption data shown above. The fitted parameters of coordination numbers and bond lengths will be used as inputs to constrain models describing these materials across short, intermediate, and long-range length scales.

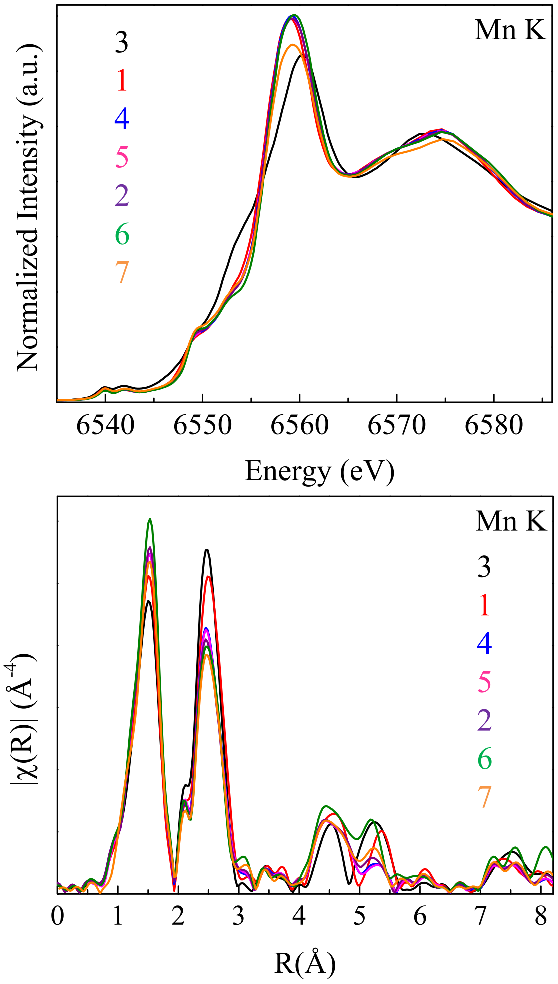

Figure V - 168: Mn K-edge XANES (top) and EXAFS (bottom) data for the samples listed in the Table V - 8

Synthesis of ^{62}Ni-enriched composites: The contrasting positive and negative scattering lengths for ^{58}Ni (68.3% abundance) and ^{62}Ni (3.6% abundance), respectively, allows the possibility of completely negating Ni contributions in neutron pair distribution function analysis (PDF) for samples having the right combination of these isotopes. This promises an unparalleled view of the local to mid-range structure in complex composite materials containing Mn and Ni as the main transition metal constituents. One of the challenges with such experiments is the synthesis of ^{62}Ni-enriched composites. To demonstrate the feasibility of ^{62}Ni-enriched composite cathodes materials, natural Ni, in metallic form, was chosen as the initial source of Ni. The Ni metal was first annealed in air to produce

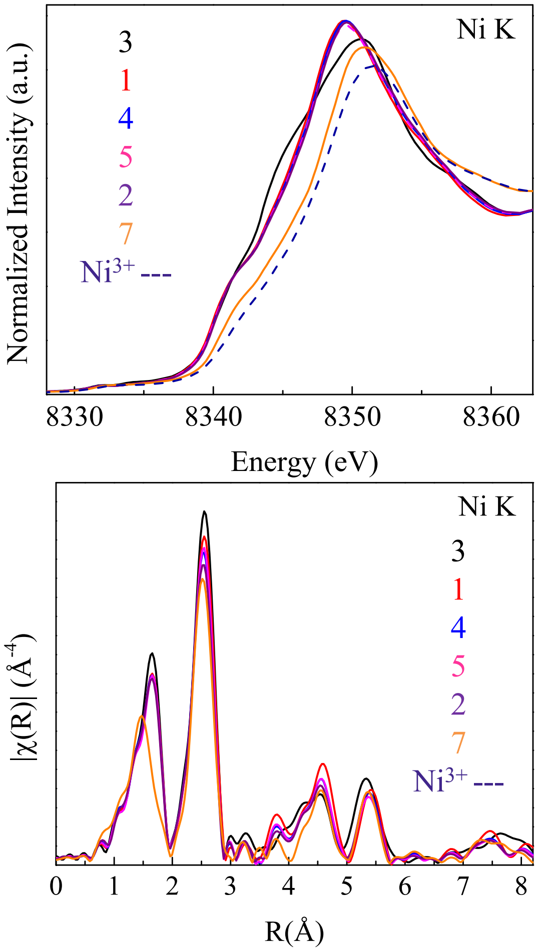

Figure V - 169: Ni K-edge XANES (top) and EXAFS (bottom) of the samples listed in Table V - 8

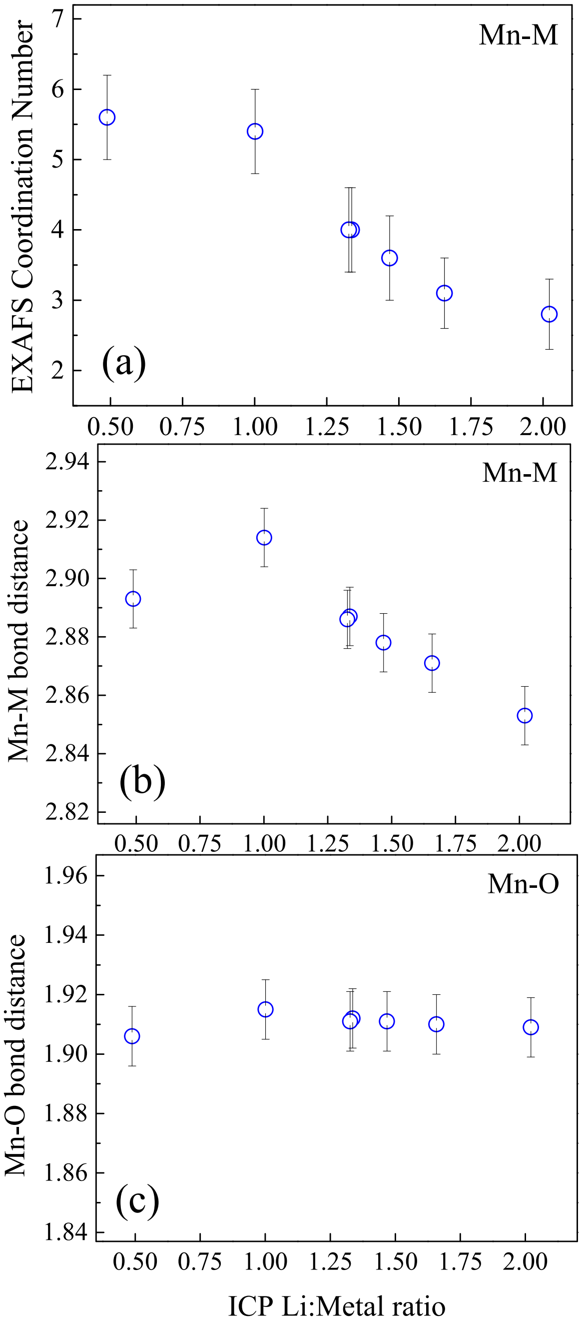

Figure V - 170: (a) First-shell, Mn-M Coordination numbers, (b) Mn-M bond distances, and (c) Mn-O bond distances as a function of Li to TM ratios, determined by ICP analysis for the samples listed in Table V - 8

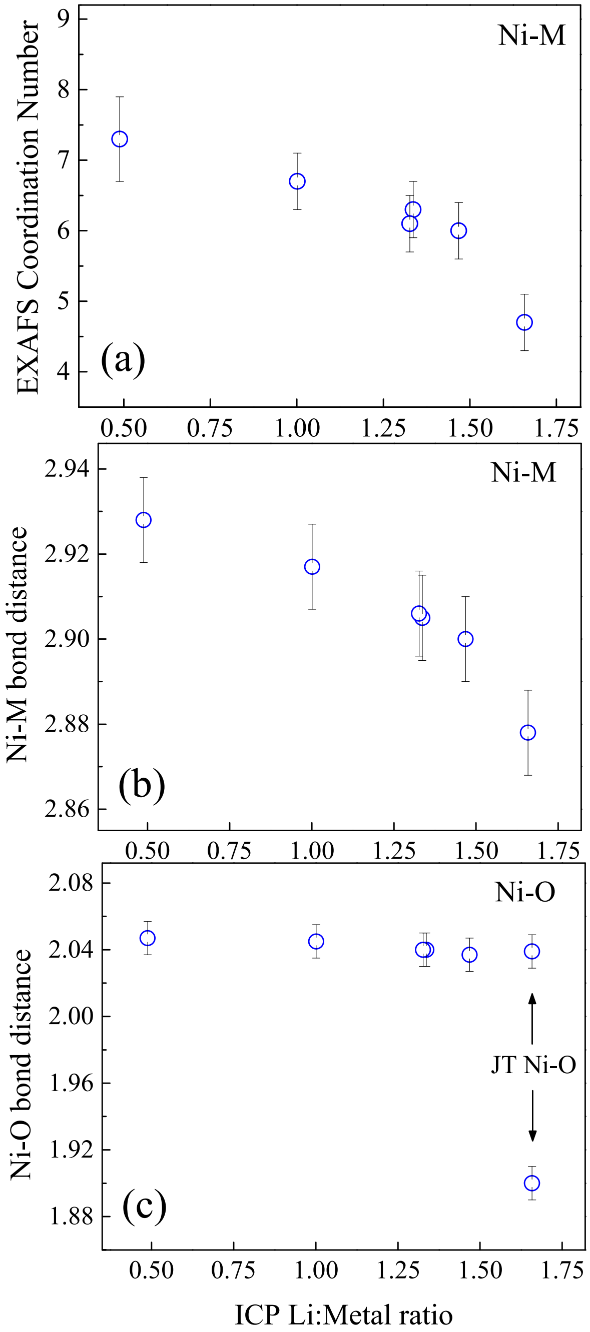

Figure V - 171: (a) First-shell, Ni-M Coordination numbers, (b) Ni-M bond distances, and (c) Ni-O bond distances as a function of Li to TM ratios, determined by ICP analysis, for the samples listed in Table V - 8

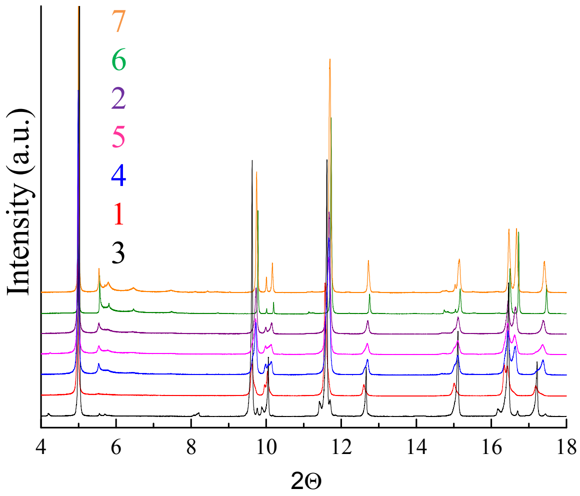

Figure V - 172: HR-XRD of the samples listed in Table V - 8

NiO. Subsequently, the NiO was dissolved in a solution of nitric acid, HNO_3, to produce nickel nitrate, $Ni(NO_3)_2$. This form of nickel has previously been shown to be compatible with a novel synthesis method in which layered Li_2MnO_3 is used as a precursor for producing a variety of integrated, composite materials. Figure V - 173(a) and (b) show the electrochemical performance of a $0.5Li_2MnO_3•0.5LiMn_{0.5}Ni_{0.5}O_2$ cathode, synthesized as described above, in a lithium half-cell. The characteristic, first-cycle plateau is observed with a charge capacity of ~300 mAh/g. Subsequent cycles show altered profiles revealing typical performance of conventionally-prepared composite materials, including voltage fade. Figure V - 173(b) shows that the cell delivered between 230-240 mAh/g over ~15 cycles on test. These data confirm that the synthetic route chosen is a viable option for the synthesis of ^{62}Ni-enriched composite materials.

The ion-exchange method using Li_2MnO_3 precursors was also explored for the synthesis of Mn- and Ni-containing layered-layered-spinel (LLS) cathode materials. Figure V - 173(c) shows Mn K-edge data of a $0.5Li_2MnO_3•0.5LiMn_{0.5}Ni_{0.5}O_2$ baseline material along with increasing amounts of an integrated $LiMn_{1.5}Ni_{0.5}O_4$ spinel component. Changes are observed in going from 0% to 100% pure spinel which reveal local structural changes to the Mn environment. However, the oxidation state of Mn remains Mn^{4+} throughout the series, as expected for both the $0.5Li_2MnO_3•0.5LiMn_{0.5}Ni_{0.5}O_2$ and $LiMn_{1.5}Ni_{0.5}O_4$ components. Further analyses of these materials are currently underway.

Collaboration with Rutherford Laboratory, UK

The series of samples listed in Table V - 8 have been sent for neutron studies at ISIS (Rutherford Lab, UK) under the direction of Professor Bill David. Data collection and preliminary analyses have been completed. The data show that defects in the materials and, in particular, stacking faults in the Li_2MnO_3 end-member, provide extremely complex structures on a local scale. A complete description of these defects is now being pursued in order to elucidate their structural role in the electrochemical performance of composite electrode structures.

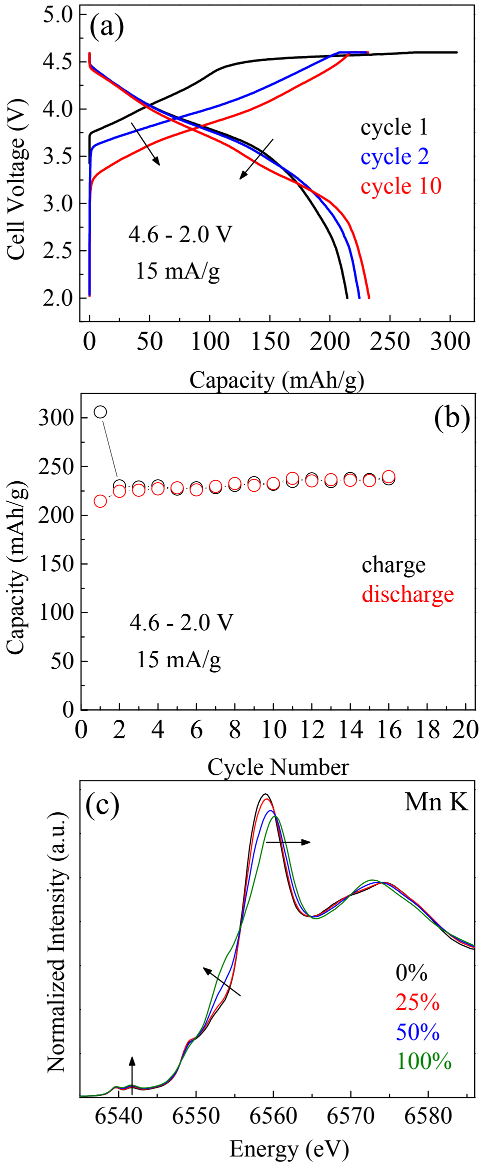

Figure V - 173: Electrochemical performance, (a) and (b), of $0.5Li_2MnO_3$•$0.5LiMn_{0.5}Ni_{0.5}O_2$ cathodes synthesized via natural Ni→NiO→$Ni(NO_3)_2$→ion-exchnage with Li_2MnO_3. (c) Mn K-edge XANES of $0.5Li_2MnO_3$•$0.5LiMn_{0.5}Ni_{0.5}O_2$ with increasing integration of a $LiMn_{1.5}Ni_{0.5}O_4$ spinel component

Conclusions and Future Directions

A synchrotron-based study on the complex structures of $y\{xLi_2MnO_3\bullet(1-x)LiMO_2\}\bullet(1-y)LiM_2O_4$ electrodes has been initiated. XAS, HR-XRD, and neutron powder diffraction data have been collected on a series of end-member and composite compositions of interest. A detailed analysis of the X-ray absorption data, giving local structures including coordination and bond distances, will be combined with HR-XRD and neutron PDF analysis to build a model of these structurally integrated cathodes across multiple length scales. These models will then be applied to cycled systems to better understand the structure-electrochemical properties of the electrodes. A synthesis method has been tested and evaluated for making ^{62}Ni-enriched composite cathodes. Enrichment potentially allows for an unprecedented look into the complexities of these structures. Future work will include high-resolution electron microscopy (HR-TEM) as well as computational modeling and simulation.

V.F.2 Advanced *In situ* Diagnostic Techniques for Battery Materials (BNL)

Xiao-Qing Yang
Brookhaven National Laboratory

Chemistry Department
Building 555
Upton, NY 11973
Phone: (631) 344-3663; Fax: (631) 344-5815
E-mail: xyang@bnl.gov

Xiqian Yu (Co-PI)
Chemistry Department
Building 555
Upton, NY 11973
Phone: (631) 344-4142; Fax: (631) 344-5815
E-mail: xyu@bnl.gov

Start Date: October 2013
Projected End Date: September 2014

Objectives

- To determine the contributions of electrode materials changes, interfacial phenomena, and electrolyte decomposition to the cell capacity and power decline.
- To develop and apply synchrotron-based *in situ* X-ray techniques such as X-ray diffraction (XRD) and X-ray absorption spectroscopy (XAS) to study materials in an environment that is close to real operating conditions.
- To perform diagnostic studies of the potentially low cost and high energy density cathode materials such as spinel structured $LiNi_xMn_{2-x}O_4$.
- To develop new diagnostic tools for battery studies.

Technical Barriers

- Li-ion and Li-metal batteries with long calendar and cycle life.
- Li-ion and Li-metal batteries with superior abuse tolerance.
- High production cost of PHEV batteries.

Technical Targets

- Complete the studies of the kinetic properties of $Li_{1.2}Ni_{0.15}Co_{0.1}Mn_{0.55}O_2$ high energy density cathode materials during constant current charge using X-ray absorption spectroscopy.
- Complete the development of using quick X-ray absorption spectroscopy technique to study the kinetic properties of high energy density cathode materials during constant voltage charge.
- Complete the *in situ* XRD and absorption studies of Fe-substituted, high-voltage spinel during heating.

Accomplishments

- Used newly developed "quick XAS" technique to study the kinetics of high energy density cathode materials for Li-ion batteries during electrochemical delithiation.
- Carried out thermal stability studies of Fe-substituted high voltage cathode material $LiNi_{1/3}Mn_{4/3}Fe_{1/3}O_4$ during heating.
- Carried out studies on relationship between thermal stability and structural changes of Fe-substituted high voltage cathode material $LiNi_{1/3}Mn_{4/3}Fe_{1/3}O_4$ during heating, using XRD and XAS.

✧ ✧ ✧ ✧ ✧

Introduction

Li-rich layered oxides are becoming more appealing as high-energy density cathode materials for Li-ion batteries recently as they exhibit high capacities over 250 mAh g^{-1} with a high operating voltage. However, the rate capability of this material is not satisfactory and needs to be improved. There are two important factors affecting the transport property, the structural factor and the elemental factor. The structural factor considers the different reaction rates between the $LiMO_2$ and Li_2MnO_3 components. Experimental results distinguishing the kinetic property of each component in the composite would be very helpful in understanding the fundamentals of the kinetic properties. For the elemental factor, the charge transfer rate of each individual transition metal element (Ni, Co, and Mn) is quite important. Therefore, the in-depth understanding with elemental selectivity for the delithiation kinetics distinguishing the $LiMnO_2$ and Li_2MnO_3 components in bulk will provide valuable guidance for the optimization of Li-rich layered materials with improved rate capability.

$LiNi_{0.5}Mn_{1.5}O_4$ (LNMO) with high operating voltage is a very good candidate for serving as high energy density cathode material in Li-ion batteries. However, In order to be used in EVs, the thermal stability of LNMO needs to be significantly improved. It has been reported that charged LNMO starts oxygen release at around 250°C, showing far worse than its parent material $LiMn_2O_4$ (LMO). The Fe-substituted LNMO designed and synthesized by the group shows dramatic thermal stability improvement, but maintains comparable high voltage capacity as the non-substituted LNMO. The structural changes of this new material during cycling and heating were studied.

Approach

Synchrotron based X-ray diffraction (XRD), X-ray absorption spectroscopy (XAS), especially the "quick-XAS" techniques were used to elucidate and differentiate the contribution from each component and element to the capacity.

Synchrotron based XRD and XAS, as well as combined time resolved XRD in combination with MS techniques were used during electrochemical cycling and heating.

Results

High energy density $Li_{1.2}Ni_{0.15}Co_{0.1}Mn_{0.55}O_2$ material: Figure V - 174a shows the 1st charge curve of the $Li_{1.2}Ni_{0.15}Co_{0.1}Mn_{0.55}O_2$/Li cell during *in situ* XAS experiments. The normalized Mn, Co and Ni K-edge X-ray absorption near edge structure (XANES) spectra of $Li_{1.2}Ni_{0.15}Co_{0.1}Mn_{0.55}O_2$ electrode during charge are shown in Figure V - 174b.The K-edge XANES spectra for Ni shown in Figure V - 174b exhibit the entire rigid edge shift towards higher energy continuously until the charging voltage reached 4.4 V, indicating the oxidation of the Ni^{2+} to close to Ni^{4+} in this charging region. Upon further charging up to the voltage plateau, only slight change of the XANES profile can be observed in comparison to the 4.4 V charged state, with no further change of the K-edge energy position, which indicates very little further oxidation of Ni in this voltage range. For Mn, the shape of the XANES spectra continuously changes during charge, but the inflection point of the K-edge spectra stays at an almost constant value of approximately 6556 eV throughout the whole charging process, implying that the oxidation state of Mn may remain close to Mn^{4+} throughout the charging process. All of the XANES shape changes at the Mn K-edge are mainly caused by the variation of local structure during Li deintercalation. Similar to the Mn XANES feature, the shape of the Co K-edge spectra continuously changes but the energy position of the absorption edge basically does not shift at all. Previous work has proposed that the charge compensation for the Li deintercalation process in a similar cathode system could be achieved mainly at both oxygen and cobalt sites simultaneously. Figure V - 174c presents the Fourier transformed (FT) EXAFS spectra of Mn, Co and Ni *in situ* collected during initial charging.

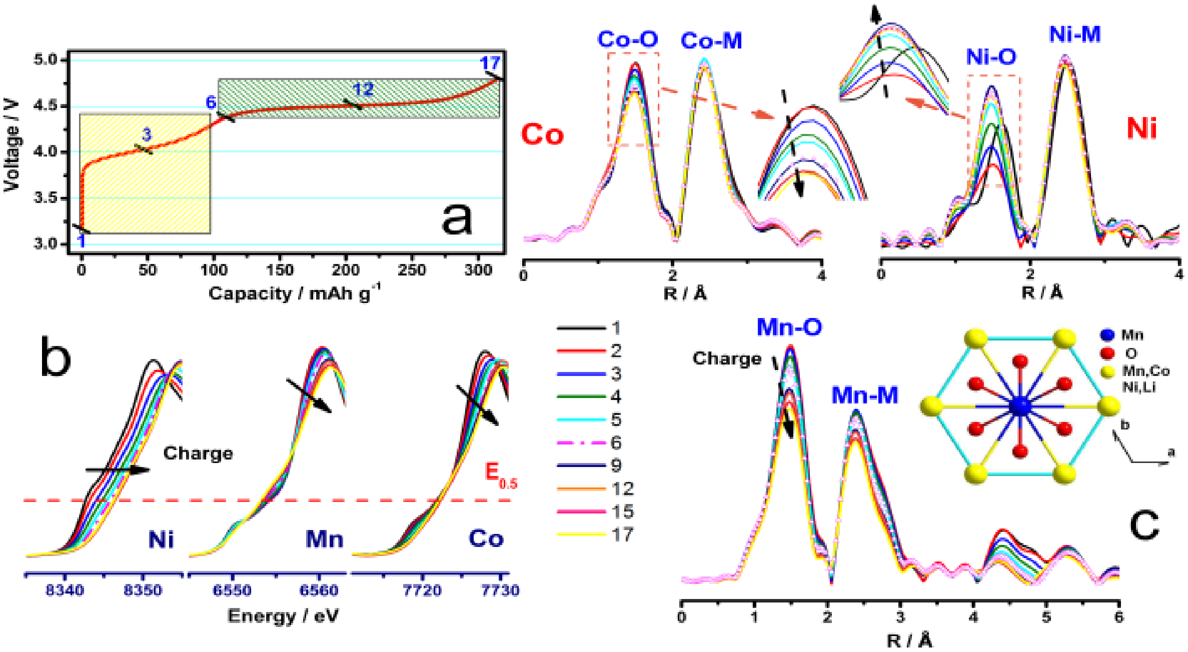

Figure V - 174: (a) The first charging curve of $Li_{1.2}Ni_{0.15}Co_{0.1}Mn_{0.55}O_2$ during *in situ* XAS experiment (under constant current), selected XAS scan numbers are marked on the charge curves; (b) Normalized XANES spectra and (c) Magnitude of Fourier transformed Mn, Co and Ni K-edge spectra collected during initial charge. Inset is the schematic view of the coordination environment around transition metal ions

The first peak corresponds to the Metal-Oxygen interaction and the second peak is related to the Metal-Metal interaction, as labeled in each spectrum. The most significant changes in intensity are observed at the first peak of the Metal-Oxygen bonding for all Mn, Co and Ni during initial charge. A closer inspection reveals that the Ni-O and Co-O peaks completed most of their intensity changes when the voltage reached 4.4V. After that, during further charging through the voltage plateau region, they only exhibit slight changes. In contrast, the Mn-O peak continues its intensity changes in the voltage plateau above 4.4 V all the way to the end of charge at 4.8 V. This suggests that in the voltage slope region (3V-4.4V), the delithiation reaction is mostly related to the oxidation of Ni and Co, while in the voltage plateau region, it is mostly related to the Mn sites during initial charge.

The comparative Fourier transformed magnitude of the corresponding Ni, Co, Mn K-edge EXAFS spectra during constant voltage charge at 5V are plotted in Figure V - 175 by using color scale.

For Ni, the first coordination peaks (Ni-O) show dramatic changes in both position and intensity within the first 100 seconds, which represents the charge compensation occurring at the Ni sites. The peak intensities decreased first (from 0 to *ca.* 60 sec) due to the Jahn-Teller distortion caused by the oxidation of Ni^{2+} to Ni^{3+}, then turned around to increase with further oxidation of Ni^{3+} to Ni^{4+}. The EXAFS features remain unchanged after 160 seconds, indicating the oxidation of Ni^{2+} to Ni^{4+} was almost completed within the first three minutes. For Co and Mn, the first coordination shell peak (Co-O and Mn-O) intensities show a continuous decrease. No obvious Co-O peak intensity changes can be observed after 200 seconds at 5V charge while Mn-O peak intensities continued to decrease in the whole observation time scale (900 second), indicating a much slower delithiation kinetics around Mn sites. These results show that Mn sites have much poorer reaction kinetics both before and after initial "activation" of Li_2MnO_3, comparing with Ni and Co, providing valuable guidance in designing various Li-rich layered materials with desired balance of energy densities and rate capabilities for different applications.

High-voltage, Fe-substituted LNMO: The results of *in situ* XRD spectra for Fe-substituted $LiNi_{1/3}Fe_{1/3}Mn_{4/3}O_4$ sample are shown in Figure V - 176 together with the charge-discharge curves.

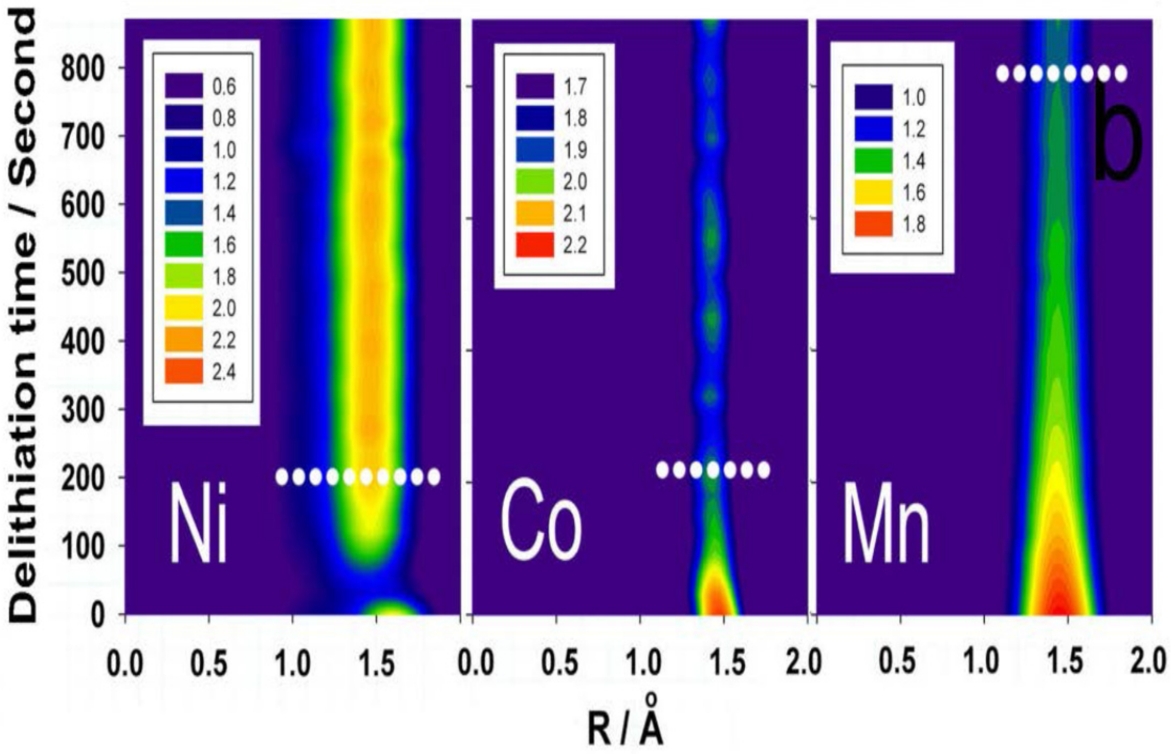

Figure V - 175: EXAFS spectra of $Li_{1.2}Ni_{0.15}Co_{0.1}Mn_{0.55}O_2$ during constant voltage charging at 5V. Ni, Co, Mn reacted simultaneously using time-resolved XAS technique. Projection view of corresponding Ni-O, Co-O, Mn-O peak magnitudes of the Fourier transformed K-edge spectra as functions of charging time

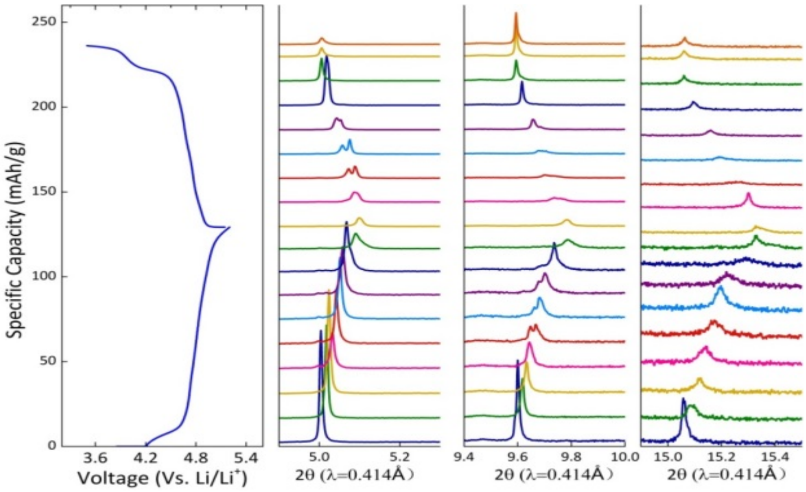

Figure V - 176: *In situ* XRD spectra for Fe-substituted $LiNi_{1/3}Fe_{1/3}Mn_{4/3}O_4$ high voltage spinel sample during charge-discharge cycle between 3.6 V to 5.0V

During charge, it is clearly seen that the reaction proceeds in a solid-solution fashion until 0.4Li was extracted from the material. After that, phase separation occurs and each phase reacts in a solid-solution fashion, leading to two solid-solution reactions. This is also what happened in the following discharge process until around 0.6Li was inserted back into the material. After that, the two phases merge into one and react in a solid-solution fashion until the end of discharge. This behavior is quite different from the non-substituted, high-voltage spinel $Li_xNi_{0.5}Mn_{1.5}O_4$. These results are being further analyzed for reporting in future publications.

The results of *in situ* XAS spectra for Fe-substituted $LiNi_{1/3}Fe_{1/3}Mn_{4/3}O_4$ sample during heating at Fe-K-edge, Mn K-edge, and Ni K-edge are shown in Figure V - 177 together with the schematic of the migration of Fe to the tetrahedral sites. The stabilizing role of Fe is further confirmed by *in situ* XANES study of charged $LiNi_{1/3}Fe_{1/3}Mn_{4/3}O_4$ sample as shown in Figure V - 177. By examining the changes of pre-edge part during the heating process, it is clear that the pre-edge of Fe increases significantly with increasing temperature. In contrast, pre-edges for Mn and Ni are almost invariant in the whole process. Since the intensity of pre-edge is very sensitive to the local environment of transition metal, such great intensity increase implies Fe ions migrate from octahedral sites to the tetrahedral sites. This process is illustrated in Figure V - 177d.

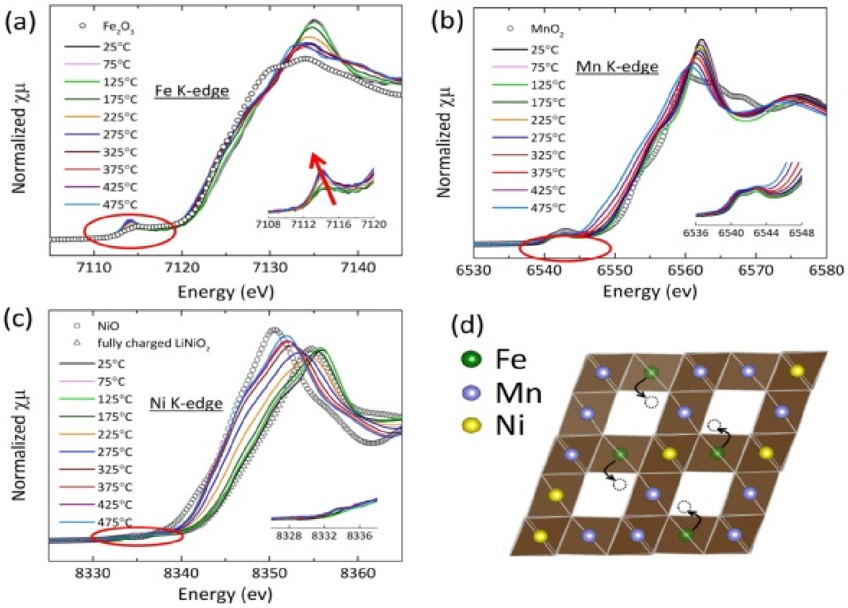

Figure V - 177: *In situ* (a) Fe (b) Mn and (c) Ni K-edge XANES spectra of fully charged $LiNi_{1/3}Mn_{4/3}Fe_{1/3}O_4$ during heating up to 475°C. (d) illustration of Fe migration to the tetrahedral sites

For $Li_{1.2}Ni_{0.15}Co_{0.1}Mn_{0.55}O_2$ materials, by collaborating with Khal Amine's group at ANL, the elementally related delithiation kinetic behaviors studied by time-resolved XAS technique during 5V constant voltage charging show that the Li extraction with a concomitant oxidation of Ni^{2+} to Ni^{4+} has fast reaction kinetic. In contrast, much poorer delithiation kinetic was revealed in Mn region during and after the activation process. These results show that Mn sites have much poorer reaction kinetics comparing with Ni and Co, providing valuable guidance in designing various Li-rich layered materials with desired balance of energy densities and rate capabilities for different applications.

For the high-voltage Fe-substituted LNMO, the origin of the thermal stability improvement effect of Fe substitution has been discovered and the contribution of Fe for maintaining comparable capacity was studied.

For future studies, the thermal stability of a series of blended $LiMn_2O_4$ (LMO) and $LiNi_{1/3}Co_{1/3}Mn_{1/3}O_2$ (NCM) cathode materials with different weight ratios will be studied using time-resolved XRD and mass spectroscopy techniques. The structural evolution of $Li_{2-x}MoO_3$ high-energy density cathode materials will be studied using *in situ* XAS and XRD during charge-discharge cycling.

FY 2014 Publications/Presentations

1. Yang, X.-Q.; Nam, K.-W. (June 2014). "Advanced *in situ* Diagnostics Techniques for Battery Materials." Presented at the 2014 DOE Annual Merit Review and Peer Evaluation Meeting, Washington, D.C.
2. Yu, X.; Yang, X.-Q.; *et.al*. (2013). *Nano Letters* (13); pp. 4721-4727.
3. Xiao, J.; Yang, X.-Q.; *et. al*. (2013). *Journal of Power Sources* (242); pp: 736-741.
4. Wan, W.; Yang, X.-Q.; *et. al*. (2014). *Rsc Advances* (4), pp: 19878-19882, DOI: 10.1039/c4ra01166j.
5. Xu, Z.L.; Yang, X.-Q. (Yang, Xiao-Qing) *et. al*., (2014). *ACS Applied Materials & Interfaces* (6); pp: 1219-1227.
6. Hu, E.Y.; Yang, X.-Q.; *et. al*. (2014). *Chemistry of Materials* (26); pp: 1108-1118.
7. Lee, S.W.; Yang, X.-Q.; *et. al*. (2014). *Journal of Physical Chemistry C* (118); pp: 2834-2843.
8. Kim, M.C.; Yang, X.-Q.; *et. al*. (2014). *Chemsuschem* (7); pp: 829-834, DOI: 10.1002/cssc.201301037.
9. Yu, X.; Yang, X.-Q.; *et. al*. (2014). *Advanced Energy Materials* (4). DOI: 10.1002/aenm.201300950.
10. Xie, Y; Yang, X.-Q.; *et. al*. (2014). *Journal of the American Chemical Society* (136); pp: 6385-6394.
11. Kim, J.W.; Yang, X.-Q.; *et. al*. (2014). *Journal of Power Sources* (254); pp: 190-197.
12. Ma, J.; Yang, X.-Q.; *et. al*. (2014). *Chemistry of Materials* (26); pp: 3256-3262.
13. Guo, B.K.; Yang, X.-Q.; *et. al*. (2014). *Energy & Environmental Science* (7); pp: 2220-2226.
14. He, K.; Yang, X.-Q.; *et. al*. (2014). *ACS Nano* (8); pp: 7251-7259.
15. Ma, J.; Yang, X.-Q.; *et. al*. (2014). *Chemistry-A European Journal* (20); pp: 8723-8730.
16. Shadike, Z.; Yang, X.-Q.; *et. al*. (2014). *Journal of Power Sources* (260); pp: 72-76.
17. Zhou, Y.-N.; Yang, X.-Q.; *et. al*. (forthcoming). "Tuning Charge-discharge Induced Unit-cell-breathing through Metal-Metal Bonding in Layer-structured Cathode Materials for Lithium-ion Batteries." *Nature Comm*.
18. Yang, X.-Q.; Amine, K. (October 2013). "The Studies on the Crystal and Local Structure Changes of Layer Structured Cathode Materials during Multiple Cycling and their Kinetic Behaviors Using Synchrotron Based XRD and X-Ray Absorption Spectroscopy." Presented at the 54th Battery Symposium in Japan, Osaka, Japan.
19. Zhou, Y.-N.; Yu, X.; Hu, E.Y.; Bak, S. Yang, X.-Q.; Lee, H.S.; Li, H.; Huang, X.; Chen, L.; Nam, K.-W.; Cho, S.-J. (June 2014). "Using Synchrotron Based Advanced Characterization Techniques to Study the New Electrode Materials for Next Generation of Batteries." Presented at the Conference of International Battery Frontier 2014 (CIBF2014), Shenzhen, China.
20. Yang, X.-Q. (August 2014). "An Overview of Selected Diagnostic Studies of Electrode Materials for Next Generation Electric Vehicle Batteries." Presented at the 9th U.S.-China Electric Vehicle and Battery Technology Workshop, Seattle, WA.

V.F.3 Interfacial Processes – Diagnostics (LBNL)

Robert Kostecki
Lawrence Berkeley National Laboratory

Environmental Energy Technologies Division
1 Cyclotron Road, MS 90R3029B
Berkeley, CA 94720
Phone: (510) 486-6002; Fax: (510) 486-5454
E-mail: r_kostecki@lbl.gov

Start Date: October 2012
Projected End Date: September 2016

Objectives

- Unveil the structure and reactivity at hidden or buried interfaces and interphases that determine battery performance and failure modes.
- Obtain detailed insight into the dynamic behavior of molecules, atoms, and electrons at electrode/electrolyte interfaces of intermetallic anodes (Si) and high voltage Ni/Mn-based materials.
- Establish clear connections between diagnostics, theory/modelling, materials synthesis, and cell development efforts.
- Provide remedies to interface instability e.g., artificial surface layers (e.g., ALD) and/or structures, novel electrode architecture, electrolyte additives, co-intercalation of secondary metals/ions, etc.
- Characterize active material/electrode/cell degradation modes, improve long-term stability of high-energy Li-ion systems.
- Develop and deploy novel *in situ* far- and near-field optical multifunctional probes.
- Achieve spatial and temporal resolutions that correspond to the size and rate of basic chemical steps and structural, building blocks.

Technical Barriers

This project addresses the following technical barriers related to the battery technology development effort of the DOE Office of Vehicle Technologies:

- Inadequate Li-ion battery energy (related to cost).
- Poor Li battery calendar/cycle lifetime for PHEV and EV applications.
- High electrode impedance that limits power density
- Need for new advanced battery materials and composite electrodes with acceptable specific energy, durability, costs, and safety characteristics.

Technical Targets

- Cycle life: 5,000 (deep) and 300,000 (shallow) cycles.
- Available energy: 200 Wh/kg.
- Calendar life: 15 years.

Accomplishments

- Determined the mechanism of interfacial processes on $LiNi_{0.5}Mn_{1.5}O_4$ and chemical cross-talk in high-energy Li-ion cells.
- Mn and/or Ni dissolution leads to formation of Ni(II) and Mn(II) coordination complexes, which diffuse toward the anode and get integrated in the SEI at the graphite surface (SEI Mn/Ni poisoning).
- Insoluble electrolyte decomposition products form electronic and ionic barriers in composite cathodes and contribute to the impedance rise in graphite anodes in Li-ion cells.
- *In situ* and *ex situ* studies revealed that the nature and kinetics of interfacial processes are strongly dependent on the electrode surface structure.
- The composition and effectiveness of the SEI layer on β-Sn single crystal electrodes in EC-DEC $LiPF_6$ electrolytes varies strongly with the Sn crystal surface orientation. The irreversible capacity observed on polycrystalline β-Sn strongly depends on the surface distribution of theses crystal domains with different reactivity.
- Presence of residual SnO_2 strongly affects Sn surface reactivity, chemistry of the SEI and the irreversible capacity.
- Oxygen-free Sn surfaces produce compact and stable SEI layers!
- Near-field FTIR spectra of the SEI layers are similar to far-field spectra for reference compounds. However, the SEI layer constituents are not homogenously distributed across the electrode surface.
- Spectra of real samples display nano-FTIR peaks associated with compounds thought to be in the SEI.

✧ ✧ ✧ ✧ ✧

Introduction

The main objective of this task is to obtain detailed insight into the dynamic behavior of molecules, atoms, and electrons at electrode/electrolyte interfaces of intermetallic anodes (Si) and high voltage Ni/Mn-based materials at a spatial resolution that corresponds to the size of basic chemical or structural building blocks. The aim of these studies is to unveil the structure and reactivity at hidden or buried interfaces and interphases that determine battery performance and failure modes. To accomplish these goals, novel far- and near-field optical multifunctional probes must be developed and deployed *in situ*. The proposed work constitutes an integral part of the concerted effort within the BATT Program and it attempts to establish clear connections between diagnostics, theory/modeling, materials synthesis, and cell development efforts.

This project provides a better understanding of the underlying principles that govern the function and operation of battery materials, interfaces and interphases, which is inextricably linked to the successful implementation of high energy density materials such as Si and high voltage cathodes in Li-ion cells for PHEVs and EVs. This task also involves the development and application of novel innovative experimental methodologies to study and understand the basic function and mechanism of operation of materials, composite electrodes, and Li-ion battery systems for PHEV and EV applications.

Approach

Design and employment of novel and sophisticated *in situ* analytical methods to address the key problems of the BATT baseline chemistries. The proposed experimental strategies combine imaging with spectroscopy aimed at probing electrodes at an atom, molecular, or nanoparticulate level to unveil structure and reactivity at hidden or buried interfaces and determine electrode performance and failure modes in baseline Li_xSi-anodes and high-voltage LMNO cathodes. The main goal is to gain insight into the mechanism of surface phenomena on thin-film and monocrystal Sn and Si intermetallic anodes and evaluate their impact on the electrode long-term electrochemical behavior. Comprehensive fundamental study of the early stages of SEI layer formation on polycrystalline and single crystal face Sn and Si electrodes will be carried out. *In situ* and *ex situ* far- and near-field scanning probe spectroscopy will be employed to detect and monitor surface phenomena at the intermetallic anodes high-voltage (>4.3 V) model and composite cathodes.

Results

The mechanism of Ni and Mn dissolution from $LiNi_{0.5}Mn_{1.5}O_4$ and $LiMn_2O_4$ spinel electrodes: The effect of Ni and Mn dissolution and migration from $LiNi_{0.5}Mn_{1.5}O_4$ cathode toward the graphite anode and the mechanism of their interaction with the SEI layer were studied. The nature and distribution of Ni and Mn species incorporated in the SEI layer at the graphite anode were probed using optical fluorescence microscopy and x-ray absorption spectroscopy.

Fluorescence spectroscopy measurements were carried out both *in situ* on binder- and carbon additive-free $LiNi_{0.5}Mn_{1.5}O_4$ and $LiMn_2O_4$ spinel electrodes and *ex situ* on graphite electrodes from a cell that was cycled 625 times against a $LiNi_{0.5}Mn_{1.5}O_4$ composite electrode. While the electrochemical data of the $LiMn_2O_4$ electrode did not reveal significant fluorescence rise despite reversible redox of Mn(IV)/(III), the $LiNi_{0.5}Mn_{1.5}O_4$ electrode exhibits a strong fluorescence signal rise correlated with the Ni electro-catalytic activity. Interestingly, *ex situ* fluorescence measurement performed on pristine electrodes is free of fluorescence, whereas graphite and $LiNi_{0.5}Mn_{1.5}O_4$ cycled electrodes exhibit non-uniform fluorescence pattern. A plausible explanation of the observed fluorescence must involve formation of fluorescent organo-metallic compounds by reaction between Ni metal ions and the electrolyte decomposition products. As the concentration of the metal-ion center increases, the fluorescence intensity rises

Since in this case Mn metal ions do not form fluorescent species, X-ray absorption near edge spectroscopy (XANES) measurements were carried out on the cycled graphite to analyze the oxidation state and local bonding of Ni and Mn in the SEI layer. The normalized XANES spectra for five different locations are very similar, which indicates that the chemical state and structure of the Ni or Mn species are identical throughout the whole measurement area. A direct comparison of the nickel/manganese K-edge transmission XANES spectra with reference spectra indicates that (II) is the dominant valence state of Ni and Mn in the SEI layer and that their molecular environments are very similar to that of metal oxalate vs. $LiNi_{0.5}Mn_{1.5}O_4$ (Figure V - 178).

These results support the general idea of Ni and Mn dissolution from $LiNi_{0.5}Mn_{1.5}O_4$ and their transport across the electrolyte toward the anode. However the observed fluorescence suggests that manganese and nickel do not diffuse/migrate as free Mn(II) and Ni(II) ions, which then get incorporated into the SEI layer through the ion exchange mechanism with mobile Li^+.

The fluorescent background of the Raman spectrum of the cycled graphite electrode is very similar to that of Mn(II)acetylacetonate and confirms the presence of Mn metal complexes with β-diketone ligands. This is supported by the Mn K-edge transmission X-ray absorption near edge spectra (XANES) of the graphite negative electrode shown in Figure V - 178, which exhibit spectral features similar to that of Mn(II) bisacetylacetonate and Mn(II) oxalate. A linear combination analysis revealed that the Mn species present within the SEI are mainly Mn(II)(acac)$_2$.

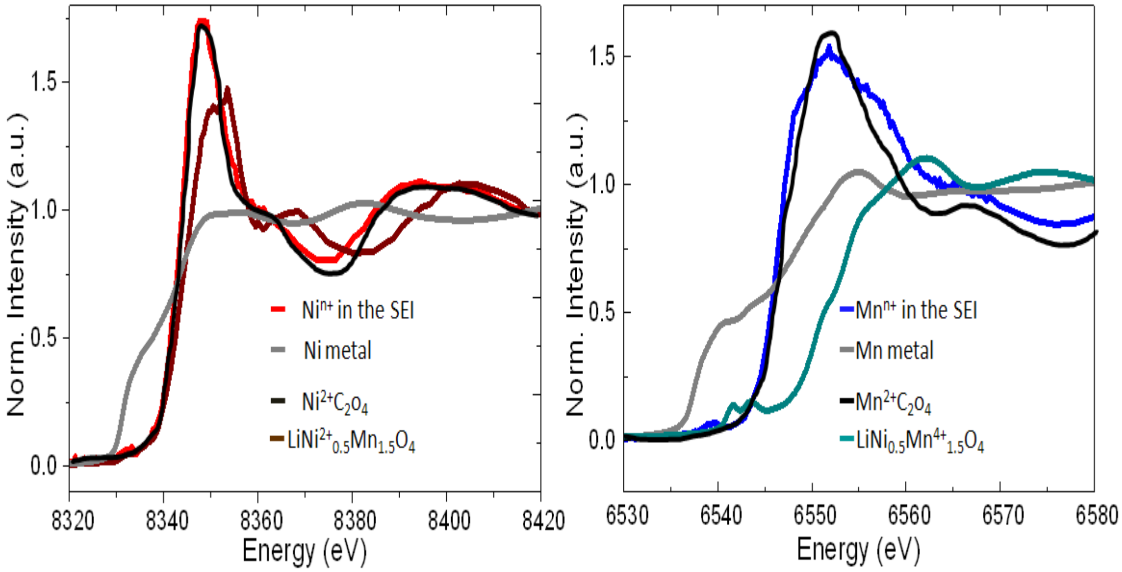

Figure V - 178: Normalized nickel and manganese K-edge transmission XANES spectra of the cycled graphite electrode compared with references

These new results are consistent with recent literature reports of Ni(II) and Mn(II) species in the SEI layer. However, the exact nature of these species revealed in this work clearly points at Ni(II) and Mn(II) complexes. A non-uniform distribution of these compounds in the SEI layer accumulate may indicate different chemical affinity of those species to the SEI basic building blocks. *In situ* and *ex situ* LIB and near-field IR measurements are underway to study further the mechanism of formation of the metal complexes and their detrimental effect on Li-ion transport in the SEI layer and the electrode impedance (Milestone 4 FY2014).

Interfacial phenomena on Si single crystal electrodes: The SEI formation on the facets (100), (110) and (111) was controlled electrochemically during the first potentiostatic charge in a three electrode cell from 2.5 V, to 500 mV (before Si-Li alloying) and 10 mV versus Li/Li$^+$. The effect of VC and FEC additives was evaluated by using the following electrolyte compositions: 1 M LiPF$_6$, EC/DEC (3:7), 1 M LiPF$_6$ 2% VC, EC/DEC (3:7) and 1 M LiPF$_6$ 10% FEC, EC/DEC (3:7). Composition, structure and morphology of the SEI layer were investigated by a combination of *ex situ* FTIR, SEM-EDX, LIBS and XPS.

The SEI layer formation in the electrolyte with and without vinylcarbonate (VC) or fluoroethyl carbonate (FEC) additives starts at the potential ca. 2.2 V (Figure V - 179). Variations of the I-V polarization profiles and the charge consumed in the electrolyte reduction process indicate different mechanisms of the SEI layer formation and their passivating behavior. Consistently, the SEI morphology also varies greatly with the electrolyte composition. Spectroscopic analysis of the SEIs revealed different ratios of LiF, alkyl carbonates and Si-O-F (Figure V - 179). However, the observed discrepancies between EDX and XPS data may indicate non-uniform decomposition products distribution at the surface and in the bulk of the SEI layers.

The Si surface crystal orientation also strongly affects the electrochemical and spectroscopic response of Si in organic carbonate electrolytes. The composition of the SEI layer is quite dissimilar at Si (100), Si (110) and Si (001) particularly at the beginning of the electrolyte reduction process. Most importantly, these differences in the surface chemistry are still visible upon full lithiation of Si when the original surface crystal structure turned totally amorphous. A plausible explanation involves possible differences in Si surface reactivity, surface reconstruction effects and Li-ion diffusion pathways.

Development of novel characterization techniques: *In situ* double-femtosecond (fs) pulse laser-induced breakdown spectroscopy (LIBS) in a collinear configuration was used to improve the sensitivity of LIBS analysis of interfacial layers on Si(100) and SEI formed on Si(100) electrodes submerged in liquid electrolytes (Figure V - 180). Initial experiments were aimed towards improvement of excitation parameters for optimization of emission intensities. Significant emission signal enhancements were observed in the double- vs. the single-pulse LIBS of Si (100) in 1M LIPF$_6$ in EC/DEC (Figure V - 180). The emission of specific lines (Li and C$_2$) of Si(100) and SEI grown on Si(100) was also compared in preliminary experiments in 1M LIPF$_6$ in EC/DEC, demonstrating emission intensity differences between the two electrodes associated with elemental and molecular concentration variations at two solid/liquid interfaces.

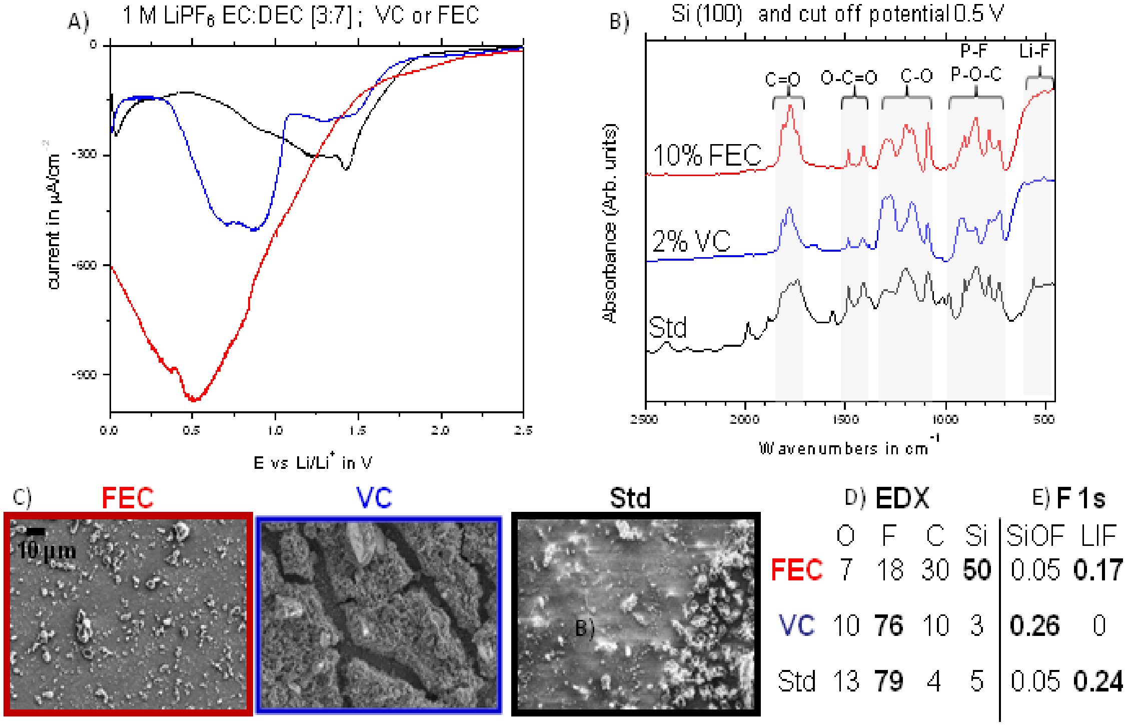

	D) EDX				E) F 1s	
	O	F	C	Si	SiOF	LIF
FEC	7	18	30	**50**	0.05	**0.17**
VC	10	**76**	10	3	**0.26**	0
Std	13	**79**	4	5	0.05	**0.24**

Figure V - 179: A) I-V polarization plots,, B) FTIR spectra, C) SEM images, D) EDX and E) XPS analysis of the SEI layer on the Si (100) electrode in 1 M LiPF6, EC/DEC (3:7), electrolyte with VC or FEC additives

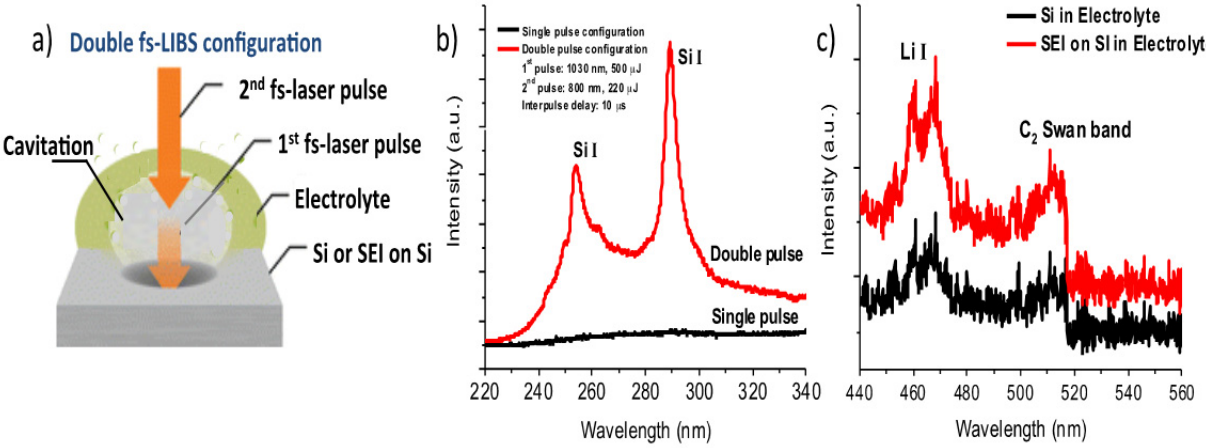

Figure V - 180: a) Double fs-pulse LIBS scheme used for analysis of SEI layers in liquid electrolytes. b) Signal enhancement of Si (100) in 1M LIPF$_6$ EC/DEC electrolyte with the double-pulse configuration. c) Comparison of double fs-pulse LIBS signals of Si and SEI on Si in the same electrolyte

In situ near-field characterization techniques to study electrochemical interfaces involved the development of a liquid cell similar to those available in some commercial atomic force microscopes. The engineering complications associated with retrofitting the near-field microscope proved this approach infeasible. The approach was altered to one using graphene as a thin model electrode. It has been shown previously that graphene can be used as a Li-ion electrode whereas the monatomic thickness of the graphene layer will allow the optical probe near-field to interact with the dielectric properties of the surface layer on the obverse side. As a proof of principle, the group proposes to observe the domain structure of a block copolymer spin-coated on graphene without cycling, and if this experiment yields positive results, move on to the *in situ* configuration described above.

Conclusions and Future Directions

- LMNO electrode/electrolyte interface exhibits a fluorescence rise correlated with the beginning of the Ni^{2+} (ca. 4.2 V) oxidation.
- Ni(II) and Mn(II) coordination complexes form at the $LiNi_{0.5}Mn_{1.5}O_4$ surface via reaction between interfacial atoms and the organic carbonate solvents oxidation products.
- The Ni(II) and Mn(II) coordination complexes with β-keto esters ligands partially dissolve in the electrolyte, diffuse towards the anode and get integrated in the SEI at the graphite surface.
- The SEI layer formed at the graphite surface contains Ni(II) and Mn(II) not metallic Mn and Ni as proposed in the literature.
- The mechanism of the SEI layer “poisoning” by the Ni(II) and Mn(II) coordination complexes remains unclear at this moment but it can be used to study basic functions and operation of SEIs in Li-ion systems.
- *In situ* and *ex situ* studies revealed that the nature and kinetics of interfacial processes strongly dependent on the electrode surface structure.
- The composition and effectiveness of the SEI layer on β-Sn single crystal electrodes varies strongly with the Sn crystal surface orientation.
- Presence of residual SnO_2 strongly affects Sn surface reactivity, chemistry of the SEI and the irreversible capacity.
- Near-field FTIR spectra of the SEI layer are similar to far-field spectra for reference compounds. However, the SEI layer constituents are not homogenously distributed across the electrode surface.
- Spectra of real samples display nano-FTIR peaks associated with compounds thought to be in the SEI.
- Apply novel far- and near-field optical multifunctional probes to obtain detailed insight into the dynamic behavior of molecules, atoms, and electrons at electrode/electrolyte interfaces of intermetallic anodes (Si) and high voltage Ni/Mn-based materials at a spatial resolution that corresponds to the size of basic chemical or structural building blocks.
- Unveil the structure and reactivity at hidden or buried interfaces and interphases that determine battery performance and failure modes.
- Develop novel innovative experimental methodologies to study and understand the basic function and mechanism of operation of materials, composite electrodes, and molecular cross talk in Li-ion cells.
- Understand the mechanism of chemical “poisoning’ of SEI by metal coordination complexes formed at the LMNO cathode. Identify underlying principles that govern charge and mass transport phenomena in the SEI layer using model systems and well-defined chemistry e.g., monomolecular films on intermetallic anodes.
- Cooperate with the BATT Task Groups Intermetallic Anodes, High-Voltage Cathodes and industrial partners to investigate the effect of material structure, morphology on formation of the SEI layer.

FY 2014 Publications/Presentations

1. Kostecki, R. (June 2014). “Interfacial Processes in EES Systems Advanced Diagnostics.” Presented at the 2014 DOE Annual Merit Review and Peer Evaluation Meeting, Washington, D.C.
2. Qiao, R.; Lucas, I.T.; Karim, A.; Syzdek, J.; Liu, X.; Chen, W.; Persson, K.; Kostecki, R.; Yang, W. (2014). *Adv. Mater. Interfaces*; p: 1300115; DOI: 10.1002/admi.201300115.
3. Lux, S.F.; Chevalier, J.; Lucas, I.T.; Kostecki, R. (2014). Electrochemistry Comm. (46); pp. 5-8. DOI:10.1016/j.elecom.2014.05.030.

V.F.4 Microscopy Investigation on the Fading Mechanism of Electrode Materials (PNNL)

Chong-Min Wang
Pacific Northwest National Laboratory

Environmental Molecular Sciences Laboratory
902 Battelle Boulevard, Mail Stop K8-93
Richland, WA 99352
Phone: (509) 371-6268; Fax: (509) 371-7866
E-mail: Chongmin.wang@pnnl.gov

Start Date: July 1, 2013
Projected End Date: September 30, 2016

Objectives

- Use *in situ* and *operando* high-resolution transmission electron microscopy (TEM) and spectroscopy to probe the fading mechanism of electrode materials.
- Understand how the structure and chemistry of electrode materials evolve at a dimension ranging from atomic-scale to meso-scale during the charge and discharge cycles.
- Understand the correlation of the structural and chemical change to the fading and failure of lithium (Li)-ion batteries.
- Understand how the interfaces evolve between the electrode and the electrolyte and how they depend on the chemistry of electrolytes.

Technical Barriers

- Capacity and voltage fading occur for Li-ion batteries.
- High theoretical capacity of electrode materials cannot be fully extracted reversibly.

Technical Targets

- Develop new *ex situ*, *in situ,* and *operando* TEM diagnostic techniques for directly probing the structural evolution of electrode and interfaces.
- Identify the quantitative correlation of the structural and chemical change with the fading and failure of Li-ion batteries.
- Use in situ and operando TEM studies to guide smart microstructure design concepts for high capacity and long-cycle-life Li-ion batteries.

Accomplishments

- Demonstrated the first nano battery under *operando* TEM condition. A liquid cell based on closed window technique has been developed. This work paved the road for detailed study of SEI layer.
- Established a detailed mechanism on how the surface native oxide layer and artificial coating layer function in Si anode related to capacity fading and Coulombic efficiency.
- Discovered that capacity/voltage fading of $Li_{1.2}Ni_{0.2}Mn_{0.6}O_2$ cathode is closely related to Ni segregation, dissolution, corrosion, fragmentation, and phase transformation of the materials

✧ ✧ ✧ ✧ ✧

Introduction

Most previous microscopic investigations on the structural/chemical evolution of electrode materials and the solid-electrolyte interphase (SEI) layer formation have been either *ex situ* studies or used low-vapor-pressure/solid electrolytes for *in situ* TEM studies. Therefore, these results do not reveal fully detailed dynamic information under practical conditions. It is necessary to develop new *operando* characterization tools to characterize the structural/chemical evolution of electrode and SEI formation and electrode/electrolyte interaction using a practical electrolyte. This will be critical for making new breakthroughs in this field. The success of this work will increase the energy density of Li-ion batteries and accelerate market acceptance of electrical vehicles (EV), especially for plug-in hybrid electrical vehicles (PHEV) required by the EV Everywhere Grand Challenge proposed by DOE/EERE.

Approach

Extend and enhance the unique *ex situ* and *in situ* TEM methods for probing the structure of Li-ion batteries, especially for developing a biasing liquid electrochemical cell that uses a real electrolyte in a nano-battery configuration. Use various microscopic techniques, including *ex situ*, *in situ*, and especially the *operando* TEM system, to study the fading mechanism of electrode materials in batteries. This project will be closely integrated with other research and development efforts on high-capacity cathode and anode projects in the BATT Program to 1) discover the origins of voltage and capacity fading in high-capacity layered cathodes and 2) provide guidance for overcoming barriers to long cycle stability of silicon (Si)-based anode materials.

Results

1. Developed an *Operando* TEM Electrochemical Liquid Cell: In this study, an *operando* TEM electrochemical liquid cell has been successfully developed as illustrated in Figure V - 181. The liquid cell provides the configuration of a real battery with a practical liquid electrolyte. To demonstrate this novel technique, the lithiation/delithiation behavior of single Si nanowires was studied. Some of lithiation/delithiation behaviors of Si obtained using the liquid-cell are consistent with the results from the open-cell studies. However, we also discovered new insights different from the open cell configuration - the dynamics of the electrolyte and, potentially, a future quantitative characterization of the SEI layer formation and structural and chemical evolution.

This liquid-cell nano-battery approach provides indispensable complementary information to the widely applied open-cell approach. The complete electrochemical process can be more fully understood by combining open-cell and liquid cell battery TEM techniques. The open-cell approach provides important information regarding the composition, phase transformation, and atomic resolution structural changes of the electrode itself, allowing high resolution microscopy to be obtained. On the other hand, the liquid-cell allows the usage of any form of liquid electrolyte that is relevant to real battery and full emersion of the electrodes. Therefore, the liquid cell had tremendous potential for the study of the electrolyte-electrode interaction: the SEI formation and growth kinetics. In order to successfully and quantitatively measure the SEI layer using this liquid-cell battery approach, optimized cell development and electron dose calibrations are underway. Our results using this *in situ* liquid electrochemical cell open a new avenue for the study of the SEI formation in all the electrochemical reactions inside a working battery cell.

2. *In situ* TEM Probing of Native Oxide and Artificial Layers on Silicon Nanoparticles for Lithium Ion Batteries: Thin layer of coating on silicon nanoparticles has been found to be an effective way for improving the cyclic performance of electrode materials in lithium ion batteries. However, the behavior and the functioning mechanism of such a coating layer have never been fully understood, which is even further complicated by the inevitable existence of a native oxide layer of typically several nanometers on the particle surface. Using *in situ* transmission electron microscopy, we explored the behavior of both native oxide layer and aluminum glycerol (ALGL) coating on silicon nanoparticle upon cyclic lithiation/delithiation. This research discovered that upon initial lithiation, the native oxide layer converts to Li_2O, which essentially increases the impedance and exert mechanical confinement on the particle, resulting in incomplete lithiation/delithiation or inactive particle.

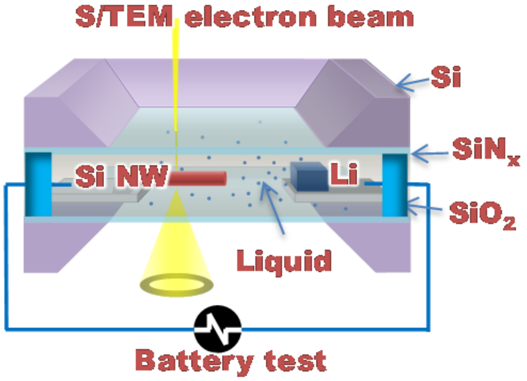

Figure V - 181: Schematic drawing showing the setup of the liquid cell battery

Fabrication of ALGL coating can eliminate the native oxide layer on the silicon nanoparticle. The ALGL has been observed to be rather mechanically flexible and electron and Li^+ conductive, enabling fast and complete lithiation/delithiation of the particle. Further, the ALGL has been found to serve as a separator, effectively preventing the coalescence of the particles during the lithiation/delithiation process. This study clarifies the role of the native oxide on silicon nanoparticle on cycle performance and provides vivid picture of how coating layer works on preserving capacity. This study is summarized in the schematic drawing of Figure V - 182.

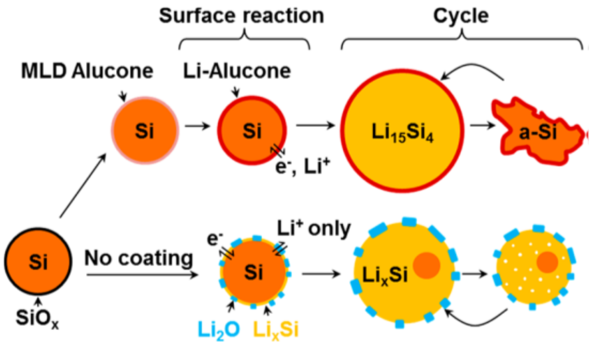

Figure V - 182: Schematics of surface reactions and cycle behaviors of silicon nanoparticles with native oxide layer and artificial coating layer

3. Multiscale structural and chemical characterizations of $Li_{1.2}Ni_{0.2}Mn_{0.6}O_2$ and correlation with the capacity and voltage fading: Voltage and capacity fading of layer structured lithium and manganese rich (LMR) transition metal oxide is directly related to the structural and composition evolution of the material during the cycling of the battery. However, understanding such evolution at atomic level remains elusive. Using aberration-corrected scanning-transmission electron microscopes (S/TEM) equipped with high angle annular dark field/annular bright field (HAADF/ABF) detectors, advanced energy dispersive X-ray spectroscope (EDS) and electron energy loss spectroscope (EELS), we systematically studied the pristine and charge-discharge cycled $Li_{1.2}Ni_{0.2}Mn_{0.6}O_2$ (LMR) cathode materials. Based on atomic level structural imaging, elemental mapping of the pristine and cycled samples and density functional theory calculations, it is found that accompanying the hopping of Li ions is the simultaneous migration of Ni ions towards the surface from the bulk lattice, leading to the gradual depletion of Ni in the bulk lattice and thickening of a Ni enriched surface reconstruction layer (SRL). Furthermore, Ni and Mn also exhibit concentration partitions within the thin layer of SRL in the cycled samples where Ni is almost depleted at the very surface of the SRL, indicating the preferential dissolution of Ni ions in the electrolyte. Accompanying the elemental composition evolution, significant structural evolution is also observed and identified as a sequential phase transition of C2/m →I41→Spinel (Figure V - 183). For the first time, it is found that the surface facet terminated with pure cation is more stable than that with a mixture of cation and anion. These findings firmly established how the elemental species in the lattice of LMR cathode transfer from the bulk lattice to surface layer and further into the electrolyte, clarifying the long standing confusion and debate on the structure and chemistry of the surface layer and their correlation with the voltage fading and capacity decaying of LMR cathode. Therefore, this work provides critical insights for designing of cathode materials with both high capacity and voltage stability during cycling.

Conclusions and Future Directions

A major step forward for the battery research is the demonstration of the *operando* TEM for rechargeable battery. This work is a milestone work that marks the starting of the detailed studying of the SEI layers for rechargeable battery. A combination of *ex situ* and *in situ* TEM and STEM techniques were used to study the structural and chemical evolution of both anode and cathode materials for Li-ion batteries. Si nanoparticles have been extensively studied as anode material for lithium-ion battery. The nanoparticle surface is always covered with a thin layer of native oxide. The function and behavior of the native oxide as well as the artificial coating layer have been clarified by *in situ* TEM. For cathode materials, typically such as $Li(Li_{0.2}Ni_{0.2}Mn_{0.6})O_2$, detailed atomic level information has been captured regarding the structural and chemical evolution of the materials and the correlation with the capacity and voltage fading of the cathode. We discovered that the dopant may selectively segregate in certain crystallographic plane, which will affect the Li-ion transport; and, therefore, the charge/discharge rate of battery. The layer to spinel phase transformation, corrosion, and segmentation are the main factors that contribute to the capacity and voltage fading of the cathode.

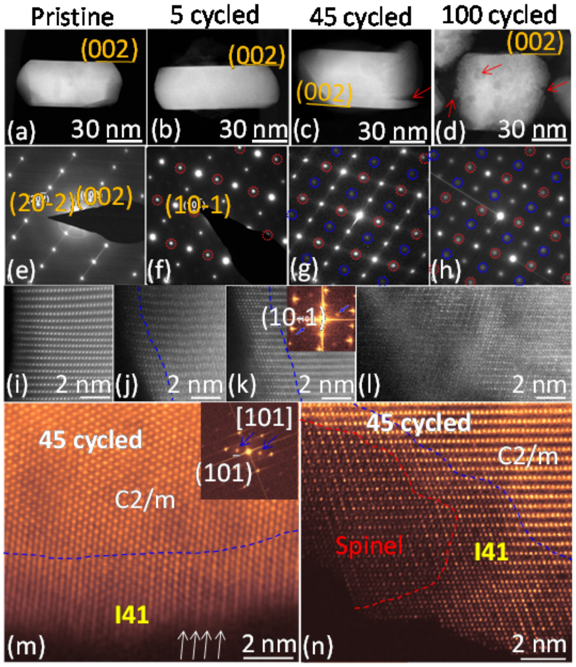

Figure V - 183: (a-d) Low magnification STEM-HAADF images to show cycling induced corrosion. Cracks and pits are highlighted by red arrows. (002) surface planes show strong resistance to corrosion. (e-h) [010] zone axis SAED patterns. Extra diffraction spots appeared in cycled samples, which are highlighted by red and blue circles. Red circles indicated the formation of ordered structure. (10-1) ordered plane is clearly seen after cycling. Blue circles come from double diffraction. (i-l) High resolution STEM-HAADF images to show the cycling induced structure change on particle surfaces. Pristine samples (i) shows homogeneous structure from surface to bulk. Dashed lines in (j, k) highlight the thickness of the SRL. In (l), the whole areas were transformed. (m) [101] zone axis STEM-HAADF image and its fast Fourier transformation image. The white arrows indicate the ordered features of (20-2) planes and extra diffraction spots. (n) [010] zone axis STEM-HAADF image to show spinel structure and I41 structure in a 45 cycled sample

Future work will focus on the following areas:
(1) Atomic level probing of the capacity and voltage fading mechanism of LMR material, especially phase stability of the high-voltage cathode material ($Li(Li_{0.2}Ni_{0.2}Mn_{0.6})O_2$) and modified NCM.
(2) *Operando* TEM investigation of the fundamental characteristics of the SEI layer on a Si anode and its correlation with the chemistry of electrolyte as well as

the battery fading mechanism. (3) Operando TEM will be used to directly observe the characteristics of $Li(Ni_{0.2}Mn_{0.6}Li_{0.2})O_2$-electrolyte interface structures with respect to different electrolyte additives and surface coatings. The future work will intend to answer questions such as: What is the structure between the cathode particle and the electrolyte, and how does this structure evolve during Li-ion transport? How does the phase transformation happen? How does electrolyte additive affect the phase stability and the interface structure and their correlation with the voltage and capacity stability?

FY 2014 Publications/Presentations

1. M. Gu, L.R. Parent, B. L. Mehdi, R. R. Unocic, M. T. McDowell, R. L. Sacci, W. Xu, J. Connell, P. Xu, P. Abellan, X. Chen, Y.i Zhang, D.l E. Perea, J. E. Evans, L. J. Lauhon, J. G. Zhang, J. Liu, N. D. Browning, Y. Cui, I. Arslan, and C. M. Wang, “Demonstration of an Electrochemical Liquid Cell for Operando Transmission Electron Microscopy Observation of the Lithiation/ Delithiation Behavior of Si Nanowire Battery Anodes”, Nano Letters, 2013, 13, 6106−6112.
2. Y. He, C. Ban, A. Genc, L. Pullan, J. Liu, J. G. Zhang, S. Mao, and C. M. Wang, “*In situ* Transmission Electron Microscopy Probing of Native Oxide and Artificial Layers on Silicon Nanoparticles for Lithium Ion Batteries”, ACS Nano, 2014. Online published.
3. M. Gu, H. Yang, D. E. Perea, J. G. Zhang, S. Zhang, and C. M. Wang, “Bending induced Symmetry Breaking of Lithiation in Germanium”, Nano Letter., 14, 4622-4627, 2014.
4. C. M. Wang, invited talk on “Multiscale operando TEM probing of structural and chemical evolution of electrode materials for lithium ion batteries and beyond”, 2014 MRS Spring Meeting, April, 2014, San Francesco.

V.F.5 NMR and Pulse Field Gradient Studies of SEI and Electrode Structure (Cambridge U)

Clare Grey
Cambridge University

Department of Chemistry
Lensfield Road
Cambridge, CB2 1EW
Phone: +44(1223)336509; Fax: +44(1223)336362
E-mail: cpg27@cam.ac.uk

Start Date: October 2012
Projected End Date: September 2016

Objectives

- Identify major SEI components, their spatial proximity, and how they change with cycling.
- Contrast SEI formation on Si vs. graphite and high voltage cathodes.
- Correlate Li^+ diffusivity in particles and composite electrodes with rate.
- Explore how additives modify the SEI.
- Develop new NMR-based methods for identifying different components in the SEI and their spatial proximities within the SEI, which will be broadly applicable to study the SEI formation on a much wider range of electrodes.
- Investigate local structural changes of high voltage/high capacity electrodes on cycling.

Technical Barriers

Capacity fade due to significant surface electrode interphase (SEI) formation (focusing on Si); Reduced rate performance due to SEI formation; High energy density; High power

Technical Targets

- Specific power: 300 W/kg.
- Life: 10 years.
- Capacity fade: <20%.

Accomplishments

- Used solid state NMR spectroscopy to determine the extent of ordering in high voltage $Li(Ni_{0.5}Mn_{1.5})O_4$ spinels and correlate with performance.
- Developed method for studying lithiation of Si nanowires *in situ* by NMR spectroscopy.
- Established protocol for investigating SEI in Si with NMR spectroscopy.
- Examined the effect of various Si coatings on SEI formation.
- Used *in situ* NMR methodology to distinguish between solid and liquid components in the Li-S battery.

✧ ✧ ✧ ✧ ✧

Introduction

The formation of a stable surface electrode interphase (SEI) is critical to the long-term performance of a battery, since the continued growth of the SEI on cycling/aging results in capacity fade (due to Li consumption) and reduced rate performance due to increased interfacial resistance. Although arguably a (largely) solved problem with graphitic anodes/lower voltage cathodes, this is not the case for newer, much higher capacity anodes such as Si, which suffer from large volume expansions on lithiation, and for cathodes operating above 4.3 V. Thus it is essential to identify how to design a stable SEI.

The major technique used in this work is NMR and our SEI studies are complemented by studies that focus on eludidating the short range changes that occur within the electrodes themselves.

Approach

Perform multinuclear nuclear magnetic resonance (NMR) studies of local structure; *in situ* NMR studies of Li^+ transport. Pulse Field Gradient (PFG) measurements of electrolyte diffusivity and tortuosity; SIMS and XPS of SEI composition.

Results

New approach for performing *in situ* NMR of Si nanowires: A new approach for performing *in situ* NMR of Si nanowires has been developed, which allows for an *in situ* study of the whole electrode structure over multiple charge-discharge cycles. Si nanowires grown via CVD methods (as shown by Chan, C. K. et al., “High-performance lithium battery anodes using silicon nanowires” *Nat Nanotechnol.* 3, 31-35, (2008)) were used, but instead of growing the Si wires on stainless steel, the typical support, they were grown on commercially available carbon supports, providing an extremely effective, binder-free model system for *in situ* NMR studies (Figure V - 184).

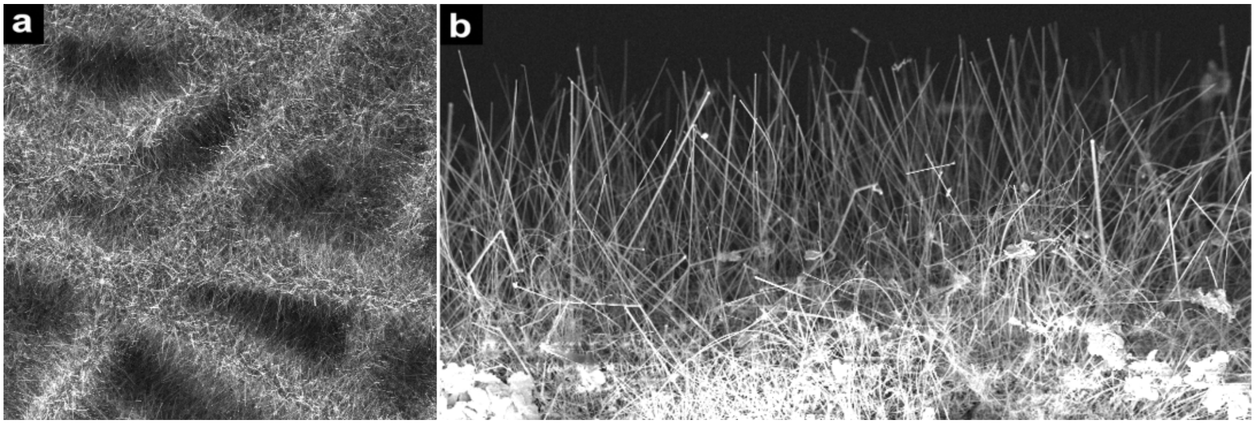

Figure V - 184: Approx. 60 nm Si wires grown on a carbon fiber support

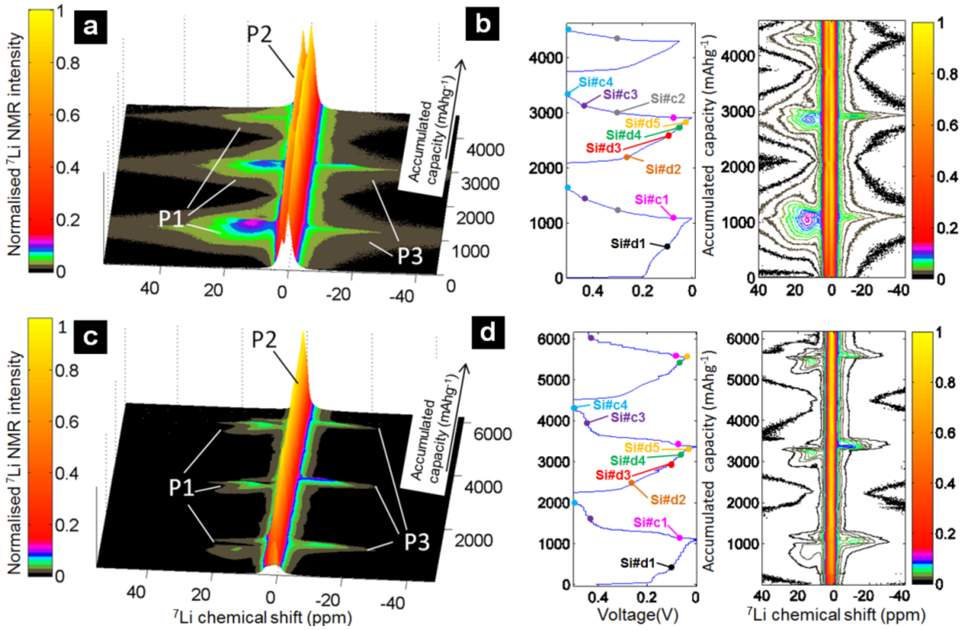

Figure V - 185: Galvanostatic (a, b) and SPECS with 50 mV steps (c, d) cycling of Si nanowires. The formation of small Si clusters (P1 resonance) and the overlithiated crystalline phase $Li_{15+x}Si$ (P3) are clearly seen by ^{7}Li NMR. If all the amorphous phase is converted to $Li_{15}Si$ (c and d) then the system takes a different path on charge, $Li_{15}Si$ reacting to form a low Li content amorphous Si phase (P1 is largely absent)

The method allows study of the wires beyond the 1st cycle (required to convert the crystalline Si into an amorphous phase), which was not possible in earlier studies (in part due to problems associated with maintaining electrical contact between the Si particles and the current collector within the earlier *in situ* NMR design). The approach has been used to date to identify the previously unobserved electrochemical signature associated with the over-lithiation of c-$Li_{3.75}Si$ below 50 mV and investigate the origin of the large hysteresis seen on charging a fully discharge electrode. Spectra of sufficient quality are obtained with only *ca.* 0.5 mg of Si allowing key electrochemical signatures to be mapped onto distinct structural changes. Specifically, by performing NMR studies under SPECS (stepped potential electrochemical spectroscopy) (Figure V - 185), it was possible to identify structurally how the Si local environments were affected by the mode of cycling. An important result was the observation of Si-Si clusters on delithating $Li_{15}Si_4$. It was suggested that the energetics of the formation of these clusters (within this phase) set the voltage for the conversion of $Li_{15}Si_4$ to a-Li_xSi, providing an explanation for the voltage hysteresis in this system. This also provides a robust method for studying the SEI and the effect of different additives on SEI growth, which is currently being pursued.

Study of silicon nanoparticle coatings: A systematic study of silicon nanoparticle coatings has been initiated. Experiments were performed with (3-aminopropyl)triethoxysilane (APTES), 2-cyanoethyl-triethoxysilane, tritriethoxy(octyl)silane (TEOOS), (3-glycidyloxypropyl)trimethoxysilane, and poly(methyl-vinylether-alt-maleic anhydride (Figure V - 186) to examine how various surfaces affect SEI formation and the coulombic efficiencies observed on cycling 15-20 nm Si particles (Figure V - 187). Small Si particles were chosen for initial experiments so as to maximize potential surface reactions. The low-resolution TEM results indicate that the coating procedure resulted in increased particle agglomeration, with a coating surrounding the particle agglomerates. Control experiments will thus be needed to separate effects from any morphological changes induced by the surface treatments from those due to the coatings.

Si electrodes, composed of 1/3 active Si nano particles, 1/3 carboxymethyl cellulose (CMC), and 1/3 super P carbon, were cycled vs. Li metal with 1M $LiPF_6$ in EC/DMC as the electrolyte. Noticeable improvements in coulombic efficiency were observed for all the coatings with APTES showing the best performance (Figure V - 188). Improved rate performance was also observed possibly due to the formation of a thinner SEI. NMR experiments were used to characterize (i) the nature of the coating both before and after electrochemical cycling and (ii) the nature of the SEI with and without the coating. Preliminary NMR experiments confirm that the SEI coating is less thick (as quantified via both ^1H and ^{13}C NMR). Experiments are ongoing to investigate the nature of the coating/grafting of molecules and how this affects SEI formation.

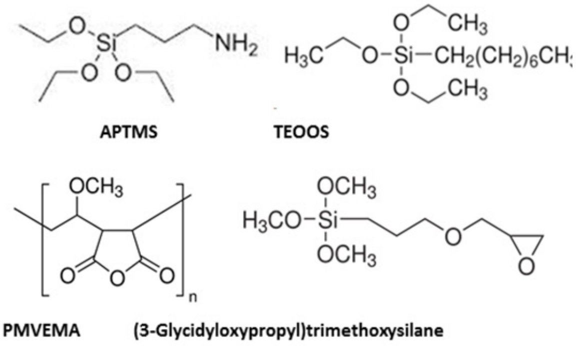

Figure V - 186: Molecules used for Si nanoparticle coating

Investigation of decomposition SEI products: The decomposition SEI products that form on silicon have been investigated by using NMR methods. Initial experiments have focused on a Si-carbon electrode with no binder, so as to maximize the amount of SEI that is formed (Figure V - 189). Electrodes have been investigated at the top of charge so as to avoid complications due to air and moisture sensitive Li_xSi phases. A range of NMR probes have been used including ^1H, ^7Li, ^{19}F and ^{13}C NMR single and double resonance experiments to probe spatial proximity between species. The first challenge to be addressed was how to work up the electrodes for further NMR analysis. In initial experiments, the electrodes were soaked in DMC to remove excess electrolyte. However, this resulted in considerable removal of the SEI, leading to very few observable signals in the NMR measurements. Therefore, it was decided to not rinse any of the samples before performing the experiments, realizing that this would result in considerable electrolyte being trapped in the SEI. However, the goal was to identify all the products of the SEI. Shorter washing treatments in future experiments

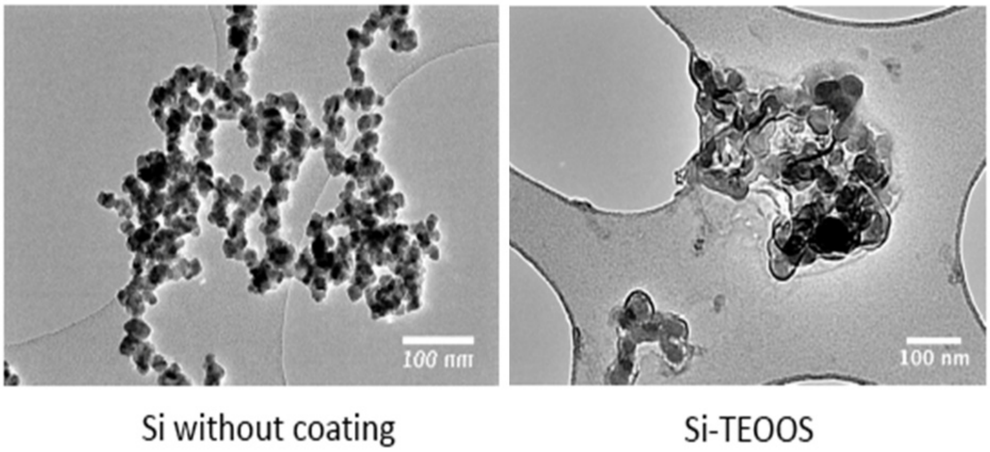

Si without coating

Si-TEOOS

Figure V - 187: TEM results of the Si particles before (left) and after (right) Si-TEOOS coating

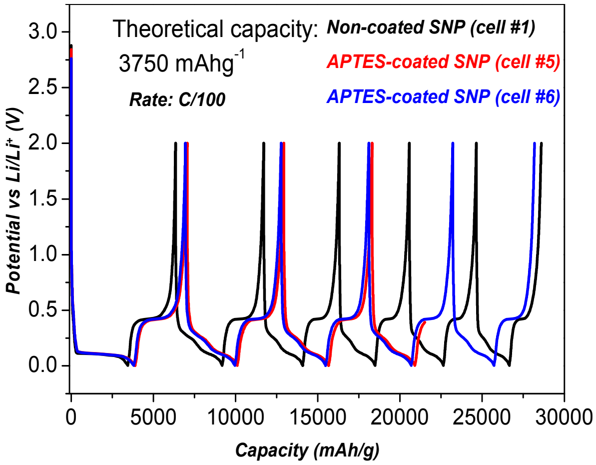

Figure V - 188: Cycling experiments performed with and without the APTES coating

will be explored, once a baseline of all the species that are present is established. Initial experiments used ^1H and were dominated by $LiPF_6$ signals from dried electrolyte. LiF was also observed, but this phase was only observed in significant concentrations when samples were exposed to moisture (by, e.g., washing with reagents that had not been dried carefully, leaving samples in nominally air- tight NMR rotors, etc.). Thus, the LiF that forms in the system (at least) reflects moisture introduced by the subsequent handling of the electrode and is not inherent to the SEI formation mechanism per se. This may be very different when, e.g., CMC binders are used, which are more difficult to dry fully. ^7Li 1D NMR spectra, while being less useful diagnostically, were combined with 2D NMR experiments to determine which phases contained lithium. The ^1H spectra were also dominated by EC, but when combined with ^1H-^{13}C correlation experiments provided signatures for a series of decomposition products. Experiments are now in progress to analyze the 1 and 2D ^{13}C spectra in more detail. Recent SEI studies have focused on a comparison between graphite and Si.

Li-S battery: The *in situ* NMR method was used to investigate the different components in Li-S cell in collaboration with R. Seshadri (UCSB). The Li-S phase diagram was first explored using computational techniques. Both the computational and experimental studies are consistent with the suggestion that the only solid product formed in the cell is Li_2S. No Li_2S_2 was observed. *In situ* NMR spectroscopy also allows the direct observation of both soluble Li^+-species and solids (Li_2S) during cell discharge. It was suggested that during the first discharge plateau, S is reduced to soluble polysulfide species concurrently with the formation of a solid component (Li_2S), Li_2S forming near the beginning of the first plateau, in the cell configuration studied here. The NMR data suggests that the second plateau is defined by the reduction of the residual soluble species to solid product (Li_2S). A ternary phase diagram was developed which helps explain why Li_2S formation is seen initially in this study, but is only seen on the second plateau in some other studies. (See Figure V - 190.)

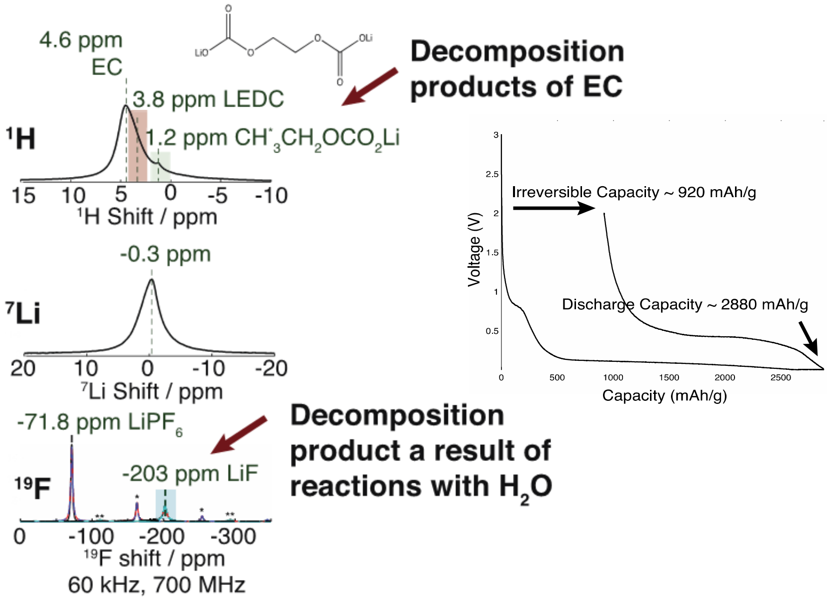

Figure V - 189: NMR spectra obtained after 1 charge discharge cycle (right) of a Si:superP carbon electrode (1:1 Si:C ratio by mass). Electrolyte = EC/DMC. Galvanostatic cycling was performed at a rate of C/75 based on a theoretical capacity of 3579 $mAhg^{-1}$

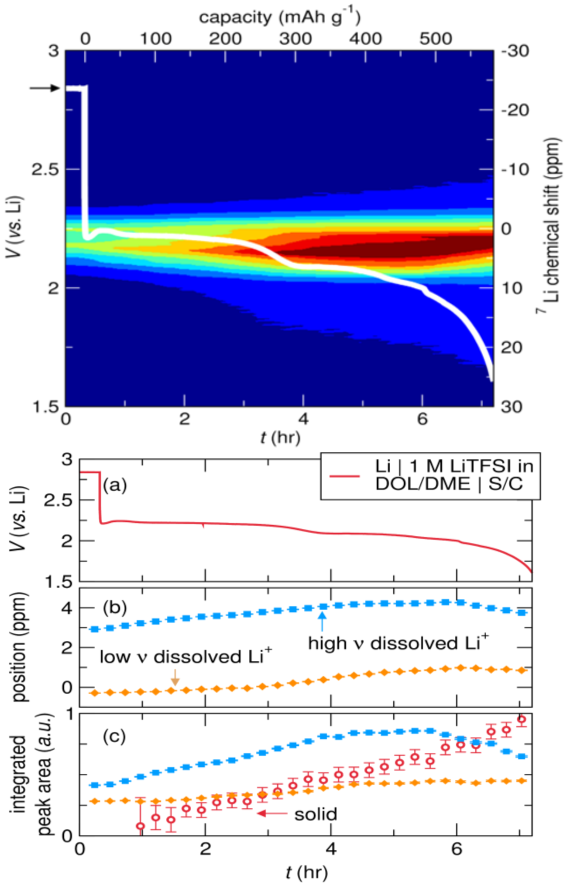

Figure V - 190: Top: The *in situ* ^{7}Li NMR signal overlaid on the electrochemical discharge curve for a Li-S bag cell discharged galvanostatically at a rate corresponding to C/20, using a 1 M LiTFSI in DOL/DME electrolyte. A spectrum is recorded every 15 mins. The cell is held at open circuit for 15 min before discharge. The Li metal resonance at ca. +250 ppm is not shown. Bottom: (a) Discharge profile of the same Li-S bag cell. The spectra were fit using three components (two liquid (high and low frequency) and one solid) to extract the changes in (b) chemical shift and (c) integrated intensities as a function of discharge

Conclusions and Future Directions

The use of *in situ* NMR spectroscopy to probe structural changes (in silicides) following multiple cycles has been demonstrated. Key findings include insight into the large voltage hysteresis seen between discharge and charge. The NMR approach has been extended to investigate the Li-S cell, to determine when Li_2S is formed on discharge. The NMR results, together with DFT calculation results, are used to show that Li_2S is the only solid phase that is formed and to help understand why some studies see Li_2S on the 1st plateau and others do not. The NMR method will continued to be applied to a wider range of systems, focusing on paramagnetic cathode materials.

A detailed study of SEI formation on Si has been performed for the first cycle and major organic components have been identified. The effect of various coatings has been explored. Future directions will include a more detailed study of SEI formation as a function of cycle number and depth of discharge. MR Imaging and pulsefield gradient experiments to explore electrode tortuosities will be continued along with more detailed coating studies.

FY 2014 Publications/Presentations

1. Grey, C. (June 2014). “First Principles Calculations and NMR Spectroscopy of Electrode Materials.” Presented at the 2014 DOE Annual Merit Review and Peer Evaluation Meeting, Washington, D.C.
2. Ogata, K.; Salager, E.; Kerr, C.J.; Fraser, A.E.; Ducati, C.; Morris, A.J.; Hofmann, S.; Grey, C.P. (2014). “Revealing lithium-silicide phase transformations in nano-structured silicon-based lithium ion batteries via *in situ* NMR spectroscopy.” *Nature Commun.* (5); p. 3217.
3. Kim, J.C.; Li, X.; Moore, C.J.; Bo, S.H.; Khalifah, P.G.; Grey, C.P.; Ceder, G. (2014). “Analysis of Charged State Stability for Monoclinic $LiMnBO_3$ Cathode.” *Chem. Mater.* (26); pp. 4200-4206.
4. Duncan, H.; Hai, B.; Leskes, M.; Grey, C.P.; Chen, G. (2014). “Relationships between Mn3+ Content, Structural Ordering, Phase Transformation, and Kinetic Properties in $LiNi_xMn_{2-x}O_4$ Cathode Materials”, *Chem. Mater.* (26); pp. 5374-5382.
5. Grey, C.P. (December 2013). Presentation at MRS Fall Meeting, Boston, M.A.
6. Grey, C.P. (October 2013). Presentation at Rocky Mountain Conference, Copper Mountain.

V.F.6 Cell Failure: Electrochemical Diagnostics (LBNL)

Vincent Battaglia
Lawrence Berkeley National Laboratory

Environmental Energy Technologies Division
1 Cyclotron Road
Berkeley, CA 94720
Phone: (510) 486-7172; Fax: (510) 486-4260
E-mail: vsbattaglia@lbl.gov

Start Date: October 2012
Projected End Date: September 2016

Objectives

- To advance Li- and Li-ion-based technologies to advance their widespread use as traction batteries in vehicles.
- To develop methods and tools necessary for determining precisely the source or sources of failure of any material in a cell.

Technical Barriers

The barriers to batteries being widely deployed in vehicles to provide traction and the recapture of energy lost to breaking are the upfront cost, the limited lifetime, the weight, and the size.

Technical Targets

- Cost: 110 \$/kWh EV; 293 \$/kWh PHEV.
- Lifetime: 15 years EV; 15 years PHEV.
- Weight: 235 Wh/kg EV; 97 Wh/kg PHEV40.
- Size: 500 Wh/L EV; 145 Wh/L PHEV40.

Accomplishments

- Fabricated a Graphite/NCM pouch cell that demonstrated very good cyclability with very little impedance rise.
- Developed a method for testing transition metal dissolution from a cathode as a function of state of charge (SOC).
- Constructed 3-electrode cells that require only one separator between the electrodes and established a method for assigning impedance contributions to each electrode.
- Developed a method for independently assigning a numerical rate of the side reactions and particle isolation in a material.

✧ ✧ ✧ ✧ ✧

Introduction

The BATT Program consists of a large number of individual projects all working towards solving the technical barriers that have been preventing the widespread adoption of EVs and PHEVs. Among the list of projects, there typically exists a collection of PIs engaged with the same material. When this is the case, a Focus Group is established on that material. For 2014, the Focus Groups are 1) High-Voltage NCM and 2) Si Anodes. The responsibility in supporting the Focus Groups is to benchmark materials and to develop techniques for assessing performance and the sources of cell failure.

For the NCM Focus Group, it is anticipated that the material may experience gassing as it is pushed to higher voltages. The responsibility is to find a way to make cells large enough to generate a significant amount of gas and a means of collecting and sampling the gas for chemical analysis that will limit the amount of external exposure. It is also anticipated that higher voltages may result in transition metal dissolution and cell impedance rise. The responsibility is to develop methods to measure the rate of dissolution and its dependence on SOC and to describe accurately the source of impedance rise.

For the Si Focus Group, it is anticipated that the material will fail partially as a result of particle isolation that comes from volume expansion during lithiation and fail as a result of side reactions on exposed surface as a result of cracking. The responsibility is to find a way to independently measure these two sources of failure, and to test the Si in full cells and establish its performance capabilities and to identify sources of failure for high-loading Si electrodes.

Approach

A Focus Group is identified by BATT Program management to zero in on a problem that may be common to a class of materials. A promising chemistry is identified specifically in the Focus Group or is appropriately selected to accentuate the problem. Methods are developed in anticipation of the problem that will accurately and definitively define and measure the problem. Battery-grade materials are obtained from reliable, industrial sources. Electrodes are fabricated using materials that accentuate the problem to be studied. Performance metrics are obtained, and eventually shared with other BATT PIs at periodic meetings and through quarterly reports. Progress is made through a group effort focused on common materials.

Results

Fabrication of high-performance pouch cells: For many cathodes pushed to a high enough potential, gas is formed. For the Focus Group on High-Voltage NCM, it is anticipated that at voltages above 4.3 V vs. Li that a change occurs in the chemistry to prevent longer term cycling. One of those changes may have to do with reactions with the electrolyte and it is possible that this will bring on different products which may be reflected in the composition of the gas. To prepare for this event, the group developed pouch cells and demonstrated that they cycle as well as coin cells, see Figure V - 191.

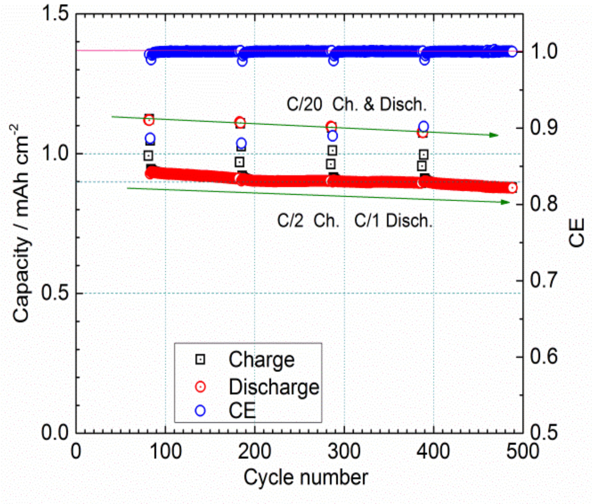

Figure V - 191: Charge and discharge capacity and coulombic efficiency vs. cycle number of a pouch cell with graphite/NCM cycled to 4.2 V

Figure V - 191 shows the cyclability of the full cell from the 80th to the 500th cycle where little capacity is lost and the coulombic efficiency remains high. What is also telling is if one plots the average voltage on charge and the average voltage on discharge to see if the data separates with cycle number or is essentially parallel. In the latter case, such a plot indicates that there is little impedance rise in the cell over the course of cycling (Figure V - 192).

Cathode dissolution: NCM and NCM-related materials are considered the next generation of cathode materials for Li-ion cells to replace $LiCoO_2$ and $LiNi_{0.8}Co_{0.15}Al_{0.05}O_2$ materials. In order to take full advantage of this material, the extraction of Li to higher voltages must not result in capacity fade. One area that is always of interest with this class of oxides is the level, rate, and mechanism of transition metal loss. This year, half-cells of NCM were assembled and held at different voltages for two weeks. The cells were disassembled and dissolved the Li in acid and measured the amount of Mn in the solution using ICP-OES. Figure V - 193 shows the results of that analysis.

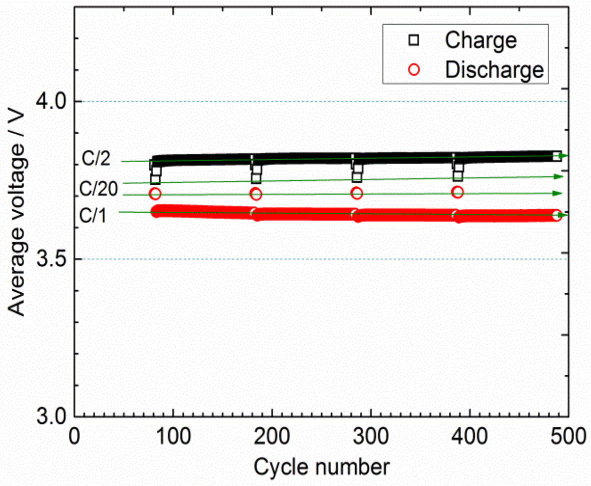

Figure V - 192: The average voltage on charge and on discharge plotted vs. cycle number for a Graphite/NCM pouch cell

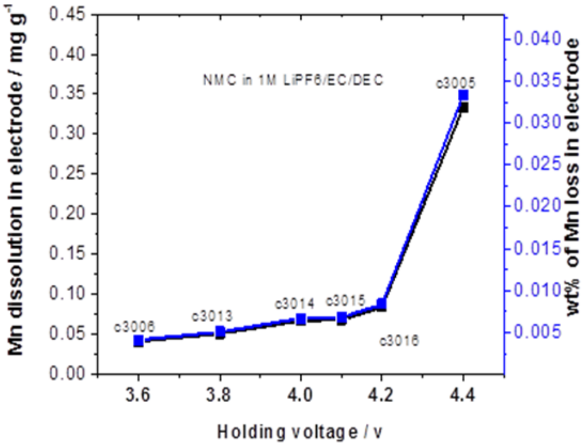

Figure V - 193: The amount of Mn found at the anode in a NCM half-cell was converted to the amount lost from the cathode while held for two weeks at different voltages

Clearly, there is a change in mechanism for Mn dissolution between 4.2 and 4.4 V. This may be a clue to why NCM cells are not cycled above 4.2 V.

Impedance data from a 3-electrode cell. For some cells chemistries, impedance and impedance rise may limit the accessible capacity, especially for cells where power pulses may be needed. Impedance data from two electrode cells can only provide the full cell impedance and does not allow one to assign the contributions specifically to the cathode or anode, even for half-cells. If one wants to assign the impedance one needs to make two identical cells, cycle them identically, disassemble them without modifying either, reassemble the cathodes together and the anodes, and repeat the impedance measurement. Even this only allows access only to one SOC and a particular time during the cycle life.

A three-electrode cell is ideal for assessing the impedance from each electrode, without cell disassembly, and can be taken at any number of SOCs and during any cycle. The problem with 3-electrode cells has been the placement of the reference, the interpretation of the data, and the possible leaking that ensues with the addition of another electrode through the casing. With regard to placement, it is typically either placed between the electrodes with the inclusion of a second separator or to the side of the cell just outside one or both electrodes.

With regard to interpretation of the data it is found that placement between electrodes necessarily blocks the current density in that section of the cell which distorts the data. Placement outside of the cell is also circumspect as for coin cells or other cylindrical electrodes, where one is cut larger than the other so that the larger overlaps the other all the way around the cell-leading to a uniform edge effect all the way around the cell. The potential distribution in the region near the overlap is not symmetric and this too causes a distortion of the impedance data for electrodes placed in this area. The impedance data from each electrode to the reference, when added together, sum to give the two-electrode impedance data, as it should. However, the impedance of one electrode vs. the reference contains contributions from itself that appear greater than what is calculated for a symmetric cell and contributions from the other electrode are also present. For the other electrode, negative contributions are present that can be associated with the other electrode and the contributions from it are smaller than what one would calculate. In other words, one electrode is dominant and contains contributions from both electrodes and the other is subordinate and contains negative contributions from the dominant electrode and smaller contributions from itself. By comparing the contributions from each electrode with the two electrode data, one can identify smaller, larger, and negative contributions which allows one to assign them to one electrode or the other.

Figure V - 194 shows the impedance data of a graphite/ $LiNi_{1/2}Mn_{3/2}O_4$ cell where cell impedance and the impedance rise in during the first three cycles has shown to greatly reduce the cyclable capacity. However, the source of the impedance was not clear. Using a 3-electrode cell, it was determined that the cathode contributed 2/3 of the cell impedance and most of this came from charge transfer resistance. However, the resistance rise in the cell and the falling capacity with cycle number was coming from the anode. The anode data was confirmed by cycling two identical cells and disassembling them after 5 cycles but the cathode data was not confirmed as the cathodes fell apart during cell disassembly.

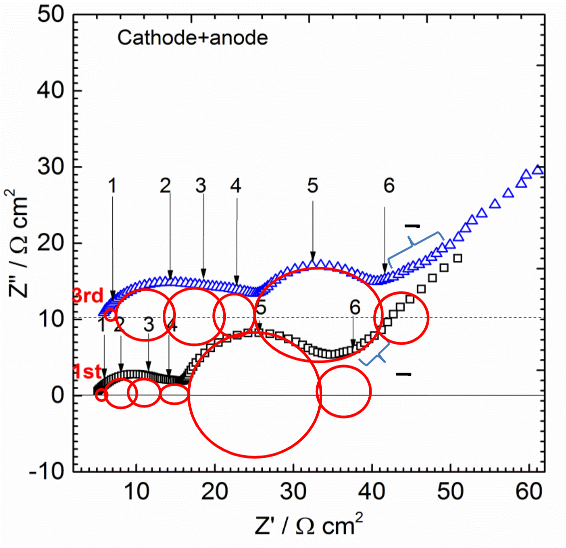

Figure V - 194: Nyquist plot of the electrochemical impedance spectroscopy of a Graphite/$LiNi_{1/2}Mn_{3/2}O_4$ cell at cycle 1 and cycle 3

Calculation of side reaction and particle isolation rates. Every battery researcher reports capacity fade as a function of cycle number. However, cells lose capacity in three ways: 1) side reactions occur on the anode consuming Li faster than the side reactions on the cathode resupply the Li, 2) loss of active sites either as a result of electronic isolation of material through cracking or the sites become less accessible on the atomic scale, and 3) resistance rise leading the cell to reach the cutoff voltage earlier than it did in the previous cycle. The group is developing techniques to distinguish these three mechanisms. This year some effort was put forward to distinguish the rate of side reactions from the other two.

Si-based electrodes were provided by the Liu Group as the baseline electrodes for the Si Anode Focus Group. This electrode was first tested in a half-cell for characterization purposes prior to being tested in a full cell with LFP as the cathode. Figure V - 195 plots the voltage vs. capacity where charge is in the positive direction and discharge in the negative direction. The first 15 cycles, cycle 100 and cycle 200 are shown. Focusing solely at the endpoints, one realizes that the discharge end point moves to the right as a result of side reactions and loss of cyclable capacity and the charge endpoint moves to the right as a result of side reactions but would move to the left as a result of loss of cyclable capacity.

Figure V - 196 re-plots just the endpoints vs. time. The slope of these curves provides the rate. Again, the rate at which the discharge endpoint moves is equal to the rate of side reactions $(\dot{SR})$ plus particle isolation

($\dot{PI}$) and the rate the discharge endpoint moves is the rate of side reactions minus particle isolation. By fitting a second order polynomials to the data in Figure V - 196 and taking the derivative with respect to time, one can add the equations to get two times the side reactions or subtract the equations to get two times the particle isolation resulting in the following two expressions.

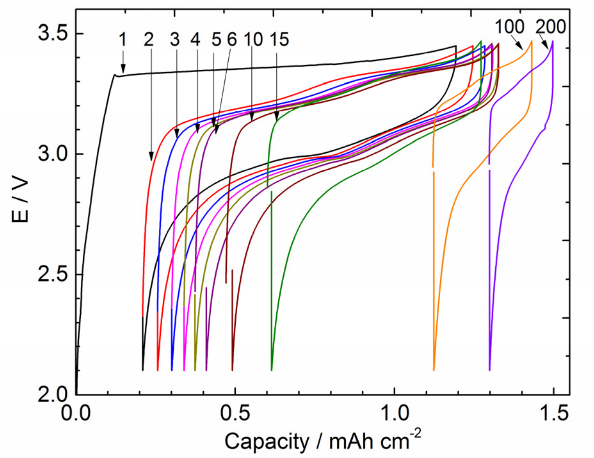

Figure V - 195: Voltage vs. capacity superimposed on each other where charge is in the positive direction and discharge in the negative direction

$$\dot{SR} = 8.7 - 0.0086 t_D \text{ [µAh/h]}$$

$$\dot{PI} = 2.8 - 0.0032 t_D \text{ [µAh/h].}$$

where t_D is the time of discharge. These equations are based on fitting the data after the 38th cycle and after the first 380 hrs and show that both decrease with time. A comparison of these rate expressions indicates that the rate of particle isolation declines more quickly than the rate of the side reactions and that shortly after switching to a C/2 cycling rate, the side reactions are a little over 3 times greater than the rate of particle isolations but by the 200th cycle (750th hour of cycling) the rate of side reactions are 5.6 times greater than the rate of particle isolation.

To re-cast the particle isolation rate in terms of capacity lost per cycle, one plots the time of discharge vs. cycle number and fits a 2nd order polynomial to this curve to get

$t_D = 273 + 3.0861N - 0.0035N^2$ [h] {starting at cycle 38}.

where N is cycle number. The capacity lost per cycle is then calculated from the expression

$$\frac{dQ}{dN} = \frac{dQ}{dt_D}\frac{dt_D}{dN} = \dot{PI}\frac{dt_D}{dN}.$$

Taking the derivative of the discharge time vs. cycle number and substituting in the expression for discharge time in terms of cycle numbers gives

$$PI = 5.941 - 0.044N + 0.0010N^2 - 7.8E(-8)N^3$$

[uAh/cycle] {starting from cycle 38}.

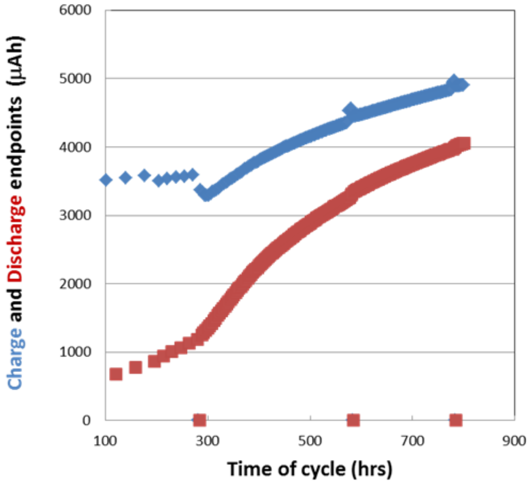

Figure V - 196: Charge (blue diamonds) and discharge (red squares) endpoints vs. time of cycling

Conclusions and Future Directions

This year saw the development of four novel experimental methods: 1) for capturing a large quantity of gas, 2) for measuring the amount of Mn dissolution as a function of voltage, 3) for determining the sources of impedance, and 4) for determining the fraction of side reactions *versus* particle isolation. It is believed that all for methods will become critical as the analysis of high voltage systems and Si anodes becomes more involved.

Future plans include developing methods for 1) measuring the gas pressure in a pouch cell, 2) measuring the composition of the gas in a pouch cell, 3) measuring the rate Mn dissolution from a cathode, 4) assessing the effect of resistance rise on capacity fade, and 5) assessing performance of proposed Li/S cell improvements.

FY 2014 Publications/Presentations

1. Battaglia, V. (June 2014). “Scale-up and Testing of Advanced Materials from the BATT Program.” Presented at the 2014 DOE Annual Merit Review and Peer Evaluation Meeting, Washington, D.C.
2. Delacourt, C.; Ridgway, P.L.; Srinivasan, V.; Battaglia, V. (2014). “Measurements and Simulations of Electrochemical Impedance Spectroscopy of a Three-Electrode Coin Cell Design for Li-Ion Cell Testing Batteries and Energy Storage.” *J. Electrochem. Soc.* (161:9); pp. A1253-A1260.

V.G Beyond Lithium-Ion Battery Technologies

V.G.1 Novel Chemistry: Lithium Selenium and Selenium Sulfur Couple (ANL)

Tien Duong (Program Manager)
Subcontractor: Argonne National Laboratory

Khalil Amine (Principal Investigator)
Argonne National Laboratory
9700 South Cass Avenue
Argonne, IL 60439-4837
Phone: (630) 252-3838; Fax: (630) 972-4520
E-mail: amine@anl.gov

Collaborators:
Ali Abouimrane, Argonne National Laboratory
Yanjie Cui, Argonne National Laboratory.
P. Y. Ren Advanced Photon Source, Argonne National Laboratory.

Start Date: October, 2013
Projected End Date: 2017

Objectives

- The objective of this project is to develop a novel SeS_x cathode material for rechargeable lithium batteries with high energy density, long life along with low cost and high safety.

Technical Barriers

The primary technical barrier is the development of a safe and cost-effective battery with 40 mile range for a plug-in hybrid electric vehicle that meets or exceeds all DOE performance goals. The actual technical barriers are:

- Cell energy density (by volume and/or weight).
- Battery cycle life and high temperature performance.

Technical Targets

When this new cathode is optimized, the following result can be achieved:

- A cell with nominal voltage of 2 V and energy density of 600 Wh/kg.
- A battery capable of operating for 500 cycles with low capacity fade.

Accomplishments

Active cathode materials containing Se, SeS_2, and SeS_7 combined with carbon were prepared and tested against Li metal anode. A discharge capacity of 350, 571, and 800 mAh/g for the Li/Se, Li/SeS_2, and Li/SeS_7 cells, respectively, was maintained for over 50 cycles. The cell capacity increased with increasing S content in the composites due to its contribution to the overall capacity. The coulombic efficiency was nearly 100% for the Li/Se and Li/SeS_2 cells. The Li/SeS_7 cell showed much higher capacity and a relatively low coulombic efficiency during the initial 20 cycles. The lithium insertion in these cathode materials was studied, and a mechanism is proposed.

✧ ✧ ✧ ✧ ✧

Introduction

State-of-the-art lithium-ion batteries are being developed for large-scale applications such as electric vehicles (EVs) and hybrid electric vehicles (HEVs). For this purpose, lithium-ion batteries must have long-term cycling performance with high capacity. Achieving this goal will need breakthroughs in the area of novel electrode materials, since commercial batteries have typical capacities of 120–160 mAh/g, which are far below the required energy demand for these applications. In terms of high energy density, Li/S and Li/O_2 batteries are attractive because they have the potential of providing 2 to 3 times the energy density of the lithium-ion batteries currently on the market. However, they all have some limitations, such as poor cycle performance, large cell polarization, and low conductivity in case of sulfur system. In 2012, our group reported for the first time that selenium and selenium-sulfur could be cycled versus both lithium and sodium. The choice of selenium, which is a d-electron-containing element of group 16 in the periodic table, is due to (a) its higher electrical conductivity compared to that of sulfur and (b) its high theoretical gravimetric capacity (678 mA·h/g) and volumetric capacity (3,268 mAh/cm^3).

Approach

Selenium has a melting point of 220 ºC and an electronic conductivity of 10^{-5} S·cm^{-1}, which is nearly 20 times higher than sulfur due to the small gap between the valence and the conduction band (10^{-5} S·cm^{-1} for Se compared with 5×10^{-30} S·cm^{-1} for S). Sulfur-selenium mixtures are miscible in all proportions, and many S-Se composites including Se_5S, Se_5S_2, Se_5S_4, SeS, Se_3S_5, SeS_2, and SeS_7 can be prepared, including materials with very low amount of Se such as SeS_{20}. Those Se-S materials can offer higher theoretical capacities than selenium alone, in the range of 675-1,550 mAh·g^{-1}, with improved conductivity compared to pure sulfur. Unlike sulfur, which melt at 120°C, selenium tends to melt at much higher temperature (220°C) which offer better safety characteristics in full cell configuration.

Results

Active cathode materials containing Se, SeS_2, and SeS_7 combined with carbon were tested against Li metal anode between 0.8 and 4.0 V, as shown in Figure V - 197a, Figure V - 197b, and Figure V - 197c, respectively. The ether-based electrolyte “D2,” i.e., 1.0 M lithium trifluoromethanesulfonylimide (LiTFSI) in 1,3-dioxolane (DOL) and 1,2-dimethoxyethane (DME), was selected for this study due to its greater stability compared to the conventional carbonate-based electrolyte. Selected voltage profiles (the 1st, 2nd, and 30th cycles) of the Li/Se cell are shown in Figure V - 197d, and suggest overall reversible electrochemical reactions for the Li/Se cell. A discharge capacity of 350, 571, and 800 mAh/g for the Li/Se, Li/SeS_2, and Li/SeS_7 cells, respectively, was maintained for over 50 cycles. The cell capacity increased with increasing S content in the composites due to its contribution to the overall capacity. The coulombic efficiency was nearly 100% for the Li/Se and Li/SeS_2 cells. By contrast, the Li/SeS_7 cell showed a relatively low coulombic efficiency during the initial 20 cycles, although much higher capacity is obtained in this case.

Specially designed coin cells were used for *in situ* high energy x-ray diffraction (HEXRD) studies. As shown in Figure V - 198a, Figure V - 198b, and Figure V - 198c, the peak intensity of the starting material (Se) decreased, while the Li_2Se peaks grew during the discharge, and the process was reversed during the charge process.

For SeS_2, as shown in Figure V - 198d, Figure V - 198e, and Figure V - 198f, no crystalline phase is present at the beginning of the discharge. When the cell is discharged to 2.08 V, the Li_2S phase first appears followed by Li_2Se crystallization at ~2.04 V. During the delithiation, Li_2Se and Li_2S remain until the cell is charged to 2.19 and 2.30 V, respectively. When the cell is charged to 2.25 V, Se peaks appear and keep increasing to the end of charge. These phenomena suggest that the charge product is a mixture of Se and S rather than SeS_2, but the S is not detected due to its weak diffraction ability.

In situ x-ray absorption spectroscopy (XAS) can be very informative when applied to a complex battery system that involves both liquid and solid (crystalline and/or amorphous) phases. Figure V - 199a shows the x-ray absorption near edge structure (XANES) spectra of commercial Se powder and synthesized Li_2Se mixed with boron nitride. The selenium K-edge absorption, at 12,658 eV, arises from the transition of Se 1s core electrons to the unoccupied 4p states. The Se K-edge of Li_2Se shifts to a higher energy at 12660 eV, which is inconsistent with the commonly observed phenomenon that the edge shifts to a higher energy with increasing oxidation state. However, the Se K-edge of Li_2Se shifts to a high energy might also be explained by a reduced screening effect, as reported in the S case. To illustrate the XANES spectra evolution, a 2D contour plot of Se’s XANES spectra recorded during the cell cycling is presented in Figure V - 199b. In addition, the Li/Se cell voltage profile is displayed on the side of the XANES spectra (Figure V - 199c). During lithiation, the critical points (at 2.04 and 1.67 V) of the electrochemical process are well-correlated with the evolution of the XANES spectra. For example, the inflection point at 2.04 V in the voltage profile coincides with the shift of the XANES spectrum to lower energy. The precipitous voltage drop at around 6 hours of discharging corresponds to the sudden appearance of the Se K-edge of Li_2Se.

To better illustrate the edge position shifts, we show the first derivatives of the XANES spectra in Figure V - 199d. The Se edges are shifted significantly with (de)lithiation. When the cell is discharged through the inflection point at 2.04 V, the edge shifts from 12,657.9 eV to 12,656.7 eV. In the following 3 hr (more than 300 mAh/g capacity), the edge positions do not change much and are accompanied by the voltage plateau around 2 V. When the cell is discharged to 1.67 V, the Se K-edge jumps to 12,660 eV, suggesting the formation of Li_2Se. During charge, the Se edges slowly shift back to lower energy. These observations indicate that polyselenides might have formed during the cycling, but in a non-crystalline state; hence, they are not detected by XRD. As a consequence, the reduced Se in the lithium polyselenides shifts the Se K-edge to a lower energy, as expected. With increasing lithiation, the elemental Se is depleted, and polyselenides are reduced to crystallized Li_2Se, which contains Se^{2-} ions in an environment surrounded by 8 Li^+. The strong coulombic interaction significantly reduces the screening effect and shifts the Se edge to a higher energy.

.

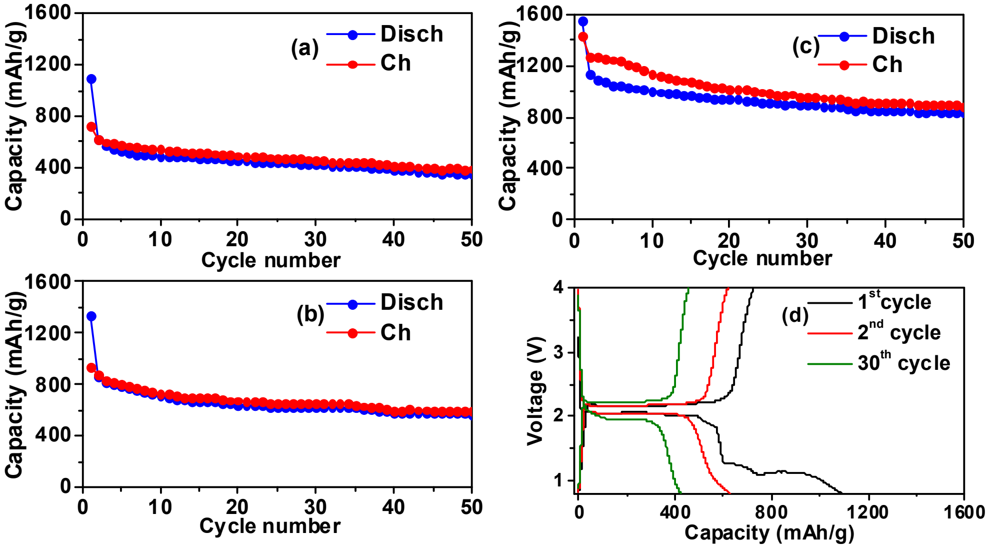

Figure V - 197: Cycle performance of lithium cells with (a) Se-, (b) SeS2-, and (c) SeS7-carbon composite cathodes in ether-based electrolyte, and voltage profile of Li/Se cell (d)

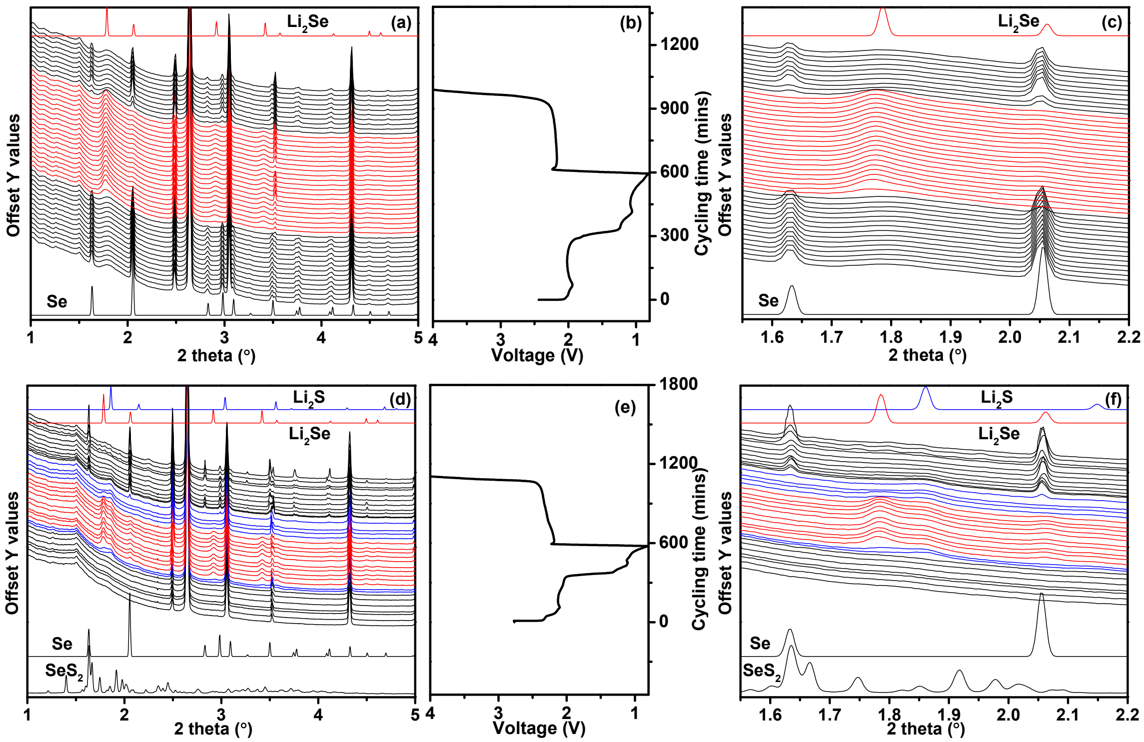

Figure V - 198: HEXRD patterns of Li/Se cell in ether-based electrolyte during the first cycle (a, c) with voltage profile in (b); HEXRD patterns of Li/SeS2 cell in the first cycle (d, f) with voltage profile in (e)

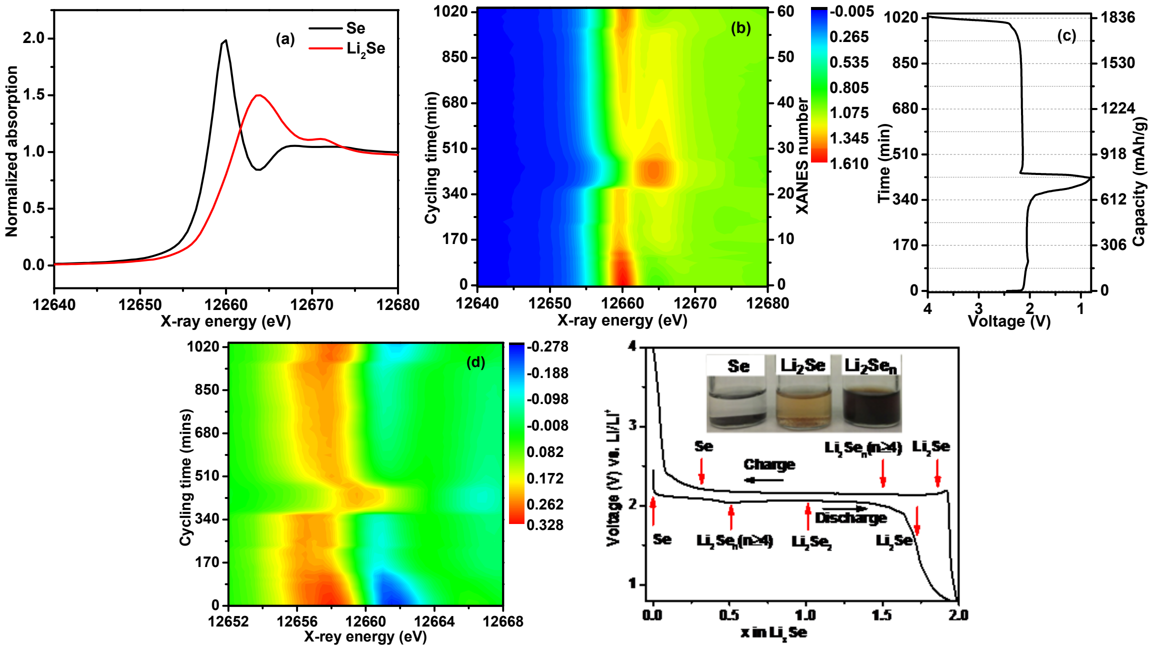

Figure V - 199: (a) Normalized Se XANES spectra of standard Se and Li2Se, (b) normalized XANES spectra of Li/Se cell during cycling, (c) battery voltage profile, (d) derivative of normalized XANES spectra of Li/Se cell during cycling, and (e) representation of cathode phase evolution during charge and discharge of a Li/Se cell in an ether-based electrolyte

Through linear combination fitting of the *in situ* XANES spectra, the HEXRD analysis, and voltage profile, we propose a mechanism for the Li/Se cell lithiation process, as shown in Figure V - 199e. Selenium is first reduced to Li_2Se_n ($n\geq4$) at 2.04 V, which is then further reduced to Li_2Se_2 and Li_2Se after discharging to 2.06 V and 0.8 V, respectively. During charging, Li_2Se is directly oxidized to Li_2Se_n ($n\geq4$) and then Se. To further demonstrate the formation of lithium polyselenides, we carried out a solubility test. We added 3.95 mg of Se to 5 ml of DOL and DME solvent (equivalent to 0.01 mol/L solution) in one container and 4.64 mg of Li_2Se to 5 ml of the same solvent in a second container (again equivalent to 0.01 mol/L solution). As shown in the inset of Figure V - 199e, neither material is completely dissolved when present alone, the solubility of Se being extremely low. However, the precipitated Se particles did dissolve when we added a few drops of saturated Li_2Se solution to the Se suspension, and the solution became dark brown. The intense color of the solution suggests the formation of highly soluble polyselenides. This test confirmed that the lithium polyselenides do exist in the D2 electrolyte and are more soluble than either Se or Li_2Se alone. We believe that the formation of soluble polyselenides could facilitate the Li/Se battery redox reaction, but it may also cause some dissolutive transport of Se to the anode, which would result in the loss of active cathode material and form Li_2Se on the Li anode, as observed in the Raman spectrum

Conclusions and Future Directions

Three compositions in the SeS_x system have been tested in ether-based electrolytes. More important, the mechanism of lithium insertion to the anode in the ether-based electrolyte is proposed. The existence of the polyselenides is further manifested by a solubility test of over-saturated Se and Li_2Se solutions in the electrolyte solvent and a mixture of the solutions. The solubility of polyselenides could facilitate the electrochemical reaction in the Li/Se cell but may cause the shuttle effect and deposition of Li_2Se on the lithium anode. Preliminary result using carbonate based electrolyte suggests that polyselenides are not formed. This might be an alternative approach to avoid the shuttle effect in the Li/Se system as well as the analogue Li/S system. The mechanism in the carbonate-based electrolyte is not well understood so far. Therefore we are going to focus on the understanding of the Li/Se system in the carbonate-based electrolyte, then improve the performance accordingly as one of the major future directions. In addition, an effective electrode structure will be developed to allow for full capacity utilization; this will entail preparing different carbon-SeS_x composites to optimize the electrochemical performance.

FY 2014 Publications/Presentations

1. (De)Lithiation Mechanism of Li/SeSx (x = 0–7) Batteries Determined by *In situ* Synchrotron X-ray Diffraction and X-ray Absorption Spectroscopy, Y. Cui, A. Abouimrane, K. Amine, et al., *J. Am. Chem. Soc.*, 2013, **135** (21), 8047.
2. Li–Se Battery: Absence of Lithium Polyselenides in Carbonate Based Electrolyte, Y. Cui, A. Abouimrane, and K. Amine et al., Chem. Commun., 2014, **50**, 5576-5579.
3. (De)Lithiation Mechanism of Se-based Lithium Batteries Determined by *In situ* Synchrotron X-ray Probes, Y. Cui, A. Abouimrane, J. Lu, T. Bolin, Y. Ren, W. Weng, C. Sun, V. A. Maroni, S. M. Heald, and K. Amine, Fall ECS Meeting, Oct. 27- Nov. 1, 2013, San Francisco, CA.
4. Se-based Positive Electrode Material for Rechargeable Battery Applications. A. Abouimrane, Y. Cui, K. Amine, TMS, 143rd Annual Meeting & Exhibition, Feb. 16-20, 2014, San Diego, CA.
5. Mechanism Understanding of New Li-Se Rechargeable Battery System, A. Abouimrane, Y. Cui, K. Amine, International Battery Association 2014 meeting, Mar. 3-7, 2014, Brisbane, Australia.
6. Controllable Lithium Polyselenides Presence in the New Li-Se Rechargeable Battery System, A. Abouimrane, Y. Cui, and K. Amine, TMS, 144th Annual Meeting & Exhibition, Mar. 15-19, 2015, Orlando, FL.
7. Mechanism Understanding of New Li-Se Rechargeable Batteries in Different Electrolytes, Y. Cui, A. Abouimrane, and K. Amine, 2014 Spring ECS Meeting, May 11-15, 2014, Orlando, FL.

V.G.2 Development of Novel Electrolytes for Lithium Air (ANL)

Tien Duong (Program Manager)
Subcontractor: Argonne National Laboratory

Khalil Amine & Larry Curtiss
Argonne National Laboratory
9700 S. Cass Avenue, Building 205
Argonne, IL 60439-4837
Phone: (630) 252-3838; Fax: (630) 972-4440
E-mail: amine@anl.gov; curtiss@anl.gov

Collaborators:
Jun Lu, Argonne National Laboratory
K. C. Lau, Argonne National Laboratory
Dean Miller, Argonne National Laboratory
R. S. Assary, Argonne National Laboratory
H.-H. Wang, Argonne National Laboratory
Y.-K. Sun, Hanyang University, Korea
S. Vajda, Argonne National Laboratory

Objectives

- Develop stable electrolytes and new cathode architectures in lithium air batteries to lower the charge overpotential, improve the cell efficiency and cycle life.
- Understand the oxygen crossover effect at the anode on the electrochemical performance of Li-air battery.

Technical Barriers

The primary technical barrier is the development of a safe and cost-effective battery with 40 mile range for a plug-in hybrid electric vehicle that meets or exceeds all DOE performance goals. The actual technical barriers are:

- **Unstable electrolytes**: electrolyte decomposition (in particular the ether-based electrolytes) in the presence of the reduced oxygen species, especially superoxide anion (O_2^-).
- **Inefficient cathode structure and catalysis**: Commonly used carbons and cathode catalysts do not access the full capacity of the oxygen electrode and cause significant charge overpotentials. This lowers rates.
- **Lithium electrode poisoning** due to oxygen crossover and reaction with the electrolyte destroys the integrity and functioning of the cell. This lowers cycle life.

Technical Targets

The goal of this project is to demonstrate that a practical Li-air battery is achievable. The targets are to achieve 300 cycles and an energy density of 600~700 Wh/kg. This will provide the necessary breakthroughs and a firm basis for follow-on optimization and incremental improvements.

Accomplishments

- Precisely engineered cathode materials were used to determine that the Li-O_2 battery discharge mechanism involves lithium superoxide and peroxide formation in the electrolyte, followed by surface nucleation and growth from the electrolyte.
- Investigations have revealed evidence for the presence of lithium superoxide in the discharge process confirming a through-electrolyte growth mechanism.
- The mechanism for electrolyte instabilities was determined for salts and oxygen crossover to lithium anodes.

✧ ✧ ✧ ✧ ✧

Introduction

Lithium-air batteries can be considered the ‘holy grail’ of lithium batteries because they offer, in principle, at least ten times the energy density of conventional lithium-ion systems. The lithium-ion cell chemistry, the best to date, would provide a theoretical specific energy of ~900 Wh/kg if the calculation is based on the masses of the anode and cathode materials alone; in practice, 150-200 Wh/kg has been accomplished at the cell level. In contrast, a lithium-air cell, when discharged to Li_2O_2 at an average 3.1 V would provide a theoretical specific energy of 3623 Wh/kg, or when discharged to Li_2O at the same voltage, 5204 Wh/kg. Note that gasoline (octane) offers a theoretical energy of ~13,000 Wh/kg if the mass of the injected oxygen is not considered in the calculation because it is supplied externally and combusted within, and exhausted from, the engine. By the same token, a lithium-air cell would offer a specific energy of ~11,000 Wh/kg if the ‘free’ oxygen supplied during discharge and released during charge is ignored in the calculation.

While the inherent energy potential of lithium metal approaches that of gasoline, today's battery manufacturers have not yet been able to unlock this potential. While today's lithium-ion batteries may provide acceptable power for hybrid electric vehicles (HEVs) and all-electric vehicles (EVs), they do not provide sufficient energy for an acceptable driving distance. This range limitation and the absence of a battery charging infrastructure have limited public interest in electric vehicles. A breakthrough in Li-air battery technology would significantly increase the possibility of extending the electric range of these vehicles with the added advantages of reducing battery cost and weight.

Li-air battery technology is still in its infancy and, no doubt, will require significant research efforts in a variety of fields to unlock its full potential. The successful implementation of non-aqueous Li-air cells has been hampered because of severe materials problems that have limited electrochemical performance: (1) the non-aqueous electrolytes are unstable at high potentials and are easily oxidized by lithium superoxide, thereby seriously limiting cycle life; (2) during discharge, the solid and insoluble Li_2O_2 and/or Li_2O products are deposited on the surface or within the pores of the carbon cathode, thereby clogging the pores and restricting oxygen flow; (3) poisoning of the lithium electrode due to oxygen crossover destroys the integrity and functioning of the cell; and (4) commonly used cathode catalysts, such as MnO_2 or Mn metal, do not access the full capacity of the oxygen electrode or enable sufficiently high rates.

The team led by Dr. Khalil Amine at Argonne National Laboratory (ANL) is working on problems that limit the electrochemical performance of the Li-air battery, including the stability of the organic electrolyte, cathode catalysts and structures, and stability of the lithium anode under oxygen-crossover conditions. This effort will lead to the development of a reversible lithium air battery that provides at least 2 times the energy density of the state-of-the-art lithium-ion battery for powering electric vehicles. The technology, if successful, can also benefit many military applications that require very high energy density such as satellite, military vehicles for silent watch and operation.

Approach

Issues that limit the performance of the Li-air battery include (1) electrolytes decomposition; (2) inefficient cathode materials; and (3) lithium electrode corrosion. During the previous year (FY13) we made significant progress in finding cathode materials that can reduce the charge overpotential that was leading to the larger inefficiencies in the performance of the $Li-O_2$ battery. Although the lower charge potential reduces sources of electrolyte instability, the cycle life remained poor. The possible reasons for this include other sources of electrolyte instabilities and cathode degradation leading to increased charge potentials with cycling.

This project addresses the cycle life problem of Li-air batteries through investigation of (a) the discharge formation mechanism and relationship to electrolytes, (b) investigation of the morphology and composition of the discharge product, and (c) investigation of electrolyte decomposition mechanisms. This understanding is being used to (a) develop new electrolytes that will be more stable than ethers towards oxygen reduction species in the electrolyte, (b) new carbon based cathodes that will promote formation of discharge morphologies such as those involving superoxides to prevent degradation of the cathode materials with cycling, and (c) investigation of techniques to protect the lithium anode.

The experimental designs to create advanced electrolytes, carbons, catalysts, cathodes, and anodes will be guided by theory and modeling. The experimental results will be thoroughly analyzed with very sophisticated analytical techniques and used to fine-tune the computational studies. Fundamental understanding of the underlying principles will be provided to greatly facilitate the next steps in the development cycle.

Results

Effect of the Size-selective Silver Clusters on Li_2O_2 Morphology in Lithium-Oxygen Batteries: In a study of $Li-O_2$ discharge product morphology based on precisely controlled size-selective subnanometer transition metal clusters (in collaboration with S. Vjda) added to the cathode, we have found a dramatic dependence on cluster size. This is the first time that size-selected subnanometer clusters have been studied in $Li-O_2$ cells. The discharge products resulting from the three cluster sizes were examined using SEM and TEM imaging and were found to dramatically depend on the Ag cluster size. The SEM images in Figure V - 200 show the carbon cathode after discharge to 2.5 V for the 1st cycle. The SEM images reveal that the discharge product resulting from the Ag_3 cluster-based cathode is film-like. In contrast, the discharge product of the Ag_9 -based cathode is largely toroid-like with rough surfaces, while that of the Ag_{15} -based cathode is characterized by toroids with relatively smooth surfaces. The Ag_9 toroids are smaller than the Ag_{15} toroids (~500 nm vs. ~1,000 nm) with the same discharge capacity. The XRD patterns in Figure V - 200 are consistent with Li_2O_2 in all three cases.

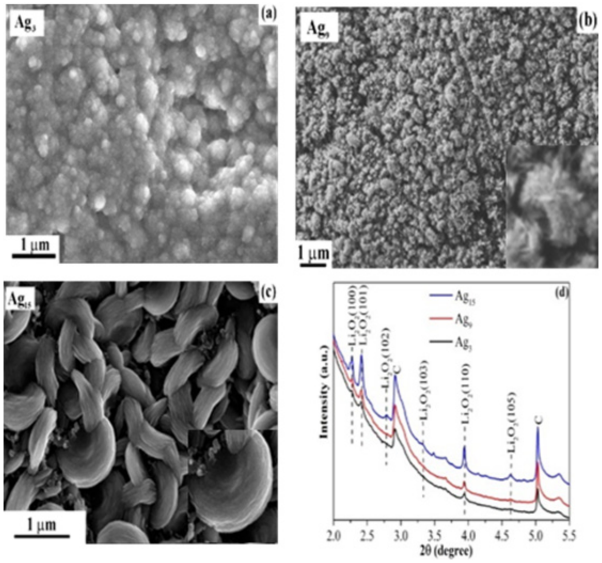

Figure V - 200: SEM images of discharge products (for (a) Ag_3, (b) Ag_9, and (c) Ag_{15} -based cathodes materials and (d) XRD patterns for the three discharge products from the three cathode materials

The lithium peroxide discharge product on the cathode was further probed by TEM imaging. The TEM images show several distinct building blocks that make up the discharge products. A TEM image of a toroid from the discharge product based on the cathode with Ag_{15} clusters indicates the presence of both nanosized grains (nanoparticles of ~10 nm size) and amorphous regions suggesting that the toroids are nanocrystalline, i.e., made up of grains and grain boundaries. The TEM image for the discharge product from the Ag9–based cathode indicates that its building blocks are elongated nanoparticles or nanorods (~100 nm in length) that are distinctly different from the smaller and more spherical-like nanoparticles found in the discharge product of the Ag_{15} based cathode. The TEM image of the Ag_3 discharge product reveals that it is largely made up of crystalline flat plates around 50-200 nm in size. Electron diffraction patterns and XRD show that the discharge products contain crystalline Li2O2.

The different morphologies of the $Li-O_2$ discharge products provide evidence, supported by DFT calculations, for discharge mechanisms involving oxygen reduction and formation of either LiO_2 or Li_2O_2 in the electrolyte, followed by surface nucleation and growth from the electrolyte as shown in Figure V - 201 The dependence of the discharge mechanisms on oxygen reduction rate can account for the differing discharge product morphologies with different charge overpotentials.

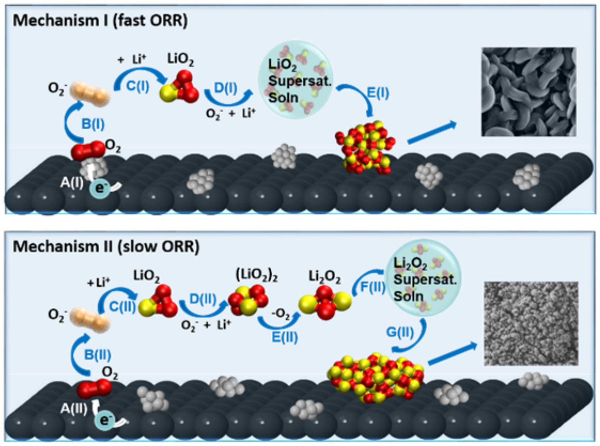

Figure V - 201: Illustration of two discharge reaction mechanisms based on an initial oxygen reduction at an active site followed by solution phase reactions and growth at a surface nucleation site. Mechanism I involves fast oxygen reduction and formation of a LiO2 supersaturated solution, while mechanism II involves slow oxygen reduction and formation of a lithium peroxide supersaturate solution. Growth and nucleation occurs via these supersaturated solutions

This study of specific and well-defined clusters on cathode surfaces provides evidence that subnanometer surface species can strongly influence the morphology of the discharge products in $Li-O_2$ cells via the through solution nucleation and growth mechanism. These results imply that characterization of the subnanometer surface structure of cathodes is a key factor in understanding the discharge and charge chemistries in lithium-air cells and the tailoring of this structure is a potential avenue to reduce the charge overpotentials, increase capacities, and increase cycle life with less reactive surface morphologies.

Evidence for Formation of a Lithium Superoxide Component in $Li-O_2$ Battery Discharge Products: Several experimental studies have been carried out that provide evidence for the presence of lithium superoxide in the discharge product based on an activated carbon cathode. The first study involved a kinetics study of the discharge process and its relationship to the charge overpotential in a $Li-O_2$ cell that revealed evidence for a first-order disproportionation reaction during discharge from lithium superoxide like component to a lithium peroxide (Li_2O_2) component. The second study involved analysis of the Raman spectra of the discharge product to provide additional confirmation for slow disproportionation required to account for the two components discharge product.

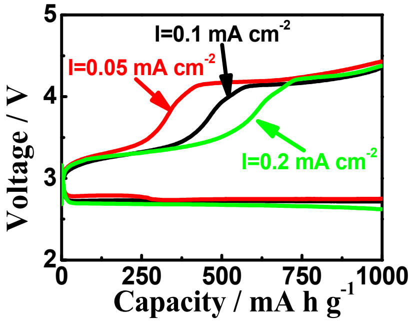

Figure V - 202: Discharge/charge curves of AC with different discharge current density and the same charge current density

The kinetics study was based on activated carbon cathode in a Li-O_2 cell that was run at various capacities and different discharge rates. The results show two distinct charge plateaus, one at 3.2-3.5 V and the other at ~4.2 V as shown in Figure V - 202. A kinetics study based on the capacity and charge density dependence of the charge plateaus provided evidence for a first-order reaction during discharge from an O-rich superoxide-like component to a Li_2O_2 component due to LiO_2 disproportionation. This points to a discharge product with the two types of domains. The oxygen-rich superoxide-like component has a much smaller potential during charge (3.2-3.5 V) than the Li_2O_2 component (~4.2 V). Characterization data from XRD shown in Figure V - 203 indicates that the superoxide character disappears after the charge reaches 3.5 V, suggesting that a phase with an oxygen-rich superoxide-like character is related to the first plateau and that Li_2O_2 is correlated with the second plateau.

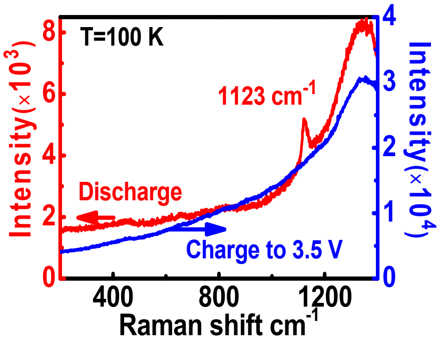

Figure V - 203: Raman spectrum of the discharged AC cathode surface showing graphite D (1330 cm-1), and LiO2-like bands (1123 cm-1 red trace). Raman spectrum of a similar AC cathode that was discharged and charged back to 3.5 V does not show the LiO2-like band (blue trace)

The discharge product containing these two components is characterized by toroids shown in Figure V - 204, which are assemblies of nanoparticles. The different evolution of the toroids during discharge and charge suggests that the formation and decomposition mechanisms are different, consistent with the kinetics analysis showing superoxide disproportionation.

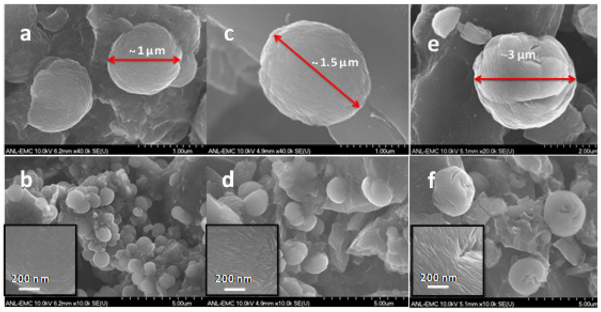

Figure V - 204: The morphologies of toroids at the same discharge capacity of 1000 mAh/g with different current densities of (a, b) 0.2, (c, d) 0.1 and (e, f) 0.05 mA/cm²

In the second study Raman spectroscopy is used to characterize the composition of toroids formed in the Li-O_2 cell based on the activated carbon cathode. Figure V - 205 shows typical Raman spectra of toroids resulting from the three different current densities. In all three spectra, there is a distinct peak at 1123 cm^{-1} (denoted as S1) associated with the presence of a LiO_2-like component in the toroids, which we identified in the previous work. With decreasing current density, the relative intensity of the peak S1 gets weaker, which means that the amount of LiO_2-like component decreases. This result is consistent with our previous conclusion from the kinetics analysis that, for a constant discharge capacity, more LiO_2 disproportionates to form Li_2O_2 and O_2 at a lower discharge current density.

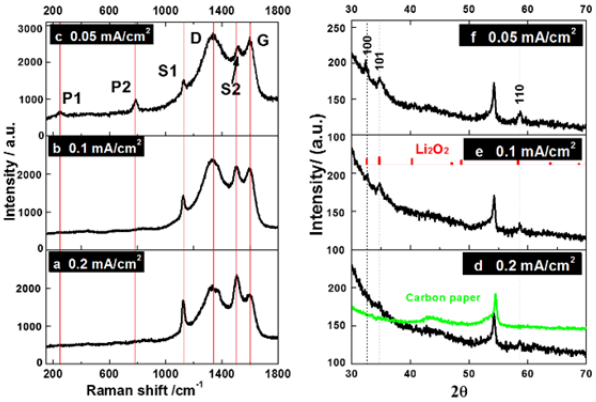

Figure V - 205: Raman spectra of the toroids on the surface of the discharged AC cathode with different current densities of (a) 0.2, (b) 0.1 and (c) 0.05 mA/cm2. XRD patterns of the discharge AC cathode at the same discharge capacity of 1000 mAh/g with different current densities of (d) 0.2, (e) 0.1 and (f) 0.05 mA/cm²

The trends in the Raman data as a function of discharge current density and charging cutoff voltage provide evidence that the toroids are made up of outer LiO_2-like and inner Li_2O_2 regions, consistent with a disproportionation reaction occurring in the solid phase. The LiO_2-like component is found to be associated with a new Raman peak identified in the carbon stretching region at ~1505 cm^{-1}, which appears only when the LiO_2 peak at 1123 cm^{-1} is present. The new peak is assigned to distortion of the graphitic ring stretching due to coupling with the LiO_2-like component based on density functional calculations. These new results on the LiO_2-like component from Raman spectroscopy provide evidence that a late stage disproportionation mechanism can occur during discharge and adds new understanding to the complexities of possible processes occurring in Li-O_2 batteries.

Mechanisms for electrolyte instabilities in Li-O_2 cells: A combined experimental and theoretical study has been carried out on the decomposition of the salt LiBOB for use in Li-O_2 cells. Experimental FTIR studies shown in Figure V - 206 show evidence of lithium oxalate in the discharge product. Through AIMD metadynamics simulations and quantum chemical calculations, we have found a mechanism for Li_2O_2 induced "ring-opening" of LiBOB and a subsequent nucleophilic substitution reaction. The strong interaction found between a Li_2O_2 molecule and LiBOB in an electrolyte suggests that a similar strong interaction of LiBOB with Li_2O_2 crystalline surfaces will also occur. In addition, the current study suggests that the reaction between Li_2O_2 and LiBOB will produce lithium oxalate during the discharge process of a Li-O_2 cell. The degradation of the LiBOB salt initiated by the chemical reaction with Li_2O_2 as found in this study suggests that stability of both solvents and salts in electrolytes against the parasitic reactions with Li_2O_2 is a serious challenge to the rechargeability of Li-O_2 cells.

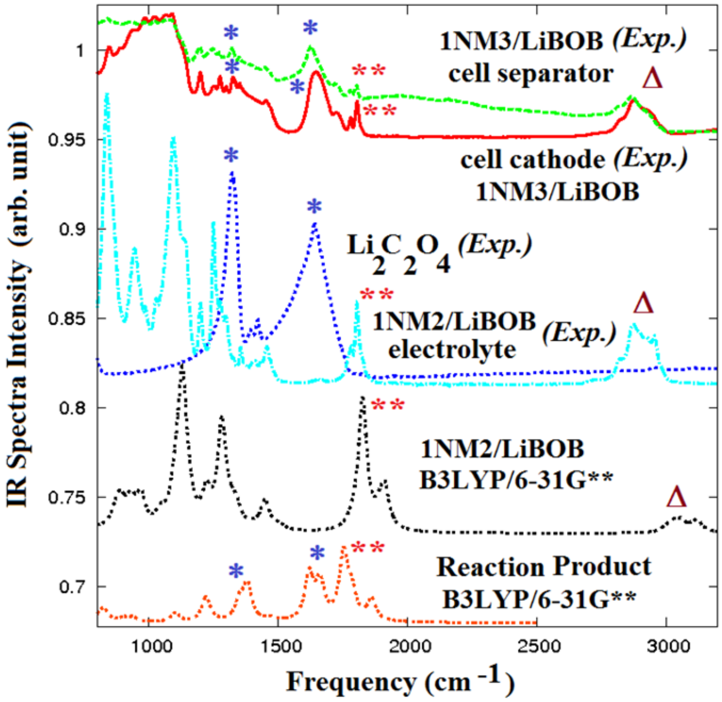

Figure V - 206: Comparison of the computed B3LYP/6-31G** IR spectra with the experimental FTIR spectra from after the first discharge of the Li-O2 cell. The (*) represents the dominant IR peak of lithium oxalate, the (**) indicates the dominant IR peaks of LiBOB, whereas the (Δ) represents the IR signatures of –CH3- and –CH2- groups in the solvent been used

In another study on electrolyte stability, a molecular-level understanding of the reactions that occur at the lithium-metal anode/electrolyte interphase Li-O_2 batteries was developed for siloxane electrolytes. Experimental and computational techniques were applied to explore the reactivity of tri(ethylene glycol)-substituted trimethylsilane (1NM3), a siloxane-based ether electrolyte, at the lithium-metal anode. *In situ*/*ex situ* X-ray diffraction and Fourier-transform infrared spectroscopy studies provided evidence of the formation of lithium hydroxide and lithium carbonates at the anode upon gradual degradation of the metallic lithium anode and the solvent molecules in the presence of oxygen. Density functional calculations performed to obtain a mechanistic understanding of the reductive decomposition of 1NM3 indicated that the decomposition does not require any apparent barrier to produce lithium hydroxide and lithium carbonates when the reduced 1NM3 solvent molecules interact with the oxygen crossing over from the cathode. This study indicates that degradation may be more significant in the case of the 1NM3 solvent, compared to linear ethers such as tetraglyme or dioxalone, because of its relatively high electron affinity. Also, both protection of the lithium metal and prevention of oxygen crossover to the anode are essential for minimizing electrolyte and anode decomposition.

Conclusions and Future Directions

In this project, an integrated experimental and theoretical approach was used to address the technical barriers for non-aqueous Li-air battery. This project addresses the cycle life and energy density of Li-air batteries through investigation of (a) the discharge formation mechanism and relationship to electrolytes, (b) investigation of the morphology and composition of the discharge product, and (c) investigation of electrolyte decomposition mechanisms. Accomplishments during the past year include:

- Precisely engineered cathode materials with size selected silver clusters were used to determine that the Li-O_2 battery discharge mechanism involves lithium superoxide and peroxide formation in the electrolyte, followed by surface nucleation and growth from the electrolyte.
- Investigations based on characterization by XRD, Raman spectra, and kinetics analysis have revealed evidence of the presence of lithium superoxide in the discharge process, confirming a through-electrolyte growth mechanism as proposed in our silver cluster results.
- The mechanisms for electrolyte instabilities were determined for the LiBOB salt and siloxane solvents and are being used to help find more stable electrolytes.

Future research will focus on an integrated effort using these results on the mechanism of lithium oxygen formation and electrolytes for increasing the cycle life and energy density of the Li-O_2 battery.

FY 2014 Publications/Presentations

1. Disproportionation in Li–O2 Batteries Based on a Large Surface Area Carbon Cathode, D. Zhai, H.-H. Wang, J. Yang, K. C. Lau, K. Li, K. Amine, and L.A. Curtiss, J. Am. Chem. Soc., 135 (41), 15364–15372 (Oct, 2013). DOI: 10.1021/ja403199d.
2. Raman Evidence for Late Stage Disproportionation in a Li−O_2 Battery, D. Zhai, H.-H. Wang, K. C. Lau, J. Gao, P. C. Redfern, F. Kang, B. Li, E. Indacochea, U. Das, H.-H. Sun, H.-J. Sun, Khalil Amine, and L. A. Curtiss, J. Phys. Chem. Lett. 5, 2705−2710 (2014) DOI: 10.1021/jz501323n.
3. Molecular-Level Insights into the Reactivity of Siloxane-Based Electrolytes at a Lithium-Metal Anode, R. S. Assary, J. Lu, X. Y. Luo, X. Y. Zhang, Y. Ren Ren, H. M. Wu, H. M. Albishri, D. Abd El-Hady, A. S. Al-Bogami, L. A. Curtiss, K. Amine, ChemPhysChem 15 2077-2083 (2014) DOI: 10.1002/cphc.201402130.
4. Investigation of the Decomposition Mechanism of Lithium Bis(oxalate)borate (LiBOB) Salt in the Electrolyte of an Aprotic Li-O_2 Battery, K. C. Lau, J. Lu, J. Low, D. Peng, H. Wu, H. M. Albishri, D. Abd Al-Hady, L. A. Curtiss, K. Amine, Energy Technology, 2, 348-354 (2014) DOI: 10.1002/ente.201300164.
5. Polymer supported organic catalysts for O-2 reduction in Li-O-2 batteries, W. Weng, C. J. Barile, P. Du, A. Abouimrane, R. S. Assary, A. A. Gewirth, L. A. Curtiss, K. Amine, Electrochimica Acta, 119, 138-143 (2014). DOI: 10.1016/j.electacta.2013.12.027.
6. Effect of the size-selective silver clusters on lithium peroxide morphology in lithium–oxygen batteries, J. Lu, L. Cheng, K. C. Lau, E. Tyo, X. Luo, J. Wen, Dean Miller, R. S. Assary, H.-H. Wang, P. Redfern, H. Wu, J.-B. Park, Y.-K. Sun, S. Vajda, K. Amine, L. A. Curtiss, Nature Communications 5, 4895 (2014) doi:10.1038/ncomms5895.
7. Jun Lu, Li Li, Jin-Bum Park, Yang-Kook Sun, Feng Wu and Khalil Amine, “Aqueous and non-aqueous Li-air Battery”, Chem. Rev., 114, 5611–5640,2014.

Invited Talks

1. "Insights into Discharge and Charge Chemistries in Li-O2 Batteries from Theory and Experiment", L. A. Curtiss & K. Amine, Materials Challenges in Alternative & Renewable Energy 2014 (MCARE 2014) Conference, February 16 - 20, 2014, Clearwater, Florida.
2. “Insights into Charge and Discharge Chemistries in Li-O2 Batteries from Theory and Experiment,” L. A. Curtiss & K. Amine, ASM Symposium, April 16, 2014, Oak Ridge National Laboratory.
3. “Computational Studies of Materials Aspects of Li-O_2 Batteries,” L. A. Curtiss Thomas Young Centre Workshop on Energy Materials, London, England, Sept. 10-12, 2014.
4. “Electronic structure of interfaces and their role in charge and discharge chemistries in lithium-oxygen batteries,” L. A. Curtiss, ACS National Meeting, San Francisco, CA August 10-15, 2014.

V.G.3 Composite Electrolyte to Stabilize Metallic Lithium Anodes (ORNL)

Nancy Dudney
Oak Ridge National Laboratory

Materials Science and Technology Division
PO Box 2008, MS 6124
Oak Ridge, TN 37831-6124
Phone: (865) 576-4874
E-mail: dudneynj@ornl.gov

Start Date: October 2011

Objectives

- Prepare composites of representative polymer and ceramic electrolyte materials to achieve thin membranes having the required combination of electrochemical and mechanical properties.
- Understand the lithium ion transport at the interface between polymer and ceramic solid electrolytes which is critical to the effective conductivity of the composite membrane.
- Identify key features of the composite composition, architecture and fabrication that optimize performance.
- Fabricate thin electrolyte membranes (to use with a thin metallic lithium anode) that provide good power performance and long cycle life.

Technical Barriers

Advanced lithium batteries, including Li-air and Li-S, require robust protection of the metallic lithium anode to maintain a mechanically and chemically stable lithium anode. Any reaction or roughening of the lithium will result in a loss of capacity, degradation of performance and possibly in compromised safety. A robust solid electrolyte to protect the lithium while ensuring rapid cycling is the clear solution, yet fabricating such an electrolyte with the required ionic transport, electrochemical stability, and mechanical strength is a technical challenge. The electrolyte must be very thin and light, and cost effective for manufacturing. To provide a lithium anode with significantly higher energy density than current Li-ion anodes, all components of the anode assembly including the packaging, current collector, protective electrolyte, and the amount of lithium itself, must be minimized.

Technical Targets

- Develop a solid electrolyte membrane that stabilizes the long-term, safe, and efficient cycling of lithium metal anodes to enable high energy density batteries.
- Provide an electrolyte-protected anode to promote the equivalent electric range of 40 miles (PHEV) and 200-300 miles (EV).
- Enable battery anodes for very high energy Li-S Battery (500 Wh/kg) by 2020 and Li-Air Battery (700 Wh/kg) by 2030.

Accomplishments

- Fabrication of composite electrolyte disks with high volume fraction of the ceramic phase (up to 80%).
- Evaluation of composites with different ceramic loading, particle size distribution and surface coating of the ceramic particles.
- Demonstration that ionic conductivity above that of the pure polymer electrolyte correlates with absorption of organic molecules from the glove box atmosphere.
- Demonstration of controlled reaction with selected organic species, assessing the amount absorbed and the effect on ionic conductivity of the pure and composite electrolytes.

✧ ✧ ✧ ✧ ✧

Introduction

This program is based on the observation that no single solid electrolyte, either polymer, ceramic, or glass, can currently meet all of the requirements for a stable interface with the active lithium anode. Many inorganic materials are not stable in contact with lithium metal and also suffer from being too brittle when thinned to a light weight membrane. Polymer electrolytes, even those with rigid block co-polymer structures, gradually roughen with lithium cycling and are too resistive for room temperature operation. Formation of a composite polymer-ceramic structure offers a pragmatic approach to optimizing the electrolyte properties. Using the wealth of known solid electrolyte materials, this program is addressing the fabrication and testing of such composites, both experimentally and through simulation. A critical aspect of such a composite is the set of properties of the interface formed between two different electrolytes, which must offer mechanical integrity while not impeding the transport of lithium ions. Characterizing and modifying these interfaces is a primary focus of this program.

This study will identify the key design strategies that should be used to prepare composite electrolytes to meet the challenging combination of physical, chemical, and manufacturing requirements to protect and stabilize the lithium metal anode for advanced batteries. By utilizing well characterized and controlled component phases, the design rules developed for the composite structures will be generally applicable toward the substitution of alternative and improved solid electrolyte component phases as they become available. Success in this program will enable these specific DOE technical targets: 500-700Wh/kg, 3,000-5,000 deep discharge cycles, and robust operation.

Approach

The program emphasizes the investigation of polymer-ceramic interfaces formed as bilayers and then as simple composite mixtures where the effects of the interface properties can be readily isolated. In general, the different ceramic materials chosen for the study are several orders of magnitude more conductive to Li^+ ions than the standard polyethylene oxide (PEO) plus Li salt polymer electrolyte, and interfaces can contribute an additional source of resistance for the composite structures. Processing conditions are varied to assess the route that gives the most conductive polymer-ceramic interfaces.

Using finite element simulations as a guide for both ion transport and mechanical stability, composites are fabricated with promising compositions and architectures. Generally, the volume fraction of the ceramic is pushed to the maximum that can still give a dense composite with the polymer matrix. The processing is restricted to dry mixing and melt consolidation methods in an inert atmosphere to eliminate uncontrolled contamination of water and other soluble species. This proves to be essential as described below. The lithium transport properties are evaluated using AC impedance and DC cycling with lithium in symmetric or half cells. General design rules will be determined that can be widely applied to other combinations of solid electrolytes.

Results

The most important result from this study is that composites containing a high loading (40-60v%) of submicron ceramic electrolyte particles dispersed in a polymer PEO electrolyte matrix are extremely sensitive to volatile organic species in the inert glove box atmosphere. This was a surprise. Several careful side-by-side comparisons with different ceramic contents demonstrated that the composites load-locked into a communal glovebox (<1ppm H_2O and O_2) could be contaminated in just the few short minutes needed to assemble, crimp, and seal the samples into a standard coin cell. An example is shown in Figure V - 207 where sister samples were crimped in two different gloveboxes, one being the 'liquid-free' glove box used to prepare the composite material (red curves) versus the standard glovebox routinely used to assemble Li-ion batteries (black curves). Initially the impedances of the samples were equal, but over the next days and weeks, the impedance of the samples diverged by orders of magnitude.

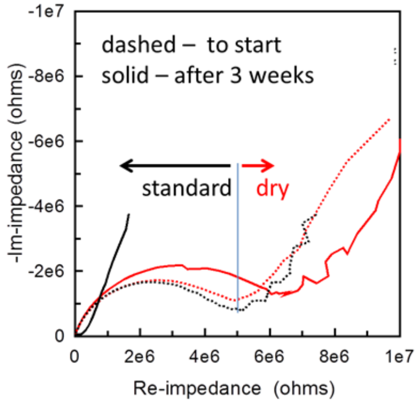

Figure V - 207: Impedance of composites assembled in coin cells using a standard (black) and liquid-free (red) glove box. Data were recorded just after assembly and after 3 weeks

Before these gas-exposure tests, the dramatic but sluggish change in conductivity with time was believed to be due to redistribution of the ceramic particles or the dissolved Li salt to form effective percolation pathways for the ion transport. Both crystallization of the polymer matrix and compression of the sample in the coin cell could drive such redistribution. Although the process resulting in the slow increase in conductivity is not understood, it clearly does not occur when the material is carefully protected from exposure to organic vapors. Figure V - 208 shows the time dependence of several samples upon crimping into the coin cell in the communal glovebox.

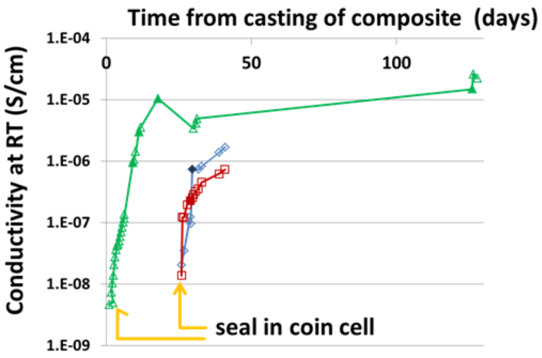

Figure V - 208: Change in conductivity of samples sealed in coin cells. Samples differ in ceramic loading and PEO molecular weight. Some jogs are due to temperature scans

Figure V - 209 shows the Arrhenius plot for two composites compared to the conductivity of the pure ceramic and the pure polymer electrolyte components. Again, the more resistive composite was protected from exposure to organic vapors.

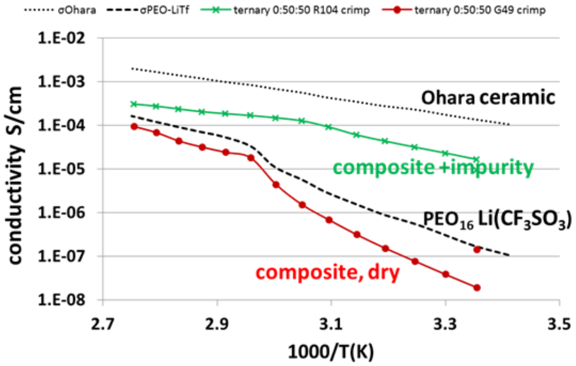

Figure V - 209: Conductivity of composites with 50v% Ohara ceramic powder assembled into coin cell in standard glove box (green) and liquid-free glove box (red), compared to pure ceramic and polymer electrolytes (black)

A number of studies related to: the size, composition and surface coating of the ceramic particles; the volume fraction of the ceramic; the processing effects of heat and pressure; and the impedance with blocking and lithium electrodes have been completed. However, in many examples the exposure to organic vapors was poorly controlled. These experiments are now secondary to the need to understand and quantify the adsorption of different selected organic vapors, the diffusion and segregation of the organic molecules, and the mechanism whereby organic molecules facilitate directly or indirectly the ionic transport by Li$^+$ or compensating anions. Dimethyl carbonate is the most reactive solvent tested so far, with large concentrations of DMC adsorbed if the source is not limited. As shown in Figure V - 210, DMC yields a high conductivity, for both the ceramic composite and the pure polymer electrolyte, and also a lower bulk modulus than the dry composite as revealed by deformation of the samples. Initial results indicate a relatively low contact resistance with a metallic electrode, but more work is underway to determine stability.

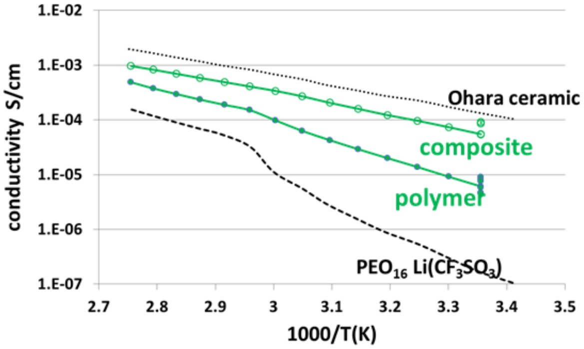

Figure V - 210 Conductivity of composite and polymer electrolytes treated in DMC. Composite is 50v% Ohara ceramic

Conclusions and Future Directions

Evidence that incidental exposure to organic vapors can result in a profound effect on the ionic conductivity has opened a new avenue of research and raised concern about the interpretation of all composite electrolyte reports in literature. The application of ceramic-polymer composite electrolytes for protection of lithium anodes may depend on these questions: Is facile Li$^+$ transport along or across the ceramic-polymer interface possible in the absence of adsorbed water or solvent molecules? Can a small concentration of the right absorbed molecule improve the interface conductivity, processing and performance of composites with a high ceramic loading without adverse effects at the lithium anode interface? These will form the core of on-going studies with aims of providing design rules and processing guidance generally applicable to a variety of solid electrolytes materials.

FY 2014 Publications/Presentations

1. 2013 Fall meeting of the Electrochemical Society *Polymer-Ceramic-Glass Electrolyte Composites: Progress Toward Achieving Stable and Safe Lithium Metal Anodes* by Nancy Dudney, Wyatt Tenhaeff, Sergiy Kalnaus, Ezhiylmurugan Rangasamy, Jeff Sakamoto.
2. 2013 Fall meeting of the Electrochemical Society *Analysis of Composite Electrolytes for Stability With Li Metal Anodes* by Sergiy Kalnaus, Wyatt Tenhaeff, Jeff Sakamoto, Adrian Sabau, Claus Daniel, Nancy Dudney.
3. 2013 Fall meeting of the Electrochemical Society *Cycling Stability, Interfacial Impedance, and Ionic*

Transport Characterization of Garnet Ceramic Electrolyte Membranes by Jeff Sakamoto, Travis Thompson, Jeff Wolfenstine, Jan Allen, Wyatt Tenhaeff, Ezhiylmurugan Rangasamy, Nancy Dudney.

4. 2013 Fall meeting of the Materials Research Society *Polymer-Ceramic-Glass Composites as Lithium Electrolytes*, Nancy Dudney, Wyatt Tenhaeff, Sergiy Kalnaus, Ezhiyl Rangasamy, Jeff Sakamoto.
5. Gordon Conference on Ceramics, July 2014. The challenge of Lithium metal batteries - using ceramic electrolytes to help meet the challenge, by NJ Dudney.
6. ASM Educational Symposium, April 2014, *Lithium protection – making lithium anodes possible* by NJ Dudney.
7. AVS Michigan Chapter Symposium, August 2014, Michigan State University, *Batteries and Battery Materials by Vapor Deposition* by NJ Dudney.
8. Toyota TRINA seminar, Ann Arbor Michigan, August 2014, *The challenge of Lithium metal batteries* by NJ Dudney.
9. Thermophysical properties of $LiFePO_4$ cathodes with carbonized pitch coatings and organic binders: Experiments and first-principles modeling, Jagjit Nanda, Surendra Martha, Wallace Porter, Hsin Wang Nancy Dudney, Maxwell Radin, Donald Siegel. J Power Sources 251 (2014) 8-13.
10. *Effect of interface modifications on voltage fade in* $0.5Li_2MnO_3$-$0.5LiNi_{0.375}Mn_{0.375}Co_{0.25}O_2$ *cathode materials*, Ira Bloom, Lynn Trahey, Ali Abouimrane, Ilias Belharouak, Xiaofeng Zhang, Qingliu Wu, Wenquan Lu, Daniel P. Abraham, Martin Bettge, Jeffrey W. Elam, Xiangbo Meng, Anthony K. Burrell, Chunmei Ban, Robert Tenet, Jagjit Nanda and Nancy Dudney, J. Power Sources 249 (2014) 509.
11. Thermophysical properties of $LiFePO_4$ cathodes with carbonized pitch coatings and organic binders: Experiments and first-principles modeling, Jagjit Nanda, Surendra Martha, Wallace Porter, Hsin Wang Nancy Dudney, Maxwell Radin, Donald Siegel. J Power Sources 251 (2014) 8-13.
12. *Resolving the grain boundary and lattice impedance of hot-pressed* $Li_7La_3Zr_2O_{12}$ *garnet electrolytes*, Wyatt E. Tenhaeff, Ezhiyl Rangasamy, Yangyang Wang, Alexei P. Sokolov, Jeff Wolfenstine, Jeffrey Sakamoto, and Nancy J. Dudney, ChemElectroChem Comm. 1 (2014) 375.

V.G.4 Lithium Dendrite Prevention for Lithium-ion Batteries (PNNL)

Wu Xu
Pacific Northwest National Laboratory
Energy & Environment Directorate
902 Battelle Boulevard, Mail Stop K2-44
Richland, WA 99352
Phone: (509) 375-6934; Fax: (509) 375-2186
E-mail: wu.xu@pnnl.gov

Ji-Guang Zhang (Co-PI)
Pacific Northwest National Laboratory
Energy & Environment Directorate
902 Battelle Boulevard, Mail Stop K2-44
Richland, WA 99352
Phone: (509) 372-6515; Fax: (509) 375-2186
E-mail: jiguang.zhang@pnnl.gov

Start Date: October 1, 2012
Projected End Date: September 30, 2016

Objectives

- Prevent lithium (Li) dendrite formation in Li-metal anode used in Li-metal batteries and to prevent Li dendrite formation in carbon anodes used in Li-ion batteries during overcharge and/or low temperature conditions.

Technical Barriers

Li dendrite growth and low Li Coulombic efficiency (CE) are the two major problems hindering the application of Li metal as an anode material in rechargeable Li batteries. Li dendrite growth on carbonaceous anodes in Li-ion batteries also has been a serious safety issue under abusive charging conditions, such as overcharging, charging at high rates, and charging at low temperatures. All of these barriers have hindered commercialization of rechargeable Li-metal batteries as well as state-of-the-art Li-ion batteries for use in plug-in hybrid electric vehicles and pure electric vehicles.

Technical Targets

- Optimize electrolyte compositions to effectively prevent Li dendrite growth on Li-metal anode.
- Identify appropriate electrolyte formulations to minimize Li dendrite growth on carbonaceous anodes.
- Identify optimal electrolyte formulations to enable Li-metal batteries to operate for more than 500 cycles without internal shorting.

Accomplishments

- Developed electrolytes to suppress Li dendrite growth on Li metal and to maintain Li CE of 97%.
- Optimized electrolytes with Cs^+ additive to maintain 500 stable cycles for Li|LFP cells without internal short circuiting.
- Discovered a Cs^+-additive that can protect the graphite anode in propylene carbonate (PC)-based electrolytes and enhance the high rate capability and high temperature cycling stability of graphite|NCA full cells.
- Filed one invention disclosure report and two U.S. Patent Applications.

✧ ✧ ✧ ✧ ✧

Introduction

Li-metal batteries have been called the “holy grail” of energy storage systems because the Li metal anode has an ultrahigh theoretical specific capacity, low density, and the lowest negative electrochemical potential, but two major problems—Li dendrite growth and low CE of Li deposition/stripping—hinder their commercial applications. For a Li-ion battery, Li plating and Li dendrite formation during overcharging or fast charging, or when charging at low temperatures, also are serious problems that must be solved. A rough or dendritic Li film generated at the anode surface can self-amplificate and lead to internal short circuiting of the battery and even more serious safety problems such as thermal runaway, fire, and explosion. A general solution to the dendrite growth problem will not only enable a series of Li-metal based energy storage systems, but also significantly improve the safety of Li-ion batteries.

Approach

The PNNL approach is to use novel electrolytes and additives to prevent Li dendrite formation on Li-metal and carbon anodes while maintaining high CE of battery operation. These electrolytes will enhance the cycling stability, rate capability and high/low temperature stability of Li metal anode, carbon anode, and various Li^+-intercalation cathode materials. Hence, the long-term stability of rechargeable Li and Li-ion batteries will be improved, especially during high rate overcharge and low-temperature operating conditions.

Results

Effects of additives on the average CE of Li deposition/stripping. In addition to Cs^+ and Rb^+ additives that we reported previously, the effects of several other additives, including $LiAsF_6$, vinylene carbonate (VC), monofluoroethylene carbonate (FEC), and their combinations on the CE and cycling stability of a Li electrode have been investigated using a baseline electrolyte of 1.0 M $LiPF_6$/PC electrolyte (E075) and Li|Cu cells. A method proposed by Aurbach et al., (*J. Power Sources* 1999, *81-82*, 95-111) has been used to evaluate the average CE of Li deposition/stripping. Table V - 9 shows that the combinations of $LiAsF_6$-VC or FEC at 2wt% for each component can increase the average CE (over 10 cycles) of Li from 73% to near 97%. Electrolyte with the VC additive also proves to be more stable than electrolytes with the FEC additive.

Table V - 9: Effects of Additives on the Average CE of Li

Electrolyte Solution	Average CE (%)
ELY075	73.2
ELY075+2wt% $LiAsF_6$	77.4
ELY075+2wt% VC	94.1
ELY075+2wt% FEC	93.7
ELY075+2wt% VC+2wt% $LiAsF_6$	96.7
ELY075+2wt% FEC+2wt% $LiAsF_6$	96.4

Long-term cycling test of Li-dendrite-suppression electrolyte in Li cells with different cathodes at low rates: The cycling performance of Li|$LiFePO_4$ (LFP), Li|$LiNi_{0.80}Co_{0.15}Al_{0.05}$ (NCA) and Li|$LiNi_{0.5}Co_{0.2}Mn_{0.3}$ (NCM) cells with three different electrolytes was tested using relatively lower charging rates. The LFP electrode was homemade with an LPF loading of ~12 mg/cm^2 or ~2.0 mAh/cm^2. The NCA and NCM electrodes were obtained from Bryant J. Polzin of Argonne National Laboratory, with code names ANL-S-C002 and ANL-A-C005, respectively. The NCA loading was 11.59 mg/cm^2 or 1.50 mAh/cm^2, and the NCM loading was 10.89 mg/cm^2 or 1.42 mAh/cm^2. The electrolytes were 1.0M $LiPF_6$ in carbonate solvents, where E004 contained EC/EMC, X1 contained EC/PC/EMC, and Cs means 0.05M $CsPF_6$ was added. The cells were first charge/discharged through two formation cycles at C/10 rate and then cycled at C/5 charging and 1C discharging in the voltage ranges of 2.8~3.9 V for LFP and 3.0~4.3 V for NCA and NCM. The long-term cycling stability of these cells is shown in Figure V - 211a, Figure V - 211b, and Figure V - 211c, respectively.

Figure V - 211 shows that the LFP cells with Cs^+-containing electrolyte (X1Cs is 1.0 M $LiPF_6$ in EC/PC/EMC with 0.05M $CsPF_6$) shows extremely stable long-term cycling during the tested 500 cycles, while the cells with two control electrolytes without Cs^+-additive exhibit fast capacity fading with cycling. The sharp capacity increase at around 60 to 100 cycles is caused by the temperature increase from 69 to 74°F in the laboratory. On the other hand, the NCA and NCM cells with Cs^+-electrolyte show cycling-stability that is very similar to the control electrolytes. One possible explanation for the observed differences among the different samples is that Cs^+ may be intercalated into NCA and NCM at higher voltage (4.3 V) but it cannot be intercalated into LFP at less than 3.9 V. Further investigation is required to verify this assumption.

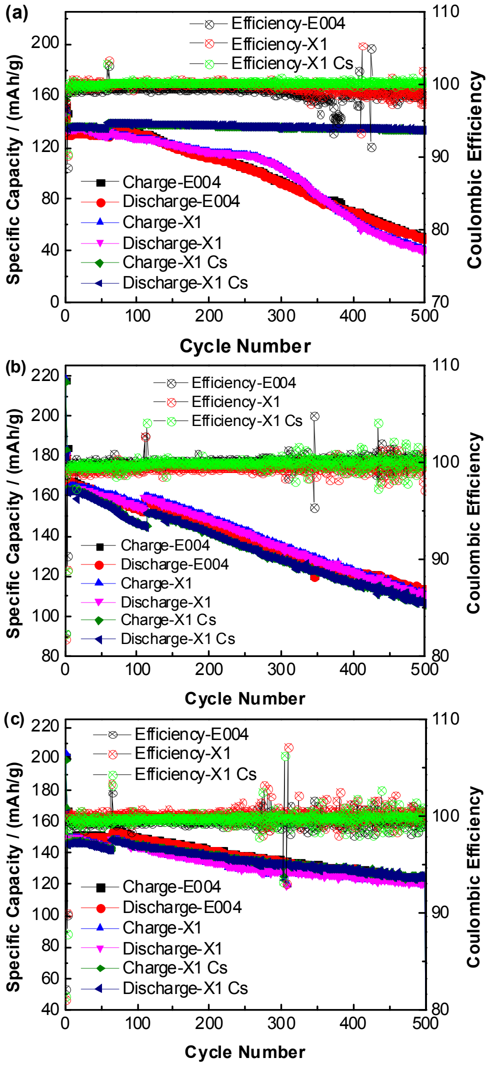

Figure V - 211: Long-term cycling performance of Li|LFP (a), Li|NCA (b) and Li|NCM (c) cells with three different electrolytes at C/5 charging and 1C discharging at room temperature

Long-term cycling test of Li-dendrite-suppression electrolyte in Li|LFP cells at high rates: Figure V - 211a demonstrates that addition of $CsPF_6$ in the Cs^+-containing electrolyte X1Cs can effectively protect Li anode morphologies at a charge current density of 0.48 mA/cm^2 for Li|LFP cells. Further investigation of Li|LFP cells at higher charging current densities (1.2 and 1.6 mA/cm^2, equivalent to C/2 and C/1.5 rates) indicates that the effect of Cs^+ additive is less dramatic when the current density is higher than 1 mA/cm^2, probably due to the formation of dead Li metal species during quick Li stripping process.

Figure V - 213 shows the impedance spectra of Li|LFP coin cells using different electrolytes and measured at different stages of cycling. The samples were charged at C/1.5 (1.60 mA/cm^2) and discharged at 1C (2.40 mA/cm^2). When no additive is used, the cell impedance increases with cycle numbers as shown in Figure V - 213 (a) and Figure V - 213 (b). In contrast, Figure V - 213 (c) shows that the addition of $CsPF_6$ in electrolyte leads to a decrease in the cell impedance during cycling. This indicates the formation of a protection layer at the electrodes/electrolyte interface when $CsPF_6$ is used. Figure V - 212 compares the surface morphologies of Li-metal electrodes imaged by scanning electron microscopy (SEM). The Li samples were taken from the disassembled Li|LFP cells after they were tested for 150 cycles in different electrolytes. The images in Figure V - 212 show that the surface of Li metal anode after cycling in the Cs^+-containing electrolyte is much smoother than those cycled in other electrolytes without the Cs^+ additive.

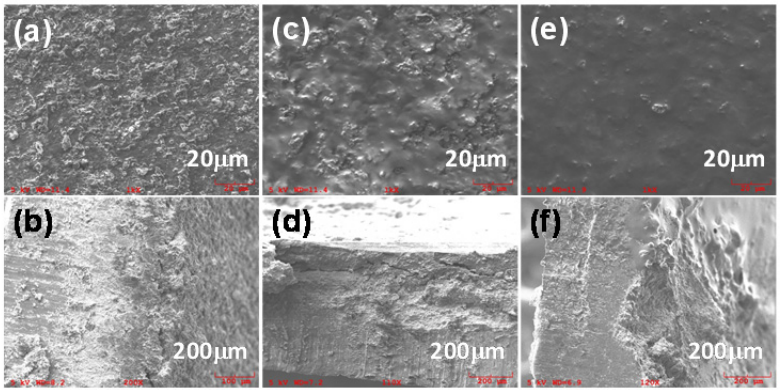

Figure V - 212: Surface (a,c,e) and cross-section (b,d,f) SEM images of Li metal anodes in Li|LFP cells with three different electrolytes after 150 cycles at C/2 (1.20 mA/cm^2) charging and 1C (2.40 mA/cm^2) discharging. The electrolytes are (a,b) E004; (c,d) X1; and (e,f) X1Cs

Effect of Cs^+-additive on Li dendrite suppression on graphite anodes: In addition to studying the effect of electrolyte additives on the stability of Li metal anodes, we also studied the effect of Cs^+ additive on the cycling stability of graphite electrode. This was accomplished by cycling Li|graphite half cells in an electrolyte (1M $LiPF_6$ in EC/PC/EMC) with 0.05 M of $CsPF_6$. Both surface and cross-sectional morphologies of deposited graphite electrode were evaluated by SEM. At fully charged condition (100% of graphite capacity), deposited Li metal was observed on the graphite surface even at a low current density of 0.2 mA/cm^2. A higher charging rate leads to more Li deposition at carbon electrode surface, but the Li morphology is not dendritic. Under 100% overcharging condition (200% of graphite capacity), severe Li dendrites formed on carbon anode surface. More dendritic Li was observed at low temperatures during the charging process.

Effect of Cs^+-additive on performance of PC-based electrolytes in graphite|NCA full cells: The cycling stability and rate capability of graphite|NCA full cells with different electrolytes are shown in Figure V - 214.

It is not surprising to see that the control electrolyte without any additive (i.e., X1) shows low capacity and poor cycling stability in graphite-based full cells (Figure V - 214a) because of the co-intercalation of PC in the electrolyte into graphite causing partial exfoliation of graphene structure in graphite anode (Figure V - 214b). After adding $CsPF_6$ or FEC additives, the graphite anodes are well protected because stable SEI layers are formed. Although no clear difference in the cycling performance was observed for the samples with Cs^+ or FEC additive cycling at room temperature (Figure V - 214a), the samples cycled with Cs^+ additive electrolyte (X1Cs) show higher discharge capacity and better cycling stability than the electrolytes with FEC and $CsPF_6$/FEC mixture at high temperature (Figure V - 214c). The sample cycled in an electrolyte containing only the Cs^+ additive also demonstrates better high-rate capability than those cycled in the electrolytes with FEC or a mixture of Cs^+ and FEC as the additives (Figure V - 214d). One possible explanation for this behavior is that Cs^+ additive can form a stable SEI layer on the surface of graphite and prevent its exfoliation by PC present in the electrolyte. The fundamental mechanism behind the improved performance in graphite|NCA cells with sole Cs^+ additive will be further investigated.

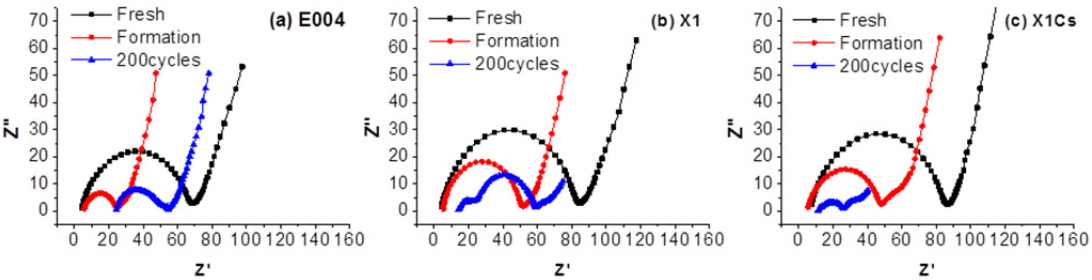

Figure V - 213: The a.c. impedance spectra of Li|LFP coin cells at the discharged state after different cycles. The samples were first charged/discharged at C/10 rate for two cycles, then charged at C/1.5 rate (1.60 mA/cm^2) and discharged at 1C rate (2.40 mA/cm^2) for 200 cycles

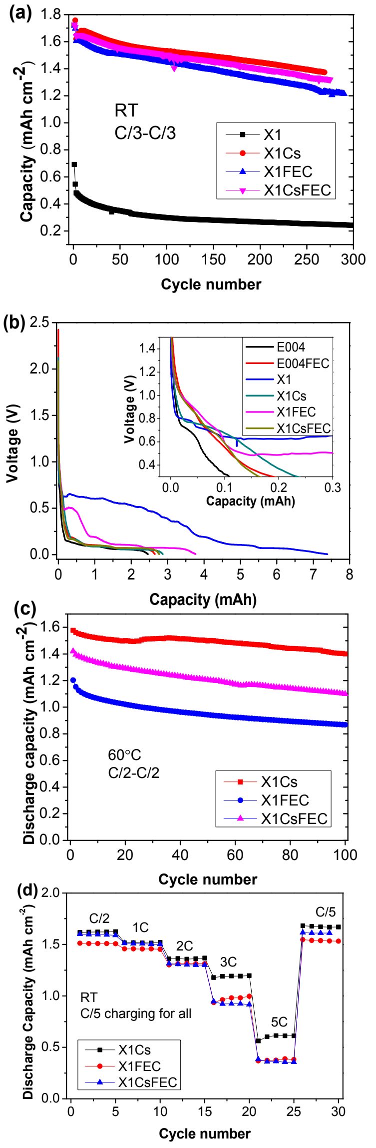

Figure V - 214: Battery performance of graphite|NCA full cells in terms of cycling stability at RT (a) and 60°C (c) and rate capability at RT (d), and discharge voltage profiles of Li|graphite cells (b)

Conclusions and Future Directions

The effects of different additives on CE of Li deposition/stripping and cycling stability of Li|Cu cell in $LiPF_6$/PC electrolyte were investigated. The combinations of $LiAsF_6$-VC or FEC at 2 wt% for each component can significantly increase the average CE of Li from 73% to ~97%. Li|LFP cells with 0.05M $CsPF_6$ in the electrolyte can be cycled for 500 cycles without fading at 0.5 mA/cm^2 charging current density while the cells with control electrolytes without Cs-additive decay rapidly after 100 cycles. The Cs^+-additive also can prevent graphite exfoliation in PC-based electrolytes and enhance high rate capability and high temperature cycling stability of graphite|NCA full cells.

The fundamental mechanism of the Cs^+-additive to protect graphite anodes and improve the performance of full cells will be further investigated. The performance of the Cs^+ additive in conventional electrolytes used in Li-ion batteries will also be investigated next year. New electrolyte additives will be investigated to prevent Li dendrite growth in Li-ion batteries operated at low temperatures.

FY 2014 Publications/Presentations

1. F. Ding, W. Xu,* X. Chen, J. Zhang, Y. Shao, M. H. Engelhard, Y. Zhang, T. A. Blake, G. L. Graff, X. Liu, and J.-G. Zhang,* “Effects of Cesium Cations in Lithium Deposition via Self-Healing Electrostatic Shield Mechanism”, *J. Phys. Chem. C*, 2014, **118**(8), 4043-4049.
2. W. Xu,* J. Wang, F. Ding, X. Chen, E. N. Nasybulin, Y. Zhang, and J.-G. Zhang,* “Lithium Metal Anodes for Rechargeable Batteries”, *Energy Environ. Sci.*, 2014, **7**(2), 513-537.
3. W. Xu,* F. Ding, X. Chen, Y. Zhang, J. Qian, E. N. Nasybulin, R. Cao, M. H. Engelhard, and J.-G. Zhang, “Dendrite-Suppression Electrolytes for Lithium-Metal and Lithium-Ion Batteries”, in *Electronic Proceedings of the 46th Power Sources*

Conference, Session 26.4, pp. 374-377, June 9-12, 2014, Orlando, FL.

4. W. Xu, X. Chen, Y. Zhang, F. Ding, E. N. Nasybulin, and J.-G. Zhang, "Dendrite-Free and High-Efficiency Rechargeable Lithium Metal Batteries", Presented at *224th ECS Meeting*, Oct. 27-Nov. 1, 2013, San Francisco, CA.
5. W. Xu, F. Ding, Y. Zhang, J. Qian, X. Chen, E. N. Nasybulin, P. Bhattacharya, R. Cao, M. H. Engelhard, and J.-G. Zhang, "Dendrite-Suppression Electrolytes for Rechargeable Lithium Batteries", Presented (Invited Talk) at *247th ACS National Meeting & Exposition*, March 16-20, 2014, Dallas, TX.
6. W. Xu, F. Ding, X. Chen, Y. Zhang, J. Qian, J. Zhang, E. N. Nasybulin, P. Bhattacharya, L. Xiao, R. Cao, H. Xiang, M. H. Engelhard, and J.-G. Zhang, "Dendrite-Suppression Electrolytes for Lithium-Metal and Lithium-Ion Batteries", Presented at *46th Power Sources Conference*, June 9-12, 2014, Orlando, FL.

V.G.5 Development of High Energy Lithium Sulfur Batteries (PNNL)

Jie Xiao
Pacific Northwest National Laboratory
Energy and Environment Directorate
902 Battelle Boulevard
Richland, WA 99352
Phone: (509) 375-4598; Fax: (509) 375-2186
E-mail: jie.xiao@pnnl.gov

Jun Liu (Co-PI)
Pacific Northwest National Laboratory
Energy and Environment Directorate
902 Battelle Boulevard
Richland, WA 99352
Phone: (509) 375-4443; Fax: (509) 371-6242
E-mail: jun.liu@pnnl.gov

Start Date: October 1, 2011
Projected End Date: September 30, 2016

Objectives

- Develop high energy lithium-sulfur (Li-S) batteries
    - Investigate the fundamental chemistry and failure mechanism in the Li-S system.
    - Apply fundamental research to help address the challenges in the practical applications.

Technical Barriers

- High cost of materials and synthesis routes.
- Limited energy density and cycling ability.

Technical Targets

- Fabrication of thick sulfur electrodes with nanostructures.
- Identify the limiting factors in Li-S cells comprised of thick cathode at a relevant scale.
- Revisit the fundamental reaction mechanism in Li-S battery system.

Accomplishments

- Developed a convenient approach to coat nano-structured S/C nanocomposite into large-area, uniform and pin-hole free electrode with adjustable sulfur loadings at 2-8 mg/cm^2.
- Identified the key factor that limits the long-term cycling of Li-S cells consisting thick sulfur electrode.
- Discovered the roles of sulfur radicals in Li-S system.

✧ ✧ ✧ ✧ ✧

Introduction

Compared to the state-of-art Li-ion battery technologies, Li-S batteries have the attributes of high energy (theoretically 2,650 Wh/kg), low cost and environmental friendliness and are therefore of paramount research interest. However, the low electrical conductivity of sulfur (5×10^{-30} S/cm) and the "shuttle reaction" caused by soluble polysulfides are detrimental to their performance, leading to low sulfur utilization rate, poor Coulombic efficiency, fast capacity fade, and severe self-discharge, not to mention concerns regarding the use of lithium metal as the anode.

Approach

Although there were many approaches reported in literature to address the challenges in Li-S systems, the sulfur content in the S/C composite, the electrode thickness, and testing conditions varied significantly in different groups, making the direct comparison or evaluation of various methods difficult. The approaches adopted in this project include:

- Fabricate and test thick sulfur electrode by using cost-effective methods.
- Revisit the failure mechanism of Li-S cells comprised of thick sulfur electrodes.
- Apply advanced characterization to investigate the species generated during the electrochemical process.

Results

1. Fabrication and investigation of thick sulfur electrode

In FY14, a facile approach (Patent application #: 61/521,191**)** has been developed to fabricate thick sulfur electrode while remaining the necessary nano-structure of sulfur/carbon (S/C) composite to promote the utilization rate of sulfur and reduce the polarization. The electrochemical properties of these thick sulfur electrodes were then further studied to identify the key challenges of Li-S batteries at a relevant scale.

Figure V - 215a compares the areal specific capacity delivered from sulfur electrodes with different sulfur loadings. 0.1C was used to enhance the electrode wetting for these electrodes. When sulfur loading was increased from 1 to 3.5 mg/cm^2, the areal specific capacity showed almost liner increase to a peak value at 4.5 mAh/cm^2, followed by a decrease. This was because with increasing electrode thickness, both the ionic and electronic conductivity of sulfur cathode decreased. Therefore, the utilization rate of sulfur decreased with increasing sulfur loading on the electrode. In the beginning, the capacity gain from packing more sulfur on the electrode exceeded the reduced utilization rate of sulfur so the whole trend of areal specific capacity kept increasing. At certain limit, e.g.3.5 mg/cm^2, the balance between maximum loading and utilization rate was reached, followed by a decreased areal specific capacity with higher sulfur loading.

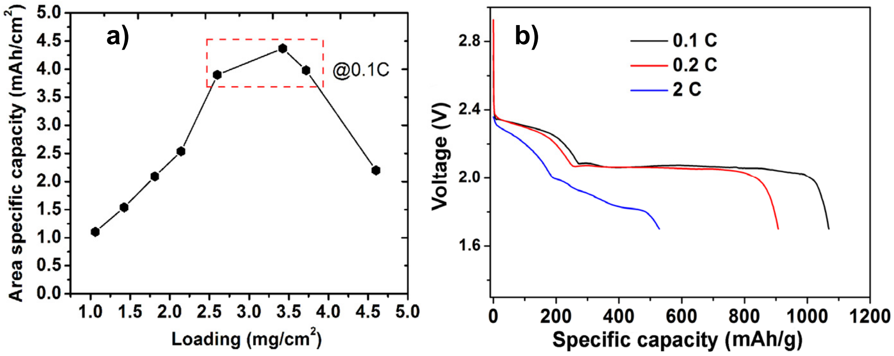

Figure V - 215: a) Areal specific capacity delivered from sulfur electrodes with different sulfur loadings. b) Rate capability of thick sulfur electrode with 3.5 mg/cm^2 loading. 1C=1000 mAh/g (PNNL unpublished results)

Of note, the optimized sulfur loading could change depending on the current density and electrode wettability. For example, it was found that the electrolyte penetration into the interior sulfur cathode became very difficult when the electrode thickness was increased. Since ether-based solvent had to be used for Li-S batteries, the application of vacuum was not feasible. If the wetting of the entire thick electrode was resolved, the optimized loading of sulfur e.g., the loading corresponding to the highest areal capacity could be further increased to benefit the practical applications.

Figure V - 215b displays the rate capability of thick sulfur electrode. At a slow rate of 0.1C, the reversible capacity is ca. 1100 mAh/g and decreases to slightly more than 900 mAh/g at 0.2C. Above 0.2C rate, the polarization became large with significantly reduced capacity to less than 600 mAh/g. While the electrode thickness was one reason, another more important reason at this stage was the insufficient electrolyte wetting on the whole electrode, leading to the poor Li$^+$ cation transport especially at high rates. The wetting issue greatly affected the maximum capacity deliverable from the thick electrode as well as the rate performance and should be first addressed.

2. Limiting factor for long-term cycling of Li-S cells comprised of thick cathode

In Li-S cells, both cathode and anode had to be considered concurrently to understand the electrochemical performances of the whole system. The main factor that limited the long-term cycling stability of Li-S cells may change with time especially when a thick cathode is used.

Figure V - 216a and Figure V - 216b shows the surface and cross-sectional SEM images of lithium metal anode harvested from Li-S cell comprised of thick sulfur electrodes after 100 cycles. Not only the anode surface became very rough, forming cracks and pores (Figure V - 216a), the electrolyte also penetrated deeply into the bulk and “corroded” the whole lithium metal anode. EDS mapping discovered a large amount of sulfur elements along with other SEI components (Figure V - 216b), implying the accumulation of inactive byproducts on the anode side with cycling. The end result was the gradual increase of cell impedance on the anode side. Figure V - 216c showed the cycling stability of Li-S cells with sulfur loading at 3.5 mg/cm^2 on the cathode. Although the first 200 cycles demonstrated a relatively stable cycling with 71% capacity retention, a sharp decrease was seen after 200 cycles due to the cell impedance increase on the anode. When coupled with thick sulfur cathode, lithium anode was deeply stripped and redeposited thus the damages on the lithium side, especially in the presence of dissolved polysulfides, were enlarged and became severe after 200 cycles. If thin-film sulfur cathode was used, only shallow cycling occurrs on the lithium side thus hundreds of stable cycles could be demonstrated (depending on the thickness of cathode), which was, however, not useful for practical applications and therefore not reported here. This project focused on thick sulfur electrode and confirmed that lithium metal became the dominant limiting factor in determining the cell stability during long-term cycling. More effort should be pursued on the anode side in Li-S cells constructed at a relevant scale.

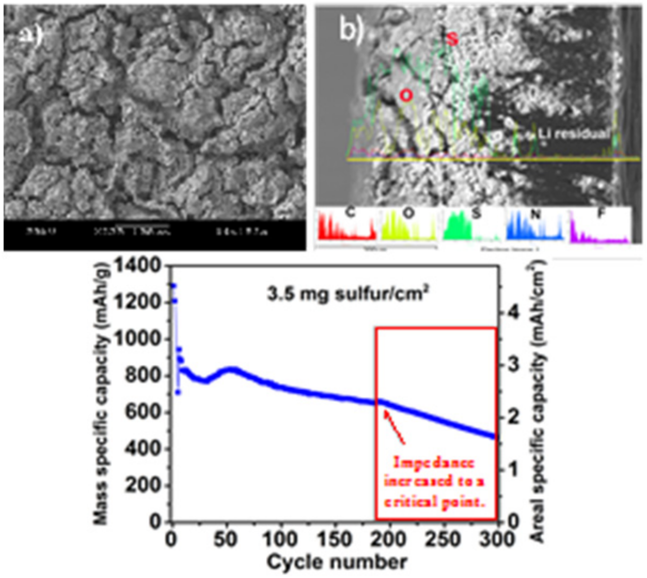

Figure V - 216: SEM images of lithium metal anode on the a)surface and b) cross-section view and EDS mapping after 100 cycles in Li-S cells comprised of thick sulfur cathode (3.5 mg/cm^2). c) showed the long-term cycling of Li-S cell. (PNNL unpublished results)

3. Roles of sulfur radicals in Li-S batteries

Although reports on Li-S batteries were quickly accumulated, it was still not conclusively known how polysulfide ring/chain participated in the whole cycling and whether the discharge and charge processes followed the same pathway. By using *in situ* electron paramagnetic resonance (EPR) technique, S_3^{*-} radical was directly observed in a functioning Li-S cell, which greatly facilitated the understanding of the different reaction pathways of the discharge/charge processes in Li-S cells.

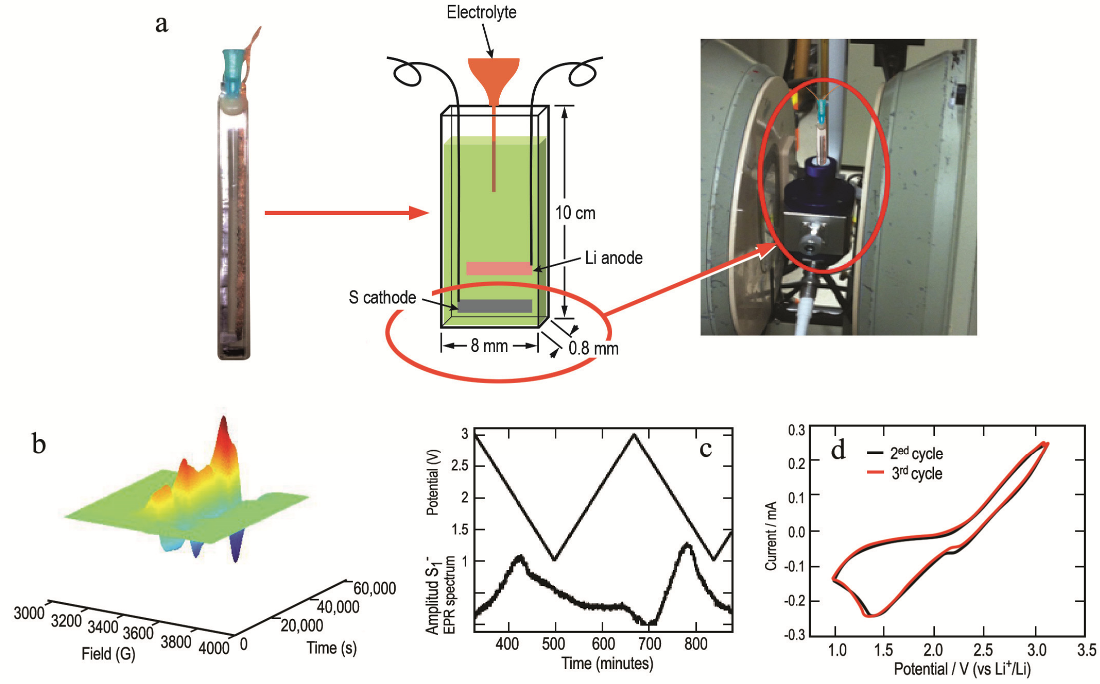

Figure V - 217: a) EPR cell design for *in situ* testing and capturing of radical resonance signals generated throughout the operation of Li-S batteries. b) 3D plot of *in situ* EPR spectra in a functioning Li-S EPR cell vs. time during CV scan. c) The concentration evolution of sulfur radicals at different time (potentials). d) The 2nd and 3rd CV curves collected concurrently from Li-S EPR cell. Both c) and d) started from the second cycle due to wetting issues. (PNNL unpublished results)

Figure V - 217a illustrates the detailed dimension of the EPR cell. Figure V - 217b shows the resonance signals from sulfur radicals, which demonstrated periodic changes with changing potentials (time) and were assigned to S_3^{*-} radicals based on its line shape/width and g-factor (2.029). To simplify discussion, the amplitude of sulfur radical concentration was plotted together with the potential changes, in Figure V - 217c. Due to the limitation of the current design of EPR cell (cell thickness: 0.8 mm), the polarization was relatively large leading to the asymmetric redox peaks (Figure V - 217d). However, a small reduction peak at 2 V was clearly seen with a second broad peak extended to 1 V due to the polarization. In general, the concentration of S_3^{*-} radicals reached its maximum at ca.2 V during negative scan, followed by a decrease till the end of positive scan, although a slight delay was also observed (Figure V - 217c).

The identification of sulfur radicals explained why traditional alkyl carbonate-based electrolyte such as ethylene carbonate (EC) and dimethyl carbonate(DMC) cannot be used in Li-S batteries. This was because S_3^{*-} easily reacted with the alkyl carbonates, which was known to be vulnerable to the radicals. Similarly, for Li-O_2 batteries, carbonate solvents intensively reacted with intermediate $O_2^{\bullet-}$ radicals through nucleophilic attack, converting discharge products to inactive carbonates. On the other hand, ether-based electrolytes or glymes were relatively more stable towards radicals. Considering the similar oxidation ability between S_3^{*-} and $O_2^{\bullet-}$, EC and DMC etc. should be excluded in the presence of S_3^{*-}.

Based on the periodic concentration changes of sulfur radicals at different potentials (Figure V - 217b-Figure V - 217c) and the electrochemical characteristics of the cell, it was revealed that the chemical and electrochemical reactions in Li-S cell are driving each other to proceed by using sulfur radicals as the media, leading to two completely different reaction pathways during discharge and charge, as proposed in Figure V - 218. The different voltage curves for discharge and charge, regardless of current density, were also well explained by the proposed radical mechanism (details not discussed here).

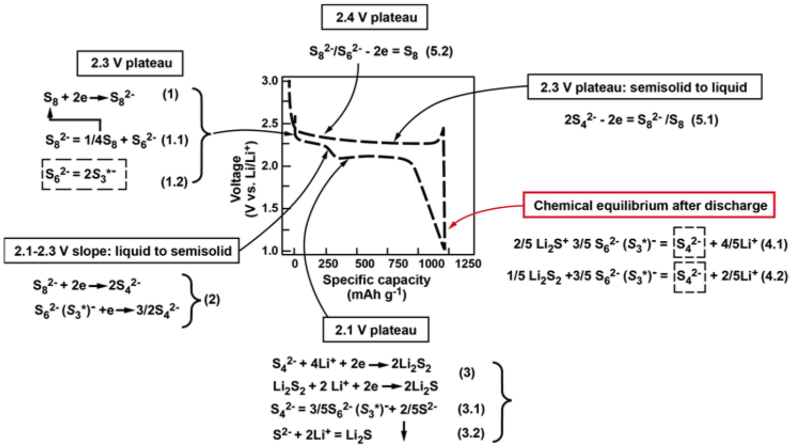

Figure V - 218: Proposed reaction mechanism for Li-S batteries during cycling. The equilibria between S_6^{2-} and S_3^{*-} always existed and shifted at different potentials. S_6^{2-} preferred to stay at relatively high potential (> 2.1 V) while S_3^{*-} was the preferred form at low potential (≤ 2.1 V). Different reaction pathways were suggested for discharge and charge processes. The Li-S cell was tested at C/5 rate between 1 V and 3 V in typical button cells.

Conclusions and Future Directions

The electrochemical properties of thick sulfur cathodes were systematically investigated and compared at different sulfur loadings. Maximum areal specific capacity was identified at 4.5 mAh/cm^2 (sulfur loading: 3.5 mg/cm^2) at C/10 rate based on the current wetting method. It was revealed that lithium anode, if coupled with thick cathode, underwent deep stripping and deposition processes, introducing a large amount of insulating byproducts with cycling. The limiting factor that controlled the stable cycling of Li-S cells, therefore, gradually shifted to the anode side due to impedance increase for the lithium metal. By using *in situ* EPR technique, the generation and concentration variation of sulfur radicals was identified throughout the whole cycling, indicating the temporal equilibrium among different polysulfides, instead of producing a single polysulfide component, at each different potential. The chemical and electrochemical reactions in the Li-S cells were driving each other to move forward via using sulfur radicals as the media. Different reaction pathways had been revealed for the discharge and charge processes of Li-S battery, which matched well with their voltage profiles and helped to further understand the electrochemical characteristics of Li-S batteries.

Future work will first address the wetting issues in thick sulfur electrodes thus the sulfur loading could be further improved without sacrificing reversible capacity. Interface reactions between the electrolyte and the anode will be carefully studied to explore appropriate electrolyte and/or additives to minimize SEI accumulation. Alternative anode will also be investigated to replace lithium metal but still enable high-energy sulfur battery technology.

FY 2014 Publications/Patents/Presentations

1. J. Zheng, D. Lu, M. Gu, C. Wang, J.-G. Zhang, J. Liu and J. Xiao, “How to Obtain Reproducible Results for Lithium Sulfur Batteries?” *J. Electrochem. Soc.*, **2013**, 160, A2288-2292.
2. J. Zheng, J. Tian, D. Wu, M. Gu,# W. Xu, C. Wang, F. Gao, J.-G. Zhang, J. Liu, and J. Xiao, “Lewis Acid-Base Interactions between Polysulfides and Metal Organic Framework in Lithium Sulfur Batteries”, *Nano Letters*, 2014, 14, 2345-2352.
3. J. Xiao, D. Lv, Y. Shao, W. Bennet, G.L. Graff, J. Zhang and J. Liu “Electrodes for Li-S batteries”, Patent Application #: 61/521,191.
4. J. Xiao, J.-G. Zhang, G.L. Graff, J. Liu, W. Wang, J. Zheng, W. Xu, Y.Shao, Z. Yang, “Energy Storage Systems Having an Electrode Comprising Li_xS_y”, Patent Application #: 13/432,166.
5. J. Xiao, D. Lv, Y. Shao, J.-G. Zhang and J. Liu “Electrolyte for lithium-sulfur batteries employing graphite as the anode”, Patent Application #:30597-E.
6. J. Xiao, D. Lv, Y. Shao, W. Bennett, J.-G. Zhang and J. Liu “Preformation of stable solid electrolyte interface (SEI) film on graphite anode”, Patent application #: 30544-E.
7. J. Xiao, J. Zheng, D. Lv, T. Lozano, J. Zhang, W. Bennett, G. Graff and J. Liu, “Lithium Sulfur Batteries: Fundamental Understanding Towards Practical Applications:, Materials Challenges in Alternative &Renewable Energy 2014 Conference, Clearwater, Florida.
8. J. Xiao, D. Lv, J. Zheng, T. Lozano, E. Walter, Y. Shao, N.T. Saenz, J.-G. Zhang, W. Bennett, G. Graff and J. Liu, “Towards the Practical Application of Lithium Sulfur Batteries: Electrochemistry and Chemistry”, Beyond Li-ion Batteries VII, Argonne National Laboratory, Argonne, June 3rd, 2014.
9. J.Xiao, D.Lv, J. Zheng, T. Lozano, E. Walter, Y. Shao, N.T. Saenz, J.-G. Zhang, W. Bennett, G. Graff and J. Liu, “Towards the Practical Application of Lithium Sulfur Batteries: Electrochemistry and Chemistry”, General Motor Global R&D Center, Warren, June 23rd, 2014.
10. J. Xiao, D. Lv, J. Zheng, T. Lozano, E. Walter, Y. Shao, N.T. Saenz, J.-G. Zhang, W. Bennett, G. Graff and J. Liu, “Towards the Practical Application of Lithium Sulfur Batteries: Electrochemistry and Chemistry”, U.S.-China Electric Vehicle and Battery Technology Workshop, Seattle, August 19, 2014.
11. J. Xiao, D. Lv, J. Zheng, T. Lozano, E. Walter, Y. Shao, N.T. Saenz, J.-G. Zhang, W. Bennett, G. Graff and J. Liu, “Towards the Practical Application of Lithium Sulfur Batteries: Electrochemistry and Chemistry”, Ulsan National Institute of Sciences and Technology, Ulsan, Korea, Sept 16, 2014.
12. J. Xiao, D. Lv, J. Zheng, T. Lozano, E. Walter, Y. Shao, N.T. Saenz, J.-G. Zhang, W. Bennett, G. Graff and J. Liu, “Towards the Practical Application of Lithium Sulfur Batteries: Electrochemistry and Chemistry”, University of Waterloo, July 24th, 2014.
13. D. Lv, Y.Shao, T. Lozano, W. D. Bennett, G. L. Graff, B. Polzin, J.-G. Zhang, M. H. Engelhard, N.T. Saenz, W.A. Henderson J. Liu and J. Xiao, “Challenges in Practical Li-S Batteries: Failure Mechanism on Lithium Metal Anode”, The 225th Electrochemical Society Meeting, Orlando, FL, May 13rd, 2014.

V.G.6 Rechargeable Lithium-Air Batteries (PNNL)

Ji-Guang Zhang
Pacific Northwest National Laboratory
Energy & Environment Directorate
902 Battelle Boulevard, Mail Stop K2-44
Richland, WA 99352
Phone: (509) 372-6515; Fax: (509) 375-2186
E-mail: jiguang.zhang@pnnl.gov

Wu Xu (Co-PI)
Pacific Northwest National Laboratory
Energy & Environment Directorate
902 Battelle Boulevard, Mail Stop K2-44
Richland, WA 99352
Phone: (509) 375-6934; Fax: (509) 375-2186
E-mail: wu.xu@pnnl.gov

Start Date: October 1, 2012
Projected End Date: September 30, 2016

Objectives

- Develop stable electrolytes, electrode materials, and catalysts to improve the cycling stability and Coulombic efficiency (CE) of rechargeable $Li\text{-}O_2$ batteries for their potential application in long-range electric vehicles.

Technical Barriers

During the discharging process, the reduced oxygen species attack all components in a $Li\text{-}O_2$ battery and significantly limit the reversibility of rechargeable $Li\text{-}O_2$ batteries. In addition, the overvoltage that occurs during the charging process of a $Li\text{-}O_2$ battery also is high (i.e., over 1 V) and leads to low Coulombic efficiency of the batteries.

Technical Targets

- To further develop stable air electrodes via surface modifications of carbon with different inert materials such as Al_2O_3, TiO_2, RuO_2, etc.
- To develop stable solid-state electrolytes based on inorganic ceramic ionic conducting glasses and polymeric electrolytes.

Accomplishments

- Systematically investigated factors that affect the extended cycle life of $Li\text{-}O_2$ batteries with Ru nanoparticle catalyst and ether-based electrolyte.
- Achieved ~100 stable cycles of $Li\text{-}O_2$ batteries with a carbon nanotube/ruthenium (CNT/Ru) composite air electrode and a DMSO-based electrolyte.
- Investigated cycling stability of $Li\text{-}O_2$ cells in four types of new electrolytes.

✧ ✧ ✧ ✧ ✧

Introduction

Li-air or $Li\text{-}O_2$ batteries have an ultra-high theoretical specific energy (~5,200 Wh/kg when the weights of Li and O_2 are included), and are expected to have a practical specific energy of around 800 Wh/kg that is about four times that of state-of-the-art Li-ion batteries (approximately 200 Wh/kg). However, development of rechargeable $Li\text{-}O_2$ batteries faces significant challenges including decomposition of electrolytes, large over-voltage that occurs during charging, design of cathode materials with high capacity and stability, and protection of Li metal anode. More importantly, highly reactive oxygen species ($O_2^{-\bullet}$, LiO_2, O_2^{2-}, LiO_2^-, and Li_2O_2) are generated on the air electrode surface via the oxygen reduction reaction (ORR) during the discharge of a $Li\text{-}O_2$ battery, and these species attack every component in $Li\text{-}O_2$ batteries and significantly limit the reversibility of the rechargeable $Li\text{-}O_2$ batteries. Therefore, the chemical and electrochemical stability of all $Li\text{-}O_2$ battery components, including the electrolyte solvent, electrolyte salt, cathode material (typically carbon-based), and binder, needs to be reevaluated in an O_2-rich environment. Also, good catalysts need to be developed to reduce the overvoltage during oxygen reduction and evolution reactions so the cycling stability of $Li\text{-}O_2$ batteries can be improved.

Approach

PNNL's approach is to develop new electrolytes (both liquid and solid-state) that are stable against the reactive reduced-oxygen species; and to explore the protected carbon air electrodes with selected oxygen evolution reaction (OER) catalysts to avoid carbon oxidation and improve the cycling stability of the rechargeable $Li\text{-}O_2$ batteries. The stability of the electrolytes and coated air electrodes during discharge-charge processes of a Li-O_2 battery will be systematically investigated to improve the performance of Li-O_2 batteries.

Results

Investigation of factors affecting extended cyclability of Li-O_2 batteries: The extended cycle life of Li-O_2 batteries with CNTs/Ru nanocomposites as electrocatalytic substrate and ether-based electrolyte has been systematically investigated. The morphologies of the electrodes after discharge/charge processes at selected cycle numbers were analyzed by scanning electron microscopy (SEM) and X-ray photoelectron spectroscopy (XPS). During the discharge process, toroidal particles (mainly Li_2O_2) can only be observed after the first discharge (Figure V - 219a). The morphology changes to dense and smooth layer at the 2nd discharge cycle. The images of the air electrodes after the 5th and 50th discharge cycles are shown in Figure V - 219b and Figure V - 219c, respectively. After charging, all electrodes restore almost all of the porosity and look similar to the pristine electrode (Figure V - 220), meaning that toroidal particles observed after the first discharge as well as the dense deposits of discharge products observed for the higher cycle numbers are effectively decomposed. However, a closer look at the images of the charged electrodes reveals certain changes on the surface of CNTs even after the first charge, from a smooth surface for the pristine CNTs to rough layers with grain-like morphologies for cycled electrodes (inserts in Figure V - 220). XPS analysis results indicate that they are the residues of decompositions of electrolytes during discharge and charge, and/or carbon during charging at >3.5 V.

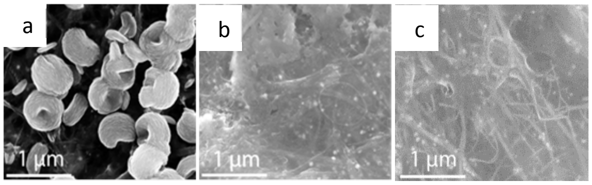

Figure V - 219: SEM images of discharged CNTs/Ru electrodes after a) 1st, b) 5th, and c) 50th cycles in the LiTf-tetraglyme electrolyte

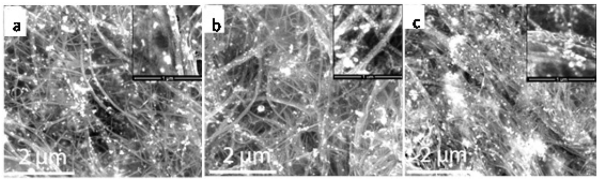

Figure V - 220: SEM images of charged CNTs/Ru electrodes after a) 1st, b) 5th, and c) 50th cycles in the LiTf-tetraglyme electrolyte

The contents of Li_2O_2 in the discharged products formed on CNT electrodes after selected cycles were analyzed using the iodometric titration method. However, this method cannot be used to analyze the Li_2O_2 content in the discharged CNTs/Ru electrodes because of the catalytic effect of Ru nanoparticles. There is ~70% current yield of Li_2O_2 (meaning that 70% of current passing through the cell was used to form Li_2O_2) after the first discharging but the yield was reduced to 33 to 42% after the 5th discharge until the 50th cycle. During charging, O_2 and CO_2 are released (Figure V - 221). With increasing cycle numbers, less O_2 but more CO_2 are detected, and the charging voltage profile also changes. In summary, the observed long cycle life of the Li-O_2 battery originates from the appropriate material selection and efficient charging process. It is important to decompose all the discharge products (Li_2O_2 and side products) during the charging step to restore the porosity of the electrode for the next cycle.

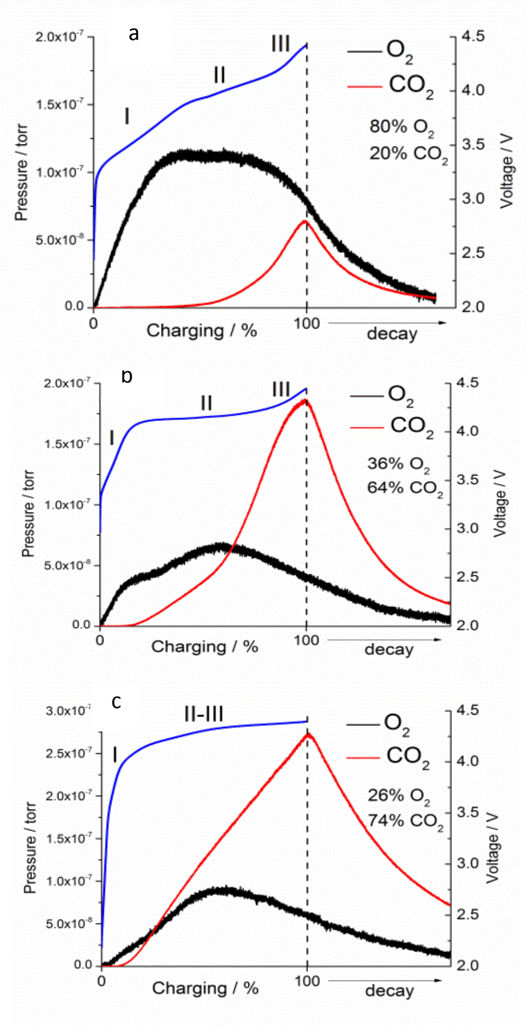

Figure V - 221: *In situ* mass spectroscopic analysis of O_2 and CO_2 evolved during charging of the batteries with CNTs/Ru electrode and LiTf-tetraglyme electrolyte at a) 1st, b) 5th, and c) 50th cycles

Long-term cycling Li-O_2 cells: Dimethylsulfoxide (DMSO)-based electrolytes have been reported to have a good stability in Li-O_2 cells. Discharge on a CNT/Ru electrode in $LiClO_4$-DMSO electrolyte results in the formation of toroidal particles similar to the LiTf-tetraglyme electrolyte, but with much smaller sizes (~100 nm) and deformed shape. Titration of the discharged air electrodes demonstrates a 69% current yield of Li_2O_2 while mass spectroscopic tests reveal a 92% O_2 release during charging. This indicates that significant portion of side products are not decomposed with CO_2 release. After charging, toroidal Li_2O_2 particles disappear, but there is an obvious residue attributed to the side products.

Cycling voltammetry (CV) analysis of the $LiClO_4$-DMSO electrolyte (bubbled with continuous flow of oxygen) on flat glassy carbon and Ru electrodes demonstrates the formation of the sharp ORR peaks at 2.25 V with nearly the same peak currents and onsets at 2.6 V except for the first cycle on Ru, which shows unexpectedly lower onset of cathodic current apparently arising for some surface adsorbed species (Figure V - 222). More importantly, cycling on glassy carbon demonstrates two distinct anodic peaks. The peak at the lower potential is attributed to the OER, while the peak at the higher potential should correspond to decomposition of side products. There also is an onset of anodic decomposition of $LiClO_4$-DMSO electrolyte at 4.2 V, and the cycling is extremely stable in the applied range (500 cycles with only a small decrease in peak current values). CV profiles with Ru as the working electrode exhibit much lower anodic peak currents but it also is very stable. However, the Ru working electrode also promotes electrolyte decomposition and eventually shifts its onset to ~4.0 V.

To avoid potential chemical and/or electrochemical instability of Li metal in $LiClO_4$-DMSO electrolyte, lithium nickel cobalt aluminum oxide was used as the lithium source for the cycling experiment. Total discharge capacity of Li-O_2 cell in $LiClO_4$-DMSO electrolyte is ~6,500 mAh g^{-1} (Figure V - 223a), which is almost three times higher than those in the LiTf-tetraglyme electrolyte. Complete charging results in severe anodic decomposition of the DMSO-electrolyte at the end of charging with the plateau at 4.3 V. To avoid electrolyte decomposition, shallow cycling was conducted at 80% (Figure V - 223b) depths of discharge (DOD). The samples exhibit a lower charging voltage (< 4 V) and maintained for 95 cycles before the cell voltage drops quickly.

Development of new electrolytes for Li-O_2 batteries: The possibility of making stable composite solid electrolytes for Li-O_2 batteries was investigated. Flexible free-standing solid electrolyte films were prepared by using a garnet-type ceramic Li^+ conductor $Li_{6.4}La_3Zr_{1.4}Ta_{0.6}O_{12}$ (LLZTO) powder and polyethylene (PE), where PE is stable against reduced oxygen species and can provide mechanical integrity and flexibility of the composite LLZTO/PE solid electrolyte. The functionality of the electrolyte with LLZTO powder (70 wt%) was tested in symmetrical Li|Li cells, but the cells could not sustain the required current densities (>0.01 mA cm^{-2}) due to the insulating nature of PE. Decreasing PE content to 15 wt% did not solve the problem of low conductivity while mechanical integrity and flexibility were lost because of the insufficient amount of PE. Additional work, especially control of solid electrolyte thickness, is required to develop functional solid-state composite electrolytes.

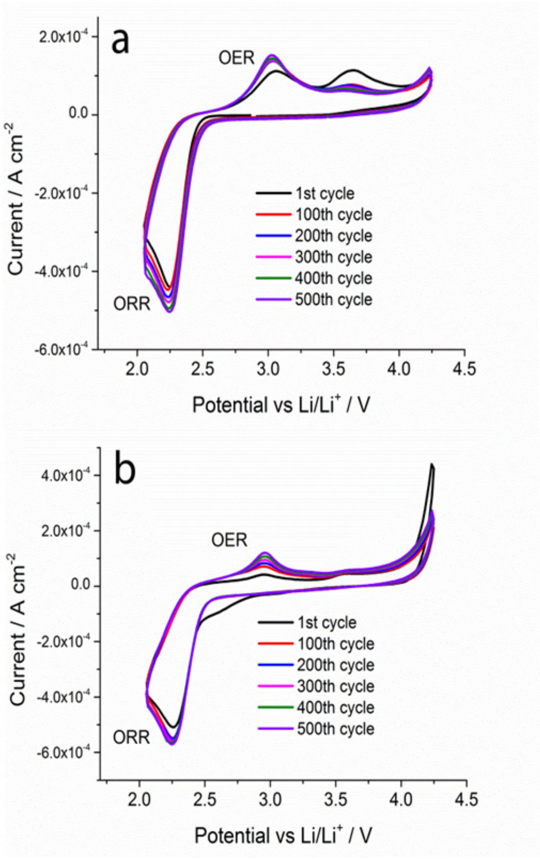

Figure V - 222: Cycling voltammetry (100 mV s^{-1}) on flat a) glassy carbon and b) Ru electrodes recorded in a $LiClO_4$-DMSO electrolyte bubbled with oxygen

Three other types of electrolytes were investigated further in Li-O_2 batteries. One approach is to use the so-called “solvent-in-salt” electrolytes. The high concentration of salt significantly increases ionic strength of the electrolyte and may alter reactivity of a solvent. For example, acetonitrile is known as a relatively stable electrolyte against the superoxide anion radical, but it is reactive with Li metal and cannot be used directly in Li-O_2 batteries. The concentrated electrolyte of 75 wt% LiTFSI in acetonitrile is stable with Li metal because a thick solid-electrolyte-interphase layer is formed on the Li surface so it can be directly applied in a Li-O_2 battery. Although there is some fluctuation in the capacity of the Li-O_2 cell, the battery demonstrates over 120 cycles with over 100 days of operation (Figure V - 224). Voltage profiles exhibit a main discharging plateau at about 2.5 V and a main charging plateau at about 4.5 V.

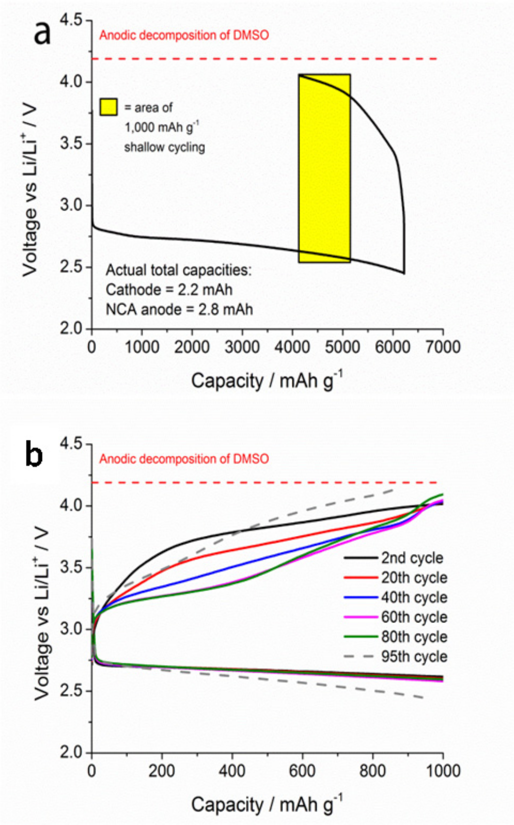

Figure V - 223: Cycling Performance of Li-O_2 Batteries with CNT/Ru electrodes in the $LiClO_4$-DMSO Electrolyte. Capacity limited (1,000 mAh g^{-1}) cycling was conducted at 80% of the total discharge capacity

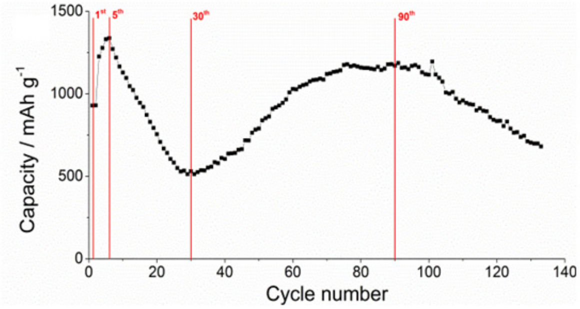

Figure V - 224: Cycling performance of a Li-O_2 battery with the electrolyte of 75 wt% LiTFSI in acetonitrile

Another electrolyte investigated consists of 50 wt% LiTFSI in 1-butyl-1-methylpiperidinium bis(trifluoromethylsulfonyl)imide (PIP14TFSI). This electrolyte also can be considered as an ionic liquid electrolyte. The electrolyte is a solid at room temperature, and the tests were conducted at 60°C. The batteries demonstrate a capacity of 2,700 mAh g^{-1} at 0.05 mA cm^{-2}. However, only a few stable discharge/ charge cycles are obtained before capacity drops sharply. The low yield of Li_2O_2 after the first discharge (32% by titration) may indicate limited electrolyte stability.

To avoid an unstable organic cation (PIP14), an electrolyte that is a mixture of LiTFSI (T_m=235°C) and CsTFSI (T_m=130°C) with a eutectic composition (x_{LiTFSI}=0.07 and x_{CsTFSI}=0.93) and a melting point of 117°C was tested in a Li-O_2 battery at 120°C. The battery delivers a high discharge capacity of about 3,000 mAh g^{-1} and relatively stable cycling performance. The discharge voltage plateau is about 2.2 V, which is ~ 500 mV lower than the typical values observed during the discharge of Li-O_2 batteries. This reduced discharge voltage may be the result of poor electrolyte conductivity. The fluctuation in the charge voltage profiles can be attributed to the decomposition of $TFSI^-$ anion at elevated temperatures.

Conclusions and Future Directions

The extended cycling behavior of Li−O_2 batteries based on CNTs was systematically investigated by several approaches. Important conditions that lead to long cyclability are appropriate material selection (including catalyst an electrolyte) and an efficient charging protocol to achieve efficient decomposition of discharge products including Li_2O_2 and side products. Approximately 100 stable cycles were obtained for the Li_2O_2 batteries with CNT/Ru nanocomposites as an electrocatalytic substrate and a DMSO-based electrolyte. Solvent-in-salt type electrolytes also showed promising cycling behavior.

Future work will focus on developing solvent-in-salt electrolytes that are stable against reactive reduced-oxygen species. The OER catalysts will be further studied to reduce charging overvoltage and improve cyclability of Li-O_2 batteries.

FY 2014 Publications/Presentations

1. E. N. Nasybulin, W. Xu,* B. L. Mehdi, E. Thomsen, M. H. Engelhard, R. C. Masse, P. Bhattacharya, M. Gu, W. Bennett, Z. Nie, C. Wang, N. D. Browning, J.-G. Zhang,* "Formation of Interfacial Layer and Long-Term Cyclability of Li-O_2 Batteries", *ACS Appl. Mater. Interfaces*, 2014, **6**, 14141-14151.
2. E. N. Nasybulin, M. H. Engelhard, W. Xu, and J.-G. Zhang, "Evaluating the Stability of Li-O_2 Battery Components on Cathode/Electrolyte Interface by XPS", Presented at AVS 60th International Symposium & Exhibition, Oct. 27-Nov. 1, 2013, Long Beach, CA.

3. E. N. Nasybulin, W. Xu, M. H. Engelhard, E. C. Thomsen, M. Gu, B. L. Mehdi, J. Zheng, Z. Nie, and J.-G. Zhang, "The Development of Catalytic Systems for the Rechargeable Li-O_2 Batteries", Presented at 224th ECS Meeting, Oct. 27-Nov. 1, 2013, San Francisco, CA.
4. E. N. Nasybulin, W. Xu, B. L. Mehdi, E. C. Thomsen, M. H. Engelhard, R. C. Masse, P. Bhattacharya, M. Gu, W. D. Bennett, Z. Nie, C. M. Wang, N. D. Browning, and J.-G. Zhang, "Formation of Interfacial Layer and Long-term Cycling of Li-O_2 Batteries", Presented at 225th ECS Meeting, May 11-15, 2014, Orlando, FL.

V.G.7 Simulations and X-Ray Spectroscopy of Li-S Chemistry (UCB)

Nitash Balsara
University of California, Berkeley
Department of Chemical and Biomolecular Engineering
201 C Gilman Hall
Berkeley, CA 94720
Phone: (510) 642-8973; Fax: (510) 642-5033
E-mail: nbalsara@berkeley.edu

David Prendergast (Co-PI)
Lawrence Berkeley National Laboratory
1 Cyclotron Road, MS 67R3207
Berkeley, CA 94720
Phone: (510) 486-4948; Fax: (510) 486-7424
E-mail: dgprendergast@lbl.gov

Start Date: October 2013
Projected End Date: September 2016

Objectives

- Develop a unique diagnostic tool to study Li-S battery reaction intermediates that employs X-ray spectroscopy and molecular modeling.
- Elucidate Li-S battery charge/discharge reaction mechanisms.
- Examine physical and chemical nature of Li-S battery reaction intermediates in electrolyte environment.

Technical Barriers

As Li-S batteries are charged and discharged, Li_2S_x reaction intermediates formed can leave the cathode, causing capacity to fade and battery failure. Redox reaction mechanisms that form Li_2S_x intermediates are still unclear. Elucidation of reaction pathways requires an experimental tool that can differentiate Li_2S_x intermediates in their native environment. Little is known about the physical and chemical nature of Li_2S_x intermediates dissolved in electrolytes.

Technical Targets

- Obtain X-ray absorption spectroscopy (XAS) signatures for Li_2S_x intermediates dissolved in polymer electrolytes of poly(ethylene oxide) (PEO) and a diblock copolymer of polystyrene-poly(ethylene oxide) (SEO) by experiment and by simulations.
- Develop Li-S cells that facilitate use of soft and hard X-ray spectroscopy during charge-discharge cycles
- Perform detailed (first-principles or empirical force-field) molecular dynamics simulations to interpret associated X-ray spectra and reveal molecular nature of Li_2S_x intermediates in electrolyte.

Accomplishments

- Experimental XAS were obtained for Li_2S_x (x = 2, 4, 6, 8) intermediates dissolved in poly(ethylene oxide) (PEO) and a diblock copolymer of polystyrene-poly(ethylene oxide) (SEO).
- First ever theoretical calculation of sulfur K-edge XAS of isolated Li_2S_x species in tetraglyme, and more recently, lithium polysulfide radical anion species performed.
- The effect of other lithium salts (i.e. $LiNO_3$) on polysulfide speciation was probed via XAS and MD simulations.
- Newly designed Li-S cells for *in situ* XAS experiments were built and tested.

✧ ✧ ✧ ✧ ✧

Introduction

The objectives of this work are to: (a) elucidate mechanisms by which redox reactions in the sulfur cathode proceed, and (b) study the physical and chemical nature of Li_2S_x intermediates. Past studies of Li-S battery reaction mechanisms have been inconclusive due to the difficulty of differentiating Li_2S_x spectroscopically. Standards for single Li_2S_x species cannot be obtained as they cannot be isolated as single components. Instead polysulfides exist only in solutions, and as mixtures of different Li_2S_x resulting from reversible disproportionation reactions. The equilibrium constants and reaction kinetics governing disproportionation are system-dependent, making it difficult to conclusively obtain spectral standards for each polysulfide compound. The approach to solve these issues and elucidate polysulfide chemistry is to couple experimental X-ray spectroscopy (XAS) to theoretical XAS and molecular dynamic simulations. This coupling provides us with an unprecedented ability to obtain spectra for single Li_2S_x molecules, and enables a rigorous approach to understand lithium polysulfide disproportionation and Li-S battery reaction mechanisms.

Approach

Molecular dynamic (MD) simulations of Li_2S_x molecules dissolved in tetraglyme are used to determine the free energy of formation for each Li_2S_x molecule as well as the optimal conformation/geometry of both single molecules and molecules existing in concentrated systems. Excited Core Hole (XCH) simulations are used to obtain theoretical lithium polysulfide anion and Li polysulfide radical anion X-ray signatures for representative *ab initio* molecular dynamic motifs. Theoretical spectra and MD simulation findings are used to support experimental findings.

Previously, Li_2S_x species were dissolved in poly(ethylene oxide) and a block copolymer polystyrene-poly(ethylene oxide). Sulfur K-edge XAS were obtained for these systems. Principal component analysis (PCA) was used to understand the underlying chemistry. More recently, spectra have been obtained for polysulfide systems at different polysulfide concentrations, as well as in the presence of other Li salts. Theoretical simulations are being employed to explain the effects of concentration and Li salt additives.

Solid-state Li-S pouch cells have been modified to allow soft X-ray probing of both the anode and cathode. These cells will enable *in situ* XAS of battery reaction mechanisms. Theoretical calculations, as well as understanding of X-ray overabsorption and the effects that polysulfide concentration and Li salt additives have on Li_2S_x spectra will allow us to rigorously explain Li-S redox reaction mechanisms.

Results

Theoretical XAS calculations of Li_2S spectra: As validation of the XCH approach to calculating theoretical X-ray spectra, the experimental spectrum for lithium sulfide (Li_2S) powder is compared to the calculated spectra for Li_2S, as shown in Figure V - 225. Excellent agreement was found between the experimental and calculated spectra. The experimental spectrum is characterized by three main peaks at 2473.8, 2476.1, and 2484.0 eV, which are reproduced by the XCH calculated spectral peaks at 2473.8, 2476.0 and 2484.1 eV, respectively. The green peak, representing the calculated X-ray spectrum for a static crystal Li_2S, and the gold spectra, representing the ensemble structure of Li_2S obtained from 298K first principals DFT simulation are very similar, having only small changes that are attributable to thermal broadening.

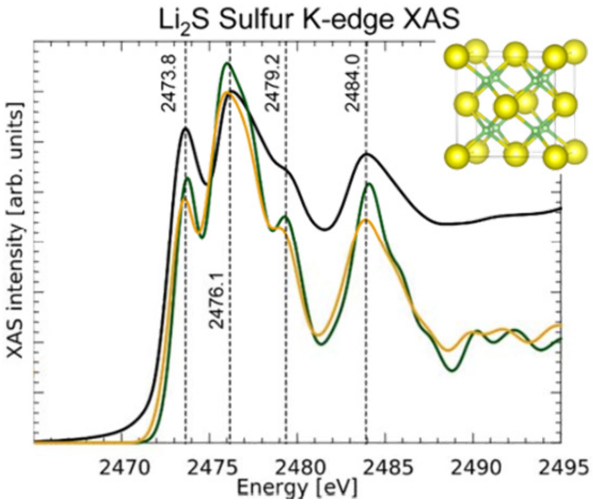

Figure V - 225: Sulfur K-edge XAS of Li_2S: experimental (black) and theoretical (green – static crystal; gold – 298K)

Theoretical XAS calculations for Li_2S_x species dissolved in TEGDME: Figure V - 226 shows the first-principles simulation of sulfur K-edge XAS of Li polysulfide species dissolved in tetraethylene glycol dimethylether (TEGDME). As previously reported, the spectra can be characterized by two peaks, a strong main-edge peak between 2472.6 and 2473.9 eV and a pre-edge peak occurring between 2470.6 and 2471.5 eV. These features arise from two differently coordinated sulfur atoms on the same molecule: terminal sulfur atoms (at the end of polysulfide chains) and internal sulfur atoms. Density functional theory (DFT) calculations indicate that terminal atoms have increased charge compared to internal atoms. This increase in electronic charge of terminal sulfur atoms leads to reduced binding energy of the 1s core-electrons. This leads to the red shift of the absorption onset with respect to the absorption feature of the internal sulfur atoms.

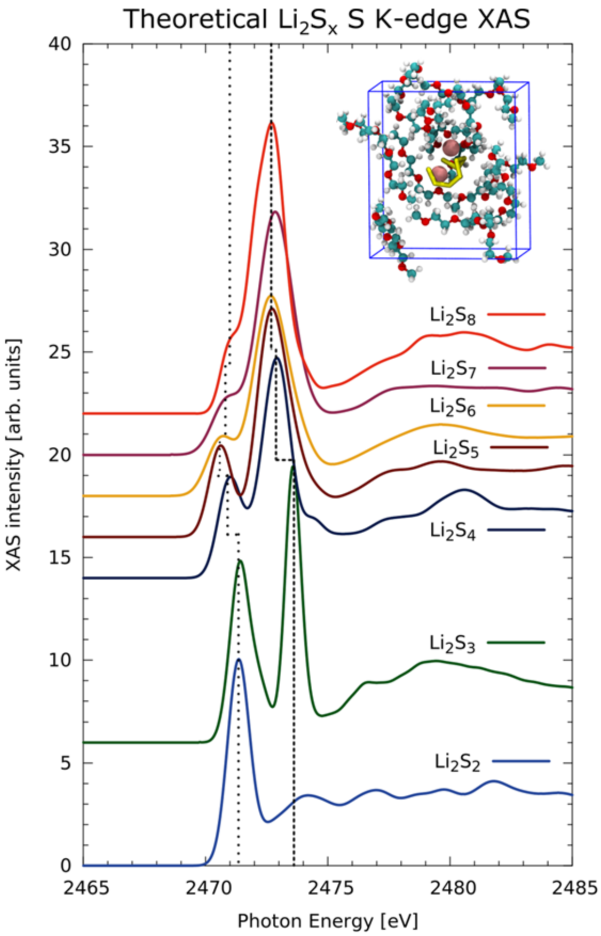

Figure V - 226: Calculated sulfur K-edge XAS of Li_2S_x ($2 \leq x \leq 8$) dissolved in TEGDME

Comparison of experimental and theoretical results: The spectral features shown in the above polysulfide spectra and previously shown in experimental polysulfide spectra raise the possibility of distinguishing polysulfides based on main/pre-edge intensities. It is expected that as polysulfide chain length increases, the pre-edge feature will decrease, as the overall number of terminal sulfur atoms decreases relative to internal sulfur atoms. As shown in Figure V - 227, this expectation is proven to be true. However, a more accurate approach was shown to distinguishing polysulfide species that may be used to instead compare the overall peak areas of internal and terminal sulfur atoms (assuming a Gaussian line shape for each peak). Bond length fluctuations at finite temperature can increase peak broadening, and perhaps decrease peak intensity. Employing the peak area incorporates the subtle finite temperature dependence of spectral features and gives way to a more accurate metric by which polysulfides can be differentiated.

Similar calculations were performed for previously shown experimental spectra of Li_2S_8 and Li_2S_4 dissolved in PEO. The resulting peak intensity and area ratios for these spectra follow similar trends to the theoretically calculated case, the area ratio being higher than the intensity ratio for Li_2S_8.

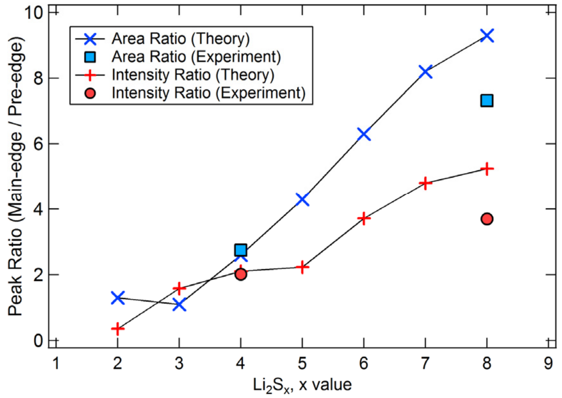

Figure V - 227: Comparison of peak intensity and area ratios

Identification of unique sulfur K-edge peak in lithium polysulfide radical anions. Previous studies of Li-S redox reactions suggest the presence of Li polysulfide radical anions during the charge or discharge process. Obtaining a spectral standard for these species experimentally is naturally very difficult. Theoretical methods were used to calculate sulfur K-edge XAS for radical sulfur anions that can be used in future *in situ* studies. The resulting spectra, shown in Figure V - 228, have a unique feature (highlighted by an arrow) that is vacant in the Li_2S_x spectra. This will enable detection of radical species during *in situ* reactions.

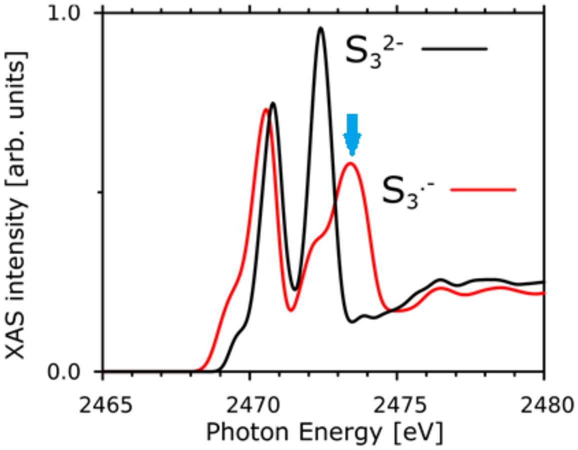

Figure V - 228: Calculated sulfur K-edge XAS of S_3^{2-} and $S_3^{\cdot -}$. Unique radical feature highlighted by arrow

Effect of Li salt additives on polysulfide spectra: Thin films of PEO containing Li_2S_8 and $LiNO_3$ were probed using XAS at the sulfur K-edge. Figure V - 229 shows a significant decrease in main-edge intensity in the X-ray spectrum of Li_2S_8 as $LiNO_3$ concentration increases. These changes may be due to disproportionation reactions or fundamental changes in the X-ray spectra, perhaps due to changes in electron distribution as the surrounding molecular environment becomes more Li-ion rich. MD simulations and theoretical XAS calculations are being used to explain this phenomena.

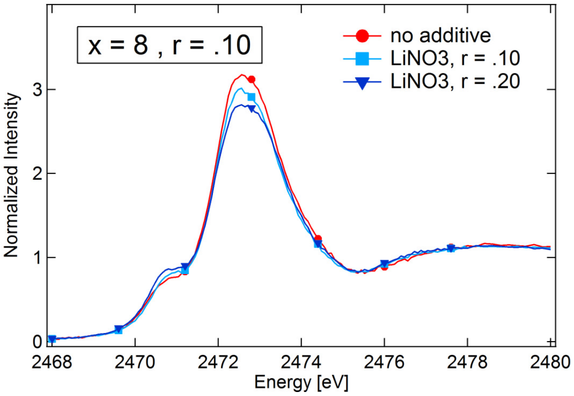

Figure V - 229: Effect of $LiNO_3$ on Li_2S_x, x = 8 X-ray spectrum, where 'r' denotes the ratio of total lithium ions per ethylene oxide monomer

Preparation of *in situ* cell: Solid-state Li-S cells containing a Li metal anode, a block copolymer electrolyte SEO containing $LiClO_4$, and a cathode containing carbon black, elemental sulfur, and SEO have been constructed as shown in Figure V - 230. The pouch cell has been modified with a thin Mylar film window that allows soft X-rays to probe the battery. The corresponding first discharge curve for the cell described here is shown in Figure V - 231, and mimics typical behavior of conventional Li-S cells. These cells will be used to perform *in situ* XAS experiments during upcoming beamtime.

Figure V - 230: Modified Li-S pouch cell for *in situ* XAS experiments

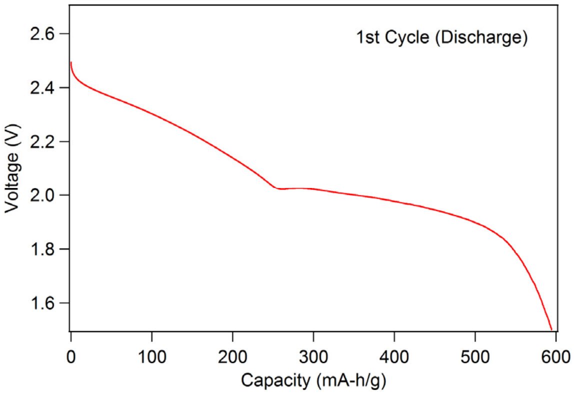

Figure V - 231: First discharge curve for Li-S cell shown in Figure V - 230

Conclusions and Future Directions

Molecular dynamic simulations and theoretical XAS calculations have obtained X-ray spectra for single, isolated Li_2S_x species. Accuracy of the theoretical approaches has been shown both in comparison of calculated spectra to experimental spectra of lithium sulfide as well as Li_2S_x species dissolved in PEO. It was also shown that the calculated ratio between main-edge and pre-edge peak area, rather than intensity, enables one to distinguish Li_2S_x species with increased accuracy. This calculation, shown in Figure V - 227, shows just how similar the theoretical and experimental results are. More recently, sulfur K-edge spectra have been calculated for radical anion polysulfide species. These standards are difficult to obtain experimentally and will allow detection of radical sulfur species during *in situ* XAS studies.

In future work, *in situ* Li-S pouch cells will be used to study Li-S battery reaction mechanisms. Elucidation of the effects of polysulfide concentration, salt additives, overabsorption, and polysulfide agglomeration on obtained X-ray spectra will assure a rigorous analysis of resulting spectroelectrochemical data.

FY 2014 Publications/Presentations

1. Balsara, N. (June 2014). "Fundamental Studies of Lithium-Sulfur Cell Chemistry." Presented at the 2014 DOE Annual Merit Review and Peer Evaluation Meeting, Washington, D.C.
2. Pascal, T.A.; Prendergast, D. (March 2014). "Finite temperature effects on the X-ray absorption spectra of energy related materials." Presented at the Bulletin of the American Physical Society, Denver, CO.

3. Pascal, T.A.; Prendergast, D. (April 2014). “First Principles X-Ray Absorption Spectroscopy Applied to Lithium Sulfur Batteries – Investigating The Solution Phase Chemistries of Dissolved Polysulfide Species.” Presented at the 2014 MRS Spring Meeting, San Francisco, CA.
4. Pascal, T.A.; Prendergast, D. (July 2014). “Thermodynamics and X-ray Absorption Spectra of Dissolved Lithium Polysulfides near Solid Interface.” Presented at the Workshop on Charged Systems and Solid/Liquid Interfaces, Santa Barbara, CA.
5. Pascal T.A.; Wujcik, K.; Velasco-Velez, J.; Wu, C.; Teran, A.A.; Cabana, J.; Guo, J.; Salmeron, M.; Balsara, N.; Prendergast, D. (2014). “X-ray Absorption Spectra of Dissolved Polysulfides in Lithium–Sulfur Batteries from First-Principles.” *J. Phys. Chem. Lett.* (5); pp. 1547−1551.
6. Wujcik, K.; Velasco-Velez, J.; Wu, C.; Pascal, T.; Terana, A.; Marcus, M.; Cabana, J.; Guo, J.; Prendergast, D.; Salmeron, M.; Balsara, N. (2014). “Fingerprinting lithium-sulfur battery reaction products using X-ray absorption spectroscopy.” *Journal of the Electrochemical Society* (161:6); pp. A1100-A1106.

V.G.8 Lithium Batteries with Higher Capacity and Voltage (UTA)

John B. Goodenough
University of Texas at Austin
Department of Mechanical Engineering
204 East Dean Keeton
C2201, ETC 9.184
Austin, Texas 78712
Phone: (512) 471-1646; Fax: (512) 471-7681
E-mail: jgoodenough@mail.utexas.edu

Start Date: January 2013
Projected End Date: December 2016

Objectives

- To develop a solid Li^+ electrolyte that
  - Can block dendrites from a Li^0 anode.
  - Has a Li+ conductivity σLi > 10-4 S cm-1.
  - Is stable in different liquid electrolytes at anode and cathode.
  - Has a low impedance for Li+ transfer across a solid/liquid electrolyte interface.
  - Is capable of low-cost fabrication as a thin, mechanically robust film.

Technical Barriers

To develop a solid electrolyte membrane for a Li-air cell with an aqueous catholyte, the solid electrolyte must be stable in water. However, Li^+ can be easily exchanged with protons, which limits the use of ceramic electrolyte membranes.

The PEO/Al_2O_3 polymer electrolyte membranes developed during the last project year has a low Li^+ conductivity since the single bond oxygen of the PEO component does not allow fast Li^+ transport. The C-O unit needs to be replaced to reduce interaction between Li^+ and the polymer backbone.

Technical Targets

- Determine TEM garnet surface structure in contact with a liquid electrolyte. Design of a surface coat of a garnet membrane to minimize impedance of Li^+ transfer across garnet surface.
- Prepare dense Li^+-electrolyte alternative to garnet and test impedance of Li^+ transfer across it.
- Construct and test a Li-S cell with a solid Li^+-electrolyte separator.

Accomplishments

- Identified chemical instability of the garnet-type solid electrolytes in water.
- Fabricated mesh-type crosslinked polymer membranes with fluorine, sulfone, and ester functional groups.
- Constructed and tested Li-S and Na-S cells with polymer electrolyte membranes.

✧ ✧ ✧ ✧ ✧

Introduction

A Li metal anode can provide higher capacity and voltage in an electrochemical cell. It also enables a battery fabricated in a charged state. To use a Li metal anode, it is essential to develop a solid electrolyte membrane that can block Li dendrites. The solid state separators may also enable an aqueous catholyte as well as aprotic solvents. A hybrid aprotic catholyte battery with a PEO/Al_2O_3 polymer composite membrane and Li metal anode was developed last year, but, to scale the cell up to grid scale energy storage, the possibility of an aqueous catholyte also needs to be checked since it can reduce production cost. Based on this idea, chemical stabilities in water for several solid electrolyte compositions were tested. It turned out that developing a Li^+ solid electrolyte stable in water is difficult because of a proton exchange reaction.

The solid separator can benefit Li-S cell development by blocking polysulfide crossover and eliminating shuttle currents. Several polymer membranes with different functional groups in polymer backbones were synthesized to control the chemical interaction between Li^+ and polymer. Different monomers brought unique polymer characteristics and electrochemical performance.

Approach

A solid state Li^+ electrolyte, e.g., garnet-structured ceramics, has been tested to check chemical stability in water since that is important to develop a Li-air cell with an aqueous catholyte.

In parallel, a polymer composite membrane has been studied to make a thin, flexible, and mechanically robust Li^+/Na^+ ion conducting separator that has higher ionic conductivity than that of the PEO/Al_2O_3 composite membrane developed last year. Chemical interaction between Li^+/Na^+ and the polymer backbone has been tuned by changing functional groups in the polymer.

Results

Chemical stability of garnet in water: The Li-ion conductors “$Li_{6.5}La_3Zr_{1.5}Ta_{0.5}O_{12}$” (LLZT) and “$Li_7La_3Zr_2O_{12}$” (LLZ) with garnet structure were prepared by solid-state reaction in an alumina crucible; their stability in water was investigated at room temperature.

The prepared LLZT and LLZ samples were crushed into powder for the ion-exchange reaction. The ion-exchange reaction was performed by placing 0.5 g of the garnet oxides in a flask containing 100 ml water of pH = 7. The experiments were carried out under constant stirring at room temperature. The duration of the exchange process was 48 hours. The dried samples were characterized by TGA, ^7Li and ^{27}Al MAS NMR, neutron diffraction, and TEM. (See Figure V - 232.)

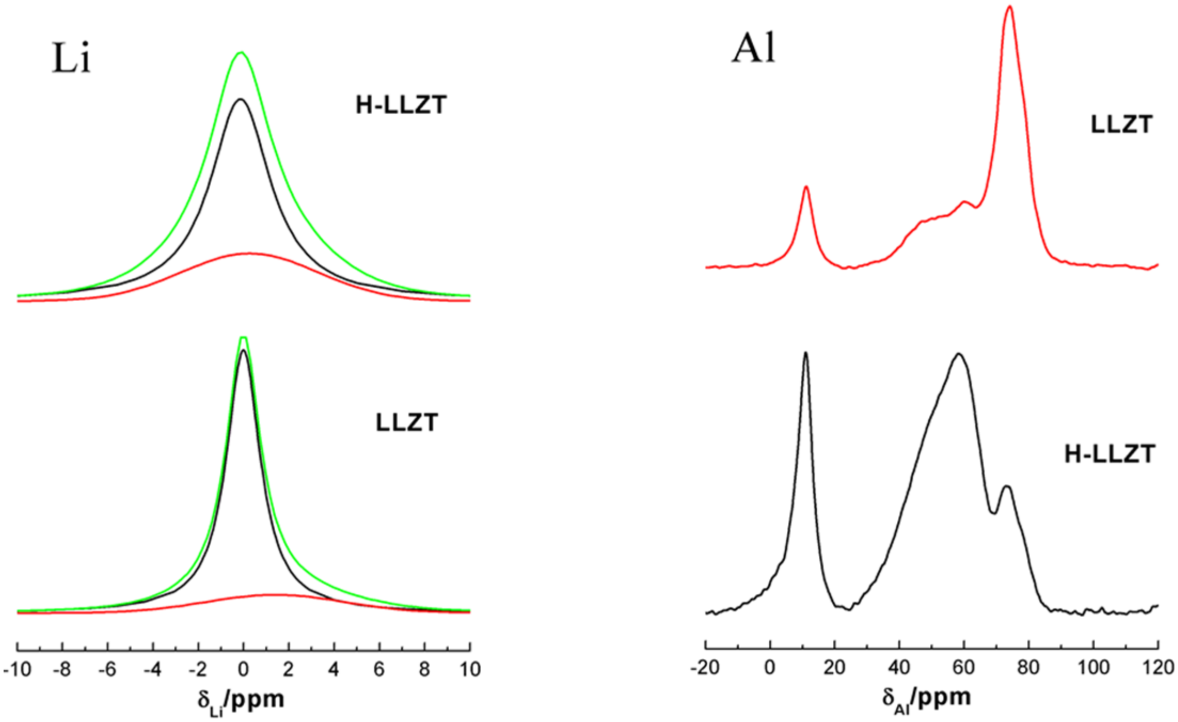

Figure V - 232: ^7Li and ^{27}Al MAS NMR spectra of LLZT and H-LLZT at room temperature, the line shape of ^7Li is fit as a sum of broad and narrow components associated with slow and fast Li-ion domains

It was found that both the bulk garnet and grain-boundary phases are unstable in water. The exchanged protons distort the Li-O octahedra and reduce the occupancy of Li on the octahedral sites of the bulk phase. The amorphous phase $LiAlO_2$ in the grain boundary is dissolved after ion exchange, which inhibits the Li transport in the grain boundary. The total (bulk+grain-boundary) conductivities of the garnets $Li_{6.5-x}H_xLa_3Zr_{1.5}Ta_{0.}5O_{12}$ at 25°C is 3.2×10^{-5} S cm^{-1} with an activation energy of 0.38 eV. The lowering of σ_{Li} and increase in E_a after reaction with water could be attributed primarily to a greater grain-boundary resistance.

Li-S cell with crosslinked polymer separator membranes: A Li-S cell was constructed using a Li^+ polymer-electrolyte separator and compared its performance with a cell having the same Li_2S_6 cathode trapped in porous carbon and a carbon-fiber paper for capturing mobile Li_xS soluble species. The membranes were made by thiol-ene chemistry which enabled fabrication of mesh-type polymer chain structures. The tetrathiol crosslinker was used in all batches since fewer thiol units (e.g., trithiol crosslinker) and less crosslink density brought more polysulfide crossover. The monomers in each membrane are mainly composed of (1) tri(ethylene glycol), (2) double vinyl ester, (3) perfluorohexane, and (4) double vinyl sulfone. Monomers for the (2-4) cases were chosen to have less chemical and electrochemical interactions with Li^+ in the liquid electrolyte. The perflurohexane-tetrathiol membrane showed severe rolling after soaking in liquid electrolyte, probably owing to the hydrophobic-hydrophilic combination of chain units, which made the cell test impossible. The double vinyl sulfones-tetrathiol membrane was notably stiff and did not absorb the liquid electrolyte, which prevented Li^+ transport through the membrane. (See Figure V - 233.)

The other two membranes with ethylene glycol and ester absorbed an ether-based liquid electrolyte, and coin cell tests proceeded. The tests showed little crossover to the anode side, but an osmosis problem prevented a good performance. No lithium nitrate was added in the electrolyte to see whether the crosslinked mesh structure in the membrane could block the polysulfide crossover. There was no endless charging in the voltage curves, but, instead, large polarization was observed. It was found that the interface between Li metal and the membranes were dried out after cycling, which suggests a possible osmosis issue in this case. The osmosis problem was solved by adding solvent to the anolyte. However, Li-S cell contains concentrated Li_2S_6 catholyte while the anolyte does not have any polysulfide molecules, which brings a variable strong driving force for the osmosis across the membrane.

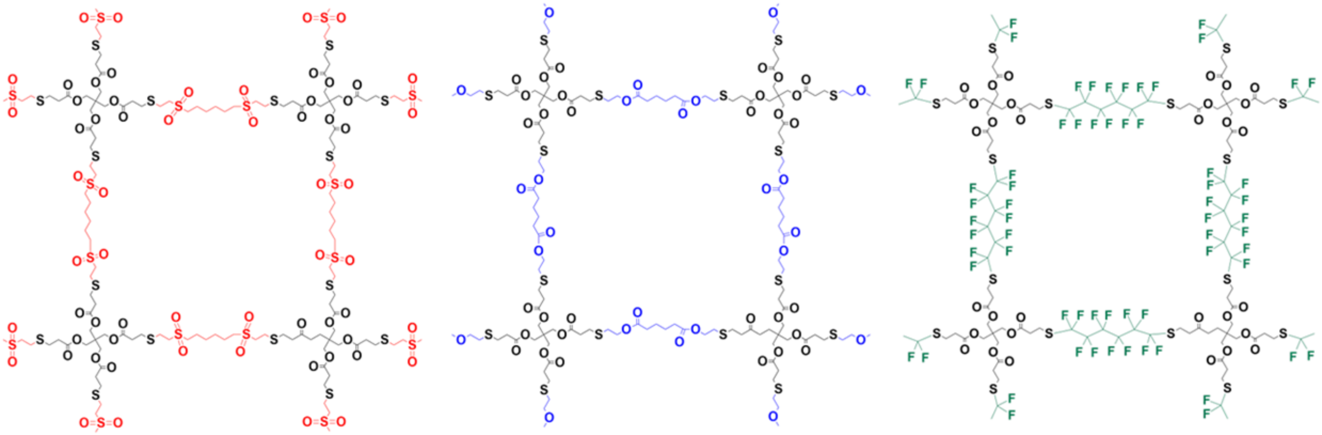

Figure V - 233: Crosslinked polymer membranes with double vinyl sulfone, double vinyl ester, and perfluorohexane units (from the top)

Conclusions and Future Directions

The data demonstrates that a separator that blocks dendrites is not sufficient as a practical metallic-Li anode. An interface layer between the polymer and a Li^0 anode needs to be developed which provides stable polymer-Li^0 contact on repeated cycling. To solve the problem and to avoid osmosis problem, an alkali-ion anode needs to be developed which makes contact with a polymer separator without contacting the liquid electrolyte and is stable on repeated cycling. For this development, a solid alkali-ion electrolyte between the metallic anode and a polymer containing a liquid electrolyte is necessary. In order to do this, a way must be discovered to retain bonding between the anode, the interface solid, and the polymer during cycling.

FY 2014 Publications/Presentations

1. Goodenough, J.B. (June 2014). "Lithium Batteries with Higher Capacity and Voltage." Presented at the 2014 Annual Merit Review and Peer Evaluation Meeting, Washington, D.C.
2. Park, K.; J. H. Cho, K. Shanmuganathan, J. Song, J. Peng, M. Gobet, S. Greenbaum, C. J. Ellison, J. B. Goodenough. (2014). *J. Power Sources* (263); pp. 52–58.

V.G.9 Exploratory Studies of Novel Li-Air Battery Systems (BNL, UM Boston)

Xiao-Qing Yang
Brookhaven National Laboratory
Chemistry Department
Building 555
Upton, NY 11973
Phone: (631) 344-3663; Fax: (631) 344-5815
E-mail: xyang@bnl.gov

Deyang Qu
University of Massachusetts Boston
Department of Chemistry
100 Morrissey Boulevard
Boston, MA 02482
Phone: (617) 287-6035; Fax: (617)-287-6185
E-mail: deyang.qu@umb.edu

Start Date: October 2013
Projected End Date: September 2014

Objectives

- To alleviate the chemical interaction between superoxide ($O_2^{\cdot -}$) and electrolyte.
- To enhance the rechargability of Lithium-air batteries.

Technical Barriers

- Li-Air batteries: long calendar and cycle life.
- Li-Air batteries: superior abuse tolerance.
- PHEV batteries: high production cost.

Technical Targets

- Complete *in situ* electrochemical ESR study for the oxygen reduction in varioius electrolytes.
- Complete studies of the impact of borate additives to the GDE rechargeability.
- Complet studies of catalytic disproportionation of superoxide formed during the reduction of oxygen.
- Complete the preliminary design of the Li-air flow cell.

Accomplishments

- Completed *in situ* electrochemical ESR study for the oxygen reduction in varioius electrolytes.
- Completed studies of the impact of borate additives to the GDE rechargeability.
- Completed studies of the catalytic disproportionation of superoxide formed during the reduction of oxygen.
- Completed the preliminary design of the Li-air flow cell.

✧ ✧ ✧ ✧ ✧

Introduction

O_2 reduction is one of the most important reactions in the arena of energy storage. O_2 cathodes make both fuel cells and metal air cells attractive, because of the abundance of O_2 in air. The mechanism of the O_2 redox reaction in aprotic electrolytes has been subjected to extensive investigation recently due to the elevated interest in rechargeable Li-air batteries. The reduction of O_2 in aprotic electrolytes has been investigated for decades. The first step of the electrochemical O_2 reduction in an aprotic electrolyte is believed to be a one-electron process yielding superoxide ($O_2^{\cdot -}$). The redox couple ($O_2/O_2^{\cdot -}$) is reversible in some organic electrolytes. $O_2^{\cdot -}$ ions remain stable in many solvents e.g., dimethyl sulfoxide (DMSO) and pyridine. In those solvents, the stability of $O_2^{\cdot -}$ depends on the trace amount of H_2O in the solvent, a small amount of water in the electrolyte will lead to a protonation of O_2^-, and the $O_2^{\cdot -}$ will rapidly disproportionate to O_2 and HO_2^-. Electron spin resonance (ESR), also known as electron paramagnetic resonance (EPR), is a unique technique for the investigation of species containing unpaired electrons. $O_2^{\cdot -}$ is a paramagnetic species, thus it can be detected by ESR spectroscopy. ESR can improve the understanding of surface and electrochemical phenomena, but the stability and line-width of $O_2^{\cdot -}$ impede the detection at room temperature, making *in situ* spectro-electrochemical detection very difficult without a spin trap. Only recently was electrochemically generated superoxide (O_2^-) detected directly on a Pt electrode without using a spin trap. Porous carbon electrodes are important in many energy storage systems, since they are commonly used in making gas diffusion electrodes, where O_2 reduction takes place in metal air and fuel cells. *In situ* electrochemical ESR investigation of the O_2 reduction reaction (ORR) on a gas diffusion electrode made with high surface area porous carbon is tedious. High surface area carbon itself has dangling bonds on the surface, particularly in the region between the graphitic crystallites, where the ORR likely occurs. The unpaired electrons associated with the surface functional groups can become delocalized into the conduction band of the carbon under certain conditions, thus rapid electron exchange would average out electron-nuclear interaction. Of course, unpaired electrons on the carbon surface can also localize an electron from the conduction band to form an electron pair. Therefore a relatively sharp signal from the unpaired electron of $O_2^{\cdot-}$ would superimpose upon a broad ESR signal of charge carriers, since the dangling bonds on the surface groups manifest themselves throughout the entire conducting bands of the carbon material. Here we reports the first *in situ* electrochemical ESR studies of $O_2^{\cdot-}$ anions during the O_2 reduction on a high surface area porous carbon electrode in aprotic electrolytes.

Approach

Electron spin resonance (ESR) spectroscopy is the key technique used for this project, which was carried out with an X-band spectrometer (CMS 8400, Adani). The temperature controlling experiment was operated by ESR temperature control unit (MN82VT, Resonance Instrument) and a gas flow cryostat in H_{102} cavity. Reference standard was MnO diluted in MgO (1:500 weight ratio) and mounted inside the cavity to measure the Q-factor of the cavity.

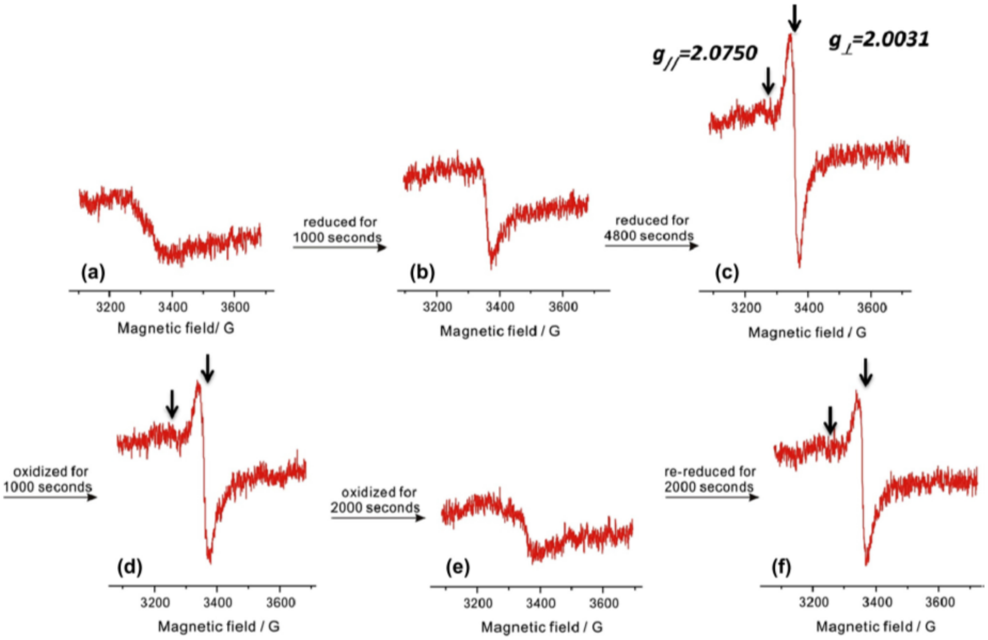

Figure V - 234: ESR signal for the carbon electrode during reduction and oxidation (2 μA) in a 0.1 M Bu4NBF4 DMSO electrolyte saturated O2 (a) before polarization; (b) after reducing for 1000 sec; (c) after reducing for 4800 sec (accumulated); (d) after oxidizing for 1000 sec; (e) after oxidizing for 2000 sec; (f) after re-reducing for 2000 sec

Results

In situ ESR spectro-electrochemical investigation of the superoxide anion radical during the electrochemical O_2 reduction reaction in aprotic electrolyte. For the first time, electrochemically generated superoxide ions on a porous carbon electrode are investigated by means of *in situ* electrochemical ESR technique at ambient conditions. Superoxide ions ($O_2^{\cdot-}$) are detected as the product of the electrochemical O_2 reduction reaction. The redox couple ($O_2/O_2^{\cdot-}$) is reversible in DMSO electrolyte. The superoxide ions are believed to be absorbed and de-mobilized on the carbon surface. Overlapping a symmetric carbon ESR signal, the anisotropic signal of the superoxide is observed. The *g*-factor of the carbon ESR spectra is found to be 2.0025, which is almost identical to that of a free electron; Anisotropic *g*-factors for the $O_2^{\cdot-}$ are $g_{\perp}$=2.0031, $g_{//=}$ 2.0750.

The ESR signals after 1,000 sec and 4,000 sec reductions are shown in Figure V - 234b and Figure V - 234c, respectively. Clearly, a sharp and intense ESR signal which can be attributed to $O_2^{\cdot-}$ was developing. The g⊥ and g// were calculated as 2.0031 and 2.0750, respectively, based on Figure V - 234c. The axially symmetric g-factors are similar with those reported in the literature, e.g., g⊥=2.006, g// = 2.103 in a formate solution at 95K, and g⊥=2.005, g// = 2.098 in a DMSO at 77K. The decrease in the symmetry of $O_2^{\cdot-}$ resulted from the adsorption of the electrochemically generated $O_2^{\cdot-}$ on the surface of the porous electrode, especially from the possible interaction between $O_2^{\cdot-}$ and the functional groups on the carbon surface along with those adsorbed on the carbon basal and edge sites. Dissolved in a free solvent, the $O_2^{\cdot -}$ signal height decreased sharply with the temperature increase, the phenomenon could be related to the mobility of $O_2^{\cdot -}$ in the free solvent and variation of spin-lattice relaxation time. Functional groups on a high surface area carbon electrode could make the $O_2^{\cdot -}$ localized, if the $O_2^{\cdot -}$ were generated on a porous electrode and attached to the functional groups. Those functional groups could then act as a spin trap.

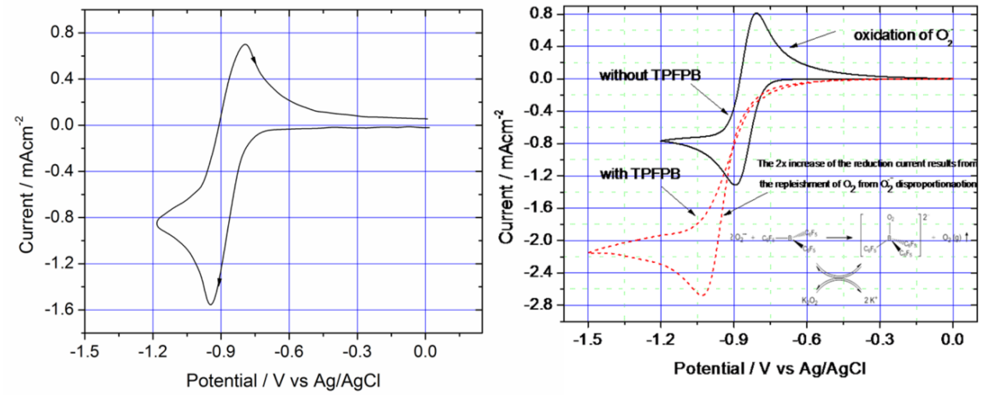

Figure V - 235: (left) Cyclic voltammograms at 300 mV/sec in 1 M TEABF4 PC electrolyte saturated with O2 on a glassy carbon disc electrode, (right) Cyclic voltammograms in 1 M TEABF4 acetonitrile electrolyte (solid line) and 1 M TEABF4 acetonitrile electrolyte containing 40mM TPFPB (dash line) on the same glass disc electrode at 300 mAs-1 scan rate. The glassy carbon electrode area 0.07 cm2; Counter electrode: Pt-mesh; Ag/AgCl as reference electrode

Borate compound is proven to be an efficient catalyst for the disproportionation of superoxide. The kinetics for the superoxide disproportionation was found much faster than its chemical interaction with PC. As shown in Figure V - 235, it is clear that at a high scan rate (300 mVs^{-1}), a pair of relatively symmetric reduction (-0.95 V.s Ag/AgCl) and oxidation (-0.79 V.s Ag/AgCl) peaks are evident, which can be correlated to O_2 reduction and O_2^- oxidation, respectively. The ratio between the anodic and cathodic peak area is almost a unit when acetonitrile was used as solvent (solid black line in right figure). When PC was used as solvent, although a clear oxidation peak was evident, the ratio is less than one (left figure), which demonstrated that part of $O_2^{\cdot -}$ reacted with PC before becoming oxidized. If borate compound was added in the ACN electrolyte, all $O_2^{\cdot -}$ became disproportionated before they can be oxidized, no oxidation peak can be observed (red dash line in right figure). Interestingly, the regenerated O_2, from the disproportionation of O_2^-, will be re-reduced on-site simultaneously with the O_2 diffused from the electrolyte on the electrode surface. Therefore, the electrochemical reduction of O_2 in the TPFPB containing electrolyte would be a pseudo 2-electron reaction. The reduction current density is increased via replenishment of O_2 from the catalyzed disproportionation of O_2^- with the final product being O_2^{2-}.

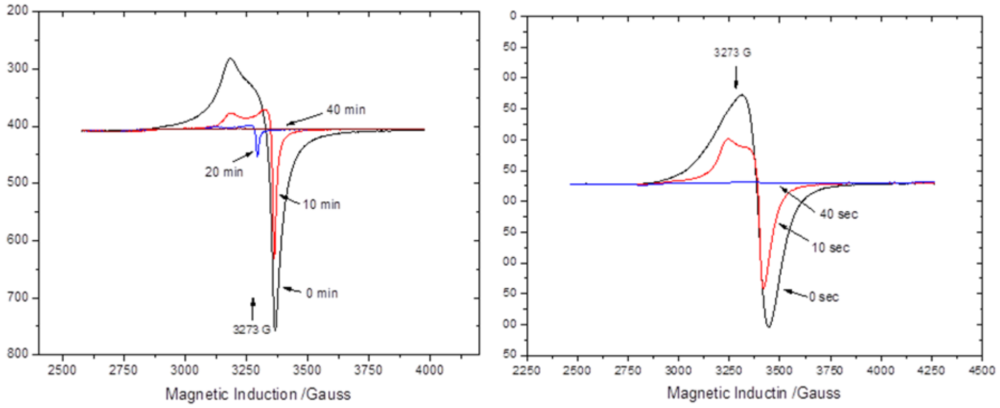

Figure V - 236: Left: (a) ESR spectra of O2- in DMSO taken at different times after the addition of TPFPB. Mole ratio of TPFPB and O2- was approximately 1:1. Right: ESR spectra of O2- in DMSO taken at different times after adding PC. Mole ratio of O2- and PC was 1:1

In situ ESR studies of O_2 reduction in DMSO electrolyt containing PC and TPFPB.

Borate compound is proven to be an efficient catalyst for the disproportionation reaction for superoxide. The kinetics for the catalytic O_2^-

disproportionation is much faster than the direct chemical reaction between PC and O_2^-. Therefore, with the addition of BNL synthesized boron compoundtris(pentafluorophenyl) borane (TPFPB), the consumption of PC by the O_2^- produced from the reduction of O_2 can be suppressed. The kinetics for the catalyzed $O_2^{\cdot-}$ disportionation again its chemical interaction with PC have been studied using ESR spectroscopy. The results are shown in Figure V - 236. The right figure clearly show that there was no detectable O_2^- remaining in the solution after 30 seconds in the presence of TPFPB. Results shown in the left figure of Figure V - 236 demonstrates that O_2^- was indeed consumed by reacting with PC. However, the catalytic disproportionation of O_2^- proceeds much faster than the chemical reaction between PC and O_2^-. Thus, before reacting with the carbonate components of the electrolyte, the O_2^- ions formed during the electrochemical reduction of O_2 would disproportionate to O_2 and O_2^{2-} in the presence of TPFPB. Therefore the undesired reaction between the carbonate solvents and O_2^- can be avoided.

Conclusions and Future Directions

In conclusion, an electrochemically generated $O_2^{\cdot-}$ specie was detected in an *in situ* electrochemical ESR measurement on a porous carbon electrode. A two-line ESR spectrum of $O_2^{\cdot-}$ with anisotropic *g*-factor can be observed at room temperature. The *g*-factors were consistent with that of free $O_2^{\cdot-}$ in frozen solvents. The $O_2^{\cdot-}$ is believed to be adsorbed on the carbon surface, thus its mobility was restrained thus the spin-lattice relaxation as would be in a frozen condition. Although overlapping the broad ESR signal from the carbon, which demonstrated a symmetric ESR signal of free electrons, the narrow anisotropic $O_2^{\cdot-}$ can be distinguished. The *in situ* spectra-electrochemical investigation on the O_2 reduction in an aprotic electrolyte confirmed the previously proposed one-electrode mechanism for the O_2 reduction, and reversibility of the redox ($O_2/O_2^{\cdot-}$) reaction. This would be a powerful method for the *in situ* investigation of gas diffusion electrode in Li-air battery systems.

FY 2014 Publications/Presentations

1. 2014 DOE Annual Peer Review Meeting Presentation.
2. Q. Wang, D. Zheng, M.E. McKinnon, X.Q. Yang, D.Y. Qu, “Kinetic Investigation of Catalytic Disproportionation of Superoxide Ions in the Non-aqueous Electrolyte used in Li-Air Batteries”, J. Power Sources in press.

Invited Presentations

1. “Oxygen Reduction on a Carbon-based Gas Diffusion Electrode in Non-aqueous Electrolyte for Li-air Batteries”, 9th US-China Electric Vehicle Workshop, sponsored Seattle, Washington, 08/18-08/19/2014.
2. “Elimination of the superoxide radicals during the discharge of Li-air battery” The International Conference on the Frontier of Advanced Batteries, CIBF2014, 06/20/2014 – 6/22/2014, Shenzhen, China.

V.G.10 Exploratory Studies of Novel Sodium-Ion Battery Systems (BNL)

Xiao-Qing Yang
Brookhaven National Laboratory
Chemistry Department
Building 555
Upton, NY 11973
Phone: (631) 344-3663; Fax: (631) 344-5815
E-mail: xyang@bnl.gov

Xiqian Yu
Brookhaven National Laboratory
Chemistry Department
Building 555
Upton, NY 11973
Phone: (631) 344-4142; Fax: (631) 344-5815
E-mail: xyu@bnl.gov

Start Date: October 2013
Projected End Date: September 2014

Objectives

- To determine the contributions of electrode materials changes, interfacial phenomena, and electrolyte decomposition to the cell capacity and power decline for Na-ion batteries.
- To develop and apply synchrotron based *in situ* X-ray techniques such as x-ray diffraction (XRD) and x-ray absorption spectroscopy (XAS) to study materials in an environment that is close to the real operating conditions for na-ion cells.
- To develop new diagnostic tools for Na-ion battery studies.

Technical Barriers

- Na-ion batteries with long calendar and cycle life.
- Na-ion batteries with superior abuse tolerance.
- To reduce the production cost of a PHEV batteries.

Technical Targets

- Complete the *in situ* x-ray diffraction studies of $Li_4Ti_5O_{12}$ during chemical sodiation. $Li_4Ti_5O_{12}$ is considered as a potential anode materials for Na-ion batteries. Complete the development of using quick x-ray absorption spectroscopy technique to study the kinetic properties of high energy density cathode materials during constant voltage charge.
- Complete the Ti K-edge x-ray absorption spectroscopy (XAS) of $Li_4Ti_5O_{12}$, $Li_7Ti_5O_{12}$ (lithiated $Li_4Ti_5O_{12}$) and fully sodiated $Li_4Ti_5O_{12}$ ($Li_7Ti_5O_{12}$ and $Na_6 LiTi_5O_{12}$ in 1:1 ratio). These compounds are considered potential anode materials for Na-ion batteries.
- Complete the *in situ* x-ray diffraction studies of $NaCrO_2$ during electrochemical chemical de-sodiation. $NaCrO_2$ is considered as a potential cathode material for Na-ion batteries.
- Complete the x-ray absorption studies of $NaCrO_2$ at different sodiation levels.

Accomplishments

- A novel characterization technique using the combination of chemical sodiation and synchrotron based *in situ* X-ray diffraction (XRD) has been developed. The power of this new technique was demonstrated in elucidating the structure evolution of $Li_4Ti_5O_{12}$ upon sodium insertion.
- *In situ* x-ray absorption studies of $Li_4Ti_5O_{12}$ during chemical sodiation have been carried out.
- *In situ* x-ray diffraction studies of $NaCrO_2$ during electrochemical chemical de-sodiation have been carried out.
- *In situ* x-ray absorption studies of $NaCrO_2$ during electrochemical chemical de-sodiation have been carried out.

✧ ✧ ✧ ✧ ✧

Introduction

In order to develop new electrode materials for the next generation of energy storage devices such as batteries and supercapacitors with higher energy and power density, longer cycling life and better safety characteristics, an in-depth understanding of the relationship between structural change and electrochemical performance of electrode materials is quite critical. Recently, due to the abundant sodium resources and their potentially low cost in raw materials, research and development of room-temperature sodium (Na)-ion batteries have attracted extensive interest for application in large-scale stationary energy storage and smart grid. Unlike what might be assumed (that sodium insertion and extraction is similar to lithium), recent detailed structural studies on Na_xCoO_2, Na_xVO_2 and Sb show that sodium storage mechanisms in most cathode/anode materials could be quite complicated and significantly different from that for corresponding lithium compounds. Unfortunately, for many electrode materials used in Na-ion batteries, the sodium storage mechanisms and the relationship between the structural changes and their electrochemical performance are not well-understood. Therefore, completely structural or physical characterization of the materials is quite necessary and the development of new and facile *in situ* techniques, especially dedicated to sodium storage system, will be very desirable. Here we report our recent progress in developing a new novel characterization technique using the combination of chemical sodiation and *in situ* X-ray diffraction to study the structural changes of $Li_4Ti_5O_{12}$ during sodium insertion. In contrast with most reported *in situ* XRD experiments (Na-ion batteries) performed during electrochemical cycling, which require special designed electrochemical cells, the chemical sodiation reported herein was carried out in a capillary, making it a relatively easy procedure. The chemical method also demonstrates its advantages and uniqueness: very clean and high quality XRD patterns can be obtained for detailed structural analysis. Recent work shows that sodium can also be reversibly inserted/extracted into/from $Li_4Ti_5O_{12}$ framework through a complicated three-phase transition behavior. The detailed studies reported herein reveal that sodium storage behaviors in $Li_4Ti_5O_{12}$ are size-dependent.

Approach

Synchrotron based X-ray diffraction (XRD), X-ray absorption spectroscopy (XAS), especially the “quick-XAS” techniques were used to elucidate and differentiate the contribution from each component and element to the capacity.

Results

In situ **XRD studies of $Li_4Ti_5O_{12}$ during chemical sodiation**

A novel characterization technique using the combination of chemical sodiation and synchrotron based *in situ* X-ray diffraction (XRD) has been developed. The schematic of this new technique and the results obtained for $Li_4Ti_5O_{12}$ upon sodium insertion are plotted in Figure V - 237. A solid solution reaction behavior in a wide range has been revealed during sodium insertion into the nano-sized $Li_4Ti_5O_{12}$ (~44 nm), which is quite different from the well-known two-phase reaction of $Li_4Ti_5O_{12}/Li_7Ti_5O_{12}$ system during lithium insertion, and also has not been fully addressed in the literature so far. Based on this *in situ* experiment, the apparent Na^+ ion diffusion coefficient (D_{Na+}) of $Li_4Ti_5O_{12}$ was estimated in magnitude of 10^{-16} cm^2 s^{-1}, close to the values estimated by electrochemical method, but 5 order of magnitudes smaller than the Li^+ ion diffusion coefficient (D_{Li+}~10^{-11} cm^2 s^{-1}), indicating a sluggish Na^+ ion diffusion kinetic in $Li_4Ti_5O_{12}$ comparing with that of Li^+ ion. Nanosizing the $Li_4Ti_5O_{12}$ will be critical to make it a suitable anode material for sodium-ion batteries. The application of this new *in situ* chemical sodiation method reported in this work provides a facile way and a new opportunity for *in situ* structure investigations of various sodium-ion battery materials and other systems.

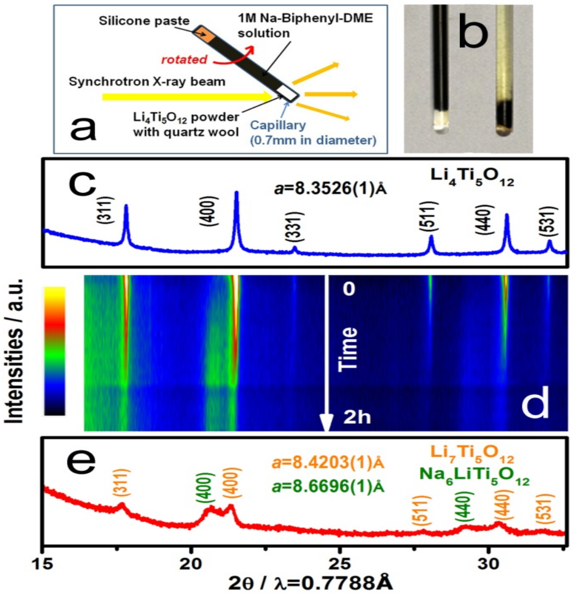

Figure V - 237: The evolution of XRD patterns during *in situ* chemical sodiation of nano-sized (44nm) $Li_4Ti_5O_{12}$: (a) Schematic of the *in situ* chemical sodiation experiment setup by using a quartz capillary. 1M Na: 1M biphenyl /L 1,2-dimethoxyethane (DME) solution was used as reducing agent; (b) capillaries before (left) and after (right) *in situ* sodiation; (c) XRD pattern for the $Li_4Ti_5O_{12}$ at the beginning of reaction; (d) contour plot of peak intensities as a function of reaction time; (e) XRD pattern for the final sodiated $Li_4Ti_5O_{12}$ at the end of reaction

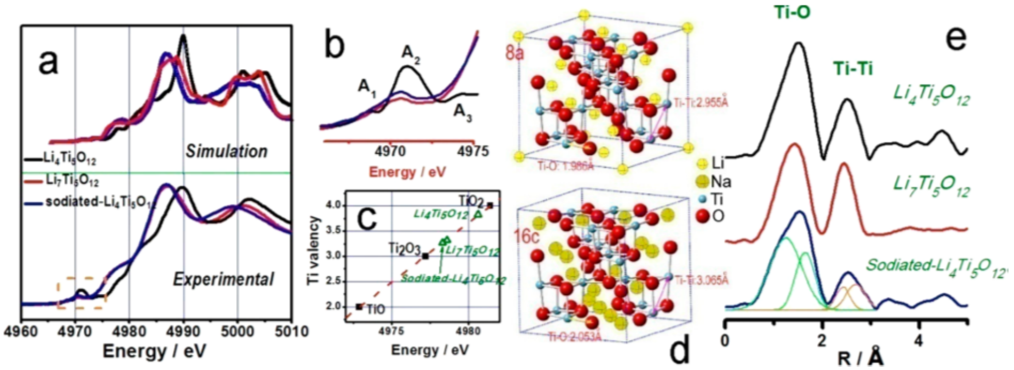

Figure V - 238: (a) Experimental/calculated Ti K-edge XANES spectra; (b) enlarged view of the XANES pre-edge region as marked by rectangle in panel a; (c) Ti valences of the $Li_4Ti_5O_{12}$, $Li_7Ti_5O_{12}$and sodiated $Li_4Ti_5O_{12}$estimated by comparing with standard titanium oxides; (d) crystal structure of $Li_4Ti_5O_{12}$and $Na_6(Li_6)LiTi_5O_{12}$; and (e) experimental EXAFS spectra of $Li_4Ti_5O_{12}$, $Li_7Ti_5O_{12}$ (lithiated $Li_4Ti_5O_{12}$), and fully sodiated $Li_4Ti_5O_{12}$ ($Li_7Ti_5O_{12}$ $Na_6LiTi_5O_{12}$ in 1:1 ratio)

Figure V - 238 shows both experimental and calculated (using the density functional theory (DFT) method) Ti K-edge X-ray absorption near edge structure (XANES) spectra. For fully sodiated $Li_4Ti_5O_{12}$, the calculated spectrum is averaged with that of $Li_7Ti_5O_{12}$ and $Na_6LiTi_5O_{12}$ in ratio of 1:1. It was found that the calculated spectra match the experimental ones very well, further proving the $Na_6LiTi_5O_{12}$ phase formed during sodium insertion. Both experimental and calculated spectra shift to lower energy along with sodium insertion, indicating the reduction of Ti ion during sodium insertion. The pre-edge features shown in Figure V - 238b also suggest the reduction of the $Li_4Ti_5O_{12}$ during Li or Na insertion. The three prepeaks, named as A1−3, correspond to transitions of the titanium 1s-core electrons toward the unoccupied Ti 3d-4s/4p hybridized states, which are semilocalized states surrounding the Ti atom. The A1 peak is due to a bonding t2g band-like bonding-state whereas A2 is the result of nondirectional e_g antibonding states. Transition A3 has predominantly Ti-4p character hybridized with the Ti-4s and/or O-2p orbital. The decrease in intensity of the A1 peak suggests a partial filling of the Ti-3d t2g band by the charge compensating electrons entering the crystallite accompanying the Li or Na insertion. The average valence state of Ti (in bulk level) is estimated by comparing the half energy position with reference titanium oxides. The valence state of sodiated $Li_4Ti_5O_{12}$ is very close to that for $Li_7Ti_5O_{12}$. This further proves that almost an equal amount of Na has been inserted to $Li_4Ti_5O_{12}$ as in the case of Li insertion. The EXAFS spectra analysis was as shown in Figure V - 238d. The Fourier transformed (FT) spectra of Ti in pristine, lithiated, and sodiated $Li_4Ti_5O_{12}$ are compared in Figure V - 238e. The first peak at around 1.5 Å in the FT spectra is due to the titanium−oxygen interaction while the second peak at around 2.9 Å is due to the titanium−titanium interaction, as labeled in the spectra and shown schematically in Figure V - 238d. Compared with $Li_4Ti_5O_{12}$ and $Li_7Ti_5O_{12}$, the significant non-Gaussian line-shape of the fully sodiated $Li_4Ti_5O_{12}$ indicates multiple peaks present in both the first and second FT spectrum peaks. This suggests that there are two different Ti−O and Ti−Ti coordination environment within sodiated $Li_4Ti_5O_{12}$, corresponding to the $Li_7Ti_5O_{12}$ and $Na_6LiTi_5O_{12}$ phases as also evidenced by XRD analysis.

In situ x-ray diffraction studies of $NaCrO_2$ during electrochemical chemical de-sodiation

Figure V - 239 shows the *in situ* XRD patterns of $NaCrO_2$ along with the first charge curve. At the beginning of the charge, (003) peak continuously shifted to the lower two-theta angles, indicating that a solid solution reaction was involved with c-axis expansion. When x = 0.08 was reached, a new (003) peak emerged from the left side of the original (003) peak with increasing intensity with further charging. As we know, the (003) peak is a single-fold peak. Thus, every new (003) peak is a fingerprint for the formation of a new phase. In the range of $0.08 < x < 0.2$, two phase coexistence could be observed. The intensity of (003) peak for the second phase increased with further charging in expense of that for the first one, while the position of (003) peak of the second phase shifted to lower two theta angles. When x = ~0.25 was reached, the second phase dominated the structure while the first phase disappeared. When x = 0.3 was reached, another (003) peak appeared and the (003) peak of the second phase became broader indicating the formation of the third phase. When x = 0.4 was reached, only the third phase can be observed. In the range of $0.4 < 0.48$, the (003) peak of the third phase shifted to lower angles but the shifting two theta angle range for the third phase was smaller than the second phase. The peak at 62.4° in the first pattern corresponds to (110) reflection of the O3-type structure. The position changes of this peak represent the structure changes of the *a*-*b* plane.

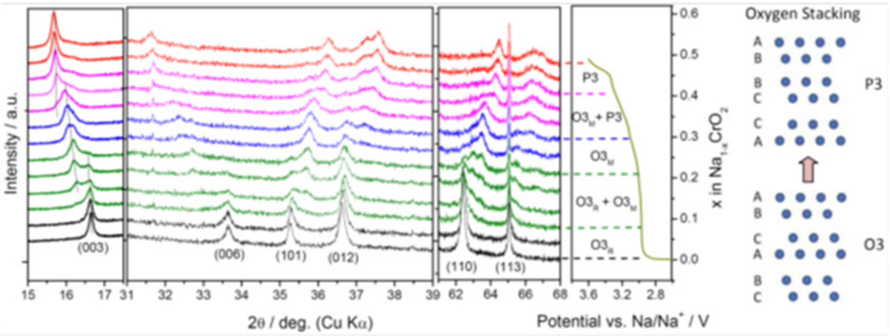

Figure V - 239: ***In situ*** **X-ray diffraction patterns collected during the first charge (up to 3.6 V at C/12 rate) for a $NaCrO_2$/Na cell. Corresponding voltage-composition profile is given on the right of XRD patterns. Oxygen stacking of O3 and P3 structure is given on the right**

During charge, the original sharp (110) peak decreased in intensity and became broader and broader in peak shape, indicating some lattice distortion in the *a*-*b* plane. The (110) peak shifting to the higher two theta angles indicates the contraction of the '*a*' and '*b*' lattice parameters. Based on the variation of all Bragg peaks, it can be concluded that the structure evolution took place through phase transitions of three solid-solution phases with two two-phase co-existence regions.

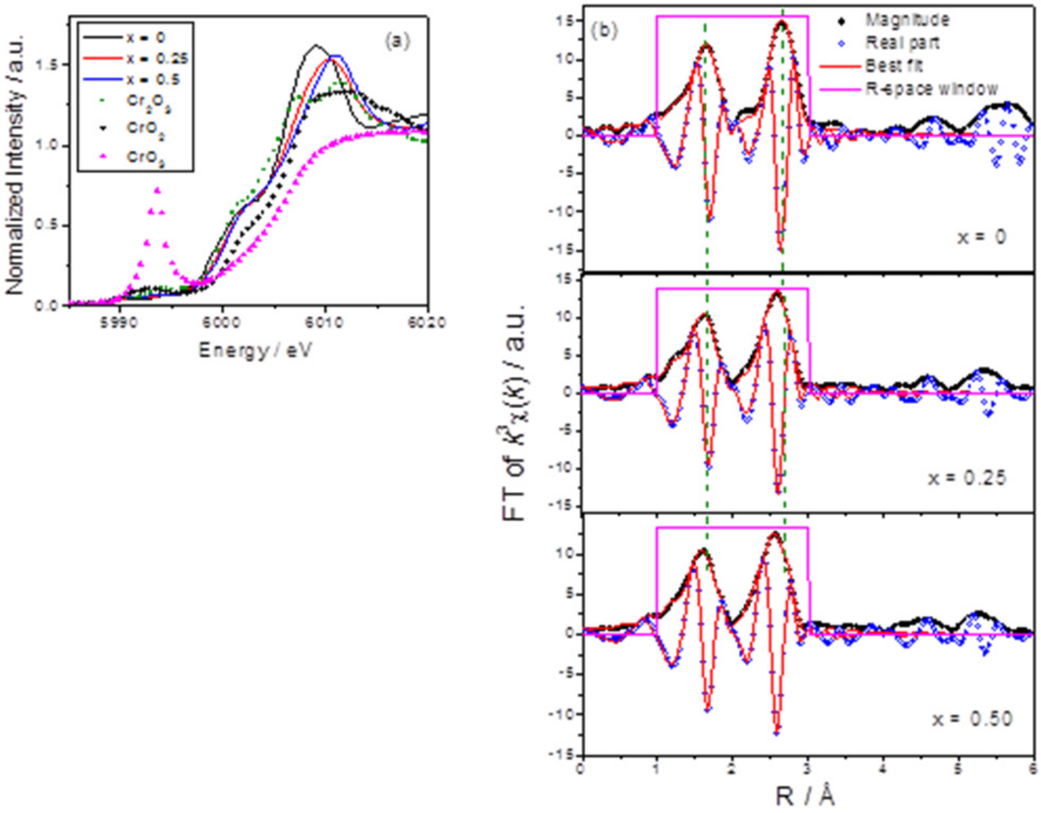

Figure V - 240: (a) Cr K-edge XANES spectra of pristine (x = 0), half charged (x = 0.25), fully charged (x = 0.5) Na1-xCrO2 and CrOx references (Cr_2O_3, CrO_2 and CrO_3); (b) Least-square fits of calculated FT-EXAFS phase and amplitude functions (solid red lines) to the experimental EXAFS spectra (solid and open circles) for pristine (x = 0), half charged (x = 0.25) and fully charged (x = 0.5) $Na_{1-x}CrO_2$. Phase shift was not corrected in the FT magnitude of EXAFS spectra

Figure V - 240 (a) shows the *ex-situ* x-ray absorption near edge spectroscopy (XANES) of the pristine (x = 0), half charged (x= ~0.25) and fully charged (x= ~ 0.5) $Na_{1-x}CrO_2$ electrodes with CrO_x references for Cr^{3+}, Cr^{4+} and Cr^{6+}. It can be seen that the white line shifted to higher energy during charge, indicating the oxidation of Cr^{3+} cations to higher oxidation states. Due to the quite different shape of the edge structure for the pristine, half and fully charged samples, it is difficult to quantify the edge-shift energy. However, comparing with the references for Cr^{3+} and Cr^{4+}, it can be roughly estimated that Cr^{3+} was oxidized to around $Cr^{3.5+}$ at the fully charged state. The Fourier Transformed EXAFS spectra of the pristine (x=0), half charged (x=0.25) and fully charged (x=0.5) $Na_{1-x}CrO_2$, were plotted in Figure V - 240 (b). The first peak at R= ~1.7 Å was due to contribution from the nearest Cr-O_6 octahedra while the second peak at R= ~2.7 Å was attributed to Cr-Cr_6 hexagon on a-b plane in the second coordination shell. Note that the FT-EXAFS spectra were not phase corrected so that the actual bond lengths were approximately 0.3 Å longer. The results of FT-EXAFS spectra analysis using least-square fits of phase and amplitude functions are plotted in Figure V - 240 (c). The fitted (red lines) and experimental (solid and open circles) FT-EXAFS spectra for the three samples match very well.

Conclusions and Future Directions

In conclusion, we have developed a new synchrotron based *in situ* XRD technique to study sodium ion battery materials during chemical sodiation. The power of this new *in situ* technique has been demonstrated through the investigation of the phase transition behavior of $Li_4Ti_5O_{12}$ anode material during sodium insertion. A solid solution reaction behavior in a wide range has been revealed during Na^+ insertion into the nano-sized $Li_4Ti_5O_{12}$ (~44 nm). This solid solution reaction behavior, which is quite different from the well-known two-phase reaction of $Li_4Ti_5O_{12}/Li_7Ti_5O_{12}$ system during lithium insertion, has not been fully addressed in the literature so far. However, we also want to point out that the phase transition of $Li_4Ti_5O_{12}$ upon sodium insertion is more complicate than during lithium insertion, since a new phase $Na_6LiTi_5O_{12}$ and three-phase reaction are involved. The kinetic governed phase transition pathway changes should also not be neglected and worthwhile for further detailed investigations. Based on this *in situ* experiment, the apparent Na^+ diffusion coefficient (D_{Na+}) of $Li_4Ti_5O_{12}$ was estimated to be in the magnitude of 10^{-16} cm^2 s^{-1p}, 5 order of magnitudes smaller than the Li^+ diffusion coefficient (D_{Li+}~10^{-11} cm^2 s^{-1}), indicating a sluggish Na^+ diffusion kinetic in $Li_4Ti_5O_{12}$ comparing with Li^+.

FY 2014 Publications/Presentations

1. 2014 DOE Annual Peer Review Meeting Presentation.
2. Shadike, Z (Shadike, Zulipiya); Zhou, YN (Zhou, Yong-Ning); Ding, F (Ding, Fei); Sang, L (Sang, Lin); Nam, KW (Nam, Kyung-Wan); Yang, XQ (Yang, Xiao-Qing); Fu, ZW (Fu, Zheng-Wen), "The new electrochemical reaction mechanism of Na/FeS_2 cell at ambient temperature", *JOURNAL OF POWER SOURCES*, Volume: 260, Pages: 72-76, DOI: 10.1016/j.jpowsour.2014.03.011, Published: AUG 15 2014.
3. He, K (He, Kai); Zhou, YN (Zhou, Yongning); Gao, P (Gao, Peng); Wang, LP (Wang, Liping); Pereira, N (Pereira, Nathalie); Amatucci, GG (Amatucci, Glenn G.); Nam, KW (Nam, Kyung-Wan); Yang, XQ (Yang, Xiao-Qing); Zhu, YM (Zhu, Yimei); Wang, F (Wang, Feng); Su, D (Su, Dong), "Sodiation via Heterogeneous Disproportionation in FeF2 Electrodes for Sodium-Ion Batteries", ACS NANO, Volume: 8, Pages: 7251-7259, DOI: 10.1021/nn502284y, Published: JUL 2014.

Invited Presentations

1. Yongning Zhou, Xiqian Yu, Enyuan Hu, Seongmin Bak, Xiao-Qing Yang, Hung Sui Lee, Hong Li, Xuejie Huang, Liquan Chen, Kyung-Wan Nam, and Sung-Jin Cho "Using Synchrotron Based Advanced Characterization Techniques to Study the New Electrode Materials for Next Generation of Batteries, presented at the Conference of International Battery Frontier 2014 (CIBF2014), June 20-22, 2014, Shenzhen, China. **Invited.**

V.G.11 Nanostructured Design of Sulfur Cathodes for High Energy Lithium-Sulfur Batteries (Stanford U)

Yi Cui (Principal Investigator)
Subcontractor: Stanford University

Department of Material Science and Engineering
476 Lomita Mall, McCullough 343
Stanford. CA 94305
Phone: (650) 723-4613; Fax: (650) 725-4034
E-mail: yicui@stanford.edu

Start Date: August 2013
Projected End Date: July 2017

Objectives

This study aims to enable sulfur cathodes with high capacity and long cycle life by developing them from the perspective of nanostructured materials design, which will be used to combine with lithium metal anodes to generate high-energy lithium-sulfur batteries. Novel sulfur nanostructures as well as multifunctional coatings will be designed and fabricated to overcome issues related to volume expansion, polysulfide dissolution and insulating nature of sulfur.

Technical Barriers

The poor cycle life of lithium-sulfur battery is caused by multiple materials challenges: 1) large volume expansion of sulfur upon lithiation; 2) dissolution of intermediate discharge product lithium polysulfides in the electrolyte; 3) insulating nature of sulfur. These problems result in the following technical barriers to good battery performance:

- Loss of active materials.
- Rapid capacity decay.
- Low Coulombic efficiencies.
- Poor rate performance.
- Low areal mass loading of active materials.

Technical Targets

- Develop fundamental material guidelines through structure and property correlations.
- Design novel nanostructured sulfur cathodes to address the material challenges outlined above.
- Develop conductive coatings to improve the rate performance of lithium-sulfur batteries.
- Discover novel nanostructured materials that can trap polydulfide species.

Accomplishments

- Designed and synthesized various conductive polymer-encapsulated sulfur nanostructured cathodes to achieve a superior battery rate performance.
- Developed conductive hydrogen reduced TiO_2 inverse opal 3-D structures for sulfur and polysulfides confinement.
- Discovered the use of conductive Ti_4O_7 as highly effective matrix to bind with polysulfide species to improve the capacity and cycling of sulfur cathode.
- Developed a novel design of a thin conductive coating on the separator to prevent formation of the deactivation layer on the electrode surface.

✧ ✧ ✧ ✧ ✧

Introduction

Lithium-sulfur batteries can bring about significant improvements to the current state of the art battery technologies due to its high specific energy, energy density and cost saving. The capacity decay of lithium-sulfur battery during cycling is a multifaceted problem. There exist multiple materials challenges that prevent it from reaching the cycling performance suitable for portable electronics and electrical vehicles. The rapid capacity decay of sulfur cathodes can be attributed to several reasons: 1) significant volumetric expansion (~80% change) when sulfur is reduced to lithium sulfide (Li_2S); 2) dissolution of intermediate lithium polysulfides (Li_2S_x, $4 \leq x \leq 8$) in the electrolyte; 3) low ionic and electronic conductivity of both sulfur and Li_2S.

Approach

We tackled the sulfur cathode problems using the following approaches:

1) Engineer empty space into sulfur cathode to accommodate the volume expansion of the electrode.

2) Develop novel sulfur nanostructures with multi-functional coatings for the confinement of both sulfur and lithium polysulfides and the improvement of the electrode conductivity.

3) Develop new nanostructured materials that can capture the polysulfide dissolved in the electrolyte.

Results

Conductive polymer-coated sulfur nanosphere cathodes: We demonstrated stable and high performance sulfur cathodes made from conductive polymer-coated hollow sulfur nanospheres. Polyaniline (PANI), polypyrrole (PPY), and poly(3,4-ethylenedioxythiophene) (PEDOT), three of the most well-known conductive polymers, were coated onto monodisperse hollow sulfur nanopsheres through a facile, versatile, and scalable polymerization process in aqueous solution at room temperature (Figure V - 241).

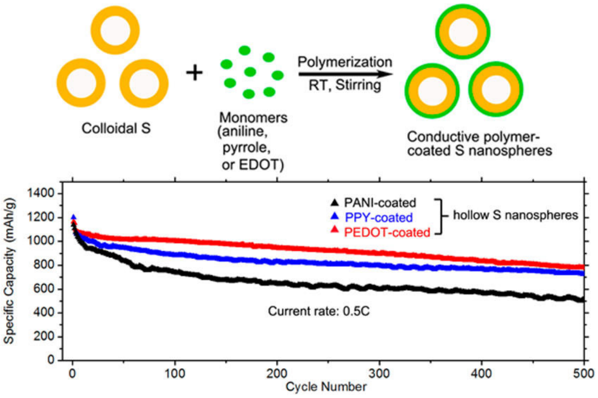

Figure V - 241: Schematic illustration of the fabrication process of conductive polymer-coated hollow sulfur nanospheres. RT, room temperature (upper); Cycling performances of the cells made from hollow sulfur nanospheres with PANI, PPY and PEDOT coatings of at C/2 rate for 500 cycles (lower)

Since all the conductive polymer-encapsulated sulfur particles in our system possess the same hollow structure except with different coatings, they act as ideal models to accurately compare the influence of different conductive polymers on sulfur cathode by ruling out the factor of sulfur volume expansion. We also performed *ab initio* simulations to elucidate the significance of chemical bonding between these conductive polymers and Li_xS ($0<x\leq2$) species in enhancing the cycling stability. Comparing the performance of batteries made from PANI-, PPY-, and PEDOT-encapsulated hollow sulfur nanospheres, we found that the ability of these three polymers in enabling long cycle life and high-rate performance decreased in the order of PEDOT > PPY > PANI. After 500 discharge/charge cycles at C/2 rate, the cells made from PEDOT- and PPY-encapsulated hollow sulfur nanospheres still delivered high reversible capacities of 780 and 726 mAh/g, respectively (a decay of only 0.066% and 0.08% per cycle). As to rate capability, even at high current of 4C, a capacity of 624, 440, and 329 mAh/g can be achieved for the cells made from PEDOT-, PPY- and PANI-coated sulfur particles, respectively. Therefore, among the three conductive polymers, PEDOT was found to be the best choice that can enable long cycle life and high-rate capability for sulfur cathode.

Sulfur cathodes with hydrogen reduced titanium dioxide inverse opal structure: We developed a 3-D electrode structure to achieve both sulfur physical encapsulation and polysulfides binding simultaneously. The electrode is based on hydrogen reduced TiO_2 with an inverse opal structure that is highly conductive and robust toward electrochemical cycling (Figure V - 242). The openings at the top surface allow sulfur infusion into the inverse opal structure. In addition, chemical tuning of the TiO_2 composition through hydrogen reduction was shown to enhance the specific capacity and cyclability of the cathode. With such a TiO_2 encapsulated sulfur structure, the sulfur cathode could deliver a high specific capacity of 1100 mAh/g in the beginning, with a reversible capacity of 890 mAh/g after 200 cycles of charge/discharge at a C/5 rate. The Coulombic efficiency was also maintained at around 99.5% during cycling. The results showed that inverse opal structure of hydrogen reduced TiO_2 represents an effective strategy in improving lithium sulfur batteries performance.

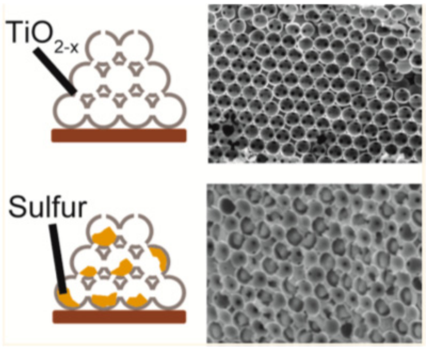

Figure V - 242: Schematics and SEM characterizations of the reduced TiO_2 inverse opal structure before (upper) and after sulfur infusion (lower)

Strong sulfur binding with conductive magnéli-phase Ti_4O_7 nanoparticles: We discovered that conductive Magnéli phase Ti_4O_7 can function as highly effective matrix to bind with sulfur species (Figure V - 243). Compared with the TiO_2-Sulfur composite cathode, the Ti_4O_7-S cathodes exhibit higher reversible capacity and improved cycling performance. It delivers high specific capacities at various C-rates (1342, 1044, and 623 mAh/g at 0.02, 0.1, and 0.5 C, respectively) and remarkable capacity retention of 99% (100 cycles at 0.1 C). The superior properties of Ti_4O_7-S are attributed to the strong adsorption of sulfur species on the low-coordinated Ti sites of Ti_4O_7. Our study demonstrates the importance of surface coordination environment in strongly influencing the S-species binding. These findings can be also applicable to numerous other metal oxide materials.

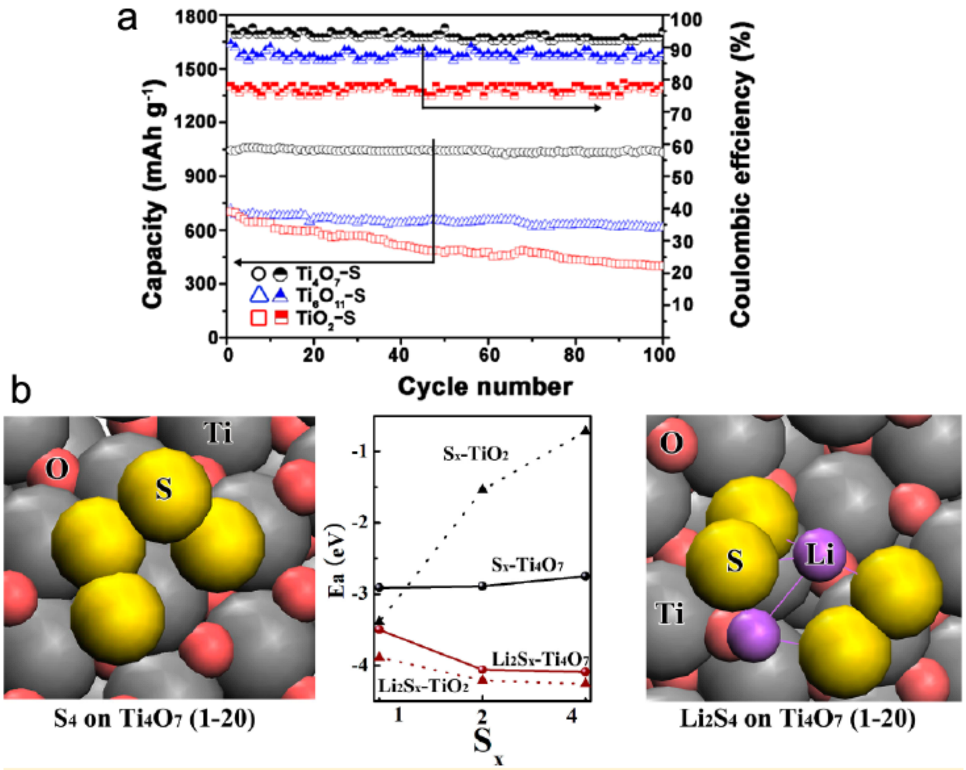

Figure V - 243: (a) Cycling performance of the cathodes with different titanium oxides for 100 cycles at C/10. (b) DFT analysis of the adsorption of S species on Ti_4O_7(1−20) surface. Legend: gray, Ti; pink, O; yellow, S; purple, Li

Improved lithium-sulfur batteries with a conductive coating on the separator: We demonstrated the role of the separator in the capacity decay of the lithium-sulfur battery, namely that it can accommodate a large amount of polysulfides inside which it then precipitates as a thick layer of inactive S-related species. We discovered the use of a thin layer of conductive coating on the separator can prevent the formation of the inactive S-related species layer (Figure V - 244). The large surface area of the conducting coating increased the utilization of the polysulfides accommodated in the separator. We showed that the specific capacity and cycling stability of the lithium-sulfur battery are both improved significantly compared to the battery with a pristine separator.

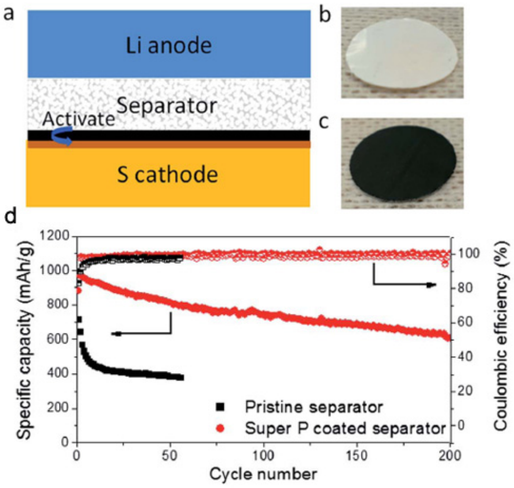

Figure V - 244: (a) Schematic Li–S battery model with the conductive surface design of the separator. (b) and (c) Photographs of the pristine separator and the Super P coated separator, respectively.(d) The cycling stability comparison of the Li–S battery (~60 wt% sulfur in the cathode) with different separators at C/10

Conclusions and Future Directions

Much progress has been made on this project this year. We successfully designed and synthesized various conductive polymer-encapsulated sulfur nanosphere cathodes and achieved superior rate performance for lithium-sulfur batteries. We demonstrated effective trapping and binding of polysulfides using conductive polymer coatings, 3-D titanium dioxide inverse opal structure, and conductive magnéli-phase Ti_4O_7 nanoparticles, showing greatly improved battery performances in terms of high capacity and excellent cycling stability. We also demonstrated a rational design of coating a conductive layer onto the separator to improve battery performance by preventing the formation of the inactive S-related species layer.

Future directions include: 1) increasing the mass and the percentage of sulfur loading in the electrode; 2) tuning different electrolyte additives to improve the Coulombic efficiency and cycling stability; 3) screening a wide range of oxide materials for effective polysulfide trapping.

FY 2014 Publications/Presentations

1. W. Li, Q. Zhang, G. Zheng, Z. W. Seh, H. Yao, and Y. Cui, "Understanding the Role of Different Conductive Polymers in Improving the Nanostructured Sulfur Cathode Performance," *Nano Letters*, 2013, 13, 5534-5540.
2. Z. Liang, G. Zheng, W. Li, Z. W. Seh, H. Yao, K. Yan, D. Kong, and Y. Cui, "Sulfur Cathodes with Hydrogen Reduced Titanium Dioxide Inverse Opal Structure", *ACS Nano*, 2014, 8, 5249-5256.
3. X. Tao, J. Wang, Z. Ying, Q. Cai, G. Zheng, Y. Gan, H. Huang, Y. Xia, C. Lian, W. Zhang and Y. Cui, "Strong Sulfur Binding with Conducting Magneli-Phase Ti_nO_{2n-1} Nanomaterials for Improving Lithium-Sulphur Batteries", *Nano Letters*, 2014, 14, 5288-5294.
4. H. Yao, K. Yan, W. Li, G. Zheng, D. Kong, Z. W. Seh, V. K. Narasimhan, Z. Liang, and Y. Cui, "Improved lithium-sulfur batteries with a conductive coating on the separator to prevent the accumulation of inactive S-related species at the cathode-separator interface", *Energy & Environmental Science*, 2014, 7, 3381-3390.

Appendix A: List of Contributors and Collaborators

Contributor/ Collaborator	Affiliation	FY 2014 Annual Progress Report Section(s)
Abouimrane, Ali	Argonne National Laboratory	IV.C.1, IV.C.2, IV.C.3, IV.C.4, IV.C.5, IV.D.1, V.G.1
Abraham, Daniel	Argonne National Laboratory	IV.B.2, IV.C.1, IV.C.2, IV.C.3, IV.C.4, IV.C.5, IV.E.2, IV.B.1
Ahmed, Shabbir	Argonne National Laboratory	III.A.1
Alamgir, Mohamed	LG Chem Power	II.A.3
Albano, Fabio	XALT Energy	IV.E.4, II.B.2
Albers, Tracy	GrafTech International	IV.E.4
Allu, S.	Oak Ridge National Laboratory	III.C.3
Amine, Khalil	Argonne National Laboratory	IV.B.2, IV.C.1, IV.C.2, IV.C.3, IV.C.4, IV.C.5, IV.D.1, V.G.1, V.G.2
Amin-Sanayel, Ramin	Arkema	IV.E.2
Andrews, Joy	SLAC National Accelerator Laboratory	V.B.5
Aoun, Bachir	Argonne National Laboratory	IV.C.1, IV.C.2, IV.C.3, IV.C.4, IV.C.5
Arnold, John	Miltec UV International	II.C.2
Arsenault, Renata	USABC Program Manager	II.A.2, II.A.4
Assary, R. S.	Argonne National Laboratory	V.G.2
Ayyakkannu, Manivannan	National Energy Technology Laboratory	V.C.6
Bae, Chulheung	USABC Program Manager	II.A.3, II.A.7, II.A.8
Balasubramanian, Mahalingam	Argonne National Laboratory	IV.C.1, IV.C.2, IV.C.3, IV.C.4, IV.C.5, V.F.1
Balbuena, Perla	Texas A&M University	V.C.11
Balsara, Nitash	University of California, Berkeley	V.G.7
Ban, Chunmei	National Renewable Energy Laboratory	IV.C.1, IV.C.2, IV.C.3, IV.C.4, IV.C.5, V.C.7
Banas, James	JSR Micro	IV.E.4
Bareño, Javier	Argonne National Laboratory	IV.B.4
Barsoum, Michel W.	Drexel University	V.C.3
Basco, John	Argonne National Laboratory	III.B.1
Battaglia, Vincent	Lawrence Berkeley National Laboratory	V.E.4, V.F.6
Belharouak, Ilias	Argonne National Laboratory	IV.C.1, IV.C.2, IV.C.3, IV.C.4, IV.C.5
Bender, Guido	National Renewable Energy Laboratory	IV.E.3

Contributor/ Collaborator	Affiliation	FY 2014 Annual Progress Report Section(s)
Benedek, Roy	Argonne National Laboratory	IV.C.1, IV.C.2, IV.C.3, IV.C.4, IV.C.5
Bettge, Martin	Argonne National Laboratory	IV.B.1, IV.C.1, IV.C.2, IV.C.3, IV.C.4, IV.C.5
Billings, J.	Oak Ridge National Laboratory	III.C.3
Bloom, Ira D.	Argonne National Laboratory	III.B.1, III.B.3, IV.B.4, IV.C.1, IV.C.2, IV.C.3, IV.C.4, IV.C.5
Brodie, Brad	DENSO International	II.B.7
Bugga, Ratnakumar	Jet Propulsion Laboratory	IV.C.1, IV.C.2, IV.C.3, IV.C.4, IV.C.5, IV.E.1
Burgman, Jack	PPG Industries	IV.E.4
Burrell, Anthony K.	Argonne National Laboratory	IV.E.1, IV.C.1, IV.C.2, IV.C.3, IV.C.4, IV.C.5
Burton, Evan	National Renewable Energy Laboratory	III.A.2, III.A.3
Busbee, John	Xerion Advanced Battery Corp.	II.A.4
Carlson, Steven A.	Optodot Corp	II.C.4
Ceder, Gerbrand	Massachusetts Institute of Technology	V.E.5
Chahar, Bharat	Zenyatta Ventures	IV.E.4
Chen, Guoying	Lawrence Berkeley National Laboratory	V.B.4
Chen, Zonghai	Argonne National Laboratory	IV.C.1, IV.C.2, IV.C.3, IV.C.4, IV.C.5, IV.D.1
Cheng, Yang-Tse	University of Kentucky	V.C.4
Chiang, Yet-Ming	Massachusetts Institute of Technology	V.E.6
Christophersen, Jon P.	Idaho National Laboratory	III.B.3, III.B.2
Croy, Jason R.	Argonne National Laboratory	IV.E.1, V.F.1, IV.C.1, IV.C.2, IV.C.3, IV.C.4, IV.C.5, V.B.1
Cui, Yangie	Argonne National Laboratory	IV.D.1
Cui, Yanjie	Argonne National Laboratory	V.G.1
Cui, Yi	Stanford University	V.G.11, V.C.10, V.C.14
Cunningham, Brian	Department of Energy	II.D, III
Curtiss, Larry	Argonne National Laboratory	V.G.2
D. Vu, Anh	Argonne National Laboratory	IV.C.2
Daniel, Claus	Oak Ridge National Laboratory	IV.C.1, IV.C.2, IV.C.3, IV.C.4, IV.C.5, IV.E.3, IV.E.4
David, Bill	Rutherford Appleton Lab	V.F.1
Dees, Dennis W.	Argonne National Laboratory	IV.B.2, III.A.1, IV.C.1, IV.C.2, IV.C.3,

Contributor/ Collaborator	Affiliation	FY 2014 Annual Progress Report Section(s)
		IV.C.4, IV.C.5, IV.B.1
Deppe, John B.	Deppe Consulting	All
Dietz Rago, Nancy	Argonne National Laboratory	IV.B.4
Doeff, Marca	Lawrence Berkeley National Laboratory	V.B.3
Dogan, Fulya	Argonne National Laboratory	IV.C.1, IV.C.2, IV.C.3, IV.C.4, IV.C.5
Dudney, Nancy	Oak Ridge National Laboratory	V.G.3
Duffield, Michael	SAFT	II.A.6
Dunn, Jennifer	Argonne National Laboratory	III.A.5
Duong, Tien	Department of Energy	V
Dzwiniel, Trevor	Argonne National Laboratory	IV.E.2
Eitouni, Hany	Seeo	II.B.5
Elwasif, W.	Oak Ridge National Laboratory	III.C.3
Faguy, Peter	Department of Energy	IV
Fenton, Kyle R.	Sandia National Laboratories	IV.B.3
Feridun, Ozgenur K.	Argonne National Laboratory	IV.E.1
Finamore, Thomas	Energetics, Incorporated	All
Forbes, Jerry	Frontier Industrial Technology	IV.E.3
Gaines, Linda	Argonne National Laboratory	III.A.5
Gallagher, Kevin G.	Argonne National Laboratory	III.A.1, IV.C.1, IV.C.2, IV.C.3, IV.C.4, IV.C.5
Gao, Feng	Ashland	IV.E.4
Gao, Huajian	Brown University	V.C.4
Garcia-Ontiveros, Javier Bareno	Argonne National Laboratory	IV.C.1, IV.C.2, IV.C.3, IV.C.4, IV.C.5
Geller, Tony	Sandia National Laboratories	III.C.8
George, Steve M.	University of Colorado, Boulder	V.C.7, IV.B.3
Gogotsi, Yury	Drexel University	V.C.3
Goliaszewski, Alan	Ashland	IV.E.4
Goodenough, John B.	University of Texas, Austin	V.G.8
Graf, Peter	National Renewable Energy Laboratory	III.C.10
Grapf, Peter	National Renewable Energy Laboratory	III.C.1
Grey, Clare	Cambridge University	V.F.5
Gross, Oliver	USABC Program Manager	II.A.1

Contributor/ Collaborator	Affiliation	FY 2014 Annual Progress Report Section(s)
Halalay, Ion	General Motors	IV.E.2
Halalay, Ion	USABC Program Manager	II.A.9
Han, Taeyoung	General Motors	III.C.4
Hart, Terry	PPG Industries	IV.E.4
Hartridge, Steve	CD-adapco	III.C.5
Hellring, Stuart	PPG Industries	IV.E.4
Hendershot, Ron	Daikin	V.D.3
Henriksen, Gary L.	Argonne National Laboratory	IV.B.2, IV.C.1, IV.C.2, IV.C.3, IV.C.4, IV.C.5
Hickner, Michael A.	Pennsylvania State University	V.C.8
Hotchman, Amit	ANSYS	III.C.10
Howell, David	Department of Energy	I, II
Iddir, Hakim	Argonne National Laboratory	IV.C.1, IV.C.2, IV.C.3, IV.C.4, IV.C.5
Ingram, Brian J.	Argonne National Laboratory	IV.C.1, IV.C.2, IV.C.3, IV.C.4, IV.C.5
Jansen, Andrew N.	Argonne National Laboratory	IV.B.2, IV.B.3, IV.C.1, IV.C.2, IV.C.3, IV.C.4, IV.C.5, IV.B.1, IV.E.4
Jeka, Gerald	Argonne National Laboratory	IV.E.1
Johnson, Christopher	Argonne National Laboratory	IV.B.2, IV.C.1, IV.C.2, IV.C.3, IV.C.4, IV.C.5, IV.E.1
Johnson, Christopher	National Energy Technology Laboratory	II.B.2, II.B.6, II.B.7, II.C.1, II.C.5, IV.D.5, IV.D.6
Jorgensen, Scott	USABC Program Manager	II.A.5
Judes, Avie	Johnson Controls	II.A.2
Jun, Myungsoo	National Renewable Energy Laboratory	III.C.10
Juzkow, Marc	Leyden Energy	II.A.7
Kaczmarek, Susan	Energetics, Incorporated	All
Kalhammer, Fritz	Electric Power Research Institute	III.A.1
Kalnaus, S.	Oak Ridge National Laboratory	III.C.3
Kee, R.	Colorado School of Mines	III.C.8
Kepler, Keith	Farasis	IV.D.3
Kercher, Andrew	Oak Ridge National Laboratory	V.B.6
Key, Baris	Argonne National Laboratory	IV.C.1, IV.C.2, IV.C.3, IV.C.4, IV.C.5
Keyser, Matthew	National Renewable Energy Laboratory	III.B.4
Kiggans, Jim	Oak Ridge National Laboratory	V.B.6

Contributor/ Collaborator	Affiliation	FY 2014 Annual Progress Report Section(s)
Kim, Gi-Heon	National Renewable Energy Laboratory	III.C.1, III.C.10, III.C.2, III.C.4, III.C.7
Kostecki, Robert	Lawrence Berkeley National Laboratory	V.F.3
Kras, Mike	Argonne National Laboratory	IV.E.1
Krumdick, Gregory K.	Argonne National Laboratory	IV.C.1, IV.C.2, IV.C.3, IV.C.4, IV.C.5, IV.E.1, IV.E.2
Kumar, Bijayendra	Energetics, Incorporated	All
Kumta, Prashant N.	University of Pittsburgh	V.C.13, V.C.6
Lamb, Joshua	Sandia National Laboratories	III.B.3
Lau, K. C.	Argonne National Laboratory	V.G.2
Lee, Eungje	Argonne National Laboratory	IV.C.1, IV.C.2, IV.C.3, IV.C.4, IV.C.5
Lee, Sehee	University of Colorado, Boulder	V.C.7
Li, Genong	ANSYS	III.C.10
Li, Jianlin	Oak Ridge National Laboratory	IV.C.1, IV.C.2, IV.C.3, IV.C.4, IV.C.5, IV.E.3, IV.E.4
Li, Yan	Argonne National Laboratory	IV.B.1, IV.C.1, IV.C.2, IV.C.3, IV.C.4, IV.C.5
Lin, Chi-Kai	Argonne National Laboratory	IV.C.1, IV.C.2, IV.C.3, IV.C.4, IV.C.5
Liu, Gao	Lawrence Berkeley National Laboratory	IV.B.2, IV.D.1, IV.E.2, V.C.5
Liu, Jun	Pacific Northwest National Laboratory	V.C.9, V.G.5
Liu, Yijin	SLAC National Accelerator Laboratory	V.B.5
Long, Brandon R.	Argonne National Laboratory	IV.E.1, V.F.1, IV.C.1, IV.C.2, IV.C.3, IV.C.4, IV.C.5
Looney, J. Patrick	Brookhaven National Laboratory	V.B.2
Lopatin, Sergey	Applied Materials	II.C.3
Lopez, Herman	Envia Systems	II.A.1
Lu, Jun	Argonne National Laboratory	IV.D.1, V.G.2
Lu, Wenquan	Argonne National Laboratory	III.A.1, IV.B.1, IV.B.2, IV.C.1, IV.C.2, IV.C.3, IV.C.4, IV.C.5, IV.E.1, IV.E.2
Lucht, Brett	University of Rhode Island	V.D.1
Lytle, Gregg	Solvay Specialty Polymers	IV.E.4
Manthiram, Arumugam	University of Texas, Austin	V.B.9
Martin, Jerry	Boulderionics	IV.E.2
Mazzeo, Brian	Brigham Young University	V.E.1
McDonald, Joe	Environmental Protection Administration	III.A.1

Contributor/ Collaborator	Affiliation	FY 2014 Annual Progress Report Section(s)
Meng, Ying Shirley	University of California, San Diego	V.B.8
Michelbacher, Christopher J.	Idaho National Laboratory	III.B.2
Miller, Dean J.	Argonne National Laboratory	V.F.1, V.G.2, IV.C.1, IV.C.2, IV.C.3, IV.C.4, IV.C.5
Miller, James	Argonne National Laboratory	I
Mixer, Bruce	National Energy Technology Laboratory	II.B.1, II.B.5, IV.D.4
Moffat, Harry	Sandia National Laboratories	III.C.8
Mohanty, Debasish	Oak Ridge National Laboratory	IV.C.1, IV.C.2, IV.C.3, IV.C.4, IV.C.5, IV.E.3, IV.E.4
Mukherjee, Partha	Texas A&M University	III.A.4
Nagasubramanian, Ganesan	Sandia National Laboratories	IV.B.3
Nagpure, Shrikant	Oak Ridge National Laboratory	IV.E.3, IV.E.4
Nanda, Jagjit	Oak Ridge National Laboratory	IV.C.1, IV.C.2, IV.C.3, IV.C.4, IV.C.5, V.B.5
Nelson, Paul A.	Argonne National Laboratory	III.A.1
Neubauer, Jeremy	National Renewable Energy Laboratory	III.A.2, III.A.3
Orendorff, Christopher J.	Sandia National Laboratories	IV.E.2, IV.E.4, III.B.3, IV.B.3
Pannala, S.	Oak Ridge National Laboratory	III.C.2, III.C.3, III.C.8
Park, Joong Sun	Argonne National Laboratory	V.F.1
Park, Kyungjin	SK Innovation	II.A.8
Payzant, Andrew	Oak Ridge National Laboratory	IV.C.1, IV.C.2, IV.C.3, IV.C.4, IV.C.5
Pekala, Richard W.	ENTEK Membranes	II.A.9
Persson, Kristin	Lawrence Berkeley National Laboratory	V.E.3
Pesaran, Ahmad	National Renewable Energy Laboratory	III.A.2, III.A.3, III.B.4, III.C.2, III.C.7, III.B.3
Polzin, Bryant	Argonne National Laboratory	IV.B.2, IV.C.1, IV.C.2, IV.C.3, IV.C.4, IV.C.5, IV.E.1, IV.E.4
Polzin, Bryant J.	Argonne National Laboratory	IV.B.1
Powell, Bob	General Motors	IV.E.2
Prendergast, David	Lawrence Berkeley National Laboratory	V.G.7
Prezas, Panos	Argonne National Laboratory	III.B.1
Privette, Rob	XG Sciences	IV.B.3, IV.E.4
Pupek, Krzysztof Kris	Argonne National Laboratory	IV.E.2
Qi, Yue	Mihigan State U.	V.C.4

Contributor/ Collaborator	Affiliation	FY 2014 Annual Progress Report Section(s)
Qu, Deyang	University of Massachusetts, Boston	V.G.9
Reilly, Frank	Ceres Technologies	IV.E.3
Rempel, Jane	TIAX	IV.D.6
Ren, P. Y.	Argonne National Laboratory	V.G.1
Ren, Yang	Argonne National Laboratory	IV.C.1, IV.C.2, IV.C.3, IV.C.4, IV.C.5
Rinaldo, Steven G.	Argonne National Laboratory	IV.C.1, IV.C.2, IV.C.3, IV.C.4, IV.C.5
Risco, Andrew	Boulderionics	IV.E.2
Robertson, David	Argonne National Laboratory	III.B.1
Ross, Philip	Lawrence Berkeley National Laboratory	V.C.12
Rousseau, Aymeric	Argonne National Laboratory	III.A.1
Ruther, Rose	Oak Ridge National Laboratory	V.B.5
Santhanagopalan, Shriram	National Renewable Energy Laboratory	III.C.2, III.B.4, III.C.11, III.C.6, III.C.7
Santini, Dan	Argonne National Laboratory	III.A.1
Saxon, Aron	National Renewable Energy Laboratory	III.B.4
Sazhin, Sergiy V.	Idaho National Laboratory	III.B.2
Seminario, Jorge M.	Texas A&M University	V.C.11
Shaffer, Christian	EC Power	III.C.6, III.C.9
Sheldon, Brian W.	Brown University	V.C.4
Shembel, Elena	Enerize	IV.E.3
Shi, Ying	National Renewable Energy Laboratory	III.B.4
Shin, YoungHo	Argonne National Laboratory	IV.E.1
Shirk, Matthew G.	Idaho National Laboratory	III.B.2
Simunovic, S.	Oak Ridge National Laboratory	III.C.3
Singh, Jagat D.	3M Company	II.B.4, IV.D.2
Slater, Michael D.	Argonne National Laboratory	IV.C.1, IV.C.2, IV.C.3, IV.C.4, IV.C.5
Smith, Kandler	National Renewable Energy Laboratory	III.C.2, III.A.2, III.A.3, III.A.4, III.C.10, III.C.5
Somorjai, Gabor	University of California, Berkeley	V.C.12
Son, YK	Johnson Controls	II.C.1
Sopori, Bhushan	National Renewable Energy Laboratory	IV.E.3
Spotnitz, Robert	Battery Design, LLC	III.C.5
Sprague, Michael A.	National Renewable Energy Laboratory	III.C.11, III.C.7
Srinivasan, Venkat	Lawrence Berkeley National Laboratory	V.E.7

Contributor/ Collaborator	Affiliation	FY 2014 Annual Progress Report Section(s)
Steele, Leigh Anna M.	Sandia National Laboratories	III.B.3
Stefan, Ionel	Amprius	II.B.1
Stoneberg, Allen	Maxwell Technologies	II.A.5
Strand, Deidre	Wildcat Discovery Technologies	V.D.4
Suchomel, Matthew	Argonne National Laboratory	V.F.1
Sun, Y.-K.	Hanyang University	V.G.2
Sunstrom, Joe	Daikin	V.D.3
Tabacchi, John G.	National Energy Technology Laboratory	II.B.3, II.B.4, II.C.2, II.C.3, IV.D.2, II.C.4
Tataria, Harshad	USABC Program Manager	II.A.6
Telep, David	XALT Energy	IV.E.3, IV.E.4
Tenant, Robert	National Renewable Energy Laboratory	IV.C.1, IV.C.2, IV.C.3, IV.C.4, IV.C.5
Tenent, Robert	National Renewable Energy Laboratory	IV.E.5
Thackeray, Michael M.	Argonne National Laboratory	IV.E.1, V.B.1, V.F.1, IV.C.1, IV.C.2, IV.C.3, IV.C.4, IV.C.5
Tomsia, Antoni P.	Lawrence Berkeley National Laboratory	V.E.6
Trask, Stephen E.	Argonne National Laboratory	IV.B.1, IV.B.2, IV.C.1, IV.C.2, IV.C.3, IV.C.4, IV.C.5
Tselepidakis, Dimitrios	ANSYS	III.C.10
Turner, John A.	Oak Ridge National Laboratory	III.C.2, III.C.3
Ulsh, Mike	National Renewable Energy Laboratory	IV.E.3
Vajda, S.	Argonne National Laboratory	V.G.2
Vaughey, John T.	Argonne National Laboratory	V.C.1, IV.C.1, IV.C.2, IV.C.3, IV.C.4, IV.C.5
Venkatachalam, Subramanian	Envia Systems	IV.D.4
Vijayagopal, Ram	Argonne National Laboratory	III.A.1
Voelker, Gary E.	Miltec UV International	II.C.2
Vu, Anh D.	Argonne National Laboratory	IV.C.1, IV.C.3, IV.C.4, IV.C.5
Walker, Lee	Argonne National Laboratory	III.B.1
Wang, Chong-Min	Pacific Northwest National Laboratory	V.F.4
Wang, Donghai	Pennsylvania State University	II.B.6, IV.D.5, V.C.8
Wang, Feng	Brookhaven National Laboratory	V.B.2
Wang, H.-H.	Argonne National Laboratory	V.G.2

Contributor/ Collaborator	Affiliation	FY 2014 Annual Progress Report Section(s)
Wanta, Mark	Superior Graphite	IV.E.4
Wheeler, Dean	Brigham Young University	V.E.1
Whittingham, M. Stanley	Binghamton University	V.C.2
Wixom, Mike	Navitas Systems	IV.E.3, IV.E.4, II.C.5
Wood, David L.	Oak Ridge National Laboratory	IV.C.1, IV.C.2, IV.C.3, IV.C.4, IV.C.5, IV.E.3, IV.E.4
Wood, Eric	National Renewable Energy Laboratory	III.A.2, III.A.3
Wu, Huiming	Argonne National Laboratory	IV.C.1, IV.C.2, IV.C.3, IV.C.4, IV.C.5, IV.D.1
Wu, Qingliu	Argonne National Laboratory	IV.B.1, IV.B.2, IV.C.1, IV.C.2, IV.C.3, IV.C.4, IV.C.5
Xiao, Jie	Pacific Northwest National Laboratory	V.B.7, V.G.5
Xiao, Xingcheng	General Motors	V.C.4
Xu, Kang	Army Research Laboratories	V.B.5, V.D.2
Xu, Wu	Pacific Northwest National Laboratory	V.G.4, V.G.6
Yang, Chuanbo	National Renewable Energy Laboratory	III.C.10, III.C.7
Yang, Xiao-Qing	Brookhaven National Laboratory	IV.C.1, IV.C.2, IV.C.3, IV.C.4, IV.C.5, IV.D.1, V.D.2, V.F.2, V.G.10, V.G.9
Yang, Zhenzhen	Argonne National Laboratory	IV.C.1, IV.C.2, IV.C.3, IV.C.4, IV.C.5
Yassin-Lakhsassi, Khadija	Argonne National Laboratory	IV.B.2
Yu, Xiqian	Brookhaven National Laboratory	V.F.2, V.G.10
Zaghib, Karim	Hydro-Québec/IREQ	V.E.2
Zhang, Chao	National Renewable Energy Laboratory	III.C.11, III.C.7
Zhang, Ji-Guang	Pacific Northwest National Laboratory	V.B.7, V.C.9, V.G.4, V.G.6
Zhang, Zhengcheng (John)	Argonne National Laboratory	V.D.2, IV.B.2
Zhao, Hui	Lawrence Berkeley National Laboratory	IV.B.2
Zhou, Hui	Oak Ridge National Laboratory	V.B.5
Zhu, Ye	Argonne National Laboratory	IV.B.1, IV.C.1, IV.C.2, IV.C.3, IV.C.4, IV.C.5
Zhu, Yimin	OneD Material	II.B.3

Appendix B: Acronyms

3M	Minnesota Mining and Manufacturing Company
AABC	Advanced Automotive Batteries Conference
AB	Acetylene black
ABA	Anion Binding Agent
ABDT	ANSYS Battery Design Tool
ABR/ABRT	Applied Battery Research for Transportation
AC	Alternating Current
ACS	American Chemical Society
AE	Available energy
AER	All electric range
AEV	All-electric vehicle
AEY	Auger electron yield
AF	Antiferromagnetic
AFM	Atomic force microscopy
AIMD	Ab initio molecular dynamics
ALD	Atomic layer deposition
AMO	Advanced Manufacturing Office
AMR	Annual Merit Review
ANL	Argonne National Laboratory
AP-ALD	Atmospheric pressure atomic layer deposition
AP-CVD	Atmospheric pressure chemical vapor deposition
API	Application Programming Interface
APS	Advanced Photon Source
APTES	with (3-aminopropyl)triethoxysilane
ARC	Accelerated rate calorimetry
ARL	Army Research Laboratory
ARPA-E	Advanced Research Projects Agency - Energy
ARRA	American Recovery & Reinvestment Act
ASI	Area-specific impedance
ASM	American Society for Metals
ASME	American Society of Mechanical Engineers
ASR	Area specific resistance
ATR	Attenuated total reflection
ATR-FTIR	Attenuated total reflection-Fourier transform infrared spectroscopy
AVS	American Vacuum Society
BATT	Batteries for Advanced Transportation Technologies
BDOD	1,4-benzodiozane-6,7-diol
BDS	Battery Design Studio
BERC	Berkeley Energy and Resources Collaborative
BES	Basic Energy Sciences (DOE Office)
BET	Brunauer, Emmett, and Teller surface area
BEV	Battery electric vehicle

BLAST	Battery Lifetime Analysis Simulation Tool
BMF	Battery manufacturing facility
BMR	Battery Materials Research (Program)
BMS	Battery management system
BNL	Brookhaven National Laboratory
BOL	Beginning of life
BOM	Battery ownership model
BSF	Battery scaling factor
BTC	Battery Technology Center
BTMS	Battery thermal management system
BYU	Brigham Young university
CAD	Computer-aided Design
CAE	Computer-aided engineering
CAEBAT	Computer-aided engineering of batteries
CAFE	Corporate Average Fuel Economy (Standards)
CAMP	Cell analysis, modeling, and prototyping facility
CB	Carbon black
CCD	Charge-coupled device
CCSE	California Center for Sustainable Energy
CD	Charge depleting
CDM	Cell domain model
CDNUF	Current density non-uniformity factor
CE	Coulombic efficiency
CEES	Center for Electrical Energy Storage
CEF	Cathode Energy Factor
CERC	Clean Energy Research Center
CFD	Computational Fluid Dynamics
CFF	Cell Fabrication Facility
CG	Concentration gradient
CLP	Cycled laminate particle
CMC	Sodium Carboxy Methyl Cellulose
CMD	Classical molecular dynamics
CMP50V	Copper metaphosphate/vanadate
CN	Coordination number
CNT	Carbon nano-tubes
CO	Certificate of Occupancy
COP	ConocoPhillips
COTS	Commercial-Off-The-Shelf
CPI	Compact Power Inc.
CPU	Central Processing Unit
CRADA	Cooperative Research and Development Agreement
CS	Charge-sustaining
CSE	Cumulative strain energy
CSWG	Crash Safety Work Group
CT	(X-ray) Computed tomography

CV	Cyclic voltammogram
CVD	Chemical vapor deposition
CVO	Cu-V-O (compound)
CWRU	Case Western Reserve University
CWU-FRION	Lithium [(2,5-bis(diethylphosphoryl) catecholato) oxalatoborate]
CY	Calendar year
DADT	Developmental and applied diagnostic testing
DC	Direct current
DCFC	DC fast charger
DCM	Demand charge management
DCR	Direct current resistance
DDPM	Discrete diffusion particle model
DEC	Diethyl carbonate
DFT	Density function theory
DMC	Dimethyl carbonate
DME	Dimethyl ether
DMSO	Dimethylsulfoxide
DOD	Depth-of-discharge
DOE	Department of Energy
DOL	1,3-dioxolane
DOT/NHTSA	Department of Transportation/National Highway Traffic Safety Administration
DPA	Destructive physical analysis
DSC	Differential scanning calorimetry
DST	Dynamic stress test
EADL	Electrochemical Analysis and Diagnostic Laboratory (ANL)
EC	Ethylene carbonate
ECM	Equivalent Circuit Model
ECP	EC Power
ECS	Electrochemical Society
ED	Electrode domain
EDAX	Energy dispersive X-ray analysis
EDM	Electrode-domain model
EDS	Energy dispersive spectroscopy
EDV	Electric Drive Vehicle
EDX	Energy-dispersive x-ray (spectroscopy)
EELS	Electron energy loss spectroscopy
EERE	Energy Efficiency and Renewable Energy (DOE Office)
EES	Electrochemical energy storage
EESTT	Electrical Energy Storage Tech Team
EFRC	Energy Frontier Research Center
EIS	Electrochemical Impedance Spectroscopy
EMC	Electron Microscopy Center
EOC	End-of-charge
EOL	End of life
EOP	End of period

EPA	Environmental Protection agency
EPMA	Electron probe micro-analysis
EPR	Electron paramagnetic resonance
EPRI	Electric Power Research Institute
EQCM	Electrochemical quartz crystal microbalance
EREV	Extended range electric vehicle
ES	Ethylene sulfite
ESR	Electron spin resonance
ESS	Energy storage system
EUCAR	European Council for Automotive Research and Development
EV	Electric vehicle
EVI	Electric Vehicle Initiative
EXAFS	Extended X-ray absorption fine structure
FA	Fluorinated acrylic (hybrid latex binder)
FBP	Filtered Back-projection
FCG	Full concentration gradient
FCTO	Fuel Cell Technologies Office (at DOE)
FEC	Fluoro ethylene carbonate
FFT	Fast Fourier Transforms
FIB	Focused Ion Beam
FIR	First cycle irreversible loss
FMVSS	Federal Motor Vehicle Safety Standards
FOA	Federal Opportunity Anouncement
FP	First principles
FT	Fourier Transform
FTA	Fault Tree Analysis
FTIR	Fourier Transform InfraRed spectroscopy
FWHM	Full width at half maximum
FY	Fiscal year
G&A	General and administrative (costs)
GC	Gas chromatography
GC-MS	Gas chromatography - mass spectroscopy
GDE	Gas-diffusion-electrodes
GHG	Green house gases
GITT	Galvanostatic intermittent titration technique
GM	General Motors
GO	Graphene oxide
GREET	Greenhouse gases, Regulated Emissions, and Energy use in Transportation (model)
GSAS	General Structure Analysis System
GUI	Graphic user interface
HAADF	High Angle Annular Dark Field
HCA	High capacity anode
HCC	High capacity cathode
HCMRTM	High capacity manganese rich cathode materials
HD	High dielectric

HE	High energy
HEMM	High energy mechanical milling
HEV	Hybrid electric vehicle
HEXRD	High energy X-ray diffraction
HF	Hydrofluoric acid
HL-NMC	High lithium NMC
HP	High power
HPC	High performance computing
HPLC	High performance liquid chromatograph
HPPC	Hybrid pulse power characterization
HQ	Hydro-Québec
HREM	High resolution electron micrograph
HRTEM	High resolution transmission Electron Microscopy
HR-TEM	High resolution transmission electron microscopy
HS-CAN	High Speed Controller Area Network
HSE	Heyd-Scuseria-Ernzerhof (exchange-correlation functional)
HVC	High voltage cathode
IA	(IEA) Implementing Agreement
IA-HEV	Implementing Agreement - hybrid electric vehicles
IAPG	Interagency Advanced Power Group
IBA	International Battery Materials Association
ICA	Incremental capacity analysis
ICE	Internal combustion engine
ICL	Irreversible capacity loss
ICP	Inductively coupled plasma
ICV	Internal combustion engine vehicle
ID	Intensity of the carbon D-band
IEA	International Energy Agency
IEA-HEV	International Energy agency - hybrid electric vehicle
IEA-HEV-IA	International energy Agency - Hybrid Electric Vehicles - Implementing Agreement
IEEE	Institute of Electrical and Electronics Engineers
IMTP	Injection-molded thermoplastic polymer
INL	Idaho National Laboratory
INW	Inorganic nanowire
IP	In-plane (signal)
IR	Infra-red
IRCL	Irreversible Capacity Loss
IS	Impedance spectroscopy
ISC	Internal short circuit
JCI	Johnson Controls, Incorporated
JPL	Jet Propulsion Laboratory
JT	Jahn-Teller (distortion environment)
LATP	14 Li_2O•$9Al_2O_3$•$38TiO_2$•$39P_2O_5$ (lithiated glass ceramic)
LBMP	Lithium-bearing mixed polyanion
LBNL	Lawrence Berkeley National Laboratory

LCA	Life cycle analysis
LCMP50V	Lithium copper metaphosphate/vanadate (glass)
LCO	Lithium cobalt oxide
LCV	Lower cutoff voltage
LEDC	Lithium diethylcarbonate
LEESS	Lower-energy energy storage systems
LFP	Li iron phosphate
LIB	Lithium-ion battery
LIBS	Laser induced breakdown spectroscopy
LL	Layered-layered
LLNL	Lawrence Livermore National Laboratory
LLS	Layered-layered spinel
LLTO	$(Li,La)TiO_3$
LLZ	$Li_7La_3Zr_2O_{12}$
LLZT	$Li_{6.5}La_3Zr_{1.5}Ta_{0.5}O_{12}$
LMCO	$Li_{1.211}Mo_{0.467}Cr_{0.3}O_2$
LMNO	Lithium manganese nickel oxide
LMO	Lithium manganese oxide
LMR	Lithium Manganese-rich (layered cathode material)
LNMO	LiNi0.5Mn0.5O2
LNO	Lithium nickel oxide (material)
LP	Laminate particle
LPV	Linear Parameter Variable
LS	Low spin
LSV	Linear sweep voltammetry
LTI	Linear Time Invariant
LTO	Lithium titanate, $Li_4Ti_5O_{12}$
LUMO	Lowest unoccupied molecular orbital
LVO	Lithium vanadium oxide (LiV_3O_8)
LVOPF	$Li(Na)_{1+x}VOPO_4F_x$
LVP	$Li_3V_2(PO_4)_3$
MAB	Modified water soluble amine based (binder)
MAS	Magic angle spinning
MB	Methyl butyrate
MBP	Midland Battery Park
MCMB	Mesocarbon micro beads
MD	Molecular dynamics
MEF	Materials Engineering Facility
MERF	Materials Engineering Research Facility
MIT	Massachusetts Institute of Technology
MLD	Molecular layer deposition
MNO	Manganese nickel oxide
MOSS	Multibeam Optical Stress Sensor
MP	Methyl propionate
MRC	Manganese rich cathode

MRS	Materials Research Society
MS	Mass spectroscopy
MS&T	Materials Science and Technology (conference)
MSDS	Material Safety Data Sheet
MSMD	Multi-scale, multi-dimensional
MSS	Meso-porous sponge-like Si (particles)
MW-ST	Microwave-assisted solvothermal
MYPP	Multi-year program plan
NASA	National Aeronautics and Space Administration
NASA-JSC	NASA, Johnson Space Center
NASICON	Sodium (Na) Super Ionic CONductor
NCA	$LiNi_{0.8}Co_{0.15}Al_{0.05}O_2$
NCEM	National Center for Electron Microscopy
NCM	$Li_{1+w}[Ni_xCo_yMn_z]_{1-w}O_2$
NCSU	North Carolina State University
NDA	Non-Disclosure Agreement
NDE	Non-destructive evaluation
NEDO	New Energy and Industrial Technology Development Organization (Japan)
NEI	Natural Energy Institute (Hawaii)
NERSC	National Energy Research scientific Computing Center
NETL	National Energy Technology Laboratory
NG	Natural graphite
NHTSA	National Highway Transportation Safety Administration
NIST	National Institute of Standards and Technology
NIU	Northern Illinois University
NMC	$LiNi_{1/3}Co_{1/3}Mn_{1/3}O_2$
NMP	N-methylpyrrolidone
NMR	Nuclear magnetic resonance
NRC	National Research Council
NREL	National Renewable Energy Laboratory
NSLS	National Synchrotron Light Source
NSWC	Naval Surface Warfare Center
NTGK	Newman-Tiedemann-Gu-Kim (model)
OAS	Open architecture software
OCP	Open-circuit potential
OCV	Open circuit voltage
OEM	Original equipment manufacturer
OER	Oxygen evolution reaction
ORNL	Oak Ridge National Laboratory
ORR	Oxygen reduction reaction
PAA	Polyacrylic acid
PAHEV	Power-assist hybrid electric vehicle
PAN	Polyacrylonitrile
PANI	Polyaniline
PBE	Perdew Burke Ernzerhof (correlation)

PC	Propylene carbonate
PCA	Principal component analysis
PCM	Polarized continuum model
PDCA	Plan-Do-Check-Act (cycle)
PDF	Pair density function
PDM	particle-domain model
PDOS	Projected density of states
PE	Polyethylene
PEDOT	Poly(3,4-ethylenedioxythiophene)
PEDOT-SP	PEDOT - Super P carbon
PEFC	Polymer electrolyte fuel cell
PEFM	Poly(2,7-9,9-dioctylfluorene-co-2,7-9,9-(di(oxy-2,5,8-trioxadecane)) fluorine-co-2,7-fluorenone-co-2,5-1-methylbenzoic ester)
PEG	Polyethylene glycol
PEO	Polyethyleneoxide
PEV	Plug-in electric vehicle
PFG	Pulse field gradient
PFM	Poly(9,9-dioctylfluorene-co-fluorenone-co-methylbenzoic ester)
PFO	Poly(9,9-dioctylfluorene)
PFO-PBE	Phenyl boronic perfluorooctyl ethylene glycol ester
PHEV	Plug-in hybrid electric vehicle
PHEV10	PHEV with 10-mile range
PHEV40	PHEV with 40-mile range
PI	Principal Investigator
PMAA	Poly(methacrylic acid)
PNNL	Pacific Northwest National Laboratory
POD	Proper Orthogonal Decomposition
PS	Polystyrene
PSU	Pennsylvania State University
PTC	Positive temperature coefficient (device)
PTFE	Poly(tetrafluoroethylene)
PVDF	Poly(vinylidenefluoride)
R&D	Research and Development
R2R	Roll-to-roll
RAL	Rutherford Appleton Laboratory
RC	Resistance-Capacitor
REM	Regulation energy management
RF	Radio frequency
RFP	Request for proposals
RFPI	Request for proposal information
RMS	Root mean square
ROM	Reduced Order Modeling
RPM	Revolutions per minute
RPT	Reference performance test
RS	Representative sandwich (model)
RT	Room temperature

RTS	Reaction temperature sensing (sensor)
RVE	Representative volume element
SAE	Society of Automotive Engineers
SAED	Selected area electrode diffraction
SBG	Si/B4C/graphite
SBIR	Small Business Innovation Research
SBIR/STTR	Small Business Innovation Research/Small Business Technology Transfer
SD	Standard deviation
SEI	Solid electrolyte interphase
SEM	Scanning electron microscopy
SEM/FIB	Scanning electron microscopy/focused ion beem
SEM-EDS	Scanning electron microscopy/Energy Dispersive X-ray spectroscopy
SEO	Poly(styrene)-b-poly(ethylene oxide)
SFG	Sum Frequency Generation
SFS	Silica-filled separator
SG	Sol-gel (method)
SIC	Single ion conducting
SIMS	Secondary ion mass spectrometry
SLAC	Stanford acceleration laboratory
SLMP	Stabilized lithium metal powder
SLP	Single layer pouch (cells)
SNL	Sandia National Laboratories
SNS	Spallation Neutron Source
SOA	State of the art
SOC	State of charge
SOF	State of function
SOW	Statement of Work
SP	Super-P (carbon)
SPECS	Stepped potential electrochemical spectroscopy
SPEEK	Sulfonated poly(ether ether ketone) (binder)
SPPC	Single Potential-Pair Continuum
SRL	Surface reconstruction layer
SRS	Safety Reinforcing Separator
SSA	Specific surface area
SSRL	Stanford Synchroton Radiation Lightsource
STEM	Scanning transmission electron microscopy
STEM/EELS	Scanning transmission electron microscopy/electron energy loss spectroscopy
STTR	Small Business Technology Transfer Program
SUNY	State University of New York
SVM	State Variable Model
TAC	Technical Advisory Committee
TALE	Total arbitrary Lagrangian Eulerian
TAMU	Texas A&M University
TARDEC	(United States) Army Tank Automotive Research, Development and Engineering Center
TBACL	Tetrabutylammonium chloride

TDI	4,5-dicyano-2-(trifluoromethyl)imidazolide
TEGDME	Tetraethyleneglycoldimethyl
TEM	Transmission electron microscopy
TEY	Total electron yield
TFSI	Bis(trifluoromethanesulfonyl)imide
TGA	Thermal gravimetric analysis
TM	Transition metal
TMA	Tri-methyl aluminum
TOF-SIMS	Time-of-flight – secondary ion mass spectroscopy
TPB	Thermal protective barrier
TPFPB	Tris(pentafluorophenyl) borane
TPP	Tri(2-furyl)phosphine
TPPB	Tetraphenylphosphonium bromide
TR-XRD	Time-resolved X-ray diffraction
TXM	Transmission X-ray Microscopy
TXM-XANES	Transmission X-ray microscopy with X-ray near edge absorption spectroscopy
TXRD	Temperature-controlled in situ XRD
UC	University of California
UCB	University of California, Berkeley
UCSD	University of California, San Diego
UCV	Upper cut-off voltage
UDDS	Urban Dynamometer Driving Schedule
UHMWPE	Ultra High Molecular Weight Polyethylene
URI	University of Rhode Island
USABC	United States Advanced Battery Consortium
USCAR	United States Council for Automotive Research
USDRIVE	Driving Research and Innovation for Vehicle efficiency and Energy sustainability
UTA	University of Texas, Austin
UV	Ultraviolet
VACNT	Vertically aligned carbon nanotube
VASP	Vienna Ab-initio Simulation Package
VC	Vinylene carbonate
VCU	Virginia Commonwealth University
VEC	Vinyl ethylene carbonate
VF	Voltage fade
VIBE	Virtual Integrated Battery Environment
VLS	Vapor-liquid-solid (method)
VT, VTO	Vehicle Technologies Office
VTO	Vehicle Technologies Office
WBG	Wide bandgap
WDT	Wildcat Discovery Technologies
WLTP	Worldwide harmonized light vehicles test procedure
XAFS	X-ray absorption fine structure
XANES	X-ray absorption near edge structure
XAS	X-ray absorption spectroscopy

XCH	eXcited Core Hole
XEDS	X-ray energy dispersive spectroscopy
XPS	X-ray photoelectron spectroscopy
XR	X-ray reflectivity
XRD	X-ray diffraction
XRF	X-ray fluorescence spectroscopy

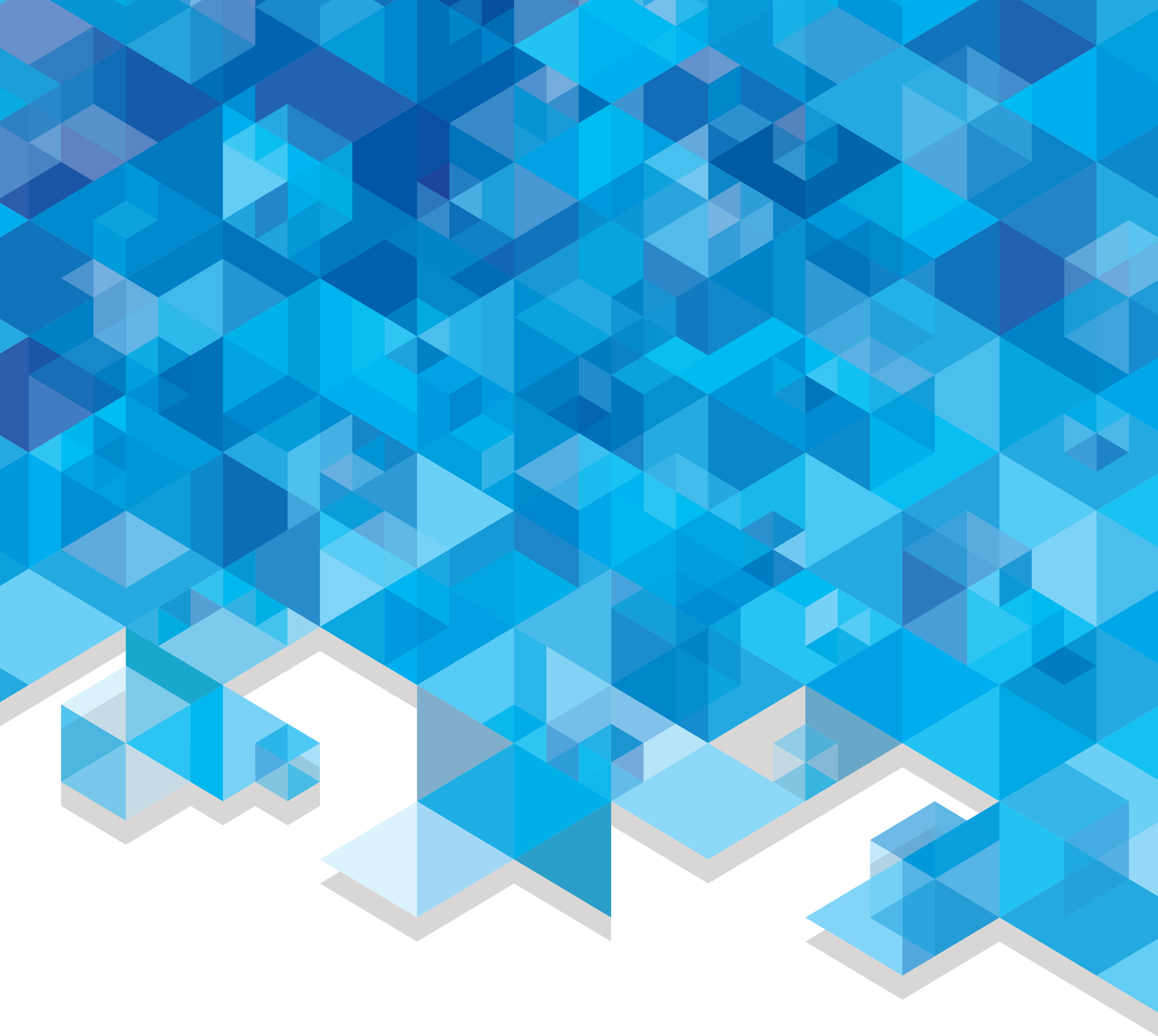

U.S. DEPARTMENT OF
ENERGY

Energy Efficiency &
Renewable Energy

For more information, visit: energy.gov/eere

DOE/EE-1162 • March 2015